

REPORT DOCUMENTATION PAGE

oved
14-0188

Public reporting burden for this collection of information is estimated to average 1 hour per response, including the time for reviewing existing information, gathering new data sources, gathering and maintaining the data needed, and completing and reviewing the collection of information, including suggestions for reducing this burden, to Washington Headquarters Services, Directorate for Information Operations and Reports, 1204, Arlington, VA 22202-4302, and to the Office of Management and Budget, Paperwork Reduction Project (0704-0188) Washington, DC 20503.

data sources, gathering
act of this collection of
n Davis Highway, Suite

0773

1. AGENCY USE ONLY (Leave Blank)		2. REPORT DATE November, 1994		3. REPORT TYPE AND DATES COVERED Final	
4. TITLE AND SUBTITLE USAF Summer Research Program - 1993 Summer Research Extension Program Final Reports, Volume 4A, Wright Laboratory				5. FUNDING NUMBERS	
6. AUTHORS Gary Moore					
7. PERFORMING ORGANIZATION NAME(S) AND ADDRESS(ES) Research and Development Labs, Culver City, CA				8. PERFORMING ORGANIZATION REPORT NUMBER	
9. SPONSORING/MONITORING AGENCY NAME(S) AND ADDRESS(ES) AFOSR/NI 4040 Fairfax Dr, Suite 500 Arlington, VA 22203-1613				10. SPONSORING/MONITORING AGENCY REPORT NUMBER	
11. SUPPLEMENTARY NOTES Contract Number: F4962-90-C-0076					
12a. DISTRIBUTION AVAILABILITY STATEMENT Approved for Public Release				12b. DISTRIBUTION CODE	
13. ABSTRACT (<i>Maximum 200 words</i>) The purpose of this program is to develop the basis for continuing research of interest to the Air Force at the institution of the faculty member; to stimulate continuing relations among faculty members and professional peers in the Air Force to enhance the research interests and capabilities of scientific and engineering educators; and to provide follow-on funding for research of particular promise that was started at an Air Force laboratory under the Summer Faculty Research Program. Each participant provided a report of their research, and these reports are consolidated into this annual report.					
14. SUBJECT TERMS AIR FORCE RESEARCH, AIR FORCE, ENGINEERING, LABORATORIES, REPORTS, UNIVERSITIES				15. NUMBER OF PAGES	
				16. PRICE CODE	
17. SECURITY CLASSIFICATION OF REPORT Unclassified	18. SECURITY CLASSIFICATION OF THIS PAGE Unclassified	19. SECURITY CLASSIFICATION OF ABSTRACT Unclassified	20. LIMITATION OF ABSTRACT UL		

**Reproduced From
Best Available Copy**

UNITED STATES AIR FORCE
SUMMER RESEARCH PROGRAM -- 1993
SUMMER RESEARCH EXTENSION PROGRAM FINAL REPORTS

VOLUME 4A
WRIGHT LABORATORY

RESEARCH & DEVELOPMENT LABORATORIES
5800 Uplander Way
Culver City, CA 90230-6608

Program Director, RDL
Gary Moore

Program Manager, AFOSR
Major David Hart

Program Manager, RDL
Scott Licoscas

Program Administrator, RDL
Gwendolyn Smith

Program Administrator, RDL
Johnetta Thompson

Submitted to:

AIR FORCE OFFICE OF SCIENTIFIC RESEARCH
Bolling Air Force Base
Washington, D.C.
November 1994

19981211 025

PREFACE

This volume is part of a five-volume set that summarizes the research of participants in the 1993 AFOSR Summer Research Extension Program (SREP). The current volume, Volume 4A of 5, presents the final reports of SREP participants at Wright Laboratory.

Reports presented in this volume are arranged alphabetically by author and are numbered consecutively -- e.g., 1-1, 1-2, 1-3; 2-1, 2-2, 2-3, with each series of reports preceded by a 35 page management summary. Reports in the five-volume set are organized as follows:

VOLUME	TITLE
1A	Armstrong Laboratory (part one)
1B	Armstrong Laboratory (part two)
2	Phillips Laboratory
3	Rome Laboratory
4A	Wright Laboratory (part one)
4B	Wright Laboratory (part two)
5	Arnold Engineering Development Center Frank J. Seiler Research Laboratory Wilford Hall Medical Center

1993 SREP FINAL REPORTS

Armstrong Laboratory

VOLUME 1A

Report #	Report Title Author's University	Report Author
1	Three-Dimensional Calculation of Blood Flow in a Thick -Walled Vessel Using the University of Missouri, Rolla, MO	Dr. Xavier Avula Mechanical & Aerospace AL/AO Engineering
2	A Study of the Contrast Detection Modeling for Human Eye and its Application to Wright State University, Dayton, OH	Dr. Jer-sen Chen Computer Science & AL/CF Engineering
3	An Approach to On-Line Assessment and Diagnosis of Student Troubleshooting Knowl New Mexico State University, Las Cruces, NM	Dr. Nancy Cooke Psychology AL/HR
4	An Experimental Investigation of Hand Torque Strength for Tightening Small Fast Tennessee Technological University, Cookeville, TN	Dr. Subramaniam Deivanayagam Industrial Engineering AL/HR
5	Determination of Total Peripheral Resistance, Arterial Compliance and Venous Com North Dakota State University, Fargo, ND	Dr. Dan Ewert Electrical Engineering AL/AO
6	A Computational Thermal Model and Theoretical Thermodynamic Model of Laser Induc Florida International University, Miami, FL	Dr. Bernard Gerstman Physics AL/OE
7	A Comparison of Various Estimators of Half-Life in the Air Force Health Study University of Maine, Orono, ME	Dr. Pushpa Gupta Mathematics AL/AO
8	The Effects of Exogenous Melatonin on Fatigue, Performance and Daytime Sleep Bowling Green State University, Bowling Green, OH	Mr. Rod Hughes Psychology AL/CF
9	A New Protocol for Studying Carotid Baroreceptor Function Georgia Institute of Technology, Atlanta, GA	Dr. Arthur Koblasz Civil Engineering AL/AO
10	Adaptive Control Architecture for Teleoperated Freflex System Purdue University, West Lafayette, IN	Dr. A. Koivo Electrical Engineering AL/CF
11	A New Construct for Interpreting the Fundamental Dilemma of Insufficient Tissue University of Tennessee, Memphis, TN	Dr. Robert Kundich Biomedical Engineering AL/CF
12	An Empirical Test of a Method for Comparison of Alternative Multiship Aircraft Arizona State University, Tempe, AZ	Dr. William Moor Industrial & Management AL/HR Engineering
13	Remote Monitoring and Reduction of Emotionality in Air Force Laboratory Primates University of Georgia Research, Athens, GA	Dr. B. Mulligan Psychology AL/OE

1993 SREP FINAL REPORTS

Armstrong Laboratory

VOLUME 1B

Report #	Report Title Author's University	Report Author
14	Simulation of the Motion of Single and Linked Ellipsoids Representing Human Body Wright State University, Dayton, OH	Dr. David Reynolds Biomedical & Human AL/CF Factors
15	Bioeffects of Microwave Radiation on Mammalian Cells and Cell Cultures Xavier University of Louisiana, New Orleans, LA	Dr. Donald Robinson Chemistry AL/OE
16	Analysis of Isocyanate Monomers and Oligomers in Spray Paint Formulations Southwest Texas State University, San Marcos, TX	Dr. Walter Rudzinski Chemistry AL/OE
17	Development of the "Next Generation" of the Activities Interest Inventory for Se Wayne State University, Detroit, MI	Dr. Lois Tetrick Industrial Relations Prog AL/HR
18	Investigations on the Seasonal Bionomics of the Asian Tiger Mosquito, Aedes Albo Macon College, Macon, GA	Dr. Michael Womack Natural Science and AL/OE Mathematics
19	Difficulty Facets Underlying Cognitive Ability Test Items Ohio State University, Columbus, OH	Dr. Mary Roznowski Psychology AL/HR
20	A Simplified Model for Predicting Jet Impingement Heat Transfer North Carolina A & T State University, Greensboro, NC	Mr. Mark Kitchart Mechanical Engineering AL/EQ
21	Geostatistical Techniques for Understanding Hydraulic Conductivity Variability Washington State University, Pullman, WA	Dr. Valipuram Manoranjan Pure and Applied AL/EQ Mathematics
22	An Immobilized Cell Fluidized Bed Bioreactor for 2,4-Dinitrotoluene Degradation Colorado State University, Fort Collins, CO	Dr. Kenneth Reardon Agricultural and Chemical AL/EQ Engineering
23	Applications of Superconductive Devices in Air Force Alfred University, Alfred, NY	Dr. Xingwu Wang Electrical Engineering AL/EQ

1993 SREP FINAL REPORTS

Phillips Laboratory

VOLUME 2

Report #	Report Title Author's University	Report Author
1	Optimal Passive Damping of a Complex Strut-Built Structure Iowa State University, Ames, IA	Dr. Joseph Baumgarten Mechanical Engineering PL/VT
2	Theoretical and Experimental Studies on the Effects of Low-Energy X-Rays on Elec University of Arizona, Tucson, AZ	Dr. Raymond Bellem Electrical & Computer PL/VT Engineering
3	Ultrawideband Antennas with Low Dispersion for Impulse Radars University of Alabama, Huntsville, AL	Dr. Albert Biggs Electrical Engineering PL/WS
4	Experimental Neutron Scattering Investigations of Liquid-Crystal Polymers Arkansas Technology University, Russellville, AR	Dr. David Elliott Engineering PL/RK
5	High Temperature Spectroscopy of Alkali Metal Vapors for Solar to Thermal Energy University of Iowa, Iowa City, IA	Mr. Paul Erdman Physics and Astronomy PL/RK
6	A Detailed Investigation of Low-and High-Power Arcjet Plume Velocity Profiles Us University of Southern California, Los Angeles, CA	Dr. Daniel Erwin Aerospace Engineering PL/RK
7	Measurements of Ion-Molecule Reactions at High Temperatures University of Puerto Rico, Mayaguez, PR	Dr. Jeffrey Friedman Physics PL/GP
8	Final Design and Construction of Lidar Receiver for the Starfire Optical Range Georgia Institute of Technology, Atlanta, GA	Dr. Gary Gimmetstad Research Institute PL/LI
9	Dynamics of Gas-Phase Ion-Molecule Reactions Carnegie Mellon University, Pittsburgh, PA	Dr. Susan Graul Chemistry PL/WS
10	A Numerical Approach to Evaluating Phase Change Material Performance in Infrared University of Texas, San Antonio, TX	Mr. Steven Griffin Engineering PL/VT
11	An Analysis of ISAR Imaging and Image Simulation Technologies and Related Post University of Nevada, Reno, NV	Dr. James Henson Electrical Engineering PL/WS
12	Optical and Clear Air Turbulence Worcester Polytechnic Institut, Worcester, MA	Dr. Mayer Humi Mathematics PL/LI
13	Rotational Dynamics of Lageos Satellite North Carolina State University, Raleigh, NC	Dr. Arkady Kheifets Mathematics PL/LI
14	Study of Instabilities Excited by Powerful HF Waves for Efficient Generation of Polytechnic University, Farmingdale, NY	Dr. Spencer Kuo Electrical Engineering PL/GP

1993 SREP FINAL REPORTS

Phillips Laboratory

VOLUME 2 cont'd

Report #	Report Title Author's University	Report Author
15	Particle Stimulation of Plasmas University of Missouri, Kansas City, MO	Dr. Richard Murphy Physics PL/WS
16	A Universal Equation of State for Shock in Homogeneous Materials California State University, Northridge, CA	Dr. Jon Shively Engineering & Computer Science PL/VT
17	Speed-Up of the Phase Diversity Method Via Reduced Region & Optimization Dimen. University of Houston, Victoria, TX	Dr. Johanna Stenzel Arts & Sciences PL/LI
18	Analysis of Solwind P-78 Fragmentation Using Empirical And Analytical Codes Alabama A & M University, Normal, AL	Dr. Arjun Tan Physics PL/WS
19	Experimental Investigations of Homogeneous and Heterogeneous Nucleation/Condensa University of Missouri, Rolla, MO	Dr. Philip Whitefield Physics PL/LI

1993 SREP FINAL REPORTS

Rome Laboratory

VOLUME 3

Report #	Report Title Author's University	Report Author
1	Analysis and Code for Treating Infinite Arrays of Tapered Antennas Printed on Bo California State University, Sacramento, CA	Dr. Jean-Pierre Bayard Electrical & Electronic RL/ER Engineering
2	Comparing Pattern Recognition Systems Syracuse University, Syracuse, NY	Dr. Pinyuen Chen Mathematics RL/IR
3	Wideband ATM Networks for the Dynamic Theater Environment University of Southwestern Louisiana, Lafayette, LA	Dr. Robert Henry Electrical & Computer RL/C3 Engineering
4	Congestion Control For ATM Network in a Tectical Theater Environment Polytechnic University, Brooklyn, NY	Mr. Benjamin Hoe Electrical Engineering RL/C3
5	Automated Natural Language Evaluators (ANLF) Southwest Texas State College, San Marcos, TX	Dr. Khosrow Kaikhah Computer Science RL/IR
6	System Analysis and Applications for a Photonic Delay Line Le Moyne College, Syracuse, NY	Dr. Evelyn Monsay Physics RL/OC
7	An Exploratory Investigaton of Multimedia Data Reinforcement for Large-Scale Inf Syracuse University, Syracuse, NY	Dr. Michael Nilan Information Studies RL/C3
8	Supporting Systematic Testing for Reusable Software Components University of Alabama, Tuscaloosa, AL	Dr. Allen Parrish Computer Science RL/C3
9	Use of Turnable Fiber Ring Lasers in Optical Communications SUNY/Institute of Technology, Utica, NY	Dr Salahuddin Qazi Optical Communications RL/OC
10	Further Monte Carlo Studies of a Theoretical Model for Non-Gaussian Radar Clutte SUNY College at Cortland, Cortland, NY	Dr. Jorge Romeu Assistant Prof. of RL/OC Mathematics
11	Hierarchical Modeling and Simulation Syracuse University, Syracuse, NY	Dr. Robert Sargent Engineering and Computer RL/XP Science
12	Metamodel Applications Using TAC Brawler Virginia Polytechnic Institute, Blacksburg, VA	Dr. Jeffery Tew Industrial & Systems RL/IR Engineering
13	Automatic Detection of Prominence in Spontaneous Speech New Mexico Institute of Mining, Socorro, NM	Dr. Colin Wightman Electrical Engineering RL/IR

1993 SREP FINAL REPORTS

Wright Laboratory

VOLUME 4A

Report #	Report Title Author's University	Report Author
1	Integrated Estimator/Guidance/Autopilot for Homing Missiles University of Missouri, Rolla, MO	Dr. S. Balakrishnan Mechanical & Aerospace WL/MN Engineering
2	Studies of NTO Decomposition Memphis State University, Memphis, TN	Dr. Theodore Burkey Chemistry WL/MN
3	Investigation of Ray-Beam Basis Functions for Use with the Generalized Ray Expan Ohio State University, Columbus, OH	Dr. Robert Burkholder Electrical Engineering WL/AA
4	Wave Mechanics Modeling of Terminal Ballistics Phenomenology Louisiana Tech University, Ruston, LA	Dr. Eugene Callens, Jr. Mechanical and Industrial WL/MN Engineer
5	Modeling for Aeroelastic Parameter Estimation of Flexing Slender Bodies in a Bal University of California, Berkeley, CA	Dr. Gary Chapman Mechanical Engineering WL/MN
6	Using VHDL in VSL Bist Design Synthesis and its Application to 3-D Pixel Graphic Wright State University, Dayton, OH	Dr. Chien-In Chen Electrical Engineering WL/EL
7	Study of Part Quality and Shrinkage for Injection Molded Aircraft Transparencies Florida International University, Miami, FL	Dr. Joe Chow Industrial and Systems WL/FI Engineering
8	Implementation of Noise-Reducing Multiple-Source Schlieren Systems Purdue University, West Lafayette, IN	Dr. Steven Collicott Aeronautics and WL/FI Astronautical Engineering
9	Performing Target Classification Using Fussy Morphology Neural Networks Iowa State University, Ames, IA	Dr. Jennifer Davidson Electrical Engineering WL/MN
10	Turbulent Heat Transfer In Counter-Rotating Disk System University of Dayton, Dayton, OH	Dr. Jamie Ervin Mechanical and Aerospace WL/ML Engineering
11	Modelling of Biomaterials for Non-Linear Optical Applications University of Virginia, Charlottesville, VA	Dr. Barry Farmer Materials Science and WL/ML Engineering
12	Passive Ranging, Roll-angle Approximation, and Target Recognition for Fuze Appli Florida State University, Tallahassee, FL	Dr. Simon Foo Electrical Engineering WL/MN
13	A Role of Oxygen and Sulfur Compounds in Jet Fuel Deposit Formation Eastern Kentucky University, Richmond, KY	Ms. Ann Gillman Chemistry WL/PO
14	Effect of Aeroelasticity on Experimental Nonlinear Indicial Responses Measured Ohio University, Athens, OH	Dr. Gary Graham Mechanical Engineering WL/FI

1993 SREP FINAL REPORTS

Wright Laboratory

VOLUME 4A cont'd

Report #	Report Title Author's University	Report Author
15	Virtual Reality Information Presentation Technology for Avionics New Mexico Highlands University, Las Vegas, NM	Dr. Elmer Grubbs Electrical Engineering WL/AA
16	An Investigation of the Thermal Stability of an AlC/Ti-22Al-23Nb Metal Matrix Co University of Delaware, Newark, DE	Dr. Ian Hall Materials Science WL/ML
17	Investigation of the Combustion Characteristics of Confined Coannular Jets with Brigham Young University, Provo, UT	Dr. Paul Hedman Chemical Engineering WL/PO
18	Morphology of High-Velocity Perforation of Laminated Plates University of New Orleans, New Orleans, LA	Dr. David Hui Mechanical Engineering WL/FI

1993 SREP FINAL REPORTS

Wright Laboratory

VOLUME 4B

Report #	Report Title Author's University	Report Author
19	Evaluation of Variable Structure Control for Missile Autopilots Using Reaction Auburn University, Auburn, AL	Dr. Mario Innocenti Aerospace Engineering WL/MN
20	Laser Imaging and Ranging (LIMAR) Processing Wright State University, Dayton, OH	Dr. Jack Jean Computer Science & WL/AA Engineering
21	Applications of Wavelet Subband Decomposition in Adaptive Arrays Lafayette College, Easton, PA	Dr. Ismail Jouny Electrical Engineering WL/AA
22	Micromechanics of Matrix Cracks In Brittle Matrix Composites With Frictional Int University of South Florida, Tampa, FL	Dr. Autar Kaw Mechanical Engineering WL/ML
23	A Physics-Based Heterojunction Bipolar Transistor Model Including High-Current, Universtiy of Central Florida, Orlando, FL	Dr. Juin Liou Electrical and Computer WL/EL Engineering
24	Electrical and Thermal Modeling of Switched Reluctance Machines San Francisco State Univesity, San Francisco, CA	Dr. Shy-Sheng Liou Engineering WL/PO
25	Process Migration Facility for the quest Distributed VHDL Simulator University of Cincinnati M.L., Cincinnati, OH	Mr. Dallas Marks Electrical and Computer WL/AA Engineering
26	Investigation of Third Order Non-Linear Optical Properties of Strained Layer Sem Columbia University, New York, NY	Dr. Mary Potasek Applied Physics WL/ML
27	Development of Control Design Methodologies for Flexible Systems with Multiple Arizona State University, Tempe, AZ	Dr. Armando Rodriguez Electrical Engineering WL/MN
28	Enhanced Liquid Fuel Atomization Through Effervescent Injection Virginia Polytechnic Inst & State Coll., Blacksburg, VA	Dr Larry Roe Mechanical Engineering WL/PO
29	Sensor Fusion for IR/MMW Dual-Mode Sensors Using Artificial Neural Networks Auburn University, Auburn, AL	Dr. Thaddeus Roppel Electrical Engineering WL/MN
30	Characterizing the Solid Fragment Population in a Debris Cloud Created by a Hype University of Alabama, Huntsville, AL	Dr. William Schonberg Civil and Environmental WL/MN Engineering
31	Digital Signal Processing Algorithms for Digital EW Receivers Wright State University, Dayton, OH	Dr. Arnab Shaw Electrical Engineering WL/AA
32	An Analytical Model of Laminated Composite Plates for Determination of Stresses University of Cincinnati, Cincinnati, OH	Mr. Robert Slater Mechanical & Industrial WL/FI Engineering

1993 SREP FINAL REPORTS

Wright Laboratory

VOLUME 4B

cont'd

Report #	Report Title Author's University	Report Author
33	Detection of Internal Defects in Multilayered Plates By Lamb Wave Acoustic Micro Universtiy of Arizona, Tucson, AZ	Dr. Kundu Tribikram Civil Engineering and WL/ML Engineering
34	Wavelet Analysis of Ultrasonic Signals for Non-Destructive Evaluation of Composi University of Dayton, Dayton, OH	Dr. Theresa Tuthill Electrical Engineering WL/ML
35	Stochastic Modeling of MBE Growth of Compoud Semiconductors University of Nevada, Las Vegas, NV	Dr. Ramasubrama Venkatasubraman Electrical and Computer WL/ML Engineering
36	Performance Evaluation And Improvement of a Resonant DC Link Inverter With A Lim North Dakota State University, Fargo, ND	Dr. Subbaraya Yuvarajan Electrical Engineering WL/PO
37	Three Component LDV Measurements in a Swirl Combustor North Carolina State University, Raleigh, NC	Dr. Richard Gould Mechanical and Aerospace WL/PO Engineering

1993 SREP FINAL REPORTS

VOLUME 5

Report #	Report Title Author's University	Report Author
Arnold Engineering Development Center		
1	Performance Enhancement for a TI TMS320C40 version of Multigraph Vanderbilt University, Nashville, TN	Mr. Ben Abbott Electrical Engineering AEDC/
2	System Integration Software for Parallel Hardware Architectures Vanderbilt University, Nashville, TN	Dr. Csaba Biegl Electrical Engineering AEDC/
3	Heat Load Structural Failure Prediction for the AEDC Heat-Hi Test Unit Nozzle Georgia Institute of Technology, Atlanta, GA	Dr. Kurt Gramoll Aerospace Engineering AEDC/
4	Coupling of an Inductive Generator with Plasma Erosion Opening Switch (PEOS) to Morehouse College, Atlanta, GA	Dr. Carlyle Moore Physics AEDC/
Frank J Seiler Research Laboratory		
5	Active and Passive Control Designs for the FJSRL Flexible Structure Testbeds Old Dominion University, Norfolk, VA	Dr. Thomas Alberts Mechanical Engineering FJSRL/
6	Three Dimensional Characterization of Non-Linear Optical Thin Films University of Colorado, Colorado Springs, CO	Dr. Thomas Christensen Physics FJSRL/
7	Electrochemistry of Lithium in Room Temperature Molten Salt Electrolytes Houghton College, Houghton, NY	Dr. Bernard Piersma Chemistry FJSRL/
Wilford Hall Medical Center		
8	Enhanced Physiologic Monitoring of Patients with Closed Head-Injury Memphis State, Memphis, TN	Dr. Michael Daley Electrical Engineering WHMC/
9	Rheological, Biochemical and Biophysical Studies of Blood at Elevated Temperatures University of Miami, Coral Gables, FL	Dr. Walter Drost-Hansen Chemistry WHMC

1993 SUMMER RESEARCH EXTENSION PROGRAM (SREP) MANAGEMENT REPORT

1.0 BACKGROUND

Under the provisions of Air Force Office of Scientific Research (AFOSR) contract F49620-90-C-0076, September 1990, Research & Development Laboratories (RDL), an 8(a) contractor in Culver City, CA, manages AFOSR's Summer Research Program. This report is issued in partial fulfillment of that contract (CLIN 0003AC).

The Summer Research Extension Program (SREP) is one of four programs AFOSR manages under the Summer Research Program. The Summer Faculty Research Program (SFRP) and the Graduate Student Research Program (GSRP) place college-level research associates in Air Force research laboratories around the United States for 8 to 12 weeks of research with Air Force scientists. The High School Apprenticeship Program (HSAP) is the fourth element of the Summer Research Program, allowing promising mathematics and science students to spend two months of their summer vacations working at Air Force laboratories within commuting distance from their homes.

SFRP associates and exceptional GSRP associates are encouraged, at the end of their summer tours, to write proposals to extend their summer research during the following calendar year at their home institutions. AFOSR provides funds adequate to pay for 75 SREP subcontracts. In addition, AFOSR has traditionally provided further funding, when available, to pay for additional SREP proposals, including those submitted by associates from Historically Black Colleges and Universities (HBCUs) and Minority Institutions (MIs). Finally, laboratories may transfer internal funds to AFOSR to fund additional SREPs. Ultimately the laboratories inform RDL of their SREP choices, RDL gets AFOSR approval, and RDL forwards a subcontract to the institution where the SREP associate is employed. The subcontract (see Appendix 1 for a sample) cites the SREP associate as the principal investigator and requires submission of a report at the end of the subcontract period.

Institutions are encouraged to share costs of the SREP research, and many do so. The most common cost-sharing arrangement is reduction in the overhead, fringes, or administrative charges institutions would normally add on to the principal investigator's or research associate's labor. Some institutions also provide other support (e.g., computer run time, administrative assistance, facilities and equipment or research assistants) at reduced or no cost.

When RDL receives the signed subcontract, we fund the effort initially by providing 90% of the subcontract amount to the institution (normally \$18,000 for a \$20,000 SREP). When we receive the end-of-research report, we evaluate it administratively and send a copy to the laboratory for a technical evaluation. When the laboratory notifies us the SREP report is acceptable, we release the remaining funds to the institution.

2.0 THE 1993 SREP PROGRAM

SELECTION DATA: A total of 719 faculty members (SFRP Associates) and 286 graduate students (GSRP associates) applied to participate in the 1992 Summer Research Program. From these applicants 185 SFRPs and 121 GSRPs were selected. The education level of those selected was as follows:

1992 SRP Associates, by Degree			
SFRP		GSRP	
PHD	MS	MS	BS
179	6	52	69

Of the participants in the 1992 Summer Research Program 90 percent of SFRPs and 25 percent of GSRPs submitted proposals for the SREP. Ninety proposals from SFRPs and ten from GSRPs were selected for funding, which equates to a selection rate of 54% of the SFRP proposals and of 34% for GSRP proposals.

1993 SREP: Proposals Submitted vs. Proposals Selected			
	Summer 1992 Participants	Submitted SREP Proposals	SREPs Funded
SFRP	185	167	90
GSRP	121	29	10
TOTAL	306	196	100

The funding was provided as follows:

Contractual slots funded by AFOSR	75
Laboratory funded	14
Additional funding from AFOSR	<u>11</u>
Total	100

Six HBCU/MI associates from the 1992 summer program submitted SREP proposals; six were selected (none were lab-funded; all were funded by additional AFOSR funds).

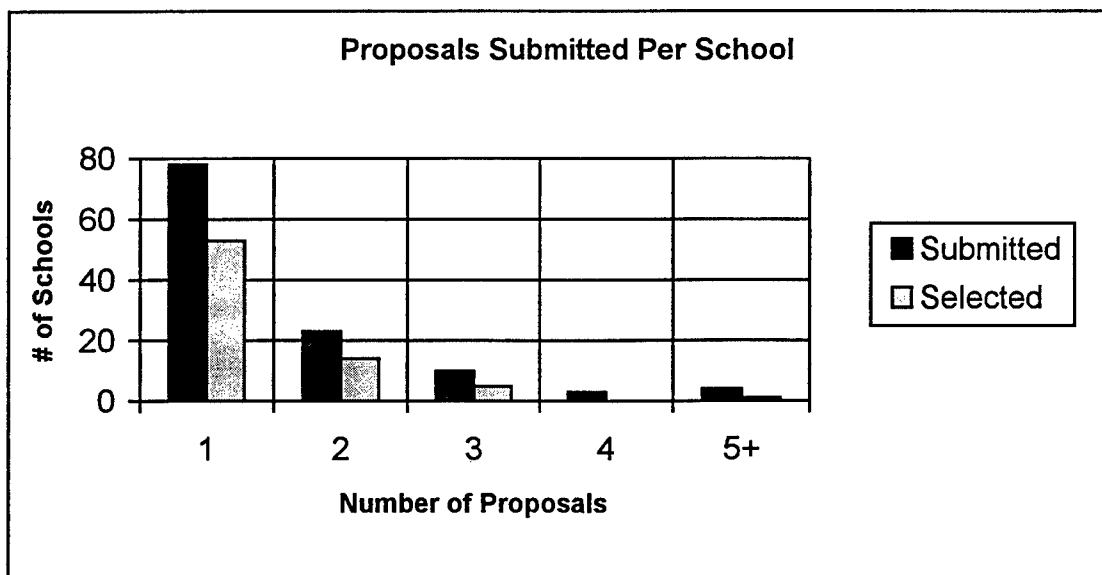
Proposals Submitted and Selected, by Laboratory		
	Applied	Selected
Air Force Civil Engineering Laboratory	9	4
Armstrong Laboratory	41	19
Arnold Engineering Development Center	12	4
Frank J. Seiler Research Laboratory	6	3
Phillips Laboratory	33	19
Rome Laboratory	31	13
Wilford Hall Medical Center	2	1
Wright Laboratory	62	37
TOTAL	196	100

Note: Phillips Laboratory funded 3 SREPs; Wright Laboratory funded 11; and AFOSR funded 11 beyond its contractual 75.

The 306 1992 Summer Research Program participants represented 135 institutions.

Institutions Represented on the 1992 SRP and 1993 SREP		
Number of schools represented in the Summer 92 Program	Number of schools represented in submitted proposals	Number of schools represented in Funded Proposals
135	118	73

Forty schools had more than one participant submitting proposals.



The selection rate for the 78 schools submitting 1 proposal (68%) was better than those submitting 2 proposals (61%), 3 proposals (50%), 4 proposals (0%) or 5+ proposals (25%). The 4 schools that submitted 5+ proposals accounted for 30 (15%) of the 196 proposals submitted.

Of the 196 proposals submitted, 159 offered institution cost sharing. Of the funded proposals which offered cost sharing, the minimum cost share was \$1000.00, the maximum was \$68,000.00 with an average cost share of \$12,016.00.

Proposals and Institution Cost Sharing		
	Proposals Submitted	Proposals Funded
With cost sharing	159	82
Without cost sharing	37	18
Total	196	100

The SREP participants were residents of 41 different states. Number of states represented at each laboratory were:

States Represented, by Proposals Submitted/Selected per Laboratory		
	Proposals Submitted	Proposals Funded
Air Force Civil Engineering Laboratory	8	4
Armstrong Laboratory	21	13
Arnold Engineering Development Center	5	2
Frank J. Seiler Research Laboratory	5	3
Phillips Laboratory	16	14
Rome Laboratory	14	7
Wilford Hall Medical Center	2	1
Wright Laboratory	24	20

Eleven of the 1993 SREP Principal Investigators also participated in the 1992 SREP.

ADMINISTRATIVE EVALUATION: The administrative quality of the SREP associates' final reports was satisfactory. Most complied with the formatting and other instructions provided to them by RDL. Ninety seven final reports and two interim reports have been received and are included in this report. The subcontracts were funded by \$1,991,623.00 of Air Force money. Institution cost sharing totaled \$985,353.00.

TECHNICAL EVALUATION: The form used for the technical evaluation is provided as Appendix 2. ninety-two evaluation reports were received. Participants by laboratory versus evaluations submitted is shown below:

	Participants	Evaluations	Percent
Air Force Civil Engineering Laboratory	*	*	*
Armstrong Laboratory	23 ¹	20	95.2
Arnold Engineering Development Center	4	4	100
Frank J. Seiler Research Laboratory	3	3	100
Phillips Laboratory	19 ²	18	100
Rome Laboratory	13	13	100
Wilford Hall Medical Center	1	1	100
Wright Laboratory	37	34	91.9
Total	100 ³	93	95.9

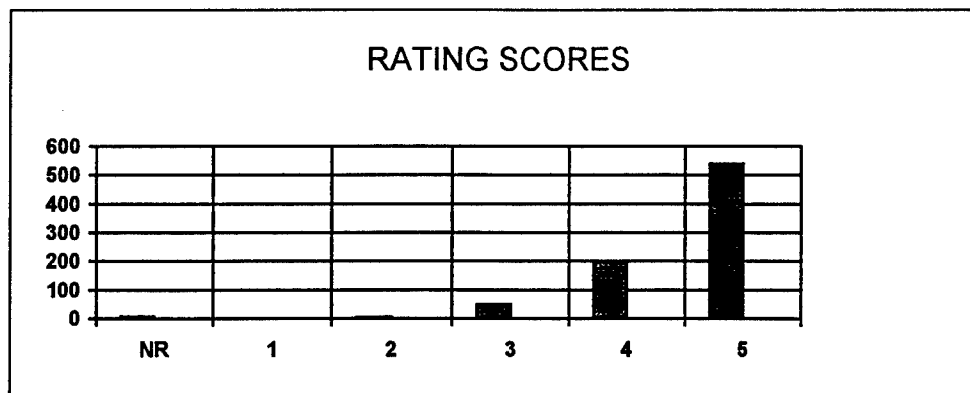
*AFCEL was combined with Wright Laboratory's Flight Dynamics Directorate and Armstrong Laboratories Environics Directorate in 1993. All four of AFCEL's SREP awards went to Armstrong Laboratories Environics Directorate, and their reports are included with Armstrong Lab.

Notes:

- 1: Research on two of the final reports was incomplete as of press time so there aren't any technical evaluations on them to process, yet. Percent complete is based upon $20/21=95.2\%$
- 2: One technical evaluation was not completed because one of the final reports was incomplete as of press time. Percent complete is based upon $18/18=100\%$
- 3: See notes 1 and 2 above. Percent complete is based upon $93/97=95.9\%$

The number of evaluations submitted for the 1993 SREP (95.9%) shows a marked improvement over the 1992 SREP submittals (65%).

PROGRAM EVALUATION: Each laboratory focal point evaluated ten areas (see Appendix 2) with a rating from one (lowest) to five (highest). The distribution of ratings was as follows:

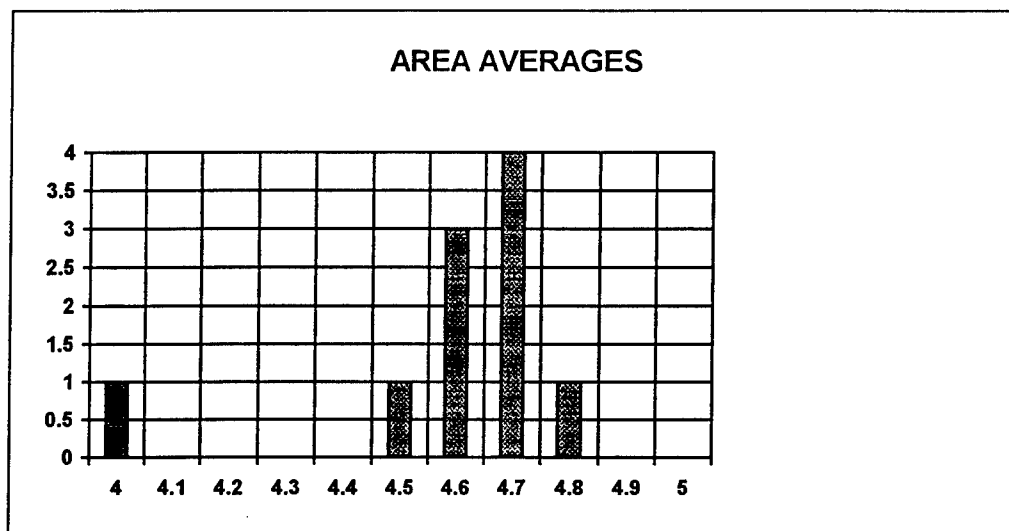


Rating	Not Rated	1	2	3	4	5
# Responses	7	1	7	62 (6%)	226 (25%)	617 (67%)

The 8 low ratings (one 1 and seven 2's) were for question 5 (one 2) "The USAF should continue to pursue the research in this SREP report" and question 10 (one 1 and six 2's) "The one-year period for complete SREP research is about right", in addition over 30% of the threes (20 of 62) were for question ten. The average rating by question was:

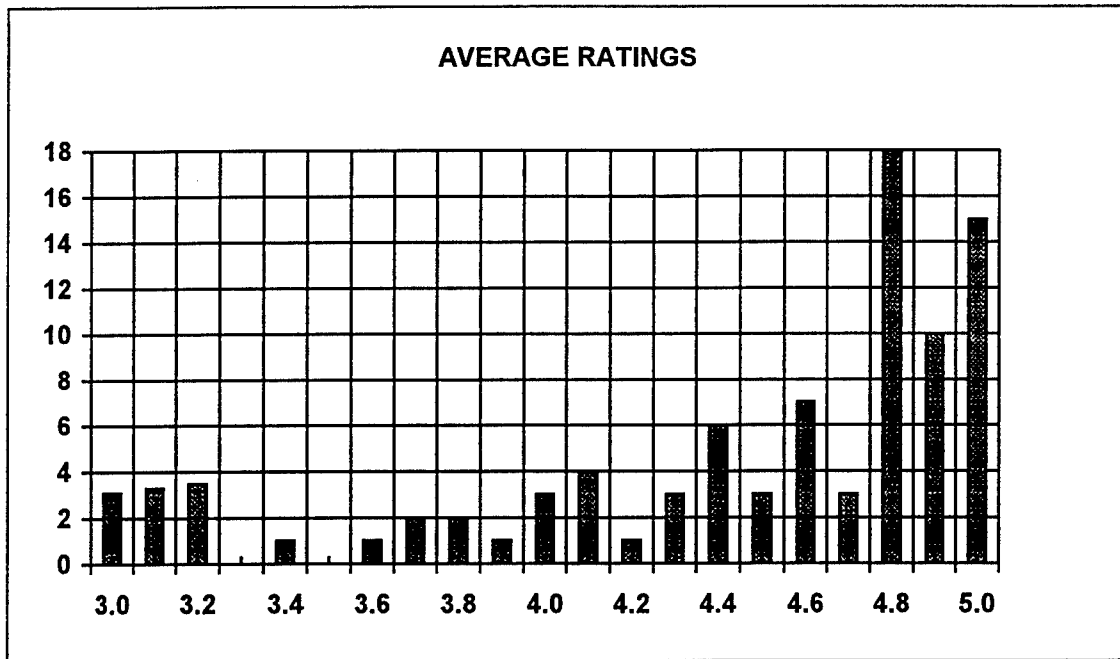
Question	1	2	3	4	5	6	7	8	9	10
Average	4.6	4.6	4.7	4.7	4.6	4.7	4.8	4.5	4.6	4.0

The distribution of the averages was:



Area 10 "the one-year period for complete SREP research is about right" had the lowest average rating (4.1). The overall average across all factors was 4.6 with a small sample standard deviation of 0.2. The average rating for area 10 (4.1) is approximately three sigma lower than the overall average (4.6) indicating that a significant number of the evaluators feel that a period of other than one year should be available for complete SREP research.

The average ratings ranged from 3.4 to 5.0. The overall average for those reports that were evaluated was 4.6. Since the distribution of the ratings is not a normal distribution the average of 4.6 is misleading. In fact over half of the reports received an average rating of 4.8 or higher. The distribution of the average report ratings is as shown:



It is clear from the high ratings that the laboratories place a high value on AFOSR's Summer Research Extension Programs.

3.0 SUBCONTRACTS SUMMARY

Table 1 provides a summary of the SREP subcontracts. The individual reports are published in volumes as shown:

<u>Laboratory</u>	<u>Volume</u>
Air Force Civil Engineering Laboratory	*
Armstrong Laboratory	1
Arnold Engineering Development Center	5
Frank J. Seiler Research Laboratory	5
Phillips Laboratory	2
Rome Laboratory	3
Wilford Hall Medical Center	5
Wright Laboratory	4A, 4B

*AFCEL was combined with Wright Laboratory's Flight Dynamics Directorate and Armstrong Laboratories Environics Directorate in 1993. All four of AFCEL's SREP awards went to Armstrong Laboratories Environics Directorate, and their reports are included with Armstrong Lab.

1993 SREP SUB-CONTRACT DATA

TABLE 1: SUBCONTRACTS SUMMARY

Report Author Author's University	Author's Degree	Sponsoring Lab	Performance Period		Contract Amount Univ. Cost Share
Abbott , Ben Electrical Engineering Vanderbilt University, Nashville, TN	M.S.	AEDC/	01/01/93	12/31/93	\$19619.00 \$0.00
Alberts , Thomas Mechanical Engineering Old Dominion University, Norfolk, VA	PhD	FJSRL/	01/01/93	04/15/94	\$20000.00 \$8000.00
Avula , Xavier Mechanical & Aerospace Engineering University of Missouri, Rolla, MO	PhD	AL/AO	01/01/93	04/15/94	\$20000.00 \$1836.00
Balakrishnan , S. Mechanical & Aerospace Engineering University of Missouri, Rolla, MO	PhD	WL/MN	12/01/92	12/14/93	\$20000.00 \$3996.00
Baumgarten , Joseph Mechanical Engineering Iowa State University, Ames, IA	PhD	PL/VT	01/01/93	04/01/94	\$19916.00 \$9083.00
Bayard , Jean-Pierre Electrical & Electronic Engineering California State University, Sacramento, CA	PhD	RL/ER	01/01/93	12/31/93	\$20000.00 \$7423.00
Bellem , Raymond Electrical & Computer Engineering University of Arizona, Tucson, AZ	PhD	PL/VT	01/01/93	02/28/94	\$19956.00 \$0.00
Biegl , Csaba Electrical Engineering Vanderbilt University, Nashville, TN	PhD	AEDC/	01/01/93	12/31/93	\$19999.00 \$0.00
Biggs , Albert Electrical Engineering University of Alabama, Huntsville, AL	PhD	PL/WS	01/01/93	12/31/93	\$19975.00 \$0.00
Burkey , Theodore Chemistry Memphis State University, Memphis, TN	PhD	WL/MN	01/01/93	12/31/93	\$20000.00 \$18648.00
Burkholder , Robert Electrical Engineering Ohio State University, Columbus, OH	PhD	WL/AA	01/01/93	12/31/93	\$20000.00 \$6727.00
Callens, Jr. , Eugene Mechanical and Industrial Engineer Louisiana Tech University, Ruston, LA	PhD	WL/MN	01/01/93	12/31/93	\$20000.00 \$5700.00
Chapman , Gary Mechanical Engineering University of California, Berkeley, CA	PhD	WL/MN	01/01/93	12/31/94	\$20000.00 \$0.00
Chen , Chien-In Electrical Engineering Wright State University, Dayton, OH	PhD	WL/EL	01/01/93	12/31/93	\$20000.00 \$32065.00
Chen , Jer-sen Computer Science & Engineering Wright State University, Dayton, OH	PhD	AL/CF	01/01/93	12/31/93	\$20000.00 \$31763.00

1993 SREP SUB-CONTRACT DATA

Report Author Author's University	Author's Degree	Sponsoring Lab	Performance Period		Contract Amount Univ. Cost Share
Chen , Pinyuen Mathematics Syracuse University, Syracuse, NY	PhD	RL/IR	01/01/93	12/31/93	\$20000.00 \$0.00
Chow , Joe Industrial and Systems Engineering Florida International University, Miami, FL	PhD	WL/FI	01/01/93	01/14/94	\$20000.00 \$2500.00
Christensen , Thomas Physics University of Colorado, Colorado Springs, CO	PhD	FJSRL/	01/01/93	12/31/93	\$20000.00 \$5390.00
Collicott , Steven Aeronautics and Astronautical Engineering Purdue University, West Lafayette, IN	PhD	WL/FI	01/01/93	12/31/93	\$20000.00 \$13307.00
Cooke , Nancy Psychology New Mexico State University, Las Cruces, NM	PhD	AL/HR	01/01/93	12/31/93	\$20000.00 \$6178.00
Daley , Michael Electrical Engineering Memphis State, Memphis, TN	PhD	WHMC/	01/01/93	12/31/93	\$20000.00 \$18260.00
Davidson , Jennifer Electrical Engineering Iowa State University, Ames, IA	PhD	WL/MN	01/01/93	02/28/94	\$19999.00 \$0.00
Deivanayagam , Subramaniam Industrial Engineering Tennessee Technological University, Cookeville, TN	PhD	AL/HR	02/01/93	12/31/93	\$20000.00 \$12491.00
Elliott , David Engineering Arkansas Technology University, Russellville, AR	PhD	PL/RK	10/01/92	08/15/93	\$20000.00 \$50271.00
Erdman , Paul Physics and Astronomy University of Iowa, Iowa City, IA	M.S.	PL/RK	01/01/93	12/31/93	\$20000.00 \$26408.00
Ervin , Jamie Mechanical and Aerospace Engineering University of Dayton, Dayton, OH	PhD	WL/ML	01/01/93	12/31/93	\$18632.00 \$3000.00
Erwin , Daniel Aerospace Engineering University of Southern California, Los Angeles, CA	PhD	PL/RK	01/01/93	12/31/93	\$19962.00 \$12696.00
Ewert , Dan Electrical Engineering North Dakota State University, Fargo, ND	PhD	AL/AO	01/01/93	12/31/93	\$20000.00 \$2100.00
Farmer , Barry Materials Science and Engineering University of Virginia, Charlottesville, VA	PhD	WL/ML	01/01/93	02/28/94	\$20000.00 \$2000.00
Foo , Simon Electrical Engineering Florida State University, Tallahassee, FL	PhD	WL/MN	01/01/93	12/31/93	\$19977.00 \$0.00

1993 SREP SUB-CONTRACT DATA

Report Author Author's University	Author's Degree	Sponsoring Lab	Performance Period		Contract Amount Univ. Cost Share
Friedman , Jeffrey Physics University of Puerto Rico, Mayaguez, PR	PhD	PL/GP	01/01/93	12/31/93	\$20000.00 \$10233.00
Gerstman , Bernard Physics Florida International University, Miami, FL	PhD	AL/OE	01/01/93	04/30/94	\$19947.00 \$2443.00
Gillman , Ann Chemistry Eastern Kentucky University, Richmond, KY	M.S.	WL/PO	01/01/93	12/31/93	\$20000.00 \$15618.00
Gimmestad , Gary Research Institute Georgia Institute of Technology, Atlanta, GA	PhD	PL/LI	01/01/93	12/31/93	\$20000.00 \$0.00
Gould , Richard Mechanical and Aerospace Engineering North Carolina State University, Raleigh, NC	PhD	WL/PO	01/01/93	12/31/93	\$20000.00 \$8004.00
Graham , Gary Mechanical Engineering Ohio University, Athens, OH	PhD	WL/FI	01/01/93	12/31/93	\$20000.00 \$5497.00
Gramoll , Kurt Aerospace Engineering Georgia Institute of Technology, Atlanta, GA	PhD	AEDC/	01/01/93	12/31/93	\$19707.00 \$14552.00
Graul , Susan Chemistry Carnegie Mellon University, Pittsburgh, PA	PhD	PL/WS	01/01/93	03/31/94	\$20000.00 \$0.00
Griffin , Steven Engineering University of Texas, San Antonio, TX	M.S.	PL/VT	01/01/93	12/31/93	\$20000.00 \$0.00
Grubbs , Elmer Electrical Engineering New Mexico Highlands University, Las Vegas, NM	PhD	WL/AA	01/01/93	12/31/93	\$20000.00 \$6747.00
Gupta , Pushpa Mathematics University of Maine, Orono, ME	PhD	AL/AO	01/01/93	12/31/93	\$20000.00 \$1472.00
Hall , Ian Materials Science University of Delaware, Newark, DE	PhD	WL/ML	01/01/93	12/31/93	\$20000.00 \$9580.00
Hedman , Paul Chemical Engineering Brigham Young University, Provo, UT	PhD	WL/PO	01/01/93	12/31/93	\$19999.00 \$7755.00
Henry , Robert Electrical & Computer Engineering University of Southwestern Louisiana, Lafayette, LA	PhD	RL/C3	12/01/92	05/31/93	\$19883.00 \$11404.00
Henson , James Electrical Engineering University of Nevada, Reno, NV	PhD	PL/WS	01/01/93	12/31/93	\$19913.00 \$9338.00

1993 SREP SUB-CONTRACT DATA

Report Author Author's University	Author's Degree	Sponsoring Lab	Performance Period		Contract Amount Univ. Cost Share
Hoe , Benjamin Electrical Engineering Polytechnic University, Brooklyn, NY	M.S.	RL/C3	09/01/92	05/31/93	\$19988.00 \$7150.00
Hughes , Rod Psychology Bowling Green State University, Bowling Green, OH	M.S.	AL/CF	01/01/93	04/15/94	\$20000.00 \$20846.00
Hui , David Mechanical Engineering University of New Orleans, New Orleans, LA	PhD	WL/FI	01/01/93	12/31/93	\$20000.00 \$0.00
Humi , Mayer Mathematics Worcester Polytechnic Institut, Worcester, MA	PhD	PL/LI	01/01/93	12/31/93	\$20000.00 \$5000.00
Innocenti , Mario Aerospace Engineering Auburn University, Auburn, AL	PhD	WL/MN	01/01/93	02/28/94	\$20000.00 \$12536.00
Jean , Jack Computer Science & Engineering Wright State University, Dayton, OH	PhD	WL/AA	01/01/93	12/31/93	\$20000.00 \$34036.00
Jouny , Ismail Electrical Engineering Lafayette College, Easton, PA	PhD	WL/AA	01/01/93	12/31/93	\$19381.00 \$4500.00
Kaikhah , Khosrow Computer Science Southwest Texas State College, San Marcos, TX	PhD	RL/IR	01/01/93	12/31/93	\$20000.00 \$0.00
Kaw , Autar Mechanical Engineering University of South Florida, Tampa, FL	PhD	WL/ML	01/01/93	12/31/93	\$20000.00 \$22556.00
Kheyfets , Arkady Mathematics North Carolina State University, Raleigh, NC	PhD	PL/LI	01/01/93	12/31/93	\$20000.00 \$2500.00
Kitchart , Mark Mechanical Engineering North Carolina A & T State University, Greensboro, NC	M.S.	AL/EQ	01/01/93	12/31/93	\$20000.00 \$0.00
Koblasz , Arthur Civil Engineering Georgia Institute of Technology, Atlanta, GA	PhD	AL/AO	01/01/93	12/31/93	\$19826.00 \$0.00
Koivo , A. Electrical Engineering Purdue University, West Lafayette, IN	PhD	AL/CF	01/01/93	06/30/94	\$20000.00 \$0.00
Kundich , Robert Biomedical Engineering University of Tennessee, Memphis, TN	PhD	AL/CF	01/01/93	12/31/94	\$20000.00 \$23045.00
Kuo , Spencer Electrical Engineering Polytechnic University, Farmingdale, NY	PhD	PL/GP	01/01/93	04/30/94	\$20000.00 \$9731.00

1993 SREP SUB-CONTRACT DATA

Report Author Author's University	Author's Degree	Sponsoring Lab	Performance Period		Contract Amount Univ. Cost Share
Liou , Juin Electrical and Computer Engineering Universtiy of Central Florida, Orlando, FL	PhD	WL/EL	01/01/93	12/31/93	\$20000.00 \$9073.00
Liou , Shy-Shenq Engineering San Francisco State Univesity, San Francisco, CA	PhD	WL/PO	01/01/93	12/31/93	\$20000.00 \$13387.00
Manoranjana , Valipuram Pure and Applied Mathematics Washington State University, Pullman, WA	PhD	AL/EQ	01/01/93	12/31/93	\$19956.00 \$10041.00
Marks , Dallas Electrical and Computer Engineering University of Cincinnati M.L., Cincinnati, OH	M.S.	WL/AA	10/01/92	06/30/93	\$20000.00 \$4731.00
Monsay , Evelyn Physics Le Moyne College, Syracuse, NY	PhD	RL/OC	01/01/93	12/31/93	\$19634.00 \$1510.00
Moor , William Industrial & Management Engineering Arizona State University, Tempe, AZ	PhD	AL/HR	01/01/93	12/31/93	\$20000.00 \$4833.00
Moore , Carlyle Physics Morehouse College, Atlanta, GA	PhD	AEDC/	01/01/93	12/31/93	\$20000.00 \$4880.00
Mulligan , B. Psychology University of Georgia Research, Athens, GA	PhD	AL/OE	01/01/93	04/15/94	\$19998.00 \$13936.00
Murphy , Richard Physics University of Missouri, Kansas City, MO	PhD	PL/WS	01/01/93	12/31/93	\$20000.00 \$13022.00
Nilan , Michael Information Studies Syracuse University, Syracuse, NY	PhD	RL/C3	01/01/93	12/31/93	\$19998.00 \$13016.00
Parrish , Allen Computer Science University of Alabama, Tuscaloosa, AL	PhD	RL/C3	01/01/93	12/31/93	\$19919.00 \$20599.00
Piersma , Bernard Chemistry Houghton College, Houghton, NY	PhD	FJSRL/	01/01/93	12/31/93	\$20000.00 \$4000.00
Potasek , Mary Applied Physics Columbia University, New York, NY	PhD	WL/ML	12/01/93	11/30/93	\$20000.00 \$7806.00
Qazi , Salahuddin Optical Communications SUNY/Institute of Technology, Utica, NY	PhD	RL/OC	01/01/93	12/31/93	\$20000.00 \$68000.00
Reardon , Kenneth Agricultural and Chemical Engineering Colorado State University, Fort Collins, CO	PhD	AL/EQ	01/01/93	01/31/94	\$19996.00 \$12561.00

1993 SREP SUB-CONTRACT DATA

Report Author Author's University	Author's Degree	Sponsoring Lab	Performance Period	Contract Amount Univ. Cost Share
Reynolds , David Biomedical & Human Factors Wright State University, Dayton, OH	PhD	AL/CF	01/01/93 06/30/94	\$20000.00 \$14063.00
Robinson , Donald Chemistry Xavier University of Louisiana, New Orleans, LA	PhD	AL/OE	01/01/93 06/30/94	\$20000.00 \$12935.00
Rodriguez , Armando Electrical Engineering Arizona State University, Tempe, AZ	PhD	WL/MN	01/01/93 12/31/93	\$20000.00 \$0.00
Roe , Larry Mechanical Engineering Virginia Polytechnic Inst & State Coll., Blacksburg, VA	PhD	WL/PO	01/01/93 12/31/93	\$20000.00 \$11421.00
Romeu , Jorge Assistant Prof. of Mathematics SUNY College at Cortland, Cortland, NY	PhD	RL/OC	01/01/93 12/31/93	\$19997.00 \$7129.00
Roppel , Thaddeus Electrical Engineering Auburn University, Auburn, AL	PhD	WL/MN	01/01/93 12/31/93	\$20000.00 \$21133.00
Roznowski , Mary Psychology Ohio State University, Columbus, OH	PhD	AL/HR	01/01/93 03/31/94	\$19953.00 \$6086.00
Rudzinski , Walter Chemistry Southwest Texas State University, San Marcos, TX	PhD	AL/OE	01/01/93 12/31/93	\$20000.00 \$10120.00
Sargent , Robert Engineering and Computer Science Syracuse University, Syracuse, NY	PhD	RL/XP	01/01/93 12/31/93	\$20000.00 \$11931.00
Schonberg , William Civil and Environmental Engineering University of Alabama, Huntsville, AL	PhD	WL/MN	01/01/93 12/31/93	\$19991.00 \$5083.00
Shaw , Arnab Electrical Engineering Wright State University, Dayton, OH	PhD	WL/AA	01/01/93 12/31/93	\$20000.00 \$4766.00
Shively , Jon Engineering & Computer Science California State University, Northridge, CA	PhD	PL/VT	01/01/93 12/31/93	\$20000.00 \$9782.00
Slater , Robert Mechanical & Industrial Engineering University of Cincinnati, Cincinnati, OH	M.S.	WL/FI	01/01/93 12/31/93	\$20000.00 \$8257.00
Stenzel , Johanna Arts & Sciences University of Houston, Victoria, TX	PhD	PL/LI	01/01/93 12/31/93	\$20000.00 \$9056.00
Tan , Arjun Physics Alabama A & M University, Normal, AL	PhD	PL/WS	01/01/93 12/31/93	\$20000.00 \$1000.00

1993 SREP SUB-CONTRACT DATA

Report Author Author's University	Author's Degree	Sponsoring Lab	Performance Period		Contract Amount Univ. Cost Share
Tetrick , Lois Industrial Relations Prog Wayne State University, Detroit, MI	PhD	AL/HR	01/01/93	12/31/93	\$20000.00 \$17872.00
Tew , Jeffery Industrial & Systems Engineering Virginia Polytechnic Institute, Blacksburg, VA	PhD	RL/IR	05/31/93	12/31/93	\$16489.00 \$4546.00
Tribikram , Kundu Civil Engineering and Engineering Universtiy of Arizona, Tucson, AZ	PhD	WL/ML	01/01/93	12/31/93	\$20000.00 \$9685.00
Tuthill , Theresa Electrical Engineering University of Dayton, Dayton, OH	PhD	WL/ML	01/01/93	12/31/93	\$20000.00 \$24002.00
Venkatasubraman , Ramasubrama Electrical and Computer Engineering University of Nevada, Las Vegas, NV	PhD	WL/ML	01/01/93	12/31/93	\$20000.00 \$18776.00
Wang , Xingwu Electrical Engineering Alfred University, Alfred, NY	PhD	AL/EQ	01/01/93	12/31/93	\$20000.00 \$10000.00
Whitefield , Philip Physics University of Missouri, Rolla, MO	PhD	PL/LI	01/01/93	03/01/94	\$20000.00 \$11040.00
Wightman , Colin Electrical Engineering New Mexico Institute of Mining, Socorro, NM	PhD	RL/IR	01/01/93	12/31/93	\$20000.00 \$1850.00
Womack , Michael Natural Science and Mathematics Macon College, Macon, GA	PhD	AL/OE	01/01/93	06/30/94	\$19028.00 \$6066.00
Yuvarajan , Subbaraya Electrical Engineering North Dakota State University, Fargo, ND	PhD	WL/PO	01/01/93	12/31/93	\$19985.00 \$22974.00

APPENDIX 1:
SAMPLE SREP SUBCONTRACT

AIR FORCE OFFICE OF SCIENTIFIC RESEARCH
1993 SUMMER RESEARCH EXTENSION PROGRAM SUBCONTRACT 93-133

BETWEEN

Research & Development Laboratories
5800 Uplander Way
Culver City, CA 90230-6608

AND

San Francisco State University
University Comptroller
San Francisco, CA 94132

REFERENCE: Summer Research Extension Program Proposal 93-133
Start Date: 01/01/93 End Date: 12/31/93
Proposal Amount: \$20,000.00

- (1) PRINCIPAL INVESTIGATOR: Dr. Shy Shenq P. Liou
Engineering
San Francisco State University
San Francisco, CA 94132
- (2) UNITED STATES AFOSR CONTRACT NUMBER: F49620-90-C-09076
- (3) CATALOG OF FEDERAL DOMESTIC ASSISTANCE NUMBER (CFDA): 12.800
PROJECT TITLE: AIR FORCE DEFENSE RESEARCH SOURCES PROGRAM
- (4) ATTACHMENTS 1 AND 2: SREP REPORT INSTRUCTIONS

*** SIGN SREP SUBCONTRACT AND RETURN TO RDL ***

1. BACKGROUND: Research & Development Laboratories (RDL) is under contract (F49620-90-C-0076) to the United States Air Force to administer the Summer Research Programs (SRP), sponsored by the Air Force Office of Scientific Research (AFOSR), Bolling Air Force Base, D.C. Under the SRP, a selected number of college faculty members and graduate students spend part of the summer conducting research in Air Force laboratories. After completion of the summer tour participants may submit, through their home institutions, proposals for follow-on research. The follow-on research is known as the Summer Research Extension Program (SREP). Approximately 75 SREP proposals annually will be selected by the Air Force for funding of up to \$20,000; shared funding by the academic institution is encouraged. SREP efforts selected for funding are administered by RDL through subcontracts with the institutions. This subcontract represents such an agreement between RDL and the institution designated in Section 5 below.
2. RDL PAYMENTS: RDL will provide the following payments to SREP institutions:
 - 90 percent of the negotiated SREP dollar amount at the start of the SREP Research period.
 - the remainder of the funds within 30 days after receipt at RDL of the acceptable written final report for the SREP research.
3. INSTITUTION'S RESPONSIBILITIES: As a subcontractor to RDL, the institution designated on the title page will:
 - a. Assure that the research performed and the resources utilized adhere to those defined in the SREP proposal.
 - b. Provide the level and amounts of institutional support specified in the RIP proposal.
 - c. Notify RDL as soon as possible, but not later than 30 days, of any changes in 3a or 3b above, or any change to the assignment or amount of participation of the Principal Investigator designated on the title page.

- d. Assure that the research is completed and the final report is delivered to RDL not later than twelve months from the effective date of this subcontract, but no later than December 31, 1993. The effective date of the subcontract is one week after the date that the institution's contracting representative signs this subcontract, but no later than January 15, 1993.
- e. Assure that the final report is submitted in accordance with Attachment 1.
- f. Agree that any release of information relating to this subcontract (news releases, articles, manuscripts, brochures, advertisements, still and motion pictures, speeches, trade association meetings, symposia, etc.) will include a statement that the project or effort depicted was or is sponsored by: Air Force Office of Scientific Research, Bolling AFB, D.C.
- g. Notify RDL of inventions or patents claimed as the result of this research as specified in Attachment 1.
- h. RDL is required by the prime contract to flow down patent rights and technical data requirements in this subcontract. Attachment 2 to this subcontract contains a list of contract clauses incorporated by reference in the prime contract.

4. All notices to RDL shall be addressed to:

RDL Summer Research Program Office
5800 Uplander Way
Culver City, CA 90230-6608

5. By their signatures below, the parties agree to the provisions of this subcontract.



Abe S. Sopher
RDL Contracts Manager

Signature of Institution Contracting Official

Typed/Printed Name

Date

Title

Institution

(Date/Phone)

ATTACHMENT 2
CONTRACT CLAUSES

This contract incorporates by reference the following clauses of the Federal Acquisition Regulations (FAR), with the same force and effect as if they were given in full text. Upon request, the Contracting Officer or RDL will make their full text available (FAR 52.252-2).

<u>FAR CLAUSES</u>	<u>TITLE AND DATE</u>
52.202-1	DEFINITIONS (SEP 1991)
52.203-1	OFFICIALS NOT TO BENEFIT (APR 1984)
52.203-3	GRATUITIES (APR 1984)
52.203-5	COVENANT AGAINST CONTINGENT FEES (APR 1984)
52.304-6	RESTRICTIONS ON SUBCONTRACTOR SALES TO THE GOVERNMENT (JUL 1985)
52.203-7	ANTI-KICKBACK PROCEDURES (OCT 1988)
52.203-12	LIMITATION ON PAYMENTS TO INFLUENCE CERTAIN FEDERAL TRANSACTIONS (JAN 1990)
52.204-2	SECURITY REQUIREMENTS (APR 1984)
52.209-6	PROTECTING THE GOVERNMENT'S INTEREST WHEN SUBCONTRACTING WITH CONTRACTORS DEBARRED, SUSPENDED, OR PROPOSED FOR DEBARMENT (NOV 1992)
52.212-8	DEFENSE PRIORITY AND ALLOCATION REQUIREMENTS (SEP 1990)
52.215-1	EXAMINATION OF RECORDS BY COMPTROLLER GENERAL (APR 1984)
52.215-2	AUDIT - NEGOTIATION (DEC 1989)
52.222-26	EQUAL OPPORTUNITY (APR 1984)
52.222-28	EQUAL OPPORTUNITY PREAWARD CLEARANCE OF SUBCONTRACTS (APR 1984)

- 52.222-35 AFFIRMATIVE ACTION FOR SPECIAL DISABLED AND VIETNAM ERA VETERANS (APR 1984)
- 52.222-36 AFFIRMATIVE ACTION FOR HANDICAPPED WORKERS (APR 1984)
- 52.222-37 EMPLOYMENT REPORTS ON SPECIAL DISABLED VETERAN AND VETERANS OF THE VIETNAM ERA (JAN 1988)
- 52.223-2 CLEAN AIR AND WATER (APR 1984)
- 52.232-6 DRUG-FREE WORKPLACE (JUL 1990)
- 52.224-1 PRIVACY ACT NOTIFICATION (APR 1984)
- 52.224-2 PRIVACY ACT (APR 1984)
- 52.225-13 RESTRICTIONS ON CONTRACTING WITH SANCTIONED PERSONS (MAY 1989)
- 52.227-1 AUTHORIZATION AND CONSENT (APR 1984)
- 52.227-2 NOTICE AND ASSISTANCE REGARDING PATENT AND COPYRIGHT INFRINGEMENT (APR 1984)
- 52.227-10 FILING OF PATENT APPLICATIONS - CLASSIFIED SUBJECT MATTER (APR 1984)
- 52.227-11 PATENT RIGHTS - RETENTION BY THE CONTRACTOR (SHORT FORM) (JUN 1989)
- 52.228-6 INSURANCE - IMMUNITY FROM TORT LIABILITY (APR 1984)
- 52.228-7 INSURANCE - LIABILITY TO THIRD PERSONS (APR 1984)
- 52.230-5 DISCLOSURE AND CONSISTENCY OF COST ACCOUNTING PRACTICES (AUG 1992)
- 52.232-23 ASSIGNMENT OF CLAIMS (JAN 1986)
- 52.237-3 CONTINUITY OF SERVICES (JAN 1991)

52.246-25	LIMITATION OF LIABILITY - SERVICES (APR 1984)
52.249-6	TERMINATION (COST-REIMBURSEMENT) (MAY 1986)
52.249-14	EXCUSABLE DELAYS (APR 1984)
52.251-1	GOVERNMENT SUPPLY SOURCES (APR 1984)

APPENDIX 2:

SAMPLE TECHNICAL EVALUATION FORM

1993 SUMMER RESEARCH EXTENSION PROGRAM

RIP NO.: 93-0092

RIP ASSOCIATE: Dr. Gary T. Chapman

Provided are several evaluation statements followed by ratings of (1) through (5). A rating of (1) is the lowest and (5) is the highest. Circle the rating level number you best feel rates the statement. Document additional comments on the back of this evaluation form.

Mail or fax the completed form to :

RDL

Attn: 1993 SREP TECH EVALS

5800 Uplander Way

Culver City, CA 90230-6608

(FAX: 310 216-5940)

- | | | | | | | |
|-----|---|---|---|---|---|---|
| 1. | This SREP report has a high level of technical merit. | 1 | 2 | 3 | 4 | 5 |
| 2. | The SREP program is important to accomplishing the labs's mission | 1 | 2 | 3 | 4 | 5 |
| 3. | This SREP report accomplished what the associate's proposal promised. | 1 | 2 | 3 | 4 | 5 |
| 4. | This SREP report addresses area(s) important to the USAF | 1 | 2 | 3 | 4 | 5 |
| 5. | The USAF should continue to pursue the research in this SREP report | 1 | 2 | 3 | 4 | 5 |
| 6. | The USAF should maintain research relationships with this SREP associate | 1 | 2 | 3 | 4 | 5 |
| 7. | The money spent on this SREP effort was well worth it | 1 | 2 | 3 | 4 | 5 |
| 8. | This SREP report is well organized and well written | 1 | 2 | 3 | 4 | 5 |
| 9. | I'll be eager to be a focal point for summer and SREP associates in the future. | 1 | 2 | 3 | 4 | 5 |
| 10. | The one-year period for complete SREP research is about right | 1 | 2 | 3 | 4 | 5 |

****USE THE BACK OF THIS FORM FOR ADDITIONAL COMMENTS****

LAB FOCAL POINT'S NAME (PRINT): _____

OFFICE SYMBOL: _____ PHONE: _____

**APPROXIMATE ANALYTICAL GUIDANCE AND ESTIMATION SCHEMES
FOR HOMING MISSILES**

**S. N. Balakrishnan and Donald T. Stansbery
Department of Mechanical and Aerospace Engineering
and Engineering Mechanics**

**University of Missouri-Rolla
Rolla, MO 65401**

**Final Report for:
Research Initiation Program
Wright Laboratory / Armament Directorate
Eglin Air Force Base, FL 32542**

**Sponsored by:
Air Force Office of Scientific Research
Bolling Air Force Base, Washington, D.C.**

December 1993

APPROXIMATE ANALYTICAL GUIDANCE AND ESTIMATION SCHEMES FOR HOMING MISSILES

S. N. Balakrishnan and Donald T. Stansbery
Department of Mechanical and Aerospace Engineering
and Engineering Mechanics
University of Missouri-Rolla

ABSTRACT

In this study polar coordinates are used to obtain a family of analytical guidance laws for homing missiles. Closed form solutions for the guidance laws are developed using modern control techniques. In order to develop the guidance laws, the dynamic equations of the target-intercept problem are decoupled through introduction of a pseudo-control in the radial direction. The commanded acceleration in the radial direction is determined through the use of pseudo-control and the commanded acceleration in the transverse direction is determined from the solution to a two-point boundary value problem. The two-point boundary value problem is solved through the use of the state transition matrix of the intercept dynamics. The resulting optimal guidance law is compared with the solutions for other guidance laws such as True Proportional Navigation and Ideal Proportional Navigation. An approximate analytical filter is developed in polar coordinates for use with guidance laws. Analysis of numerical results from using this filter is given.

APPROXIMATE ANALYTICAL GUIDANCE AND ESTIMATION SCHEMES FOR HOMING MISSILES

S. N. Balakrishnan and Donald T. Stansbery

I. INTRODUCTION

The idea of tactical missile guidance originated in Germany during the 1940's. Although Germany gave birth to the idea of tactical missile guidance during World War II, they had little success in using the ideas to produce effective missile-target engagements [1]. Many forms of tactical missile guidance have been developed and implemented since the early stages of its existence. Most guidance and control laws used in current tactical missiles are based on classical control design techniques developed in the 1950's [2]. There are many guidance laws which can guide a missile to the intercept of a target, such as, line of sight angle guidance, line of sight rate guidance and advanced guidance based on optimal control theory. For a two-point homing missile guidance problem the line of sight rate guidance is typically used. Three well known homing guidance laws which use only the observed motion of the missile-target line of sight (LOS) are pursuit guidance, constant-bearing guidance, and proportional navigation guidance.

Pursuit guidance is based on the concept that the missile is always flying directly toward the target like a dog chasing a rabbit (Figure 1). This requires the missile to constantly turn during the engagement unless it is in a head-on or a tail-chase scenario. This guidance law has the advantage that it is easy to implement and is less sensitive to noise. The disadvantage of this guidance law is that it will always end up in a tail-chase and if the target is maneuvering, the missile acceleration requirements will be extremely high near the end of the engagement. With this guidance law, the missile velocity vector direction must be sensed to steer the missile.

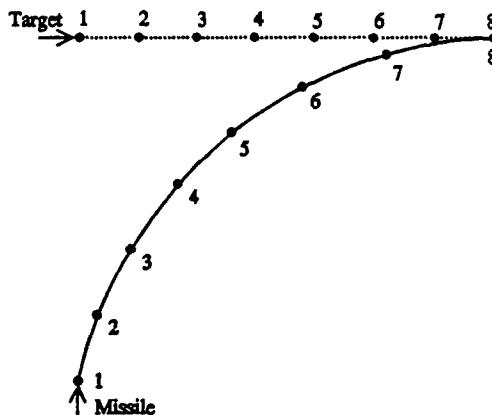


Figure 1 Pursuit Guidance

Constant-bearing guidance is based on keeping the missile on a straight-line path to the target (Figure 2), which is accomplished by keeping the LOS between the missile and the target constant (LOS is always parallel to itself [2]). To keep the LOS constant, the relative velocity between the missile and target must be aligned with the LOS. This requires proper orientation of the missile velocity at guidance initiation, which will lead the target by some angle. If the LOS can be kept constant the missile will always intercept the target even if the target is maneuvering. Constant bearing guidance is more efficient and less demanding than the pursuit guidance. However, this method is effective only if the target path can be predicted correctly. If the missile is launched with a non-zero bearing angle, the missile must perform maneuvers to get on the required course which requires additional use of fuel. Another disadvantage of constant-bearing guidance is that it requires the missile to be able to detect and correct any changes in the LOS instantaneously.

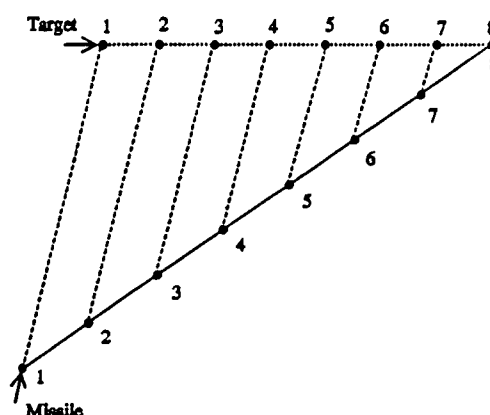


Figure 2 Constant-Bearing Guidance

The third guidance scheme, proportional navigation guidance, is the most widely used guidance law. Proportional navigation was first successfully used with the Lark missile in 1950. Since that first success in 1950, proportional navigation has been used in almost every tactical radar guided missile in the world [1]. Proportional navigation was developed due to the fact that constant-bearing guidance resulted in a collision course even with a maneuvering target. To be able to approximate a constant-bearing course, the missile heading rate is made proportional to the missile-target LOS rate, which keeps the LOS from rotating. If the missile is launched on a collision course, the heading rate is zero and the bearing angle is constant. If the missile is not launched on a collision course, there will be some correction in the heading rate so the bearing angle can be driven to a constant. This guidance law is simple, effective and easy to implement and the maximum missile acceleration is less than what is required for pursuit guidance. Proportional navigation has difficulty in engagements where the target velocity is much larger than the missile velocity and when the target is highly maneuverable. This guidance law also assumes that the missile is able to respond to changes in the LOS immediately.

With the advancement of technology in the areas of aircraft and missile survivability and maneuverability, improved methods for missile homing guidance are necessary. The goals for the improved guidance laws are to make the missile more reliable, more effective, less sensitive to target maneuvers and increase the missiles operating range. The performance of these guidance laws, which is measured by the miss distance between missile and target, must also be improved upon. There is a choice as to how the performance of the missile can be improved, by developing more sophisticated hardware or more sophisticated software. The existing classical guidance and control schemes are easy to implement but require complex hardware to improve their performance. New modern guidance and control techniques can be developed which have better, more complex solutions that do not require complex hardware. This makes it more feasible to develop a new homing guidance law using modern guidance and control techniques. Figure 3 demonstrates the modern missile guidance and control approach in block diagram form.

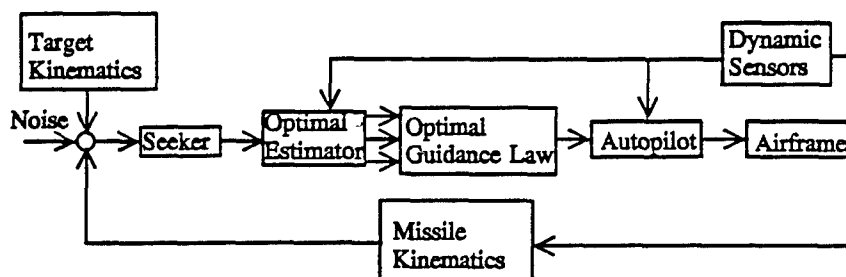


Figure 3 Modern Missile Guidance and Control

In this study, polar coordinates are used to obtain a closed form solution for an optimal guidance law for a target-intercept problem [3]. The reason for formulating this problem in polar coordinates is that polar coordinates are the natural reference system to solve the target-intercept problem since the measurements are bearing angle, range and range rate. In order to obtain a closed form solution for the commanded accelerations in the radial and transverse directions, the equations of the intercept dynamics must be decoupled. To decouple the dynamic equations a pseudo-control is introduced in the radial direction, which produces an optimal control problem in each direction. The closed form solution in the radial direction is found through the use of the pseudo-control and the closed form solution in the transverse direction is found by using the state transition matrix of the intercept dynamics. The closed form solution for the optimal guidance law for the target-intercept problem can then be compared with two forms of proportional navigation, namely IPN [5] and TPN [6].

The estimates of states are used in guidance laws. The objective of an optimal estimator/filter is to provide accurate estimates of the states of the system and model parameters of the optimal guidance law. These estimates depend on many factors, such as, measurements, assumed model structure, inputs to the system and many others. Modern estimation methods use measurements and known relationships between various system parameters to determine the required information needed by the optimal guidance law.

Many typical filters are developed in rectangular coordinates where the measurements are nonlinear. It has been suggested that better performance may be possible if polar coordinates are used [10,12,13]. In this study the optimal estimator/filter for the optimal guidance law will be developed in polar coordinates. In the target-intercept problem the dynamics are developed in polar coordinates where the states are range, range rate, LOS, and LOS rate. In the filter there will be angle measurements only (LOS). The other parameters will be determined based on *a priori* information about the states.

This study presents the formulation of the target-intercept problem in two dimensions and a detailed derivation of the optimal guidance law in polar coordinates. The transverse commanded acceleration, as a closed form solution to the two-point boundary-value problem, is developed using the state transition matrix of the intercept dynamics. A comparison of existing classical guidance laws with the new optimal guidance law is made. To complete the design a detailed derivation and implementation of a optimal estimator/filter is demonstrated. Section 2 will establish the two dimensional target-intercept problem in polar coordinates. The dynamic equations will be decoupled using a pseudo-control in the radial direction. A closed form solution for the optimal guidance law in the radial and transverse direction will be derived. The closed form solution for the optimal guidance law in the transverse direction results in a two-point boundary-value problem. Section 3 will present a closed form solution for the commanded acceleration in the transverse direction through the use of the state transition matrix of the intercept dynamics. Section 4 will look at D , a design parameter for the optimal guidance law, and approximations for the expression for D are investigated. The resulting solutions will then be compared to an iterative method to solve the same homing missile guidance problem. Section 5 will contain a comparison of the new optimal guidance law with two existing forms of proportional navigation, for a maneuvering and non-maneuvering target. The LOS rate and commanded acceleration, for IPN and TPN will be compared with the resulting LOS rate and commanded acceleration for the new guidance law. A comparison of the ability to intercept a maneuvering and non-maneuvering target will also be presented. A detailed derivation of the approximate analytical estimator/filter will be presented in Section 6. Results for the state estimates and error covariance from a three-degree-of-freedom simulation will be compared with simulation results for an extended Kalman filter using numerical iteration for the propagation of the states and error covariances. Section 7 will contain the conclusions and discuss the future work.

II. OPTIMAL GUIDANCE LAW IN DECOUPLED POLAR COORDINATES

Homing missile guidance is a two-point guidance system which uses the LOS rate to guide the missile towards its target. Proportional navigation and its derivatives are known to be effective LOS rate guidance systems [4,7,8,9]. With the need for improved missile performance, new methods for missile guidance have been investigated using modern control techniques. One area that is being investigated is optimal linear guidance laws [10,11,12]. This type of guidance law is typically developed in Cartesian coordinates with the relative positions, relative velocities and target accelerations as the states. These states are then used to determine the LOS rate which

is needed to guide the missile. In this section, an optimal homing missile guidance law will be developed in polar coordinates which are the natural coordinate system for a missile engagement. This allows the LOS rate to be one of the states of the system which will be found directly.

PROBLEM FORMULATION

The dynamics of a two dimensional target-intercept problem as shown in Figure 4, can be described in inertial polar coordinates by two coupled nonlinear differential equations as

$$\ddot{r} - r\dot{\theta}^2 = a_{T_r} - a_{M_r} \quad (2-1)$$

$$r\ddot{\theta} + 2\dot{r}\dot{\theta} = a_{T_\theta} - a_{M_\theta} \quad (2-2)$$

In these equations r is the relative range between the target and the missile, θ is the bearing angle, a_{T_r} and a_{T_θ} are the target accelerations in the radial and transverse directions respectively, and a_{M_r} and a_{M_θ} are the missile commanded accelerations in the radial and transverse directions respectively. Dots denote differentiation with respect to time. The target-intercept problem can be expanded into three dimensions by adding the dynamics in the elevation direction.

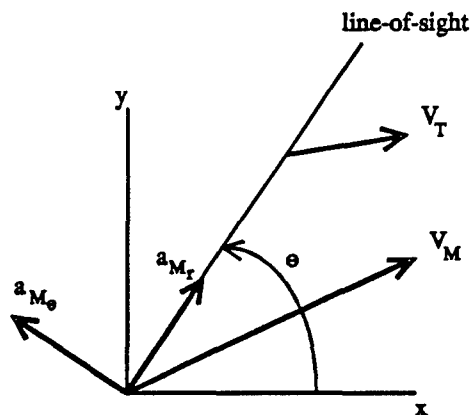


Figure 4 Engagement Geometry

In order to decouple the dynamics in the radial and transverse directions, a pseudo-control is defined in the radial direction as

$$a_{M,r} = a_{M_r} - r\dot{\theta}^2 . \quad (2-3)$$

By introducing the pseudo-control the dynamics in the radial and transverse directions are decoupled. This allows the commanded acceleration in each direction to be developed independent of the other.

The commanded accelerations will be determined by designing terminal controllers in the radial and transverse directions, which are used to bring each system close to desired conditions at the terminal time.

RADIAL (LINE OF SIGHT) COMMANDED ACCELERATION

The equation of motion in the radial direction can be put into a state space form as

$$\dot{y} = \begin{bmatrix} r & \dot{r} & a_{M,r} \end{bmatrix}^T , \quad (2-4)$$

where

$$\dot{y}_1 = y_2 , \quad (2-5)$$

$$\dot{y}_2 = y_3 - a_{M,r} , \quad (2-6)$$

$$\dot{y}_3 = -\lambda_r y_3 . \quad (2-7)$$

In Eq. (2-7), λ_r is the inverse time constant, $\frac{1}{\tau}$, associated with the radial target acceleration.

The optimal guidance law in the radial direction is obtained as a solution to minimizing the performance index, J_r , to achieve small terminal miss distances while maintaining acceptable levels of pseudo-control. The performance index in the radial direction can be written as

$$J_r = \frac{1}{2} S_f y_{1_f}^2 + \frac{1}{2} \int_0^{t_f} \gamma a_{M,r}^2 dt . \quad (2-8)$$

In Eq. (2-8), S_f is the weight on the terminal miss distance, y_{1_f} , and γ is the weight on the pseudo-control effort. The time-to-go, t_f , is approximated as $\frac{r}{|\dot{r}|}$, assuming that the relative velocity along the line-of-sight is maintained at a constant.

The pseudo-control which minimizes the performance index in Eq. (2-8) is found to be

$$a_{M_r}(t) = \frac{(t_f - t)}{\gamma} \lambda_1, \quad (2-9)$$

where λ_1 is the Lagrangian multiplier which adjoins the state in Eq. (2-6) to the performance index in Eq. (2-8).

The Lagrangian multiplier can be written as

$$\lambda_1(t) = \frac{S_{f_r} \left[y_1(t) + t_f y_2(t) + \frac{y_3(0)}{\lambda_r^2} (\exp(-\lambda_r t_f) + t_f \lambda_r - 1) \right]}{1 + \frac{S_{f_r} t_f^3}{3\gamma}}. \quad (2-10)$$

The instantaneous values of the relative range, $y_1(t)$, and relative range rate, $y_2(t)$, can be obtained through the integration of Eqs. (2-5), (2-6) and (2-7) as

$$y_1(t) = y_1(0) + t y_2(0) + \frac{y_3(0)}{\lambda_r^2} [\exp(-\lambda_r t) + t \lambda_r - 1] - \frac{(3t_f - t)t^2 \lambda_1}{6\gamma}, \quad (2-11)$$

$$y_2(t) = y_2(0) + \frac{y_3(0)}{\lambda_r} (1 - \exp(-\lambda_r t)) - \frac{t_f \lambda_1}{\gamma} + \frac{[t^2 \lambda_1]}{2\gamma}. \quad (2-12)$$

The actual missile commanded acceleration in the radial direction can be obtained from Eq. (2-3) as

$$a_{M_r}(t) = a_{M_{r1}}(t) + r(t) \dot{\theta}^2(t). \quad (2-13)$$

TRANSVERSE COMMANDED ACCELERATION

The decoupled equation of motion in the transverse direction, given by Eq. (2-2), can be rewritten as

$$\ddot{\theta} = -\frac{2\dot{r}\dot{\theta}}{r} + \frac{1}{r} a_{T_0} - \frac{1}{r} a_{M_\theta}. \quad (2-14)$$

Since r and \dot{r} are known from Eq. (2-11) and (2-12) they can be treated as functions of time only. This allows Eq. (2-14) to be expressed as a time-varying linear differential equation,

$$\ddot{\theta} = f(t) \dot{\theta} + g(t) a_{T_0} - g(t) a_{M_\theta}, \quad (2-15)$$

where $f(t) = -\frac{2\dot{r}}{r}$ and $g(t) = \frac{1}{r}$. The equation of motion in Eq. (2-15) can be put into a state space form as

$$z = [\theta \quad \dot{\theta} \quad a_{T_0}]^T, \quad (2-16)$$

where

$$\dot{z}_1 = z_2, \quad (2-17)$$

$$\dot{z}_2 = f(t)z_2 + g(t)a_{T_0} - g(t)a_{M_0}, \quad (2-18)$$

$$\dot{z}_3 = -\lambda_0 z_3. \quad (2-19)$$

In Eq. (3-19), λ_0 is the inverse time constant, $\frac{1}{\tau}$, associated with the transverse target acceleration.

The optimal guidance law in the transverse direction is obtained as a solution to minimizing the performance index, J_θ , to achieve small terminal angular rates while maintaining small angular rates and acceptable levels of control throughout the engagement. The performance index in the transverse direction can be written as

$$J_\theta = \frac{1}{2}S_f z_f^2 + \frac{1}{2} \int_0^{t_f} (\gamma_1 z_2^2 + \gamma_2 a_{M_0}^2) dt. \quad (2-20)$$

In Eq. (2-20), S_f is the weight on the final line-of-sight rate and γ_1 and γ_2 are the weights on the line-of-sight rate and the transverse commanded acceleration respectively.

The optimization of Eq. (2-20), which produces the minimizing control, results in a two-point boundary value problem:

$$\begin{bmatrix} \dot{z}_2 \\ \dot{\lambda}_2 \end{bmatrix} = \begin{bmatrix} f(t) & -\frac{g^2(t)}{\gamma_2} \\ -\gamma_1 & -f(t) \end{bmatrix} \begin{bmatrix} z_2 \\ \lambda_2 \end{bmatrix} + \begin{bmatrix} g(t)z_3(0)\exp(-\lambda_0 t) \\ 0 \end{bmatrix}, \quad (2-21)$$

where λ_2 is the Lagrangian multiplier which adjoins the states in Eq. (2-27) with the performance index in Eq. (2-20). The two-point boundary value problem can be solved numerically, by using the shooting method, or analytically if functional forms of $f(t)$ and $g(t)$ are known.

The minimizing control, a_{M_0} , in the transverse direction can be written as

$$a_{M_0} = \frac{g(t) \lambda_2}{\gamma_2} . \quad (2-22)$$

III. AN OPTIMAL GUIDANCE LAW SOLUTION USING STATE TRANSITION MATRIX

In this section, a solution to the two-point boundary value problem in Eq. (2-21) will be accomplished by using the state transition matrix of the intercept dynamics. This will produce a closed form solution for the minimizing control in the transverse direction. The solution to the two-point boundary value problem will first be found for a non-maneuvering target [2] and then the solution for a maneuvering target will be added.

NON-MANEUVERING TARGET

Without target acceleration Eq. (2-21) can be written as

$$\dot{x}(t) = A(t)x(t) , \quad (3-1)$$

where $x(t) = [z_2(t) \quad \lambda_2(t)]^T$ and $A(t)$ is

$$A(t) = \begin{bmatrix} f(t) & -\frac{g^2(t)}{\gamma_2} \\ -\gamma_1 & -f(t) \end{bmatrix} . \quad (3-2)$$

The solution to the homogeneous differential equation in Eq. (3-1) is

$$x(t) = \phi(t, \tau)x(\tau) , \quad (3-3)$$

where $\phi(t, \tau)$ is the state transition matrix, which can be written in matrix form as

$$\phi(t, \tau) = \begin{bmatrix} \phi_{11}(t, \tau) & \phi_{12}(t, \tau) \\ \phi_{21}(t, \tau) & \phi_{22}(t, \tau) \end{bmatrix} . \quad (3-4)$$

The state transition matrix can be found by solving the following equation:

$$\dot{\phi}(t, \tau) = A(t)\phi(t, \tau) ; \quad \text{with } \phi(\tau, \tau) = I, \quad (3-5)$$

where $A(t)$ comes from Eq. (3-2), $\phi(\tau, \tau)$ are the boundary conditions and I is the identity matrix. The time, τ , can be selected based on when the states, $x(\tau)$, are known (usually the states can be found at time, $\tau = 0$).

The earlier assumption, in Section 2, that the closing velocity is constant, can be translated to

$$r(t) = -\dot{r}(t)(t_f - t) . \quad (3-6)$$

Using this assumption, $f(t)$ and $g(t)$ can be written as explicit functions of time as

$$f(t) = \frac{2}{(t_f - t)} , \quad (3-7)$$

$$g(t) = \frac{t_f}{r_0(t_f - t)} . \quad (3-8)$$

By substituting Eqs. (3-7) and (3-8) into Eq. (3-2), $A(t)$ becomes

$$A(t) = \begin{bmatrix} \frac{2}{(t_f - t)} & -\frac{F}{(t_f - t)^2} \\ -\gamma_1 & -\frac{2}{(t_f - t)} \end{bmatrix} , \quad (3-9)$$

$$\text{where } F = \frac{t_f^2}{r_0^2 \gamma_2} \text{ or } F = \frac{1}{t_0^2 \gamma_2} .$$

Using Eq. (3-9) in Eq. (3-5) produces four scalar homogeneous differential equations,

$$\dot{\phi}_{11}(t, \tau) = \frac{2}{(t_f - t)} \phi_{11}(t, \tau) - \frac{F}{(t_f - t)^2} \phi_{21}(t, \tau) , \quad (3-10)$$

$$\dot{\phi}_{12}(t, \tau) = \frac{2}{(t_f - t)} \phi_{12}(t, \tau) - \frac{F}{(t_f - t)^2} \phi_{22}(t, \tau) , \quad (3-11)$$

$$\dot{\phi}_{21}(t, \tau) = -\gamma_1 \phi_{11}(t, \tau) - \frac{2}{(t_f - t)} \phi_{21}(t, \tau) , \quad (3-12)$$

$$\dot{\phi}_{22}(t, \tau) = -\gamma_1 \phi_{12}(t, \tau) - \frac{2}{(t_f - t)} \phi_{22}(t, \tau) . \quad (3-13)$$

In order to solve the four homogeneous differential equations, each equation can be converted into a function of a single dependent variable as shown.

$$\tilde{\Phi}_{11}(t, \tau) = \frac{2}{(t_f - t)} \phi_{11}(t, \tau) + \frac{(F\gamma_1 + 2)}{(t_f - t)^2} \phi_{11}(t, \tau) . \quad (3-14)$$

$$\tilde{\Phi}_{12}(t, \tau) = \frac{2}{(t_f - t)} \phi_{12}(t, \tau) + \frac{(F\gamma_1 + 2)}{(t_f - t)^2} \phi_{12}(t, \tau) , \quad (3-15)$$

$$\tilde{\Phi}_{21}(t, \tau) = \frac{(F\gamma_1 + 2)}{(t_f - t)^2} \phi_{21}(t, \tau) , \quad (3-16)$$

$$\tilde{\Phi}_{22}(t, \tau) = \frac{(F\gamma_1 + 2)}{(t_f - t)^2} \phi_{22}(t, \tau) . \quad (3-17)$$

If we assume a solution for $\phi_{21}(t, \tau)$ of the form

$$\phi_{21}(t, \tau) = K(t_f - t)^b , \quad (3-18)$$

$$\dot{\phi}_{21}(t, \tau) = -Kb(t_f - t)^{b-1} , \quad (3-19)$$

$$\ddot{\phi}_{21}(t, \tau) = Kb(b-1)(t_f - t)^{b-2} , \quad (3-20)$$

where K is a constant. Eqs. (3-18) - (3-20) can be used in Eq. (3-16) to produce a quadratic equation in b as

$$b^2 - b - (F\gamma_1 + 2) = 0 . \quad (3-23)$$

The resulting solution for b is

$$b = \frac{1}{2} \pm \frac{1}{2} D , \quad (3-22)$$

where

$$D = \sqrt{9 + 4F\gamma_1} . \quad (3-23)$$

The solution for $\phi_{21}(t, \tau)$ can now be written as

$$\phi_{21}(t, \tau) = A_1(t_f - t)^{-\frac{1}{2}(D-1)} + A_2(t_f - t)^{\frac{1}{2}(D+1)}, \quad (3-24)$$

where A_1 and A_2 are constants to be determined from the boundary conditions in Eq. (3-5). Knowing that at $t = \tau$ the boundary condition for $\phi_{21} = 0$, we can solve Eq. (3-24) for A_1 in terms of A_2 as

$$A_1 = -A_2(t_f - \tau)^D. \quad (3-25)$$

We will now use Eq. (3-12) to obtain $\phi_{11}(t, \tau)$ as a function of $\phi_{21}(t, \tau)$ and $\dot{\phi}_{21}(t, \tau)$, which can be written as

$$\phi_{11}(t, \tau) = -\frac{1}{\gamma_1} \left[\frac{2}{(t_f - t)} \phi_{21}(t, \tau) + \dot{\phi}_{21}(t, \tau) \right]. \quad (3-26)$$

$\dot{\phi}_{21}(t, \tau)$ in Eq. (3-26) can be found by differentiating Eq. (3-24) with respect to time. Substituting for $\phi_{21}(t, \tau)$ and $\dot{\phi}_{21}(t, \tau)$ in Eq. (3-26) produces a solution for $\phi_{11}(t, \tau)$ as a function of A_1 and A_2 which can be written as

$$\phi_{11}(t, \tau) = -\frac{1}{2\gamma_1} [A_1(D+3)(t_f - t)^{-\frac{1}{2}(D+1)} - A_2(D-3)(t_f - t)^{\frac{1}{2}(D-1)}]. \quad (3-27)$$

Knowing that at $t = \tau$ the boundary condition for $\phi_{11} = 1$, and A_1 as a function of A_2 from Eq. (3-27), we can solve for A_2 as

$$A_2 = \frac{\gamma_1(t_f - \tau)^{-\frac{1}{2}(D-1)}}{D}. \quad (3-28)$$

Substituting Eq. (3-28) into Eq. (3-25) gives the solution for A_1 as

$$A_1 = -\frac{\gamma_1(t_f - \tau)^{\frac{1}{2}(D+1)}}{D}. \quad (3-29)$$

Since A_1 and A_2 are known, ϕ_{11} and ϕ_{21} can be found at any time t , provided that the initial time τ is known.

If we assume the same type of solution for $\phi_{22}(t, \tau)$ as was chosen for $\phi_{21}(t, \tau)$, $\phi_{22}(t, \tau)$ can be written as

$$\phi_{22}(t, \tau) = A_3(t_f - t)^{-\frac{1}{2}(D-1)} + A_4(t_f - t)^{\frac{1}{2}(D+1)} . \quad (3-30)$$

where A_3 and A_4 are constants that can be determined in the same manner as A_1 and A_2 . The resulting solutions for A_3 and A_4 are

$$A_3 = \frac{(D - 3)}{2D(t_f - \tau)^{-\frac{1}{2}(D-1)}} , \quad (3-31)$$

$$A_4 = \frac{(D + 3)}{2D(t_f - \tau)^{\frac{1}{2}(D+1)}} . \quad (3-32)$$

Since A_3 and A_4 are known, ϕ_{12} and ϕ_{22} can be found at any time t provided that the initial time τ is known. The solution for $\phi(t, \tau)$ is now complete.

In order to solve Eq. (3-3) for the states at time t , we must be able to determine the states at time τ . The states at time τ can be found by evaluating the states at the final time, t_f . From Eq. (3-3) the final states are

$$\lambda_2(t_f) = \phi_{21}(t_f, \tau) z_2(\tau) + \phi_{22}(t_f, \tau) \lambda_2(\tau) , \quad (3-33)$$

$$z_2(t_f) = \phi_{11}(t_f, \tau) z_2(\tau) + \phi_{12}(t_f, \tau) \lambda_2(\tau) . \quad (3-34)$$

From the terminal term of the performance index, $\lambda_2(t_f)$ is known to be

$$\lambda_2(t_f) = S_{f_0} z_2(t_f) . \quad (3-35)$$

By substituting Eq. (3-34) into Eq. (3-35), $\lambda_2(t_f)$ can be found as a function of $\lambda_2(\tau)$ and $z_2(\tau)$ as

$$\lambda_2(t_f) = S_{f_0} [\phi_{11}(t_f, \tau) z_2(\tau) + \phi_{12}(t_f, \tau) \lambda_2(\tau)] . \quad (3-36)$$

By setting Eq. (3-36) equal to Eq. (3-33), $\lambda_2(\tau)$ can be found as a function of $z_2(\tau)$ as

$$\lambda_2(\tau) = \frac{[S_{f_0} \phi_{11}(t_f, \tau) - \phi_{21}(t_f, \tau)]}{[\phi_{22}(t_f, \tau) - S_{f_0} \phi_{12}(t_f, \tau)]} z_2(\tau) . \quad (3-37)$$

If the terminal line of sight rate, $z_2(t_f)$, is zero, Eq. (3-34) can be used to solve for $\lambda_2(\tau)$ as

$$\lambda_2(\tau) = -\frac{\phi_{11}(t_f, \tau)}{\phi_{12}(t_f, \tau)} z_2(\tau) . \quad (3-38)$$

In the target-intercept problem the line-of-sight rate, z_2 , is known at the initial time, $\tau = 0$ and $\phi(t_f, \tau)$ can be determined at $\tau = 0$, so λ_2 can be found at the initial time. The solution for the Lagrangian multiplier at the initial time, after some algebra, can be written as

$$\lambda_2(0) = \frac{(D+3)}{2} \frac{\gamma_2 r_0^2}{t_f} z_2(0) . \quad (3-39)$$

The resulting solution to the homogeneous differential equation in Eq. (3-3) is

$$\dot{\theta}(t) = \left(1 - \frac{t}{t_f}\right)^{\frac{1}{2}(D-1)} \dot{\theta}_0 , \quad (3-40)$$

$$\lambda_2(t) = \frac{(D+3)}{2} \gamma_2 t_f r_0^2 \left(1 - \frac{t}{t_f}\right)^{\frac{1}{2}(D+1)} \dot{\theta}_0 . \quad (3-41)$$

By substituting Eq. (3-41) into Eq. (2-22), the minimizing control in the transverse direction can be expressed as

$$a_{M_0}(t) = -\frac{(D+3)}{2} \dot{r}_0 \dot{\theta}_0 \left(1 - \frac{t}{t_f}\right)^{\frac{1}{2}(D-1)} , \quad (3-42)$$

where the notation for $z_2(0)$, the line-of-sight rate, has been changed to $\dot{\theta}_0$ (the typical notation). If $t = 0$ is assumed to be the current time, the minimizing control in the transverse direction with a non-maneuvering target becomes

$$a_{M_0} = -\frac{(D+3)}{2} \dot{r}_0 \dot{\theta}_0 . \quad (3-43)$$

MANEUVERING TARGET

The solution to the two-point boundary value problem for a maneuvering target can be obtained by adding the target acceleration to Eq. (3-1), which gives

$$\dot{x}(t) = A(t)x(t) + B(t)u(t) , \quad (3-44)$$

where $u(t) = [z_3(0) \exp(-\lambda_0 t)]$ and $B(t) = [g(t) \ 0]^T$ from Eq. (2-21).

The solution to Eq. (3-44) can be written as

$$x(t) = \phi(t,0)x(0) + \int_0^t \phi(t,\tau)B(\tau)u(\tau)d\tau . \quad (3-45)$$

In Eq. (3-45), $\phi(t,\tau)$ and $\phi(t,0)$ are known from the solution to the two-point boundary value problem for a non-maneuvering target. Eq. (3-45) produces two scalar equations for z_2 and λ_2 , which can be written as

$$z_2(t) = \phi_{11}(t,0)z_2(0) + \phi_{12}(t,0)\lambda_2(0) + q_1(t) , \quad (3-46)$$

$$\lambda_2(t) = \phi_{21}(t,0)z_2(0) + \phi_{22}(t,0)\lambda_2(0) + q_2(t) , \quad (3-47)$$

where

$$q_1(t) = \frac{z_3(0)t_f}{r_0} \int_0^t \frac{\phi_{11}(t,\tau)}{(t_f - \tau)} \exp(-\lambda_3 \tau) d\tau \quad (3-48)$$

and

$$q_2(t) = \frac{z_3(0)t_f}{r_0} \int_0^t \frac{\phi_{21}(t,\tau)}{(t_f - \tau)} \exp(-\lambda_3 \tau) d\tau . \quad (3-49)$$

In order to solve Eqs. (3-46) and (3-47) for the states at time t , we must be able to determine the states at the initial time. The states at the initial time can be found by evaluating the states at the final time, as was done for the non-maneuvering case. From Eqs. (3-46) and (3-47) the final states are

$$z_2(t_f) = \phi_{11}(t_f,0)z_2(0) + \phi_{12}(t_f,0)\lambda_2(0) + q_1(t_f) , \quad (3-50)$$

$$\lambda_2(t_f) = \phi_{21}(t_f,0)z_2(0) + \phi_{22}(t_f,0)\lambda_2(0) + q_2(t_f) , \quad (3-51)$$

where $q_1(t_f)$ and $q_2(t_f)$ are the evaluation of Eqs. (3-48) and (3-49) at the final time. Since $\lambda_2(t_f)$ is known from Eq. (3-35), and the line-of-sight is known at the initial time, $\lambda_2(0)$ can be found using Eqs. (3-50) and (3-51) as

$$\lambda_2(0) = \frac{[S_{f_0}\phi_{11}(t_f,0) - \phi_{21}(t_f,0)]}{[\phi_{22}(t_f,0) - S_{f_0}\phi_{12}(t_f,0)]} z_2(0) + \frac{[S_{f_0}q_1(t_f) - q_2(t_f)]}{[\phi_{22}(t_f,0) - S_{f_0}\phi_{12}(t_f,0)]} . \quad (3-52)$$

The first term of Eq. (3-52) is the same as the result for $\lambda_2(0)$ for the non-maneuvering target. The second term in Eq. (3-52) is due to the target acceleration. The solution for $\lambda_2(0)$, after some algebra can now be written as

$$\lambda_2(0) = \frac{(D+3)}{2} \frac{\gamma_2 r_0^2}{t_f} z_2(0) + (D+3) \gamma_2 r_0 s_1 z_3(0) \exp(-\lambda_0 t_f), \quad (3-53)$$

where

$$s_1 = \left[\frac{1}{(D+1)} + \frac{\lambda_0 t_f}{(D+3)} + \frac{\lambda_0^2 t_f^2}{2!(D+5)} + \dots \right]. \quad (3-54)$$

Note that s_1 is a function of the target acceleration model.

The resulting solution to the differential equation in Eq. (3-45) is

$$\dot{\theta}(t) = \left(1 - \frac{t}{t_f}\right)^{\frac{(D-1)}{2}} \dot{\theta}_0 + \frac{2}{t_0} \left[(3s_4 - s_5) - \left(1 - \frac{t}{t_f}\right)^{\frac{(D-1)}{2}} (3s_2 - s_3) \right] a_{T_0}(0) \exp(-\lambda_0 t_f), \quad (3-55)$$

$$\begin{aligned} \lambda_2(t) = & \frac{(D+3)}{2} \gamma_2 t_f^2 \dot{\theta}_0^2 \left(1 - \frac{t}{t_f}\right)^{\frac{(D+1)}{2}} \dot{\theta}_0 + \left[\frac{6(D+3)}{D} r_0 \gamma_2 \left(1 - \frac{t}{t_f}\right)^{\frac{(D+1)}{2}} \right] s_1 a_{T_0}(0) \exp(-\lambda_0 t_f) \\ & + \left[\frac{4\gamma_1 t_f}{t_0} \left(1 - \frac{t}{t_f}\right) \left(\frac{s_3}{D} \left(1 - \frac{t}{t_f}\right)^{\frac{1}{2}(D-1)} - s_4 \right) \right] a_{T_0}(0) \exp(-\lambda_0 t_f), \end{aligned} \quad (3-56)$$

where

$$s_2 = \left[\frac{1}{(D+1)(D-1)} + \frac{\lambda_0 t_f}{(D+3)(D-3)} + \frac{\lambda_0^2 t_f^2}{2!(D+5)(D-5)} + \dots \right], \quad (3-57)$$

$$s_3 = \left[\frac{1}{(D+1)(D-1)} + \frac{3\lambda_0 t_f}{(D+3)(D-3)} + \frac{5\lambda_0^2 t_f^2}{2!(D+5)(D-5)} + \dots \right], \quad (3-58)$$

$$s_4 = \left[\frac{1}{(D+1)(D-1)} + \frac{\lambda_0(t_f - t)}{(D+3)(D-3)} + \frac{\lambda_0^2(t_f - t)^2}{2!(D+5)(D-5)} + \dots \right], \quad (3-59)$$

$$s_5 = \left[\frac{1}{(D+1)(D-1)} + \frac{3\lambda_\theta(t_f-t)}{(D+3)(D-3)} + \frac{5\lambda_\theta^2(t_f-t)^2}{2!(D+5)(D-5)} + \dots \right]. \quad (3-60)$$

Note that s_2 , s_3 , s_4 and s_5 are all functions of the target acceleration model.

The minimizing control in the transverse direction for a maneuvering target can now be expressed as a function of time as

$$\begin{aligned} a_{M_\theta}(t) = & -\frac{(D+3)}{2} \dot{r}_0 \dot{\theta}_0 \left(1 - \frac{t}{t_f}\right)^{\frac{1}{2}(D-1)} - \frac{6(D+3)}{D} \left(1 - \frac{t}{t_f}\right)^{\frac{1}{2}(D-1)} s_1 a_{T_\theta}(0) \exp(-\lambda_\theta t_f) \\ & + (D^2 - 9) \left[s_4 - \frac{s_3}{D} \left(1 - \frac{t}{t_f}\right)^{\frac{1}{2}(D-1)} \right] a_{T_\theta}(0) \exp(-\lambda_\theta t_f), \end{aligned} \quad (3-61)$$

where the notation for $z_2(0)$, the line-of-sight rate and $z_3(0)$, the target acceleration have been changed to $\dot{\theta}_0$ and for $a_{T_\theta}(0)$ (the typical notation). If $t = 0$ is assumed to be the current time, the minimizing control in the transverse direction with a maneuvering target becomes

$$a_{M_\theta} = -\frac{(D+3)}{2} \dot{r}_0 \dot{\theta}_0 + (D+3) s_1 a_{T_\theta}(0) \exp(-\lambda_\theta t_f). \quad (3-62)$$

IV. DESIGN PARAMETER: D

In this section the expression for the design parameter D will be evaluated for various typical intercept scenarios. The range of values for D will be determined and the solutions for the commanded acceleration, for non-maneuvering and maneuvering targets will be obtained. Two methods for solving the two-point boundary value problem, for a maneuvering target, will be evaluated using a six-degree-of-freedom missile-target simulation. The two methods that will be used are the state transition matrix (STM) solution that has been presented in section 3, and an iterative shooting method (ITR) [16].

THE EXPRESSION FOR D

To this point the solution for the optimal guidance law in the transverse direction has been developed as a function of D , where D is

$$D = \sqrt{9 + 4F\gamma_1} . \quad (4-1)$$

By substituting $F = \frac{1}{\dot{r}_0^2 \gamma_2}$ into Eq. (4-1), D can be expressed as

$$D = \sqrt{9 + \frac{4}{\dot{r}_0^2} \frac{\gamma_1}{\gamma_2}} \quad (4-2)$$

The solution for D , in Eq. (4-2), will always be a positive quantity since the second term under the square root contains the weights, γ_1 and γ_2 , which are always selected to be positive and the initial relative range rate squared. Since \dot{r}_0 is squared the sign on the initial relative range rate does not matter.

From Eq. (4-2) the minimum value of D can be found. If the second term under the square root is small compared to the first term under the square root, the lower limit of D can be approximated as 3. If the second term under the square root is not small compared to the first term under the square root, the full equation for D must be used.

APPROXIMATING D AS 3

For many typical intercept scenarios, D can be approximated as 3. The reason for this approximation comes from the ratio of $\frac{\gamma_1}{\gamma_2}$ in Eq. (4-2). If the weight on the line-of-sight rate, γ_1 , is at most three orders of magnitude larger than the weight on the control effort, γ_2 , (ratio of $\frac{\gamma_1}{\gamma_2} \leq 1000$) then the approximation $D = 3$ holds, over the entire flight time, for intercept scenarios with initial ranges larger than 1000 feet.

If $D = 3$ appears in the numerator of a solution, the approximation $D = 3$ can be used, however if $D = 3$ appears in the denominator of a solution, as is the case for the maneuvering target, the full expression for D should be used since the second term under the square root becomes significant when it is in the denominator.

If $t = 0$ is considered to be the current time and D can be approximated as 3, the commanded acceleration for the STM solution with a non-maneuvering target can be written as

$$a_{M_0} = -3\dot{r}_0 \dot{\theta}_0 , \quad (4-3)$$

which is the standard proportional navigation equation.

Similarly, the commanded acceleration for the STM solution with a maneuvering target can be written as

$$a_{M_0} = -3\dot{\theta}_0 \dot{\theta}_0 + 6s_1 a_{T_0}(0) \exp(-\lambda_0 t_f), \quad (4-4)$$

where

$$s_1 = \left[\frac{1}{4} + \frac{\lambda_0 t_f}{6} + \frac{\lambda_0^2 t_f^2}{2!8} + \dots \right]. \quad (4-5)$$

USING THE COMPLETE EXPRESSION FOR D

If the weight on the line-of-sight rate, γ_1 , is more than three orders of magnitude larger than the weight on the control effort, γ_2 , (ratio of $\frac{\gamma_1}{\gamma_2} \geq 10000$) then the approximation $D = 3$ does not hold. In this case Eq. (4-2) must be used to determine D . During an engagement, if the full expression of D is used, the value of D is larger than 3 over the entire flight time.

TWO-POINT BOUNDARY-VALUE SOLUTION COMPARISON

A six-degree-of-freedom missile-target simulation was used to compare two methods for solving the two-point boundary value problem with a maneuvering target. The STM was evaluated using the complete expression for D and the approximation that $D = 3$. These methods were compared to an iterative method, which has an initial value specified for the lagrangian multiplier, λ_2 , and then iterates to find the optimal solution. In the simulation, the target performs a 9-g maneuver up and to the right, relative to its reference, until the time-to-go reaches 1 second when it rolls 180° and pulls 9-g's until conclusion. The results from the simulation are shown in Table 1.

Method	D	Range (ft.)	Aspect Angle (deg.)	Boresight Angle (deg.)	Miss Distance (ft.)	Flight Time (sec.)
STM	3	7000	60	0	0.236	3.97
ITR *	---	7000	60	0	9.345	3.97
STM	3	3000	60	0	1.76	2.37
ITR *	---	3000	60	0	122.62	2.36
STM	*3	7000	60	0	0.06	3.95
ITR	---	7000	60	0	0.71	3.95
STM	*3	3000	60	0	0.67	2.37
ITR	---	3000	60	0	2.4	2.38
STM	*3	3000	120	40	1.98	2.77
ITR	---	3000	120	40	1.98	2.77

Table 1

The first four runs were made with the ratio of $\frac{\gamma_1}{\gamma_2}$ equal to 1000. The remaining six runs were made with the ratio of $\frac{\gamma_1}{\gamma_2}$ larger than 1000. The ITR method uses an initial value of 100 for the Lagrangian multiplier.

The two runs made with the iterative method that are marked with the * had difficulty converging to an optimal solution. The result of this difficulty shows up in the large miss distances. The reason the ITR method had difficulty converging is because the Lagrangian multiplier is a nonlinear function. To correct the convergence problem one or more of the following things can be tried. Adjust the initial value for the Lagrangian multiplier or the number of iterations or the time step. The state transition matrix (STM) solution directly provides the optimal solution, with no difficulty, which results in much smaller miss distances for the same two scenarios.

Table 1 shows that the STM solution resulted in a smaller miss distances compared with the iterative solution for nine of the ten scenarios. The last run resulted in the miss distances for the two methods being equal. The run time for the simulation was also greatly reduced when the STM solution was used as apposed to the ITR method.

V. OPTIMAL GUIDANCE LAW COMPARISON WITH DIFFERENT NAVIGATION SCHEMES

In this section a comparison of the optimal guidance law solution (STM) that has been developed will be compared to two forms of proportional navigation. The two forms of proportional navigation are Ideal Proportional Navigation (IPN) [5] and True Proportional Navigation (TPN) [6]. The comparison will be done for a non-maneuvering and maneuvering target.

COMPARISON WITH IDEAL PROPORTIONAL NAVIGATION

In Ideal Proportional Navigation [5], the commanded acceleration, a_c , is applied normal to the relative velocity, v , and its magnitude is proportional to the line-of-sight rate. For a non-maneuvering target the equations of motion for the target-intercept problem are

$$\ddot{r} - r\dot{\theta}^2 = -Nr\dot{\theta}^2, \quad (5-1)$$

$$r\ddot{\theta} + 2\dot{r}\dot{\theta} = N\dot{r}\dot{\theta}, \quad (5-2)$$

where N is the effective proportional navigation constant.

The line-of-sight rate is found from Eq. (5-2) to be

$$\dot{\theta} = \dot{\theta}_0 \left(\frac{r}{r_0} \right)^{N-2}. \quad (5-3)$$

During the terminal flight phase $\dot{\theta}$ will go to infinity if $N < 2$ and to zero if $N > 2$.

The resulting commanded acceleration in the transverse direction is

$$a_{M_t} = N v_0 \dot{\theta}_0 \left(\frac{r}{r_0} \right)^{N-2}, \quad (5-4)$$

where the relative velocity is a constant. To avoid a_{M_t} going to infinity during the terminal flight phase, N must be chosen to be greater than 2.

We can compare Eqs. (5-3) and (5-4) with Eqs. (3-40) and (3-42) from the STM solution for a non-maneuvering target. The assumption made in section 3 that the closing velocity is constant, $r(t) = -\dot{r}(t)(t_f - t)$, produces the following substitution $(1 - \frac{t}{t_f}) = \frac{r}{r_0}$. If the angle between the relative velocity and the LOS is small, the substitution $-\dot{r}_0 = v_0$ can be made. Using these substitutions in Eqs. (3-40) and (3-42) produces

$$\dot{\theta} = \dot{\theta}_0 \left(\frac{r}{r_0} \right)^{\frac{1}{2}(D-1)}, \quad (5-5)$$

$$a_{M_t} = \frac{(D+3)}{2} v_0 \dot{\theta}_0 \left(\frac{r}{r_0} \right)^{\frac{1}{2}(D-1)}. \quad (5-6)$$

The equations for $\dot{\theta}$ and a_{M_t} for the two guidance law solutions, for a non-maneuvering target, are similar.

One difference that can be seen in Eqs. (5-5) and (5-6) is that $\dot{\theta}$ and a_{M_t} will always go to zero during the terminal flight phase since the minimum value of D is 3, which was shown in section 4. The reason that there is no restriction on D to keep $\dot{\theta}$ and a_{M_t} from going to infinity, as is the case for N in the IPN solution, is due to the fact that Eqs. (5-5) and (5-6) are the optimal solutions.

For a maneuvering target the equations of motion of the target-intercept problem are

$$\ddot{r} - r\dot{\theta}^2 = -Nr\dot{\theta}^2 + \frac{a_T}{v} r\dot{\theta}, \quad (5-7)$$

$$r\ddot{\theta} + 2\dot{r}\dot{\theta} = N\dot{r}\dot{\theta} - \frac{a_T}{v} \dot{r}, \quad (5-8)$$

where the target maneuver is always normal to the relative velocity.

The line-of-sight rate is found from Eq. (5-8) to be

$$\dot{\theta} = \dot{\theta}_0 \left(\frac{r}{r_0}\right)^{N-2} + \frac{a_T}{v_0(N-2)} \left[1 - \left(\frac{r}{r_0}\right)^{N-2}\right] \quad N \neq 2. \quad (5-9)$$

During the terminal flight phase, $\dot{\theta}$ goes to infinity if $N \leq 2$ and to $\frac{a_T}{v_0(N-2)}$ if $N > 2$. The first term of the line-of-sight rate is induced by the initial line of sight rate and the second term is induced by the maneuver of the target.

The resulting commanded acceleration in the transverse direction is

$$a_{M_0} = N v_0 \dot{\theta}_0 \left(\frac{r}{r_0}\right)^{N-2} + \frac{N a_T}{(N-2)} \left[1 - \left(\frac{r}{r_0}\right)^{N-2}\right] \quad N \neq 2, \quad (5-10)$$

where the relative velocity is constant. The second term in Eq. (5-10) is due to the target maneuver. To avoid a_{M_0} going to infinity during the terminal flight phase, N must be chosen to be greater than 2. With $N > 2$, the first term in Eq. (5-10) will go to zero, which results in a_{M_0} going to $\frac{N}{(N-2)} a_T$.

The target acceleration model used above, can be put in place of the exponential target acceleration model used in section 3 and alternate expressions for the LOS rate and commanded acceleration can be found. If the process in section 3 is followed, solutions for $\dot{\theta}$ and a_{M_0} are found to be

$$\dot{\theta} = \dot{\theta}_0 \left(1 - \frac{t}{t_f}\right)^{\frac{1}{2}(D-1)} - \frac{4 a_{T_0}}{r_0(D+1)(D-1)} \left[1 - \left(1 - \frac{t}{t_f}\right)^{\frac{1}{2}(D-1)}\right] \quad (5-11)$$

and

$$a_{M_0} = -\frac{D+3}{2} r_0 \dot{\theta}_0 \left(1 - \frac{t}{t_f}\right)^{\frac{1}{2}(D-1)} - \frac{(D+3) a_{T_0}}{(D+1)(D-1)} \left[D - 3 + 2 \left(1 - \frac{t}{t_f}\right)^{\frac{1}{2}(D-1)}\right]. \quad (5-12)$$

The second terms in Eqs. (5-11) and (5-12) are due to the target maneuver.

We can compare Eqs. (5-9) and (5-10) with Eqs. (5-11) and (5-12) from the STM solution for a maneuvering target. Using the same substitutions in Eqs. (5-11) and (5-12), that were used in the non-maneuvering target solution produces

$$\dot{\theta} = \dot{\theta}_0 \left(\frac{r}{r_0}\right)^{\frac{1}{2}(D-1)} + \frac{4 a_{T_0}}{v_0(D+1)(D-1)} \left[1 - \left(\frac{r}{r_0}\right)^{\frac{1}{2}(D-1)}\right], \quad (5-13)$$

$$a_{M_0} = \frac{D+3}{2} v_0 \dot{\theta}_0 \left(\frac{r}{r_0}\right)^{\frac{1}{2}(D-1)} - \frac{(D+3)a_{T_0}}{(D+1)(D-1)} \left[D - 3 + 2\left(\frac{r}{r_0}\right)^{\frac{1}{2}(D-1)} \right] . \quad (5-14)$$

The equations for $\dot{\theta}$ and a_{M_0} for the two guidance law solutions, for a maneuvering target, are also similar. One difference that can be seen during the terminal flight phase is, since the minimum value of D is 3, the first terms in Eqs. (5-11) and (5-12) will go to zero, which results in $\dot{\theta}$ always going to $\frac{4}{(D^2-1)} \frac{a_{T_0}}{v_0}$ and a_{M_0} always going to $-\frac{(D^2-9)}{(D^2-1)} a_{T_0}$. There is again no restriction on D to keep $\dot{\theta}$ and a_{M_0} from going to infinity, as is the case for N in the IPN solution, since Eqs. (5-11) and (5-12) are the optimal solutions. There exists a sign difference in the second term of the commanded acceleration because the reference frame for the IPN solution is located at the target where in the STM solution the origin is located at the missile.

COMPARISON WITH TRUE PROPORTIONAL NAVIGATION

In True Proportional Navigation [6], the commanded acceleration, a_c , is applied normal to the missile-target line-of-sight and its magnitude is proportional to the line-of-sight rate times a variable closing speed. For a non-maneuvering target the equations of motion for the target-intercept problem are

$$\ddot{r} - r\dot{\theta}^2 = 0 , \quad (5-15)$$

$$r\ddot{\theta} + 2\dot{r}\dot{\theta} = N\dot{\theta}^2 , \quad (5-16)$$

where N is the effective proportional navigation constant. To compare the following TPN solutions with the STM solutions we will assume the closing speed in the TPN solutions is constant, as was the case for the STM solution.

The line-of-sight rate is found to be the same as the line-of-sight rate for the IPN non-maneuvering target solution in Eq. (5-5), where $\dot{\theta}$ goes to infinity if $N < 2$ and to zero if $N > 2$.

The resulting commanded acceleration in the transverse direction is

$$a_{M_0} = N\dot{r}_0 \dot{\theta}_0 \left(\frac{r}{r_0}\right)^{N-2} . \quad (5-17)$$

To avoid a_{M_0} going to infinity, N must be chosen to be greater than 2.

We can compare Eq. (5-17) with Eq. (3-42) from the STM solution for a non-maneuvering target. Using the substitution, $(1 - \frac{t}{t_f}) = \frac{r}{r_0}$ in Eq. (3-42) produces

$$a_{M_0}(t) = -\frac{(D+3)}{2} \dot{r}_0 \dot{\theta}_0 \left(\frac{r}{r_0}\right)^{\frac{1}{2}(D-1)} . \quad (5-18)$$

The equations for $\dot{\theta}$ and a_{M_0} for the two guidance law solutions, for a non-maneuvering target, are similar. In Eqs. (5-5) and (5-18), $\dot{\theta}$ and a_{M_0} will always go to zero since the minimum value of D is 3. There is no restriction to keep $\dot{\theta}$ and a_{M_0} from going to infinity, as is the case for N in the TPN solution, since Eqs. (5-5) and (5-18) are the optimal solutions. The sign difference between the commanded acceleration in Eqs. (5-17) and (5-18) is because the origin of the reference frame for the TPN solution is located at the target where in the STM solution the origin is located at the missile.

For a maneuvering target the equations of motion of the target-intercept problem are

$$\ddot{r} - r\dot{\theta}^2 = 0 , \quad (5-19)$$

$$r\ddot{\theta} + 2\dot{r}\dot{\theta} = N\dot{r}\dot{\theta} - a_T , \quad (5-20)$$

where a_T is the magnitude of the target acceleration and is proportional to the closing speed as $a_T = -b\dot{r}$.

The line-of-sight rate is found from Eq. (5-20) to be

$$\dot{\theta} = \dot{\theta}_0 \left(\frac{r}{r_0}\right)^{N-2} + \frac{a_T}{\dot{r}_0(N-2)} \left[1 - \left(\frac{r}{r_0}\right)^{N-2}\right] \quad N \neq 2 . \quad (5-21)$$

During the terminal flight phase, $\dot{\theta}$ goes to infinity if $N \leq 2$ and to $\frac{a_T}{\dot{r}_0(N-2)}$ if $N > 2$. The first term of the line-of-sight rate is induced by the initial line of sight rate and the second term is induced by the maneuver of the target.

The resulting commanded acceleration in the transverse direction is

$$a_{M_0} = N\dot{r}\dot{\theta}_0 \left(\frac{r}{r_0}\right)^{N-2} + \frac{N\dot{r}a_T}{(N-2)\dot{r}_0} \left[1 - \left(\frac{r}{r_0}\right)^{N-2}\right] \quad N \neq 2 \quad (5-22)$$

The second term in Eq. (5-22) is due to the target maneuver. To avoid a_{M_0} going to infinity during the terminal flight phase, N must be chosen to be greater than 2. With $N > 2$, the first term in Eq. (5-25) will go to zero, which results in a_{M_0} going to $\frac{Na_T}{(N-2)}$.

We can compare Eqs. (5-21) and (5-22) with Eqs. (5-11) and (5-12) from the STM solution for a maneuvering target. Using the same substitution in Eqs. (5-11) and (5-12) that were used in the non-maneuvering solution produces

$$\dot{\theta} = \dot{\theta}_0 \left(\frac{r}{r_0}\right)^{\frac{1}{2}(D-1)} - \frac{4a_{T_0}}{r_0(D+1)(D-1)} \left[1 - \left(\frac{r}{r_0}\right)^{\frac{1}{2}(D-1)}\right], \quad (5-23)$$

$$a_{M_0} = -\frac{D+3}{2} \dot{r}_0 \dot{\theta}_0 \left(\frac{r}{r_0}\right)^{\frac{1}{2}(D-1)} - \frac{(D+3)a_{T_0}}{(D+1)(D-1)} \left[D - 3 + 2\left(\frac{r}{r_0}\right)^{\frac{1}{2}(D-1)}\right]. \quad (5-24)$$

The second terms in Eqs. (5-23) and (5-24) are due to the target maneuver. The equations for $\dot{\theta}$ and a_{M_0} for the two guidance law solutions, for a maneuvering target, are also similar. One difference that can be seen during the terminal flight phase is, since the minimum value of D is 3, the first terms in Eqs. (5-23) and (5-24) will go to zero, which results in $\dot{\theta}$ always going to $-\frac{4}{(D^2-1)} \frac{a_{T_0}}{\dot{r}_0}$ and a_{M_0} always going to $-\frac{(D^2-9)}{(D^2-1)} a_{T_0}$. There is again no restriction on D to keep $\dot{\theta}$ and a_{M_0} from going to infinity, as is the case for N in the TPN solution, since Eqs. (5-23) and (5-24) are the optimal solutions. The sign differences that occur in the LOS rate and commanded acceleration solutions are due to the fact that the origin of the reference frame for the TPN solution is located at the target where in the STM solution the origin is located at the missile.

VI. APPROXIMATE ANALYTICAL FILTER

Many filters for the target-intercept problem have been developed in rectangular coordinates where the measurements are nonlinear. In order to avoid the nonlinear measurement functions, filters have also been developed in polar coordinates where the measurements are linear [10,13-15]. These filters use extensive integration, at each time step, to arrive at numerical solutions for the state estimates (6 Eqs.) and the error covariance matrix (21 Eqs.). In this section an approximate analytical filter is developed in polar coordinates. The missile-target equations of motion, in polar coordinates, are used to determine the expressions for the propagation of the state estimates. The resulting state estimates are then used to determine the expressions for the propagation of the error covariance matrix. The numerical solutions for the state estimates and error covariance matrix can be determined by numerical computation, using the previous numerical estimates and error covariance matrix only. This approximate analytical filter is more time efficient than existing filters since there is no integration, at each time step, to determine the state estimates and error covariance matrix. The expressions for the state estimates and error covariance matrix, for the approximate analytical filter, are put into a 3-DOF missile-target flight simulation and the results for the state estimates and error covariance matrix are compared with the state estimates and error

covariance matrix for an extended Kalman filter.

STATE ESTIMATION

The state estimates can be determined by integrating the missile-target equations of motion with respect to time.

$$\ddot{r} - r\dot{\theta}^2 = a_{T_r} - a_{M_r}, \quad (6-1)$$

$$r\ddot{\theta} + 2\dot{r}\dot{\theta} = a_{T_\theta} - a_{M_\theta}. \quad (6-2)$$

The equations of motion can be written in a form that can be integrated to obtain the state estimates as

$$\ddot{r} = a_{T_r}(0)\exp(-\lambda_r t) + a_{M_r}, \quad (6-3)$$

$$\ddot{\theta} = \frac{2\dot{\theta}}{(t_f - t)} - \frac{a_{T_\theta}(0)\exp(-\lambda_\theta t)}{r_0(t_f - t)} + \frac{a_{M_\theta}}{r_0(t_f - t)}. \quad (6-4)$$

The state estimates in the radial direction can be found by integrating Eq (6-3) from t_k to t_{k+1} . The pseudo-control is assumed to be a constant over each time step. The resulting solution for the range rate estimate is

$$\dot{r}(t_{k+1}) = \dot{r}(t_k) + b_2[r(t_k)\dot{\theta}^2(t_k) - a_{M_r}] + c_3 a_{T_r}(t_k), \quad (6-5)$$

where

$$b_2 = t_{k+1}, \quad (6-6)$$

$$c_3 = \frac{[1 - \exp(-\lambda_r t_{k+1})]}{\lambda_r}. \quad (6-7)$$

The estimate of the range can be determined by integrating Eq (6-5) from t_k to t_{k+1} . The pseudo-control, $r(t_k)\dot{\theta}^2(t_k) - a_{M_r}$, is again assumed to be a constant over each time step. The resulting solution for the range estimate is

$$r(t_{k+1}) = r(t_k) + c_1 \dot{r}(t_k) + b_1 [r(t_k) \dot{\theta}^2(t_k) - a_{M_r}] + c_3 a_{T_r}(t_k) , \quad (6-8)$$

where

$$b_1 = \frac{t_{k+1}^2}{2} , \quad (6-9)$$

$$c_1 = t_{k+1} , \quad (6-10)$$

$$c_3 = \frac{[\lambda_r t_{k+1} - 1 + \exp(-\lambda_r t_{k+1})]}{\lambda_r^2} . \quad (6-11)$$

The estimate of the radial target acceleration is being modeled as a first order Markov process, which can be written as

$$a_{T_r}(t_{k+1}) = c_6 a_{T_r}(t_k) , \quad (6-12)$$

where

$$c_6 = \exp(-\lambda_r t_{k+1}) . \quad (6-13)$$

The state estimates in the transverse direction cannot be found by integrating Eq. (6-4) because the numerator and denominator, of the target acceleration term, are functions of time. This keeps the equation from being separated into two independent functions of the LOS and time. A transformation of variable is used to obtain an equation that can be integrated.

The transformation is accomplished by introducing a variable u as

$$u(t) = (t_f - t)^2 \dot{\theta}(t) . \quad (6-14)$$

The differential equation for u is (after some algebra)

$$\dot{u} = [a_{T_\theta}(t) - a_{M_\theta}] \frac{t_f}{r_0} (t_f - t) . \quad (6-15)$$

Eq. (6-15) can be integrated from t_k to t_{k+1} , to obtain $u(t_{k+1})$. Then Eq. (6-14) can be rearranged to obtain $\dot{\theta}(t_{k+1})$ as a function of $u(t_{k+1})$.

The resulting solution for the LOS rate state estimate is found to be

$$\dot{\theta}(t_{k+1}) = c_{10} \dot{\theta}(t_k) + c_{11} \frac{a_{T_0}(t_k)}{r(t_k)} + c_{12} \frac{1}{r(t_k)}, \quad (6-16)$$

where

$$c_{10} = \frac{t_f^2}{(t_f - t_{k+1})^2}, \quad (6-17)$$

$$c_{11} = \frac{t_f}{(t_f - t_{k+1})^2} \frac{[\lambda_\theta t_f - 1 - [\exp(-\lambda_\theta t_{k+1})](\lambda_\theta(t_f - t_{k+1}) - 1)]}{\lambda_\theta^2}, \quad (6-18)$$

$$c_{12} = \frac{a_{M_0} t_f}{2} \left[1 - \frac{t_f^2}{(t_f - t_{k+1})^2} \right]. \quad (6-19)$$

The estimate of the LOS can be determined by integrating Eq (6-16) from t_k to t_{k+1} . The resulting solution for the LOS estimate is

$$\theta(t_{k+1}) = \theta(t_k) + c_7 \dot{\theta}(t_k) + c_8 \frac{1}{r(t_k)} + c_9 \frac{a_{T_0}(t_k)}{r(t_k)}, \quad (6-20)$$

where

$$c_7 = t_f^2 \left[\frac{1}{(t_f - t_{k+1})} - \frac{1}{t_f} \right], \quad (6-21)$$

$$c_8 = \frac{a_{M_0} t_f}{2} \left[t_{k+1} - \frac{t_f^2}{(t_f - t_{k+1})} + t_f \right], \quad (6-22)$$

$$c_9 = \frac{t_f}{\lambda_\theta^2} \left[(\lambda_\theta t_f - 1) \left[\frac{1}{(t_f - t_{k+1})} - \frac{1}{t_f} \right] + \frac{[\exp(-\lambda_\theta t_{k+1})]}{(t_f - t_{k+1})} - \frac{1}{t_f} \right]. \quad (6-23)$$

The estimate of the transverse target acceleration is being modeled as a first order Markov process, which can be written as

$$a_{T_0}(t_{k+1}) = c_{13} a_{T_0}(t_k) , \quad (6-24)$$

where

$$c_{13} = \exp(-\lambda_0 t_{k+1}) . \quad (6-25)$$

A PRIORI CONDITIONAL ERROR COVARIANCE

The error covariance matrix is a 6x6 symmetric matrix. Each term in the matrix can be determined at time t_{k+1} from

$$p(k+1) = E[(x_{k+1} - \bar{x}_{k+1})(x_{k+1} - \bar{x}_{k+1})^T / z_k] , \quad (6-26)$$

where E is the expected value of the mean square error in the state, x , given the measurement, z_k , where z_k is the measurement history up to time k .

The error covariance matrix, $p(k+1)$, can be determined from using the state estimate equations developed above. The method for solving each term in the error covariance matrix will be demonstrated for $p_{11}(k+1)$. The solutions to the remainder of the terms are developed in the same manner and can be found in Reference 17. Using Eq. (6-26) and Eq. (6-8) $p_{11}(k+1)$ can be written as

$$p_{11}(k+1) = E[(r-r_e)_{k+1}(r-r_e)_{k+1}^T / \theta_k] , \quad (6-27)$$

where the subscript e denotes the estimate. $p_{11}(k+1)$ can be expanded to

$$\begin{aligned} p_{11}(k+1) = & E[(r-r_e)^2]_k + c_1^2 E[(\dot{r}-\dot{r}_e)^2]_k + b_1^2 E[(r\dot{\theta}^2 - r_e\dot{\theta}_e^2)^2]_k + c_3^2 E[(a_{T_r} - a_{T_{r_e}})^2] \\ & + 2c_1 E[(r-r_e)(\dot{r}-\dot{r}_e)]_k + 2b_1 E[(r-r_e)(r\dot{\theta}^2 - r_e\dot{\theta}_e^2)]_k + 2c_3 E[(r-r_e)(a_{T_r} - a_{T_{r_e}})]_k \\ & + 2c_1 b_1 E[(\dot{r}-\dot{r}_e)(r\dot{\theta}^2 - r_e\dot{\theta}_e^2)]_k + 2c_1 c_3 E[(\dot{r}-\dot{r}_e)(a_{T_r} - a_{T_{r_e}})]_k + 2b_1 c_3 E[(r\dot{\theta}^2 - r_e\dot{\theta}_e^2)(a_{T_r} - a_{T_{r_e}})]_k . \end{aligned} \quad (6-28)$$

All of the expected values in Eq. (6-28) are known at time k , except for the terms with $(r\dot{\theta}^2 - r_e\dot{\theta}_e^2)$ in them. The expected values with this term will have to be determined separately.

If the term with the coupled states (i.e. $r\dot{\theta}^2$) is assumed to be linear and is defined as $f(z)_k = (r\dot{\theta}^2)_k$, where

$z_k = [r \ \dot{\theta}]_k^T$, we can assume that $f(z_k) = (r_e \dot{\theta}_e^2)_k$. If this is done, $f(z)_k$ can be expanded in a Taylor series using the first two terms as

$$f(z)_k = f(z_e)_k + \frac{\partial f}{\partial z} \Big|_{z=(z_e)_k} (z - z_e)_k, \quad (6-29)$$

where $\frac{\partial f}{\partial z} \Big|_{z=(z_e)_k} = [\dot{\theta}_e^2 \ 2r_e \dot{\theta}_e]_k$.

Eq. (6-29) can be rearranged to produce

$$f(z)_k - f(z_e)_k = \frac{\partial f}{\partial z} \Big|_{z=(z_e)_k} (z - z_e)_k, \quad (6-30)$$

which results in

$$(r\dot{\theta}^2 - r_e \dot{\theta}_e^2) = [\dot{\theta}_e^2 (r - r_e) + 2r_e \dot{\theta}_e (\dot{\theta} - \dot{\theta}_e)] . \quad (6-31)$$

The other two terms with coupled states (i.e. $\frac{1}{r}$ and $\frac{a_{T_0}}{r}$) are determined in the same fashion [17].

If Eqs. (6-30) and (6-31) are used in Eq. (6-28) the solution for $p_{11}(k+1)$ can be written as

$$\begin{aligned} p_{11}(k+1) &= E[(r - r_e)(r - r_e)^T]_{k+1} \\ &= p_{11}(k) + c_1^2 p_{22}(k) + b_1^2 [\dot{\theta}_e^4 p_{11}(k) + 4r_e \dot{\theta}_e^3 p_{15}(k) + 4r_e^2 \dot{\theta}_e^2 p_{35}(k)] + 2b_1 [\dot{\theta}_e^2 p_{11}(k) + 2r_e \dot{\theta}_e p_{15}(k)] \\ &\quad + 2c_1 b_1 [\dot{\theta}_e^2 p_{12}(k) + 2r_e \dot{\theta}_e p_{25}(k)] + 2c_3 p_{13}(k) + 2c_1 c_3 p_{23}(k) + 2c_3 b_1 [\dot{\theta}_e^2 p_{13}(k) + 2r_e \dot{\theta}_e p_{35}(k)] \\ &\quad + 2c_1 p_{12}(k) + c_3^2 p_{33}(k) \end{aligned} \quad (6-32)$$

NUMERICAL RESULTS

A three-degree-of-freedom computer program, which simulates the intercept of a non-maneuvering target by a bank-to-turn, short-range, air-to-air homing missile has been used to compare the solutions for the state estimates and error covariance matrix of the approximate analytical filter with an extended Kalman filter, which uses

a fourth order Runge Kutta Integrator. The guidance scheme that computes the commanded acceleration is based on proportional navigation.

The engagement is characterized by the initial conditions: range, 3000 ft; altitude, 10,000 ft; aspect angle, 150 deg; and off-boresight angle, 0 deg. The diagonal elements of the initial state covariances are 100 ft² for the range, 100 ft²/sec² for the range rate, 0.1 rad² for the LOS, 0.1 rad²/sec² for the LOS rate, 10 ft²/sec⁴ for the radial target acceleration, and 1 ft²/sec⁴. The off-diagonal elements are zero.

Three different runs were made using each filter. In all of the figures the extended Kalman filter is represented by an * and the approximate analytical solution is represented by the solid line. The first run was made without updating the states or the error covariance matrix. This means that there are no corrections made to the states or the error covariance matrix based on the error between the true states and the state estimates. Figures 5-8 show the history of the state estimates, the commanded accelerations, the time-to-go, and the state error covariance solutions of the two filters. It can be seen from Figure 5, that the two filters estimate the states approximately the same. The commanded acceleration, in Figure 6, which is applied over the flight and the time-to-go approximation are also very close. The state covariances in Figure 7 are very close throughout the flight. The difference near the end of the flight time is because these are plots of the mean square error. The actual error is not as large as it may seem. The target acceleration error covariance plots in Figure 8 are exactly the same throughout the flight time for all three runs.

The second run was made without updating the states but the error covariance matrix was being updated. This means that there are no corrections made to the states due to the error between the true states and the state estimates, but corrections are made to the error covariance matrix based on the error between the true states and the state estimates. Figure 9 shows how the state error covariance solutions of the two filters compare. The target acceleration state error covariance solutions are the same as in Figure 8. The state estimates, commanded acceleration and time-to-go are also the same as in Figures 5-6. Figure 9 again demonstrates that the state error covariance solutions are approximately the same. The plot of the range error covariance shows the two solutions diverging toward the end of the flight time. The difference at the end of the flight, between the two solutions is 100, but this is again a plot of the mean square error, so the actual error is 10 which is smaller than the plot suggests.

The third run was made with both the states and the error covariance matrix being updated. This means that there are corrections made to the states and the error covariance matrix based on the error between the true states and the state estimates. Figures 10-12 show how the updated state estimates, the commanded accelerations, the time-to-go, and the updated state error covariance solutions of the two filters compare. The target acceleration state error covariance solutions are the same as in Figure 8. Figure 10 and 12 show that when the states and the error covariance are both updated the solutions for the two filters are almost exactly the same over the entire flight time. This is also the case, in Figure 11, for the commanded accelerations and the time-to-go approximation. The difference in the range error covariance plot can be explained in the same manner as above.

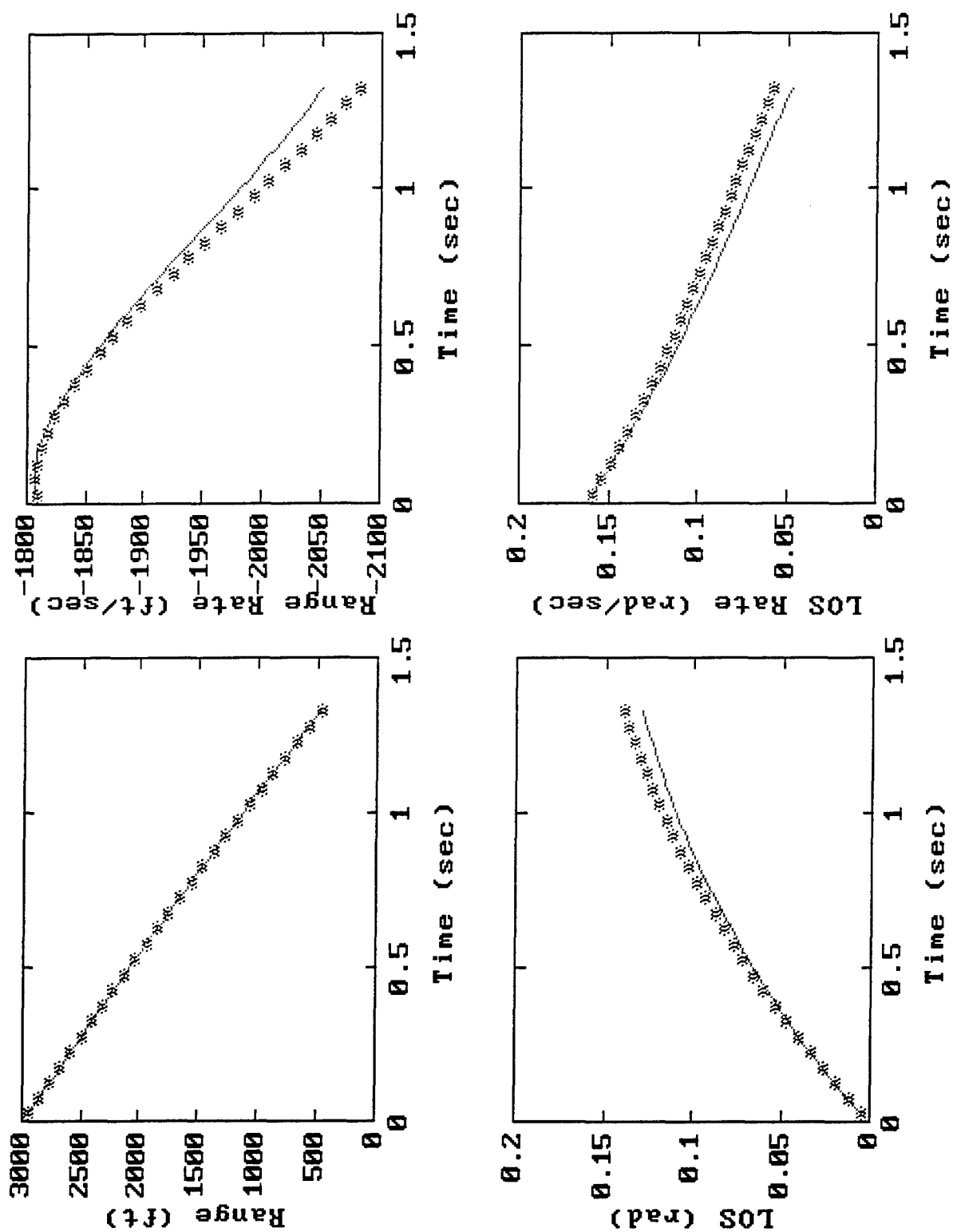


Figure 5 State Estimates (No Update)

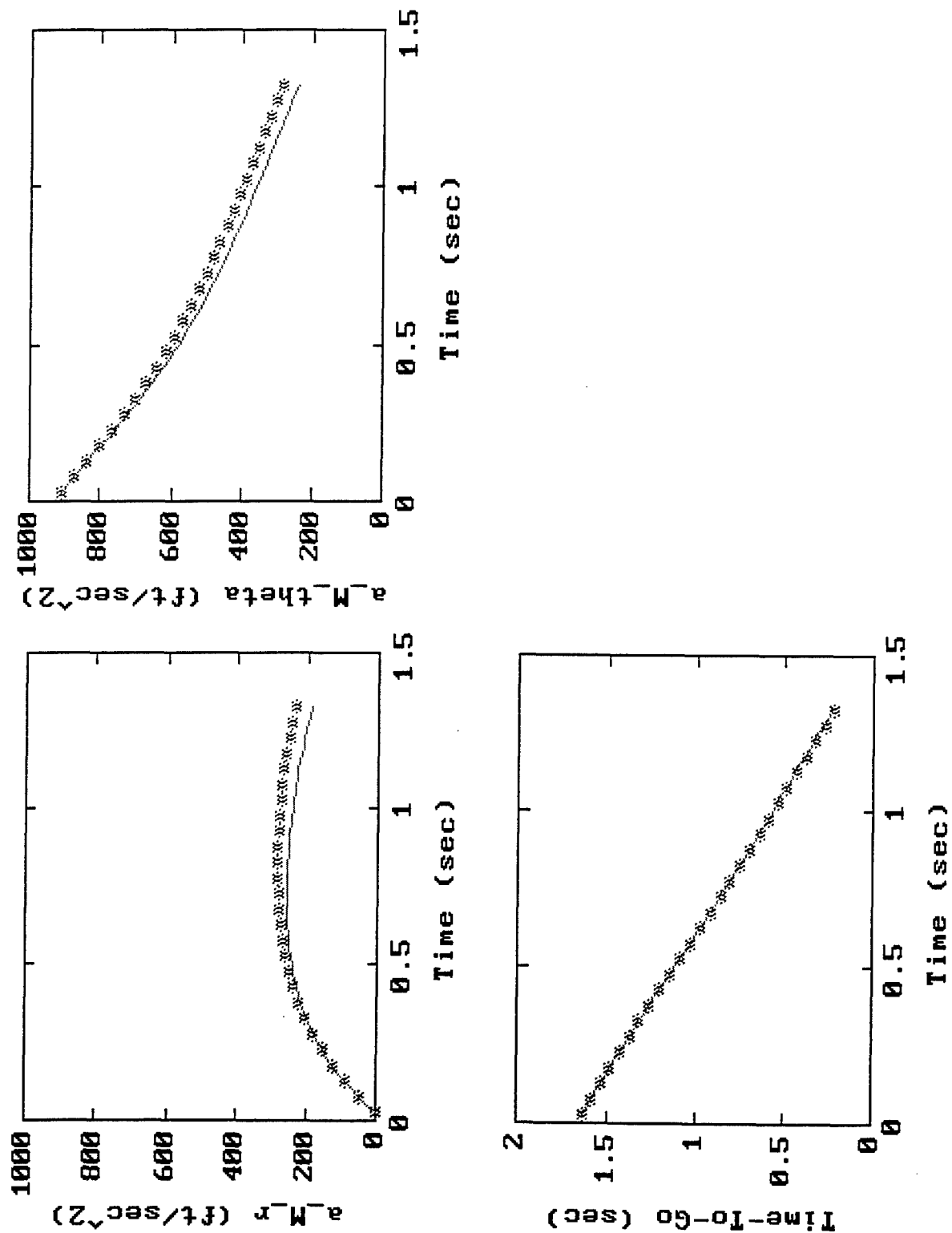


Figure 6 Commanded Accelerations and Time-To-Go (No Update)

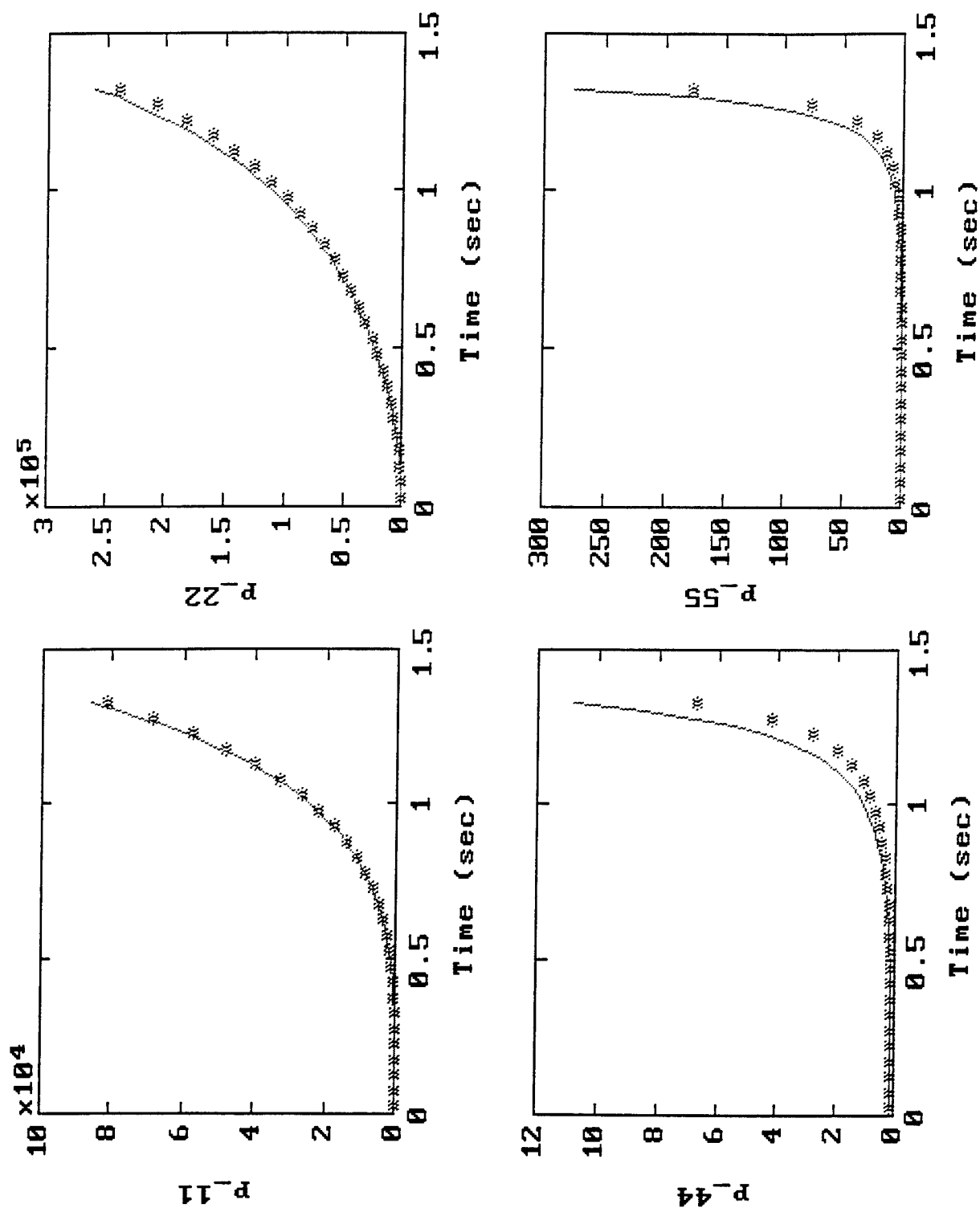


Figure 7 Error Covariance (No Update)

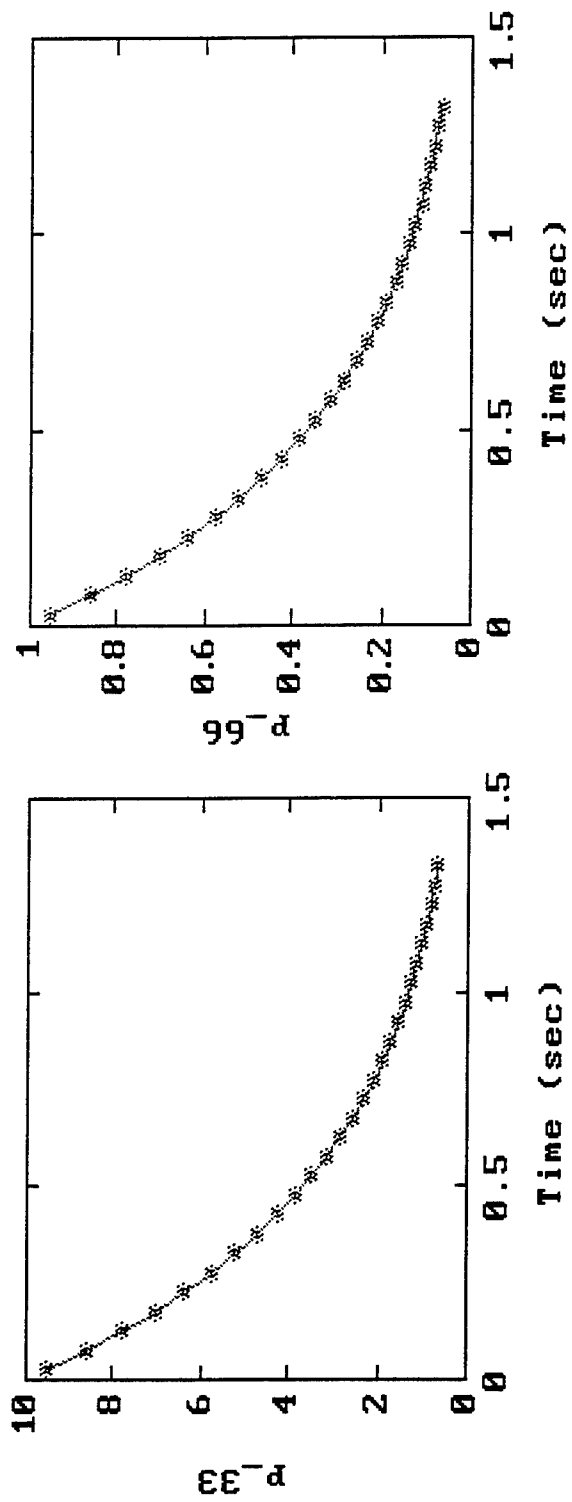


Figure 8 Error Covariance (No Update)

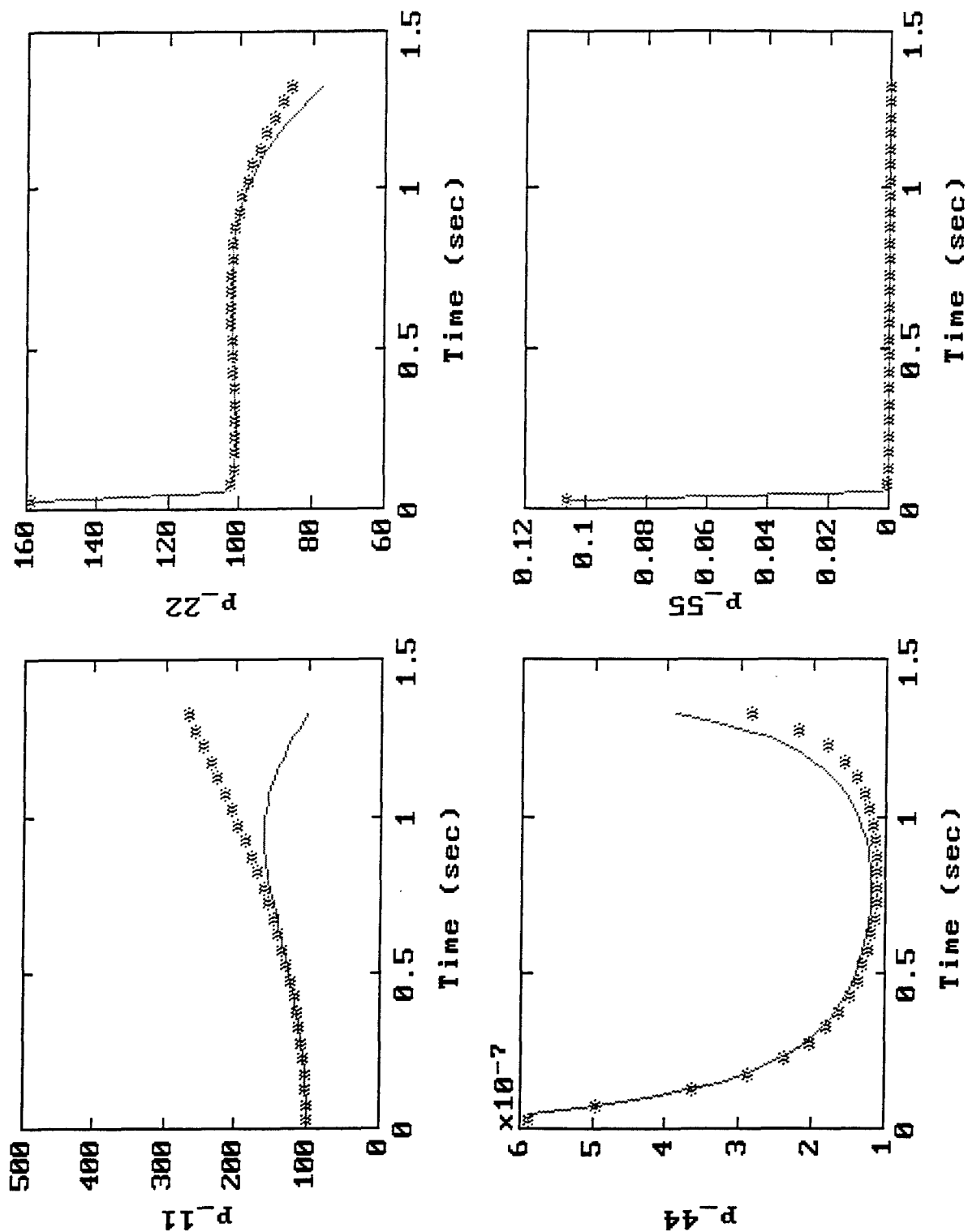


Figure 9 Error Covariance (Update)

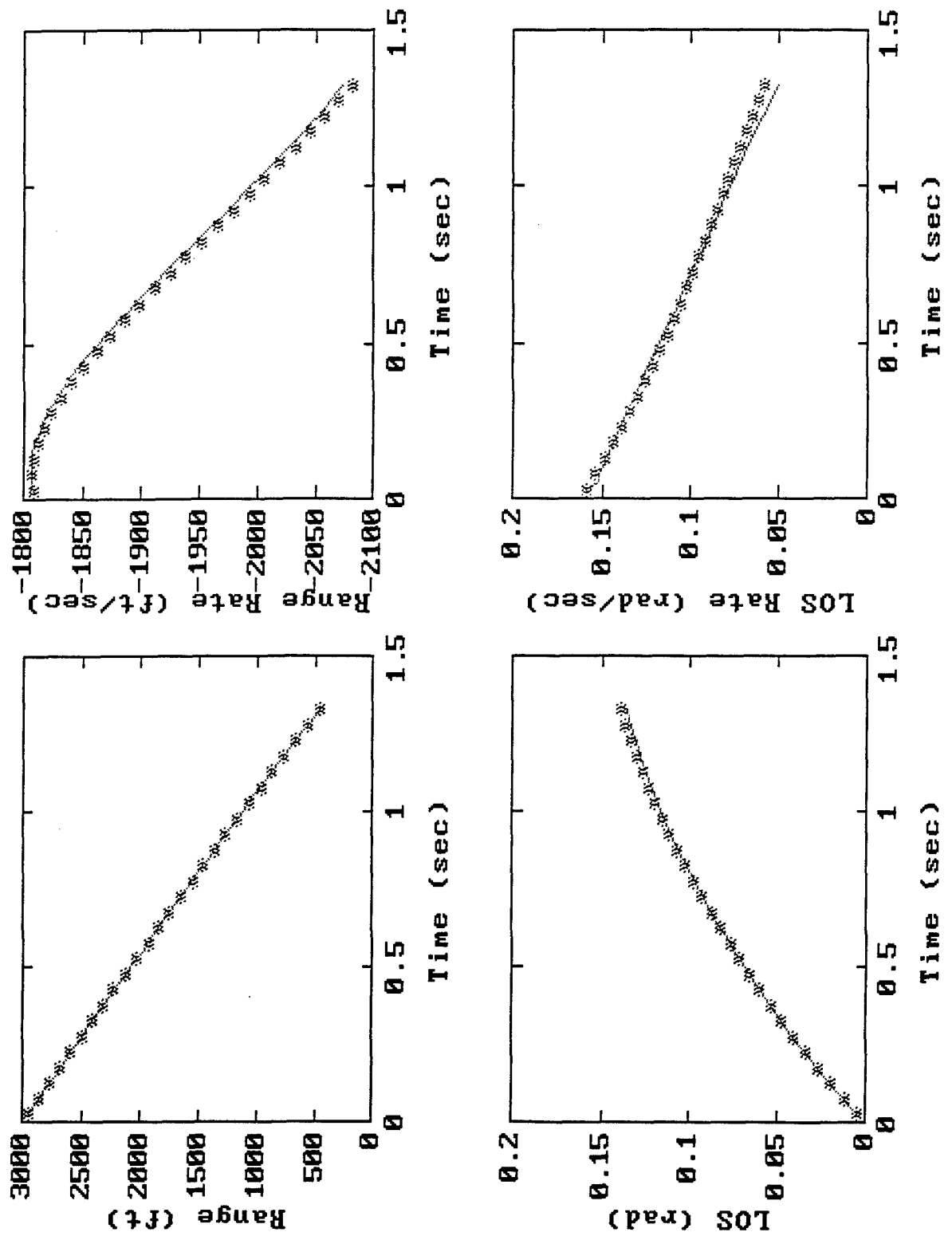


Figure 10 State Estimates (Update)

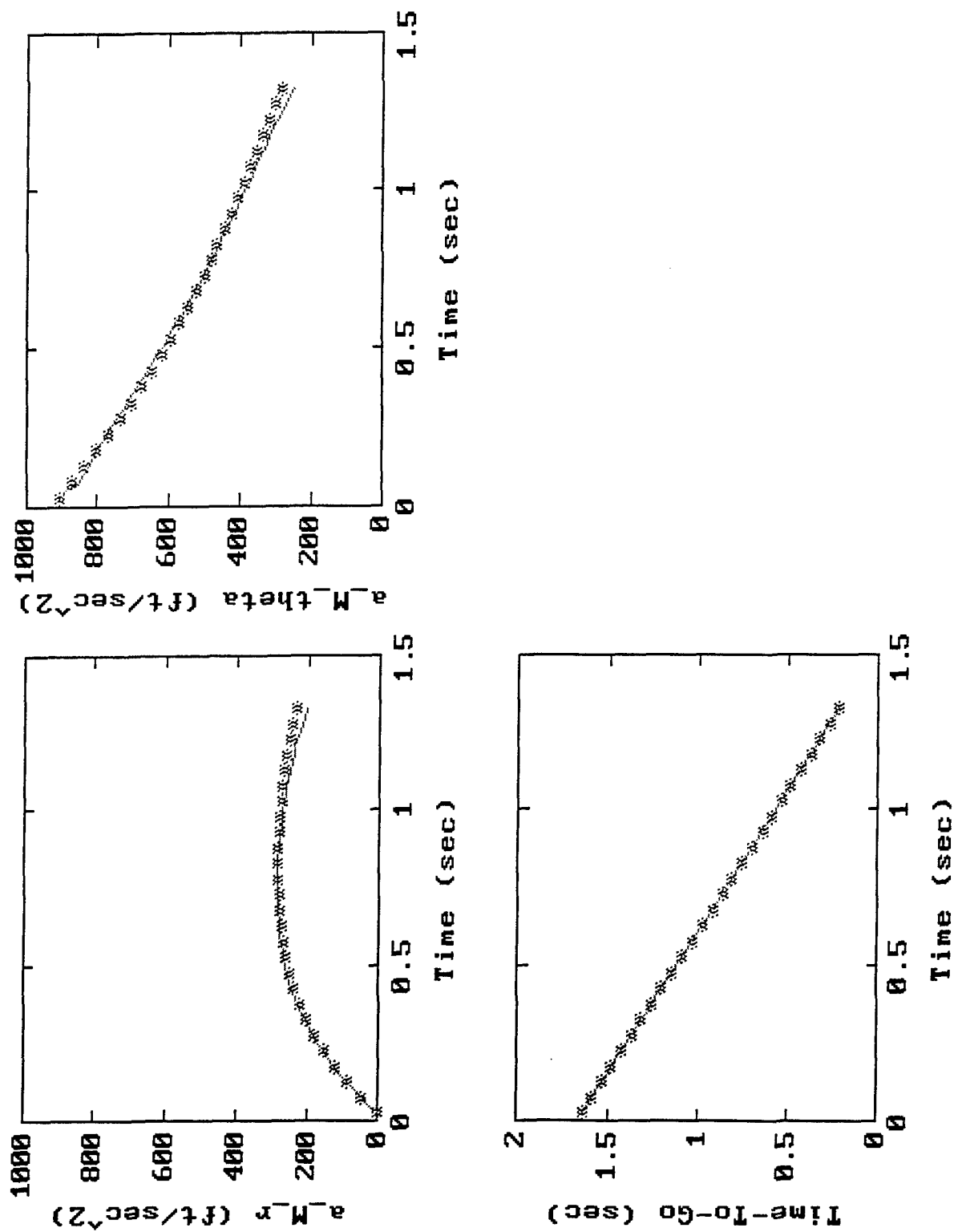


Figure 11 Commanded Acceleration and Time-To-Go (Update)

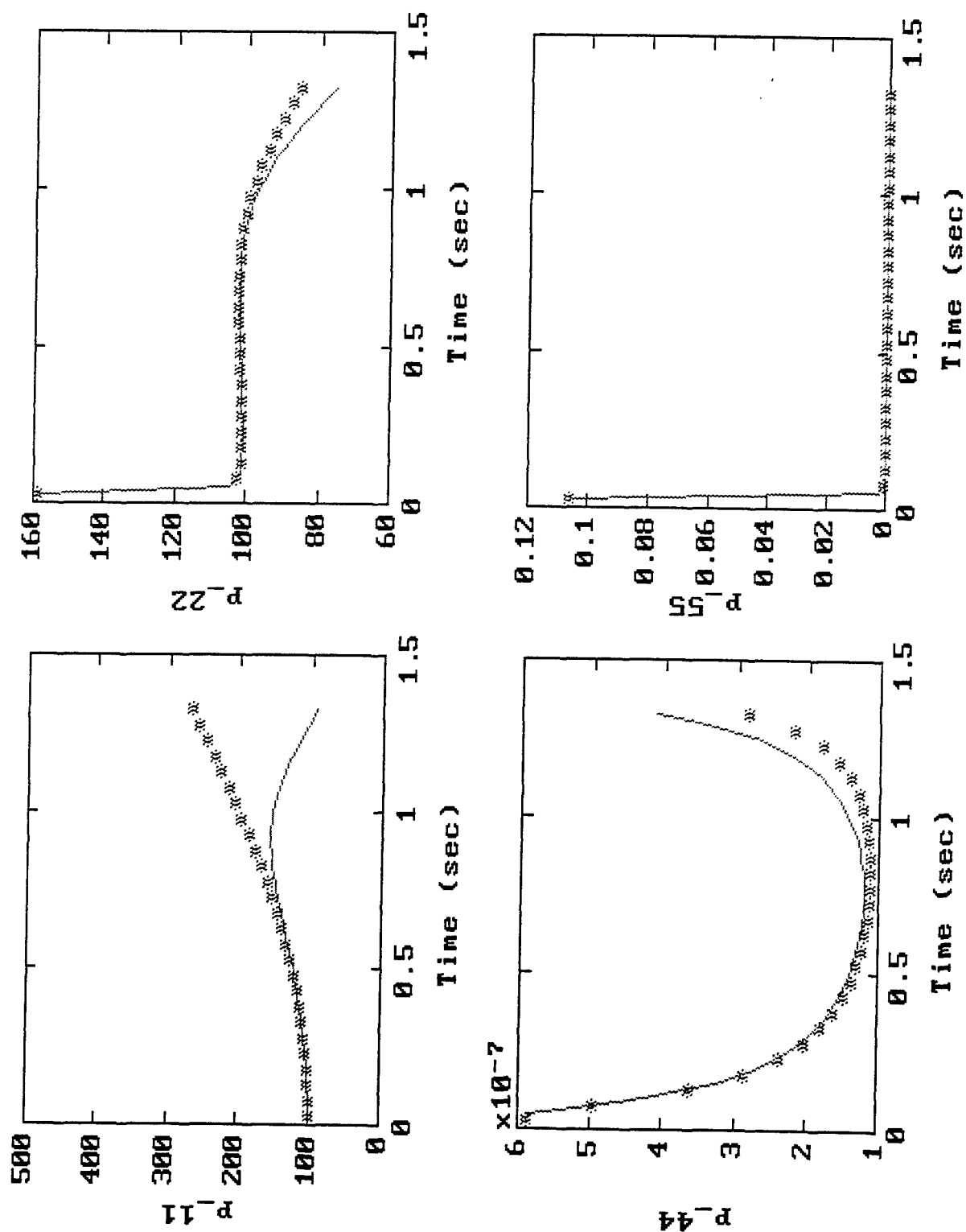


Figure 12 Error Covariance (Update)

VII. CONCLUSIONS AND FUTURE WORK

A family of analytical guidance laws has been developed in this study through approximations to the parameter time-to-go. These laws have been compared with two existing guidance laws and shown to be similar but always stable. Another contribution of this study is the development of an approximate analytical filter. This is expected to reduce the computation time in a Monte Carlo scheme considerably. Extension to a three dimensional intercept problem is considered in future work.

REFERENCES

1. Zarchan, P., *Progress in Astronautics and Aeronautics Vol. 124 - Tactical and Strategic Missile Guidance*, Washington, DC: AIAA, Inc., 1990.
2. Lin, C. F., *Modern Navigation, Guidance, and Control Processing*, Englewood Cliffs, NJ: Prentice Hall, 1991.
3. Bryson, A. E. and Ho, Y. C., *Applied Optimal Control*, Waltham, MA: Blaisdell, 1969.
4. Adler, F. P., "Missile Guidance by Three-Dimensional Proportional Navigation," *Journal of Applied Physics*, Vol. 27, No. 5, pp. 500-507, May 1956.
5. Yuan, J. P., and Chern, J. S., "Ideal Proportional Navigation," *Journal of Guidance, Control and Dynamics*, Vol. 15, No. 5, pp. 1161-1165, Sept.-Oct. 1992.
6. Yuan, J. P., and Chern, J. S., "Solutions of True Proportional Navigation for Maneuvering and Non-Maneuvering Targets," *Journal of Guidance, Control and Dynamics*, Vol. 15, No. 1, pp. 268-271, Jan.-Feb. 1992.
7. Guelman, M., "The Closed-Form Solution of True Proportional Navigation," *IEEE Trans. on Aerospace and Electronic Systems*, Vol. AES-12, No. 4, pp. 472-482, July 1976.
8. Becker, K., "Closed-Form Solution of Pure Proportional Navigation," *IEEE Transactions on Aerospace and Electronic Systems*, Vol. 26, No. 3, pp. 526-533, May 1990.
9. Shukla, U. S., "The Proportional Navigation Dilemma - Pure or True?," *IEEE Trans. on Aerospace and Electronic Systems*, Vol. 26, No. 2, pp. 382-392, March 1990.
10. Balakrishnan, S. N., "Decoupled Dynamics for Control and Estimation," *Proc. NAECON*, 1991.
11. Stansbery, D. T., Balakrishnan, S. N., Evers, J. H., and Cloutier, J. R., "Analytical Guidance Laws and Integrated Guidance/Autopilot for Homing Missiles," *IEEE Conference on Control Applications*, Vancouver, Canada, Sept. 1993..
12. Cloutier, J. R., Evers, J. H., and Feeley, J. J., "Assessment of Air-to-Air Missile Guidance and Control Technology," *IEEE Control Systems Magazine*, pp. 27-34, Oct., 1986.
13. Balakrishnan, S. N., Sammons, J. M., Speyer, J. L., and Hull, D. G., "Development and Comparison of Optimal Filters," AFATL-TR-79-87, Air Force Armament Laboratory, Eglin AFB, Florida.

14. Gelb, A., *Applied Optimal Estimation*, Cambridge, Mass: The MIT Press, 1974.
15. Balakrishnan, S. N., Speyer, J. L., "A Coordinate Transformation-Based Filter for Improved Target Tracking," *Journal of Guidance, Control and Dynamics*, Vol. 9, No. 6, pp. 704-709, Nov.-Dec. 1986.
16. Phillips, G. M., Taylor, P. J., *Theory and Applications of Numerical Analysis*, New York, NY: Academic Press, 1973.
17. Stansbery, D. T., "Approximate Analytical Guidance and Estimation Schemes for Homing Missiles", Thesis, May 1994.

STUDIES OF NTO DECOMPOSITION

Theodore J. Burkey
Associate Professor
Department of Chemistry

Memphis State University
3744 Walker Ave
Memphis, TN 38152

Final Report for:
Research Initiation Program
Wright Laboratories

Sponsored by:
Air Force Office of Scientific Research
Bolling Air Force Base, Washington, D. C.

and

Memphis State University

December 1993

STUDIES OF NTO DECOMPOSITION

Theodore J. Burkey
Associate Professor
Department of Chemistry
Memphis State University

Abstract

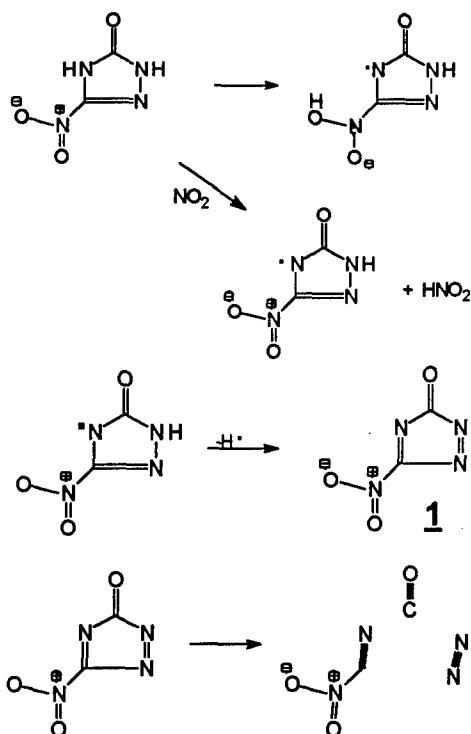
The thermal and oxidative decomposition of NTO (2,4-dihydro-5-nitro-3H-1,2,4-triazol-3-one) was studied. The gaseous products of NTO oxidation by KMnO_4 were analyzed by gas chromatography. 1.5 mole carbon dioxide and 1 mol nitrogen were observed per mol of NTO. During initial stages of the oxidation the ratio of carbon dioxide to nitrogen was 2:1. The results contradict previous analysis of gases formed upon NTO oxidation. The gas analysis will be useful in comparing the mechanism of NTO oxidation and its thermal decomposition. Ammonia, detected as a ammonium ion, is a product of oxidation with nitric acid. Likewise, thermal decomposition of NTO produces substantial amounts of ammonium ion collected by sublimation at atmospheric pressure. The ammonium counter ion and co-sublimates have yet to be identified. Small scale synthesis of NTO was optimized for preparing ^{15}N -labeled NTO. NTO on solid substrates was heated up to 194 C without observation of free radicals by ESR spectroscopy. Analysis, after oxidation, for cyanide was negative and for nitrate, inconclusive.

STUDIES OF NTO DECOMPOSITION

Theodore J. Burkey

INTRODUCTION

The Air Force plans to use NTO (2,4-dihydro-5-nitro-3H-1,2,4-triazol-3-one) as a general purpose explosive. The goal of our work is to elucidate the mechanism of NTO thermal decomposition. By avoiding conditions that promote decomposition, this will provide a rational basis for improving NTO synthesis, preparation of explosive formulations, and transportation. In addition, this information will be a guide to the development of new explosives. The safety and effectiveness of an explosive depends on its long-term stability. It is therefore important to know the extent of NTO decomposition during storage and its compatibility with other materials. Pure NTO is stable relative to conventional explosives, but it may not be compatible with other explosives.



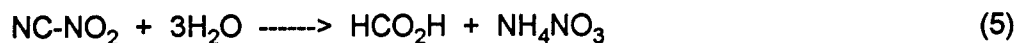
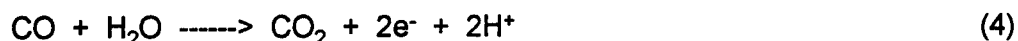
Many organic compounds thermally decompose via radical

- (1) intermediates. This fact, coupled with evidence of H abstraction discovered by Menapace and coworkers,¹ indicate that hydrogen abstractions are occurring during NTO thermal decomposition, and a second H abstraction from NTO may occur (eq 1 and 2). The product of eq 2 (1, 5-nitro-3H-1,2,4-triazol-3-one) would
- (2)
- (3)

1. Menapace, J. A.; Marlin, J. E.; Bruss, D. R.; Dasher, R. V. *J. Phys. Chem.* **1991**, *95*, 5509.

be predicted to have antiaromatic character and be a good candidate for an electrocyclic ring opening (eq 3). Such an opening would lead to three or four gaseous products, a desirable process for an explosive.² The loss of two hydrogen atoms (eq 1 and 2) is equivalent to an oxidation of NTO. We reasoned that a reaction of NTO with an oxidizing agent could afford 1 by an entirely different route. Indeed, we went on to discover that NTO reacted vigorously with $\text{KMnO}_4/\text{H}_2\text{SO}_4$ solutions to evolve CO_2 and N_2 .³ This is a facile reaction at room temperature. With excess KMnO_4 , no NTO could be detected by HPLC or NMR. NTO also reacts with ceric ammonium nitrate.^{3,4} The stoichiometry for complete destruction of NTO with KMnO_4 and Ce(IV) was 1:1 and 1:5, respectively, indicating that NTO is oxidized in a five-electron process. The oxidation with KMnO_4 appeared to proceed in at least two phases with the gas composition changing and the latter phase being slower than the first. The results were explained by eq 1-3 and 4-6. KMnO_4 oxidizes NTO in a two-electron step (equivalent to eq 1 and 2). The spontaneous ring opening of 1 produces CO , N_2 , and NC-NO_2 (eq 3). The CO_2 can be produced by KMnO_4 oxidation of CO and HCO_2H (eqs 4 and 6). The production of CO_2 from HCO_2H is limited by the hydrolysis of NC-NO_2 (eq 6)

-
2. The NC-NO_2 bond energy can be expected to be similar to the NC-NO bond energy which is only 29 kcal/mol; therefore, NCNO_2 is going to immediately decompose to NC and NO_2 radicals at elevated temperatures: Gowenlock, B. G.; Johnson, C. A. F.; Keary, C. M.; Pfab, J. J. *JCS Perkins Trans.*, **1975**, 351.
 3. Fan, P. Masters Thesis, Memphis State University, 1993.
 4. Burkey, T. J. "EFFECT OF ANTIOXIDANTS ON THERMAL DECOMPOSITION OF ENERGETIC MATERIALS" Final Report for Summer Research Program, High Explosive Research and Development, Wright Laboratories, August 1992.



accounting for the biphasic CO_2 production. In other oxidation experiments, reaction of NTO in fuming nitric acid resulted in complete decomposition of NTO, and evaporation of the acid left ammonium nitrate. Oxidation of NTO labeled at positions 1 and 2 with ^{15}N produced ammonium ion with no label, Consistent with eq 3 and 5.

Subsequent to discovering ammonium ion as a product of NTO oxidation, we also found it formed after partial NTO thermolysis. This is the first report of ammonium ions (and potentially ammonia gas) as a product of NTO decomposition. Presumably in a solid state reaction, ammonia reacts with undecomposed NTO in an acid-base reaction (pK_a of NTO is ca. 3). Every major product observed after NTO oxidation is also observed after NTO thermolysis; thus, there is considerable evidence that the two reactions may share common pathways. Because of the similarities between the products for oxidation and thermal decomposition the investigation of NTO oxidation should help identify product of NTO decomposition and aid our understanding of this process. New results in this report require modification of the proposed mechanism.

The objectives of the current project are to identify products and intermediate of NTO oxidation and decomposition and to determine if the mechanisms for the two processes are related. Species investigated include carbon dioxide, nitrogen, nitrate, cyanide, ammonium, TO (2,4-dihydro-3H-1,2,4-triazol-3-one) and free radical intermediates. ^{15}N labeled NTO will be used to identify what part of NTO a product came from and aid the identification of intermediates such as free radical. Difficulty in observing radicals will be

increased by the presence of 4 nitrogen atoms with nuclear quadrupoles, creating a spectrum with potentially 162 lines if one H were removed. The availability of ^{15}N labeled NTO will greatly enhance the ability to observe a signal. To this end extensive effort will be directed toward the synthesis of ^{15}N labeled NTO. This was necessary since labeled precursors are very expensive, and literature syntheses do not give good yields for small scale reactions.

METHODOLOGY

Preparation of samples for ESR studies. NTO (103 mg) was dissolved in 23 mL of acetone. The solution was poured over 10.1 g of alumina (Aldrich lot 04828DT, neutral Brockman I, 150 mesh, 155 m²/g). The alumina immediately turned yellow. The acetone was evaporated under a stream of argon. Similarly, NTO (102 mg) on sodium sulfate (Fisher Scientific, 10.1 g) and NTO (101 mg) on silica gel (Aldrich, 10.0 g, 70-230 mesh, 500 m²/g) were prepared. About 0.5 g of NTO/substrate was sealed in a 4 mm Suprasil after evacuating to less than 0.015 torr. Some samples were further filled with argon at 500 torr. Because of uneven heating in a sand bath some samples were heated in the ESR cavity with a quartz dewar insert and a heating gun. Temperatures within the cavity were uniform to ± 5 C.

Thermal Decomposition of NTO. An NMR tube containing NTO (50 mg) was evacuated and filled with argon at atmospheric pressure. After heating at 250 C for 20 min in a sodium nitrate/sodium nitrite/potassium nitrate (7%:40%:53%) bath, melting and browning of sample was observed. the sample was taken up in DMSO for NMR analysis.

In a different experiment, 0.21 g NTO was heated 7 hr at 250 C in a sublimber under atmospheric pressure of air (NTO sublimes under vacuum). A white solid sample (40.5 mg) was collected from the cold finger (cooled with tap water) and a brown residue (37.1 mg) remained in the sublimber flask. The residue was washed with water and dried under

vacuum at room temperature. For elemental analysis, the procedure was repeated three times to collect enough sample. Elemental analyses were obtained from Desert Analytics.

Analysis of nitrate.⁵ NTO (0.11 g) was oxidized with 10 mL $\text{Ce}(\text{SO}_4)_2$ in 1 M H_2SO_4 . Gas evolution ceased after 30 min. Addition of 5 mL of nitron acetate solution (10 g of 1,4-diphenyl-3,5-endanilaodyhyrotriazole in 50% acetic acid) resulted in a white precipitate. A control experiment with potassium nitrate yielded a brown precipitate. No further attempt was made to quantify nitrate.

Synthesis of NTO. For the standard procedure, $\text{Ba}(\text{OH})_2$ (4.85 g) was dissolved in 18 mL hot water followed by hydrazine sulfate (2.0 g). The solution was centrifuged and the supernatant was decanted from the precipitate of barium sulfate into a Parr acid digestion bomb (#4745, 23 mL Teflon liner) containing 1.0 gram of urea. The bomb was sealed and heated to 100 C for 6 hr. After cooling, the bomb was opened, the smell of ammonia could be detected, and a white crystalline precipitate was on the bottom (semicarbazide). Water was removed by rotary evaporation. To the residue, 5 mL of 97% formic acid and 1 mL concentrated HCl was added and refluxed for 4 hr. Solvent was removed by rotary evaporation leaving a white precipitate (TO). The precipitate was added to 5 mL 70% HNO_3 and heated to 60 C. Red fuming nitric acid (2 mL) was added dropwise, and the mixture was heated to 85 C for 30 min. After rotary evaporation, the residue was washed with 5 mL ice water and dried overnight under vacuum.

Analysis of Gases from NTO Oxidation. A 10-mL septum-sealed test tube containing 0.1 g NTO was evacuated, and 4 mL of 0.5 M KMnO_4 in 2 M H_2SO_4 was injected. Evolving gas was collected in a 50-mL syringe at atmospheric pressure. Duplicate

5 Furman, N. H. Standard Methods of Chemical Analysis, D. Van Nostrand, 6th ed. Vol. 1, 1966, p740.

measurements were obtained by transferring samples to a 5 mL syringe. In one case, samples were collected directly to a 5 mL syringe as the reaction progressed.

Oxidation of NTO by Nitric Acid. NTO (0.9671 g) was heated in 5 mL of fuming nitric acid at 80 C for 30 min. NTO dissolved and gas bubbles evolved. Rotary evaporation yielded a white precipitate (0.2367 g). The same results were obtained in a duplicate experiment. The amount of NH_4^+ was determined by the Nessler method.⁶

APPARATUS

An HP 5890 Series II GC with thermal conductivity detector and low temperature controller was used for gas chromatography. Gases were separated on 30' x 1/8" HayeSep D_B 100/120 Mes packed column. While lower temperatures were used, the most reproducible results were obtained for an oven temperature of 30 C and 30 mL/min He carrier flow. The column was calibrated with different samples of known composition containing commercial nitrogen and carbon dioxide. Pure gases were mixed using calibrated flow meters and sampled via syringe needle puncture of Tygon tubing downstream from the mixing point. Direct injection or a 50 μL injection loop was used.

ESR spectra were obtained on a Varian E4 ESR spectrometer with variable temperature control.

RESULTS

Oxidation of NTO by Nitric Acid. The product of oxidation by nitric acid was analyzed by ^1H NMR in DMSO-d_6 . The spectrum revealed a 1:1:1 triplet at 7.1 ppm ($J^{14}_{\text{N-H}} = 52.1$ Hz) assigned to ammonium ion. For comparison, NH_4Cl (0.02 g) in 1 mL DMSO-d_6 gives a broad peak (apparent singlet) in the proton NMR at 7.4 ppm; however, NH_4Cl (0.02 g) and 2 drops of glacial acetic acid in 1 mL DMSO-d_6 give an overlapping 1:1:1 triplet at

6 Harris, W. E.; Kratochvil, B. *Chemical Separations and Measurements*, Saunders, Philadelphia, 1974, p 119.

7.5 ppm. Apparently, greater ion pairing with chloride relative to acetate results in a more asymmetric charge distribution about the nitrogen. This increases the quadrupolar relaxation that promotes fast exchange between nitrogen spin states resulting in the collapse of coupling. No carbon was observed by ^{13}C NMR in the oxidation product. The samples contained 23% NH_4^+ by weight and corresponded to 83% yield of NH_4^+ from NTO.

Thermal decomposition of NTO. ^1H NMR analysis of NTO partially decomposed under argon (probably less than 5% decomposition) revealed ammonium ion (7.2 ppm, triplet) and a trace of TO (s, 8.0 ppm, and br s, 11.2 ppm). The NMR of genuine TO has singlets at 7.7, 11.25, and 11.4 ppm. The differences can be attributed to solvent effects caused by other compounds present.

Elemental analysis of thermal decomposition products collected with a sublimator yielded the following results. Washed residue: C 18.23%, H 1.86%, N 41.46%, and O 37.99%. The composition is very similar to NTO (C 18.47%, H 1.55%, N 43.08%, and O 36.90%) suggesting partial polymerization of NTO. Sublimate: C 28.96%, H 2.38%, N 52.38%, and O 17.36% (101.1% total). For comparison, TO: C 28.23%, H 3.56%, N 49.41%, and O 18.81%, and TO dimer: C 28.56%, H 2.40%, N 50.00%, and O 19.03%. 63% of the NTO must have escaped as gas products while 19 % appeared as sublimate and 18 % remained as residue. Interestingly, If two CO_2 and one N_2 were lost this would only account for 52 % of the weight of NTO. Clearly other gas products must be formed that are not condensing on the cold finger. We have yet to analyze by GC the gas products of thermal decomposition as we have for oxidation.

A 1:1:1 triplet (7.2 ppm) was observed for the sublimate dissolved in DMSO-d_6 . This peak is assigned to ammonium ion. A trace of TO (< 5%) was also observed in the sublimate. No simple compound fits the elemental analysis and also contains 4 hydrogens necessary for ammonium ion. It is clear the sublimate is not a pure material and purification

will be necessary. The procedure will be scaled up, and purification will entail vacuum sublimation, ion exchange, and/or recrystallization.

Radical Intermediates from Thermal Decomposition: ESR experiments.

NTO/sodium sulfate under vacuum turned yellow (unevenly) when heated for 1 min at 120 C. No observable change occurred after additional heating at 140 C for 1 to 5 min and 160 C for 5 min. After each heat treatment the tube was cooled rapidly to room temperature with water and transferred within a minute to the microwave cavity. No ESR signal was observed in each case even with signal averaging. NTO/sodium sulfate under argon was heated continuously for 50 min with discoloration and 110 min with slight yellowing. After heating at 194 C for 48 min dark spots formed on the sodium sulfate crystals. ESR spectra were accumulated continuously for each temperature, but no radicals were detected. Similar experiments for NTO/silica gel also gave negative results. No experiments were done with NTO/alumina because of the room temperature reaction between the alumina and NTO (yellowing, see METHODOLOGY). Presumably this was an NTO reaction with basic sites on alumina generating NTO anion which is yellow.

While other ESR experiments could be undertaken, it seems clear that the most fruitful method for detecting radical intermediates would be rapid heating by laser pyrolysis followed by rapid cooling on a cryogenically cooled substrate. We currently do not have the apparatus for these experiments.

Analysis of Gases from NTO Oxidation. The gas products of permanganate oxidation were carbon dioxide and nitrogen. The upper limit appears to be one mole of nitrogen and 1.5 moles of carbon dioxide for the conditions used. Only limited attempts to get further gas evolution via heating have been made at this time. Assuming the gas came from N1, N2, C3, half of C5, and the carbonyl oxygen, this would account for 48 % of the weight of NTO (compared to 63% for gases calculated for thermal decomposition). One source of the difference could be due to water that is formed during decomposition. In the

last experiment, the initial ratio of CO₂ to N₂ is that expected from our model for oxidation of NTO (2:1). As the reaction progresses this ratio decreases, indicating that either complete oxidation of the carbon from NTO is inhibited later in the reaction (perhaps via coordination of some intermediate by a reduced Mn species), or N₂ is formed from nitrogens other than at the 1 and 2 positions later in the reaction. Unfortunately, when the gas was analyzed by a scrubbing technique³ (gas bubbled through NaOH, volume decrease was attributed to CO₂ and undissolved gas was assigned to N₂) the ratio was 1:1 initially and approached 1.5:1 as the reaction progressed. Some procedures have been improved (specifically, permanganate is mixed with NTO under argon instead of a vacuum), and the gas scrubbing procedure may be repeated.

Table 1. Production of Carbon Dioxide and Nitrogen from NTO Oxidation.

NTO (g)	Total gas mL/mmol	mole ratio ^a	% CO ₂	% N ₂	CO ₂ /N ₂
0.0718	38/1.6	2.3:1	58.7	38.8	1.5
duplicate			57.2	38.8	1.5
0.0835	42/1.8	2.2:1	54.6	41.1	1.3
0.0834	41/01.7	2.1:1	58.5	39.1	1.5
duplicate			58.5	39.7	1.5
0.0737 ^b			57.4	38.8	1.5
duplicate			59.2	38.5	1.5
0.086 ^{b,c}			63.1	30.0	2.1
d			57.4	40.6	1.4

^a mole ratio of total gas to NTO. ^b total gas volume was not measured ^c sample taken at beginning of reaction .^d taken immediately after first sample

Oxidation by Other Methods. No electrolytic oxidation of NTO could be observed in DMSO or acetonitrile up to 2.4 V v AgCl reference electrode. This was also true in acidic or basic aqueous solution (1.2 V). Higher voltages result in solvent (or electrolyte) oxidation. TO was observed to oxidize at 1.7 V in DMSO. Consistent with this, TO reacts faster with KMnO_4 than NTO. It should be noted though that failure to oxidize at an electrode can occur for kinetic as well as thermodynamic reasons. Chemically, the oxidation of NTO is quite general. NTO is destroyed with KMnO_4 , Ce^{+4} , H_2O_2 , and nitric acid. Formation of gases have been examined and detected for KMnO_4 , Ce^{+4} and nitric acid. The formation of ammonium ion has been examined and detected for H_2O_2 and nitric acid.

Cyanide and Nitrate. Our mechanism suggest that a CN species at some point may be formed. If CN^- were formed, it seemed that its observation would be most likely after partial NTO oxidation. This was carried out with excess NTO (0.134 g) with 3 mL of 0.33 M KMnO_4 and 1.3 M H_2SO_4 . Cyanide could not be analyzed by precipitation with Ag^+ since NTO also gave a similar looking precipitate. Infrared analysis (KBr pellet) of the precipitate revealed no CN peak near 2100 cm^{-1} . In a control experiment, CN^- addition to KMnO_4 results in a green precipitate, but in acidic conditions with KMnO_4 it appears to be decomposed. As described in the Methodology section, a test for nitrate was inconclusive.

Synthesis of ^{15}N labeled NTO Some of the modifications of the standard synthetic procedure are described in Tables 2 and 3. Low yields of semicarbazide can result from loss of hydrazine, and the use of sealed bombs greatly improved the yield. Also, in a control experiment, excess urea reacted with semicarbazide. We also suspect the semicarbazide can hydrolyze or react further with hydrazine. Thus, extending reaction times and higher temperatures can cause destruction of semicarbazide. The isolated yields in Table 2 are for semicarbazide extracted from the residue after rotary evaporation of water, extraction of the solid with ethanol, and precipitation from ethanol with HCl.

Table 2. Synthesis of Semicarbazide (as hydrochloride)^a

run, bomb #	time (hr)	temp. (°C)	yield
1, A	5	130	60%
2, C	overnight	130	6%
3, A ^b	7	130	18%
4, B ^b	7	130	23%
5, A	9	130	11%
6, B	9	130	9%
7, C	9	130	8%
8, A	3	130	26%
9, B	4	130	40%
10, C	5	130	18%
11, A	5	100	49%
12, B	7	100	43%
13, C	9	100	38%
14, A	4	100	54%
15, B	5.5	100	42%
16, C	6.5	100	48%
17, A	3	100	61%
18, B	3	100	52%
19, C	4	100	60%

^a1.0 gram urea was used unless otherwise noted, yield based on
hydrazine sulfate (2.0 g), total volume was 23 mL. ^b1.5 g urea

For synthesis with labeled nitrogen, the semicarbazide will not be isolated. Instead
the crude products will be dissolved directly in formic acid to increase the final yield.

Table 3. Synthesis of TO^a

run	reflux time (hr)	Yield of TO
1	4	69.5%
2	4	73.1%
3	4	70.8%
4 ^b	4	19.5%
5 ^c	4	54.9%
6	6	45.0%
7	6	81.6%
8	5	73.7%
9 ^d	5	0
10	12	51.3%
11	12	100%
12	12	43.4%
13	12	46.6%

^aUrea = 0.92 g, 15 mL water, reflux in formic acid ^b K₂PO₄ 2.5 g was added to the urea/N₂H₄ in the reaction bomb, stating pH = 9, after reaction, pH = 11.

^cstarting pH = 9, ending pH = 11. ^ddid not add HCl in the synthesis of TO.

Low yields in the formation of TO

seem to correlate with the formation of ammonium ion, presumably by hydrolysis.

Although some experiments give high yields of TO, the results were not reproducible. Further work will be done to control this reaction. There appears to be impurities in the formic acid, and distillation or new reagent may rectify this problem.

The nitration is quantitative as long as reaction time is minimized. Once all steps are optimized and reproducible, labeled NTO will be prepared from 4-6 grams of hydrazine sulfate. In Table 3, the yields are for starting from hydrazine sulfate and urea without isolation of semicarbazide.

Semicarbazide for TO synthesis is as described in the METHODOLOGY section except were noted. Yield of TO was determined by NMR with acetamide as an internal standard.

Selective Isotope effects on NTO

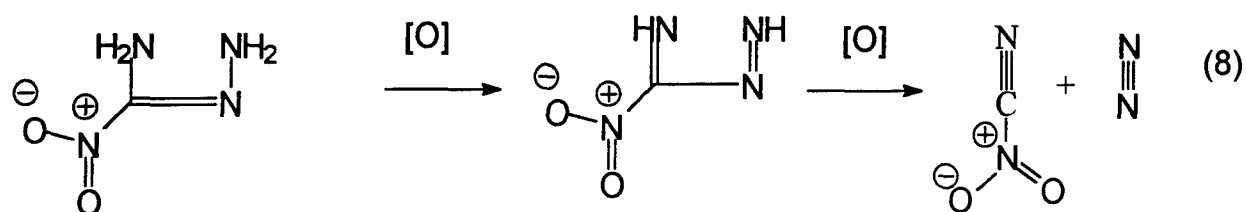
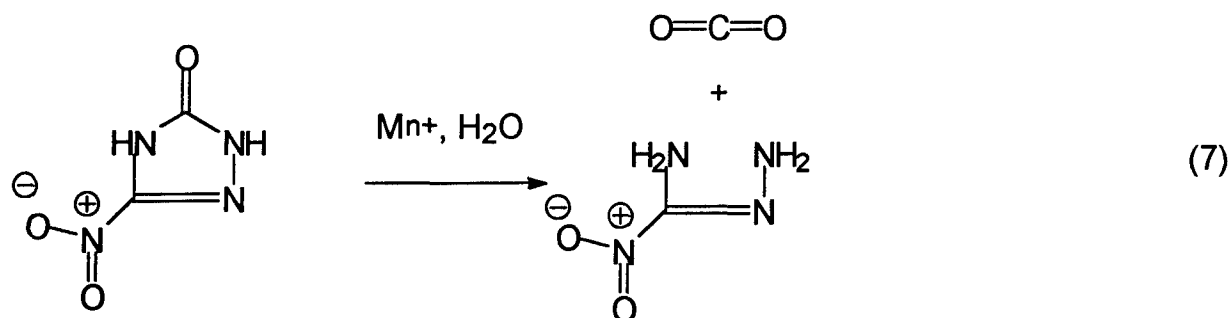
Thermal Decomposition. Menapace et. al¹ observe a global hydrogen kinetic isotope effect on the thermal decomposition of NTO. Because both positions were deuterated, their results did not show which N-H bond was responsible for the effect. Great progress in the elucidation of the mechanism of thermal decomposition could be made if it was known

which NH bond was involved. Previous results in our lab suggested that the acidic NTO proton could be selectively exchanged with acetone- d_6 . A broad NH peak at 12.8 ppm (N-4) was initially observed in a septum-sealed NMR tube but disappeared after a day. We presumed the NH peak disappear as a result of a slow enolization of acetone catalyzed by the acidic NTO NH. This would provide a means for selective deuterium exchange and the study of a selective isotope effect; however, we could not isolate 2,4-dihydro-5-nitro-3H-1,2,4-triazol-3-one-3-d. Examination of the acetone- d_6 sample at -40 C resulted in "recovery" of the peak at 12.8 ppm and a water peak at 4.2 ppm, i.e. the NH proton was exchanging with water, and no deuterium exchange had occurred. Since selective isotopic substitution of the NH peaks could not be achieved, we did not pursue isotope effects on thermal decomposition of NTO.

CONCLUSIONS

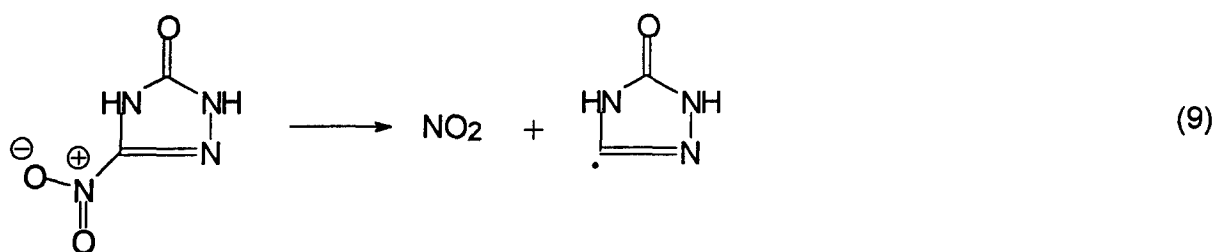
While it is unrealistic to expect that the mechanism of NTO oxidation is the same as NTO thermal decomposition, there are several results that suggest some steps are common to both reactions. The rapid and facile oxidation of NTO to carbon dioxide and nitrogen gases suggest that the mechanism is not likely to be very complex. It seems almost certain that oxidation leads to the formation of 1. Other direct oxidation reactions are very unlikely. Formation of 1 leads to the direct formation of nitrogen and carbon monoxide (eq 3), the latter getting further oxidized to carbon dioxide. The fate of $NCNO_2$ is unclear. The detection of ammonium ion indicates a hydrolysis, possibly to carbonate (carbon dioxide) and nitrate. The incomplete formation of carbon dioxide (1.5 instead of 2 mols) suggests CN may be trapped as a Mn ligand.

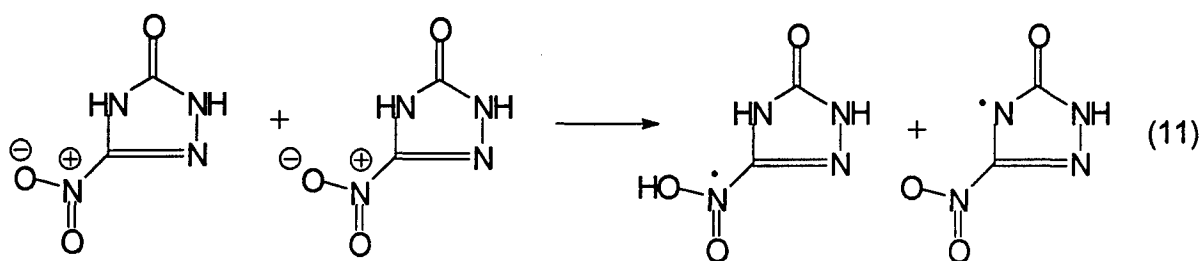
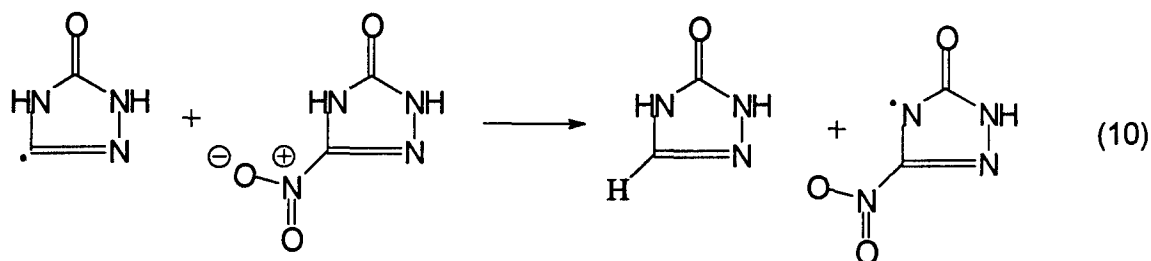
Another mechanism for NTO reaction with permanganate is possible. For example, permanganate could act as a Lewis acid catalyst in the hydrolysis of NTO (eq 7 and 8). This could lead to the same intermediates suggested in eq 3. Eq 7, of course, is not likely in the thermal decomposition.



Clearly, thermal decomposition of NTO involves more than one mechanism.

Substantial amounts of polymeric residue is formed. Of primary interest is the first step or steps that occur since they are likely to determine the course of the reaction. The formation of TO during thermal decomposition suggests that C-NO₂ scission occurs followed by hydrogen abstraction from NH (eq 9 and 10). This probably competes with the bimolecular abstraction reaction between two NTO (eq 11). Support for this reaction is the report of the observation of a hydroxy nitroxide radical, not under thermal decomposition, but rather irradiation in acetone.¹





Synthesis of NTO on a small scale can be achieved with yields greater than 70% starting from hydrazine sulfate and urea. The synthetic studies provide important conclusions for commercial or laboratory NTO synthesis. The amount of fuming nitric acid, temperature, and reaction time for nitration should be limited as much as possible since oxidation of NTO will occur and reduce the yield. Furthermore, decomposition products could persist as impurities if purification is not adequate. Oxidation may be a convenient method of disposal or selective removal of NTO. Nitric acid is probably the safest and cheapest agent we have used.

INVESTIGATION OF A GAUSSIAN RAY-TUBE BASIS FUNCTION EXPANSION
FOR COMPUTING THE ELECTROMAGNETIC SCATTERING FROM LARGE
OPEN-ENDED CAVITIES

Robert J. Burkholder
Postdoctoral Research Associate
Department of Electrical Engineering

The Ohio State University
ElectroScience Laboratory
1320 Kinnear Road
Columbus, Ohio 43212

Final Report for:
Summer Research Extension Program
Wright Laboratories AARA

Sponsored by:
Air Force Office of Scientific Research
Bolling Air Force Base, Washington, D.C.

and

The Ohio State University

December 1993

INVESTIGATION OF A GAUSSIAN RAY-TUBE BASIS FUNCTION EXPANSION FOR COMPUTING THE ELECTROMAGNETIC SCATTERING FROM LARGE OPEN-ENDED CAVITIES

Robert J. Burkholder
Postdoctoral Research Associate
Department of Electrical Engineering
The Ohio State University

Abstract

A Gaussian ray-tube basis function (GRBF) is developed for use in the generalized ray expansion (GRE) and shooting and bouncing ray (SBR) methods of analyzing the electromagnetic scattering by large open-ended cavities. GRBF's may be much larger than the ordinary geometrical optics (GO) ray-tubes used in GRE and SBR, so fewer are needed. The propagation and reflection of GRBF's are derived using the conventional Q matrix techniques of GO, with an additional Q matrix which defines the Gaussian amplitude variation transverse to the axis of propagation. Numerical results are presented which directly compare the GRBF's with ordinary GO ray-tubes in the GRE format, along with a modal reference solution. The GRBF results are generally better than conventional GRE, but the accuracy degrades considerably when oversized GRBF's are used. However, the development of the GRBF and the numerical results suggest a new elliptical ray-tube basis function (ERBF) which is tracked very similarly to the GRBF. Results using the ERBF's in the GRE expansion give better accuracy than the GRBF's and the ordinary GO ray-tubes, and the ERBF's achieve a 16-to-1 savings in ray-tubes over GO ray-tubes for the same level of accuracy.

INVESTIGATION OF A GAUSSIAN RAY-TUBE BASIS FUNCTION EXPANSION FOR COMPUTING THE ELECTROMAGNETIC SCATTERING FROM LARGE OPEN-ENDED CAVITIES

Robert J. Burkholder

I. INTRODUCTION

Two ray shooting methods have been developed to analyze the electromagnetic scattering by electrically large and realistically complex open-ended cavities [1]. The shooting and bouncing ray (SBR) method [2] launches a dense grid of parallel ray-tubes through the open end into the cavity, and tracks them inside using the laws of geometrical optics (GO). When the ray-tubes exit again through the open end, the projection of each ray-tube on the aperture plane is integrated to give the far zone scattered fields. The SBR method is extremely versatile but it tracks only the incident GO field inside the cavity, neglecting fields diffracted into the cavity by the aperture. The generalized ray expansion (GRE) technique [3] was developed to include these diffraction effects by launching GO ray-tubes radially into the cavity from an array of sources in the open end, with the ray-tubes appropriately weighted depending on the incident field. Once launched in this manner, the ray-tubes in the GRE are tracked inside the cavity and integrated exactly the same as in the SBR method. It was found in [4] that the fields diffracted into the cavity by the aperture may be especially important in the Fourier transformed time domain results because they are responsible for cavity dispersion.

A major limitation of both the GRE and SBR methods is that a very large number of ray-tubes needs to be tracked because the ray-tube cross-sections must remain electrically small. The purpose of the work reported here is to investigate a new Gaussian ray-tube basis function (GRBF) which does not have such a limitation on size, to replace the ordinary GO ray-tubes of the GRE and SBR methods.

In Section II, the GRBF is presented and the laws of propagation and reflection for a GRBF are derived. The GRBF's are then introduced into the GRE format to find the scattering from an open-ended cavity. Section III presents numerical results which com-

pare the GRBF form of GRE with ordinary GRE, along with a reference modal solution [5]. Also in Section III, a new elliptical ray basis function (ERBF) is introduced which follows logically from the GRBF and GRE methods and gives even better results. Conclusions are discussed in Section IV. An $e^{j\omega t}$ time convention is assumed and suppressed throughout the following. Z_o is the free space impedance, λ is the free space wavelength and $k = 2\pi/\lambda$ is the free space wavenumber.

II. THEORY

A GRBF is essentially an astigmatic GO ray-tube with a Gaussian amplitude profile transverse to the propagation axis. The Gaussian amplitude decays away from the propagation axis so that the GRBF is confined to a narrow axial region. The cross-section or "spot size" of a GRBF (defined by the $1/e$ amplitude contour) is elliptical in general, and the axes of the ellipse may or may not be aligned with the principal curvature directions of the GO phase-front. The Gaussian amplitude is defined in terms of an amplitude matrix analogous to the phase curvature matrix used in GO [6]. As with the phase matrix, there are simple rules for transforming the amplitude matrix as the GRBF propagates and reflects from curved walls.

The initial Gaussian amplitude variation of a GRBF is chosen based on the initial conditions of the problem of interest. In the SBR and GRE approaches, the GRBF's start out rotationally symmetric when they are launched into the cavity. After multiple reflections from the cavity walls, the cross-section may deform into an ellipse which may be twisted away from the principal curvature directions of the wavefront. As each GRBF exits the cavity, its projection on the aperture is numerically integrated and summed to give the far zone scattered field.

The Gaussian Ray-Tube Basis Function

Using a notation similar to that of [6] for a general astigmatic GO ray-tube, a GRBF for the electric field is given by

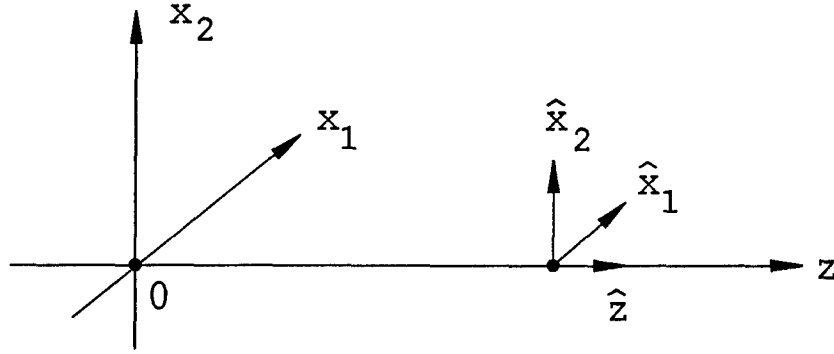


Figure 1: Local coordinate system and unit vectors associated with a general GRBF.

$$\bar{E}(x_1, x_2, z) = \bar{E}(O) \sqrt{\frac{\rho_1}{\rho_1 + z}} \sqrt{\frac{\rho_2}{\rho_2 + z}} \exp \left[-jk \left(z + \frac{1}{2} \bar{x} \cdot Q_p(z) \bar{x} \right) \right] \exp \left[-\frac{1}{2} \bar{x} \cdot Q_a(z) \bar{x} \right] \quad (1)$$

where $\bar{x} = \begin{bmatrix} x_1 \\ x_2 \end{bmatrix}$ in a $(\hat{x}_1, \hat{x}_2, \hat{z})$ coordinate system with the GRBF propagating in the $+\hat{z}$ direction along the z -axis, as shown in Figure 1. \hat{x}_1 and \hat{x}_2 are orthogonal unit vectors normal to the z -axis and define a local right-hand coordinate system according to $\hat{z} = \hat{x}_1 \times \hat{x}_2$. Q_p and Q_a are 2×2 phase curvature and amplitude matrices, respectively. $\bar{E}(O)$ is the electric field at the origin O ; both $\bar{E}(O)$ and $\bar{E}(x_1, x_2, z)$ are assumed to be polarized transverse to the axis of propagation.

$\hat{\rho}_1$ and $\hat{\rho}_2$ are the principal radii of curvature of the phase wavefront at $z = 0$. The principal curvature directions (axes) of the wavefront are denoted by \hat{x}'_1 and \hat{x}'_2 . ρ_1 is positive if the wavefront is diverging in the $\hat{x}'_1 - \hat{z}$ plane as the GRBF propagates in the $+\hat{z}$ direction, and negative if the wavefront is converging; the same is true for ρ_2 in the $\hat{x}'_2 - \hat{z}$ plane. The Q_p matrices are diagonal in the (x'_1, x'_2, z) principal curvature coordinate system, and are given by

$$Q'_p(0) = \begin{bmatrix} \frac{1}{\rho_1} & 0 \\ 0 & \frac{1}{\rho_2} \end{bmatrix}; \quad Q'_p(z) = \begin{bmatrix} \frac{1}{\rho_1 + z} & 0 \\ 0 & \frac{1}{\rho_2 + z} \end{bmatrix} \quad (2)$$

where the Q_p matrices are primed to indicate principal axes. The diagonal terms in (2) define the eigenvalues of the matrices, so the principal radii of curvature for an arbitrary

$Q_p(0)$ are given by

$$\frac{1}{\rho_{1,2}} = \frac{1}{2} \text{tr} Q_p(0) \pm \frac{1}{2} \sqrt{[\text{tr} Q_p(0)]^2 - 4 \det Q_p(0)} \quad (3)$$

in which the plus sign is associated with ρ_1 and the minus sign with ρ_2 . The trace and determinant of a matrix are defined by

$$\text{tr} Q = [Q]_{11} + [Q]_{22} \quad (4)$$

$$\det Q = [Q]_{11}[Q]_{22} - [Q]_{12}[Q]_{21}. \quad (5)$$

The correct branches of the square-root terms in (1) are defined by the following, which applies to both the ρ_1 and ρ_2 terms:

$$\sqrt{\frac{\rho_1}{\rho_1 + z}} = \begin{cases} \left| \sqrt{\frac{\rho_1}{\rho_1 + z}} \right| & : \frac{\rho_1}{\rho_1 + z} > 0 \\ j \left| \sqrt{\frac{\rho_1}{\rho_1 + z}} \right| & : \frac{\rho_1}{\rho_1 + z} < 0. \end{cases} \quad (6)$$

Notice that the square root terms are singular for $z = -\rho_1$ and $z = -\rho_2$. These are the caustic locations at which both ordinary GO ray-tubes and GRBF's are not valid. Also notice from (6) that a ray-tube undergoes a 90° phase shift as it passes through a caustic.

The exponential term in the Gaussian amplitude factor of the GRBF is $-C(x_1, x_2)$ where

$$\begin{aligned} C(x_1, x_2) &= \frac{1}{2} \bar{x} \cdot Q_a(z) \bar{x} \\ &= \frac{1}{2} \{ [Q_a(z)]_{11} x_1^2 + ([Q_a(z)]_{12} + [Q_a(z)]_{21}) x_1 x_2 + [Q_a(z)]_{22} x_2^2 \} \end{aligned} \quad (7)$$

which is a general equation for an ellipse centered transverse to the z -axis. Therefore, the cross-section of a completely general GRBF is an ellipse which may be arbitrarily rotated with respect to the principal curvature axes. To insure that the amplitude decays away from the propagation axis it is necessary that $[Q_a(z)]_{11}$ and $[Q_a(z)]_{22}$ are greater than zero. The power flow in a GRBF is given by

$$P(z) = \int_{-\infty}^{\infty} \int_{-\infty}^{\infty} |\bar{E}(x_1, x_2, z)|^2 dx_1 dx_2$$

$$\begin{aligned}
&= \frac{|\bar{E}(O)|^2 \pi}{\sqrt{[Q_a(z)]_{11}[Q_a(z)]_{22} - [Q_a(z)]_{12}[Q_a(z)]_{21}}} \left| \frac{\rho_1}{\rho_1 + z} \right| \left| \frac{\rho_2}{\rho_2 + z} \right| \\
&= \frac{|\bar{E}(O)|^2 \pi}{\sqrt{\det Q_a(z)}} \left| \frac{\rho_1}{\rho_1 + z} \right| \left| \frac{\rho_2}{\rho_2 + z} \right| \quad (8)
\end{aligned}$$

from which it follows that $\det Q_a(z) > 0$. Within these restrictions the elements of the Q_a matrix are initially chosen based on the launching conditions in the GRE and SBR methods. For a rotationally symmetric GRBF, Q_a is diagonal and the elements are equal (i.e., $[Q_a]_{11} = [Q_a]_{22}$). The procedure for determine the initial Q_a matrix is discussed later in the GRE portion of this section. The initial choice for the elements of Q_p will also be discussed.

Finally, the magnetic field of a GRBF is related to the electric field by

$$\bar{H}(x_1, x_2, z) = \frac{1}{Z_o} \hat{z} \times \bar{E}(x_1, x_2, z) \quad (9)$$

which is derived from GO.

Propagation of a Gaussian Ray-Tube

It is seen from (2) that

$$Q_p'^{-1}(z) = Q_p'^{-1}(0) + zI \quad (10)$$

where I is a 2×2 identity matrix. To translate this result to the arbitrary axes (x_1, x_2, z) , the unitary translation matrix defined by $\bar{x}' = \Theta \bar{x}$ is given by

$$\Theta = \begin{bmatrix} \hat{x}'_1 \cdot \hat{x}_1 & \hat{x}'_1 \cdot \hat{x}_2 \\ \hat{x}'_2 \cdot \hat{x}_1 & \hat{x}'_2 \cdot \hat{x}_2 \end{bmatrix} \quad (11)$$

from which it can be shown that $Q = \Theta^T Q' \Theta$ in general. (10) may be translated to

$$\Theta^T Q_p'^{-1}(z) \Theta = \Theta^T Q_p'^{-1}(0) \Theta + \Theta^T z I \Theta \quad (12)$$

which reduces to

$$Q_p^{-1}(z) = Q_p^{-1}(0) + zI. \quad (13)$$

Therefore, the result of (10) is invariant to coordinate rotation about the z -axis, and the propagation of the general phase curvature matrix from the origin O to z along the z -axis is given by

$$Q_p(z) = [Q_p^{-1}(0) + zI]^{-1}. \quad (14)$$

The propagation of the amplitude matrix $Q_a(z)$ is found by conserving power flow in the GRBF. The power flow at z is given by (8), so the power flow at $z = 0$ is given by

$$P(0) = \frac{|\bar{E}(O)|^2 \pi}{\sqrt{[Q_a(0)]_{11}[Q_a(0)]_{22} - [Q_a(0)]_{12}[Q_a(0)]_{21}}}. \quad (15)$$

Comparing this with (8) yields the solution,

$$Q_a(z) = \begin{bmatrix} \left(\frac{\rho_1}{\rho_1+z}\right)^2 [Q_a(0)]_{11} & \frac{\rho_1 \rho_2}{(\rho_1+z)(\rho_2+z)} [Q_a(0)]_{12} \\ \frac{\rho_1 \rho_2}{(\rho_1+z)(\rho_2+z)} [Q_a(0)]_{21} & \left(\frac{\rho_2}{\rho_2+z}\right)^2 [Q_a(0)]_{22} \end{bmatrix} \quad (16)$$

which has been shown to be unique by considering the 3-D GRBF as the product of two orthogonal 2-D GRBF's [7]. Using matrix notation, (16) may be written in the principal curvature coordinate system as

$$Q'_a(z) = Q'_p(z) Q_p'^{-1}(0) Q'_a(0) Q_p'^{-1}(0) Q'_p(z). \quad (17)$$

Translating this result to an arbitrary coordinate system using Θ of (11) and the property $\Theta\Theta^T = I$, yields

$$\Theta^T Q'_a(z) \Theta = \Theta^T Q'_p(z) \Theta \Theta^T Q_p'^{-1}(0) \Theta \Theta^T Q'_a(0) \Theta \Theta^T Q_p'^{-1}(0) \Theta \Theta^T Q'_p(z) \Theta \quad (18)$$

which reduces to

$$Q_a(z) = Q_p(z) Q_p^{-1}(0) Q_a(0) Q_p^{-1}(0) Q_p(z). \quad (19)$$

Therefore, (17) is invariant to coordinate rotation about the z -axis and (19) gives the general amplitude matrix at z in terms of the amplitude matrix at 0 and the phase matrices at 0 and z .

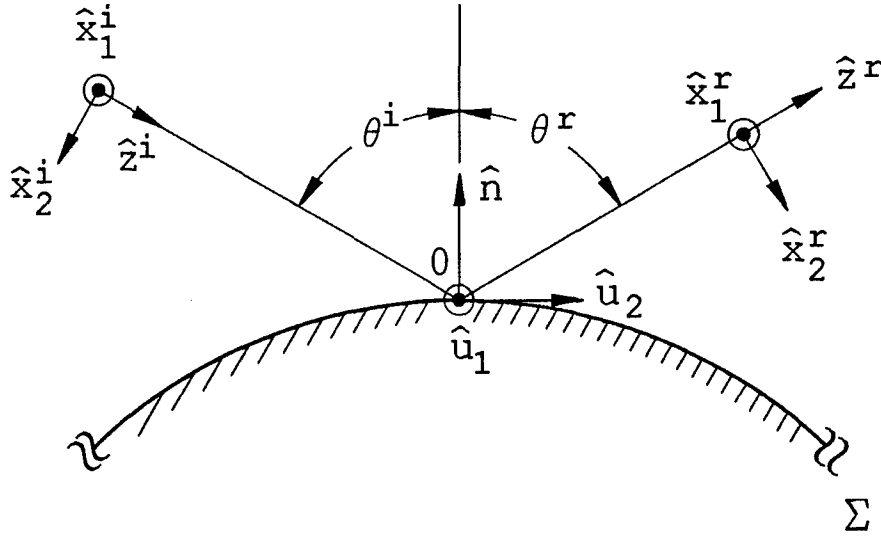


Figure 2: Geometry for the reflection of a GRBF from a curved surface.

Reflection of a Gaussian Ray-Tube

The reflection of a GRBF from an arbitrarily curved surface is found by phase and amplitude matching an incident GRBF with a reflected GRBF on the surface close to the point of reflection O . It is assumed that the surface may be described locally by a 2×2 curvature matrix around the point of reflection using the principal radii of curvature of the surface at that point. Referring to Figure 2, let the incident GRBF be given as

$$\begin{aligned} \bar{E}(x_1^i, x_2^i, z^i) &= \bar{E}^i(O) \sqrt{\frac{\rho_1^i}{\rho_1^i + z^i}} \sqrt{\frac{\rho_2^i}{\rho_2^i + z^i}} \exp \left[-jk \left(z^i + \frac{1}{2} \bar{x}^i \cdot Q_p^i(z^i) \bar{x}^i \right) \right] \\ &\quad \cdot \exp \left[-\frac{1}{2} \bar{x}^i \cdot Q_a^i(z^i) \bar{x}^i \right] \end{aligned} \quad (20)$$

and the reflected GRBF as

$$\begin{aligned} \bar{E}(x_1^r, x_2^r, z^r) &= \bar{E}^r(O) \sqrt{\frac{\rho_1^r}{\rho_1^r + z^r}} \sqrt{\frac{\rho_2^r}{\rho_2^r + z^r}} \exp \left[-jk \left(z^r + \frac{1}{2} \bar{x}^r \cdot Q_p^r(z^r) \bar{x}^r \right) \right] \\ &\quad \cdot \exp \left[-\frac{1}{2} \bar{x}^r \cdot Q_a^r(z^r) \bar{x}^r \right]. \end{aligned} \quad (21)$$

The incident and reflected GRBF's are in the (x_1^i, x_2^i, z^i) and (x_1^r, x_2^r, z^r) coordinate systems, respectively, and it is assumed the z^i and z^r axes intersect at P and lie in the

plane of incidence defined by \hat{z}^i and \hat{n} . The z^i and z^r axes make angles of θ^i and θ^r with \hat{n} , respectively. The origin of both coordinate systems is at O . \hat{u}_1 and \hat{u}_2 are orthogonal unit vectors tangent to the surface at P , and \hat{n} is the unit surface normal such that $\hat{n} = \hat{u}_1 \times \hat{u}_2$. The following coordinate relationships are chosen for convenience,

$$\begin{aligned} \hat{u}_1 &= -\hat{n} \times \hat{z}^i / |\hat{n} \times \hat{z}^i| & ; & \quad \hat{u}_2 = \hat{n} \times \hat{u}_1 \\ \hat{x}_1^i &= \hat{u}_1 & ; & \quad \hat{x}_2^i = \hat{z}^i \times \hat{x}_1^i \\ \hat{x}_1^r &= \hat{u}_1 & ; & \quad \hat{x}_2^r = \hat{z}^r \times \hat{x}_1^r, \end{aligned} \quad (22)$$

which define \hat{u}_1 , \hat{x}_1^i , and \hat{x}_1^r to be normal to the plane of incidence.

Matching the GRBF's exactly at O yields

$$\bar{E}^r(O) = \bar{\bar{\Gamma}} \cdot \bar{E}^i(O) \quad (23)$$

where $\bar{\bar{\Gamma}}$ is the diadic plane wave reflection coefficient given by

$$\bar{\bar{\Gamma}} = \begin{bmatrix} \Gamma_{\perp} & 0 \\ 0 & \Gamma_{\parallel} \end{bmatrix} \quad (24)$$

for use when \bar{E}^i is decomposed into components perpendicular (\perp) and parallel (\parallel) to the plane of incidence.

Following the procedure in [6], the equation of the surface Σ in the close vicinity to O may be written as

$$\bar{r}(\bar{t}) = \bar{t} - \frac{1}{2} [\bar{t} \cdot Q_{\Sigma} \bar{t}] \hat{n} \quad (25)$$

where $\bar{t} = t_1 \hat{u}_1 + t_2 \hat{u}_2$ and Q_{Σ} is the 2×2 curvature matrix for the surface at O . The phase of the incident GRBF on Σ is $-kS^i(\bar{r})$ where

$$\begin{aligned} S^i(\bar{r}) &= z^i + \frac{1}{2} \bar{x}^i \cdot Q_p^i(0) \bar{x}^i \\ &= \hat{z}^i \cdot \bar{r}(\bar{t}) + \frac{1}{2} \bar{x}^i \cdot Q_p^i(0) \bar{x}^i \\ &= \hat{z}^i \cdot \bar{t} + \frac{1}{2} [\bar{t} \cdot Q_{\Sigma} \bar{t}] \cos \theta^i + \frac{1}{2} \bar{x}^i \cdot Q_p^i(0) \bar{x}^i. \end{aligned} \quad (26)$$

Using the coordinate transformation $\bar{x} = \Theta^i \bar{t}$ where

$$\Theta^i = \begin{bmatrix} \hat{x}_1^i \cdot \hat{u}_1 & \hat{x}_1^i \cdot \hat{u}_2 \\ \hat{x}_2^i \cdot \hat{u}_1 & \hat{x}_2^i \cdot \hat{u}_2 \end{bmatrix} = \begin{bmatrix} 1 & 0 \\ 0 & -\cos \theta^i \end{bmatrix} \quad (27)$$

$S^i(\bar{r})$ may be written as

$$S^i(\bar{r}) = \hat{z}^i \cdot \bar{t} + \frac{1}{2} \bar{t} \cdot [Q_\Sigma \cos \theta^i + (\Theta^i)^T Q_p^i(0) \Theta^i] \bar{t}. \quad (28)$$

Similarly for the phase of the reflected GRBF,

$$S^r(\bar{r}) = \hat{z}^r \cdot \bar{t} + \frac{1}{2} \bar{t} \cdot [-Q_\Sigma \cos \theta^r + (\Theta^r)^T Q_p^r(0) \Theta^r] \bar{t} \quad (29)$$

where Θ^r is given by

$$\Theta^r = \begin{bmatrix} \hat{x}_1^r \cdot \hat{u}_1 & \hat{x}_1^r \cdot \hat{u}_2 \\ \hat{x}_2^r \cdot \hat{u}_1 & \hat{x}_2^r \cdot \hat{u}_2 \end{bmatrix} = \begin{bmatrix} 1 & 0 \\ 0 & \cos \theta^r \end{bmatrix}. \quad (30)$$

Phase-matching (28) and (29) yields

$$\theta^r = \theta^i \quad (31)$$

$$(\Theta^i)^T Q_p^i(0) \Theta^i + 2Q_\Sigma \cos \theta^i = (\Theta^r)^T Q_p^r(0) \Theta^r \quad (32)$$

which gives $Q_p^r(0)$ in terms of $Q_p^i(0)$ and Q_Σ .

The amplitude terms of the incident and reflected GRBF, $-C^i(\bar{r})$ and $-C^r(\bar{r})$, respectively, are given by

$$\begin{aligned} C^i(\bar{r}) &= \frac{1}{2} \bar{x}^i \cdot Q_a^i(0) \bar{x}^i \\ C^r(\bar{r}) &= \frac{1}{2} \bar{x}^r \cdot Q_a^r(0) \bar{x}^r. \end{aligned} \quad (33)$$

Following the same procedure as the phase matching, amplitude matching yields

$$(\Theta^i)^T Q_a^i(0) \Theta^i = (\Theta^r)^T Q_a^r(0) \Theta^r \quad (34)$$

which gives $Q_a^r(0)$ in terms of $Q_a^i(0)$. Note that the transformation of the Gaussian amplitude matrix does not depend on the surface curvature matrix Q_Σ . The transformation is entirely one of coordinate rotation.

The Generalized Ray Expansion

The generalized ray expansion (GRE) is a method of coupling incident fields into an open-ended cavity via the aperture using high-frequency asymptotic ray techniques.

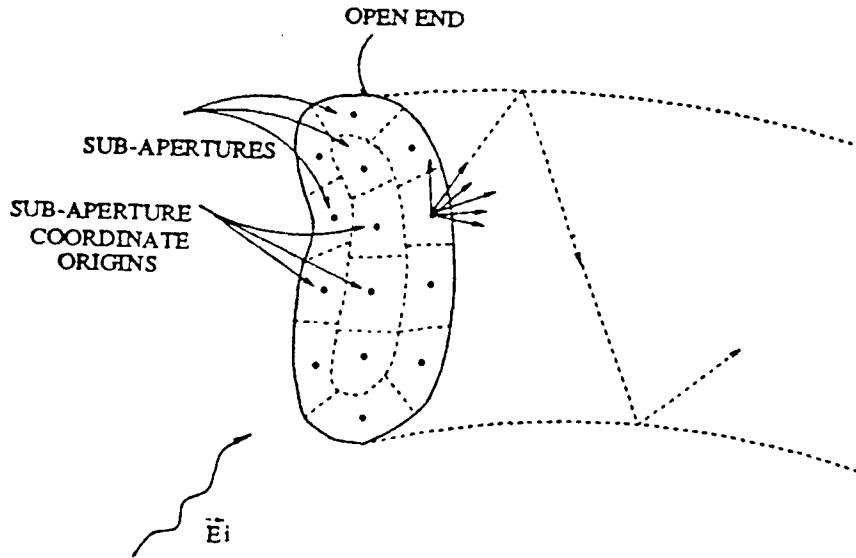


Figure 3: Aperture discretization and ray launching in the GRE method.

The aperture of the cavity is discretized into a number of subapertures and ray-tubes are launched radially into the cavity from the geometric centers of the subapertures, as illustrated in Figure 3. The ray-tubes are weighted to reproduce the far field pattern of each subaperture in the absence of the cavity, which is found by integrating the equivalent currents in each subaperture due to the incident field. Typically the Kirchhoff approximation is used to find these currents [3, 1]. After being launched into the cavity the ray-tubes are tracked through multiple reflections until they exit again through the open end. Aperture integration (again based on the Kirchhoff approximation) is used to integrate the ray-tubes to give the far zone scattered field. The GRE method intrinsically includes the fields diffracted into the cavity by the aperture, to within the Kirchhoff approximation. An added advantage of the GRE method is that the ray-tubes only need to be tracked once, independent of the excitation, because the ray launching directions do not depend on the plane wave incidence angle as they do in the SBR method.

Referring to Figure 4, the far zone free space electric field radiated by the n^{th} sub-

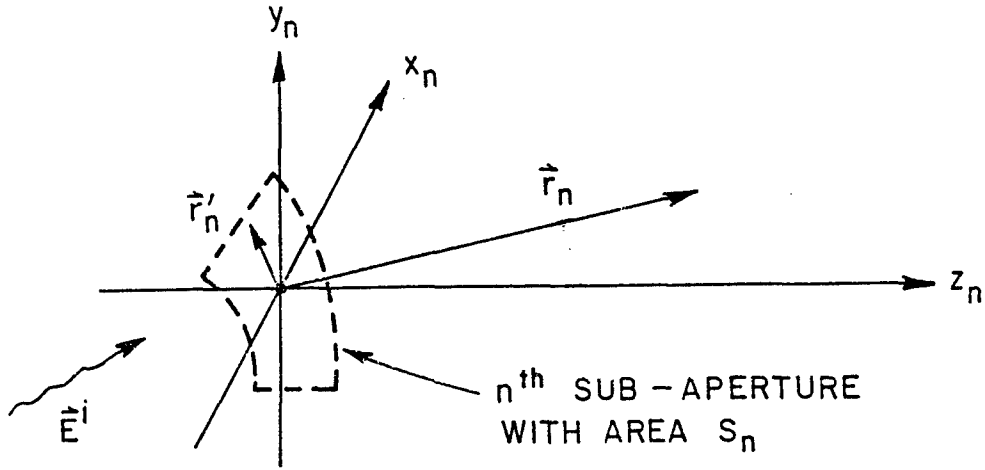


Figure 4: The n^{th} subaperture radiating in free space, excited by the incident fields \bar{E}^i and \bar{H}^i .

aperture S_n , centered at its coordinate origin O_n is given by

$$\bar{E}_n(\bar{r}_n) = jk \frac{e^{-jk r_n}}{4\pi r_n} \int_{S_n} [\hat{r}_n \times \bar{M}^i(\bar{r}'_n) + Z_o \hat{r}_n \times \hat{r}_n \times \bar{J}^i(\bar{r}'_n)] e^{jk \hat{r}'_n \cdot \bar{r}_n} dS' \quad (35)$$

where $\hat{r}_n = \bar{r}_n/r$ is a point in the far zone of the subaperture. The Kirchhoff equivalent currents are given by

$$\bar{M}^i(\bar{r}'_n) = \bar{E}^i(\bar{r}'_n) \times \hat{n} ; \bar{J}^i(\bar{r}'_n) = \hat{n} \times \bar{H}^i(\bar{r}'_n). \quad (36)$$

where \bar{E}^i and \bar{H}^i are the incident electric and magnetic fields, and \hat{n} is the unit surface normal of S_n pointing into the cavity.

(35) has the form of a spherical wave radiating from the subaperture center, with a pattern factor given by the integral term. Therefore, ray-tubes may be launched radially from O_n with an initial spherical spread factor and tracked with the cavity present. The ray-tubes may be weighted by the integral term in (35) after they have been tracked because the integral depends only on the launch direction \hat{r}_n and the incident field, independent of the cavity geometry. This allows multiple excitations to be analyzed without re-launching the ray-tubes for each new excitation.

In the conventional GRE method, a grid of ray-tubes is launched in a cone from each subaperture as shown in Figure 5. The cone angle, or maximum angle of ray launch, is

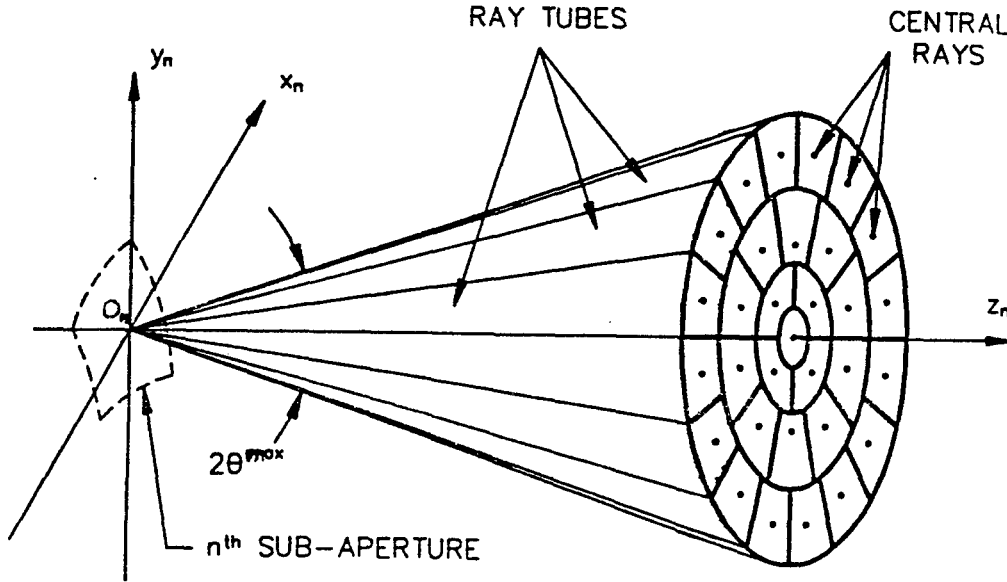


Figure 5: A grid of GRE ray-tubes launched in a cone from the n^{th} subaperture.

θ^{max} . The ray-tubes are launched with an approximately constant angular grid spacing $\Delta\theta$ and are tracked along their central (axial) rays until they exit the cavity. The field of a ray-tube is polarized transverse to its axis and is assumed to be constant over a cross-section, with the field given by tracking the axial ray according to GO. Initially, the ray-tube cross-section is approximately square as in Figure 5, but will deform after reflections from the curved cavity walls. After reflecting, the shape is no longer known. However, if the ray-tubes maintain an electrically small cross-section ($\sim \lambda^2/4$) then the exact shape is not required for the aperture integration [8]. So, unfortunately, a very large number of ray-tubes may need to be tracked for electrically large cavities. The GRBF's presented here do not have this limitation because the transverse Gaussian amplitude distribution of a GRBF is tracked along with the GO phase-front of the axial ray. So the cross-sectional shape, or spot size, is always known and is elliptical in general.

To implement GRBF's into the GRE method is very straightforward. A grid of GRBF's are launched in a cone from the subaperture centers, with an approximately constant angular grid spacing $\Delta\theta$. However, the GRBF's overlap their nearby neighbors somewhat because they are not truncated to within discrete boundaries as are ordinary

GO ray-tubes. So the initial elements of the Q_a matrix must be carefully chosen such that the far field of the each subaperture is reproduced by the GRBF expansion with sufficient accuracy. The following initial GRBF has been arrived at through theoretical considerations and trial-and-error [7]. At the first point of reflection, the initial GRBF is given by

$$\bar{E}(x_1^i, x_2^i, z^i) = \hat{p} \frac{0.5776}{z^i} \exp \left[-jk \left(z_i + \frac{1}{2} \bar{x}^i \cdot Q_p^i(z^i) \bar{x}^i \right) \right] \exp \left[-\frac{1}{2} \bar{x}^i \cdot Q_a^i(z^i) \bar{x}^i \right] \quad (37)$$

where z^i is the distance from the subaperture center from which the GRBF is launched to the first reflection point and \hat{p} is a unit polarization vector. In practice, two orthogonal polarization vectors (e.g., $\hat{\theta}$ and $\hat{\phi}$) are tracked simultaneously so that an arbitrarily polarized incident field may be handled using superposition. The initial Q matrices just before the first reflection are given by

$$Q_p^i(z^i) = \begin{bmatrix} \frac{1}{z^i} & 0 \\ 0 & \frac{1}{z^i} \end{bmatrix} ; Q_a^i(z^i) = \begin{bmatrix} \frac{\alpha^i}{(z^i)^2} & 0 \\ 0 & \frac{\alpha^i}{(z^i)^2} \end{bmatrix} \quad (38)$$

where

$$\alpha^i = \frac{8}{3} \log 4 / \Delta \theta^2. \quad (39)$$

The constant factor of 0.5776 in (37) appears due to the overlap effects of nearby GRBF's in the grid. The relationship between α^i and the angular grid spacing $\Delta \theta$ in (39) is obtained by adjusting the angular beam widths of the GRBF's to get a good reproduction of the subaperture far field pattern. The coordinates x_1^i and x_2^i may be chosen in whatever way is convenient because the initial GRBF is rotationally symmetric. The conventions in (22) are recommended.

The first reflected GRBF will have the general form of (21) with Q_p^r and Q_a^r obtained using (32) and (34), respectively. It will propagate to the next reflection point according to (14) and (19) and transform into a new GRBF after reflection. This process continues until the GRBF exits through the open end where it is summed with all other GRBF's

to give the total fields in the aperture, \bar{E}_a and \bar{H}_a , which are then integrated to obtain the far zone scattered field.

Aperture Integration

Using the Kirchhoff approximation, aperture integration gives the far zone field scattered by the cavity as

$$\bar{E}^s(\bar{r}) = jk \frac{e^{-jk r}}{4\pi r} \int_{S_a} \left[\hat{r} \times \bar{M}_a(\bar{r}') + Z_o \hat{r} \times \hat{r} \times \bar{J}_a(\bar{r}') \right] e^{jk \bar{r}' \cdot \hat{r}} dS' \quad (40)$$

where $\hat{r} = \bar{r}/r$ is the far zone observation point and \bar{r}' is a point of integration in the cavity aperture S_a . The Kirchhoff equivalent currents in the aperture are given by

$$\bar{M}_a(\bar{r}') = \bar{E}_a(\bar{r}') \times \hat{n}' ; \bar{J}_a(\bar{r}') = \hat{n}' \times \bar{H}_a(\bar{r}') \quad (41)$$

where \bar{E}_a and \bar{H}_a are the electric and magnetic fields in the aperture due to all the GRBF's which exit through the open end after being tracked within the cavity.

The integral in (40) could theoretically be evaluated in closed form for each individual GRBF and summed with the integrals of all the other GRBF's, but the integral is quite cumbersome because of the arbitrary orientation of the GRBF with respect to the aperture plane. In practice, the integral in (40) is evaluated numerically by summing over a dense grid of points in the aperture which sample the fields \bar{E}_a and \bar{H}_a . As each GRBF exits the cavity, its fields are added to the grid of field points and the integration is performed after all the GRBF's have been tracked. This is much more efficient than individually numerically integrating each GRBF.

III. RESULTS

The numerical results are in the form of co-polarized monostatic radar cross section (RCS) vs. incidence angle. The RCS (σ) is defined by

$$\sigma = \lim_{r \rightarrow \infty} 4\pi r^2 \frac{|E^s(\bar{r})|^2}{|\bar{E}^i|^2} \quad (42)$$

where $|\bar{E}^i|$ is the magnitude of the incident plane wave, and $E^s(\bar{r})$ is the component of the far zone scattered field co-polarized to the incident field. The units of RCS are decibels relative to a square meter (dBsm). In all the results presented here, the frequency

is 300 MHz so the wavelength is one meter. Both horizontal and vertical polarizations are included (with respect to the plane of incidence). No external scattering effects are included, such as the scattering from the rim at the open end. The results are compared with the hybrid modal reference solution [5]. Finally, in all the direct comparisons between the GRBF and ordinary GO ray-tube expansions, the subaperture grids and ray-tube launching patterns are identical and the maximum ray launching angle θ^{max} is 75° .

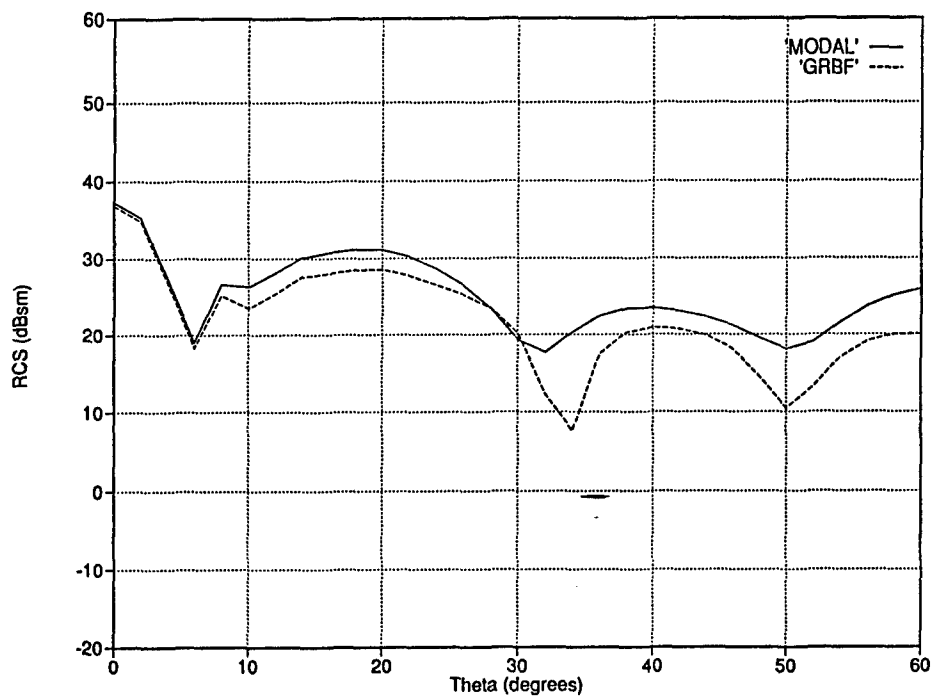
Figure 6 shows the RCS patterns of a 6 X 6 wavelength cylindrical cavity with a flat termination found using GRBF basis functions in the GRE, and Figure 7 shows the same results using ordinary GO ray-tubes in the GRE. The cross-sectional areas of the ray-tubes are approximately one wavelength squared for this ray-tube density. The GRBF results are somewhat better than the ordinary GRE results, even though GRE is expected to work fairly well for this small of ray-tubes.

Figure 8 shows the RCS patterns for the same 6 X 6 wavelength cylindrical cavity found using GRBF basis functions in the GRE, and Figure 9 shows the same results using ordinary GO ray-tubes in the GRE. The cross-sectional areas of the ray-tubes are approximately two wavelengths squared for this ray-tube density. The GRBF results are still better than the GRE, although the accuracy has degraded somewhat due to the larger ray-tubes.

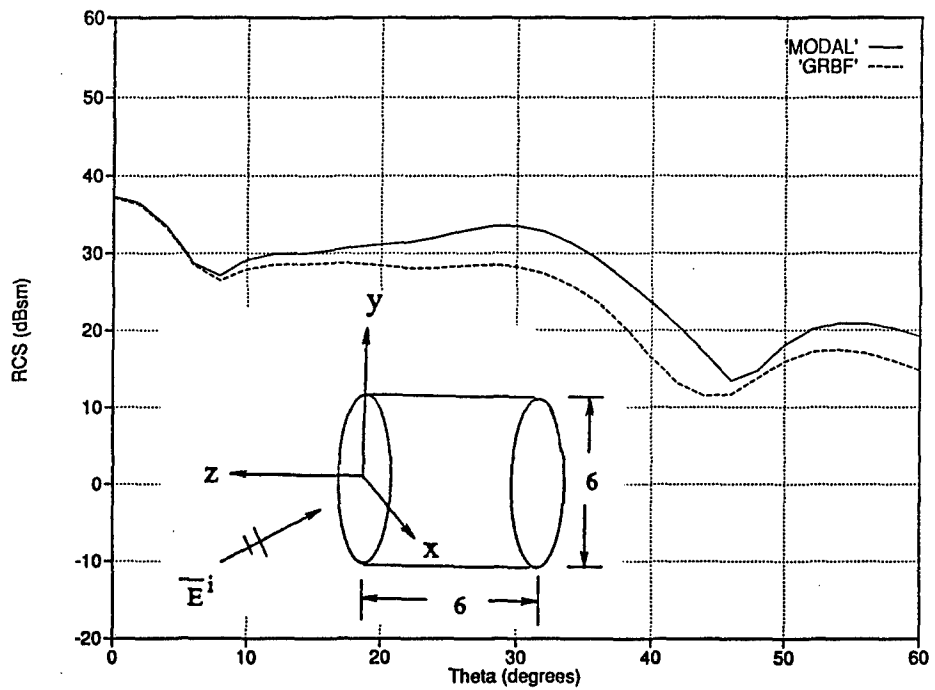
Figure 10 shows the RCS patterns for the same 6 X 6 wavelength cylindrical cavity found using GRBF basis functions in the GRE, and Figure 11 shows the same results using ordinary GO ray-tubes in the GRE. The cross-sectional areas of the ray-tubes are approximately four wavelengths squared for this ray-tube density. The accuracy of both methods has degraded considerably for this large of ray-tubes. The GRE method is expected to give poor results because the cross-sectional shapes of the ordinary ray-tubes are not known, so it is always assumed that they are circular for convenience. This assumption is only valid if the cross-section of the ray-tube is small in terms of wavelength,

which is certainly not the case in Figure 11. It was hoped that the GRBF's would maintain accuracy for larger cross-sections because their Gaussian amplitude variations are computed during the ray tracing process, but the results of Figure 10 suggest otherwise.

To see if the GRBF's may work better for a larger cavity, Figure 12 shows the RCS patterns of a 12 X 12 wavelength cylindrical cavity found using GRBF basis functions in the GRE, and Figure 13 shows the same results using ordinary GO ray-tubes in the GRE. The cross-sectional areas of the ray-tubes are again approximately four wavelengths squared for this ray-tube density. Both the GRBF and GRE results are better than the 6 X 6 cavity results of Figures 10 and 11 which use the same size of ray-tubes. However, the overall accuracy is not overly impressive.

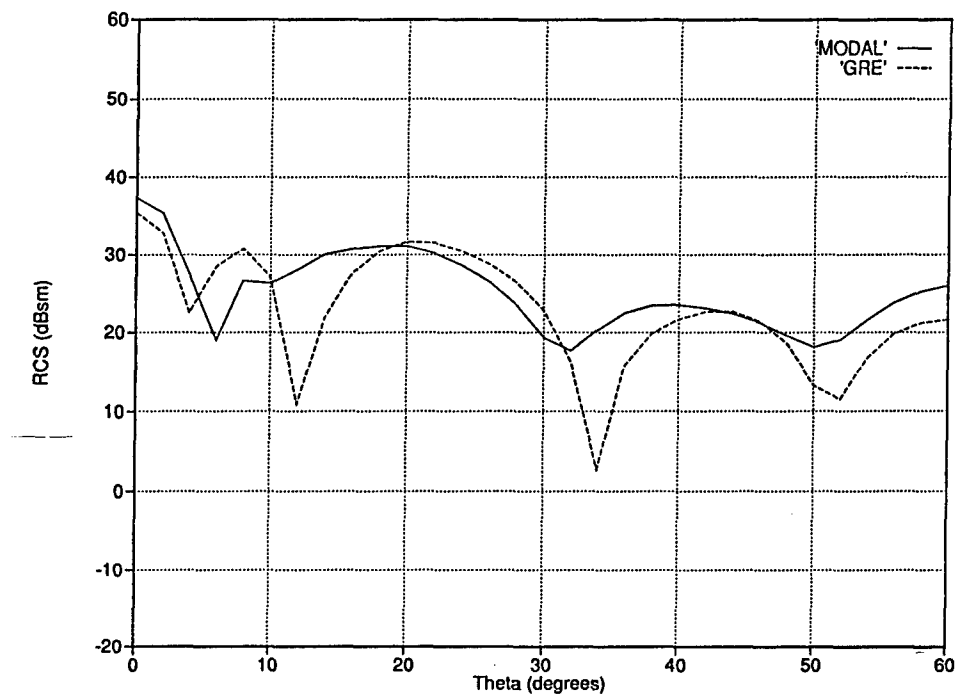


(a) Horizontal polarization.

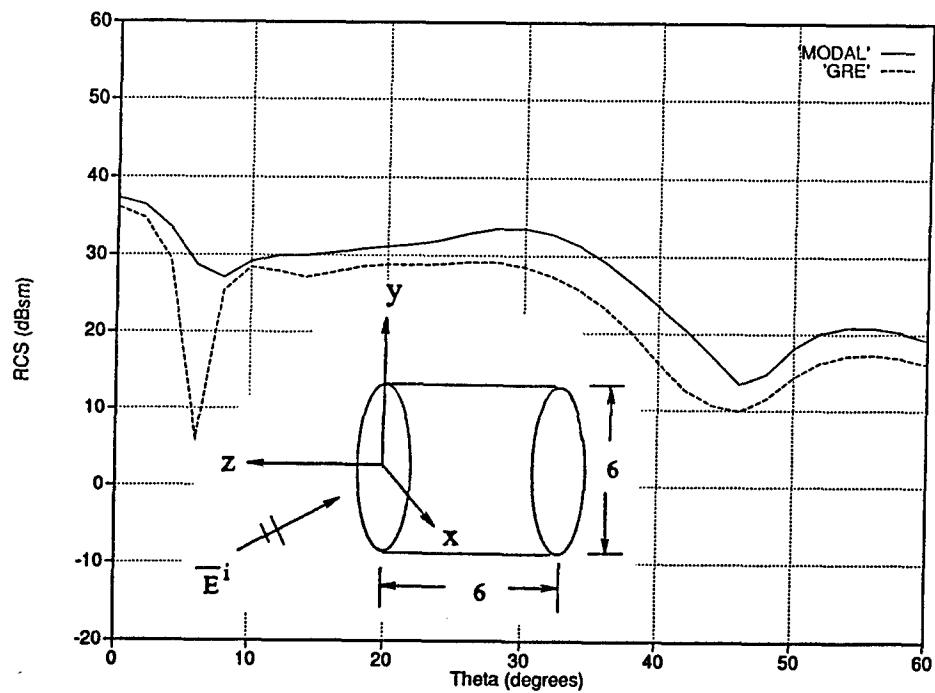


(b) Vertical polarization.

Figure 6: RCS patterns of a 6 X 6 wavelength cylindrical cavity. 32 subapertures, 84.548 GRBF's.

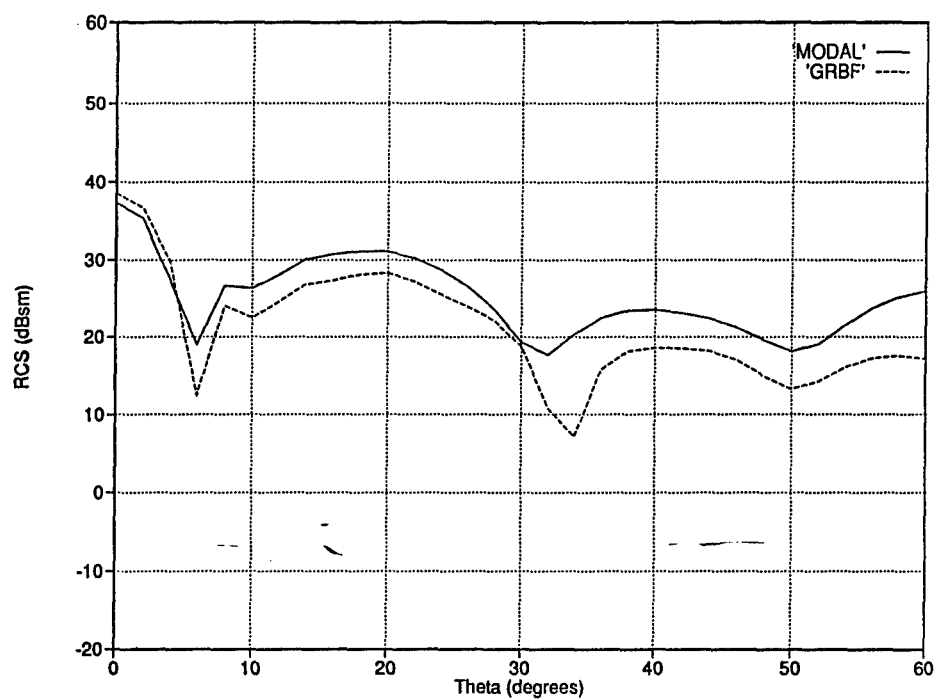


(a) Horizontal polarization.

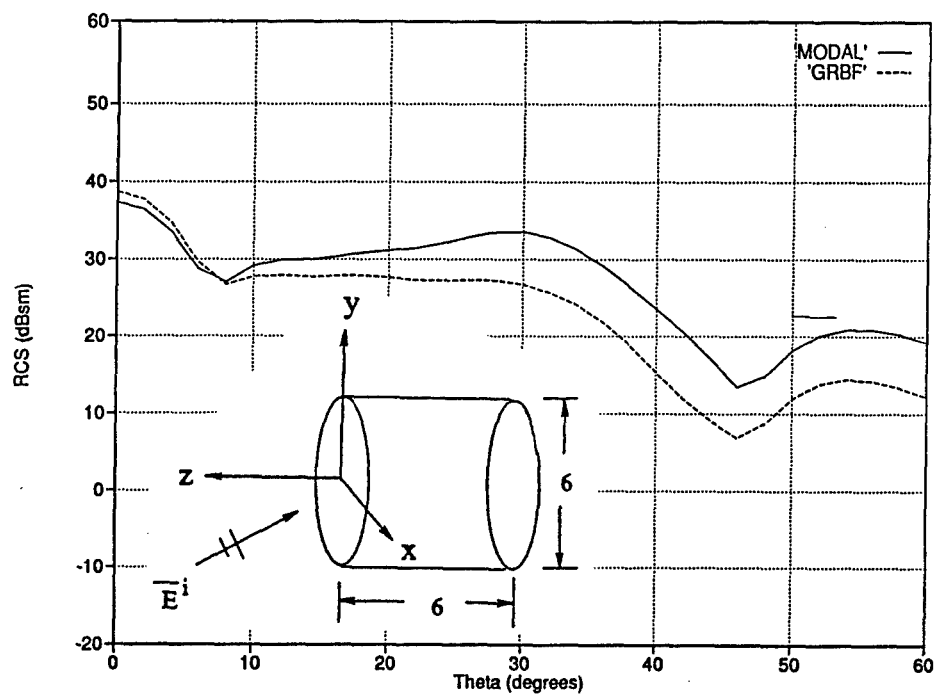


(b) Vertical polarization.

Figure 7: RCS patterns of a 6 X 6 wavelength cylindrical cavity. 32 subapertures, 84,548 GO ray-tubes.

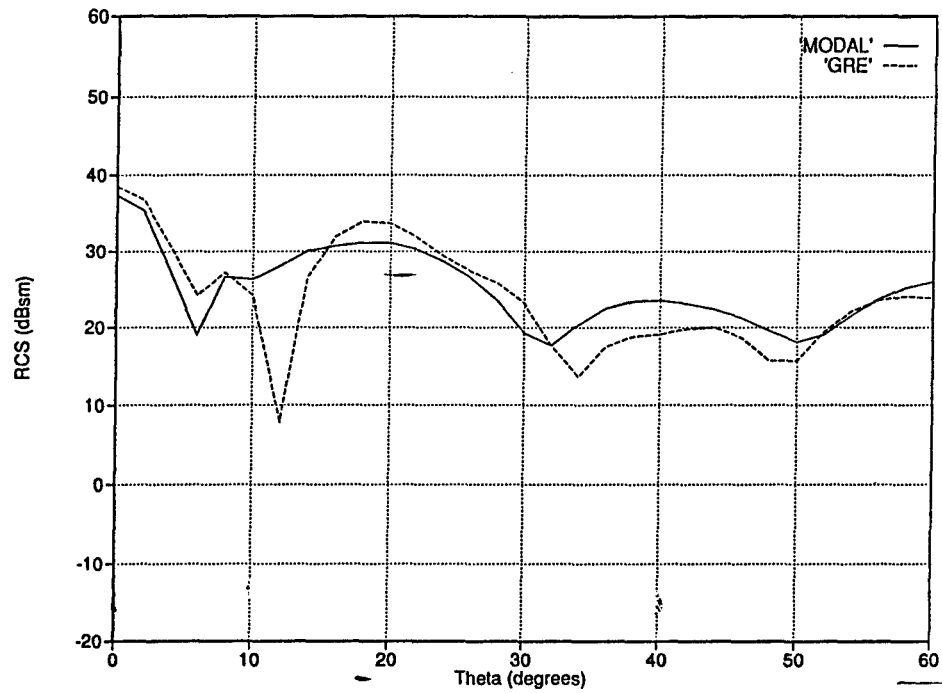


(a) Horizontal polarization.

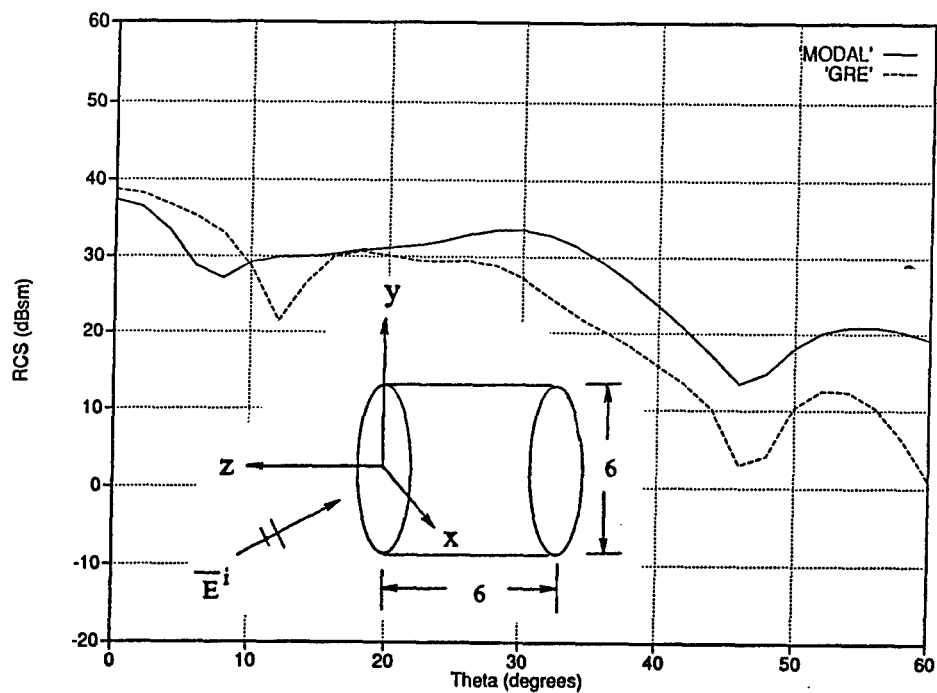


(b) Vertical polarization.

Figure 8: RCS patterns of a 6 X 6 wavelength cylindrical cavity. 32 subapertures, 17,436 GRBF's.

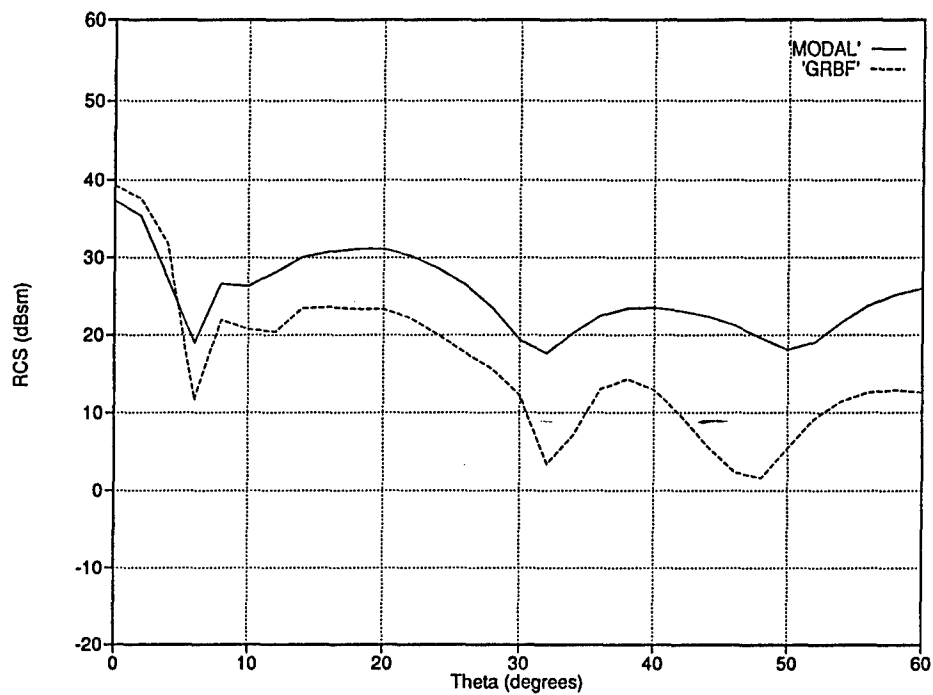


(a) Horizontal polarization.

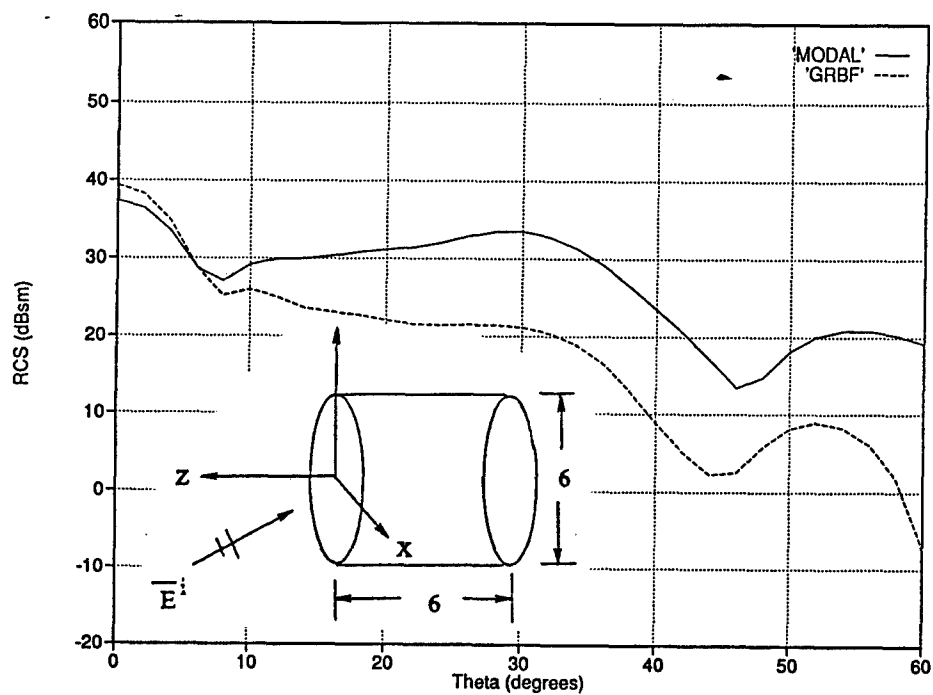


(b) Vertical polarization.

Figure 9: RCS patterns of a 6 X 6 wavelength cylindrical cavity. 32 subapertures, 17,436 GRE ray-tubes.

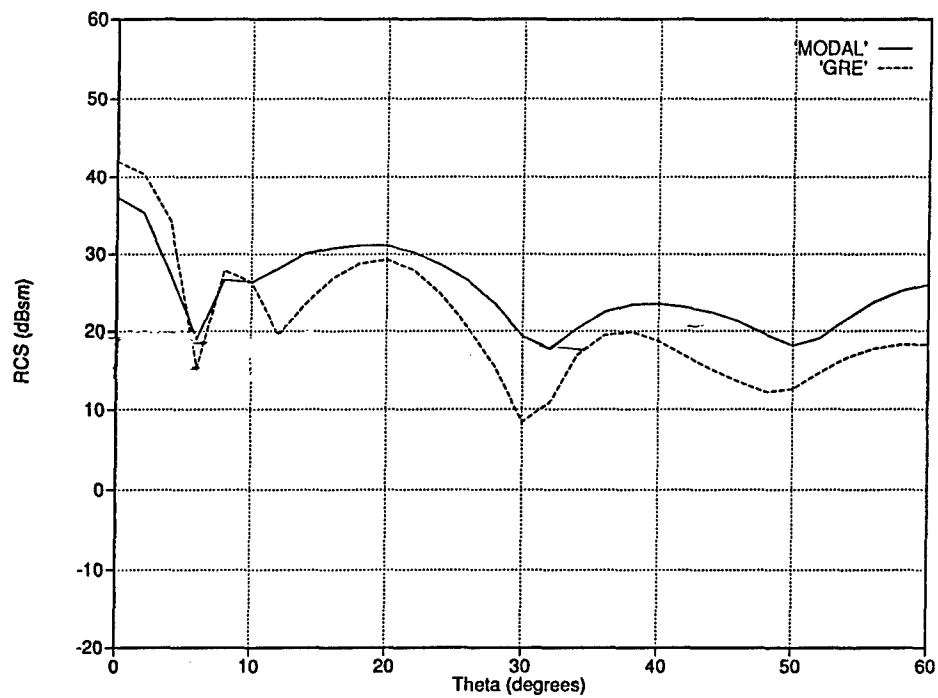


(a) Horizontal polarization.

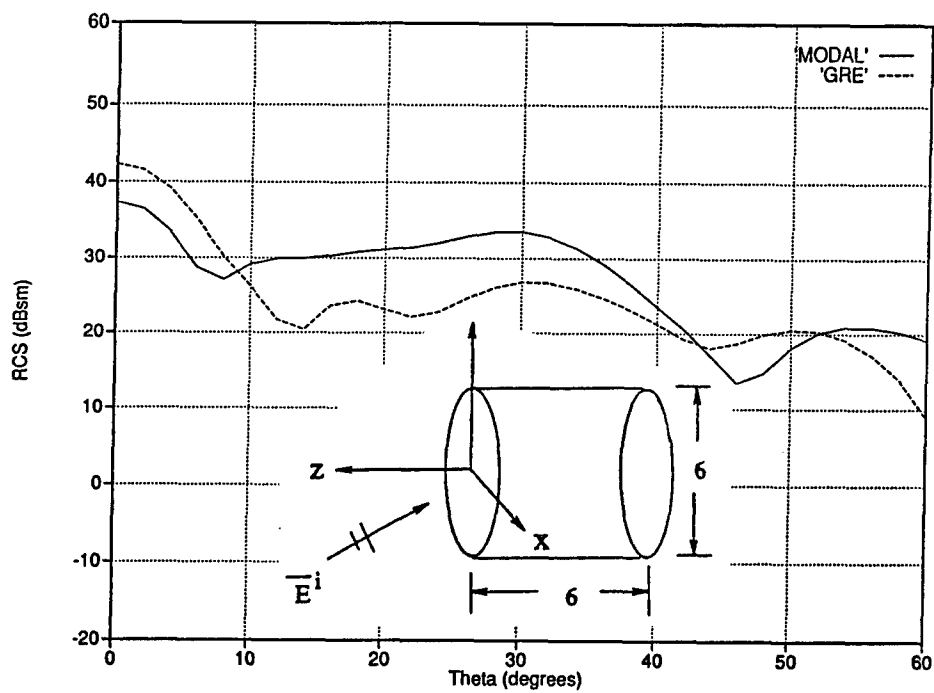


(b) Vertical polarization.

Figure 10: RCS patterns of a 6 X 6 wavelength cylindrical cavity. 32 subapertures, 3.642 GRBF's.

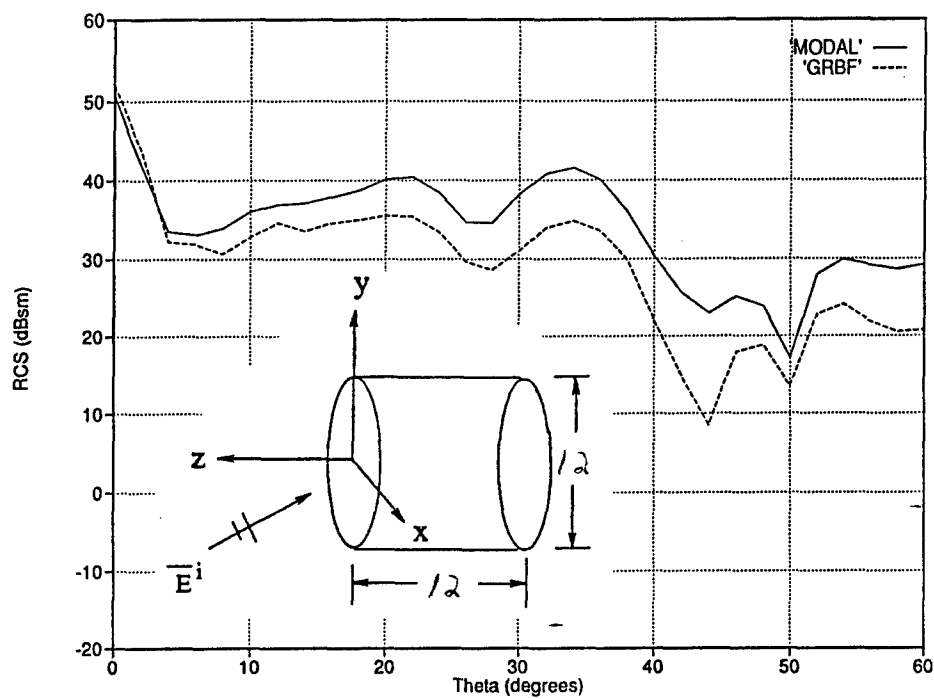


(a) Horizontal polarization.

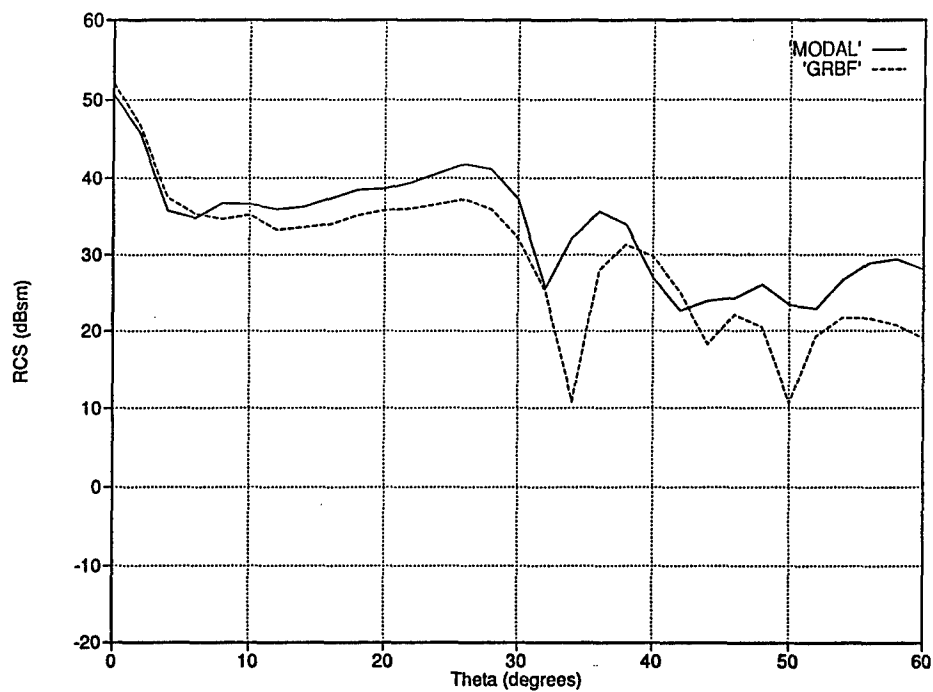


(b) Vertical polarization.

Figure 11: RCS patterns of a 6 X 6 wavelength cylindrical cavity. 32 subapertures, 3.642 GRE ray-tubes.

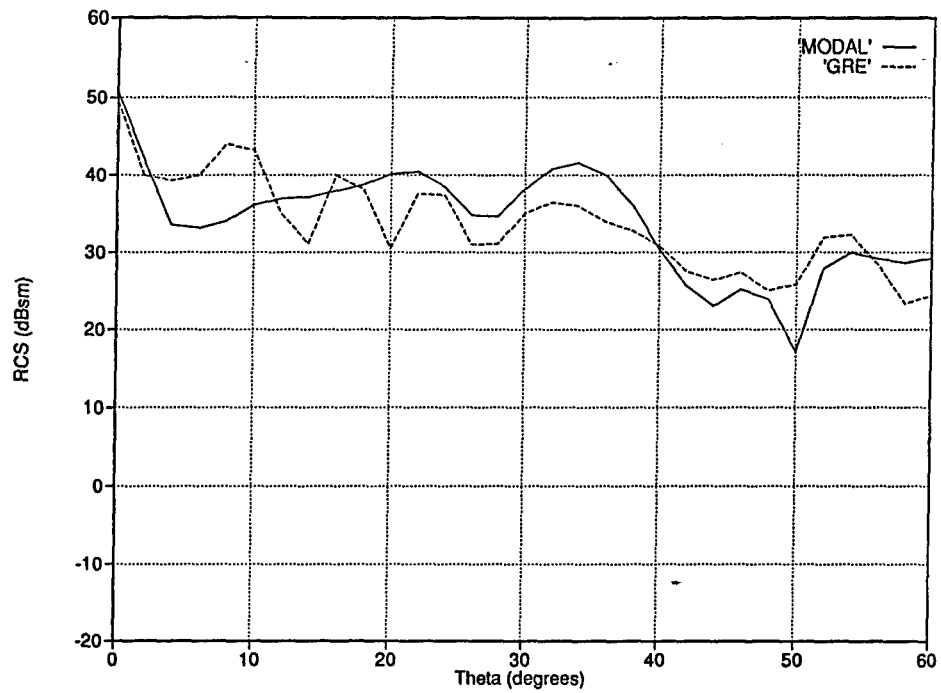


(a) Horizontal polarization.

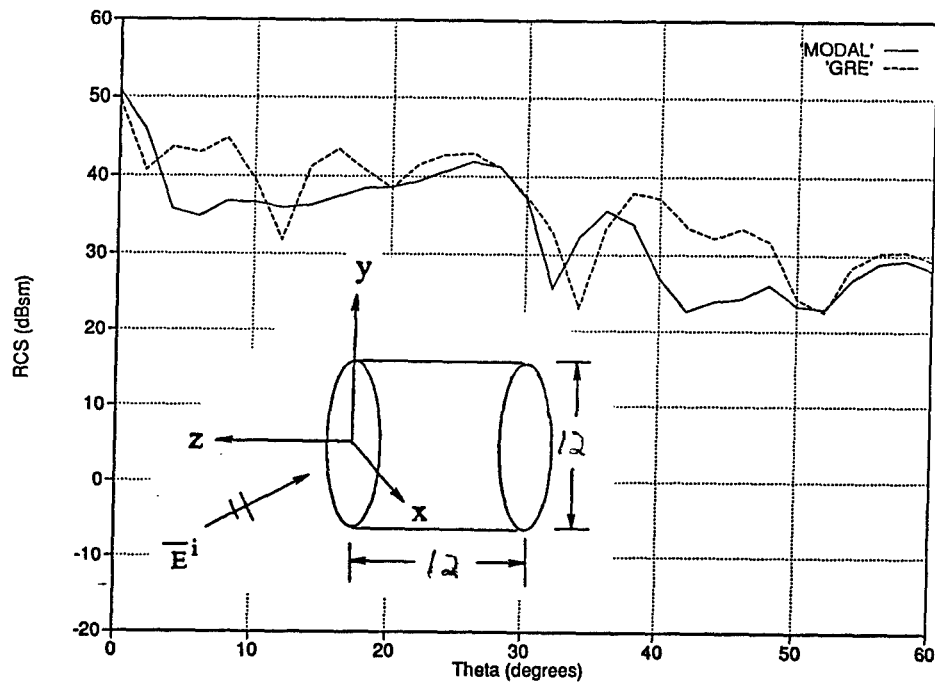


(b) Vertical polarization.

Figure 12: RCS patterns of a 12 X 12 wavelength cylindrical cavity. 32 subapertures. 60,580 GRBF's.



(a) Horizontal polarization.



(b) Vertical polarization.

Figure 13: RCS patterns of a 12 X 12 wavelength cylindrical cavity. 32 subapertures, 60,580 GRE ray-tubes.

The Elliptical Ray Basis Function

So far it has been shown that the GRBF method is generally better than the ordinary GRE method, but the GRBF's do not necessarily maintain their accuracy for larger ray-tubes as was hoped. However, the differences between the GRBF and the GRE results indicate that the shapes of the ray-tubes have a definite affect on the accuracy. With this in mind, a new basis function was tested which combines the shape-changing property of the GRBF with the concept of discrete, truncated GO ray-tubes as used in the ordinary GRE. The GRBF's have a Gaussian amplitude variation transverse to the propagation axis which gives the GRBF an elliptical cross-section, and the Q_a matrix essentially defines this ellipse at any point along the axis. So it follows that an ordinary GO ray-tube could be tracked with a general elliptical cross-section instead of the assumed circular cross-section. The elliptical ray-tube basis function (ERBF) is introduced analogous to (1) as

$$\begin{aligned} \bar{E}(x_1, x_2, z) = & \bar{E}(O) \sqrt{\frac{\rho_1}{\rho_1 + z}} \sqrt{\frac{\rho_2}{\rho_2 + z}} \exp \left[-jk \left(z + \frac{1}{2} \bar{x} \cdot Q_p(z) \bar{x} \right) \right] \\ & \cdot U [1 - \bar{x} \cdot Q_a(z) \bar{x}] \end{aligned} \quad (43)$$

where $U(\cdot)$ is the unit step function defined by

$$U(t) = \begin{cases} 1 & : t \geq 0 \\ 0 & : t < 0. \end{cases} \quad (44)$$

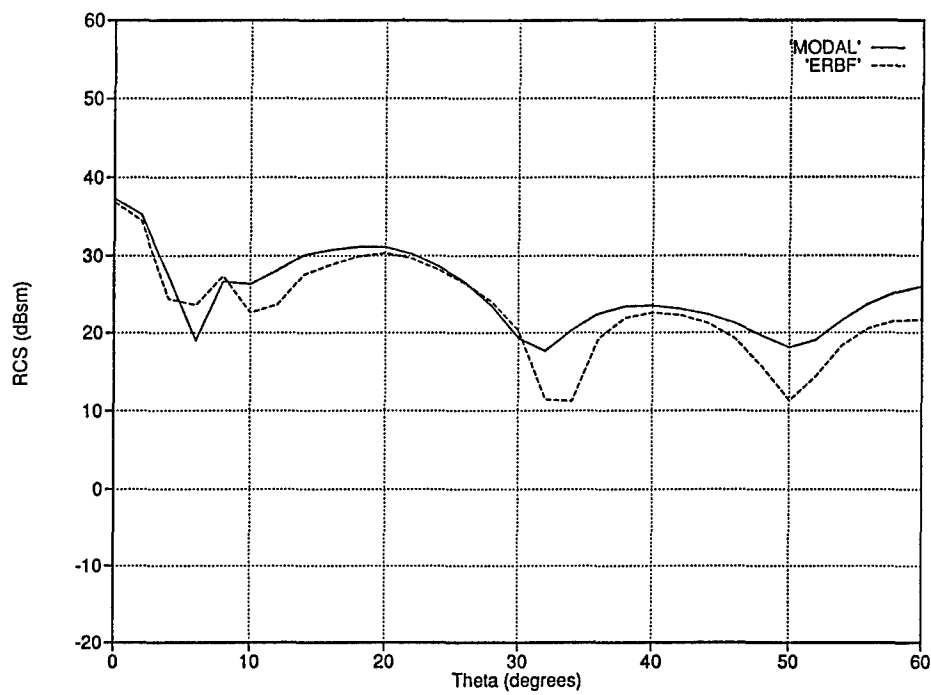
The parameters of the ellipse are defined by the Q_a matrix which is tracked using exactly the same relations as in the GRBF method. The only other difference is in the initial choice of the Q_a matrix as defined in (38). For the ERBF,

$$\alpha^i = \pi / \Delta \theta^2 \quad (45)$$

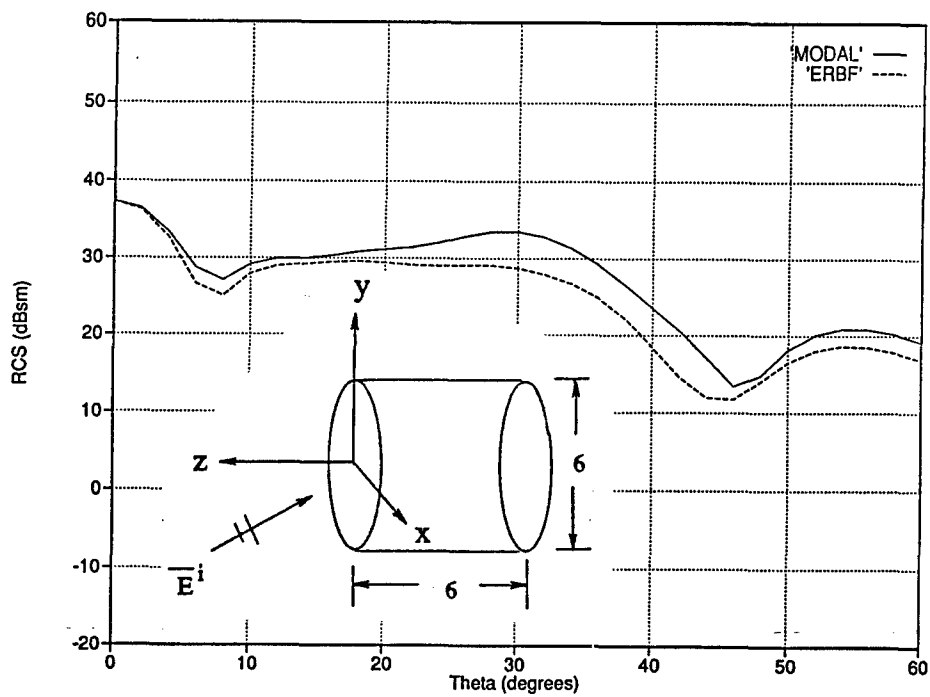
and there is no constant factor of 0.5776 as in (37).

The ERBF results are shown in Figures 14, 15, 16, and 17 which correspond to the cases of Figures 6, 8, 10, and 12, respectively. In all cases the ERBF results are better than the corresponding GRBF and GRE results. The results of Figure 17 are especially

encouraging because good accuracy has been obtained for this electrically large cavity using oversized ray basis functions, which is the goal of the work presented here.

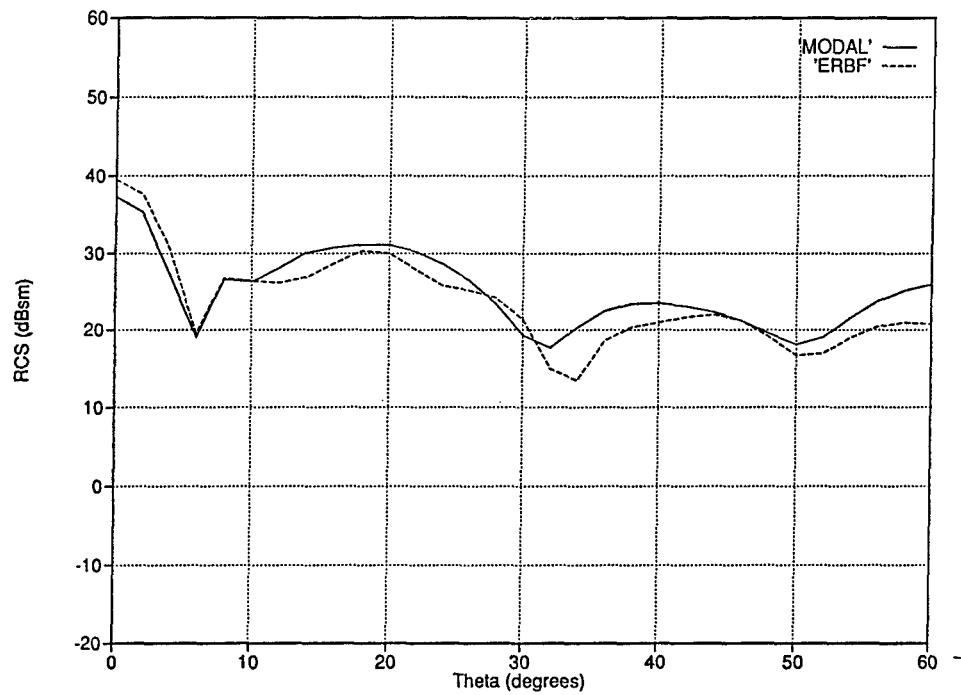


(a) Horizontal polarization.

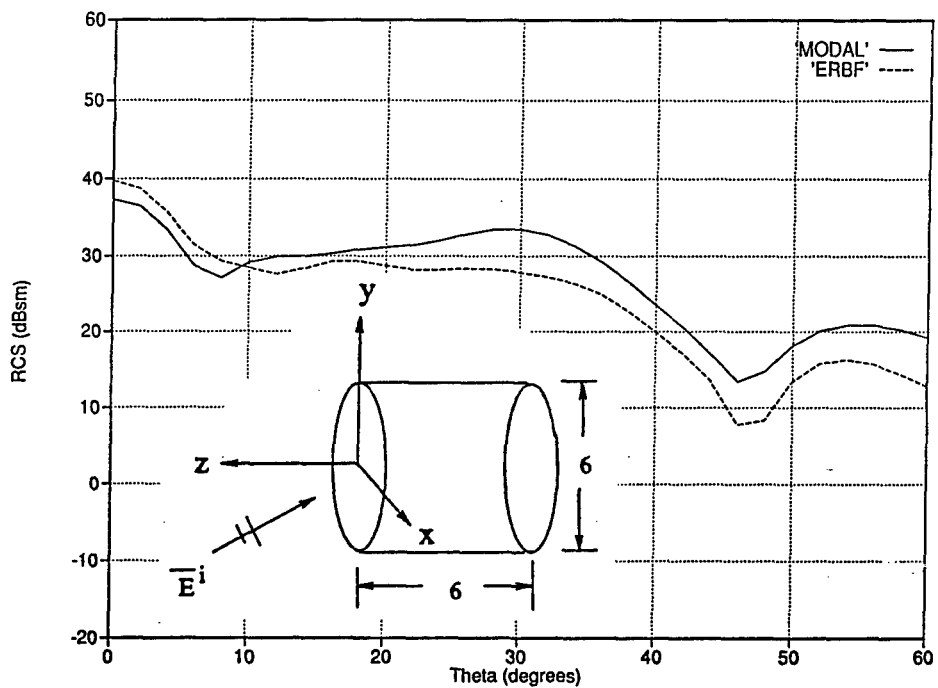


(b) Vertical polarization.

Figure 14: RCS patterns of a 6 X 6 wavelength cylindrical cavity. 32 subapertures, 84,548 ERBF's.

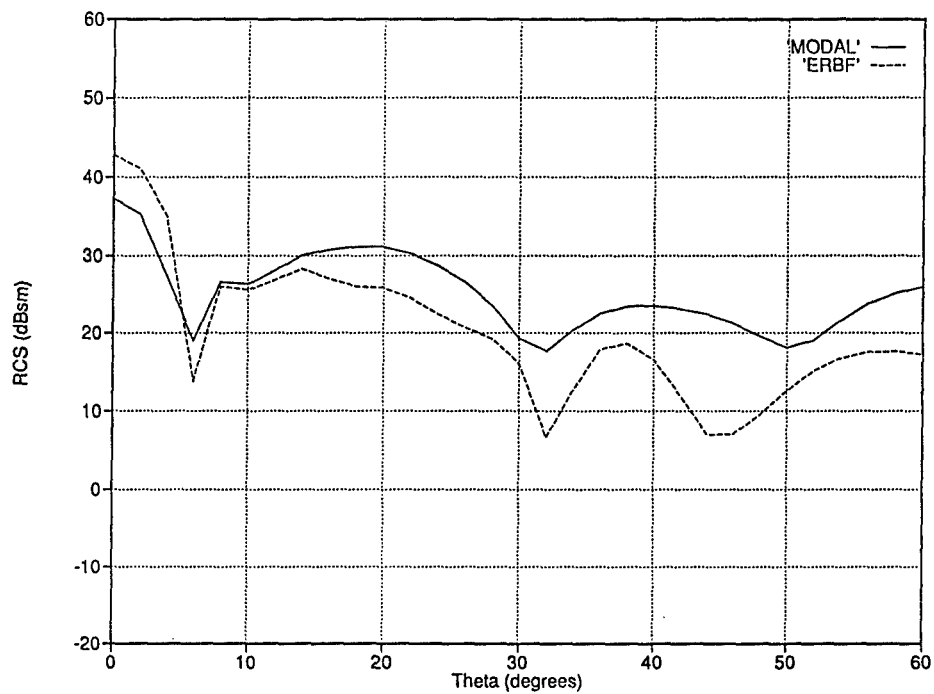


(a) Horizontal polarization.

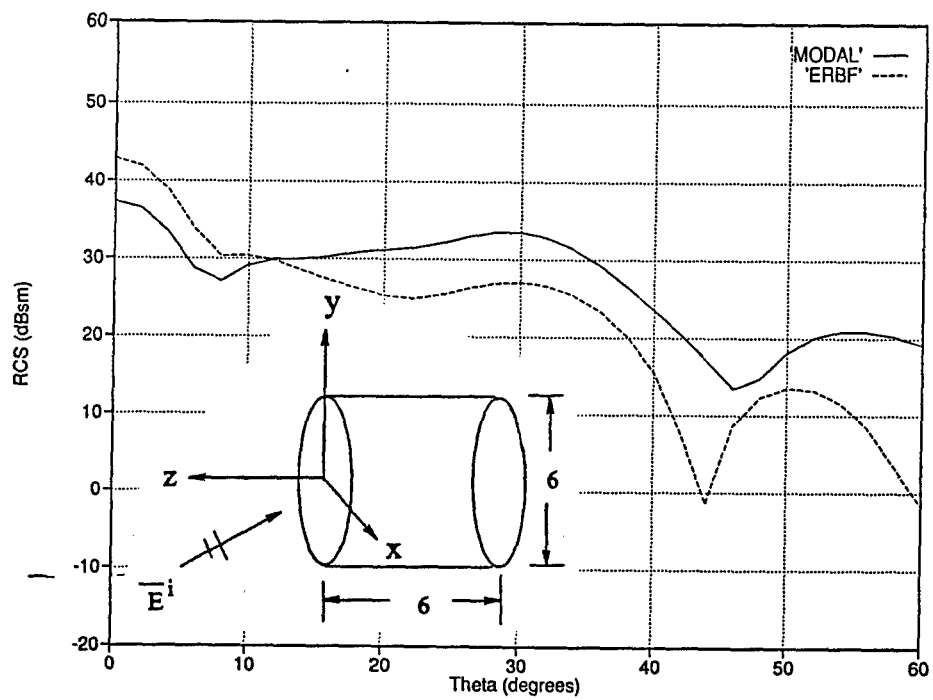


(b) Vertical polarization.

Figure 15: RCS patterns of a 6 X 6 wavelength cylindrical cavity. 32 subapertures, 17,436 ERBF's.

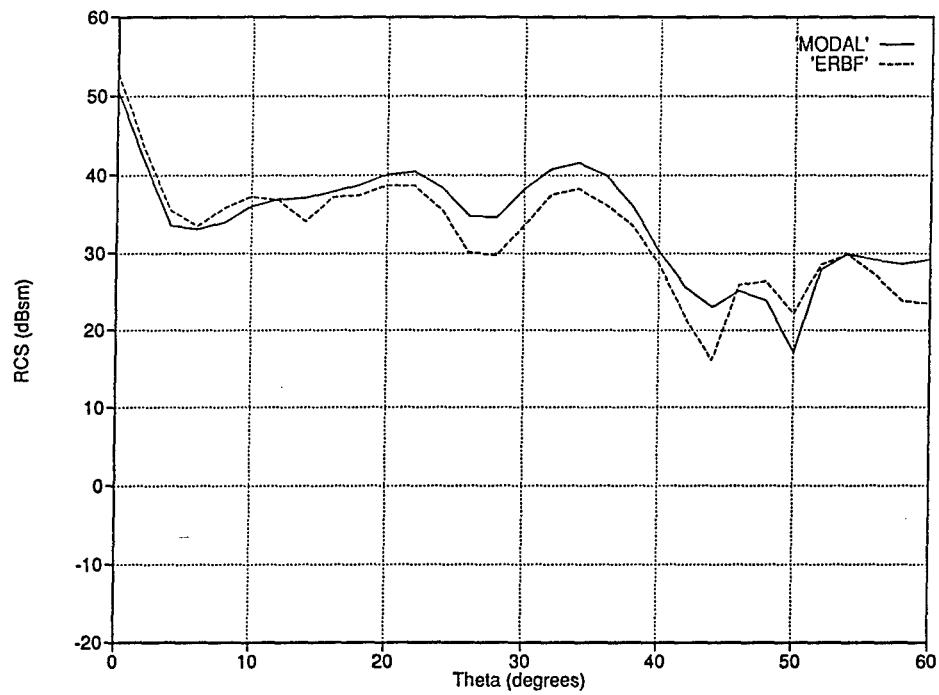


(a) Horizontal polarization.

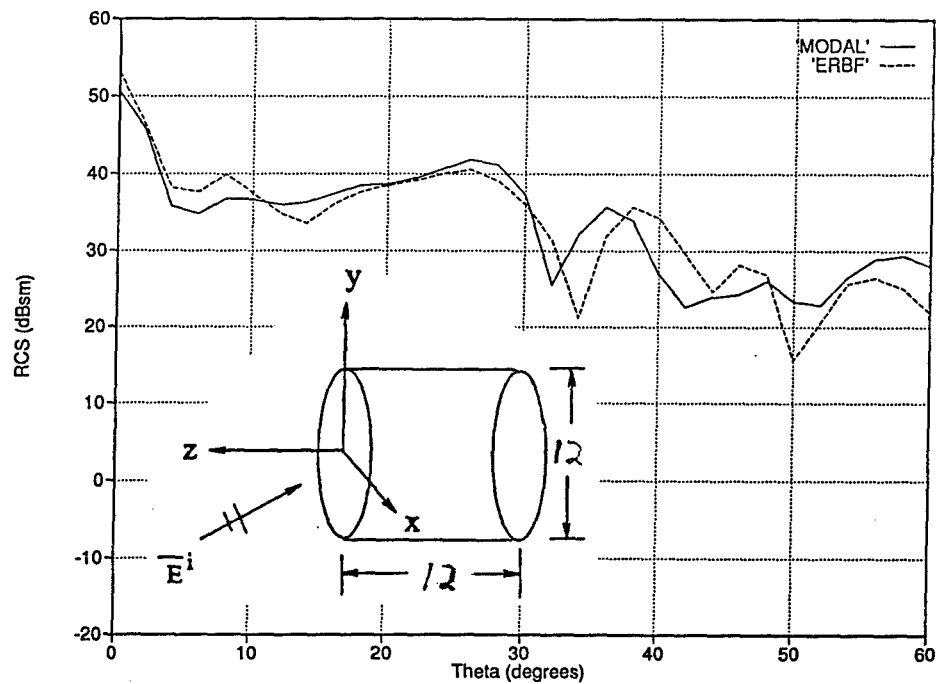


(b) Vertical polarization.

Figure 16: RCS patterns of a 6 X 6 wavelength cylindrical cavity. 32 subapertures, 3,642 ERBF's.



(a) Horizontal polarization.



(b) Vertical polarization.

Figure 17: RCS patterns of a 12 X 12 wavelength cylindrical cavity. 32 subapertures. 60,580 ERBF's.

IV. CONCLUSIONS

The goal of the work reported here was to be able to increase the efficiency of the generalized ray expansion (GRE) method by using larger ray-tube basis functions, thereby requiring far fewer rays to be tracked than by using ordinary geometrical optics (GO) ray-tubes. To this end, a new Gaussian ray-tube basis function (GRBF) was introduced and its propagation and reflection properties investigated. Using conventional techniques, simple expressions for the transformations of the phase and amplitude Q matrices were derived. The GRBF was used in the GRE format and numerical results demonstrated the advantages of GRBF's over ordinary GO ray-tubes. The results were somewhat disappointing, however, because the increase in accuracy over ordinary GRE was not very significant, especially when oversized ray-tubes were used.

Luckily, the development of the GRBF and the numerical results suggested that a new elliptical ray-tube basis function (ERBF) could be easily tested because its propagation and reflection properties are exactly the same as a GRBF. The ERBF, which is essentially an ordinary GO ray-tube with a varying elliptical cross-section, was also used in the GRE format to generate corresponding numerical results. The ERBF results were more accurate than both the GRBF and ordinary GRE results. The accuracy obtained for the larger cavity using the oversized ERBF's is very promising because one-sixteenth as many ERBF's were used compared with the number of ordinary GO ray-tubes which would be expected to give the same level of accuracy. Future work in this area should further investigate the ERBF's for larger and more realistic cavities to determine their limitations with respect to accuracy and efficiency.

References

- [1] R.J. Burkholder, R.C. Chou, and P.H. Pathak, "Two Ray Shooting Methods for Computing the EM Scattering by Large Open-Ended Cavities," *Computer Physics Communications*, Vol. 68, pp. 353-365, North Holland Science Publishers, 1991.
- [2] H. Ling, R.C. Chou, and S.W. Lee, "Shooting and Bouncing Rays: Calculating the RCS of an Arbitrarily Shaped Cavity," *IEEE Trans. Antennas and Propagation*, Vol. 37, No. 2, pp. 194-205, February 1989.
- [3] P.H. Pathak and R.J. Burkholder, "High-Frequency Electromagnetic Scattering by Open-Ended Waveguide Cavities," *J. Radio Science*, Vol. 26, No. 1, pp. 211-218, January-February 1991.
- [4] R.J. Burkholder, "Evaluation of the SBR and GRE Methods for Computing the Time Domain Electromagnetic Scattering from Large Open-Ended Waveguide Cavities," Final report for the Air Force Office of Scientific Research Summer Faculty Research Program, Wright Laboratories AARA, Wright-Patterson AFB, Ohio, September 1992.
- [5] P.H. Pathak and R.J. Burkholder, "Modal, Ray and Beam Techniques for Analyzing the EM Scattering by Open-Ended Waveguide Cavities," *IEEE Trans. Antennas and Propagation*, Vol. 37, No. 5, pp. 635-647, May 1989.
- [6] G.A. DeSchamps, "Ray Techniques in Electromagnetics," *Proc. IEEE*, Vol. 60, No. 9, September 1972.
- [7] H.T. Chou, "Development of Gaussian Ray Basis Elements for Efficient GRE Analysis of EM Backscatter from Open Cavities," Master's thesis, The Ohio State University, December 1993.
- [8] S.W. Lee, H. Ling, and R.C. Chou, "Ray-Tube Integration in Shooting and Bouncing Ray Method," *Microwave and Opt. Tech. Letters*, Vol. 1, No. 8, October 1988.

WAVE MECHANICS MODELING OF
TERMINAL BALLISTICS PHENOMENOLOGY

E. Eugene Callens, Jr.
Associate Professor
J. Scott McMurtry
Graduate Student
Department of Mechanical and
Industrial Engineering

Louisiana Tech University
Ruston, LA 71272

Final Report For:
Summer Research Extension Program

Sponsored by:
Air Force Office Of Scientific Research
Bolling Air Force Base, Washington, DC
and
Louisiana Tech University

December 1993

WAVE MECHANICS MODELING OF
TERMINAL BALLISTICS PHENOMENOLOGY

E. Eugene Callens, Jr.
Associate Professor
J. Scott McMurtry
Graduate Student
Department of Mechanical and
Industrial Engineering

Abstract

A previously developed quasi-steady wave mechanics model for penetration of structural targets by blunt penetrators is extended to include penetrators of arbitrary nosetip shape. The new model is then employed in the parametric study of the influence of nosetip shape on penetration depth for various combinations of penetrator and target density and strength as well as penetrator length to diameter ratio. Results for an ogive nosetip are compared with those for a blunt nosetip for identical penetrators, targets, and impact velocities. The wave mechanics model not only predicts the trends in penetration for the selected nosetips, but it also delineates the kinematic mechanisms that are responsible for these trends. It is shown that for a moderate to high strength target (0.8 to 2 GPa), a moderate strength penetrator (1 GPa) will flow, and there is no influence of nosetip shape on penetration depth. However, for a high strength penetrator (2 GPa) against a low to moderate strength target (0.07 to 0.5 GPa), the ogive nosetip will penetrate up to 5 times deeper than the blunt nosetip for impact velocities up to the penetrator flow initiation velocity. For impact velocities greater than this critical value, there is no difference in performance for the two nosetips. The penetrator flow initiation velocity is a function of both target and penetrator density and strength and, for typical materials of interest, this critical velocity extends from approximately 200 to 1800 m/s. The effects of these nosetip shapes on penetration depth for steel and tungsten alloy penetrators into concrete is also presented. Finally, the model is extended to include penetration into multiple layers of different target materials. Comparisons are made with experimental data for high strength steel penetrators into two-layer targets composed of concrete over aluminum for impact velocities from 610 to 1387 m/s.

WAVE MECHANICS MODELING OF
TERMINAL BALLISTICS PHENOMENOLOGY

E. Eugene Callens, Jr.
J. Scott McMurtry

INTRODUCTION

The work reported in Refs. 1 and 2 indicates that excellent agreement with experimental data is obtained for a properly formulated one-dimensional quasi-steady wave mechanics model of the penetration processes for blunt, cylindrical penetrators. The necessity of employing a wave mechanics model is rooted in the observation that the total time for the penetration process exclusive of the terminal transient is usually less than 200 microseconds. The corresponding deceleration levels are typically more than one million times greater than the standard value of gravitational acceleration. Thus, the classical differential equations for rigid body mechanics cannot adequately describe the time resolved response of either the penetrator or target material.

A major advantage of a realistic model of the governing physical mechanisms over a straight forward correlation of experimental data is that the physically based model can delineate the processes that cause the observed and predicted data trends. For example, the interaction between the hydrodynamic flow stress and the structural stresses in the penetrator and target dictate at what penetrator velocity flow is initiated in the penetrator and/or target. The initiation of flow, in turn, has a dramatic effect on the penetrator and target response as is illustrated in the parametric studies reported below and in Ref. 2.

Additionally, the exterior surface of the penetrator and the flowing surface of the target are constant pressure boundaries from which expansion waves emanate in response to incident compression waves from the high pressure interface. The interaction of these release waves with the forward propagating compression waves results in a standing wave pattern in front of the penetrator (Fig. 1). The target flow response to this free-surface type penetration is different from the flow of a continuous medium around an immersed body.

The mechanisms for momentum transfer become apparent when the principle of conservation of momentum is applied to a properly constructed control volume that encompasses the penetrator-target interface. The forces impinging upon the target are due to structural stresses in the penetrator and inertial stresses arising from the flow of the penetrator material through the interface region. Likewise, the forces in the target resisting the incursion of the penetrator are due to structural stresses in the target and inertial stresses arising from the flow of the target material through the interface region. It is the relative magnitudes of these structural and inertial stresses that determine penetrator and target response.

The formulation includes initial and terminal transients as well as the developed penetration regime. The model is based on the postulated physical behavior of one-dimensional penetrator response, axisymmetric target response, negligible thermal effects in the interface region, and steady state conditions at the interface between wave reflections. The significant consequences of the postulation of negligible thermal effects in the interface region are temperature independent material properties and the uncoupling of the energy equation. The governing equations are therefore the conservation of momentum, the conservation of mass, and a velocity component kinematic relationship.

The initial impact shock transient transitions the interface from the impact Hugoniot shock condition to the developed penetration condition. The release waves from the penetrator free-surface create tension regions at the interface during the transient process. These tensile waves follow the compression waves into the penetrator and attenuate the deceleration effect.

The penetrator deceleration is formulated in the context of wave mechanics with waves emanating from the interface region and reflecting as expansion waves from the free end. The velocity of the free end is reduced by the magnitude of twice the particle velocity with each reflection where the particle velocity is the change in velocity associated with the passage of the wave. The strength of the compression wave has a maximum value due to the presence of the penetrator free-surface. The associated particle velocity also has a corresponding maximum value. This limiting condition corresponds to the internal stress level required for incipient plastic flow. The maximum permissible stress level is the product of a function of Poisson's ratio and the static ultimate compression strength of the material.

The maximum structural stress levels in the target are known to exceed those in a penetrator of the same material by a factor of approximately 3.5. A model for this maximum permissible stress in the target is again a product of a function of Poisson's ratio and the ultimate compressive strength of the material. However, the target material immediately in front of the penetrator target interface is confined so that a higher stress level is experienced than would be the case for a free-surface compression. As in the case of the penetrator, this maximum stress level corresponds to the maximum particle velocity associated with the target compression waves.

The presence of the penetrator and crater free-surfaces causes the compression waves in both the penetrator and target to be attenuated and results in standing wave regions near the interface. In the target, this is analogous to the surface bow wave region in front of a boat. This standing bow wave region which forms after the passage of the initial Hugoniot shock transient does not include a shock wave except for the very hypervelocity case where the interface velocity exceeds the speed of sound in the target material. The structure of this bow wave region dictates the flow pattern in the interface region.

The current work extends the wave mechanics model to include arbitrary penetrator nose shapes and compound material targets. The improved model is then employed to conduct a parametric study of the effects on penetration depth of target and penetrator compressive strength and density as well as the penetrator length to diameter ratio. The study covers the entire velocity range from those values where penetration is initiated and material strength effects are dominant to the hypervelocity values where material strength effects are insignificant and the penetration process is hydrodynamic in nature. The range of material densities and strengths includes all engineering materials, and the penetrator length to diameter ratios range from 1 to 50.

QUASI-STEADY WAVE MECHANICS MODEL

The quasi-steady wave mechanics model used in this study is presented in Refs. 1 and 2 and summarized below. The governing equations are the conservation of momentum, the conservation of mass, and a velocity component kinematic relationship.

The penetrator/target interface momentum equation is

$$S'_P + \rho'_P U_{PF}^2 = \rho'_T U_{TF}^2 + S'_T \quad (1)$$

where S'_P = Stress in compressed penetrator
 S'_T = Stress in compressed target
 ρ'_P = Density of compressed penetrator
 ρ'_T = Density of compressed target
 U_{PF} = Penetrator flow velocity
 U_{TF} = Target flow velocity

The one-dimensional wave continuity equation in the penetrator is

$$\rho'_P = \rho_P \left(\frac{V_{WP}}{V_{WP} - U_{PP}} \right) \quad (2)$$

and for the target

$$\rho'_T = \rho_T \left(\frac{\bar{V}_{WT}}{\bar{V}_{WT} - \bar{U}_{PT}} \right) \quad (3)$$

where ρ_P = Penetrator initial density
 ρ_T = Target initial density
 V_{WP} = Penetrator wave velocity
 \bar{V}_{WT} = Mean target wave velocity in the bow region
 U_{PP} = Penetrator particle velocity
 \bar{U}_{PT} = Mean target particle velocity

The particle velocity is the change in velocity associated with the passage of the disturbance wave. The kinematic relationship between the various velocity components is given by

$$V_P = U_{PF} + U_{PP} + U_{TF} + \bar{U}_{PT} \quad (4)$$

where V_P = Velocity of the free end of the penetrator.

The velocities in the penetrator and target before and after the disturbance waves are shown schematically in Fig. 1 relative to the interface.

The wave velocities are given by

$$\bar{V}_{WT} = C_{WP} + S_{IT} \bar{U}_{PT} \quad (5)$$

$$V_{WP} = C_{WP} + S_{IP} U_{PP} \quad (6)$$

where C_{WP} = Zero pressure wave velocity in the penetrator

C_{WT} = Zero pressure wave velocity in the target

S_{IP} = Hugoniot constant for the penetrator material

S_{IT} = Hugoniot constant for the target material

The stress in the compressed penetrator is given by

$$S'_P = \rho_P U_{PP} V_{WP} \quad \text{for} \quad U_{PF} = 0 \quad (7)$$

$$S'_P = \rho_P U_{PPM} V_{WP} \quad \text{for} \quad U_{PF} > 0 \quad (8)$$

$$U_{PPM} = \frac{C_{SP} \sigma_{SP}}{\rho_P V_{WP}} \quad (9)$$

$$C_{SP} = v_P^{-1} \quad (10)$$

where U_{PPM} = Maximum penetrator particle velocity

C_{SP} = Penetrator free surface maximum stress constant

v_P = Poisson's ratio for the penetrator material

σ_{SP} = Penetrator compressive stress

From these relationships it is observed that either the penetrator particle velocity or flow velocity is known for any condition. If the interface pressure is below the maximum allowable penetrator stress, the flow velocity is zero, and the particle velocity is the variable. If the interface pressure is above the

maximum penetrator stress, the particle velocity is at its known maximum value and the flow velocity is the variable.

The stress in the compressed target is given by

$$S'_T = \rho_T \bar{U}_{PT} \bar{V}_{WT} \quad \text{for} \quad U_{TF} = 0 \quad (11)$$

$$S'_T = \rho_T \bar{U}_{PTM} \bar{V}_{WT} \quad \text{for} \quad U_{TF} > 0 \quad (12)$$

$$\bar{U}_{PTM} = \frac{C'_{ST} \sigma_{ST}}{\rho_T \bar{V}_{WT}} \quad (13)$$

$$C'_{ST} = C_{ST}^2 = v_T^{-2} \quad (14)$$

where \bar{U}_{PTM} = Maximum mean target particle velocity
 C_{ST}' = Target confined surface maximum stress constant
 C_{ST} = Target free surface maximum stress constant
 v_T = Poisson's ratio for the target material
 σ_{ST} = Target compressive stress

As in the case of the penetrator, either the target particle velocity or flow velocity is known for any condition. The penetrator deceleration is determined by the wave mechanics. In this model the compression wave that originates at the penetrator/target interface upon impact is tracked in the penetrator as it travels back and forth between the interface and the free end. The compression wave reflects from the free end as an expansion wave and the penetrator free-end velocity decreases by twice the particle velocity with each reflection.

When the expansion wave reflects from the interface, the sum of the penetrator and target variable velocities decrease by twice the particle velocity. The new values of these velocities are determined from the interface momentum equation and the velocity component kinematic relationship. Again, the particle velocity changes sign with each wave reflection.

The penetrator traveling wave is tracked until the penetrator velocity falls below the target flow initiation velocity. When this occurs the developed penetration phase is complete and the remainder of the penetration process is a terminal transient cylindrical expansion of the target stress and a spherical expansion of the penetrator flow stress as presented below. The change in penetrator length due to the developed penetration phase is

$$\Delta L_{PD} = -\int (U_{PF} \pm U_{PP}) dt \quad (15)$$

The change in crater depth due to the developed penetration phase is

$$\Delta L_{CD} = \int (U_{TF} + \bar{U}_{PT}) dt \quad (16)$$

The final crater diameter at each penetration location is given by

$$\frac{D_C}{D_P} = \sqrt{\frac{\rho_P' \bar{U}_{PF}^2 + C_{ST} \sigma_{ST}}{C_{ST} \sigma_{ST}}} \quad (17)$$

where D_P = penetrator initial diameter.

INITIAL AND TERMINAL TRANSIENT MODELS

The time for the initial transient is taken to be the time for the passage of the lateral release wave in the penetrator

$$\Delta t_{IT} = \frac{R_P}{V_{WPTS}} \quad (18)$$

where V_{WPTS} = Penetrator transverse impact shock velocity.

The crater length due to the initial transient is given by

$$L_{CI} = (U_{PTS} - \bar{U}_{PTM}) \Delta t_{IT} \quad (19)$$

where U_{PTS} = Target shock particle velocity.

The length of penetrator loss during the initial transient expansion is obtained from a form of the velocity kinematic relationship

$$\Delta L_{PI} = -(V_{PI} \Delta t_{IT} - L_{CI}) \quad (20)$$

The terminal transient model is a combination of a spherical penetrator flow stress expansion and a cylindrical target particle momentum expansion. The crater length due to the spherical expansion of the penetrator flow stress is

$$L_{CTPF} = \sqrt{\frac{\rho_P' U_{PF}^2}{C_{ST} \sigma_{ST}}} - 1 \quad (21)$$

The crater length due to the cylindrical expansion of the target particle momentum is

$$L_{CTPM} = R_{PR} \left(\frac{\bar{U}_{PTFI}}{U_{PTFS}} - 1 \right) \quad (22)$$

where \bar{U}_{PTFI} = Mean target particle velocity when the penetrator velocity equals the target flow initiation velocity

U_{PTFS} = Free surface target particle velocity

Also the reference radius for the cylindrical expansion is

$$R_{PR} = \frac{V_{WTL}}{V_{WTT}} R_P \quad (23)$$

where V_{WTL} = Target longitudinal wave velocity

V_{WTT} = Target transverse wave velocity

R_P = Penetrator radius

The total crater length due to the terminal transient is

$$L_{CT} = L_{CTPF} + L_{CTPM} \quad (24)$$

The time for the penetrator flow stress expansion is

$$t_{TTPF} = \frac{R_P}{2 U_{PF}} \left(\frac{L_{CTPF}}{R_P} \right)^2 \quad (25)$$

and the time for the target particle expansion is

$$t_{TTPM} = \frac{R_{PR}}{\bar{U}_{PTFI}} \left[.5 \left(\frac{L_{CTPM}}{R_{PR}} \right)^2 + \left(\frac{L_{CTPM}}{R_{PR}} \right) \right] \quad (26)$$

The total time for the terminal transient expansion is

$$t_{TT} = t_{TTPF} + t_{TTPM} \quad (27)$$

INCLUSION OF NOSETIP SHAPE EFFECTS

The inclusion of nosetip shape effects requires modification of both the penetrator/target interface momentum equation, Eqn. (1), and the target confined surface maximum stress constant equation, Eqn. (14). The hydrodynamic flow stress term for the target is multiplied by $(1 - \cos \bar{\theta})$ as obtained from a control volume analysis of momentum conservation in the interface region. The revised equation becomes

$$S'_p + \rho'_p U_{PF}^2 = \rho'_t U_{TF}^2 (1 - \cos \bar{\theta}) + S'_T \quad (28)$$

where $\bar{\theta}$ is the frontal area average turning angle for the nosetip. It is calculated as

$$\bar{\theta} = \frac{1}{A_f} \sum \theta_i A_i \quad (29)$$

where A_f = Total frontal area
 A_i = i_{th} section frontal area
 θ_i = i_{th} section angle

The target confined surface maximum stress constant must be modified because, for turning angles less than 90 degrees, the target material is not fully confined. The exponent on the target Poisson ratio is therefore a function of average turning angle. The function is approximated by a polynomial, and evaluated from the experimental data of Ref. 3 and shown in Fig. 2. The function is

$$f(\bar{\theta}) = 1.317 + 0.17614 \bar{\theta}^3 \quad (30)$$

This function gives the expected blunt penetrator value of 2 and produces the observed fit to the data in Fig. 2 for an ogive tip having an average turning angle of 18 degrees and a hemisphere tip having an average turning angle of 45 degrees. The calculated results for a blunt nosetip are also shown in Fig. 2 and illustrates increased penetration by a factor of 2 to 3 for the ogive tip over the blunt tip. The equation for the target maximum stress constant becomes

$$C'_{ST} = C_{ST}^2 = v_T^{-f(\bar{\theta})} \quad (31)$$

where $f(\bar{\theta})$ is given by Eqn. (30).

An important factor in the computational methodology is the determination of the lowest penetrator impact velocity for which the penetrator material will flow in the developed penetration regime. For velocities above this critical penetrator flow initiation velocity, it is assumed that the penetrator flows like a blunt cylinder. For velocities below this critical value, the penetrator will not deform and the revised relations, Eqns. (28) and (31), are used.

To determine this penetrator flow initiation velocity, it is assumed that the target flow at the nosetip extremity experiences the full hydrodynamic stress associated with a stagnation point, and the target structural stress is reduced to the value for the average turning angle because the target material

is not fully confined. The corresponding form of the interface momentum equation is Eqn. (1) and the target maximum stress constant is given by Eqn. (31).

The predictions of this model for nosetip shape effects were compared with experimental results from two tests conducted in the Louisiana Tech University ballistic range. For both tests, the penetrator was the tool steel core from a 30-06 armor-piercing round with a compressive strength of 1.92 Gpa. The length was 27.9 mm and the diameter was 6.22 mm for a length to diameter ratio of 4.49.

The first target was stainless steel with a compressive strength of 480 Mpa. The impact velocity was 786 m/s and the measured crater length was 28.1 mm for a ratio of penetration depth to original penetrator length (P/L) of 1.01. The measured deep crater diameter was the same as the penetrator shank, 6.22 mm. The calculated penetration depth was 27.5 mm for a P/L = 0.99, and the calculated deep crater diameter was 6.22 mm. Both of these results are well within the experimental uncertainty of ± 5 percent.

The second target was 6061-T6 aluminum with a compressive strength of 350 MPa. The impact velocity was 857 m/s and the measured crater length was 48.5 mm for a P/L = 1.74. The measured deep crater diameter was the same as the penetrator shank, 6.22 mm. The calculated penetration depth was 48.1 mm for a P/L = 1.72, and the calculated deep crater diameter was 6.22 mm. Again, the results are well within the experimental uncertainty of ± 5 percent.

PARAMETRIC STUDY OF NOSETIP SHAPE EFFECTS

The wave mechanics model with incorporated nosetip shape effects is utilized in the parametric study of penetrator and target properties on penetration depth for an ogive nosetip. The results are compared to previous calculations for a blunt nosetip as reported in Ref. 2. The wave mechanics model not only predicts the trends in penetration with variation in these properties, but is also delineates the kinematic mechanisms that are responsible for these trends.

Fig. 3 presents data in terms of the ratio of penetration depth to original penetrator length (P/L) versus penetrator impact velocity (VPI) for a high strength penetrator with an ogive nosetip into targets of six different strengths. Fig. 4 shows the same comparison for a penetrator with a blunt nosetip. The densities of both penetrator and target are approximately those of steel.

For the combination of high penetrator strength and low target strength, the ogive nosetip increases the penetration depth up to a factor of 5 over the blunt nosetip for impact velocities up to 1000 m/s. This is seen from comparing the upper curves (70 MPa) in Figs. 3 and 4.

From Fig. 3 it is also observed that for impact velocities greater than the penetrator flow initiation velocity, the penetration depth drops back to the

value for the blunt penetrator because the current model assumes that the transition is distinct at that critical velocity. In reality, the transition probably takes place over a narrow range of velocities greater than the critical value. The curve is expected to be steep in that region approximated by a discontinuity in the current approach.

It is also observed that the penetrator flow initiation velocity decreases with increasing target strength. The influence of flow initiation in the penetrator for a blunt nosetip also results in a decrease in penetration depth with increasing velocity for the lowest strength (70 MPa) target (Fig. 4). This results in a local maximum in the curve.

The decrease in penetration depth at increased impact velocity may appear to be odd from the viewpoint of dissipation of energy and conservation of momentum. The explanation is that the decrease in penetration is accompanied by an increase in crater diameter, as seen in Figs. 5 and 6. As the penetrator begins to flow, there is an associated lateral transfer of momentum and accompanying dissipation of energy.

Figs. 7 and 8 show the effect of target strength on penetration depth for a low strength penetrator (70 MPa) for an ogive and blunt nosetip, respectively. Because of the low penetrator strength, the penetrator flow initiation velocity is very low at all target strengths shown for both the ogive and blunt nosetips. These last 4 figures illustrate that there is no nosetip shape effect for low strength penetrators but there is a significant effect for high strength penetrators, particularly against low strength targets.

The effect of target strength on penetration depth is shown in Figs. 9 and 10 for a high density penetrator for an ogive and blunt nosetip, respectively. The density and strength of the penetrator correspond to a high strength tungsten or depleted uranium material. Again, the comparisons show that the ogive tip has penetration depths up to 5 times greater than the blunt nosetip against low strength targets at velocities up to 900 m/s. The reduction in penetration depth for the ogive tip is very pronounced at velocities greater than the penetrator flow initiation velocity.

This same comparison is repeated in Figs. 11 and 12 for a high strength, low density penetrator. The advantage of the ogive tip is somewhat less than before but still substantial. The penetration depth for both nosetips is significantly less for the low density penetrator than for the high density penetrator at all target strengths.

Figs. 13 and 14 present the effect of target strength on penetration depth for a high density target for an ogive and blunt nosetip, respectively. For low strength targets the ogive tip penetrates up to 4 times deeper than the blunt nosetip at relatively low velocities. The high density of the target results in low penetrator flow initiation velocities.

These same comparisons are shown in Figs. 15 and 16 for a low density target. The combination of low target strength and low target density result in very deep penetration for the ogive tip (Fig. 15) which is up to a factor of 5 greater than the penetration of the blunt nosetip (Fig. 16) over a greater range of velocity. The low strength, low density target is representative of certain polycarbonate materials.

Comparison of Figs. 17 and 18 illustrates that there is no nosetip effect against targets of sufficiently high density and strength such as high strength tool steel. Even for medium strength targets (800 MPa), the effect of nosetip shape is observed only for high strength penetrators as shown in Figs. 19 and 20. This observation remains true even if the penetrator density is increased to tungsten or depleted uranium as in Figs. 21 and 22. However the depth of penetration is significantly increased for the higher density penetrator as seen by comparing Figs. 19 and 21.

Figs. 23 and 24 illustrate that there is no nosetip effect over a wide range of target density for high strength targets (2 GPa). However, for medium strength targets (800 MPa), there is a pronounced nosetip effect for low density targets as seen in Figs. 25 and 26. The ogive tip penetrates up to 5 times deeper than the blunt nosetip up to the penetrator flow initiation velocity.

There is a significant nosetip effect for a high strength, high density penetrator against medium strength, low density targets as shown in Figs. 27 and 28. However for high strength targets (2 GPa), there is no nosetip effect for the range of penetrator density studied, as observed in Figs. 29 and 30. For medium strength targets (800 MPa), Figs. 31 and 32 show an effect for high strength, high density penetrators at relatively low velocities. For low strength targets (70 MPa), the ogive nosetips penetrate up to 5 times deeper than the blunt nosetips for high density penetrators at impact velocities less than approximately 900 m/s (Figs. 33 and 34). In Figs. 35 and 36 it is seen that this nosetip effect is confined to impact velocities less than 500 m/s for high strength, high density penetrators against medium strength, high density targets.

Comparison of Figs. 37 and 38 indicates that the pronounced penetrator length to diameter (L/D) effect observed for blunt nosetips (Fig. 38) does not exist for ogive nosetips up to the penetrator flow initiation velocity (Fig. 37). For impact velocities greater than the penetrator flow initiation velocity, the L/D effect for ogive nosetips is the same as the blunt nosetips. For a penetrator with a $L/D = 1$, the blunt nosetip penetrates deeper than the ogive nosetip at velocities below the penetrator flow initiation velocity due to the relatively large terminal transient associated with the blunt nosetip. However, the ogive nosetips penetrate deeper over this same velocity range for L/D 's greater than about 3 because the terminal transient effect becomes proportionally smaller as L/D increases.

One target material of particular interest for military application is concrete because of its use in bunkers, command centers, storage facilities, etc. The results of a parametric study of the influence of nosetip shape on penetration depth in concrete as a function of penetrator and target characteristics are presented in Figs. 39-46.

Figs. 39 and 40 illustrate the effect of target strength on penetration depth for a tungsten alloy penetrator into concrete. For the blunt nosetip, the penetration depth curves have local maxima at approximately 2,000 m/s (Fig. 40). The wave mechanics code clearly indicates that this decrease in penetration depth with increasing velocity is due to flow initiation in the tungsten alloy penetrator. For the ogive nosetip (Fig. 39), the penetration depth is increased up to a factor of 7 over the blunt nosetip at impact velocities below the penetrator flow initiation velocity. For impact velocities greater than the penetrator flow initiation velocity, the penetration depth abruptly drops to the blunt nosetip value. These same comparisons are presented in Figs. 41 and 42 for high strength steel into concrete. The qualitative results are the same as for the tungsten alloy penetrator of the same strength. However, the magnitude of penetration depth is reduced for the steel by a factor approximately proportional to the ratio of penetrator densities.

Figs. 43 and 44 present the effect of penetrator strength on penetration depth for steel into 3 ksi concrete. For the ogive nosetip, the penetration curves are the same up to the penetrator flow initiation velocity corresponding to each penetrator strength (Fig 43). The higher strength penetrators have correspondingly higher penetrator flow initiation velocities and therefore exhibit much greater penetration depth than lower strength penetrators at sufficiently high velocities. For an ogive nosetip, the penetration depth is 10 times greater for a 2 GPa penetrator than for a 1 GPa penetrator at an impact velocity of approximately 1,800 m/s as seen in Fig. 43. However, at an impact velocity of 1,000 m/s, there is no difference in penetration depth for these two strengths. These same qualitative effects are also observed for the blunt nosetip in Fig. 44. However, the ogive nosetip penetrates up to 7 times as deep as the blunt nosetip over this same range of impact velocity. These same comparisons are given in Figs. 45 and 46 for a tungsten alloy penetrator into 3 ksi concrete. The quantitative results are the same but penetration levels are increased by a factor approximately equal to the ratio of the densities.

EXTENSION TO COMPOUND MATERIAL TARGETS

The model has been developed for monolithic targets which is a good assumption for many practical applications. However, there are numerous targets of interest which are characterized by layers of different protective materials.

These are frequently various combinations of metals, ceramics, composites, concrete and earth.

A first order extension is applied to the current model for blunt penetrators. The penetration depth is monitored until the first layer has been breached. At this point the target material is switched to the second layer, and the calculation is continued using the average penetrator velocity at the time of breach with a compression wave being generated at the interface. This procedure is repeated for each subsequent layer until the penetrator either stops or is consumed.

An experimental program was conducted in the ballistic range facility at Louisiana Tech University in order to check the accuracy of this first order extension to compound material targets. A two layer target was used with concrete over 6061-T6 aluminum. Cylindrical penetrators were cut from the shanks of hardened steel drill bits. These projectiles were launched at velocities from 610 to 1387 m/s using a sabot in a 30-06 accelerator round. Two sets of data were taken for penetrator L/D ratios of nominally 2 and 3.

The concrete outside layer was nominally 16 mm thick. The compressive strength for the concrete used in the L/D = 2 tests was 53.78 MPa and in the L/D = 3 tests it was 59.5 MPa. The inner layer was 25.4 mm thick 6061-T6 aluminum having a compressive strength of 290 MPa. At these impact velocities and material thicknesses, the aluminum responded as if it were semi-infinite.

The specific test conditions and penetration data are presented in Table 1. The notations for this table are as follows:

L/D	=	Initial penetrator length to diameter ratio
V _{PI}	=	Impact velocity
L _{PI}	=	Initial penetrator length
D _p	=	Penetrator diameter
T _C	=	Concrete thickness
σ _p	=	Penetrator compressive strength
L _C	=	Crater depth (experimental and calculated)

The cumulative experimental uncertainty in the crater depth data is approximately ± 10 percent. The primary uncertainty components are target and penetrator material properties, concrete thickness, penetrator attitude at impact, and impact velocity. The calculated results are within the experimental uncertainty with the average difference for the 13 data points being less than 2 percent. These results indicate that the uncertainties are primarily random in nature as opposed to distinct biases or, if there are biases, they tend to be compensatory.

Table 1. Total Penetration Depth for Steel Into Concrete/Aluminum Targets

 $L/D = 2$

V_{PI} <u>m/s</u>	L_{PI} <u>mm</u>	D_p <u>mm</u>	T_c <u>mm</u>	σ_p <u>GPa</u>	$L_c(\text{exp})$ <u>mm</u>	$L_c(\text{cal})$ <u>mm</u>
610	11.2	5.54	14.3	1.89	16.0	17.6
610	11.1	5.54	15.9	1.71	17.6	18.6
635	11.0	5.51	15.9	1.13	17.4	18.8
876	11.2	5.51	14.3	1.58	20.2	20.8
897	11.1	5.51	15.9	1.42	21.4	21.0
942	11.1	5.51	16.7	1.31	22.6	21.9
1387	11.0	5.54	16.7	1.83	28.1	30.6

 $L/D = 3$

V_{PI} <u>m/s</u>	L_{PI} <u>mm</u>	D_p <u>mm</u>	T_c <u>mm</u>	σ_p <u>GPa</u>	$L_c(\text{exp})$ <u>mm</u>	$L_c(\text{cal})$ <u>mm</u>
807	16.6	5.59	14.7	1.80	23.4	23.8
922	16.6	5.51	14.1	1.44	27.5	27.2
925	16.6	5.51	13.1	1.65	29.2	26.9
978	16.7	5.51	15.2	1.42	26.1	28.9
1231	16.7	5.51	19.3	1.61	35.9	36.5
1262	16.7	5.49	18.9	1.75	38.9	37.0

The wave mechanics model also predicts that the decrease in penetrator length will be less than 4 percent for all of these shots. This was observed to be the case from measurements of the recovered penetrators. Also, the model predicts that the crater diameter will be equal to the penetrator diameter as all of these impact velocities are less than the penetrator flow initiation velocity. Again, this was observed to be the case from direct measurement of the craters. The experimental uncertainties associated with both the penetrator length and crater diameter results are approximately 3 percent.

These results for a first order extension to compound material targets for penetration depth are better than expected. The favorable comparisons with experimental data may be fortuitous in that there are compensating higher order effects for this combination of target materials that are neglected in this model. Other combinations of materials may not predict results with the current level of accuracy. The higher order effects associated with the influence of the

target material interface on the approaching penetrator will be objective of future research.

REFERENCES

1. Callens, E. Eugene, Jr. and J. Scott McMurtry, "One-Dimensional Wave Mechanics Model for Terminal Ballistics," Final Report for AFOSR Summer Research Program, Aug. 1992.
2. Callens, E. Eugene, Jr. and J. Scott McMurtry, "Influence of Penetrator and Target Properties on Penetration Mechanics," Final Report for AFOSR Summer Research Program, Sept. 1993.
3. Forrestal, M. J., K. Okajima, and V. K. Luk, "Penetration of 6061-T651 Aluminum Targets with Rigid Long Rods," J. Appl. Mech., Dec. 1988.

FIG. 1. FLOW AND PARTICLE VELOCITIES RELATIVE TO THE INTERFACE

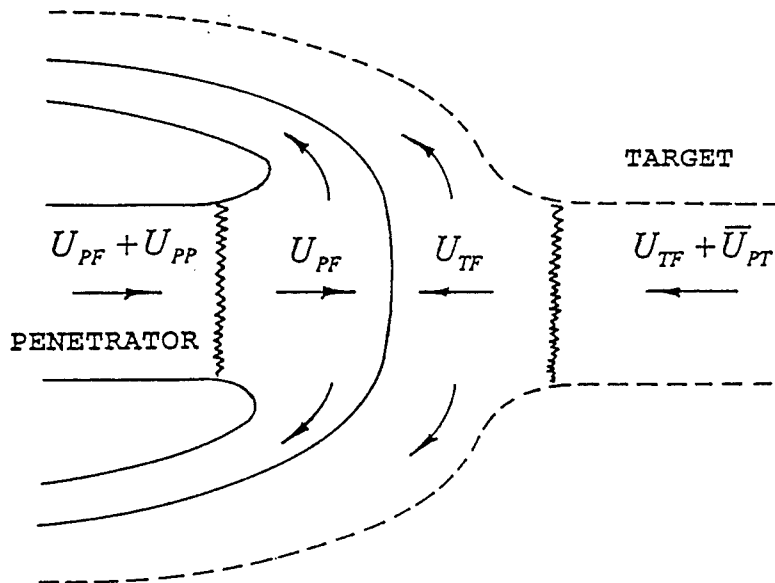


FIG. 2. EFFECT OF NOSETIP SHAPE, STEEL INTO ALUMINUM

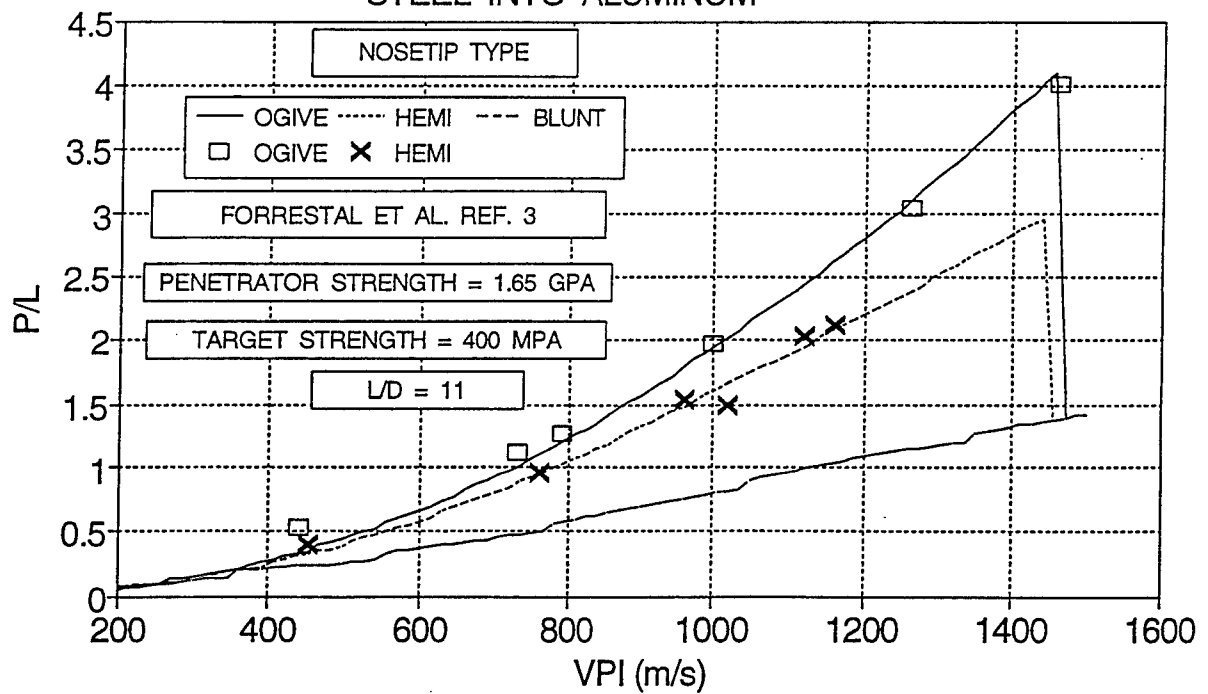


FIG. 3. EFFECT OF TARGET STRENGTH ON PENETRATION DEPTH, HIGH STRENGTH PENETRATOR, OGIVE NOSETIP

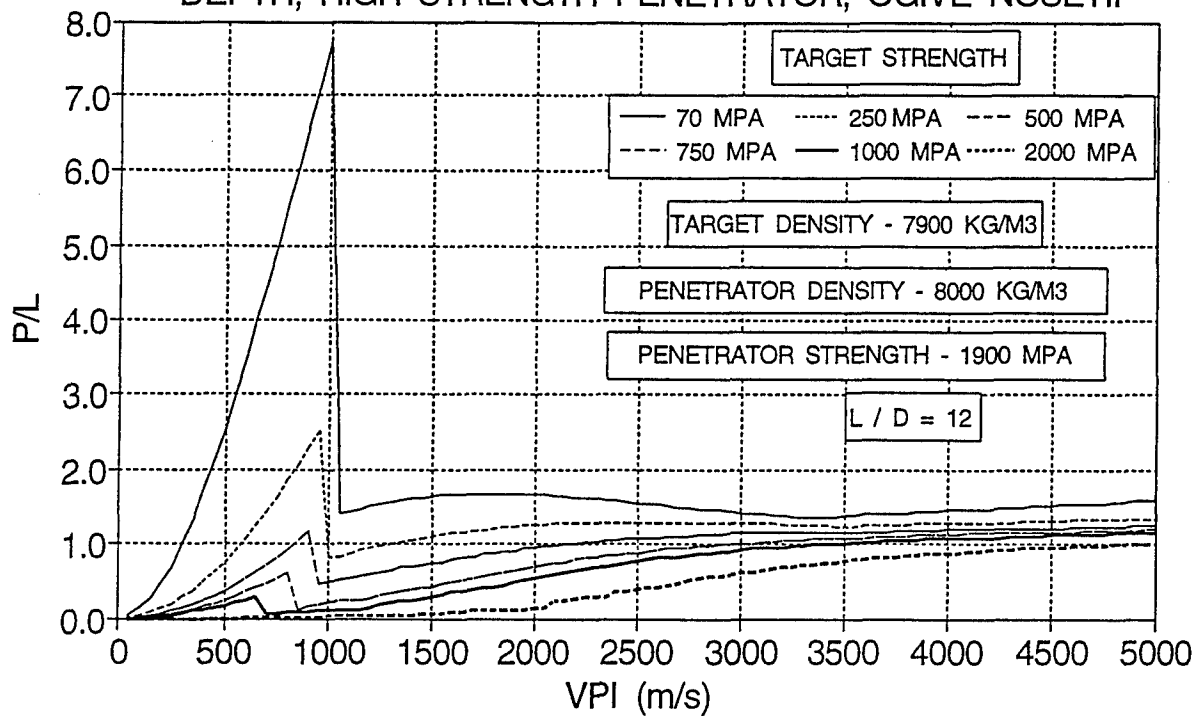


FIG. 4. EFFECT OF TARGET STRENGTH ON PENETRATION DEPTH, HIGH STRENGTH PENETRATOR, BLUNT NOSETIP

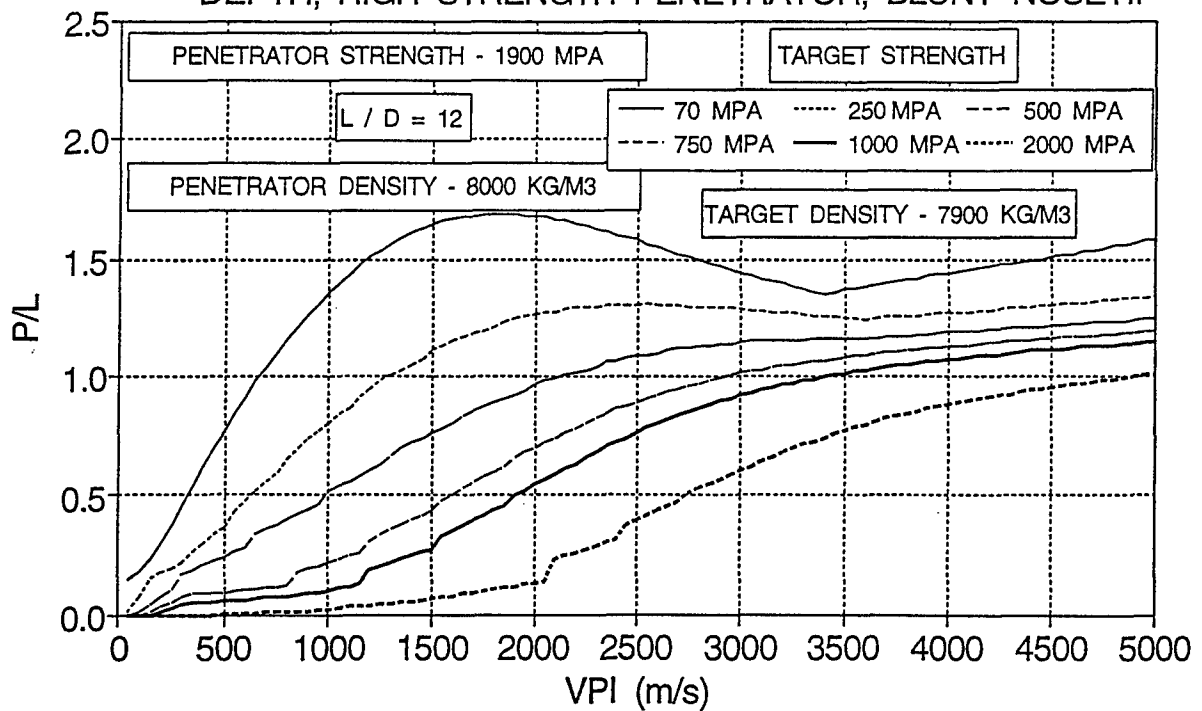


FIG. 5. EFFECT OF TARGET STRENGTH ON CRATER DIAMETER, HIGH STRENGTH PENETRATOR, OGIVE NOSETIP

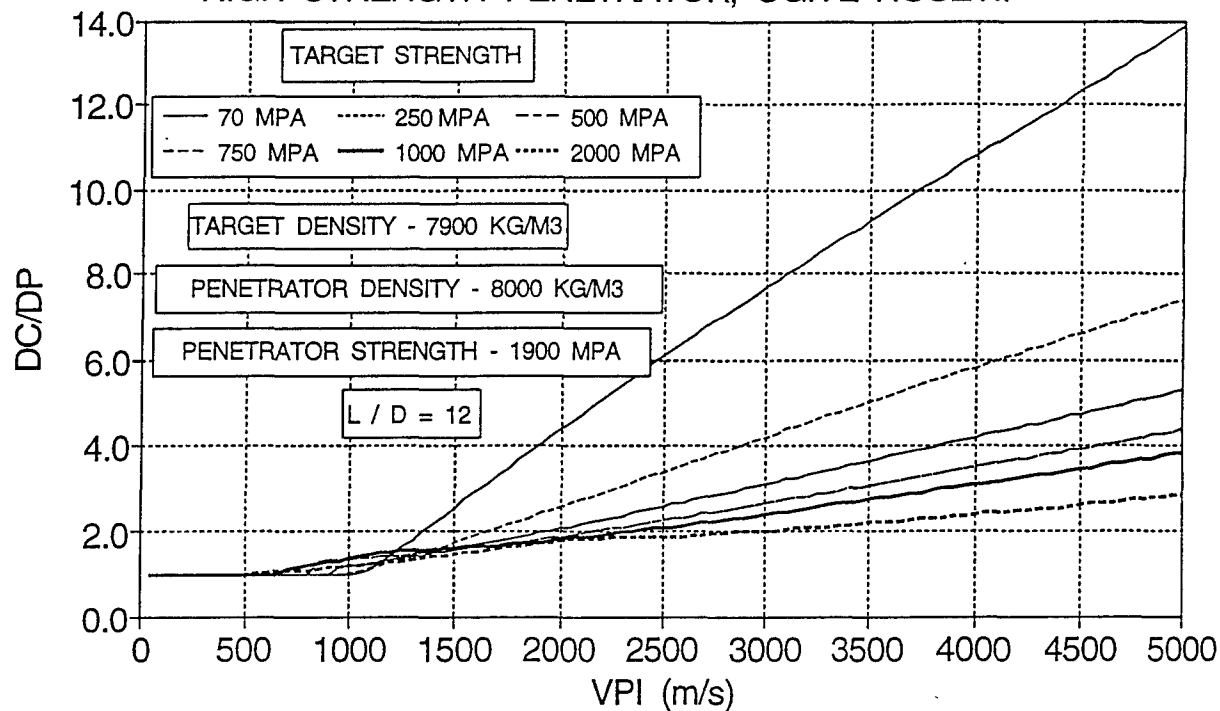


FIG. 6. EFFECT OF TARGET STRENGTH ON CRATER DIAMETER, HIGH STRENGTH PENETRATOR, BLUNT NOSETIP

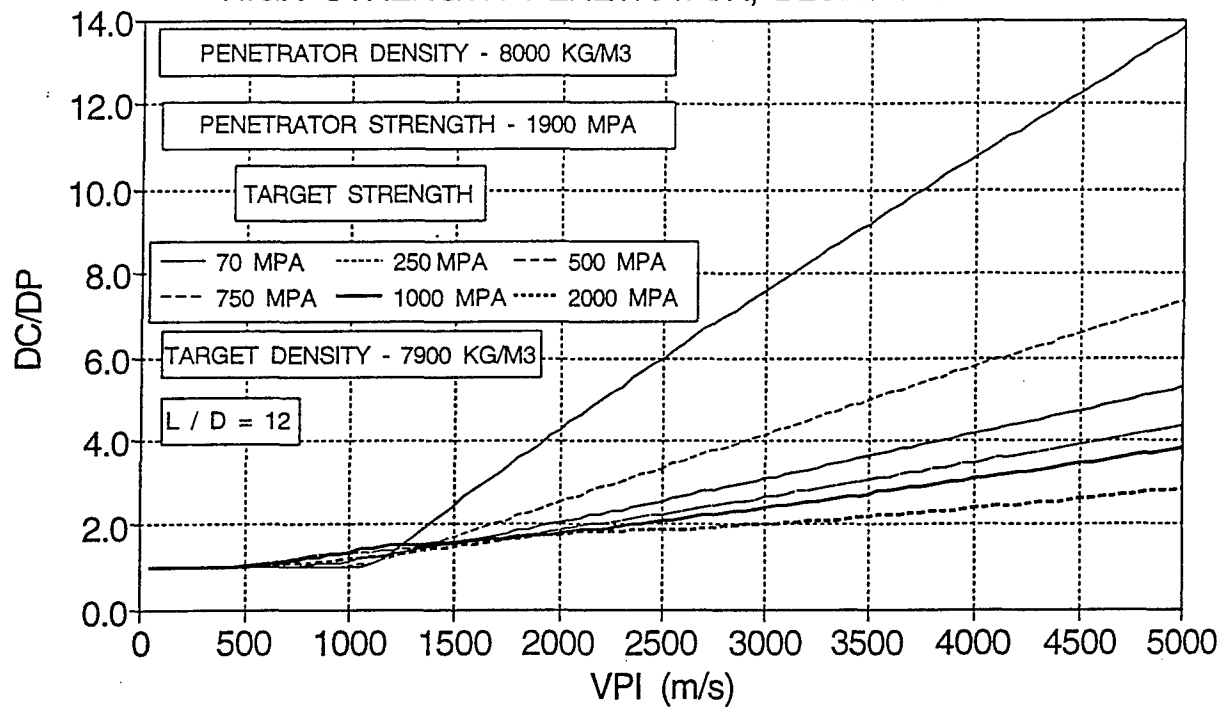


FIG. 7. EFFECT OF TARGET STRENGTH ON PENETRATION DEPTH, LOW STRENGTH PENETRATOR, OGIVE NOSETIP

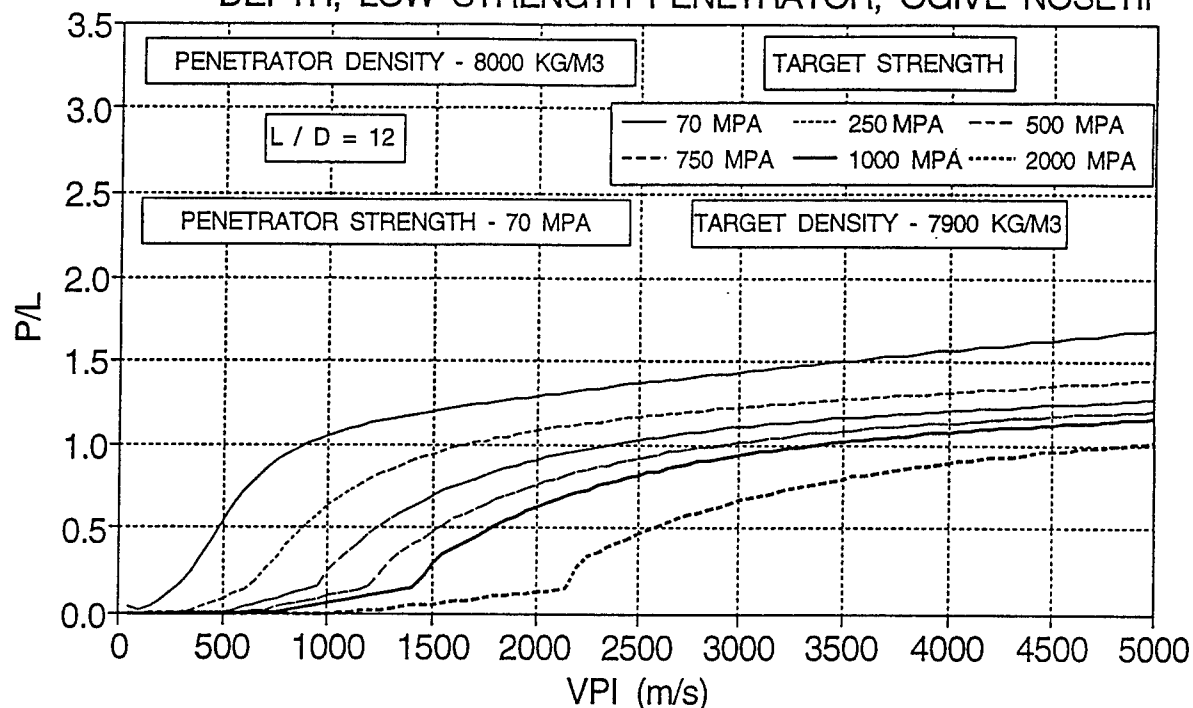


FIG. 8. EFFECT OF TARGET STRENGTH ON PENETRATION DEPTH, LOW STRENGTH PENETRATOR, BLUNT NOSETIP

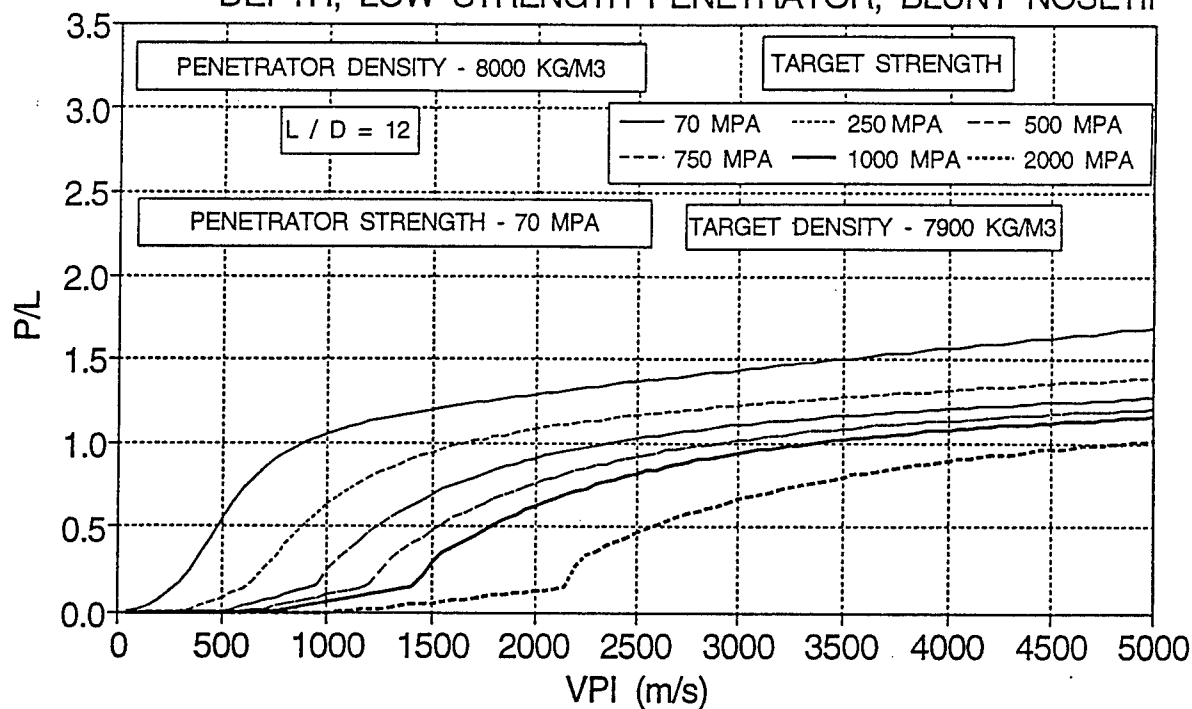


FIG. 9. EFFECT OF TARGET STRENGTH ON PENETRATION DEPTH, HIGH DENSITY PENETRATOR, OGIVE NOSETIP

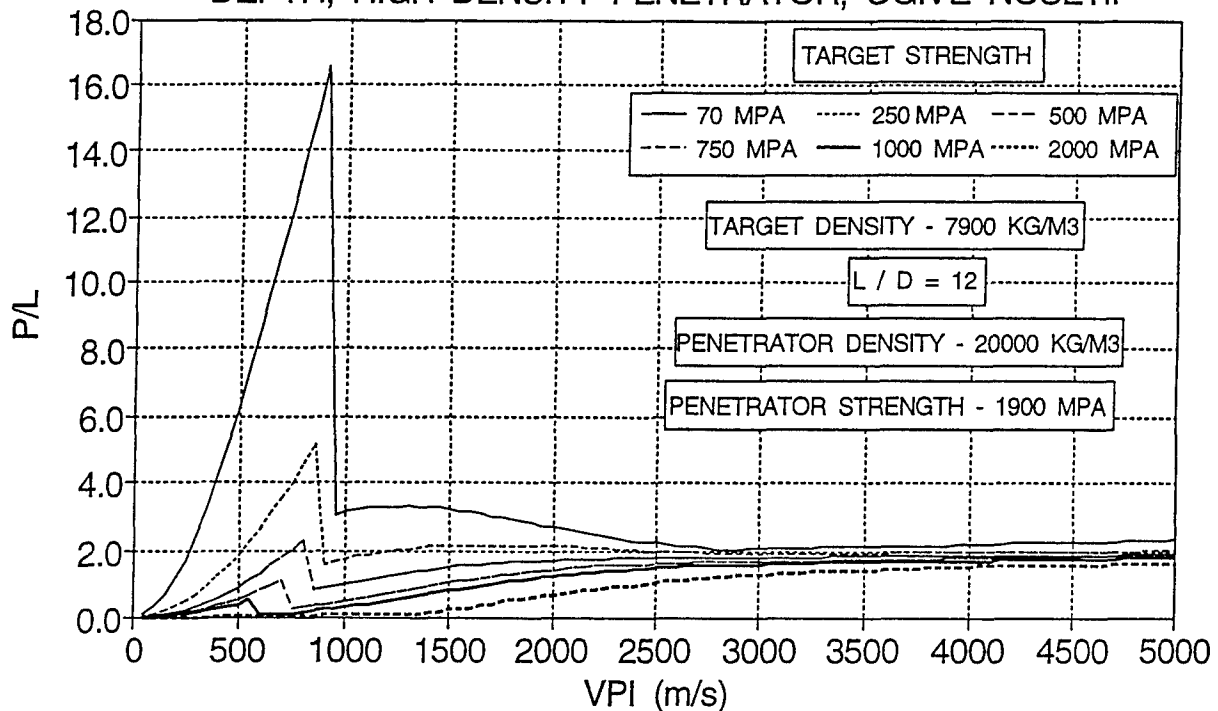


FIG. 10. EFFECT OF TARGET STRENGTH ON PENETRATION DEPTH, HIGH DENSITY PENETRATOR, BLUNT NOSETIP

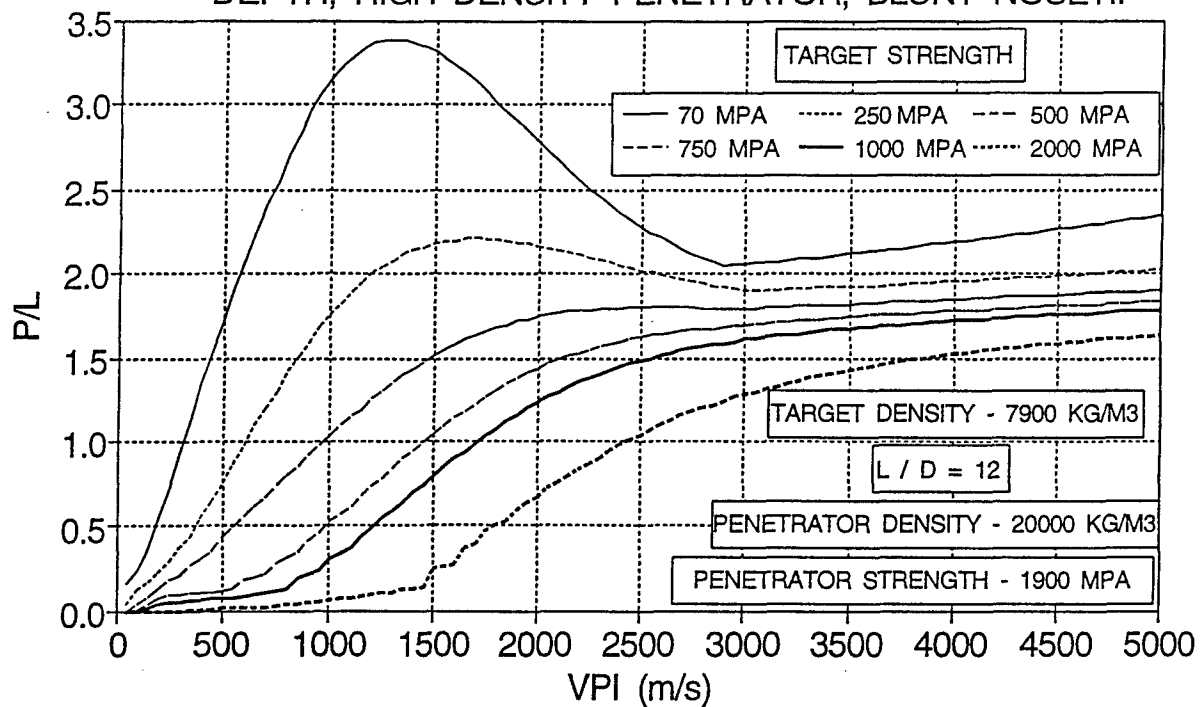


FIG. 11. EFFECT OF TARGET STRENGTH ON PENETRATION DEPTH, LOW DENSITY PENETRATOR, OGIVE NOSETIP

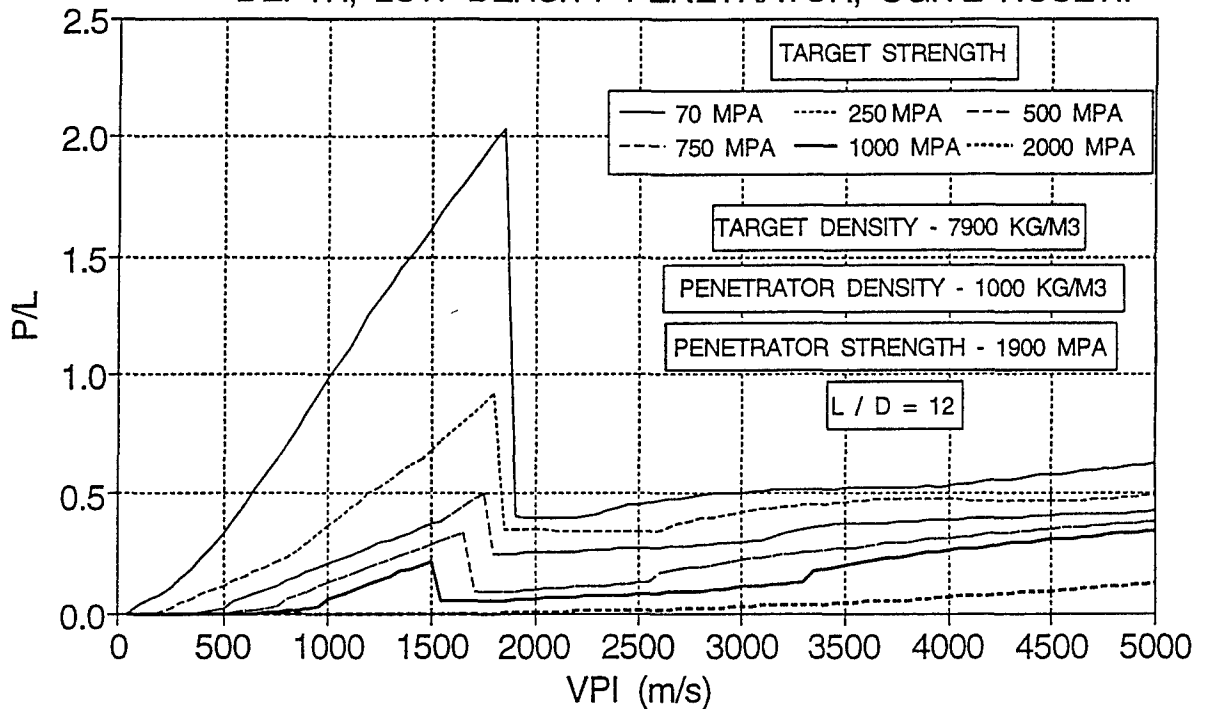


FIG. 12. EFFECT OF TARGET STRENGTH ON PENETRATION DEPTH, LOW DENSITY PENETRATOR, BLUNT NOSETIP

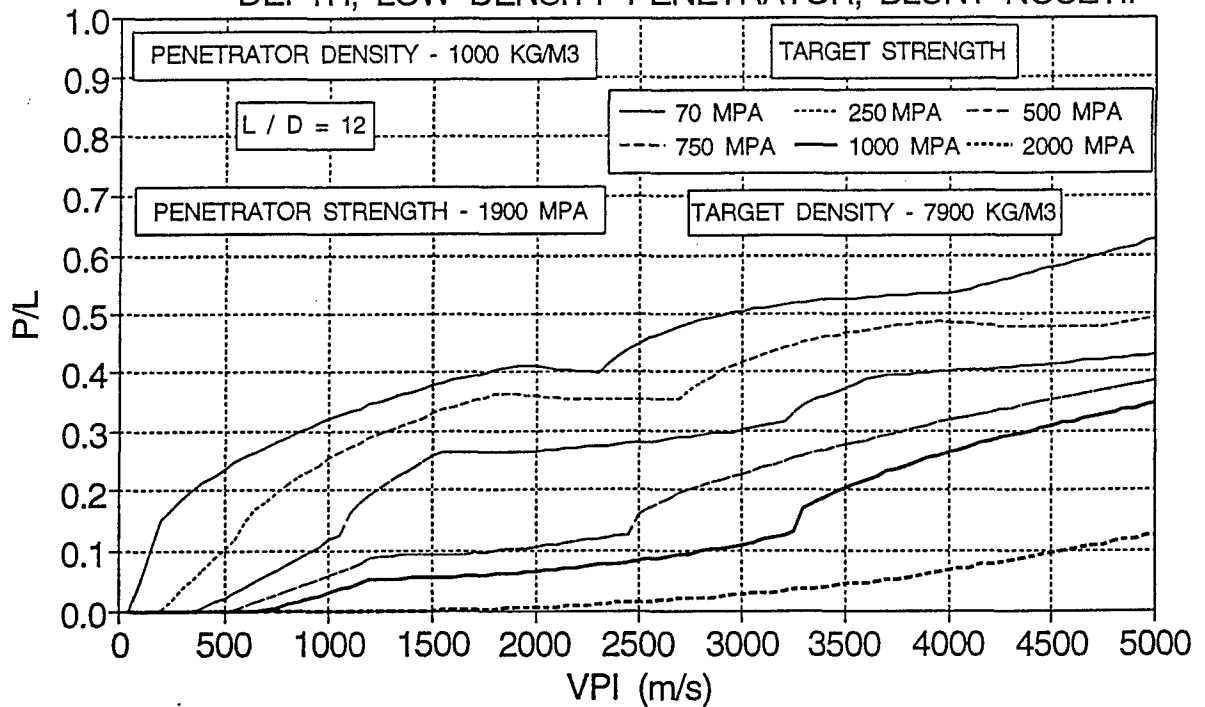


FIG. 13. EFFECT OF TARGET STRENGTH ON PENETRATION DEPTH, HIGH DENSITY TARGET, OGIVE NOSETIP

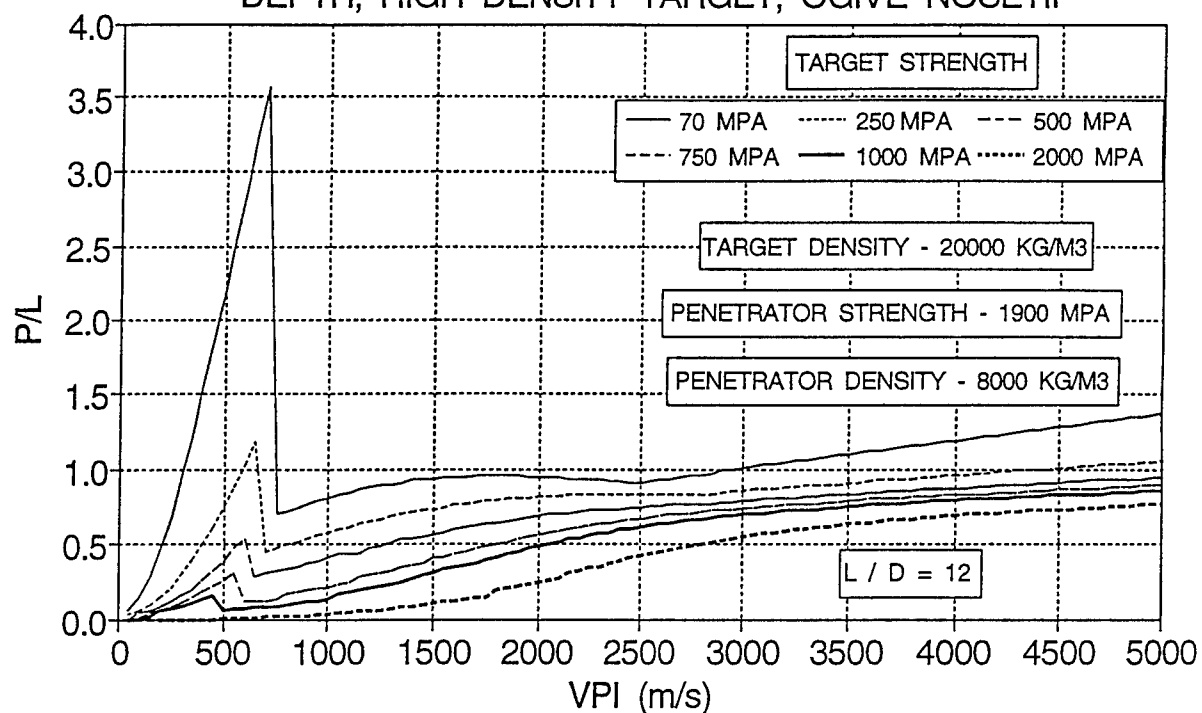


FIG. 14. EFFECT OF TARGET STRENGTH ON PENETRATION DEPTH, HIGH DENSITY TARGET, BLUNT NOSETIP

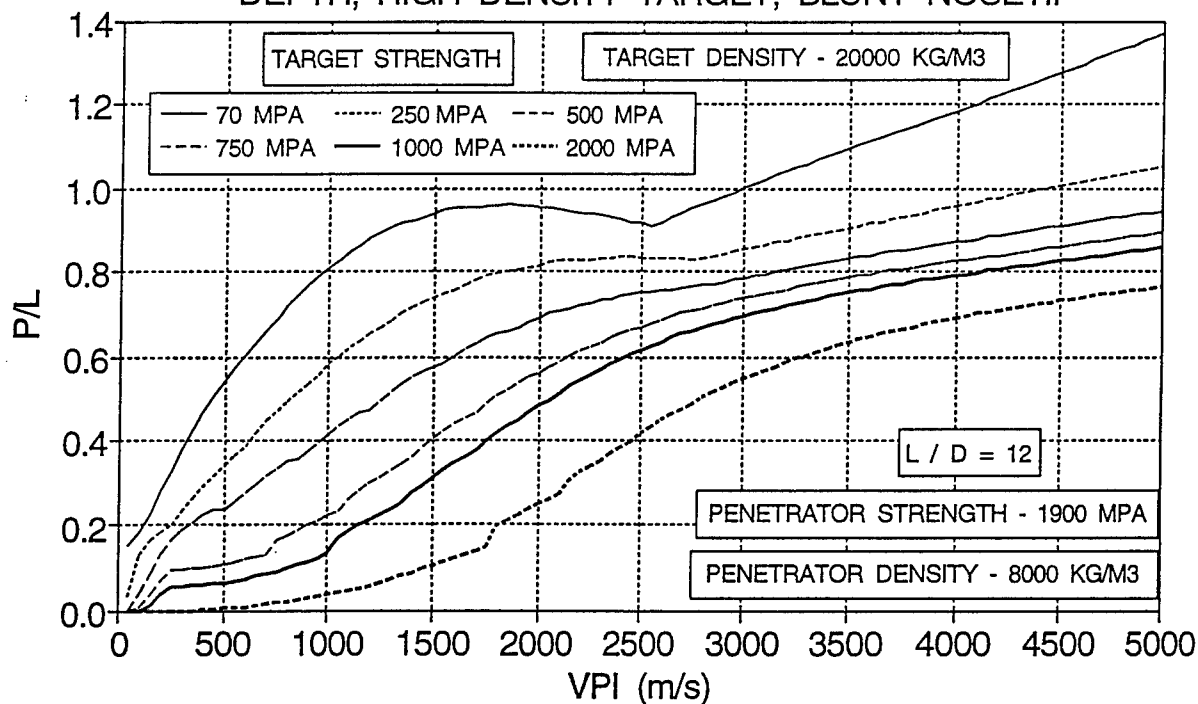


FIG. 15. EFFECT OF TARGET STRENGTH ON PENETRATION DEPTH, LOW DENSITY TARGET, OGIVE NOSETIP

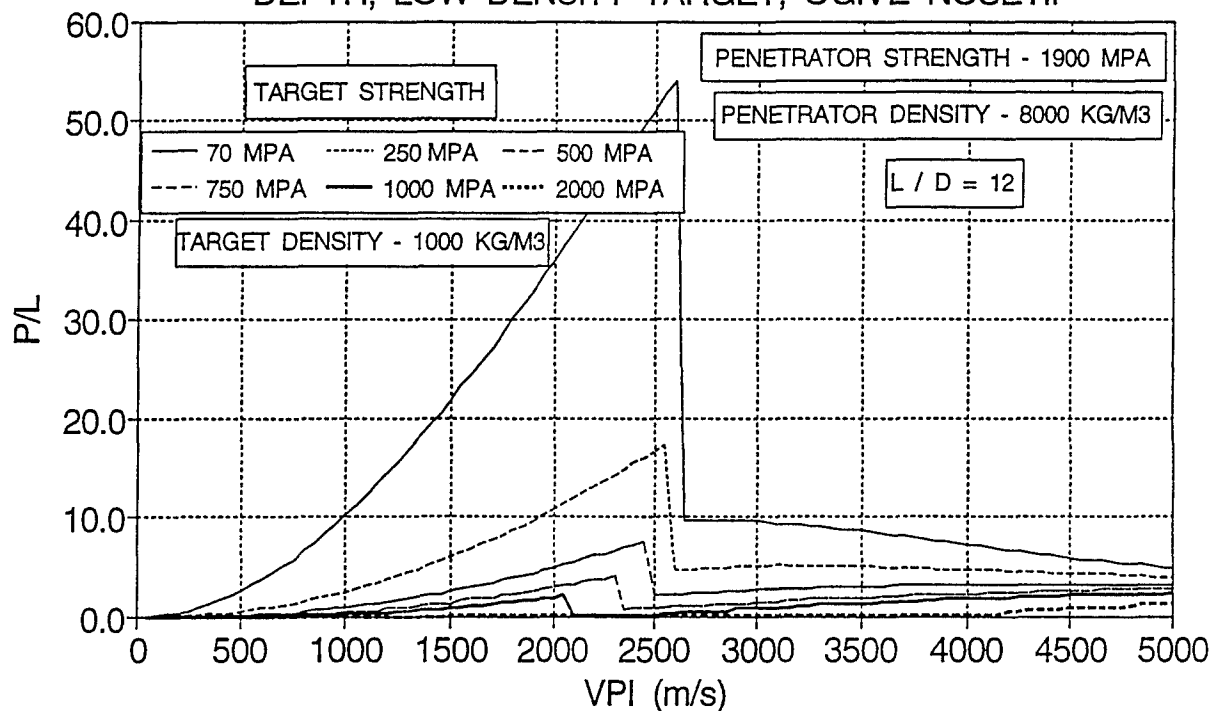


FIG. 16. EFFECT OF TARGET STRENGTH ON PENETRATION DEPTH, LOW DENSITY TARGET, BLUNT NOSETIP

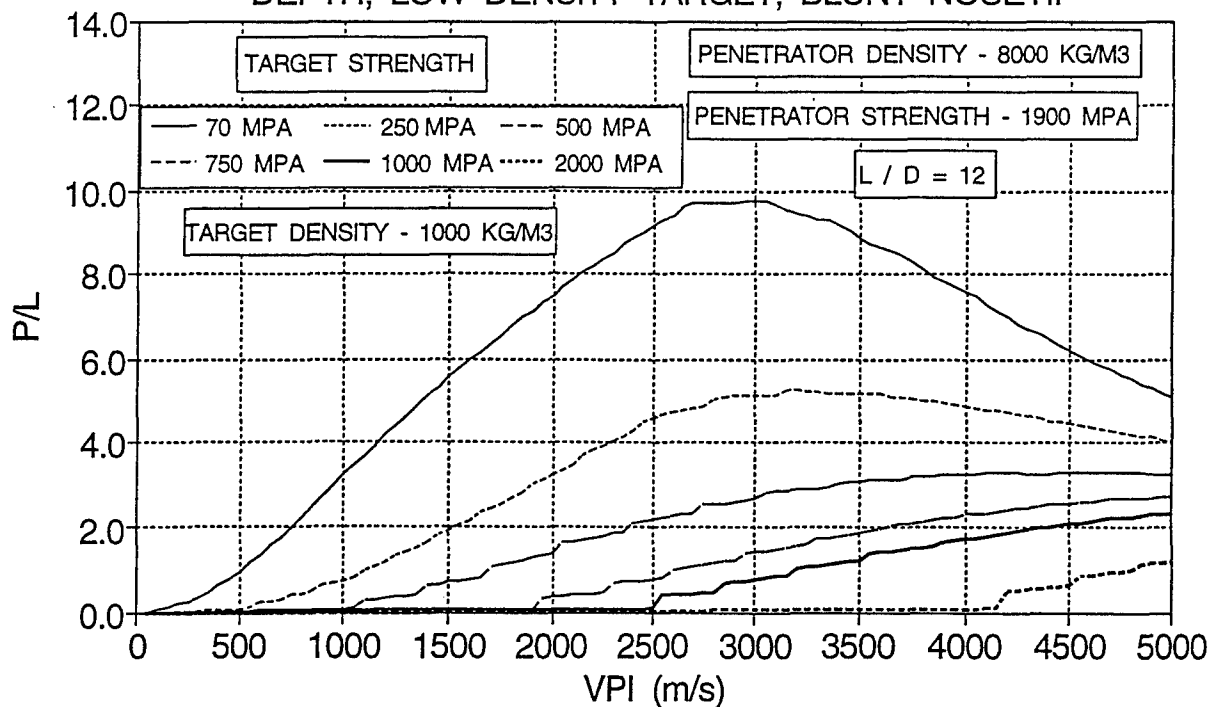


FIG. 17. EFFECT OF PENETRATOR STRENGTH ON PENETRATION DEPTH, HIGH STRENGTH TARGET, OGIVE NOSETIP

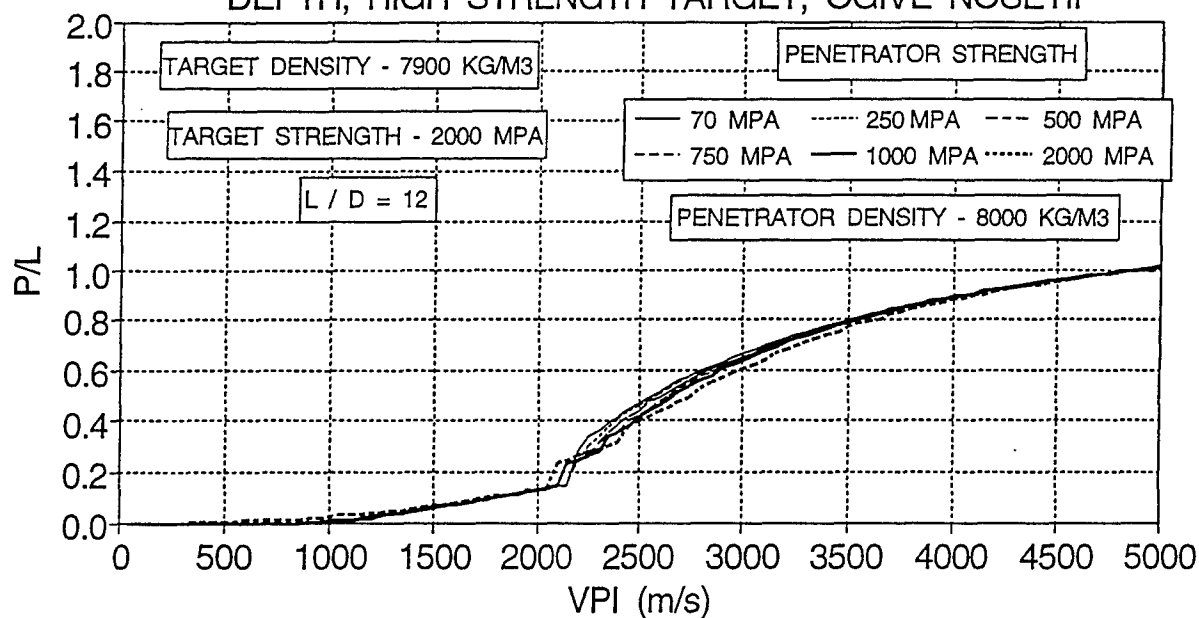


FIG. 18. EFFECT OF PENETRATOR STRENGTH ON PENETRATION DEPTH, HIGH STRENGTH TARGET, BLUNT NOSETIP

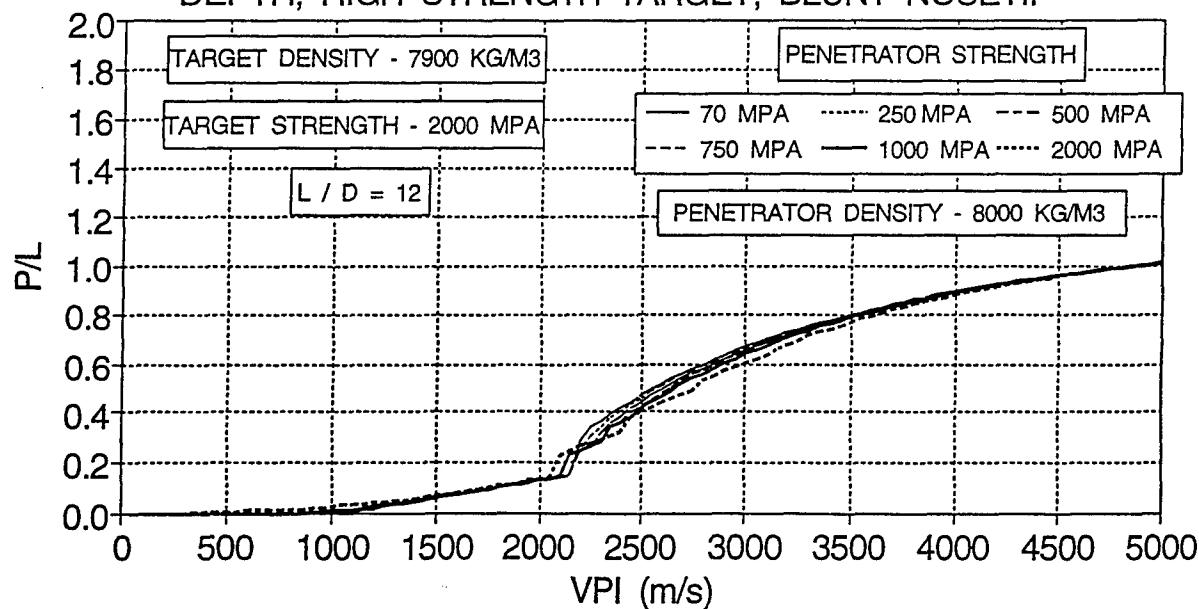


FIG. 19. EFFECT OF PENETRATOR STRENGTH ON PENETRATION DEPTH, MEDIUM STRENGTH TARGET, OGIVE NOSETIP

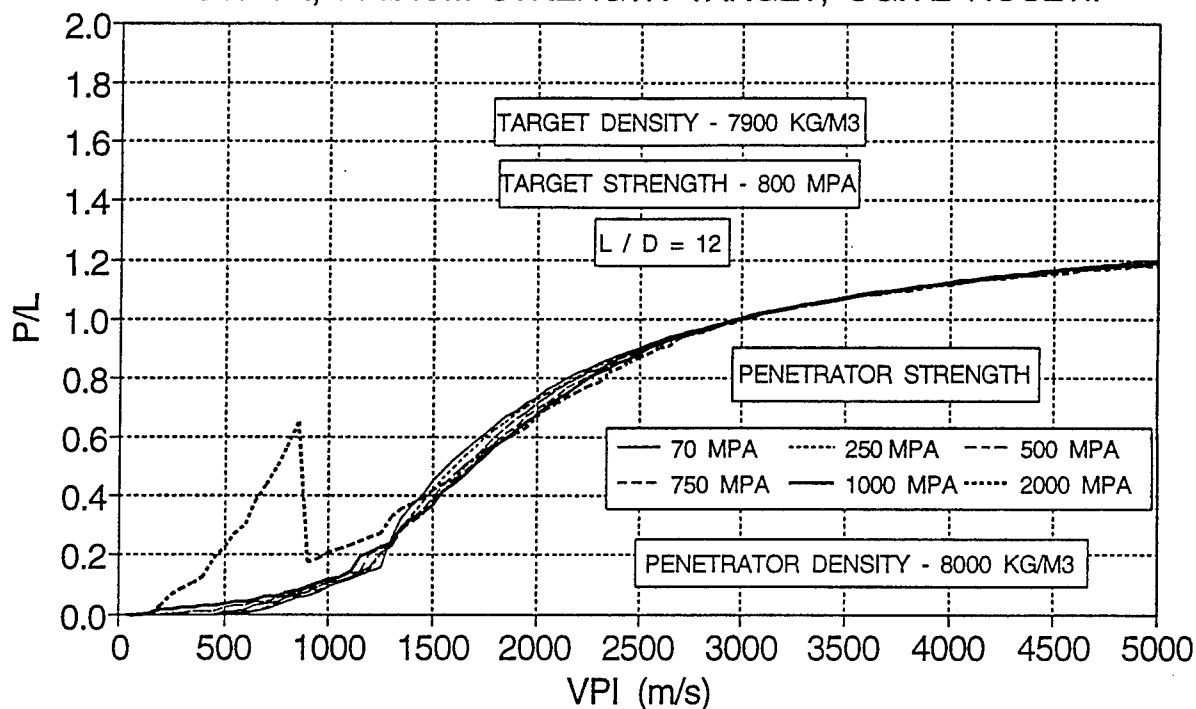


FIG. 20. EFFECT OF PENETRATOR STRENGTH ON PENETRATION DEPTH, MEDIUM STRENGTH TARGET, BLUNT NOSETIP

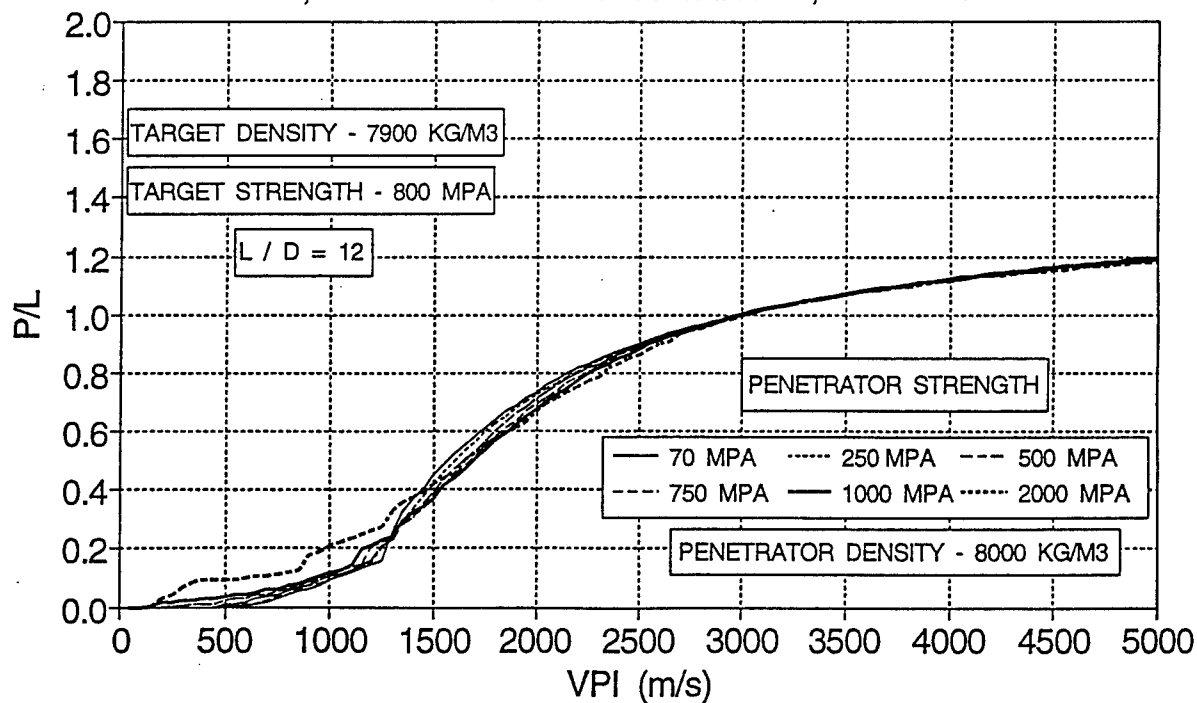


FIG. 21. EFFECT OF PENETRATOR STRENGTH ON PENETRATION DEPTH, HIGH DENSITY PENETRATOR, OGIVE NOSETIP

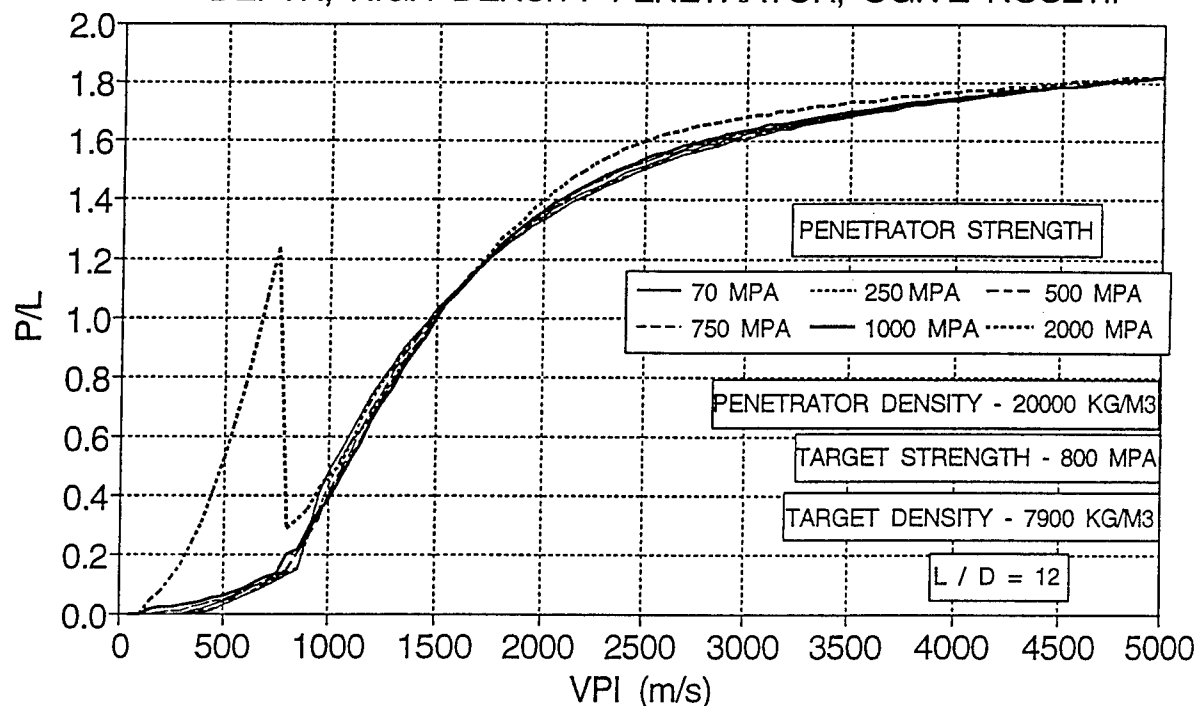


FIG. 22. EFFECT OF PENETRATOR STRENGTH ON PENETRATION DEPTH, HIGH DENSITY PENETRATOR, BLUNT NOSETIP

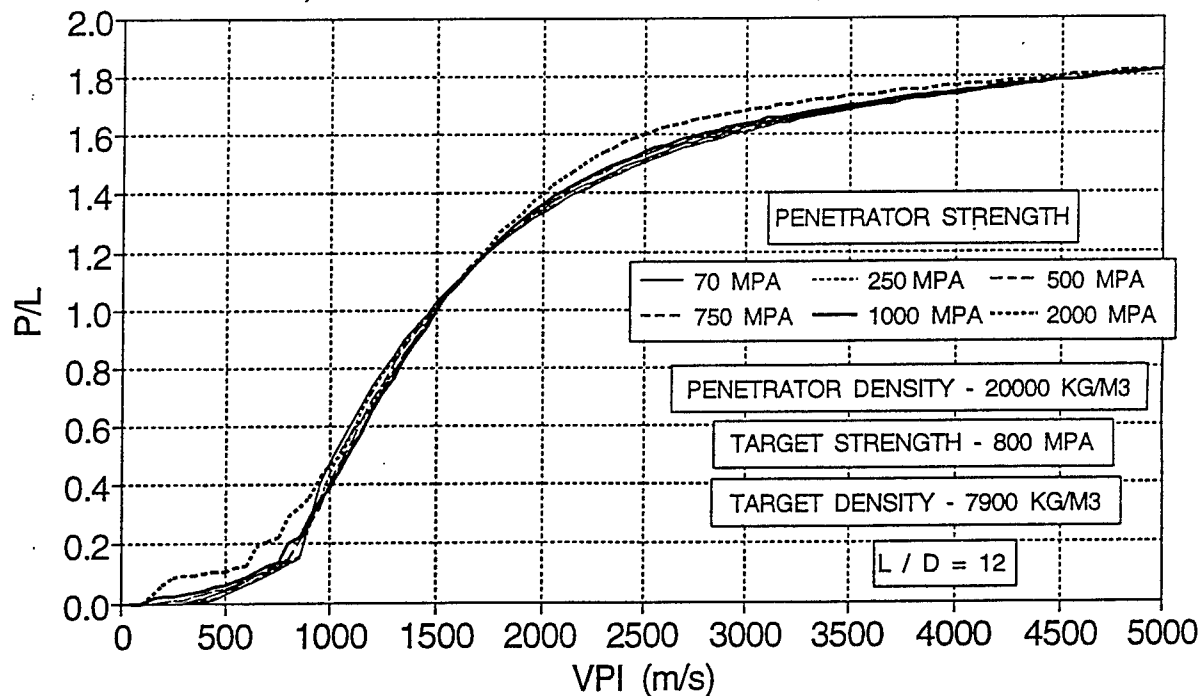


FIG. 23. EFFECT OF TARGET DENSITY ON PENETRATION DEPTH, HIGH STRENGTH TARGET, OGIVE NOSETIP

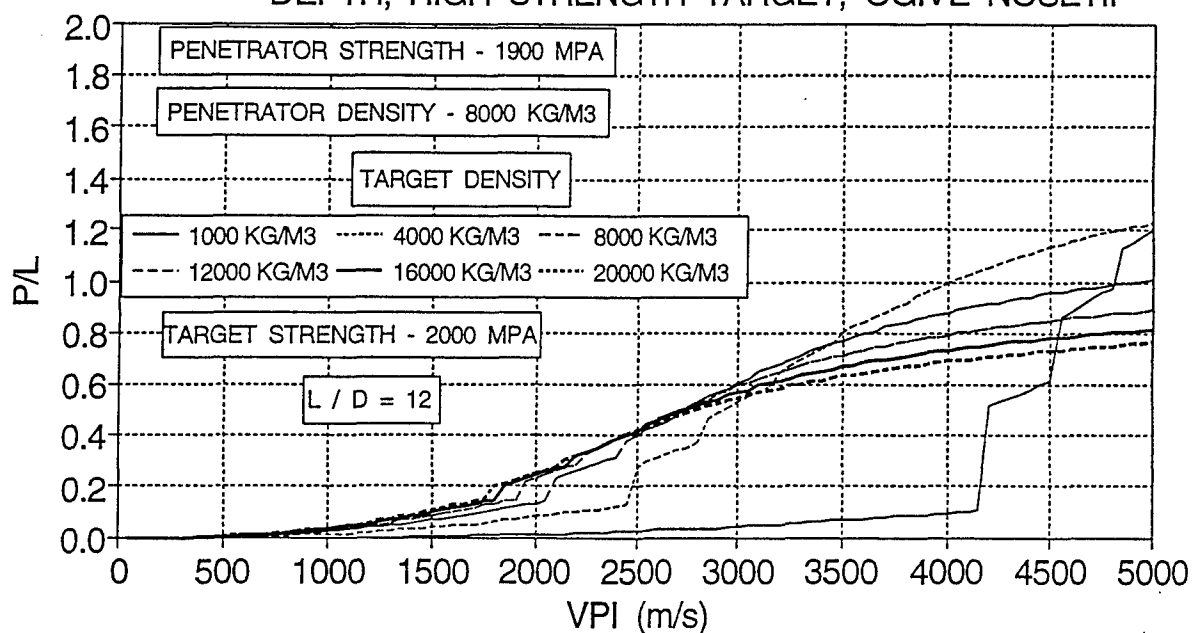


FIG. 24. EFFECT OF TARGET DENSITY ON PENETRATION DEPTH, HIGH STRENGTH TARGET, BLUNT NOSETIP

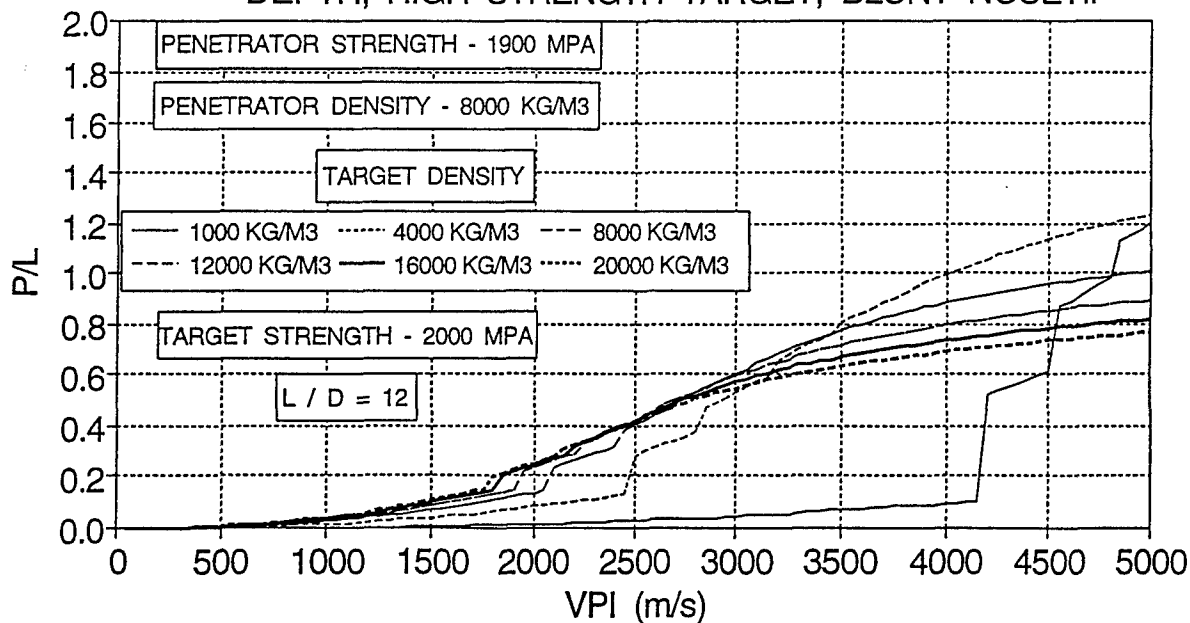


FIG. 25. EFFECT OF TARGET DENSITY ON PENETRATION DEPTH, MEDIUM STRENGTH TARGET, OGIVE NOSETIP

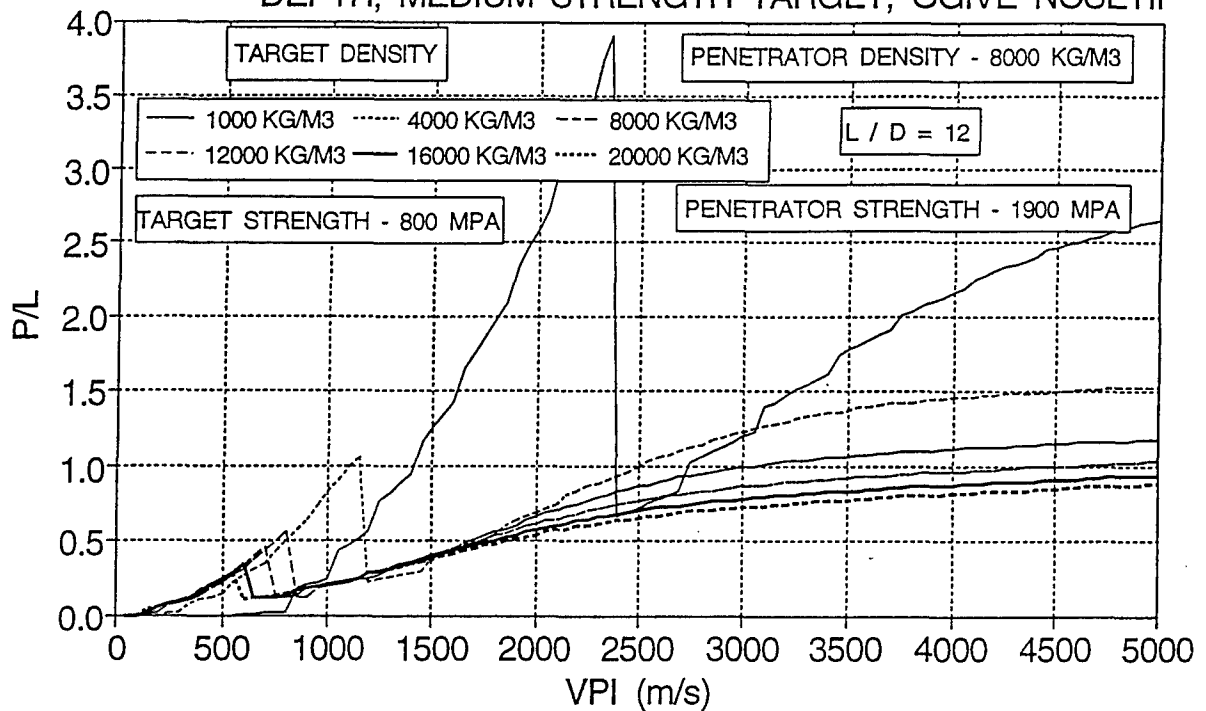


FIG. 26. EFFECT OF TARGET DENSITY ON PENETRATION DEPTH, MEDIUM STRENGTH TARGET, BLUNT NOSETIP

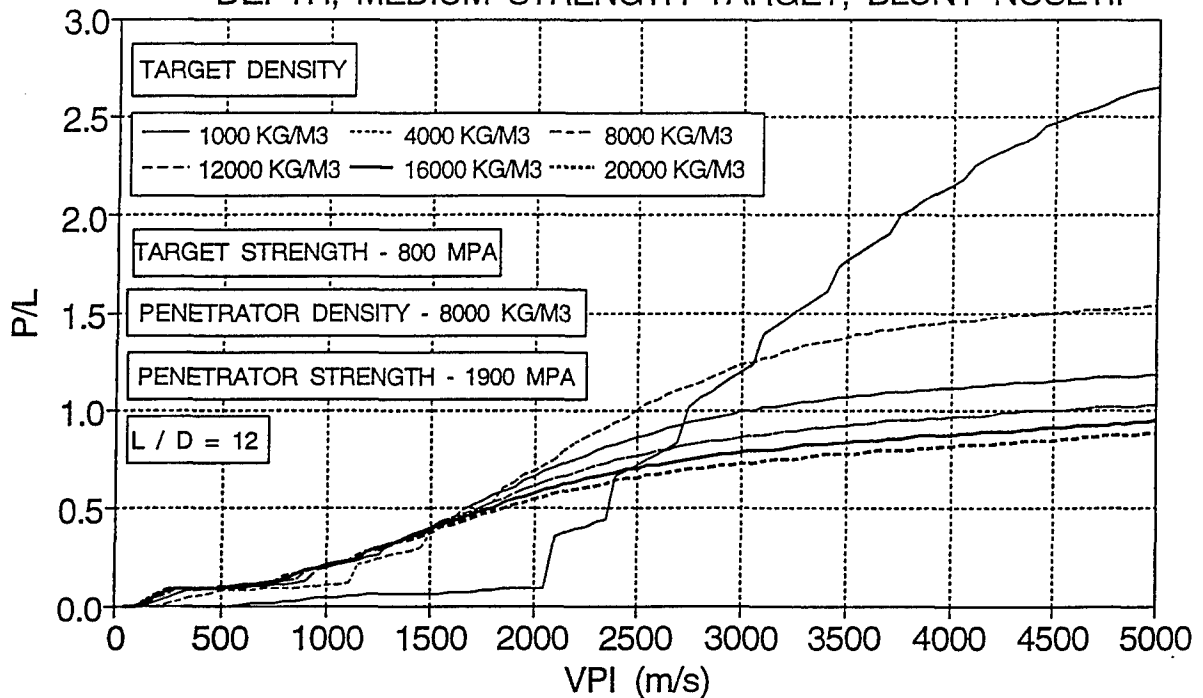


FIG. 27. EFFECT OF TARGET DENSITY ON PENETRATION DEPTH, HIGH DENSITY PENETRATOR, OGIVE NOSETIP

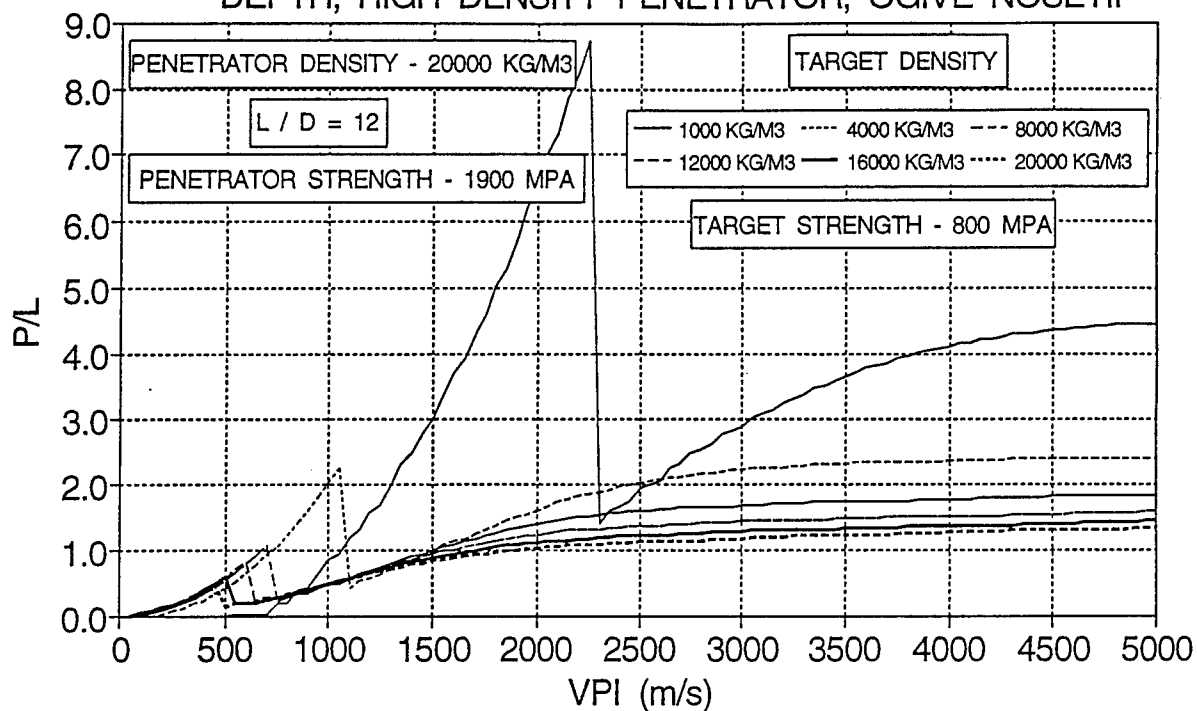


FIG. 28. EFFECT OF TARGET DENSITY ON PENETRATION DEPTH, HIGH DENSITY PENETRATOR, BLUNT NOSETIP

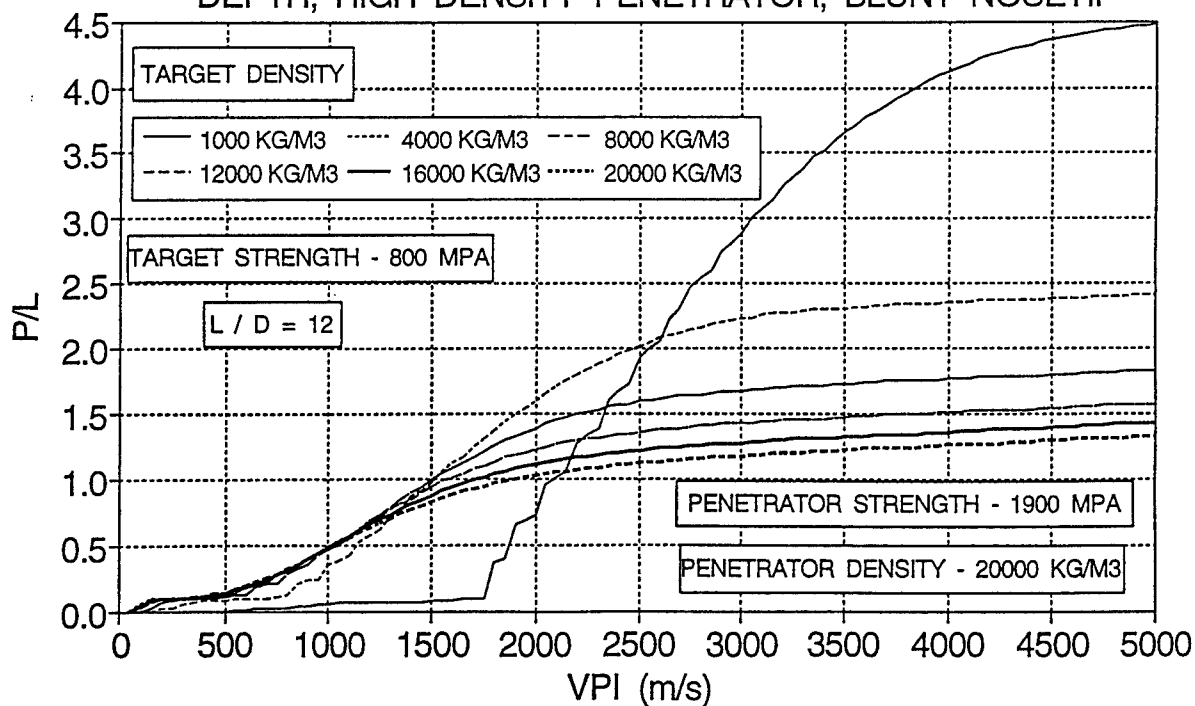


FIG. 29. EFFECT OF PENETRATOR DENSITY ON PENETRATION DEPTH, HIGH STRENGTH TARGET, OGIVE NOSETIP

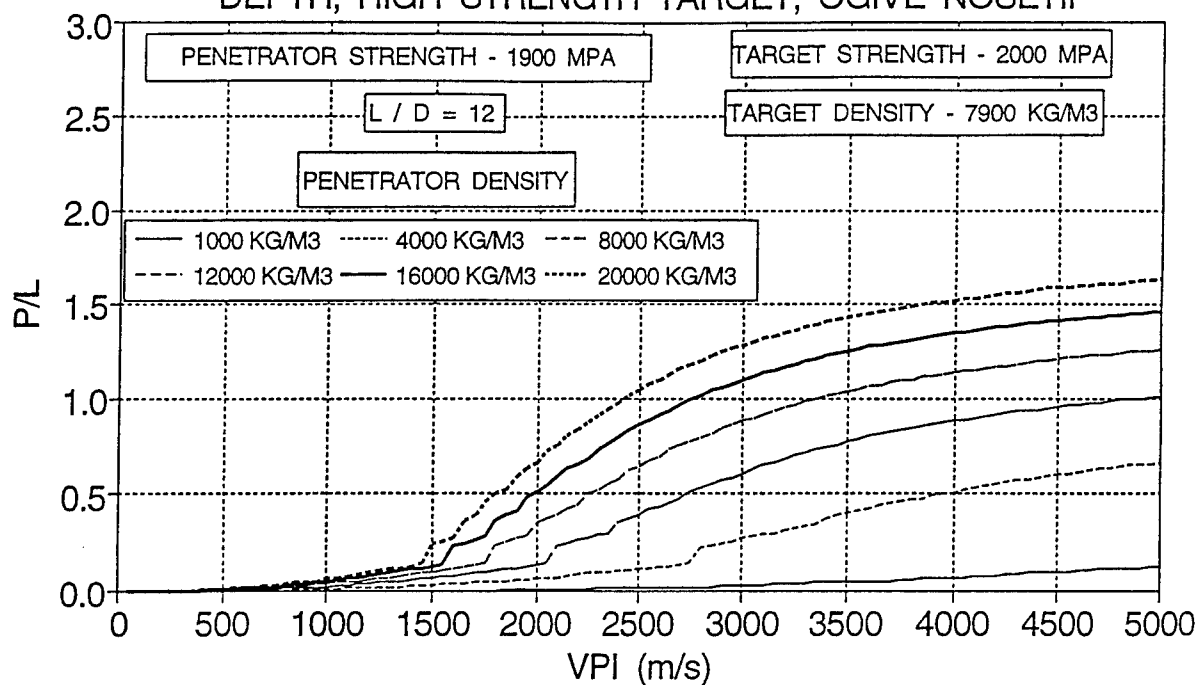


FIG. 30. EFFECT OF PENETRATOR DENSITY ON PENETRATION DEPTH, HIGH STRENGTH TARGET, BLUNT NOSETIP

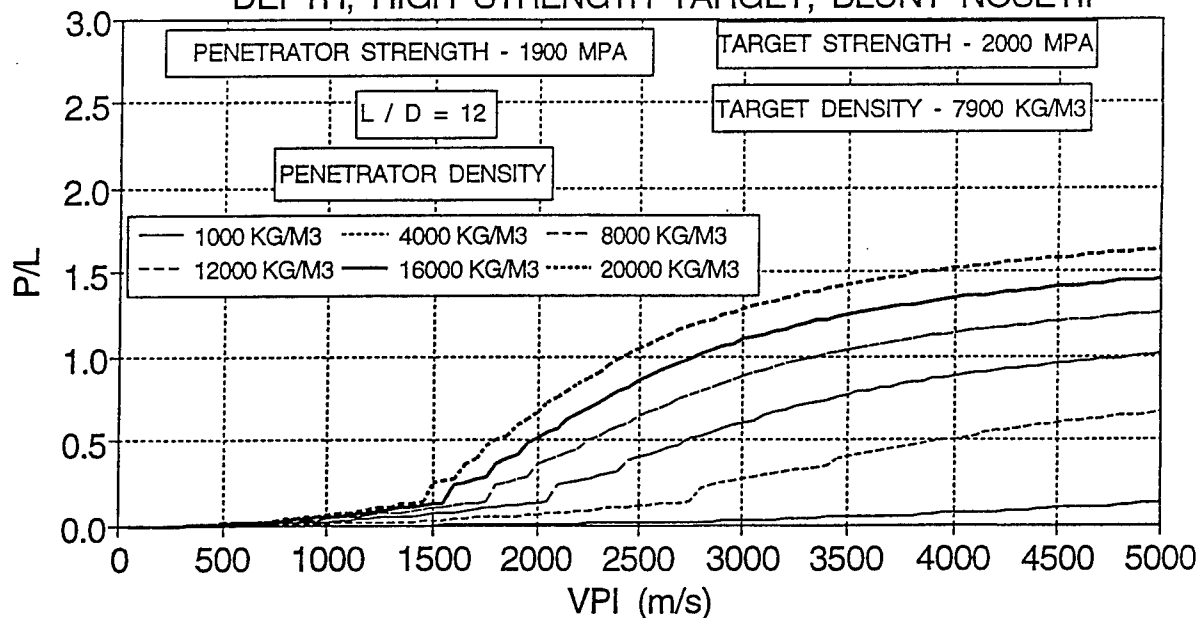


FIG. 31. EFFECT OF PENETRATOR DENSITY ON PENETRATION DEPTH, MEDIUM STRENGTH TARGET, OGIVE NOSETIP

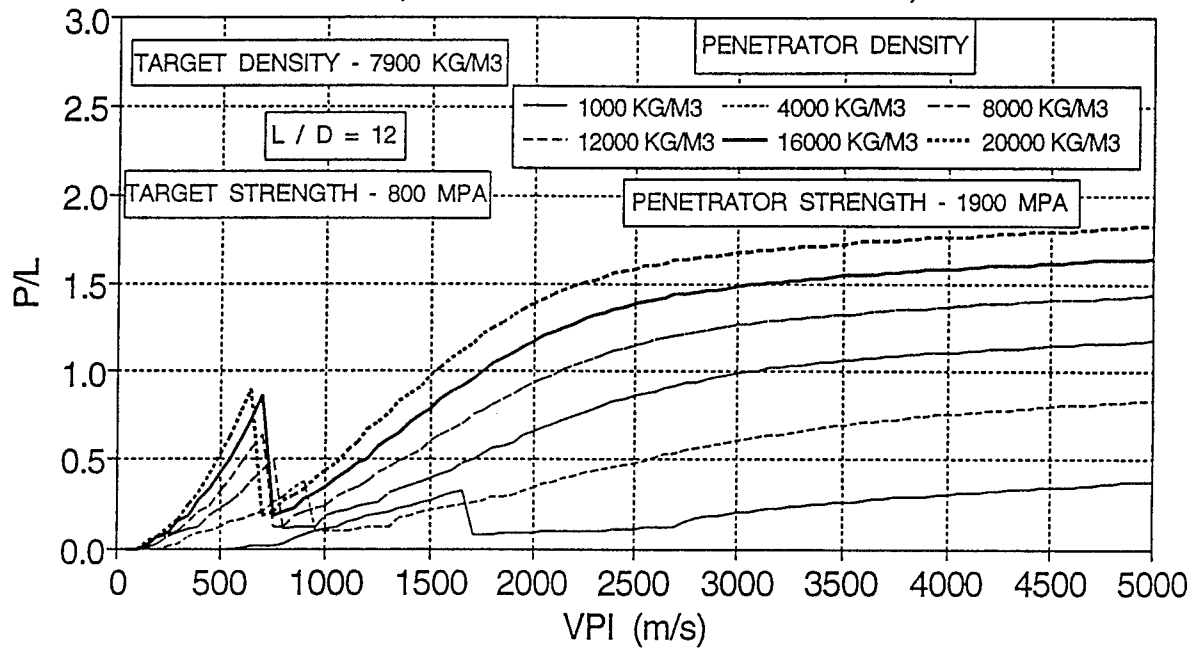


FIG. 32. EFFECT OF PENETRATOR DENSITY ON PENETRATION DEPTH, MEDIUM STRENGTH TARGET, BLUNT NOSETIP

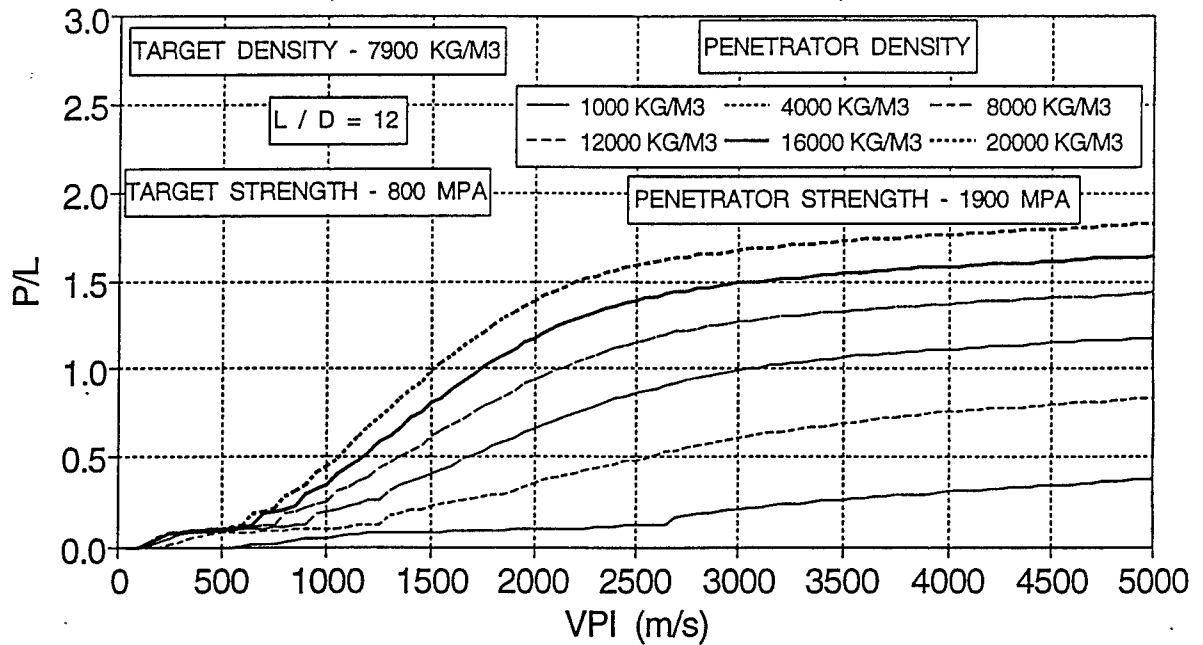


FIG. 33. EFFECT OF PENETRATOR DENSITY ON PENETRATION DEPTH, LOW STRENGTH TARGET, OGIVE NOSETIP

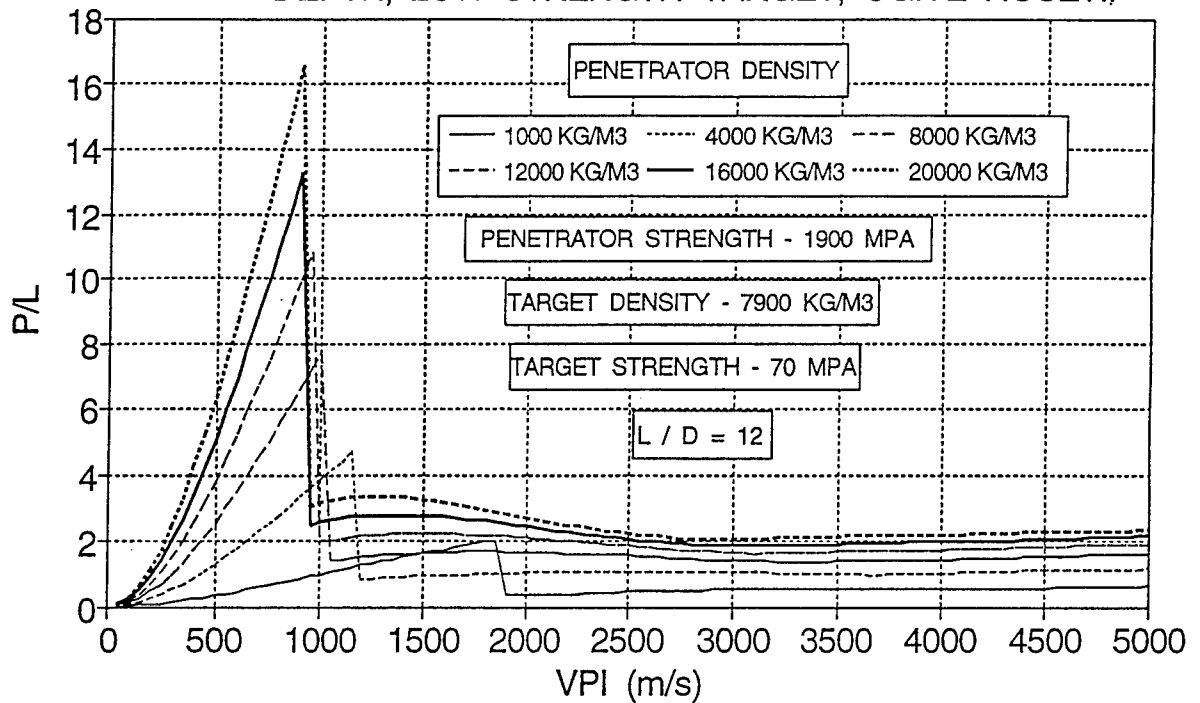


FIG. 34. EFFECT OF PENETRATOR DENSITY ON PENETRATION DEPTH, LOW STRENGTH TARGET, BLUNT NOSETIP

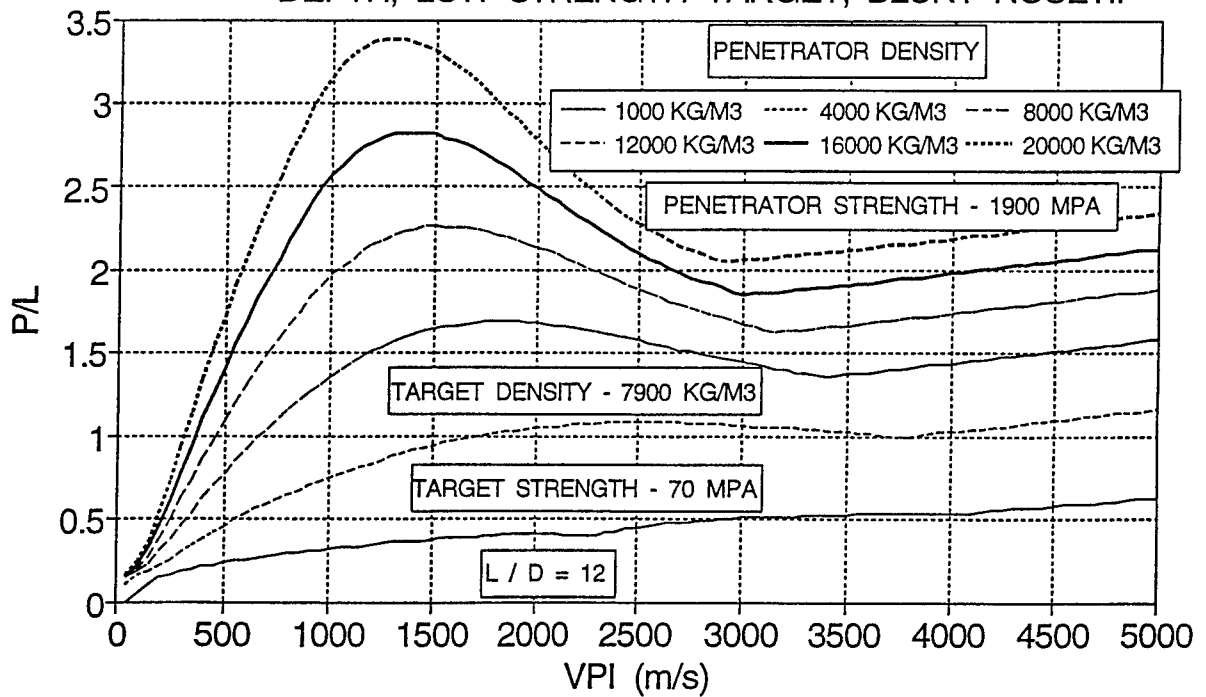


FIG. 35. EFFECT OF PENETRATOR DENSITY ON PENETRATION DEPTH, HIGH DENSITY TARGET, OGIVE NOSETIP

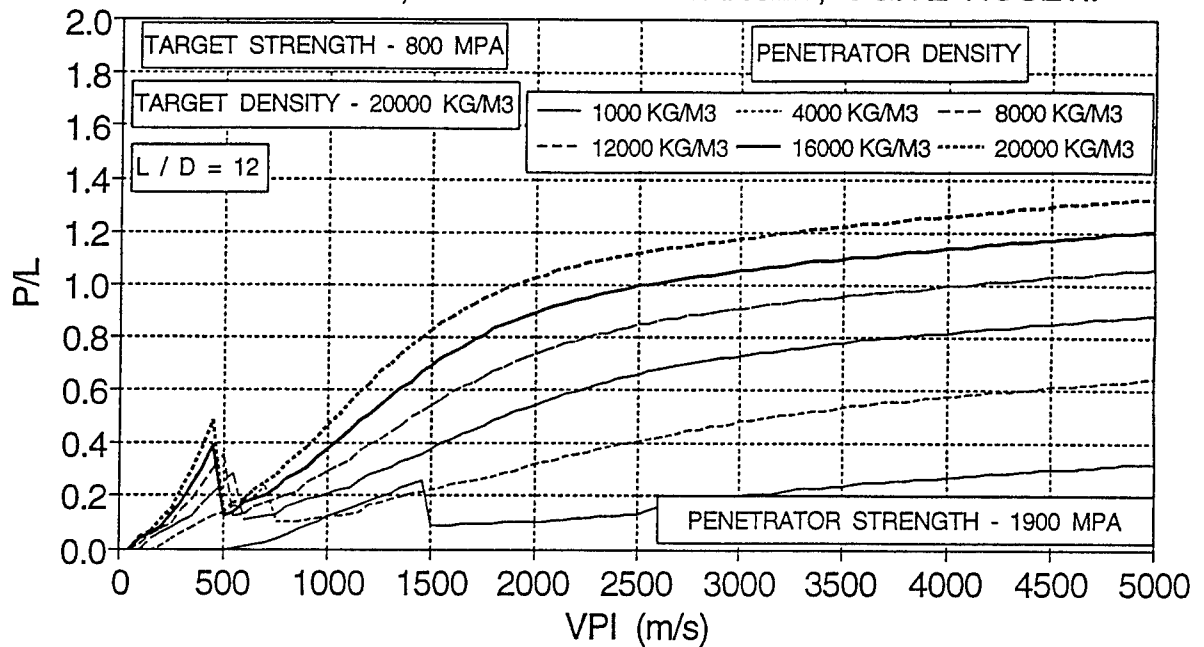


FIG. 36. EFFECT OF PENETRATOR DENSITY ON PENETRATION DEPTH, HIGH DENSITY TARGET, BLUNT NOSETIP

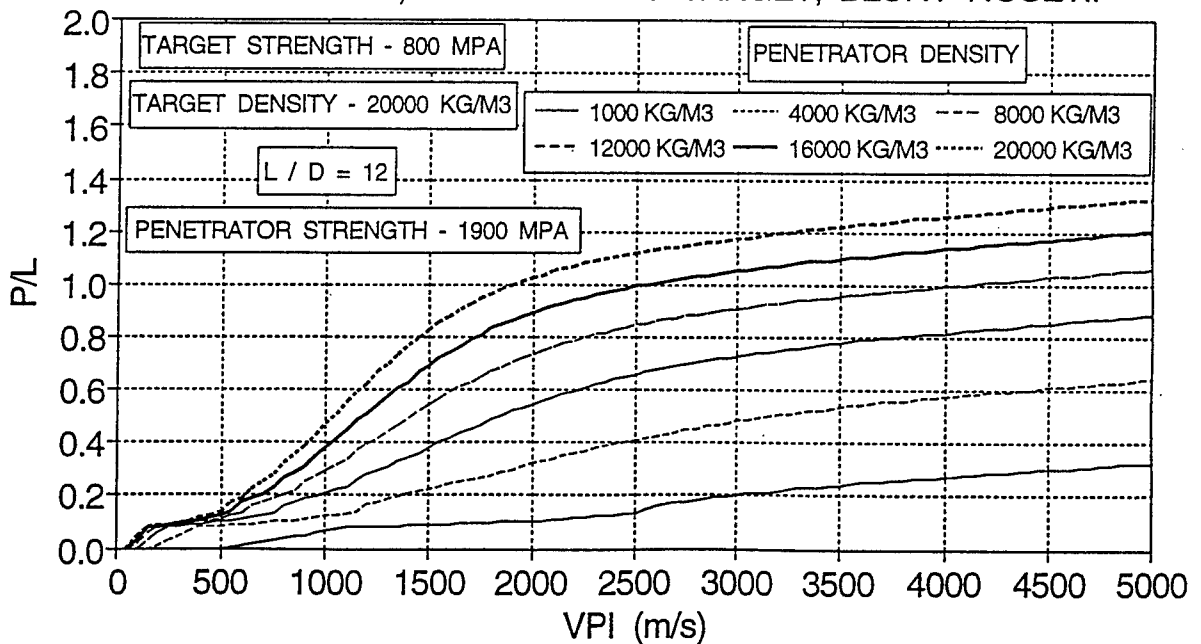


FIG. 37. EFFECT OF PENETRATOR L/D ON
PENETRATION DEPTH, OGIVE NOSETIP

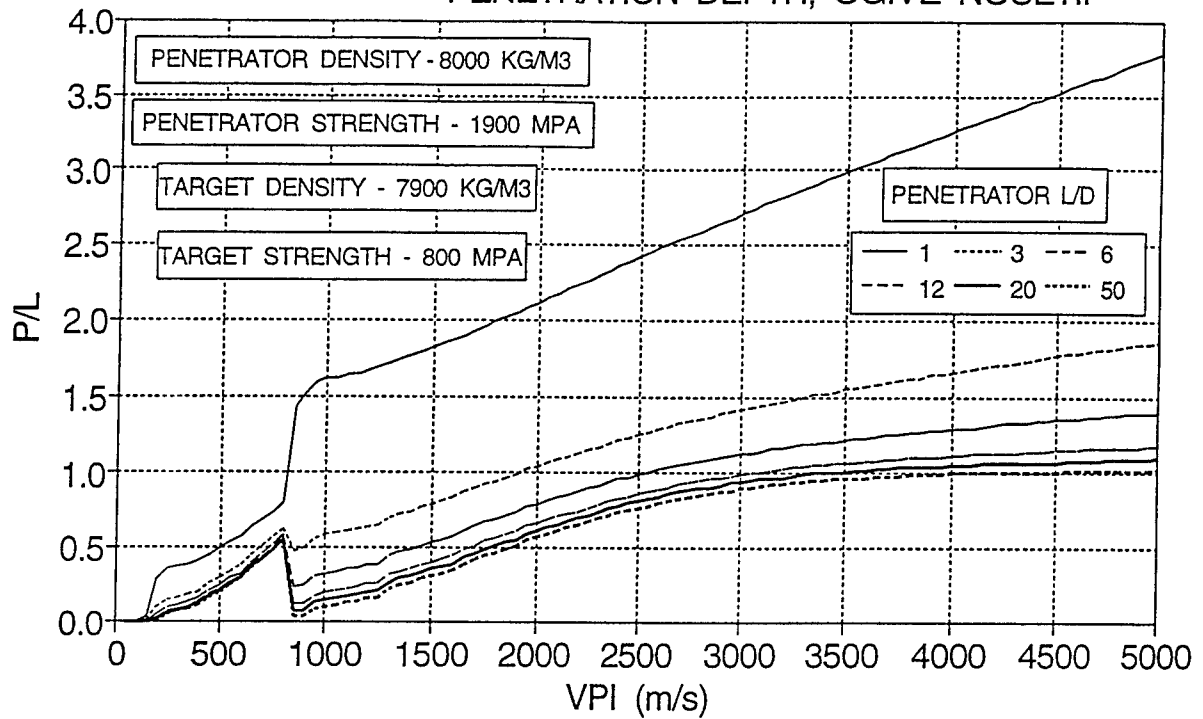


FIG. 38. EFFECT OF PENETRATOR L/D ON
PENETRATION DEPTH, BLUNT NOSETIP

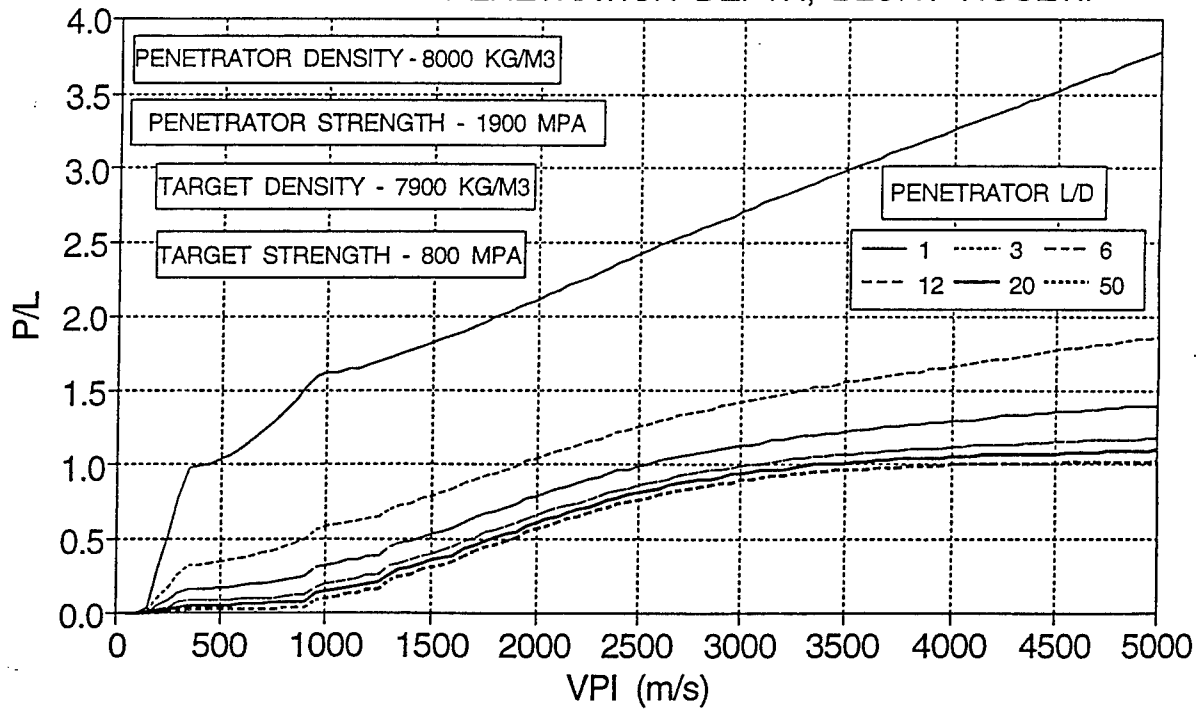


FIG. 39. EFFECT OF TARGET STRENGTH ON PENETRATION DEPTH, TUNGSTEN ALLOY INTO CONCRETE, OGIVE NOSETIP

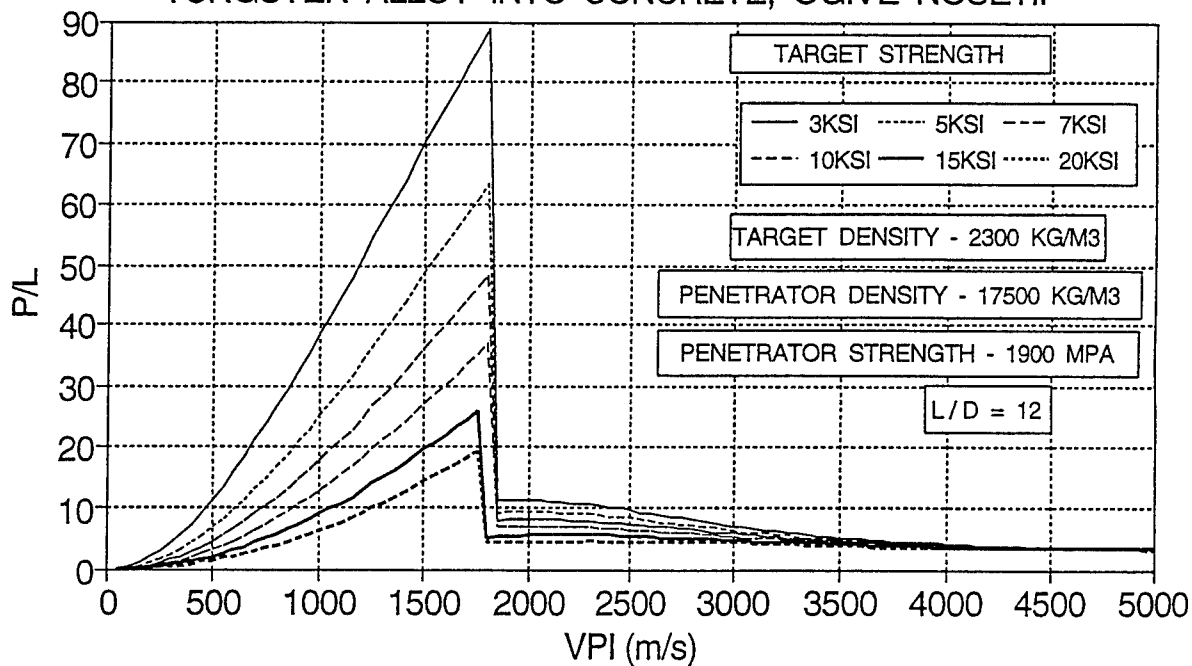


FIG. 40. EFFECT OF TARGET STRENGTH ON PENETRATION DEPTH, TUNGSTEN ALLOY INTO CONCRETE, BLUNT NOSETIP

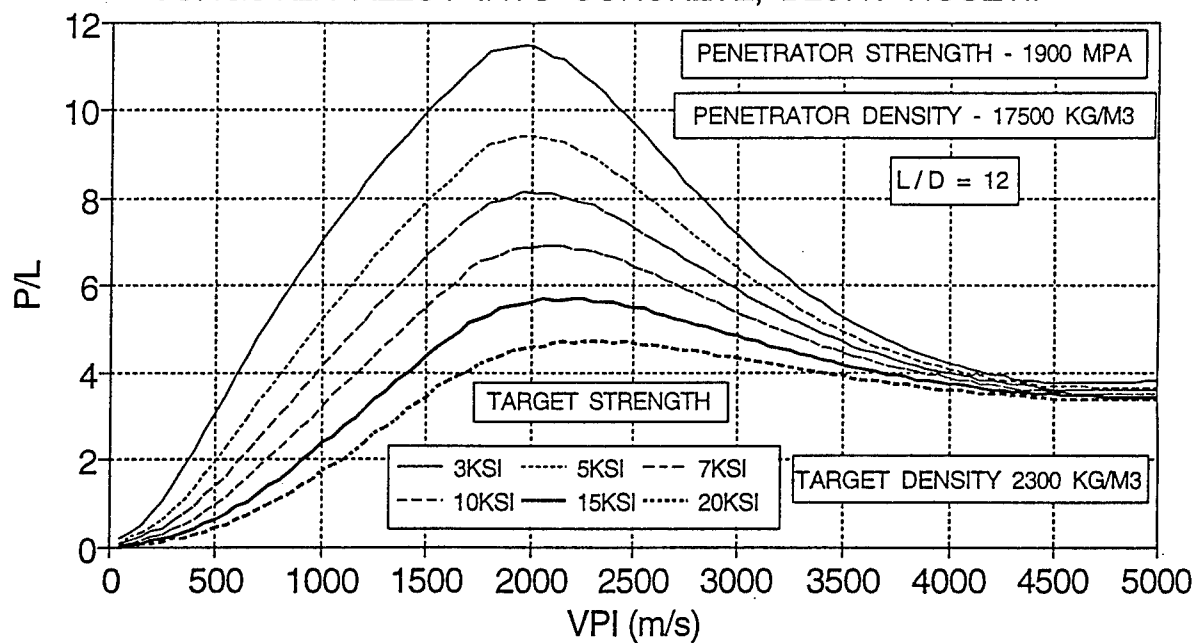


FIG. 41. EFFECT OF TARGET STRENGTH ON PENETRATION DEPTH, STEEL INTO CONCRETE, OGIVE NOSETIP

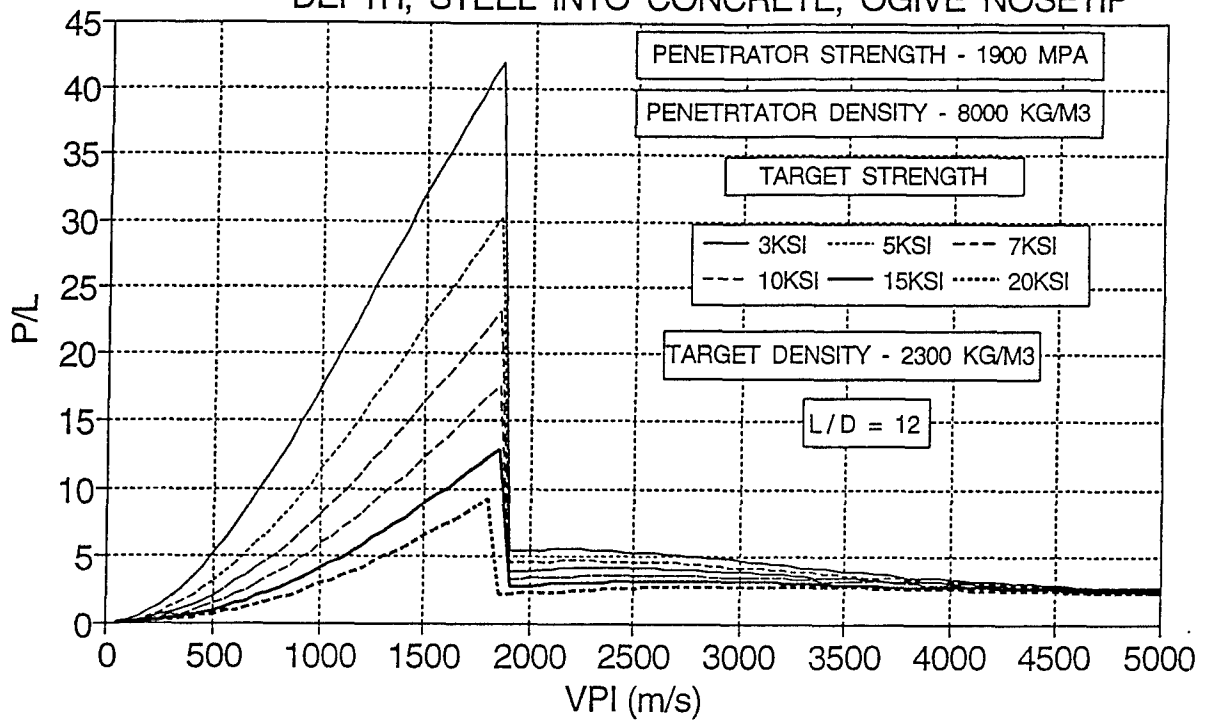


FIG. 42. EFFECT OF TARGET STRENGTH ON PENETRATION DEPTH, STEEL INTO CONCRETE, BLUNT NOSETIP

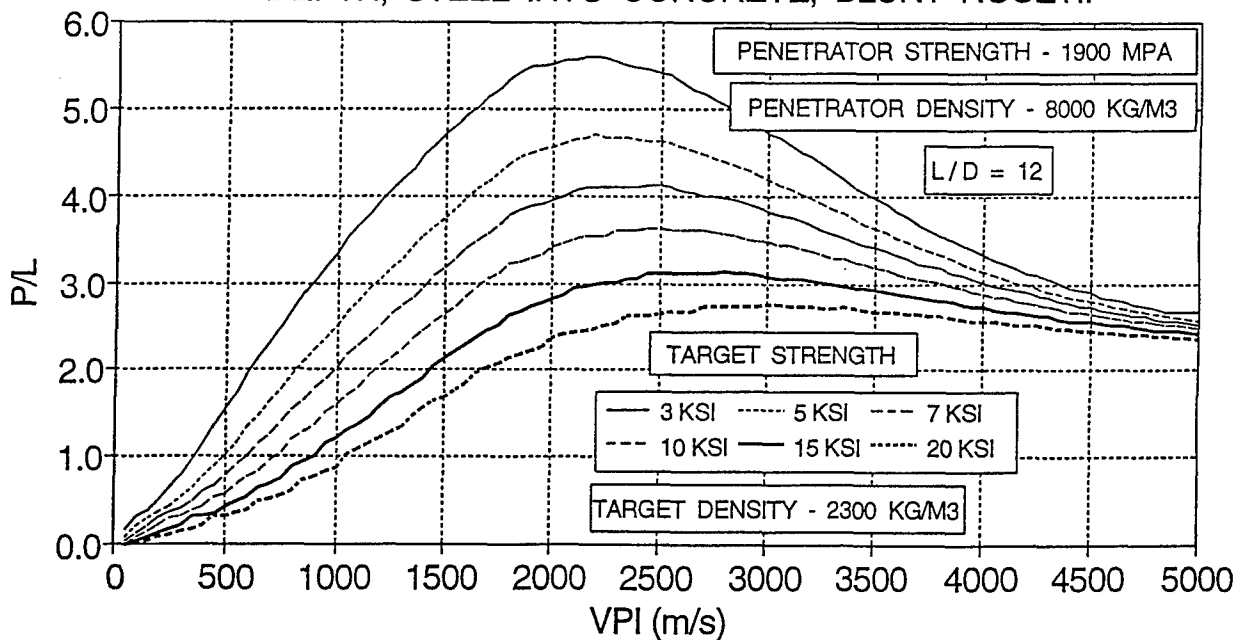


FIG. 43. EFFECT OF PENETRATOR STRENGTH ON PENETRATION DEPTH, STEEL INTO 3 KSI CONCRETE, OGIVE NOSETIP

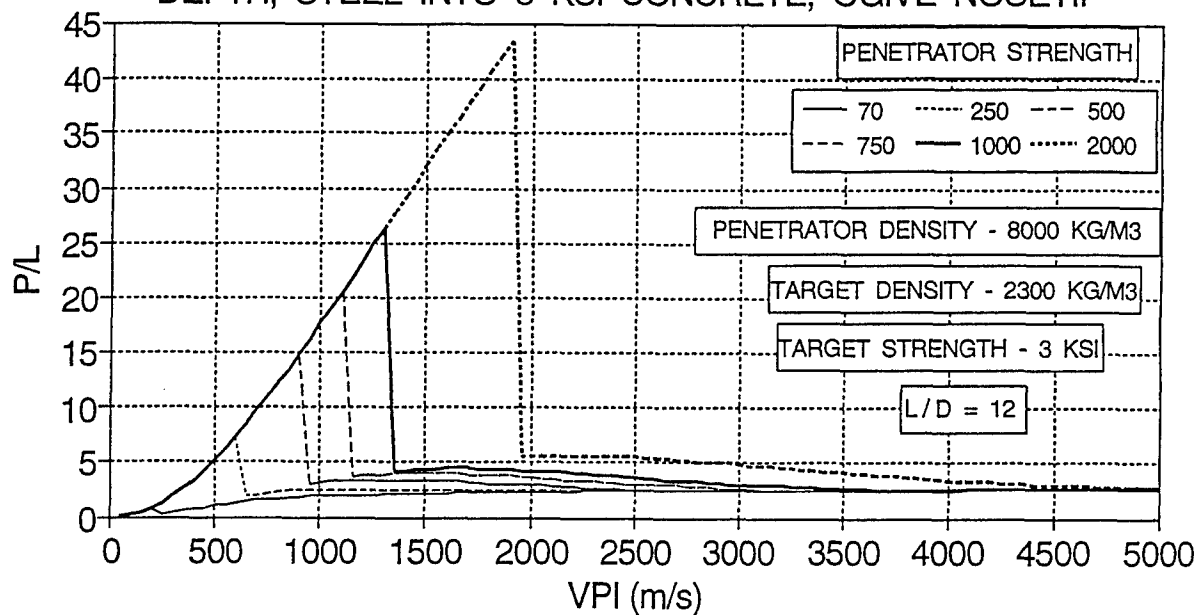


FIG. 44. EFFECT OF PENETRATOR STRENGTH ON PENETRATION DEPTH, STEEL INTO 3 KSI CONCRETE, BLUNT NOSETIP

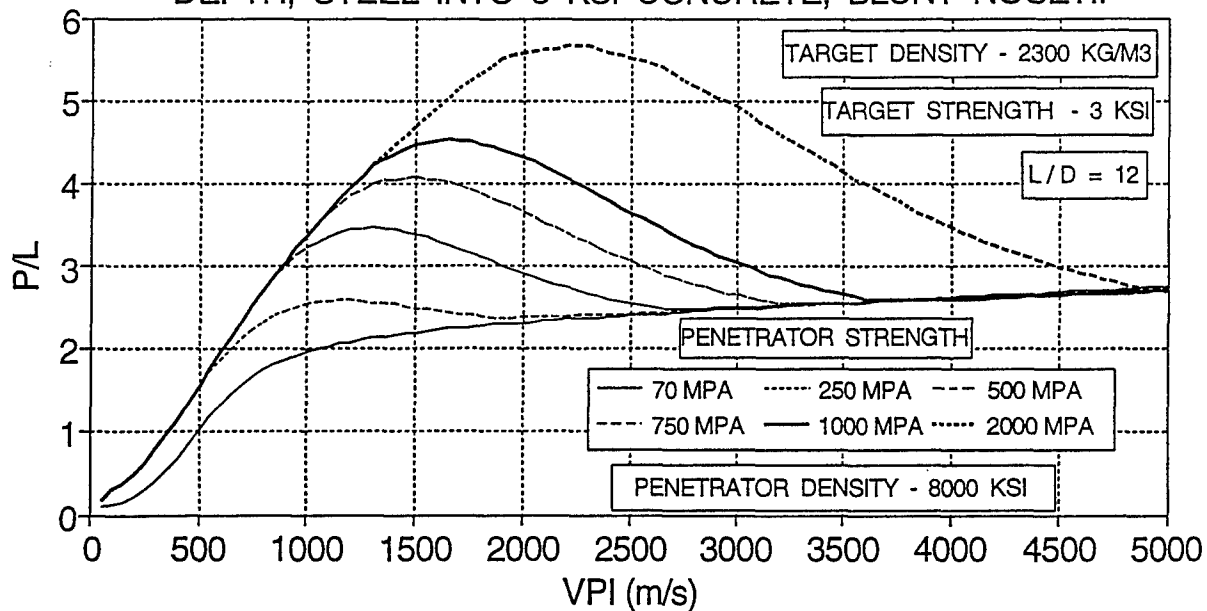


FIG. 45. EFFECT OF PENETRATOR STRENGTH ON PENETRATION DEPTH, TUNGSTEN ALLOY INTO 3 KSI CONCRETE, OGIVE NOSETIP

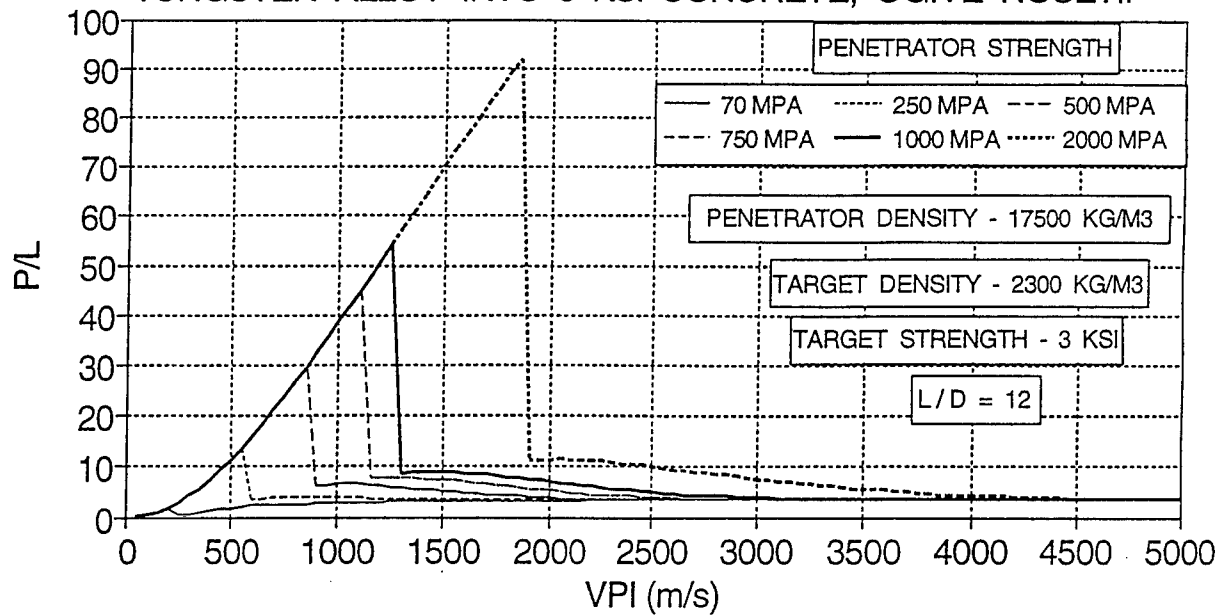
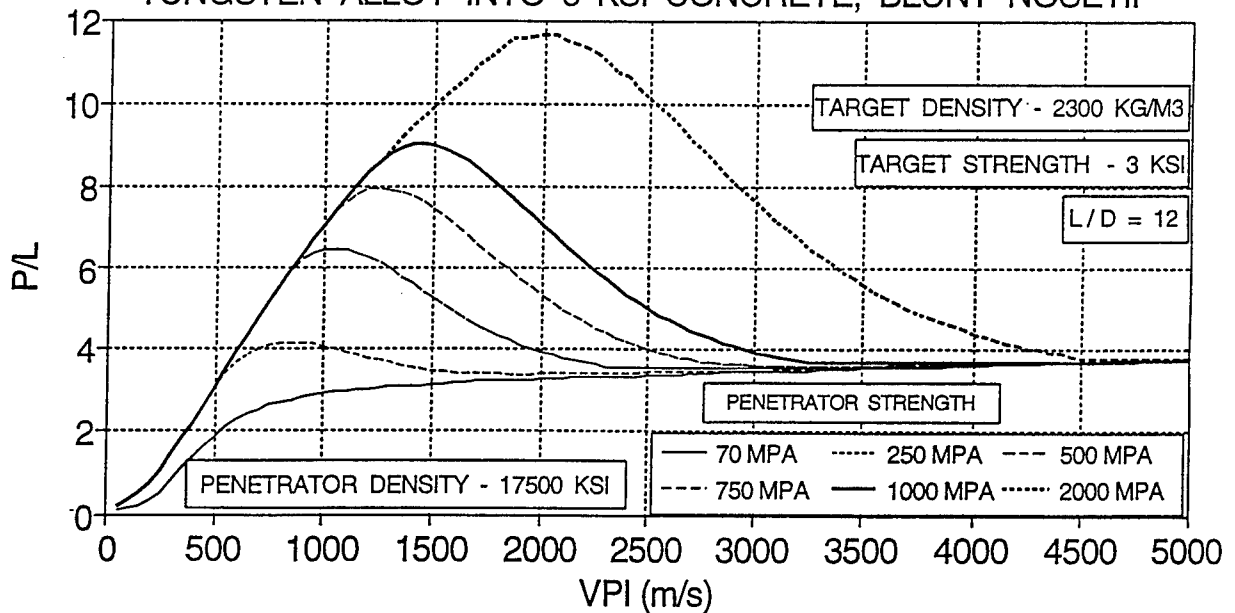


FIG. 46. EFFECT OF PENETRATOR STRENGTH ON PENETRATION DEPTH, TUNGSTEN ALLOY INTO 3 KSI CONCRETE, BLUNT NOSETIP



AN ANALYSIS OF BALLISTIC RANGE DATA REDUCTION FOR FLEXIBLE MODELS

Gary T. Chapman
Adjunct Professor
Department of Mechanical Engineering
University of California at Berkeley
Berkeley, California 94720

Final Report For:
Summer Research Extension Program

Sponsored by
The Air Force Office of Scientific Research
Bolling AFB, Washington DC

June 1994

AN ANALYSIS OF BALLISTIC RANGE DATA REDUCTION FOR FLEXIBLE MODELS

Gary T. Chapman
Adjunct Professor
Department of Mechanical Engineering
University of California at Berkeley

Abstract

The data reduction of flexible models tested in a ballistic range has been studied. The equations of motion, the aerodynamic math model, and the data acquisition system were examined. All three were examined from the point of view of two coordinate systems; one located at the instantaneous center of gravity and the other located at the center of gravity of the undeformed body. Based on the simpler set of equations and the straight forward application of existing film reading procedures it is recommended that the data analysis system should be written in terms of the instantaneous center of gravity.

An Analysis of Ballistic Range Data Reduction for Flexible Models

Gary T. Chapman

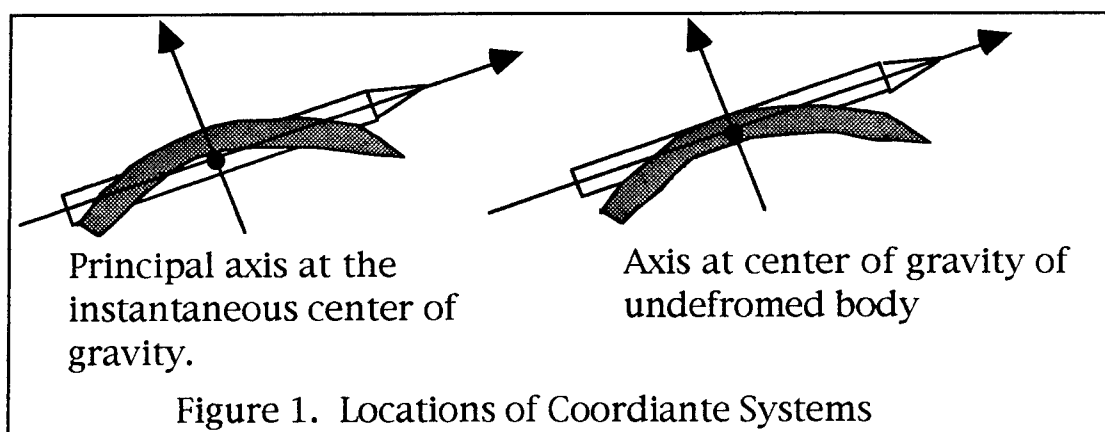
INTRODUCTION

Much work has been done on aerodynamic data reduction for rigid bodies in ballistic range tests, e.g., Ref. 1, but relatively little work has been done for deforming elastic bodies. Harkins and Courter (Ref. 2) considered the effect of a prescribed deformation on data processing and found that for small deformations there was little impact on the aerodynamic information. In many cases these deformations are not small, e. g., Ref. 3, and it would be advantageous if a method existed to reduce ballistic range data on a deforming body. This would be a very time consuming and tedious task of data acquisition if done by hand since it would require not only the six coordinates, 3 space and 3 orientation angles, but also the shape of the body would need to be determined at each ballistic range station. The advent of automated film reading technology now makes this a real possibility. The objective of the present study is to develop the set of equations for use in the data analysis of flexible models in flight in a ballistic range and the data acquisition procedure required.

THE PROBLEM

There are Three aspects to the problem of obtaining aerodynamic data on deforming bodies in a ballistic range. These are: (1) The equations of motion for an elastic body suitable for data reduction. (2) Selecting a aerodynamic math model. (3) Determining an adequate data acquisition procedure. All Three of these also depend on the coordinate system chosen. There are two candidates coordinate systems: (1) A principal axis system with the center of gravity on the instantaneous center of gravity. (2) A coordinate system with the center at the center of gravity of the

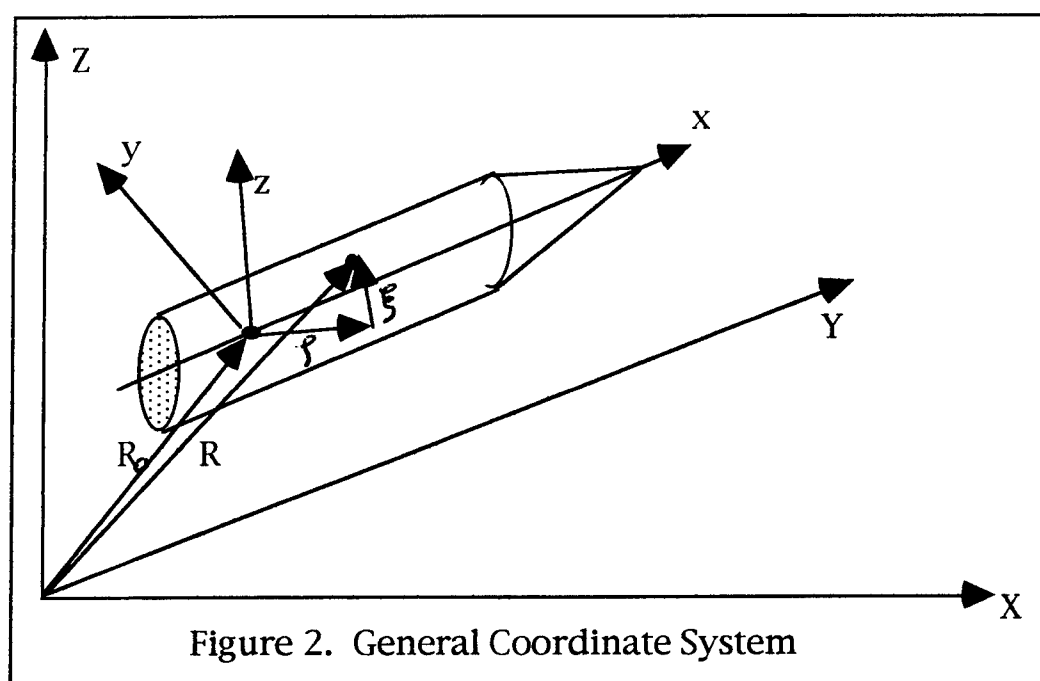
undeformed body. These two system are illustrated in figure 1.



The equations motion for an elastic body, the aerodynamic math model, and the data acquisition procedure will be examined in both coordinate systems to provide a framework for a recommendation as to which coordinate system would be the "best" for a data reduction procedure.

THE EQUATIONS OF MOTION

Consider the coordinate system illustrated in figure 2 below.



The location, velocity and acceleration of a mass element on a deforming body are given as

$$R = R_0 + \rho + \xi, \quad (\text{Eq. 1a})$$

$$\dot{R} = \dot{R}_0 + \dot{\rho} + \omega \times \rho + \dot{\xi} + \omega \times \xi, \text{ and} \quad (\text{Eq. 1b})$$

$$\begin{aligned} \ddot{R} = \ddot{R}_0 + \ddot{\rho} + 2\omega \times \dot{\rho} + \dot{\omega} \times \rho + \omega \times (\omega \times \rho) + \ddot{\xi} + 2\omega \times \dot{\xi} \\ + \dot{\omega} \times \xi + \omega \times (\omega \times \xi) \end{aligned} \quad (\text{Eq. 1c})$$

Where R is the location of the mass element in inertial space, R_0 is an arbitrary location of a coordinate system relative to the body, ρ is the location of the element of the undeformed body relative to the arbitrary location of the coordinate system, ξ is the displacement of the element from the undeformed position and ω is the angular rotation of the arbitrary coordinate system. The dot and double dot refer to first and second derivatives with respect to time.

The equation for the linear and angular momentum are

$$F = \iiint \ddot{R} dm \quad \text{and} \quad (\text{Eq. 2a})$$

$$M = \iiint r_0 \times dF = \iiint r_0 \times \ddot{R} dm \quad (\text{Eq. 2b})$$

Where F is the force vector, M is the moment vector, r_0 is the location of an elemental force relative to the center of the coordinate system being used and dm is an element of mass in the body. The integration extends over the entire body.

The equation for the vibrational degrees of freedom for an arbitrary body can be very complex. For a slender body that has only bending motion the deformation can be written as $\xi = \sum \varphi_n(t) g_n(x)$, where $g_n(x)$ are the normalized vibrational bending mode shapes and $\varphi_n(t)$ are the amplitude function for each mode. The amplitude equations for the bending modes are

$$\ddot{\varphi}_n = m_{bn} \quad (\text{Eq. 2c})$$

Which can be written as $\dot{\phi}_n = m_{bn}$, where $\dot{\phi}_n = \dot{\varphi}_n$ and m_{bn} is the generalized bending moment for the n th mode. Retaining only the first bending mode these

equations can be written as

$$\begin{Bmatrix} a_{11} & a_{12} & a_{13} & a_{14} & a_{15} & a_{16} & a_{17} \\ a_{21} & a_{22} & a_{23} & a_{24} & a_{25} & a_{26} & a_{27} \\ a_{31} & a_{32} & a_{33} & a_{34} & a_{35} & a_{36} & a_{37} \\ a_{41} & a_{42} & a_{43} & a_{44} & a_{45} & a_{46} & a_{47} \\ a_{51} & a_{52} & a_{53} & a_{54} & a_{55} & a_{56} & a_{57} \\ a_{61} & a_{62} & a_{63} & a_{64} & a_{65} & a_{66} & a_{67} \\ a_{71} & a_{72} & a_{73} & a_{74} & a_{75} & a_{76} & a_{77} \end{Bmatrix} \begin{Bmatrix} \dot{u} \\ \dot{v} \\ \dot{w} \\ \dot{p} \\ \dot{q} \\ \dot{r} \\ \dot{\phi}_1 \end{Bmatrix} = \begin{Bmatrix} f_x \\ f_y \\ f_z \\ m_x \\ m_y \\ m_z \\ m_{b1} \end{Bmatrix} \quad (\text{Eq. 3})$$

Where u , v , and w are the three components of velocity, and p , q , and r are the three components of angular velocity, f_x , f_y , and f_z , are the components of force, m_x , m_y , and m_z are the components of moment and m_{b1} is the generalized bending moment for the first mode.

Undeformed Body Coordinate System

For a coordinate system located at the center of mass of the undeformed body the forces and moments can be written as

$$\begin{aligned} f_x &= rv - qw + \left[F_{x_g} + F_{x_a} + 2(r\mu_y - q\mu_z) - p(q\delta_y + r\delta_z) \right] / m \\ f_y &= pw - ru + \left[F_{y_g} + F_{y_a} + 2p\mu_z + (p^2 + r^2)\delta_y - qr\delta_z - \alpha_y \right] / m \\ f_z &= qu - pv + \left[F_{z_g} + F_{z_a} - 2p\mu_y + (p^2 + q^2)\delta_z - qr\delta_y - \alpha_z \right] / m \\ m_x &= L - p(rI_{xy} + qI_{xz}) + (q^2 - r^2)I_{yz} + qr(I_{yy} - I_{zz}) + (qu - pv)\delta_y \\ &\quad - \underline{M}_{yz} + (ru - pw)\delta_z - p(rJ_x - qK_x) + qr \left[2(K_z - J_y) + \perp_{zz} - \perp_{yy} \right] \\ &\quad + \underline{M}_{zy} + (q^2 - r^2)(J_z + K_y + \perp_{yy}) - 2p(\dot{J}_y + \dot{K}_z + \underline{L}_{yy} + \underline{L}_{zz}) \end{aligned}$$

$$\begin{aligned}
m_y &= M - q(pI_{yz} - rI_{xy}) - (p^2 - r^2)I_{xz} + pr(I_{xx} - I_{zz}) \\
&\quad - pr(2K_z + \perp_{zz}) - (p^2 - r^2)K_x + q[rJ_x - p(J_z + K_y + \perp_{yz})] + 2p\dot{J}_x \\
&\quad - 2[q(\dot{K}_z + \underline{L}_{zz}) - r(\dot{J}_z + \underline{L}_{zy})] + (rv - qw)\delta_z \\
m_z &= N + r(pI_{yz} - qI_{xz}) + (p^2 - q^2)I_{xy} + pq(I_{xx} - I_{yy}) \\
&\quad + pq(2J_y + \perp_{yy}) + (p^2 - q^2)J_x + r[p(J_z + K_y + \perp_{yz}) - qK_x] + 2p\dot{K}_x \\
&\quad + 2[q(\dot{K}_y + \underline{L}_{yz}) - r(\dot{J}_y + \underline{L}_{yy})] + (qw - rv)\delta_y
\end{aligned}$$

Where F_{ia} and F_{ig} are the three components of the aerodynamic and gravitational force respectively and L , M , and N are the three components of the aerodynamic moment. The only inertial term from the pitch, yaw and roll motion retained in the moment for the bending moment is that due to roll as all of the rate terms appear squared and the roll term, p , is normally the only large rotation rate, hence

$$m_{b1} = B - \omega_1^2 \varphi_1 - \left[D\dot{\varphi}_1 + p^2(\perp_{yy} + \perp_{zz}) \right] / m_{g1}$$

Where B is the aerodynamic bending moment for the first mode, D is the mechanical damping, ω is the first mode bending frequency and m_{g1} is the generalized mass for the first mode. For an axially symmetric body with deflections primarily normal to the body axis the terms in the matrix of equation 3 are given as:

$$\begin{aligned}
a_{11} &= 1, a_{12} = a_{13} = a_{14} = a_{17} = 0, a_{15} = \delta_z / m, a_{16} = -\delta_y / m \\
a_{22} &= 1, a_{21} = a_{23} = a_{25} = a_{26} = a_{27} = 0, a_{24} = \delta_z / m \\
a_{33} &= 1, a_{31} = a_{32} = a_{35} = a_{36} = a_{37} = 0, a_{34} = \delta_y / m \\
a_{44} &= I_{xx} + 2(J_y + K_z) + \perp_{yy} + \perp_{zz}, a_{41} = a_{47} = 0, a_{42} = -\delta_z, \\
a_{43} &= \delta_y, a_{45} = -(I_{xy} + J_x), a_{46} = -(I_{xz} + K_x)
\end{aligned}$$

$$\begin{aligned}
a_{55} &= I_{yy} + 2K_z + \perp_{zz}, a_{51} = \delta_z, a_{52} = a_{53} = a_{57} = 0, \\
a_{54} &= -(I_{xy} + J_x), a_{56} = -(I_{yz} + K_y + J_z + \perp_{yz}) \\
a_{66} &= I_{zz} + 2J_y + \perp_{yy}, a_{61} = \delta_y, a_{62} = a_{63} = a_{67} = 0, \\
a_{64} &= -(I_{xz} + K_x), a_{65} = -(I_{yz} + K_y + J_z + \perp_{yz}) \\
a_{77} &= 1, a_{71} = a_{72} = a_{73} = a_{74} = a_{75} = a_{76} = 0
\end{aligned}$$

Where the flexibility coefficients appearing in the matrix and the forces and moments are defined as follows:

$$\begin{aligned}
\delta_i &= \int_m \xi_i dm = \varphi \beta_i & \mu_i &= \int_m \dot{\xi}_i dm = \dot{\varphi} \beta_i & \alpha_i &= \int_m \ddot{\xi}_i dm = \ddot{\varphi} \beta_i \\
J_x &= \int_m x \xi_y dm = \varphi \chi_{xy} & J_y &= \int_m y \xi_y dm \delta = \varphi \chi_{yy} & J_z &= \int_m z \xi_y dm \delta = \varphi \chi_{zy} \\
\dot{J}_x &= \int_m x \dot{\xi}_y dm = \dot{\varphi} \chi_{xy} & \dot{J}_y &= \int_m y \dot{\xi}_y dm = \dot{\varphi} \chi_{yy} & \dot{J}_z &= \int_m z \dot{\xi}_y dm = \dot{\varphi} \chi_{zy} \\
K_x &= \int_m x \xi_z dm = \varphi \chi_{xz} & K_y &= \int_m y \xi_z dm = \varphi \chi_{yz} & K_z &= \int_m z \xi_z dm = \varphi \chi_{zz} \\
\dot{K}_x &= \int_m x \dot{\xi}_z dm = \dot{\varphi} \chi_{xz} & \dot{K}_y &= \int_m y \dot{\xi}_z dm = \dot{\varphi} \chi_{yz} & \dot{K}_z &= \int_m z \dot{\xi}_z dm = \dot{\varphi} \chi_{zz} \\
\perp_{yy} &= \int_m \xi_y^2 dm = \varphi^2 \lambda_{yy} & \perp_{zz} &= \int_m \xi_z^2 dm = \varphi^2 \lambda_{zz} \\
\perp_{yz} &= \int_m \xi_y \xi_z dm = \varphi^2 \lambda_{yz} \\
\underline{L}_{yy} &= \int_m \xi_y \dot{\xi}_y dm = \varphi \dot{\varphi} \lambda_{yy} & \underline{L}_{zz} &= \int_m \xi_z \dot{\xi}_z dm = \varphi \dot{\varphi} \lambda_{zz} \\
\underline{L}_{yz} &= \int_m \xi_y \dot{\xi}_z dm = \varphi \dot{\varphi} \lambda_{yz} & \underline{L}_{zy} &= \int_m \xi_z \dot{\xi}_y dm = \varphi \dot{\varphi} \lambda_{zy} \\
\underline{M}_{yz} &= \int_m \xi_y \ddot{\xi}_z dm = \varphi \ddot{\varphi} \lambda_{yz} & \underline{M}_{zy} &= \int_m \xi_z \ddot{\xi}_y dm = \varphi \ddot{\varphi} \lambda_{zy}
\end{aligned}$$

Where

$$\beta_i = \iiint_m g_i dm, \quad \chi_{ij} = \iiint_m \rho_i g_j dm, \quad \text{and} \quad \lambda_{ij} = \iiint_m g_i g_j dm$$

Here the subscripts i and j indicate the three spatial components. Note the coordinate system for the deformation is the center of gravity of the undeformed body.

Instantaneous Center of Gravity Coordinate System

If the arbitrary coordinate system is located on the instantaneous center of gravity the formulation of the problem is nearly the same but because the coordinate system is on the instantaneous center of gravity some of the flexibility terms are zero. The development is the same up to equation 3 except the forces and moments are now given as

$$\begin{aligned} f_x &= rv - qw + \left[F_{x_g} + F_{x_a} \right] / m \\ f_y &= pw - ru + \left[F_{y_g} + F_{y_a} \right] / m \\ f_z &= qu - pv + \left[F_{z_g} + F_{z_a} \right] / m \\ m_x &= L - p(rI_{xy} + qI_{xz}) + (q^2 - r^2)I_{yz} + qr(I_{yy} - I_{zz}) + \underline{M}_{zy} \\ &\quad - \underline{M}_{yz} - p(rJ_x - qK_x) + qr \left[2(K_z - J_y) + \perp_{zz} - \perp_{yy} \right] \\ &\quad + (q^2 - r^2)(J_z + K_y + \perp_{yy}) - 2p(\dot{J}_y + \dot{K}_z + \underline{L}_{yy} + \underline{L}_{zz}) \\ m_y &= M - q(pI_{yz} - rI_{xy}) - (p^2 - r^2)I_{xz} + pr(I_{xx} - I_{zz}) + 2p\dot{J}_x \\ &\quad - pr(2K_z + \perp_{zz}) - (p^2 - r^2)K_x + q \left[rJ_x - p(J_z + K_y + \perp_{yz}) \right] \\ &\quad - 2 \left[q(\dot{K}_z + \underline{L}_{zz}) - r(\dot{J}_z + \underline{L}_{zy}) \right] \end{aligned}$$

$$\begin{aligned}
m_z = & N + r(pI_{yz} - qI_{xz}) + (p^2 - q^2)I_{xy} + pq(I_{xx} - I_{yy}) + 2p\dot{K}_x \\
& + pq(2J_y + \perp_{yy}) + (p^2 - q^2)J_x + r[p(J_z + K_y + \perp_{yz}) - qK_x] \\
& + 2[q(\dot{K}_y + \underline{L}_{yz}) - r(\dot{J}_y + \underline{L}_{yy})]
\end{aligned}$$

Here again F_{ia} and F_{ig} are the three components of the aerodynamic and gravitational forces respectively and L , M , and N are the three components of the aerodynamic moment. Again only the term in roll is retained for the bending moment and hence

$$m_{b1} = B - \omega_1^2 \varphi_1 - \left[D\dot{\varphi}_1 + p^2(\perp_{yy} + \perp_{zz}) \right] / m_{g1}$$

where B is the aerodynamic bending moment for the first mode, D is the mechanical damping, m_{g1} is the generalized mass for the first mode and ω is the first mode natural bending frequency.

For an axially symmetric body with deflections primarily normal to the body axis and the axis system located at the instantaneous center of gravity the terms in the matrix are:

$$\begin{aligned}
a_{11} &= 1, a_{12} = a_{13} = a_{14} = a_{15} = a_{16} = a_{17} = 0 \\
a_{22} &= 1, a_{21} = a_{23} = a_{24} = a_{25} = a_{26} = a_{27} = 0 \\
a_{33} &= 1, a_{31} = a_{32} = a_{34} = a_{35} = a_{36} = a_{37} = 0 \\
a_{44} &= I_{xx} + 2(J_y + K_z) + \perp_{yy} + \perp_{zz}, a_{41} = a_{42} = a_{43} = a_{47} = 0 \\
a_{45} &= -(I_{xy} + J_x), a_{46} = -(I_{xz} + K_x) \\
a_{55} &= I_{yy} + 2K_z + \perp_{zz}, a_{51} = a_{52} = a_{53} = a_{57} = 0, \\
a_{54} &= -(I_{xy} + J_x), a_{56} = -(I_{yz} + K_y + J_z + \perp_{yz}) \\
a_{66} &= I_{zz} + 2J_y + \perp_{yy}, a_{61} = a_{62} = a_{63} = a_{67} = 0, \\
a_{64} &= -(I_{xz} + K_x), a_{65} = -(I_{yz} + K_y + J_z + \perp_{yz})
\end{aligned}$$

$$a_{77}=1, a_{71}=a_{72}=a_{73}=a_{74}=a_{75}=a_{76}=0$$

Where the flexibility coefficients are defined as follows:

$$J_x = \int_m x \xi_y dm = \varphi \chi_{xy} \quad J_y = \int_m y \xi_y dm = \varphi \chi_{yy} \quad J_z = \int_m z \xi_y dm = \varphi \chi_{zy}$$

$$\dot{J}_x = \int_m x \dot{\xi}_y dm = \dot{\varphi} \chi_{xy} \quad \dot{J}_y = \int_m y \dot{\xi}_y dm = \dot{\varphi} \chi_{yy} \quad \dot{J}_z = \int_m z \dot{\xi}_y dm = \dot{\varphi} \chi_{zy}$$

$$K_x = \int_m x \xi_z dm = \varphi \chi_{xz} \quad K_y = \int_m y \xi_z dm = \varphi \chi_{yz} \quad K_z = \int_m z \xi_z dm = \varphi \chi_{zz}$$

$$\dot{K}_x = \int_m x \dot{\xi}_z dm = \dot{\varphi} \chi_{xz} \quad \dot{K}_y = \int_m y \dot{\xi}_z dm = \dot{\varphi} \chi_{yz} \quad \dot{K}_z = \int_m z \dot{\xi}_z dm = \dot{\varphi} \chi_{zz}$$

$$\perp_{yy} = \int_m \xi_y^2 dm = \varphi^2 \lambda_{yy} \quad \perp_{zz} = \int_m \xi_z^2 dm = \varphi^2 \lambda_{zz}$$

$$\perp_{yz} = \int_m \xi_y \xi_z dm = \varphi^2 \lambda_{yz}$$

$$\underline{L}_{yy} = \int_m \xi_y \dot{\xi}_y dm = \varphi \dot{\varphi} \lambda_{yy} \quad \underline{L}_{zz} = \int_m \xi_z \dot{\xi}_z dm = \varphi \dot{\varphi} \lambda_{zz}$$

$$\underline{L}_{yz} = \int_m \xi_y \dot{\xi}_z dm = \varphi \dot{\varphi} \lambda_{yz} \quad \underline{L}_{zy} = \int_m \xi_z \dot{\xi}_y dm = \varphi \dot{\varphi} \lambda_{zy}$$

$$\underline{M}_{yz} = \int_m \xi_y \ddot{\xi}_z dm = \varphi \ddot{\varphi} \lambda_{yz} \quad \underline{M}_{zy} = \int_m \xi_z \ddot{\xi}_y dm = \varphi \ddot{\varphi} \lambda_{zy}$$

$$\text{Where } \chi_{ij} = \int_m \rho_i g_j dm \quad \lambda_{ij} = \int_m g_i g_j dm$$

It should be noted that the origin of the deflection for these terms is the instantaneous center of gravity.

AERODYNAMIC MATH MODELS

To complete the equations of motion aerodynamic math models must be specified for all of the aerodynamic forces and moments in both coordinate systems.

These math models would need to include the classical terms plus terms due to bending. A complete specification of the aerodynamic math model requires some information about the specific geometry of the model and a general description is beyond the scope of this report. A slightly more detailed discussion of aeroelastic modeling is given in reference 3. Here we will focus only on the differences that occur due to bending for the two coordinate systems. At a minimum the effects of bending need to include a first order term in bending amplitude and amplitude rate, the later may not prove to be very large but is included here for completeness. For example, a pitching moment term, M , would have the following form for the contributions due to bending

$$M_{bl} = \frac{1}{2} \rho V^2 A d \left(C_{m_{\varphi_{bl}}} \varphi_{bl} + C_{m_{\dot{\varphi}_{bl}}} \dot{\varphi}_{bl} \right) \quad (\text{Eq. 4})$$

Where here ρ is the density of the air V is the model velocity, A is the reference area, d is a reference length (normally the diameter), and the two terms in brackets are the linearized pitching moment due to bending and bending rate. Similar terms would occur in all of the force and moment expressions including the bending moment. These additions to the math model for bending would not change form in the two coordinate systems, however, the coefficients may have different values.

Since the forces must remain invariant under transformation the primary effect of the different coordinate systems on the math model arises in the moment term. For the case of bending only this only amounts to an additional pitching moment term due to forces in the x direction acting away from the center of the coordinates system. Since in general this additional term will have the same form as other terms in the math model the net result is a change in magnitude of some coefficients. Hence even the effect of the coordinate system is not major.

DATA ACQUISITION

The most advanced data acquisition system for rigid body flight in a ballistic range is that by Yates (Ref. 4). In that system the film is digitized and the images processed to arrive at the location of center of area of the image and the principal axis angle relative to an inertial coordinate system. This is illustrated in figure 3.

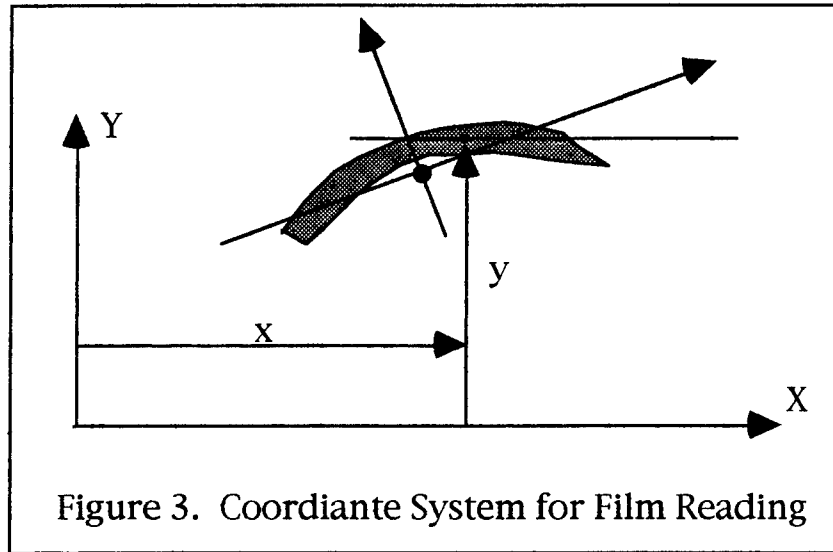


Figure 3. Coordiante System for Film Reading

With this coordinate system the center of area of the image of the model can be found as

$$x_{ci} = \frac{1}{A} \sum \rho_i x_i \text{ and } y_{ci} = \frac{1}{A} \sum \rho_i y_i. \quad (\text{Eq. 5a,b})$$

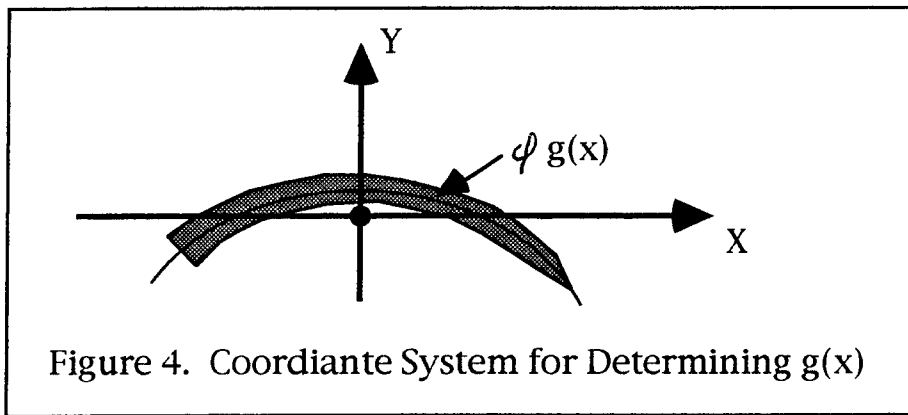
Where $A = \sum \rho_i$ is the area of the model image, and x_i , y_i and ρ_i are the x and y coordinate and density of a pixel within the model image respectively. The summation is over all picels with in the model image. The angle that the principal axis of the model image makes with the X axis is given as

$$\frac{1}{2} \tan 2\theta = \frac{\sum \rho_i (x_i - x_{ci})(y_i - y_{ci})}{\sum \rho_i [(x_i - x_{ci})^2 - (y_i - y_{ci})^2]}. \quad (\text{Eq. 5c})$$

This must be done for the two orthogonal photographic images of the model. If the

model is a homogenous slender body of revolution the centroid of the model image and its principal axis is the same as the center of gravity of the model and its principal axis. Hence we have the required information. If this is not the case the centroid of the image and the principal axis must be adjust to account for the specific model construction. This is a straight forward process.

To obtain the amplitude of the bending motion of the image, assuming a uniform model, we first must rotate the image so the principal axis lines up with the X inertial axis. This is illustrated in figure 4.



The shape of the first mode function $g(x)$ is given and hence we need only determine the amplitude of the function. Using a least square approach we get

$$\varphi = \frac{\sum \rho_i g(x_i) y_i}{\sum \rho_i g(x_i)^2} \quad (\text{Eq. 5d})$$

We now have all of the required information for a coordinate system at the instantaneous center of mass.

If the coordinate system is to be the center of mass of the undeformed body a transformation must be made from the instantaneous center of gravity to the center of gravity of the undeformed body. This is a straight forward process.

CONCLUSIONS

The equations of motion, the aerodynamic math models and the data acquisition process have all been examined in terms of two coordinate systems: One at the instantaneous center of mass and one at the center of mass of the undeformed body. The equations of motion are the simplest when written in terms of the instantaneous center of mass. The aerodynamic math model does not appear to be sufficiently different in the two coordinate systems to be a factor in making a decision. The data acquisition process is straight forward when the instantaneous center of gravity is used and just requires simple additions to existing film reading processes. The transformation required to get the data into the coordinate system on the center of mass of the undeformed body although simple represent additional complications. Therefore it would appear that the "best" axis system to use for the data reduction procedure is the instantaneous center of gravity system.

There still remains much work to convert this entire system into a full data reduction procedure.

REFERENCES

1. Chapman, Gary T., "Aerodynamic Parameter Identification in Ballistic Range Tests," Proceedings of the 1972 Army Numerical Analysis Conference, U. S. Army Research Office, ARO-D Report 72-3, Durham, NC, 1972, pp. 73-109.
2. Harkins, Thomas k. and Courter, Robert W, "Aeroelastic Effects on Range-Acquired Aerodynamic Coefficients," AIAA Aerospace Sciences Meeting, Reno NV. Jan. 1990.
3. Chapman, Gary T. and Yates, L. A., "Nonlinear Aerodynamic Parameter Estimation and Structure Identification. AIAA Atmospheric Flight Mechanics Conference, Aug. 1992, AIAA Paper No. 92-4502. (Invited Paper).
4. Yates, L. A., "Development of an Automated Film-Reading System for Ballistic Ranges, J. Spacecrafts and Rockets, Vol. 30, No. 2, March-April 1993, pp. 248-254.

**USING VHDL IN VLSI BIST DESIGN SYNTHESIS
AND ITS APPLICATION TO 3-D PIXEL GRAPHICS CHIP**

Chien-In Henry Chen
Assistant Professor
Department of Electrical Engineering
Wright State University
Dayton, OH 45435

Final Report for:
Research Initiation Program
Wright Laboratory

Sponsored by:

Air Force Office of Scientific Research
Bolling Air Force Base, Washington, D.C.

and

Wright State University

December 1993

USING VHDL IN VLSI BIST DESIGN SYNTHESIS AND ITS APPLICATION TO 3-D PIXEL GRAPHICS CHIP

Chien-In Henry Chen, Assistant Professor
Department of Electrical Engineering
Wright State University
Dayton, OH 45435

ABSTRACT

Machine-readable descriptions of integrated circuit designs have become an important factor in designing VLSI circuits. These descriptions are often defined in terms of design languages that, like computer languages, have specific syntax and semantics. Such design languages have been used to describe circuits from the geometrical level up through the architectural level. VHDL (VHSIC Hardware Description Language) is a hardware description language which has been used to characterize both the function and structure of designs from logical primitives through architectural descriptions. As new designs become extremely dependent on CAD tools, VHDL descriptions become extremely important in both academy and industry. With the growth in the complexity of VLSI circuits, the cost of testing a chip, too, has become an important part of the overall design and manufacturing cost. To keep chip testing costs within reason, designers have turned to the use of self-testing techniques. Indeed, Built-In Self-Test (BIST) is proving to be an essential design strategy in many situations. The proposed VLSI BIST synthesis system is implemented as part of VLSI Testability Synthesis Tool (VTST), which is able of accepting VHDL as input circuit format and generates the BIST mechanisms as the output. We'll first describe the developed VHDL parsers which generate the gate level netlist used in the BIST synthesis system. Then, we'll present the developed BIST Design and Testability Analysis (BISTDaTA) tool which is integrated with VHDL parsers to achieve the BIST design synthesis using VHDL. Experimental results show that the BIST synthesis system is very efficient and feasible for very large scale integrated circuit designs.

USING VHDL IN VLSI BIST DESIGN SYNTHESIS AND ITS APPLICATION TO 3-D PIXEL GRAPHICS CHIP

Chien-In Henry Chen

1. INTRODUCTION

As digital technology has progressed over the last two decades, dramatic improvements in the architectural design, power consumption, new device development, and other characteristics have enabled the construction of larger and more complex systems into a single chip. The complexity of VLSI chips has increased to a point that designers can no longer carry out their tasks without aid from various design tools. Furthermore, traditional testing techniques are costly and ineffective because of the difficult accessibility of internal circuit nodes (i.e. controllability and observability). The only way to test circuits cost effectively is not simply to use computer-aided design tools, but also to make use of testable structure in the design process - design for testability. Crosscheck Inc. is currently marketing a CAD based circuit design system which has a high degree of success in fault detection for it includes automatic inclusion of built-in self-test (BIST) circuitry. However drawbacks to the system relative to the amount of silicon overhead (e.g. 25% for 99% fault detection) have caused many designers to rethink their test requirements. Most research in design synthesis has not included testability consideration. Although many researchers stress that testability should be considered during the early stages of design, most testability research has been done after a structural design solution is defined with no feedback to the original synthesis process for finding more testable designs. Therefore, it becomes very important to develop a supporting set of design synthesis tools which includes testability as an integral part of design as well as efficiently handles the rapidly increasing complexity of the creative design process.

1.1 Automated Synthesis Systems

In recent years, there has been considerable interest in automated synthesis at a higher level of the design hierarchy. The reasons are as follows:

1. *To shorten the design time.* The economics of producing a digital system weighs heavily in favor of a short design cycle. The cost of the design time itself is a major portion of the final system cost, and the profitability of the system is highly sensitive to how quickly it can be made available to the market.

2. *To reduce the design errors.* If the automated design system is itself verified to be correct, then the final design it produces will correspond to its initial specification. This will mean fewer errors and less debugging time for the produced design.

3. *To explore the design space.* A good automated design system can produce several designs for the same specification in a reasonable amount of design time. This allows the designers to choose the best design to meet their constraints.

Traditionally, synthesis techniques have been classified in three levels. The high level is behavioral level synthesis which generates logic representations. The middle level is logic level synthesis which optimizes gate level representations. The low level is physical level synthesis which deals with the geometric view of chip.

Logic level synthesis has matured to a point that the designers commonly use tools based on such techniques to analyze and optimize digital designs. In general, logic level synthesis provides two capabilities: technology independent circuit optimization and technology dependent library cells. Most available systems have been conceived for combinational logic design and then extended to support synchronous circuit design. At present, a common way of entering a digital design is to use programs that capture the logic schematic. The designer's major task is to transform the hardware specification into logic schematic, which is generally validated by simulation. Tools for physical level synthesis are also very common. Several physical level design system are available in marketing or distributed from universities to support the geometric design of chip. Traditionally the prime objective of layout algorithms is to minimize the total layout area by carefully placing the given modules and making all required interconnects. These placement schemes try to shorten the net lengths among modules by placing the modules with more net connections closer together. However, the circuit performance is decided by a clock rate inserted to the circuit. The maximum clock rate is determined (or bounded) by the longest path delay presented in the circuit. Therefore, the performance of a design tends to be path-oriented in nature and the minimization of total net length may not lead to the improvement of the performance. Research in this area is focusing more on the problems of timing related emerging design methodology, for example, timing driven layout.

The high-level synthesis task is to map an input specification for a hardware design into a structure that implements the behavior while satisfying the goals and constraints. The input specification normally contains

behavior information. By behavior we mean the way the system or its components interact with their environment, i.e., the mapping from the inputs to outputs. Structure refers to the interconnected components that make up the system. Usually, there are a number of different structures that can be used to realize a given behavior. One of the tasks of high-level synthesis is to find the structure that best meets the constraints such as speed, cost, chip area, pin count, power consumption, testability, test time and design time.

Why is automated synthesis system difficult to achieve? The major problem is that, in the search for optimal designs, the combinatorial exploration of the synthesis possibilities occur at every stage of the design process. Moreover, there is interaction between different steps in the process. For example, chip area, speed, testability, test time and power consumption can not be accurately estimated until the final physical design process has been completed.

1.2 Design for Testability and Built-In Self-Test

With the growth in the complexity of VLSI circuits, the cost of testing a chip, too, has become an important part of the overall design and manufacturing cost. The only way to reduce the testing cost is to make use of the testable structure during the design process - design for testability. Testability can be defined as the ease of testing, or the ability to test circuits easily or cost effectively. Testability should be adopted as one of the circuit design parameters by the fact that the cost of hardware is decreasing steadily relative to the cost of testing.

Approaches to testing can be divided into two categories: External testing and built-in self-test. In external testing, the test patterns are supplied to the circuit under test (CUT) by an external tester that is capable of storing test patterns and the corresponding correct response. However, such external testers are quite expensive. In addition, there are some problems in using external testers:

1. The turnaround time to obtain the test patterns and the computation cost are becoming too long and too high, respectively.
2. The tester can not efficiently handle a very large number of test patterns.
3. Testing is too slow because of the reliance on slow test sets to supply the test patterns and analyze the results.

These problems make the testing cost grow rapidly every year as technological capability increases without a corresponding increase in circuit accessibility. To keep chip testing costs within reason, designers have turned to the use of self-testing techniques. Indeed, Built-In Self-Test (BIST) is proving to be an essential design strategy in many situations. BIST includes on-chip circuitry to provide test patterns and to analyze output response. It can perform the testing internal to the chip, so that the need for complex external testing equipment is greatly reduced. Using BIST, a significant reduction in test volume can be achieved, and many of the traditional testing problems mentioned above can be overcome.

While the BIST approach has many positive aspects, many improvements are needed such as the following:

1. reducing the hardware overhead of the on-chip circuitry,
2. reducing the test length while still obtaining a high fault coverage (98%-99%),
3. developing a computationally efficient procedure for the design of the required BIST hardware modules.

2. METHODOLOGY

VTST is a VLSI testability synthesis tool which can interface with existing VLSI design and layout CAD/CAE tools to introduce testability as an integral part of the design process. VTST provides a solution to the testability design deficiencies present in existing tools for design and synthesis of complex VLSI circuits. To incorporate testability constraints into synthesis, the synthesis systems will work in an orthogonal manner. That is, the synthesis systems do area optimization, timing optimization, and testability implementation independently of one another, and the information of design constraints in each synthesis level will be passed among them for possible solutions to the speed-testability or area-testability trade off. Therefore, the final design will satisfy the testability requirements within the given constraints.

VTST is an integrated set of tools which not only performs synthesis of digital system design from behavioral description to physical layout, but also performs the testability analysis and generates a BIST design that meets the area, performance and testability requirements. Figure 1 describes an overview of the information flow among the VTST and other commercial computer-aided design tools at the system level. VTST

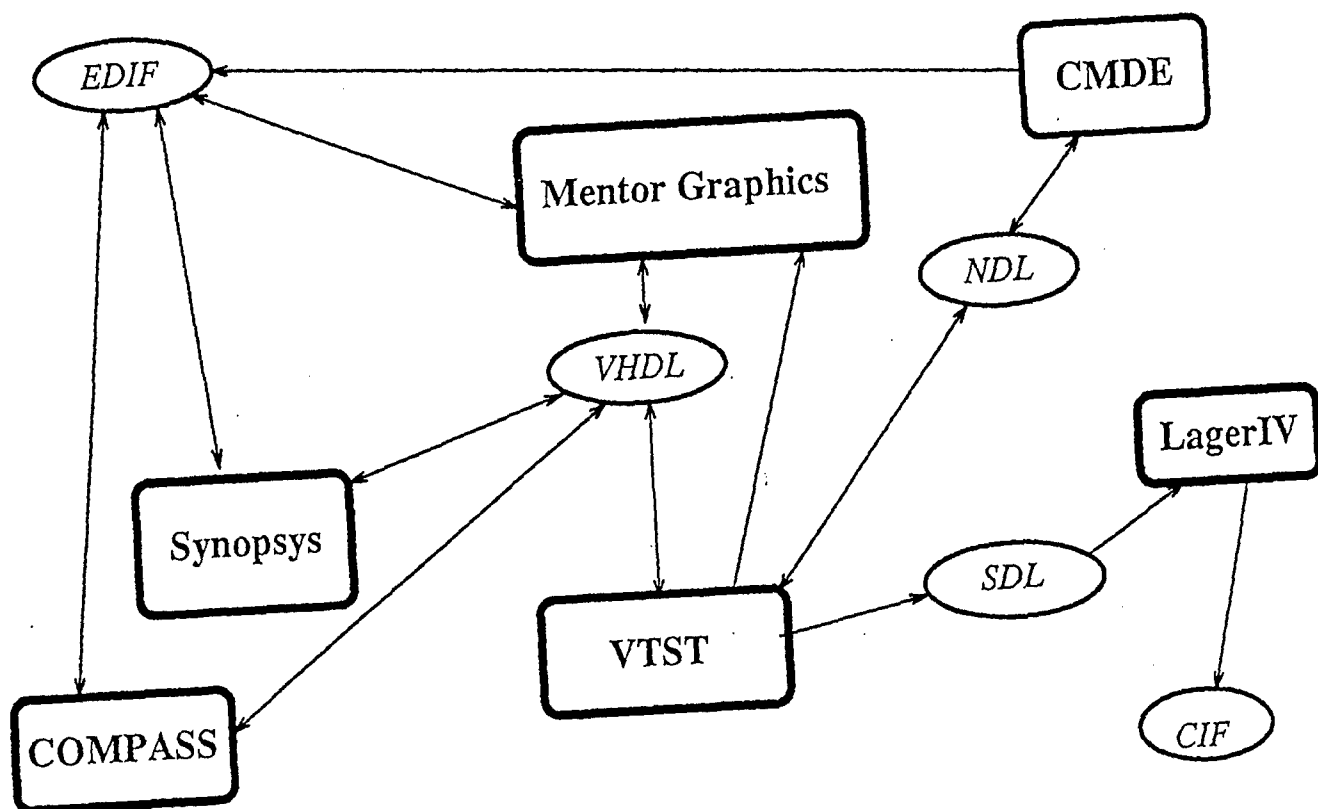


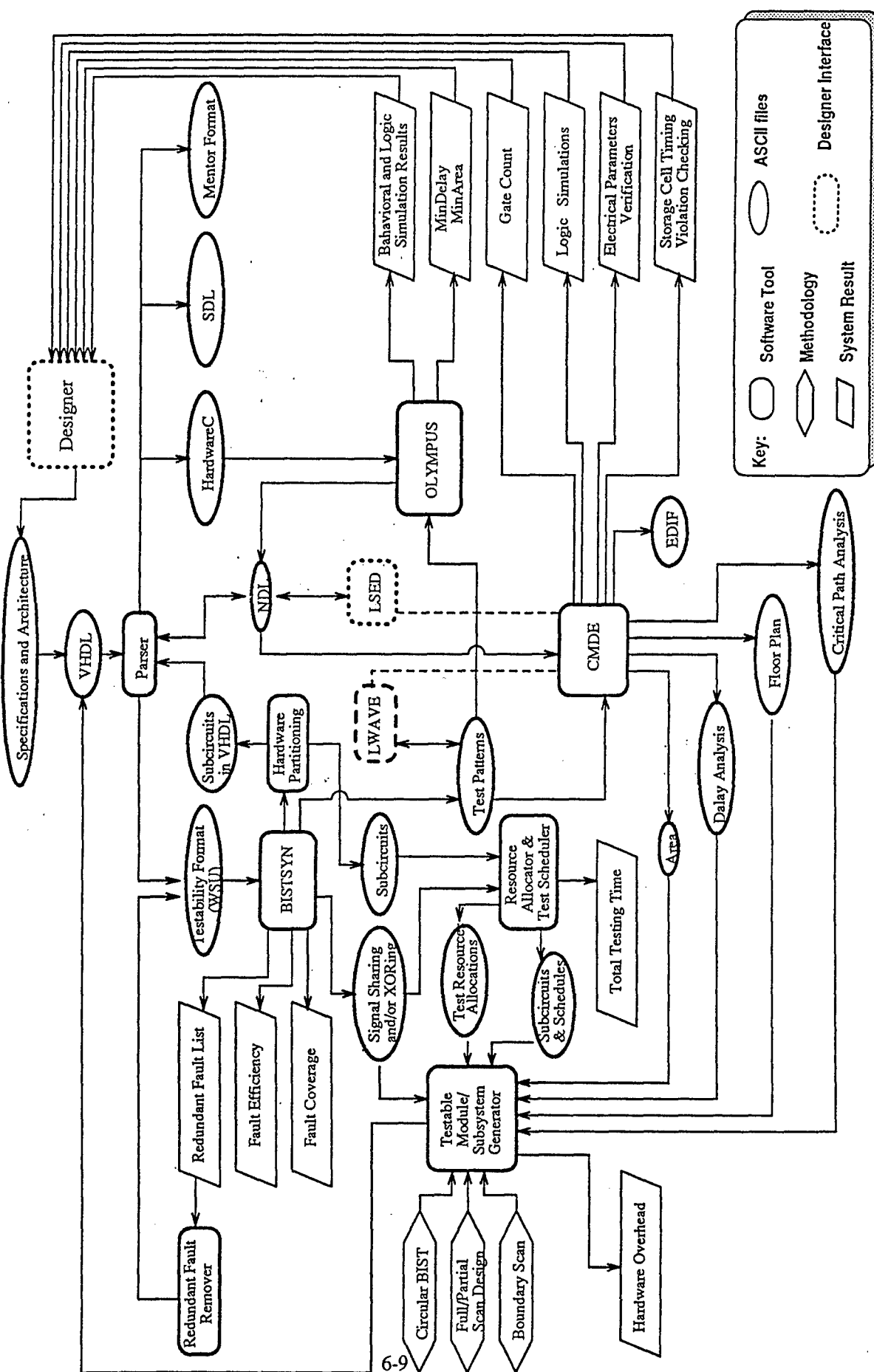
Figure 1: System Overview of VTST to Commercial CAD Tools

mainly accepts the VHDL description and the LSI logic level NDL (Network Description Language) description, and the EDIF physical-level description through the interface with other CAD tools. VTST generates several output formats: VHDL format accepted by Synopsys synthesis tool, Compass tool and Mentor Graphics tool, NDL format accepted by LSI Logic's Concurrent Modular Design Environment (CMDE) system, SDL format for LAGER silicon compiler, and EDIF format accepted by LSI Logic's CMDE, Synopsys, Compass and Mentor Graphics tools.

VTST comprises three major design tools: BIST Design and Testability Analysis Tool (*BISTDaTA*) developed by Wright State University (WSU), *OLYMPUS* synthesis system developed by Stanford University, and *CMDE* Application Specific Integrated Circuit (ASIC) design system developed by LSI Logic. Figure 2 provides an overall description of VTST. Each subsystem in VTST is an individual design tool for distinct purpose. Given the design specifications and architecture of a digital system will be specified by the designer in the early stage. *BISTDaTA* is a design for testability system which will take the given design and synthesize it into a self-testable design meeting the testability requirements such as hardware overhead, fault coverage, and total self-testing time. *OLYMPUS* is a synthesis system which will perform behavioral, structural and logic syntheses with series of translations and optimizations. *OLYMPUS* also performs technology mapping and simulation. The *CMDE* design system is an ASIC design tool to enable designers to perform logic design, logic simulation, chip planning, performance analysis, and logic-to-production verification. Since these three unique systems have different circuit input formats, VTST must be equipped with a well-developed *Parser* for testability synthesis. The final testable design will meet the design specifications such as testability constraints (fault coverage, total self-testing time and hardware overhead), performance requirements (area and delay) and architecture of the specified design. These five different circuit formats are used both internal to the VTST system and external to other commercial CAD tools. They are: (1) *WSU testability format*, (2) *NDL*, (3) *SDL*, (4) *HardwareC*, and (5) *NDL like format* used in Mentor Graphics tool.

2.1 VHDL Parsers

VHDL (VHSIC Hardware Description Language) is a hardware description language which is used to characterize both the function and structure of designs from logical primitives through architectural descriptions. The proposed VLSI testability synthesis tool (*VTST*) will be able of accepting VHDL as input circuit

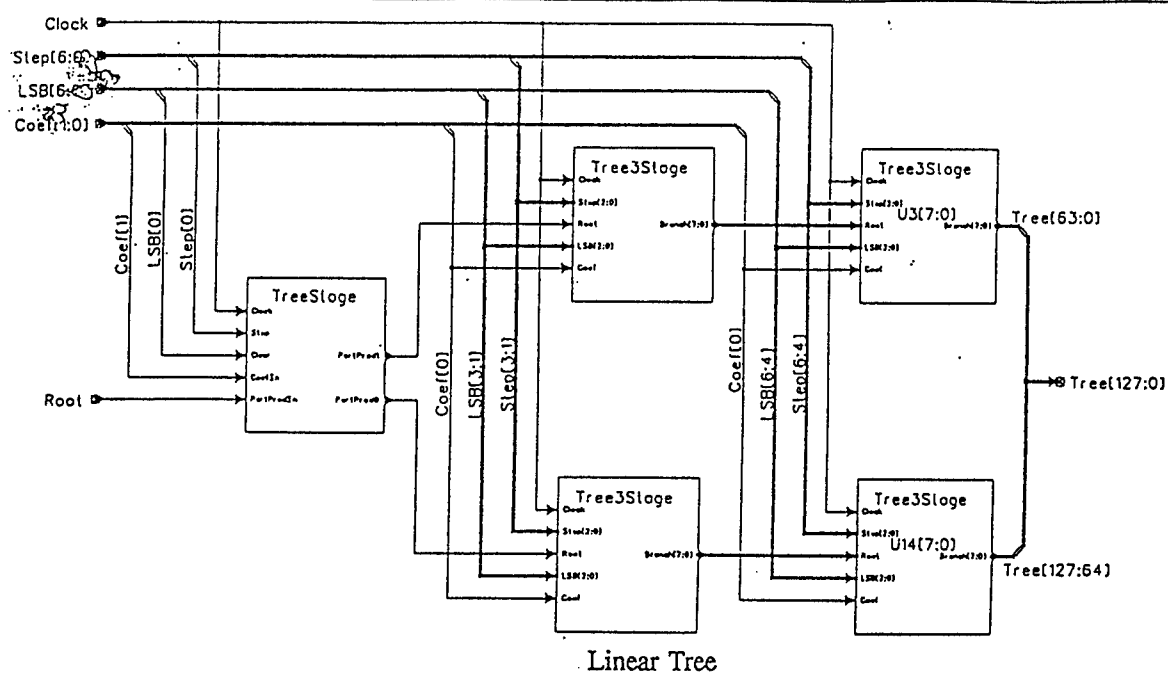
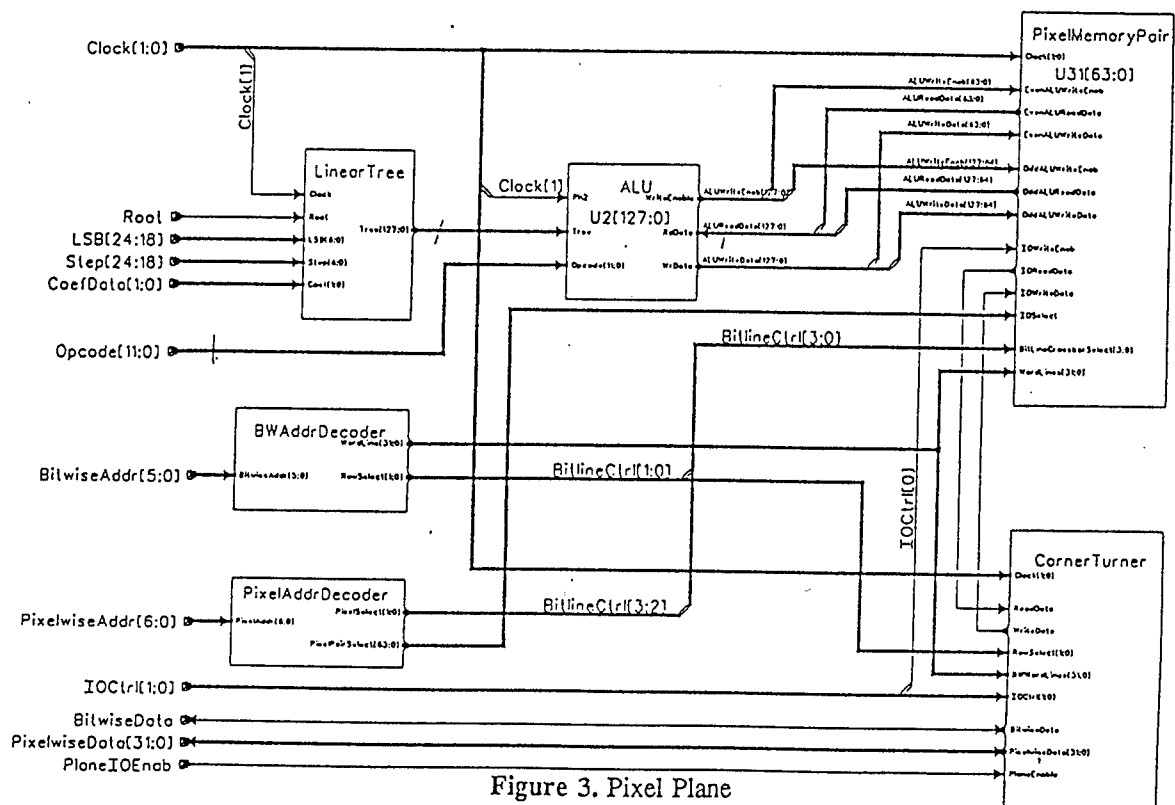
Figure 2: *VLSI Testability Synthesis Tool (VTST)*

format for top-down design. After testability synthesis, VTST will be able of generating VHDL and EDIF as output circuit format compatible with CAD/CAE commercial framework.

VHDL was developed for the design, description, and simulation of VHSIC components. VHSIC is the acronym for the Very High Speed Integrated Circuits. VHDL is primarily concerned with description of the functional operation and the logic organization of circuit designs. This description is accomplished first by specifying the inputs and outputs of a system or device. Then either its behavior (outputs as functions of inputs) or its structure (in terms of interconnected subcomponents) is specified. The primary abstraction in VHDL is called a design entity. A design entity has two ports: the interface description and one or more body descriptions.

An interface description performs several functions. It defines the logical interface to outside world. It specifies the I/O ports and their characteristics. Additionally, operating conditions and characteristics may be included. To accomplish this, the interface description provides a *port declaration* for each I/O of design entity. Each port declaration includes a port *name* and an associated *mode* and *type*. The mode specifies direction as *in*, *out*, *inout*, *buffer*, or *linkage*. The type qualifies the data that flows through a *port*. Standard types include *BIT*, *INTEGER*, *REAL*, *CHARACTER*, and *BIT_VECTOR*.

VHDL parsers are implemented by C language, using CC, yacc, lex compilers and Motif running in X window system. In this report, we use the linear tree subsystem in the PIXEL chip as an example. The linear tree is essentially a parallel, bit-serial multiplier, taking in data from the three bit-serialized streams of A, B, and C coefficients. Its outputs are the function $F(x,y) = Ax + By + C$, where x and y are the coordinates of the pixel on the display. The pixel plane is shown in Figure 3 and the linear tree subsystem including the tree submodules: *tree3stage*, *treestage*, and full adder is shown in Figure 4. To describe the VHDL parsers, due to the limited space, we use the *treestage* and full adder as examples. The VHDL descriptions of *treestage* and full adder are shown in Figures 5 and 6. VHDL Parsers were developed with the capability of parsing these VHDL descriptions to (1) WSU testability format (International Symposium of Circuits and Systems (ISCAS) test benchmark circuit format) for BIST synthesis, (2) NDL format (Figure 7) for ASIC design analysis, (3) HardwareC (Figure 8) for high-level, structural and logic synthesis, and (4) SDL format (Figure 9) for LAGER silicon compiler layout synthesis. Using the generated NDL formate, the CMDE can generate the schematics



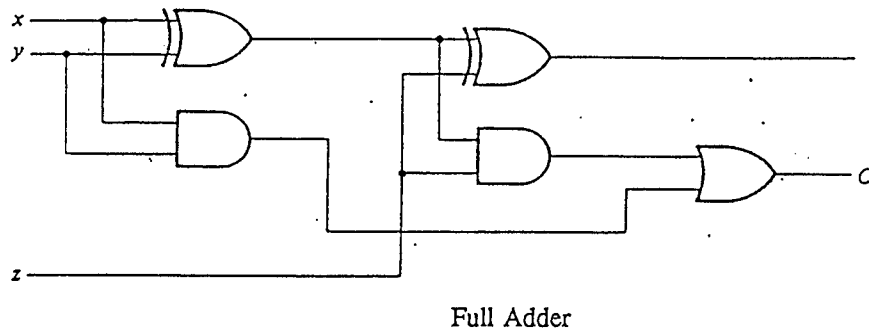
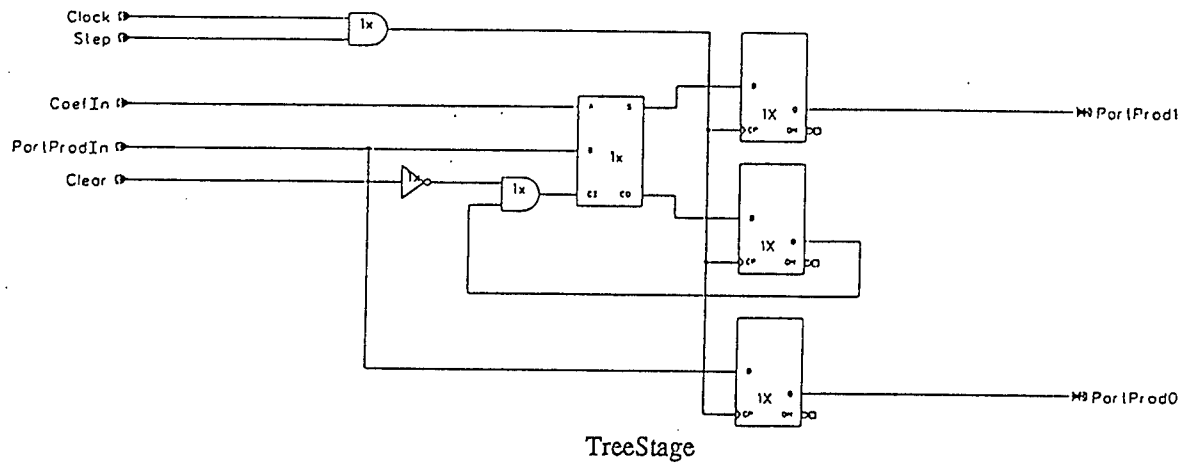
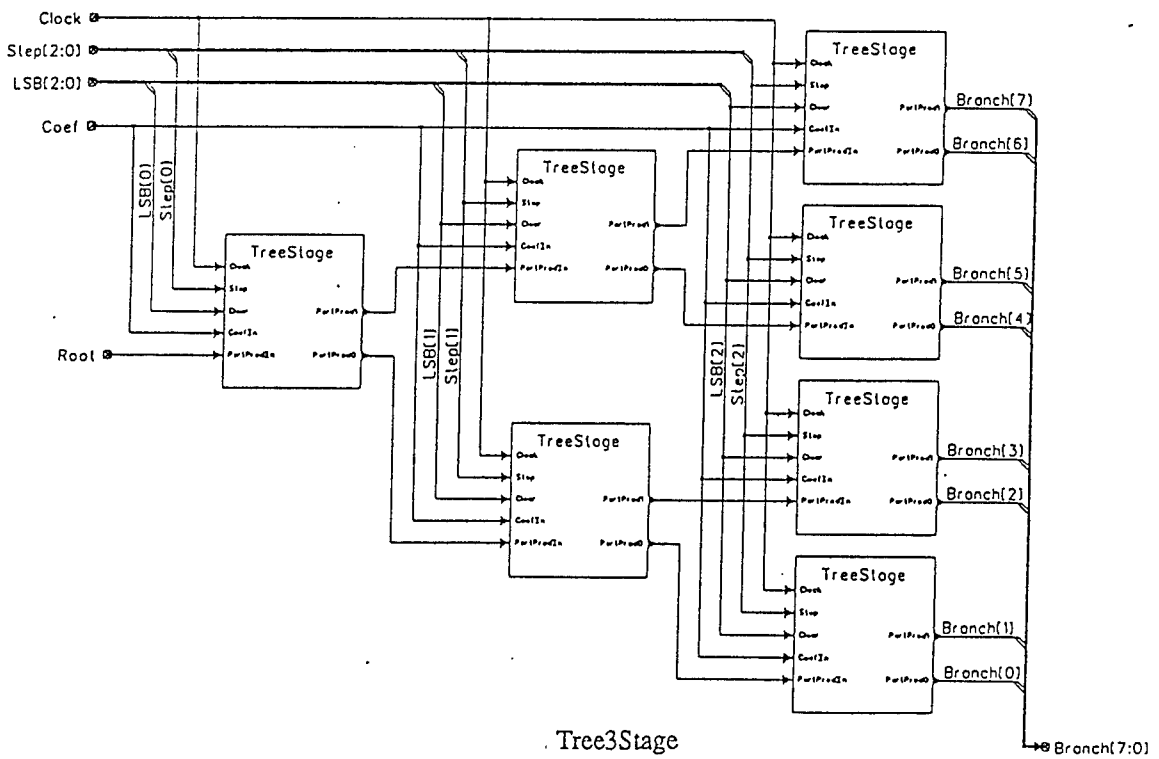


Figure 4: Schematics of linear tree subsystem using COMPASS tools.



VHDL of TreeStage

Wright State University
Electrical Engineering

```
Library Lib;
use Lib.all;

entity treestage is
port(CoefIn,PartProdIn,Clear,clk: Bit;
     PartProd1,PartProd0: OUT Bit);
end treestage;

architecture Structure of treestage is
component FullAddder
port(A1,B1,CIN2: in Bit; SUM,CO: out Bit);
-- entity type is described in lib
end component;
for all : FullAddder use entity Lib.FullAddder(structure);

component fdla
port(D, Cp: in Bit; Q,QN:out Bit);
-- entity type is described in lib
end component;
for all : fdla use entity Lib.fdla(behavior);

component AND2A
generic (const : integer;
        delay : time);
port(A,B: in Bit; Z: out Bit);
-- entity type is described in lib
end component;
for all : AND2A use entity Lib.AND2A(behavior);

component N1a
generic (const : integer;
        delay : time);
port(A: in Bit; Z : out Bit);
-- entity type is described in lib
end component;
for all : N1a use entity Lib.N1a(behavior);

signal U0_out1 : Bit;
signal U1_in0 : Bit;
signal U1_in1 : Bit;
signal U1_out2: Bit;
signal U2_in0 : Bit;
signal U2_out1: Bit;
signal U2_out2: Bit;

signal U3_in1 : Bit;
signal U3_out2: Bit;
signal U4_in1 : Bit;
signal U4_out1: Bit;
signal U4_out2: Bit;
signal U5_out2: Bit;

begin

U3: fdla
port map(U3_in1,clk,PartProd1,U3_out2);
U3_in1 <= U2_out1;

U4: fdla
port map(U4_in1, clk,U4_out1,U4_out2);
U4_in1 <= U2_out2;

U5: fdla
port map(PartProdIn, clk, PartProd0, U5_out2);

U0: N1a

generic map (0, 1 ns)
port map(Clear, U0_out1);

U1: AND2A
generic map (0, 0 ns)
port map(U1_in1, U1_in0, U1_out2);
U1_in1 <= U4_out1;
U1_in0 <= U0_out1;

U2: fulladder
port map(CoefIn,PartProdIn,U2_in0,U2_out1,U2_out2);
U2_in0 <= U1_out2;

end Structure;
```



VHDL of FullAdder

Wright State University
Electrical Engineering

```

Library Lib;
use Lib.all;

entity fulladder is
port(A1,B1,CIN2: Bit;
      SUM,CO: OUT Bit);
end FullAdder;

architecture Structure of FullAdder is
component AND2A
generic (const : integer;
        delay : time);
port(A,B: Bit; Z: out Bit);
-- entity type is described in lib
end component;
for all : AND2A use entity Lib.AND2A(behavior);

component EO2A
generic (const : integer;
        delay : time);
port(A, B: Bit; Z:out Bit);
-- entity type is described in lib
end component;
for all : EO2A use entity Lib.EO2A(behavior);

component OR2A
generic (const : integer;
        delay : time);
port(A,B: Bit; Z:out Bit);
-- entity type is described in lib
end component;
for all : OR2A use entity Lib.OR2A(behavior);

signal U0_out : Bit;
signal U1_out2: Bit;
signal U2_in1 : Bit;
signal U3_in1 : Bit;
signal U3_out2: Bit;
signal U4_in0 : Bit;
signal U4_in1 : Bit;
signal U2O: Bit;

```

```

begin
U0: EO2A
generic map (0, 0 ns)
port map(B1,A1,U0_out);

U1: AND2A
generic map (0, 0 ns)
port map(B1,A1, U1_out2);

U2: EO2A
generic map (0, 0 ns)
port map(CIN2, U2_in1, U2O);
U2_in1 <= U0_out;
SUM <= U2O;

U3: AND2A
generic map (0, 0 ns)
port map(CIN2,U3_in1,U3_out2);
U3_in1 <= U0_out;

U4: OR2A
generic map (0, 0 ns)
port map(U4_in1,U4_in0,CO);
U4_in1 <= U1_out2;
U4_in0 <= U3_out2;

end Structure;

```

Figure 6: VHDL of full adder.



NDL of TreeStage

Wright State University
Electrical Engineering

```

/*****
**
**
** Netlist copyright (C) 1988 LSI Logic Corporation
** Created by WSU VTST parser
**
**
**
*****/

compile;
directory master;

module treestage;
inputs      clk, clear, partprodin, coefin;
outputs     partprod0, partprod1;

level function;
define
/* implicit connectors *****/
    clk- = (clk);
    clear- = (clear);
    partprodin- = (partprodin);
    coefin- = (coefin);
    partprod0- = (partprod0);
    partprod1- = (partprod1);

/* part instances *****/
    u3-(partprod1-q, u3_out2--qn) = fdla(u2_out1--d, clk--cp) ;
    u4-(u4_out1--q, u4_out2--qn) = fdla(u2_out2--d, clk--cp) ;
    u5-(partprod0--q, u5_out2--qn) = fdla(partprodin--d, clk--cp) ;
    u0-(u0_out1--z) = nla(clear--a) ;
    u1-(u1_out2--z) = and2a(u4_out1--a, u0_out1--b) ;
    u2-(u2_out1--sum, u2_out2--co) = fulladder(coefin--al,
        partprodin--b1, u1_out2--cin2) ;

/* extractors *****/

/* type converters *****/

end module;
end compile;
end;
```

Figure 7: NDL of treestage.



NDL of FullAdder

Wright State University
Electrical Engineering

```

/*****
/**
/**
/** Netlist copyright (C) 1988 LSI Logic Corporation **/
/** Created by WSU VIST parser **/
/**
/**
/**
/*****/

compile;
directory master;

module fulladder;  cin2, b1, a1;
inputs
outputs  co, sum;

level function;
define
/* implicit connectors *****/

    cin2- = (cin2);
    b1- = (b1);
    a1- = (a1);
    co- = (co);
    sum- = (sum);

/* part instances *****/

u0-(u0_out--z) = eo2a(b1--a, a1--b) ;
u1-(u1_out2--z) = and2a(b1--a, a1--b) ;
u2-(sum--z) = eo2a(cin2--a, u0_out--b) ;
u3-(u3_out2--z) = and2a(cin2--a, u0_out--b) ;
u4-(co--z) = or2a(u1_out2--a, u3_out2--b) ;

/* extractors *****/

/* type converters *****/

end module;

end compile;

end;
```



HC of TreeStage 1 of 3

Wright State University
Electrical Engineering

```
#include "treestage_ps.hc"
block treestage (
    coefin,
    partprodin,
    clear,
    clk,
    partprod1,
    partprod0
)
in port coefin;
in port partprodin;
in port clear;
in port clk;
out port partprod1;
out port partprod0;

instance fulladder_ps u2;
instance DFF_ps u3, u4, u5;
instance AND2_ps u1;
instance INV_ps u0;
boolean u0_out1;
boolean u1_in0;
boolean u1_in1;
boolean u1_out2;
boolean u2_in0;
boolean u2_out1;
boolean u2_out2;
boolean u3_in1;
boolean u3_out2;
boolean u4_in1;
boolean u4_out1;
boolean u4_out2;
boolean u5_out2;

u2 (
    coefin,
    partprodin,
    u1_out2,
    u2_out1,
    u2_out2 );

u3 (
    u2_out1,
    clk,
    partprod1,
    u3_out2 );

u4 (
    u2_out2,
    clk,
    u4_out1,
    u4_out2 );

u5 (
    partprodin,
    clk,
    partprod0,
    u5_out2 );

u1 (
    u4_out1,
    u0_out1,
    u1_out2 );

u0 (
    clear,
    u0_out1 );
```

Figure 8: Hardware C of treestage.



HC of TreeStage 2 of 3

Wright State University
Electrical Engineering

```
treestage_ps.hc
#include "treestage_pd.hc"
process fulladder_ps(
    bl,
    cin2,
    sum,
    co)
    in port al;
    in port bl;
    in port cin2;
    out port sum;
    out port co;
    {
        instance fulladder u0;
        u0(
            al,
            bl,
            cin2,
            sum,
            co);
    }

process DFF_ps(D, CK, Q, Qb)
    in port D, CK;
    out port Q, Qb;
    {
        instance DFF u0;
        u0(D, CK, Q, Qb);
    }

process AND2_ps(A, B, out_)
    in port A;
    in port B;
    out port out_;
    {
        instance AND with (2) u0;
        out_ = u0(A & B);
    }

process INV_ps(D, out_)
    in port D;
    out port out_;
    {
        instance INVERTOR u0;
        out_ = u0(D);
    }

treestage_pd.hc
#include "../BaseGate.hc"
procedure fulladder (
    al,
    bl,
    cin2,
    sum,
    co)
    in boolean al;
    in boolean bl;
    in boolean cin2;
    out boolean sum;
    out boolean co;
    {
        instance AND with (2) u1, u3;
        instance XOR with (2) u0, u2;
        instance OR with (2) u4;
        boolean u0_out;
        boolean u1_out2;
        boolean u2_in1;
        boolean u3_in1;
        boolean u3_out2;
        boolean u4_in0;
        boolean u4_in1;
        boolean u2o;
        u1_out2 = u1 (
            bl &
            al );
        u3_out2 = u3 (
            cin2 &
            u0_out );
        u0_out = u0 (
            bl &
            al );
        sum = u2 (
            cin2 &
            u0_out );
        co = u4 (
            u1_out2 &
            u3_out2 );
    }
}
```




HC of TreeStage

3 of 3

Wright State University
Electrical Engineering

```
BaseGate.hc
/** high trigger **/
procedure D_LATCH (D, CK, Q, Qb)
in boolean D, CK;
out boolean Q, Qb;
static prevQ=0;
static prevCK=0;
if (CK)
{
    Q = D;
    Qb = !D;
    prevQ = D;
}
else
{
    Q = prevQ;
    Qb = !prevQ;
}
prevCK = myclock;

***** rising edge dff *****/
procedure DFF (D, myclock, Q, Qb)
in boolean D, myclock;
out boolean Q, Qb;
static prevQ;
static prevCK;
if (myclock && !prevCK)
{
    Q = D;
    Qb = !D;
    prevQ = D;
}
else
{
    Q = prevQ;
    Qb = !prevQ;
}
prevCK = myclock;

***** falling edge *****/
procedure DFF (D, myclock, Q, Qb)
in boolean D, myclock;
out boolean Q, Qb;
static prevQ;
static prevCK;
if (!myclock && prevCK)
{
    Q = D;
    Qb = !D;
    prevQ = D;
}
else
{
    Q = prevQ;
    Qb = !prevQ;
}
prevCK = myclock;

*****/

template function OR(Din) with (size) return boolean[1]
in boolean Din[size];
{
    int i;
    boolean temp;
    temp = Din[0];
    for i = 1 to size -1 do
        temp = temp | Din[i];
    return_value = temp;
}

template function NOR(Din) with (size) return boolean[1]
in boolean Din[size];
{
    int i;
    boolean temp;
    temp = Din[0];
    for i = 1 to size -1 do
        temp = temp | Din[i];
    return_value = !temp;
}

template function XOR(Din) with (size) return boolean[1]
in boolean Din[size];
{
    int i;
    boolean temp;
    temp = Din[0];
    for i = 1 to size -1 do
        temp = temp ^ Din[i];
    return_value = temp;
}

template function XNOR(Din) with (size) return boolean[1]
in boolean Din[size];
{
    int i;
    boolean temp;
    temp = Din[0];
    for i = 1 to size -1 do
        temp = temp ^ Din[i];
    return_value = !temp;
}

function INVERTOR(D) return boolean[1]
{
    in boolean D;
    return_value = !D;
}

template function AND(Din) with (size) return boolean[1]
in boolean Din[size];
{
    int i;
    boolean temp;
    temp = Din[0];
    for i = 1 to size -1 do
        temp = temp & Din[i];
    return_value = temp;
}

template function NAND(Din) with (size) return boolean[1]
in boolean Din[size];
{
    int i;
    boolean temp;
    temp = Din[0];
    for i = 1 to size -1 do
        temp = temp & Din[i];
    return_value = !temp;
}
```

93/12/25
11:02:53

treestage.sdl

1

```

(parent-cell treestage
(SIVMASTER "treestage")
)

(layout-generator Flint)

(subcells
(n1a u0 ((const 0)))
(nd2a u1 ((const 0)))
(fulladder u2)
(fd2a u3)
(fd2a u4)
(fd2a u5)
)

(net Vdd (NETTYPE SUPPLY))
(net GND (NETTYPE GROUND))

(instance u0 (
(Vdd Vdd)
(GND GND)
(a clear)
(z u0_out1)
))

(instance u1 (
(Vdd Vdd)
(GND GND)
(a u1_in1)
(b u0_out1)
(z u1_out2)
))

(instance u2 (
(Vdd Vdd)
(GND GND)
(a1 coefin)
(b1 partprodin)
(cin2 u1_out2)
(sum u2_out1)
(co u2_out2)
))

(instance u3 (
(Vdd Vdd)
(GND GND)
(d u2_out1)
(cp clock)
(q partprod1)
))

(instance u4 (
(Vdd Vdd)
(GND GND)
(d u2_out2)
(cp clock)
(q u1_in1)
))

(instance u5 (
(Vdd Vdd)
(GND GND)
(d partprodin)
)

(cp clock)
(q partprod0)
))

(instance parent (
(coefin coefin)
(partprodin partprodin)
(clear clear)
(clock clock)
(partprod1 partprod1)
(partprod0 partprod0)
(Vdd Vdd)
(GND GND)
))

(parent-cell fulladder
(SIVMASTER "fulladder")
)

(layout-generator Flint)

(subcells
(eo2a u0 ((const 0)))
(nd2a u1 ((const 0)))
(eo2a u2 ((const 0)))
(nd2a u3 ((const 0)))
(nr2a u4 ((const 0)))
)

(net Vdd (NETTYPE SUPPLY))
(net GND (NETTYPE GROUND))

(instance u0 (
(Vdd Vdd)
(GND GND)
(a b1)
(b a1)
(z u0_out)
))

(instance u1 (
(Vdd Vdd)
(GND GND)
(a b1)
(b a1)
(z u1_out2)
))

(instance u2 (
(Vdd Vdd)
(GND GND)
(a cin2)
(b u0_out)
(z sum)
))

(instance u3 (
(Vdd Vdd)
(GND GND)
(a cin2)
(b u0_out)
(z u3_out2)
))

(instance u4 (
(Vdd Vdd)
(GND GND)
(a u1_out2)
(b u3_out2)
(z co)
))

(instance parent (
(a1 a1)
(b1 b1)
(cin2 cin2)
(sum sum)
(co co)
(Vdd Vdd)
(GND GND)
))

```

which are shown in the Figures 10, 11, 12 and 13. The simulation of treestage is shown in Figure 14. Notice that the instance of each logic gate in the schematic design is the name of a LSI Logic library cell, which is selected based on the technology. Using the generated HardwareC, the OLYMPUS generates the simulation shown in Figure 15 which is consistent with the simulation from CMDE shown in Figure 14. Using the generated SDL format, LAGER silicon compiler generates the layouts shown in Figures 16 and 17.

2.2 BIST Design and Testability Analysis (BISTDaTA) Tool

The BISTDaTA Tool is a design system with the capability of analyzing the testability of input circuit designs. BISTDaTA primarily focuses on synthesizing the BIST for a VLSI design. As shown in Figure 2, BISTDaTA consists of five different software tools which perform different tasks. These five softwares are: (1) built-in self-test synthesizer (BISTSYN), (2) circuit partitioning tool (AUTONOMOUS), (3) redundant fault remover (VACUMN), (4) testable modules/subsystems generator (TESTGEN), and (5) resource allocator and test scheduler (RATS). Each subsystem will perform particular design work and interdependent of the outputs generated by the other. The primary objectives of these five tools are described below.

2.2.1 BISTSYN

BISTSYN [Chen 89, 91a] will perform: (1) automated synthesis of the pseudo-exhaustive test generator implemented by linear feedback shift registers (LFSR) with low hardware overhead, (2) minimization of the number of test patterns that are required for pseudo-exhaustive test, (3) testability analysis by generating test patterns to evaluate the circuit's fault coverage, fault efficiency and to list the redundant faults embedded in the circuit.

2.2.2 AUTONOMOUS

For those conventional circuits which are extremely unsuitable for pseudo-exhaustive test, BISTSYN employs a network partitioning tool, named AUTONOMOUS [Chen 92a, 93] to partition the combinational portions of the circuit into different structural subcircuits so that each subcircuit can be pseudo-exhaustively tested. BISTSYN can be performed on both the entire input circuit and the subcircuits after circuit partitioning.

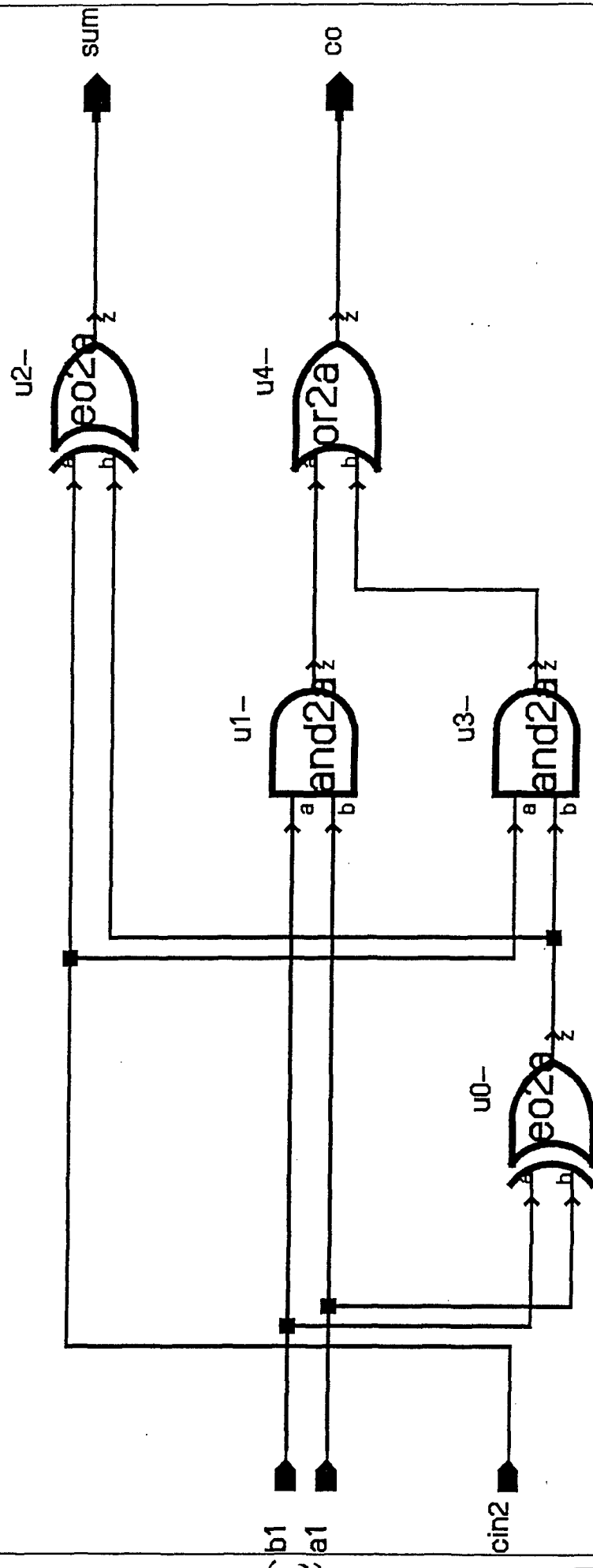


Figure 10: CMDE schematic of full adder.

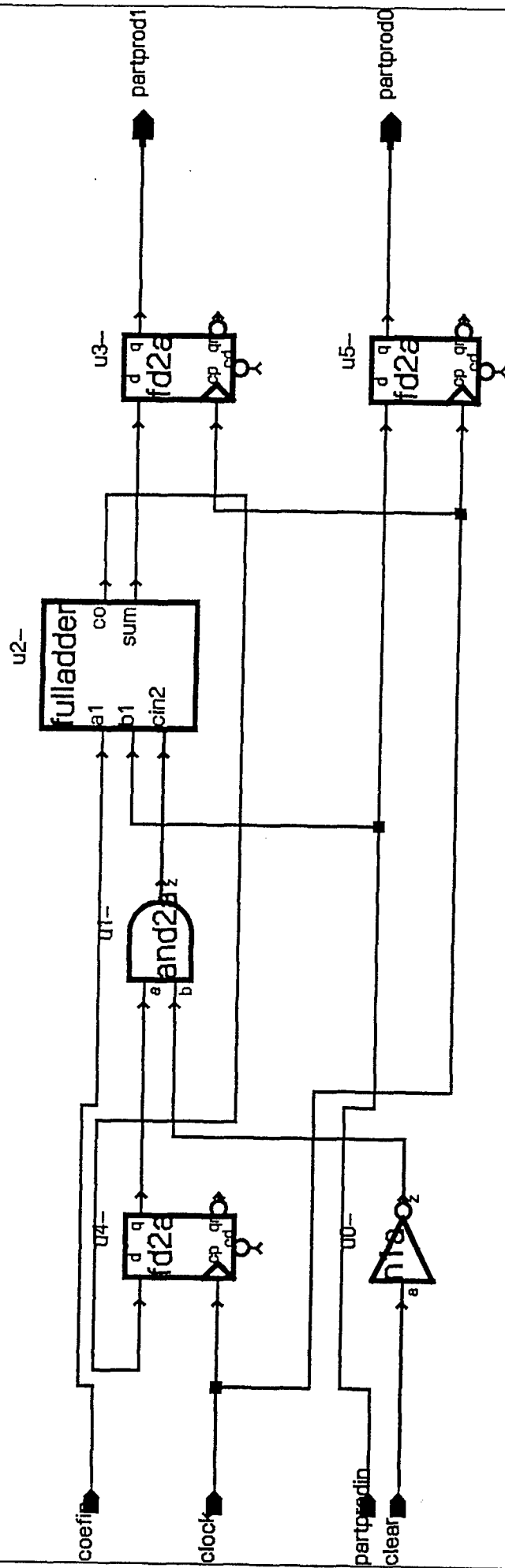


Figure 11: CMDE schematic of treestage.

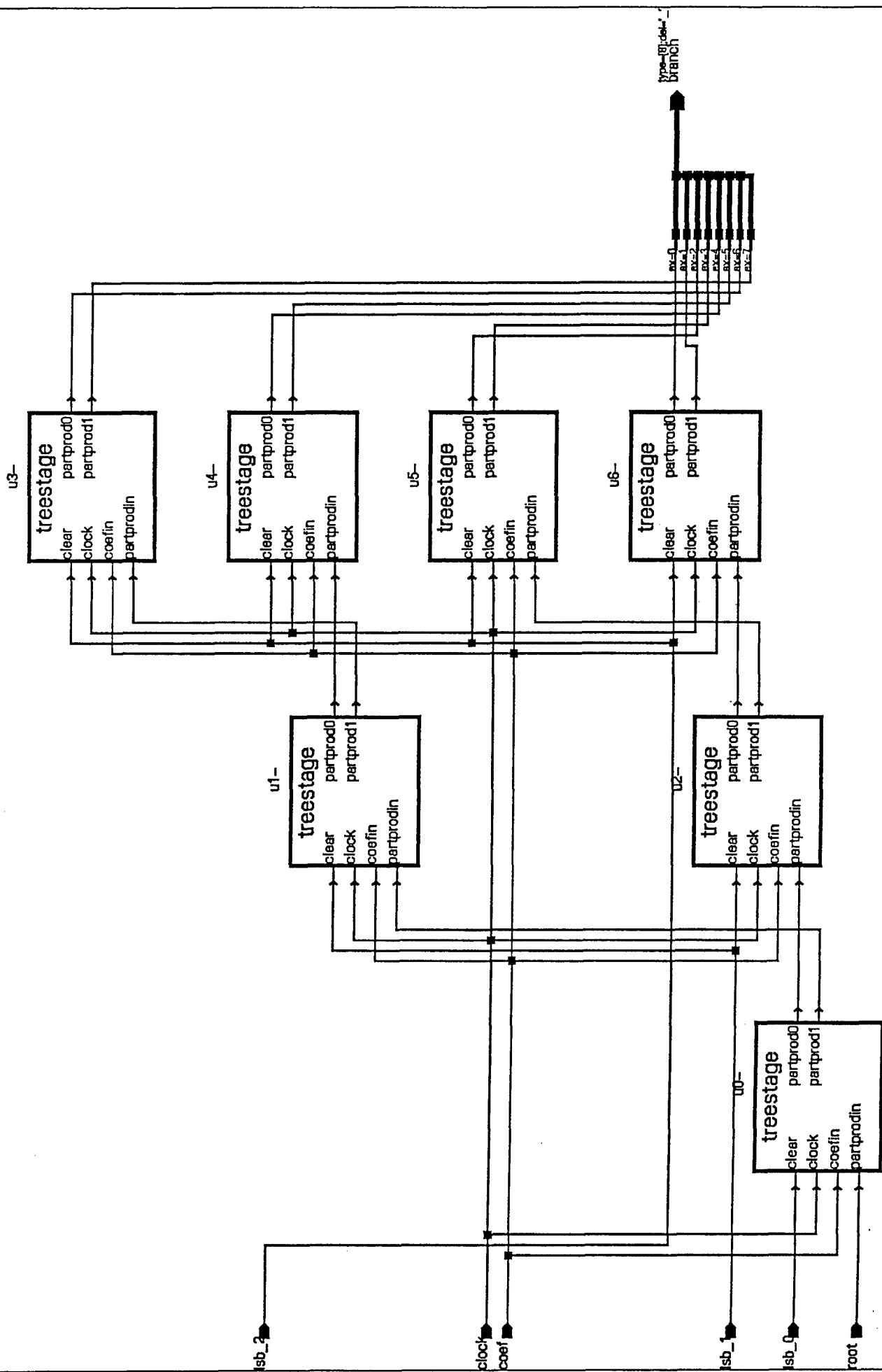


Figure 12: CMDE schematic of tree3stage.

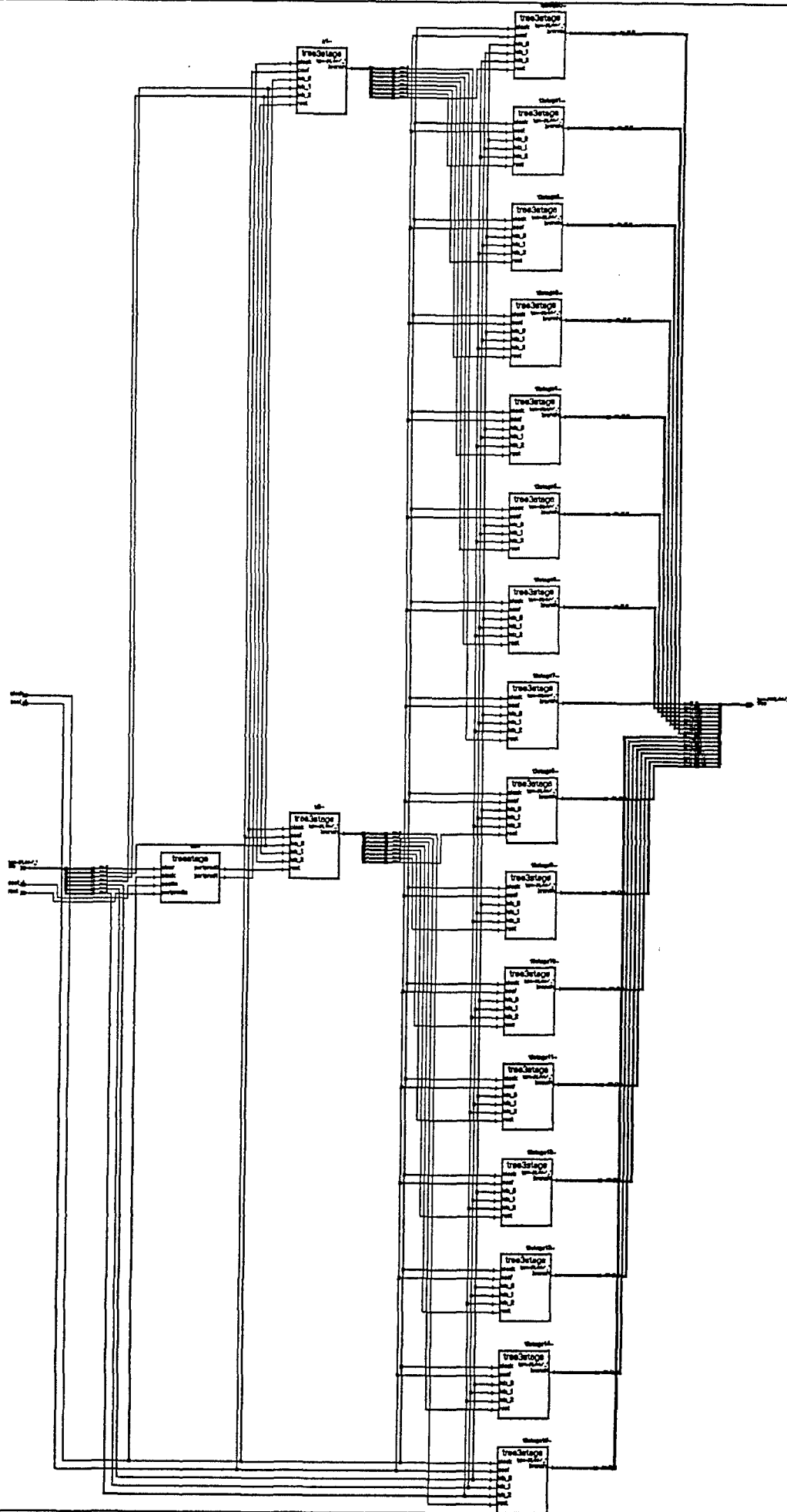


Figure 13: CMDE schematic of linear tree.



Wright State University
Electrical Engineering

Ex: TreeStage

CMDE Simulation

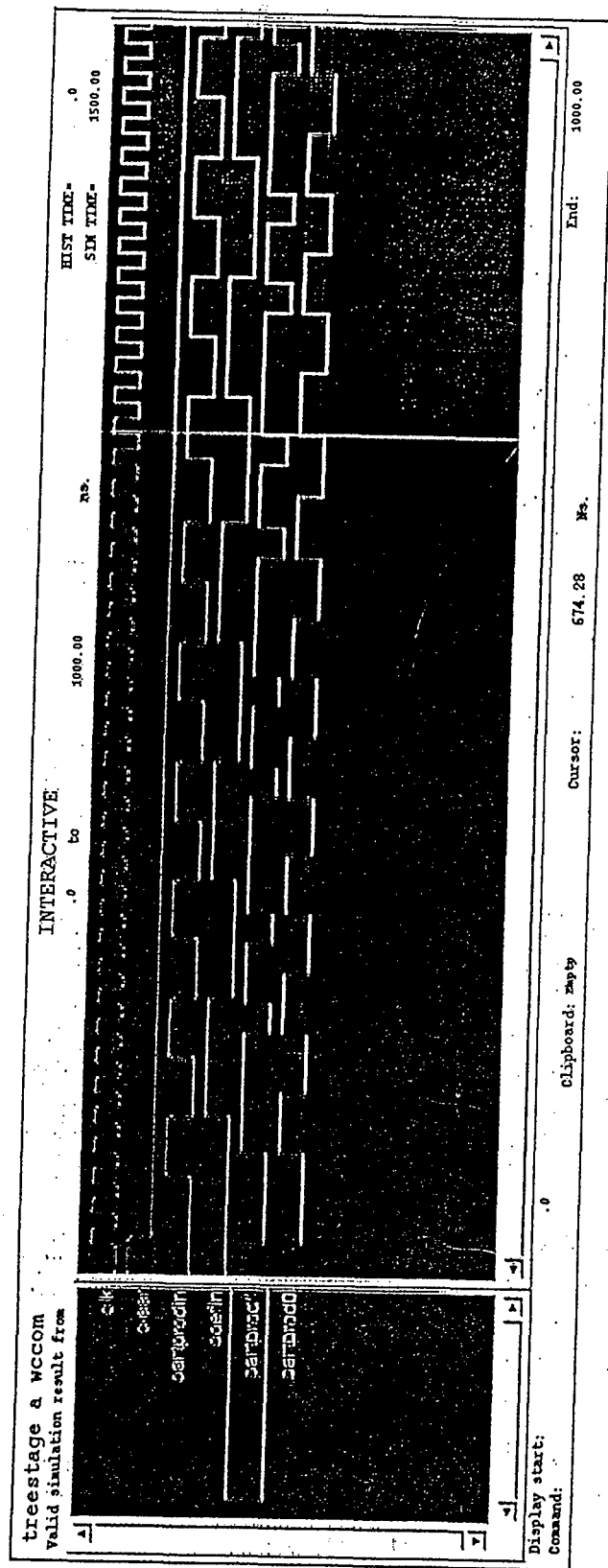


Figure 14: CMDE simulation of treestage.



VHDL to NDL and HC

Wright State University
Electrical Engineering

Ex: TreeStage

Olympus Simulation

FORMAT	SCROLL	VIEW	WINDOW	ZOOM	PRINT	QUIT																			
BIN	DEC	HEX	<	>	1	2	3	4	5	6	7	8	9	0	.	e	E	+	-	*	/	%	^	~	!@#\$%^&*~

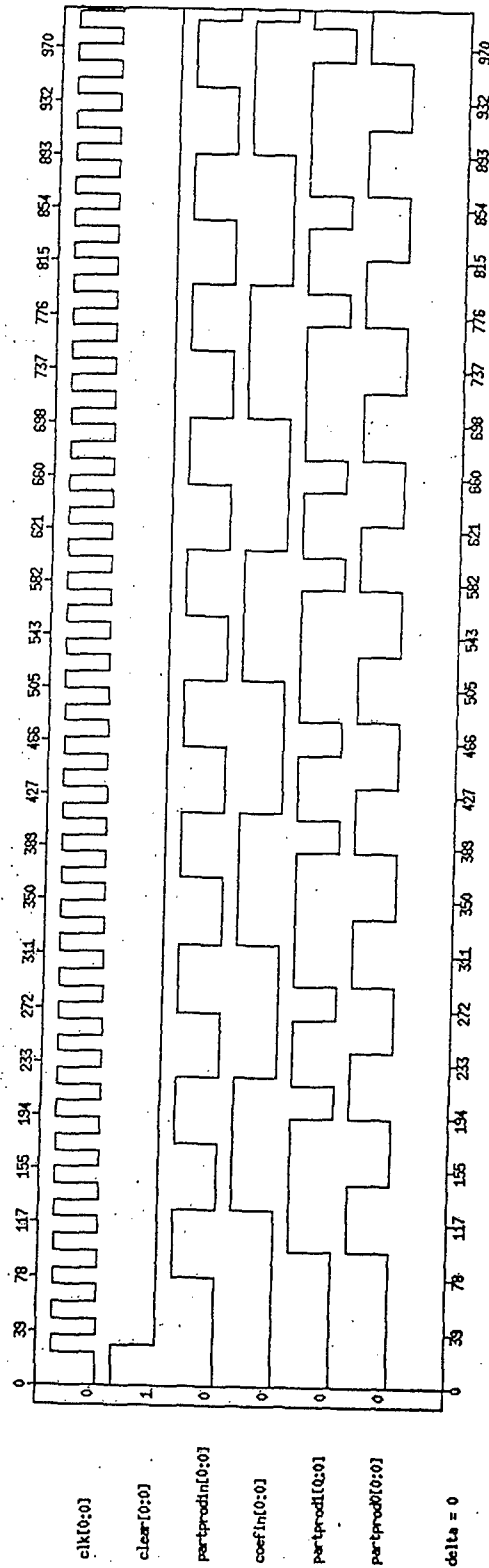


Figure 15: OLYMPUS simulation of treestage.

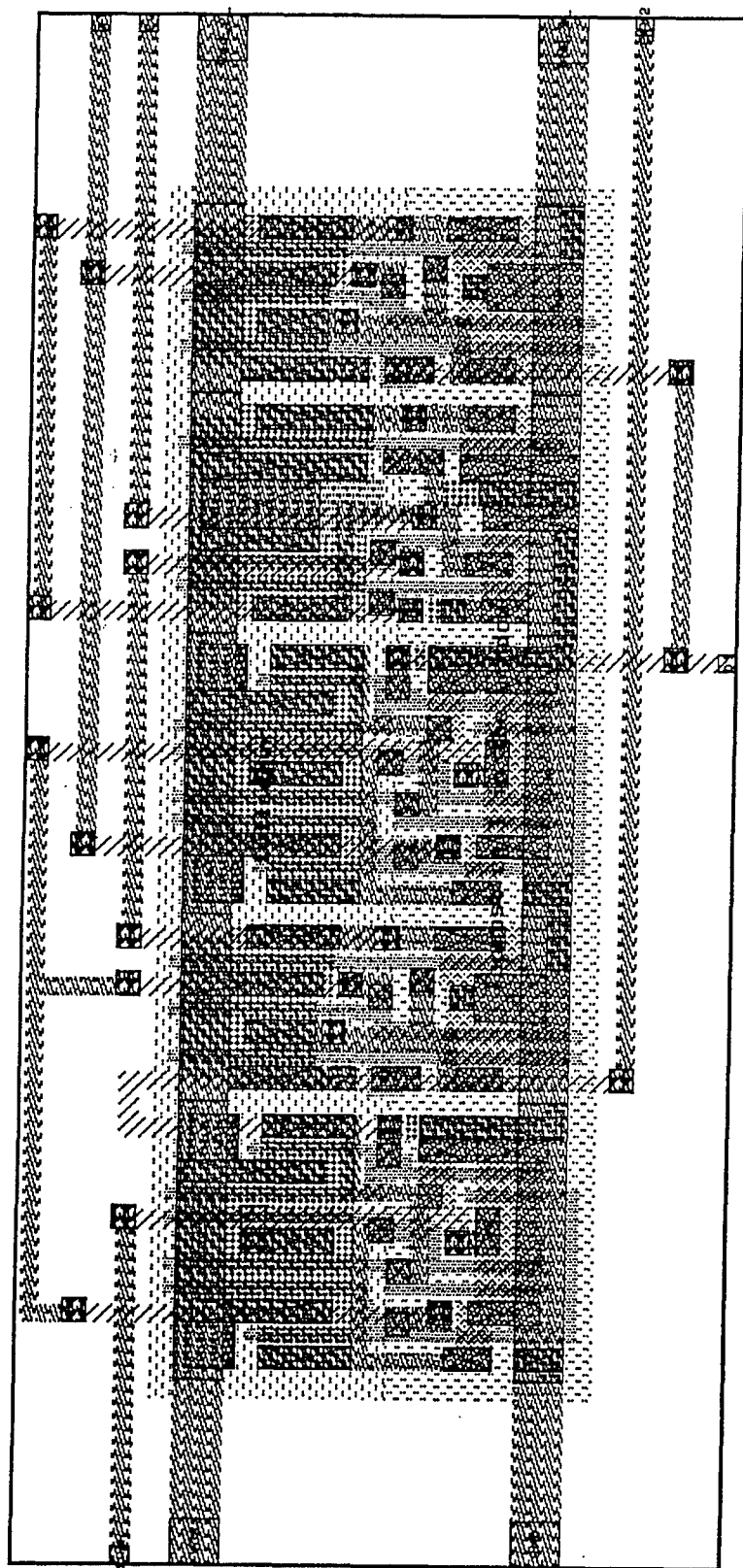


Figure 16: Layout of full adder.

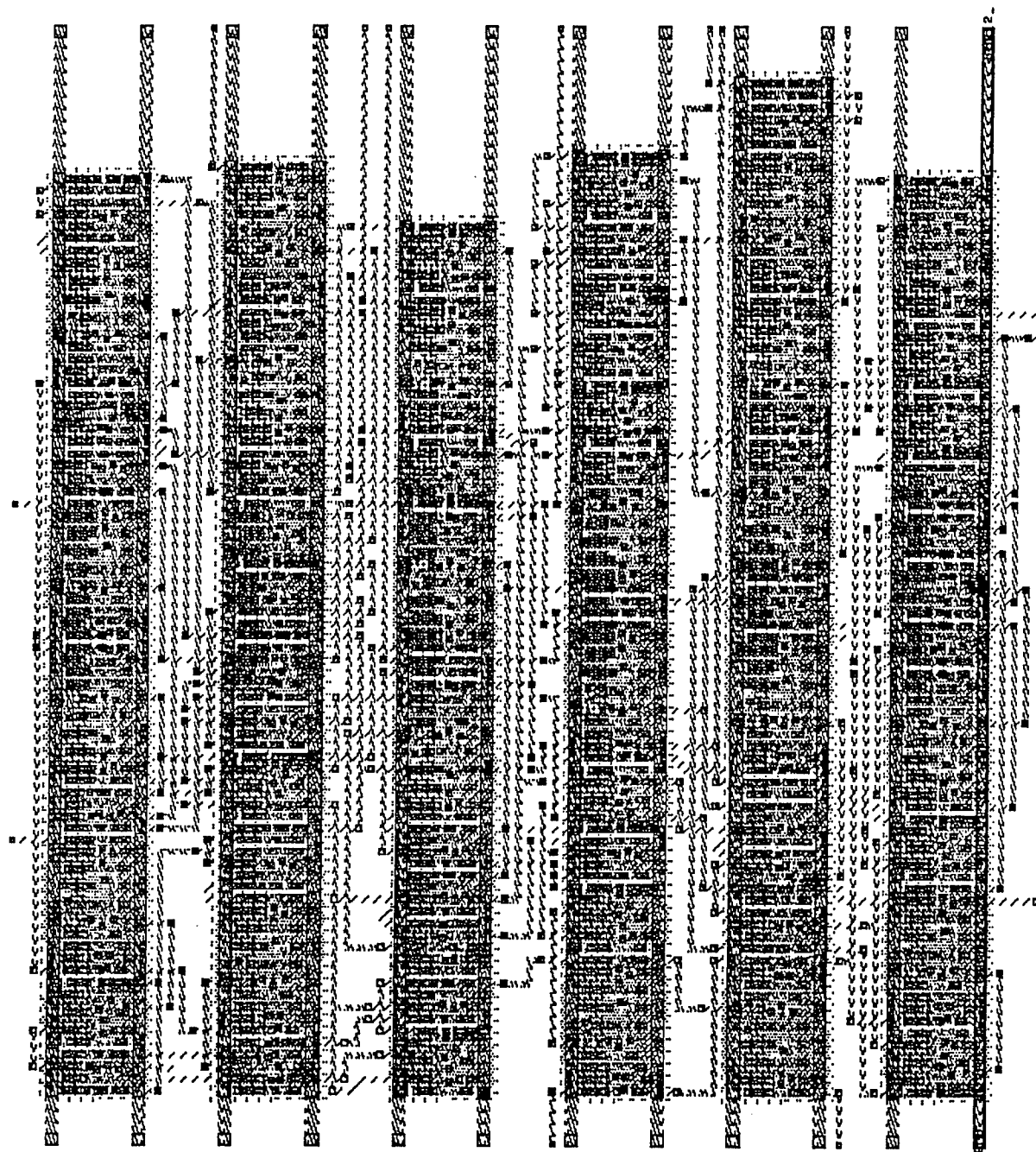


Figure 17: Layout of tree3stage.

2.2.3 VACUMN

VACUMN is a tool to remove the listed redundant faults by means of adding test points, and resynthesizing the local logic containing the redundant faults according to the redundancy removal rules. After all possible redundant faults are removed, the netlist will be input to BISTSYN for BIST design and testability analysis and also to AUTONOMOUS for circuit partitioning. The VHDL description of the BIST circuit or subcircuit will be generated and then be translated by the parser into different formats for the synthesis process.

2.2.4 RATS

The RATS [Chen 91b, 92b, 92c] performs test resource allocation and scheduling for maximizing the test resource utilization and minimizing the total self-testing time based on the test results of each module/subsystem generated by BISTSYN. The total testing time for the BIST system design is then calculated as an output.

2.2.5 TESTGEN

TESTGEN is a knowledge-based system that assists the designer in creating easily testable designs. Specifically, the TESTGEN knowledge base contains information from the tools BISTSYN, AUTONOMOUS, RATS and information from a number of testable design methodologies including full/partial scan, circular BIST, circular BIST with partial scan, memory testing and boundary scan. Also, the results from CMDE such as the area estimation, delay analysis, critical path analysis, and floor plan estimation are important factors used by TESTGEN to generate the testable design.

When the above criteria are ready, an initial phase of the testable design will be generated and described in VHDL. The newly generated VHDL file will be input to the VHDL Parser and then translated to different desired formats for other design system use such as CMDE, OLYMPUS, Mentor Graphics. Figure 18 shows the process of generating a testable design.

The VHDL description of linear tree subsystem was parsed to the WSU testability format for BIST design and testability analysis. The total gate count of linear tree is 1,535. The number of primary inputs and outputs of linear tree is 11 and 128 respectively. The testability analysis is summarized as follows. Using full

scan techniques, the total number of equivalent faults is 3,317 and the test patterns required for testing the linear tree is 30. The fault coverage is 100%. All the D flip-flops need to be changed to scan D flip-flops. After *BISTSYN* is applied, the test signals required for pseudo-exhaustively testing the combinational circuit of linear tree is 4. The total number of equivalent faults is 3,322 and the test patterns required is 16.

2.3 Additional Test Methodologies

2.3.1 Full/Partial Scan

The difficulty in testing general sequential circuits arises due to the poor controllability and observability of the memory elements, ie, flip-flops and latches. Although full scan plus combinational test generation is viewed as a satisfactory solution to the sequential testing problem, there are several disadvantages of this approach including:

- the increase of the length of circuit delay paths caused by the added hardware,
- the area overhead required by the added hardware,
- the length of the resulting tests due to extensive serial shifting of patterns and responses.

This situation has led to renewed interest in sequential test generation with design for testability in the form of *partial scan* which applies serial scan only to a selected subset of all memory elements. VTST will evaluate the circuit's full scan and partial scan designs in terms of fault coverage, overhead, and test cycles.

2.3.2 Circular BIST

Testability of a circuit is a major responsibility of a logic designer. To tackle the problem of testing a number of methods have been proposed. Among them self-testing has come to occupy a place of importance. Self-testing is particularly useful for low-volume specific application integrated circuit.

Most of the built-in self test circuits employ a pseudo-exhaustive/pseudo-random test pattern generator using LFSR and the test response is analyzed using a MISR. This idea, however, necessitates the conversion of conventional registers into a BILBO. This architectural modification results in an increased silicon overhead and makes test controller design and signal distribution a difficult task. In view of the preceding problems circular self-test path is implemented as a possible solution.

A sequential circuit that consists of combinational logic and registers is first considered. It is also assumed that we have a global reset line and that each register can be set to a desired state. This idea may be extended to circuits that do not possess the facility of a global reset. In circular self-test path we choose a few registers, based on fault coverage requirements, and connect them into one long circular shift register with data compaction capability. To do this the input of each selected register is augmented with an XOR gate. This gate exors the functional input with the output of the preceding cell as shown in Figure 19. After having made the modifications the selected flip flops can be joined in a circular path as shown in Figure 20 [Krasniweski 89]. There are two modes of operation for the registers. The multiplexer at the input of the modified cell selects the mode of operation. In the normal mode operation, all cells of the circular path serve as conventional flip flop. In the test mode, illustrated in Figure 21, after resetting the chip, the circular path provides combinational logic (CL) blocks with test patterns and, simultaneously, the compaction of CL responses is performed in much the same way as in parallel signature analyzers. The fault analysis is done by comparing the streams of bits available at the chosen output of the circuit with its fault free output. A decision of pass/fail is done by comparing the results with the precomputed correct responses. The option of selecting some or all flip flops for circular path depends upon the availability of global reset signal. Should a global reset signal be available, then all flip flops connected to the primary input and output are selected. This affords greater controllability and observability. If the global reset line is not available, then scan technique can be used to initialize the circuit to a known state. Clearly the addition of this facility will make the hardware overhead more. The scan chain must contain besides input/output registers a set of internal registers so that at least one of them is a cell of the circular path. Scanning data into this cell would automatically initialize all other flip flops in the chain. The circular self-test path idea can be extended to Circular Built-In Self-Test. The striking feature of the CBIST methodology is that the chip can be tested in single session. This saves considerable amount of time compared to other BIST techniques that require multiple sessions of testing. Other attractive attributes of CBIST are:

- the silicon overhead is substantially lower than that of earlier BIST techniques,
- as the circular path may include an arbitrarily selected set of circuit registers, the overhead can be traded-off with efficiency of the test pattern generation,

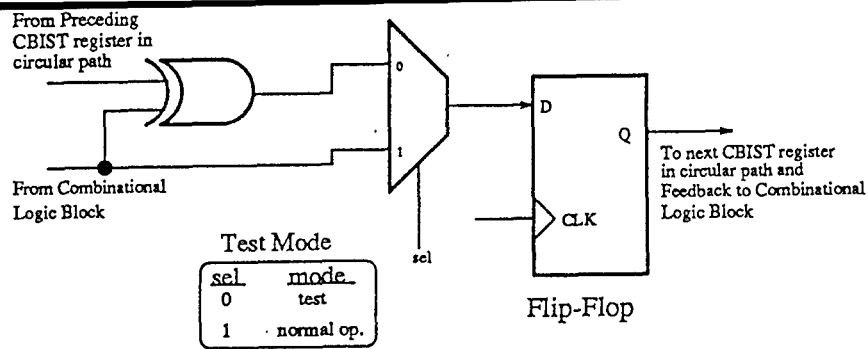


Figure 19: Single cell of CBIST.

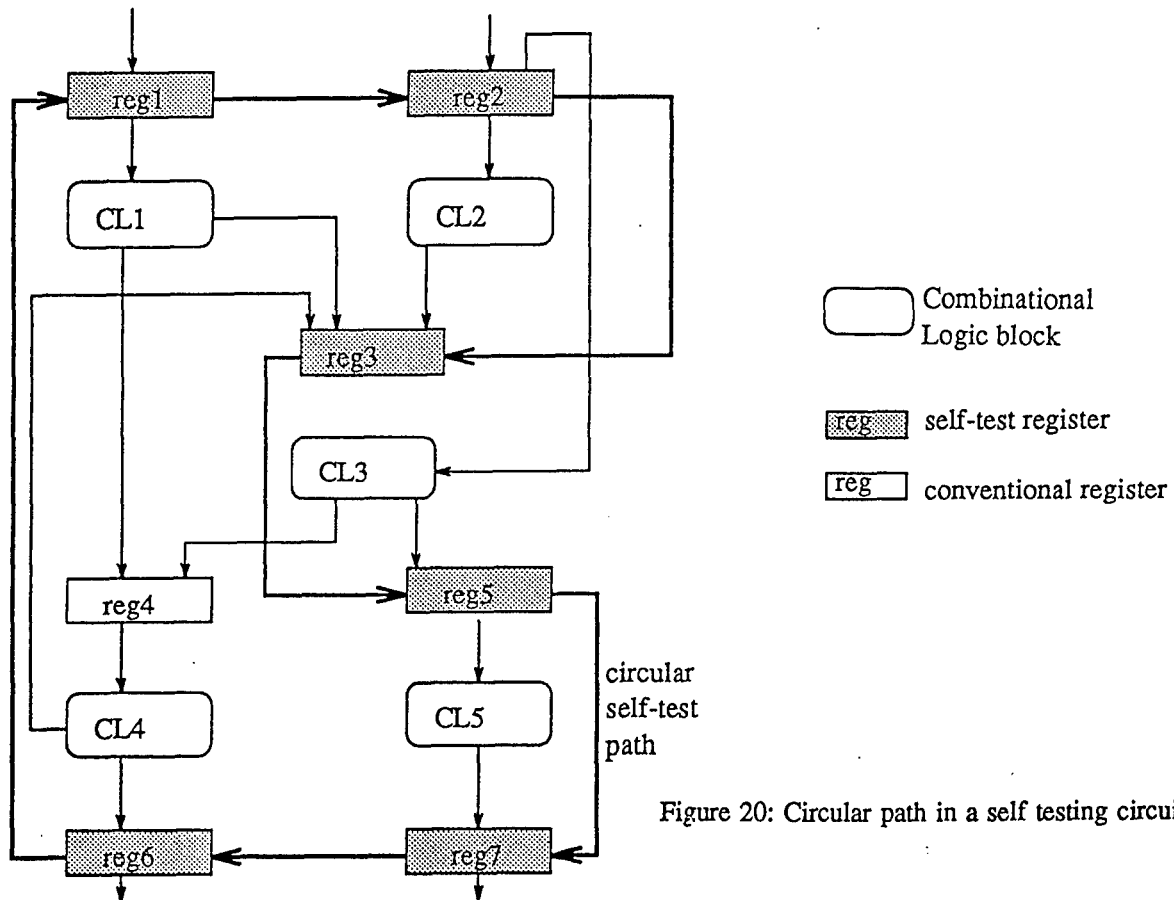


Figure 20: Circular path in a self testing circuit.

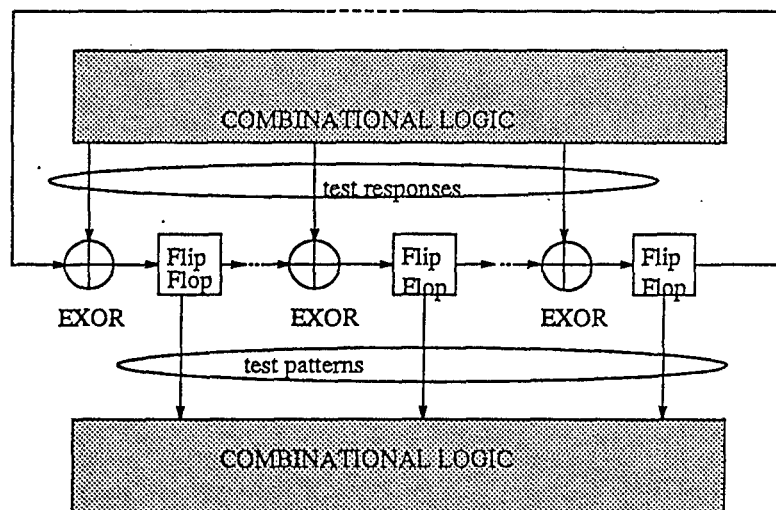


Figure 21: Circular self test path in test mode.

- the CSTP technique lends itself very well to design automation.

A cell of the circular path implements parallel load for normal operation and data compaction for testing. A scan is used only when there is no reset signal available. In sharp contrast to a multifunctional BILBO that requires complex mode switching, circular self test path offers a fairly simple circuitry. Notwithstanding the advantages of simplicity of design and cost effectiveness, major concern about the CSTP technique is the quality of testing. The quality of self testing circuit depends upon two factors:

- efficiency of test pattern generation,
- efficiency of test response compaction.

A linear feedback shift register consists of flip flops connected as shift registers and XOR gates which allow output of certain cells to be fed back to the input cell of LFSR. A n stage pseudorandom pattern generator will generate $2^n - 1$ non zero, non repetitive patterns. Such a generator is often used to test VLSI circuits. The test patterns produced by the circular path are neither pseudorandom nor purely random. This is because the patterns generated depend upon the functionality of the circuit under test. Another problem associated with Circular Built-In Self-Test is aliasing where the faulty response is the same as correct response. This problem is particularly serious because the characteristic polynomial of the circular path, $1+x^k$, is a nonprimitive polynomial which makes compaction less efficient. However, the length of the compactor is higher than those of the conventional signature registers. Also, as the whole circuit is tested in one session the number of responses that are compressed is high. This makes the aliasing probability low.

Using CBIST technique in linear tree subsystem, the total number of equivalent faults is 5,862 and the test patterns required for testing the linear tree is 286. The fault coverage is 100%. All the D flip-flops need to be changed to CSTP registers.

2.3.3 Circular BIST with Partial Scan

Most of the scan design require the decomposition of a circuit into a purely combinational part and a scan path. At times such a division may not be possible due to the presence of asynchronous flip flops or the because of the extra cost involved in implementing it. To circumvent this problem, incomplete scan design has been proposed. In this method only a few selected flip flops are chained in a scan path. In a full scan the

remaining circuit after the removal of scan path is purely combinational. However, in partial scan the remaining circuit after removing the scan path is still sequential. The following factors must be kept in mind before implementing partial scan:

1. The scan connection in the scan path must be used as a source of information and not as a point to receive information.

2. Whether or not a flip flop should be linked into a scan path depends upon the following rules:

- All flip flops that are easily controllable and observable from primary input and output need not be included in the scan path.

- Flip flops that are not easily accessible must be linked into the scan path.

- When easily controllable asynchronous flip flops cannot be linked into the scan path, they must be at least isolated from the influence of the scan path.

Partial scan techniques have been employed to test the sequential circuits with high fault coverage and reduced overhead. The flip flops selected for partial scan can be chosen on the basis of testability analysis or by using functional vectors in conjunction with a combinational test generator. It is believed that flip flops in a loop have poor controllability and observability. Some circuits can be easily handled by a test generator while others may take enormous computation time. It has been found that the test length is related to the cycle length defined as the maximum number of flip flops in a feedback cycle. The longer the test length the longer it takes to generate the test vectors.

The approach is first to implement the circular BIST capability into BISTDaTA to provide a low cost BIST alternative. All the blocks in the circuit are tested in one session. Secondly, the undetected faults as the results from circular BIST are reported to the user. Then, a "minimal" set of flip-flops are selected by the system to perform as scan registers. The test generation for partial scan design is then performed, which will report the necessary test patterns to detect all possible undetected fault as results from the circular BIST only. The clock of these scan flip-flops is given a separate control to allow insertion of scan sequences between the vector sequences produced by test generator. For a large circuit, we anticipate the use of less than 5% of the available flip-flops for partial scan to supplement circular BIST.

2.4 ASIC Design Tool Analysis

LSI Logic's CMDE system is an extensive set of software tools and technology libraries that support logic and system-level design, chip planning, layout, circuit performance analysis and design-to-production verification. CMDE system is an extensive set of software tools and technology libraries that support logic and system-level design, chip planning, layout, circuit performance analysis and design-to-production verification.

The VHDL Parser translates the VHDL description of the digital system to LSI Logic's NDL format which can be read by CMDE graphic interface schematic editor, *LSED*. *LSED* generates the schematic logic diagram of the digital design. On the other hand, the designer can use the *LSED* to design the logic schematic of the digital system. *LSED* generates the NDL format from the schematic for CMDE compilation. After CMDE compiles the NDL netlist and generates internal representations of the circuit, the simulation, verification and performance analysis will start. A waveform editor, *LWAVE*, is a graphic interface tool that enable the designer to input the test patterns graphically and then examine the response of the design. The input test signals generated by *LWAVE* will be used for simulation in normal, worst and best cases under commercial, industrial and military conditions. During simulation, CMDE can perform the delay prediction, can support multiple time block simulation as well as multiple version simulation.

CMDE design system is integrated with BISTDaTA and OLYMPUS to perform testability synthesis. The result of area estimation, floor-planning, critical path analysis and delay analysis by CMDE design system will be feedback to the BISTDaTA for the synthesis of the BIST design. The generated testable design by BISTDaTA will be input to the CMDE for analysis.

3. CONCLUSIONS

Figure 1 describes an overview of the relationship between VTST and other VLSI design systems. The VHDL Parser provides the link between VTST and other systems. BISTDaTA is a design for testability system which will take the given design and synthesize it into a self-testable design meeting the testability requirements such as hardware overhead, fault coverage, and total self-testing time. LAGER IV is a synthesis tool which will read in the SDL format generated by the VHDL Parser and produces the physical layout via

the layout generator. The physical layout format can be translated to a CIF file for chip fabrication through MOSIS. LAGER IV also includes a logic simulator named IRSIM to evaluate the functionality of the design, and provides standard cell libraries for the VLSI hierarchical design use.

For the use of VTST with other commercial tools, designers can choose their own preferences. VTST is compatible with several major commercial CAD tools: Synopsys, COMPASS, LSI Logic's CMDE and Mentor Graphics. The EDIF format for fabrication can also be generated through these tools.

4. REFERENCES

[Chen 89] C.-I. H. Chen and G. E. Sobelman, "An Efficient Approach to Pseudo-Exhaustive Test Generation for BIST Design," *IEEE International Conference on Computer Design*, pp. 576-579 (1989).

[Chen 91a] C.-I. H. Chen, "BISTSYN - A Built-In Self-Test Synthesizer," *Proc. of IEEE International Conference on Computer-Aided Design*, PP. 240-243, (1991).

[Chen 91b] C.-I. H. Chen, "Graph Partitioning for Concurrent Test Scheduling in VLSI Circuit," *Proc. of 28th IEEE/ACM Design Automation Conference*, pp. 287-290, (1991).

[Chen 92a] C.-I. H. Chen, J. Yuen and J. Lee, "Autonomous - Tool for Hardware Partitioning in a Built-In Self-Test Environment," *Proc. of IEEE Int. conf. on Computer Design*, pp. 264-267, (1992).

[Chen 92b] C.-I. H. Chen and J. Yuen, "An Efficient Approach to Pipeline Scheme for Concurrent Testing of VLSI Circuits," *Proc. of IEEE International Symposium on Circuits and Systems*, pp. 256-259, (1992).

[Chen 92c] C.-I. H. Chen and J. Yuen, "Concurrent Test Scheduling in VLSI BIST Environment," *Proc. of IEEE International conference on Computer Design*, PP. 256-259, (1992).

[Chen 93] C.-I. H. Chen and J. Yuen, "Logic Partitioning to Pseudo-Exhaustive Test for BIST Design," in *Proc. of IEEE/ACM International Conference on Computer-Aided Design*, pp. 646-649, (1993).

[Krasniweski 89] K. Krasniweski and S. Pilarski, "Circular Self-Test Path: A Low Cost BIST Technique for VLSI Circuits," *IEEE Trans. on CAD*, PP. 46-55, Jan., (1989).

**STUDY OF PART QUALITY AND SHRINKAGE
FOR
INJECTION MOLDED AIRCRAFT TRANSPARENCIES**

**Joe G. Chow
Associate Professor
Dep. of Industrial and Systems Engineering
Florida International University
Miami, FL 33199**

**Final Report for
Summer Research Extension Program**

**Sponsored by

Air Force Office of Scientific Research
Bolling AFB, Washington DC
and Florida International University**

December 31, 1993

**STUDY OF PART QUALITY AND SHRINKAGE
FOR
INJECTION MOLDED AIRCRAFT TRANSPARENCIES**

Joe G. Chow

Associate Professor

**Department of Industrial and Systems Engineering
Florida International University**

Abstract

The directly formed frameless transparency program was initiated by WL/FIVR to improve design efficiency and reduce manufacturing costs for aircraft transparencies. The specific goal is to develop the technology necessary to design and fabricate a frameless transparency using a low pressure, long cycle time injection molding process. As part of this effort, a total of 145 confirmation frameless transparencies (CFT) were molded at Envirotech Molded Products in Salt Lake City, Utah. Visual inspections, several types of testing, and measurements have been performed on the molded CFTs to identify the best combinations of molded quality and process conditions. Experimental results indicate that the injection molded transparencies have better material and optical qualities and higher dimensional accuracy than F-16 canopies manufactured by the current bent-from-sheet method. To reduce future development effort for the mold design and process development, an analytic simulation using C-MOLD software was conducted. The simulation results were compared to the CFT experimental data. The effectiveness and limitations in simulating large thick-walled parts are also discussed.

STUDY OF PART QUALITY AND SHRINKAGE FOR INJECTION MOLDED AIRCRAFT TRANSPARENCIES

Joe G. Chow

1. Introduction

Presently, transparency panels for high performance fighter and trainer type aircraft are manufactured by bending and forming flat extruded, laminated, plastic sheets. After forming, the transparency panel is trimmed to the final shape by machining its peripheral edges and drilling fasteners holes along the edges. The panel is then bolted to metal/composite frames and attached to an aircraft frame as a windshield/canopy. This process is labor intensive, expensive, and often produces rejected parts resulting from poor optical quality. Crazes, cracks, and delamination usually originate at the machined edges and fastener holes. The transparency's dimensional accuracy tends to be poor and its service life is usually fairly limited.

WL/FIVRB initiated the "Frameless Transparency Program" several years ago to study feasibility of directly formed, frameless aircraft transparencies. This program was being developed for two related concepts: direct forming and frameless. Direct forming entails manufacture of an aircraft transparency directly from molten thermoplastic resin in one thermal process. The frameless transparency eliminates the peripheral frame by incorporating thickened sill edges of the same material as the optical area.. It also includes molded-in hardware to facilitate its attachment to aircraft. The frameless concept depends on direct forming technology and offers all of the advantages of direct forming. If proven viable, directly formed, frameless aircraft transparencies can reduce costs, extend service life, and improve performance (Ref. 1).

Technology for Frameless Transparency Program has been developed in two phases:

- A contracted study, conducted by Loral Defense Systems, identified low pressure, long cycle injection molding as a candidate for forming thick-walled and impact resistant transparent panels. To demonstrate the feasibility of this proposed method,

Loral and WL/FIVRB molded and tested sub scale flat and conical panels. This study was completed in June 1988 and its results indicated that injection molding process is a viable technology for producing large, thick-walled, transparent parts.

- Develop technology required to design and fabricate directly formed, frameless transparencies. The emphasis of this phase has been the development and validation of analytical design package (ADP), an integrated design tool for aircraft transparencies. This phase also includes design of a confirmation frameless transparency (CFT), fabrication of a mold, molding and testing of the CFT, and utilizing test data to confirm the ADP.

This research, CFT molding and testing, is one of the tasks in the second phase. The objective of this study is to further explore the feasibility of direct forming the aircraft transparency. The specific goal is to mold frameless transparencies that possess part quality and material properties superior to those of transparencies produced by the current bent-from-sheet method. This can be achieved by identifying optimum molding conditions that are capable of producing excellent molded quality and material properties. Also, analytical simulation of injection molding using C-MOLD was carried out to illustrate how these simulations can be utilized to eliminate the need for trial-and error in mold design and process development. The discrepancies between existing simulations and the specialized process needed to produce aircraft transparencies are also identified.

2. CFT Molding and Testing

The molding trials were performed at a custom molder: Envirotech Molded Products, Salt Lake City, Utah. Premolding tasks, such as simulating the process using C-Mold, testing the H/C system, and calibrating thermocouples and pressure sensors, started in June of '93. The molding trials and on-site testing began in early September and were completed in late October. The experiment and testing were conducted by the Air Force Molding Team made up of personnel from Wright Patterson Air Force Base, University of Dayton Research Institute, Lockheed, and the principal investigator. The following paragraphs provide background information and the details of the CFT molding trials and testing procedure.

2.1 Process background

Part geometry

The part geometry for the molding trials is shown in Figure 1. The overall CFT dimension is approximately 49 " long, 32 " wide and 22" tall. The CFT is the first transparency to be designed, fabricated, and tested under the FTP. Although it was not designed as an actual flight item, it approximates the forward half of the F-16 A/C transparency. The CFT consists of a nominal three-quarter-inch optical section with two inch thickened sill edges. The thickened edges would permit four molded-in aluminum inserts to latch the transparency to a simulated aircraft sill plane. Also, the CFT incorporates a thickened aft edge that will provide structural stiffness and represent a windshield/canopy interface.

Molding Machine

The molding was conducted on one of the newest and largest injection molding machines at Envirotech Molded Products. The machine, possessing excellent computer controls, has the following dimensions and capabilities:

Injection capacity :	400 bounds
Platen size:	96 in by 120 in
Max. injection press:	2,000 psi
Screw diameter:	3.5 in

The machine uses an accumulator to store the molten resin for the next injection. Therefore, molten resin that went in the accumulator first was pushed out last. This has effectively increased residence time in the accumulator for some resin and would degrade polycarbonate quality. Thus, residence time has become a critical factor in determining CFT's molded quality.

Transparency Material

In previous moldings of sub scale panels, different materials from several manufacturers, such as GE's Lexan PPC-4701, Mobay's DP 9-9350, Dow's Calibre 300-06, Calibre 200-04, and Calibre 300-04, have been used. Dow's Calibre 300-06 was selected as the resin for molding CFTs based upon performance in molding, drop impact tests, insert pullout tests, material tests, and availability.

Mold Design

A single cavity collapsing mold was designed and fabricated for the molding of CFTs. Figure 2 shows photographs of the mold cavity and core, respectively. A 2.75 inch diameter sprue bushing is transitioned to the shape of the most forward CFT cross section by a single fan gate. Since the interior of the CFT "wraps around", sliding blocks are used in the mold core to provide clearance for its removal from the mold. Based on experience in molding sub scale conical panels, the mold cavity thickness was tapered to correct for the effects of nonuniform shrinkage (Ref. 2). A constant scale factor was also used to size up the mold cavity uniformly to account for thermal expansion effects. The objective of mode cavity sizing is to produce a constant thickness optical area and CFT design dimensions.

The CFT mold was made of solid billets of P20 tool steel. The cavity surface was polished to a 1200 diamond paste mirror finish. Cavity surfaces were hardened by ion nitriding for durability. Blocks for retention of latch and threaded inserts were fitted into the mold core billet. These blocks secured inserts during injection and were removed from the mold with the CFT. Thirty seven channels were drilled for heating/cooling (H/C) oil to control the temperature of the mold. A total of 33 thermocouples and 8 pressure transducers are located in cavity, core, slide, and slide mechanism billets to monitor mold cavity temperatures and pressures.

The H-C system developed for the CFT has the capacity for independently heating and cooling eight mold zones. The temperature in each mold zone can be set at a value anywhere between 37 and 500 deg F. Set temperatures and temperature ramps are achieved for each mold zone by a feed back control system. As many as eight temperature ramps can be programmed for each of the eight mold zones during the molding cycle. Programming, control, and monitoring of the H-C system were accomplished by a series of virtual instruments within LabView software residing on a Macintosh computer. The LabView system continuously recorded output from each

of the mold thermocouple and pressure sensors. Data from these sensors can be used to assess causes for molded transparency defects and the effects of cycle changes on the quality of molded parts.

2.2 CFT Molding Trials

The molding experiment was divided into the following two phases :

Phase 1: Process Development Molding

A total of 145 parts were molded in four series. The first 120 injection molding "shots" conducted in the first 3 series were devoted to the development of an optimum molding process for forming the CFT. During this molding phase, process parameters, such as injection pressure, packing pressure, packing and cooling times, and mold temperatures, were varied and resulting molded CFTs inspected and tested at the molding site to assess effects. The optimum molding condition for molding the CFT is listed as follows:

Injection pressure:	1,000 psi
Packing pressure:	1,900 psi
Melt temperature:	575 deg F
Filling time :	40 second
Packing time:	19 minutes
Cooling time:	10 minutes
Mold temperatures	200-310 deg F

Phase 2: Test Item Molding

The optimum molding condition identified in the first phase was used to mold an additional 25 CFTs in the 4th series. These CFTs will be subjected to off-site testing and measurements such as bird strike impact resistance testing and CMM dimensional mapping (Ref 3).

Molding Cycle

Before each shot, the dried resin was first melted and stored in the accumulator. When molding began, the piston in the accumulator pushed the molten plastic into the mold cavity through the sprue bushing. A constant pressure of approximately 1000 - 1900 psi was applied during the filling time of 35- 54 seconds. At the end of filling, the packing pressure of 1000-1900 psi was held constant for about 1200-2000 seconds. This was then followed by cooling until the part was sufficiently rigid to be removed from the mold. After the part was removed by the part removal system, the mold was closed again to begin the next injection cycle. The cycle clock for the molding is shown in Figure 3.

2.3 CFT On-Site Testing and Measurements

During process development molding, each molded CFT was tested to assess the effects of process changes and to evaluate CFT quality, repeatability, and performance. The results of this testing were used by the molding team to direct the evolution of the CFT molding process. The on-site testing and measurements include the following:

Inspection and evaluation Visual inspection were conducted by looking at, and through, the transparency and noting surface quality (gel spot, orange peel, etc.) internal defects (black specs, bubbles, etc.) and signs of polymer degradation. A single grading value was assigned for each molding defects and the overall quality.

Measurement of overall dimensions. Dimension measurement using instruments such as height gauge and caliper were made on every process development CFT. These measurements consist of lengths and widths at various locations. This data can establish conformance to design and repeatability, and can be used to evaluate methods for sizing the CFT mold cavity.

Drop dart impact testing This test was to establish the impact resistance of molded material after each CFT had reached ambient temperature. Six inch square coupons were cut from four CFT locations, held in apparatus which matched the local curvature of each coupons, and subjected to the impact of a 60 pound dart dropped from heights up to 22 feet. Coupons were subjected to impact on both inside and outside CFT surfaces.

Micrometer measurement of thickness at the edges of drop dart test coupons This data was indicative of actual thickness distribution in the CFT optical area. Data was compared to mold cavity thickness distribution based on dimensional mapping of the mold cavity and core. The effectiveness of the WL/FIVR method for shrinkage distribution in mold cavity design was assessed.

Optical distortion mapping The mapping was conducted utilizing an on-site optical test fixture (OTF) (Ref. 4). Angular deviations in azimuth and elevation were measured over the CFT optical surface from the designer's eye point. An F-16 canopy was also tested and compared to CFT data.

Light transmittance and haze This test was conducted for drop dart coupons before impact. Effects of process changes was assessed.

3. Results and Discussion

One of the unique characteristics of the CFT molding process is that low pressure was used to inject the molten plastic into the mold. The injection pressures used in the trials are shown in Figure 4. The main advantage of molding the part at low pressure is that the clamping pressure would also be lower. Thus, for a given clamp capacity, much larger parts can be molded. Low injection pressures require that the molds be heated to produce a smooth surface finish. This results in very long cycle times required to cool the part and to pack in additional material as the part shrinks. With a long cycle time (30 to 60 minutes), the hot mold is a natural annealing fixture; therefore, large, thick-walled parts will have lower molded-in-stress.

The experience of most molders with large thick-walled parts is that thick sections tend to have sink marks and/or voids especially where flow is from thin to thick sections. This is because thick sections take more time to solidify and shrink more than thin sections. This experiment showed that by choosing a packing pressure that is higher than the injection pressure, one can force more material into the mold cavity and greatly reduce sink marks and voids. The packing pressure chosen in these trials are also displayed in Figure 4.

In addition, the mold temperatures were also varied to reduce sinks and other defects. Figure 5 shows the zone temperatures for data collected during the last

series. Mold temperatures in zones 7 and 8, located near the thickened sill edges and aft plane, were lowered to remove the heat from the thickened sections. The temperatures in zones 1, 4, and 5 were raised up to 310 deg F to promote filling and surface quality and to make the gate area stay hot for a longer period of time. This would avoid premature freezing of the gate which would prevent additional resin from going into thickened edges during packing. During cooling, the temperatures in all zones were lowered down to 160 deg F for part removal. As the mold opened, the zone temperatures were heated back to the initial values, making it ready for the next cycle.

Other defects that are usually encountered during molding of the small thin-walled parts, such as splay, orange peel, surface slips, gate blemish, gel spots, brown streaks, voids and black specs were also observed in the trials. However, by choosing molding parameters intelligently, most of the defects could be minimized or eliminated. As a result, the overall quality for the CFTs molded during the 4th series are better than the ones produced during the first 3 series. This comparison can be seen in Figure 6. However, one of the defects, black specs, was always present in the molded parts. This can be attributed to polycarbonate sensitivity to the effects of prolonged heating in the accumulator, which can only be eliminated by using different machine designs.

One of the main advantages for injection molding is that the part dimensions can be repeated and closely controlled. Figure 7 shows the overall length (L19) and the sill-to-sill width at the aft arch (W1) for the CFT. The nominal values for these two dimensions are 46.8 "and 23.85", respectively. The discrepancies between measured and nominal values are fairly small, compared to those for F-16s. Also the parts molded using the optimum condition have more accurate and repeatable dimensions, in comparison to those molded in the first 3 series .

The micrometer thickness for typical data collected during the 4th series is shown in Figure 8. Four coupons were cut from the part and measured with the micrometer. The results indicated that the mold cavity thickness data at the first 3 coupons (A, B, and C) are generally oversized , but not more than by 0.010". This variation is better than the one seen in the bent-from-sheet canopies which may have as much as 0.020" variation. The thickness data for the coupon D is significantly larger than the desired value 0.75", probably caused by

overcompensation for the nonuniform shrinkage during mold cavity sizing. The CFT thickness distribution will be dimensionally mapped using a CMM and an in-depth study will be initiated to determine the CFT shrinkage pattern.

A comparison of angular deviations for the elevation component for both a CFT and a F-16 is shown in Figure 9. The OTF plots show that the deviation contours for CFT are more widely spread in the optical area, especially in the HUD area where the pilot looks out to target an object. As a result, the pilot will experience less distortion with a CFT. In contrast, contours in the F-16 are much closer together, concentrating on three bands. In particular, there is a sign change between the contours in the lower band and the ones in the middle. This change of sign in the deviation contours will make the object first appear higher than it actually is then look lower than its actual position or vice versa when the pilot's line of sight moves up or down in that region. This result clearly indicates that the CFT possesses better optical properties than the F-16 canopy.

Most panels successfully passed the maximum testing capacity of the drop dart test, 1320 ft-lb. A few failed due to poor selection and setting of used molding parameters. When F-16 laminated coupons were tested under the same condition, some coupons either cracked or fractured. One can thus conclude that the molded CFT panel is tougher than the F-16 laminated counterpart. However, to find out its resistance to a object flying at a high speed, the CFT panels need to be tested using a birdstrike impact resistance testing apparatus

4. Simulation of CFT Molding

Mold design is an iterative process. Complexity and cost of injection molds dictate that the molding process and inputs to the mold design should not be built by trial and error. By using CAD software, preliminary mold design parameters can be evaluated on computer instead of doing expensive and time consuming molding trials. In this research, analytical simulations were carried out to determine their effectiveness in predicting the experimental results and designing the future mold for full scaled aircraft transparencies.

The software currently being used by WL/FIVRB in the development of direct forming technology is a commercial off the shelf package, C-MOLD, available from

At the end of the filling stage, the entrance pressure predicted by C-FLOW is of the same order as that read off the molding machine.

C-PACK

C-PACK simulates the entire molding process including fluid flow and heat transfer within the polymer as the resin fills the cavity, solidifies during the packing process, and cools to a temperature suitable for part removal from the mold. Mold wall temperature is not varied during the C-PACK analysis. As an example of C-PACK output, Figure 12 shows temperature variation through the thickness of CFT nodes at 1040 seconds into the cycle time. A much higher temperature exists at the center of the 2 inch thick aft arch than at nodes in the optical area where the thickness is .75 inches. Also it is obvious that the packing pressure should not be removed at this time since the aft arch has not cooled significantly.

C-PACK can also be used to predict sinks and voids in the molded parts. During the post-filling stage, additional material is packed into the cavity to compensate for shrinkage as the material solidifies. Sinks or voids may form as a result of insufficient resin supply. C-PACK provides a qualitative index for the prediction of such defects. Due to the transparency design and process conditions used, there is a significantly high sink-index distribution along the edge of the transparency. The high sink prediction from C-PACK was qualitatively verified by experimental observations.

C-COOL

C-COOL calculates the heat transfer coefficients for heat exchange between the mold and the coolant. In addition to this heat transfer, heat transfer within the polymer melt and heat transfer within the mold material is also considered. Heat removed by each channel is predicated and can be used to size pumps and temperature controllers. Uneven cooling when comparing cavity and core wall temperatures can be identified.

The process conditions used in the molding trials involve changing the coolant temperature during the cycle (see Figure 5). As a simulation system, C-MOLD has the capability to model independent zones in the mold, but the temperature and flow

rate of coolant is constant for the cycle and the temperature is not normally greater than the temperature for opening the mold. The assumption in C-COOL breaks down under these conditions, and a fully transient three dimensional mold-cooling analysis is needed to account for transient variations in cooling temperature. As an engineering approximation, the average coolant temperature over the entire process was used in the analysis to estimate the CFT mold wall temperature and heat-flux distribution.

Based on this on-site simulation at Envirotech, the applicability of the C-MOLD analysis modules can be classified into the following categories;

If the coolant temperature in each channel is held constant throughout the molding cycle, all C-MOLD analysis are directly applicable to this process. Since the overall linear dimensions of the CFT are much larger than its thickness, the generalized Hele-Shaw formulation for mold-filling and post-filling analyses is still applicable to this process. The melt-front-advance and pressure drop predictions should match the experimental observations closely, especially in the constant thickness optical area.

If the coolant temperature in any channel varies with time, the constant coolant temperature assumption made in C-COOL is no longer applicable to this process and a fully-transient mold-cooling analysis would be needed. Such a feature is not yet available in C-COOL; therefore, a special development effort is required.

5. Conclusions

CFT Molding and Testing

1. A low pressure, long cycle injection molding process has been demonstrated for forming thick-walled, impact resistant and transparent panels from polycarbonate resins. A typical molded CFT is shown in Figure 13.
2. The direct forming technology has many advantages: design flexibility, closely controlled and repeatable part dimensions, excellent optical and material properties, and lower manufacturing costs.

Analytic Simulation

1. Simulation of injection molding for aircraft transparencies permits identification and correction of problems related to transparency design, mold design, and process parameters during the design stage. This prevents the need for costly modification of molds and other molding hardware after they are built.
2. Commercial off-the-shelf simulation package are currently capable of simulating the filling, packing, and cooling phases of anticipated aircraft transparency injection molding cycles with steady state coolant temperatures. To simulate for varying cooling channel temperatures, special effort is required for the additional computer code development.

6. References

1. Pinnell, W. R., "Development of Directly Formed and Frameless Aircraft Transparency Technology", Conference on Aerospace Transparent Materials and Enclosures, San Diego, CA 9-13, August 1993.
2. Chow J. G. and Roach K. P., "Analysis of Transparency Panel Shrinkage Characterization and their Application to Transparency Mold Design", Conference on Aerospace Transparent Materials and Enclosures, San Diego, CA 9-13, August 1993.
3. "Molding and Test Plan - Confirmation Frameless Transparency" Technical report submitted to WL/FIVR by General Dynamics at Fort Worth Division, Oct 1991.
- 4 Robson, T. L. and Pinnell, W. R., "Optical Evaluation of Transparencies Utilizing New Test Apparatus", Conference on Aerospace Transparent Materials and Enclosures, San Diego CA 9-13, August, 1993.

CONFIRMATION FRAMELESS TRANSPARENCY (CFT)

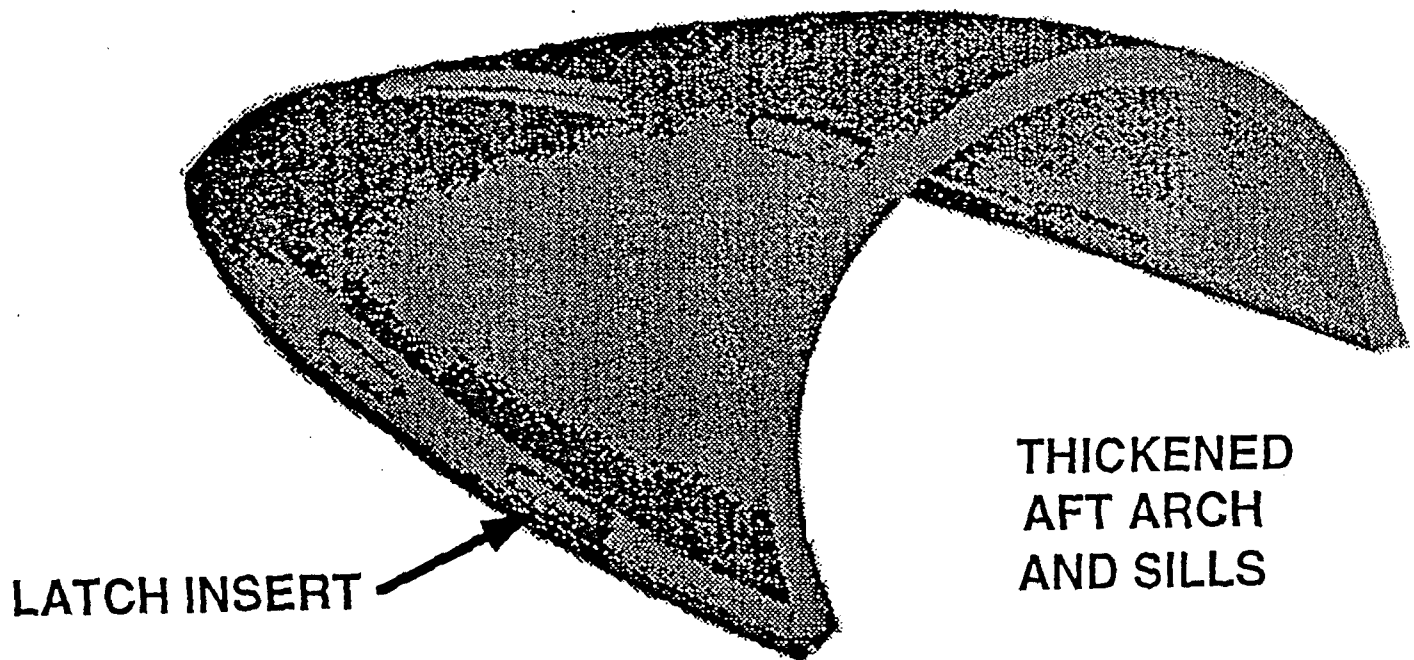
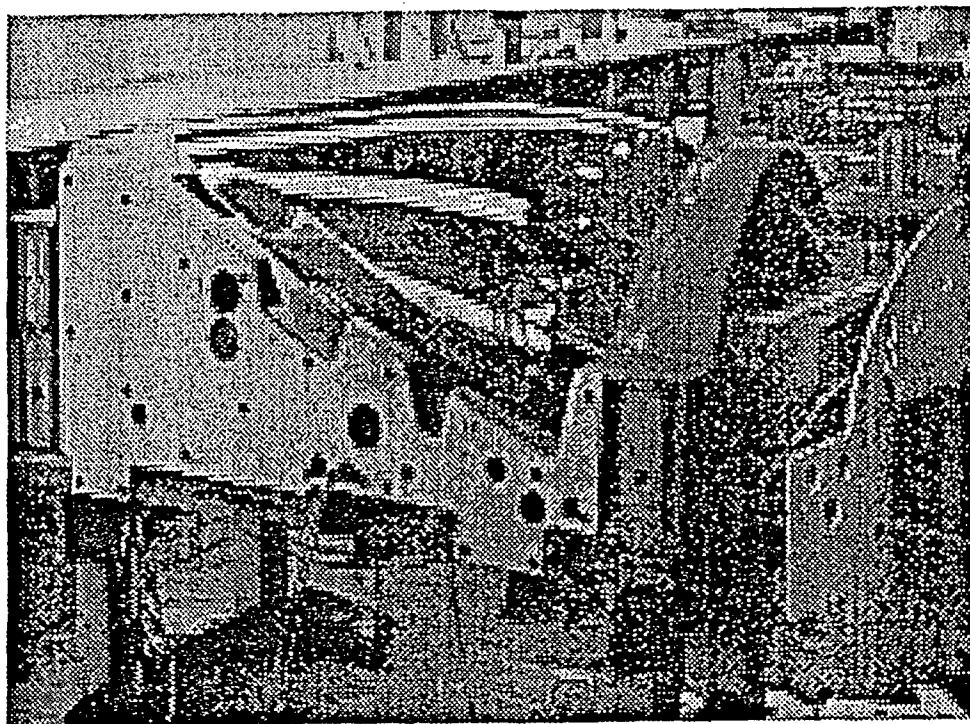
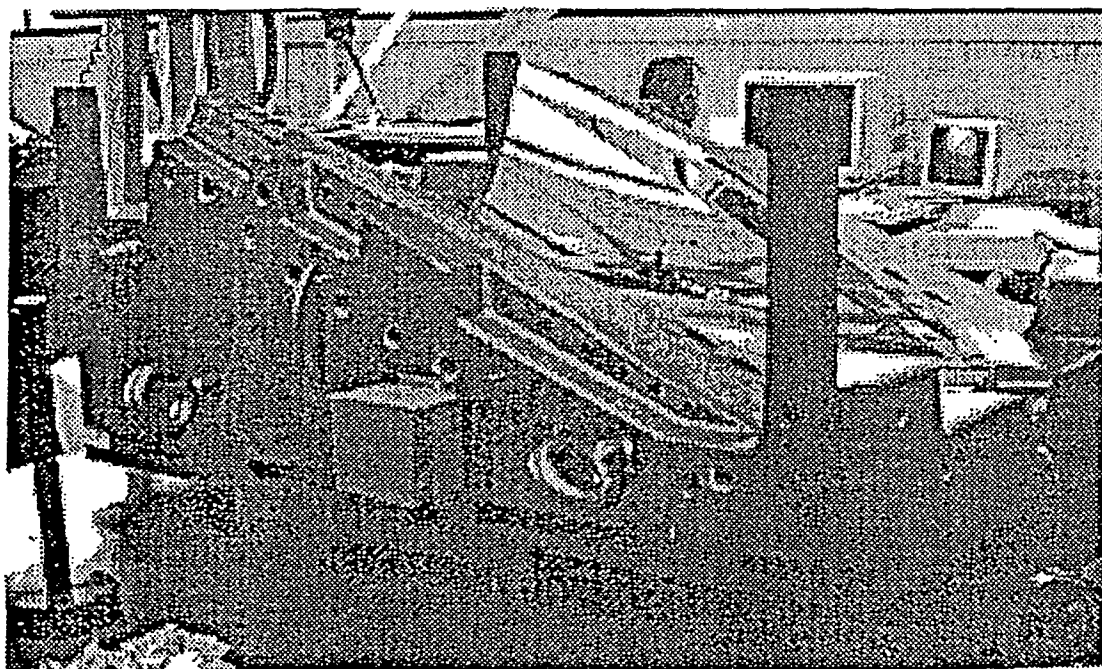


Figure 1. CFT geometry



CORE



CAVITY

Figure 2. CFT Mold Cavity and Core

TYPICAL INJECTION MOLDING CYCLE

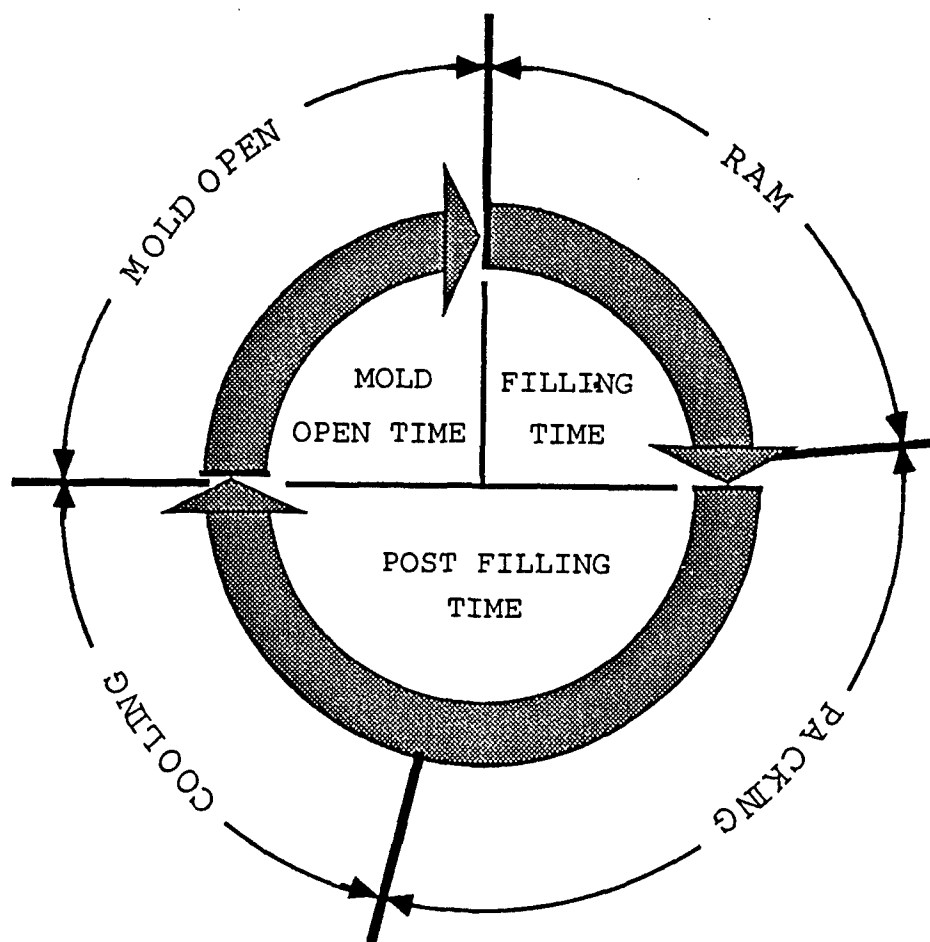


Figure 3. Molding cycle for CFT

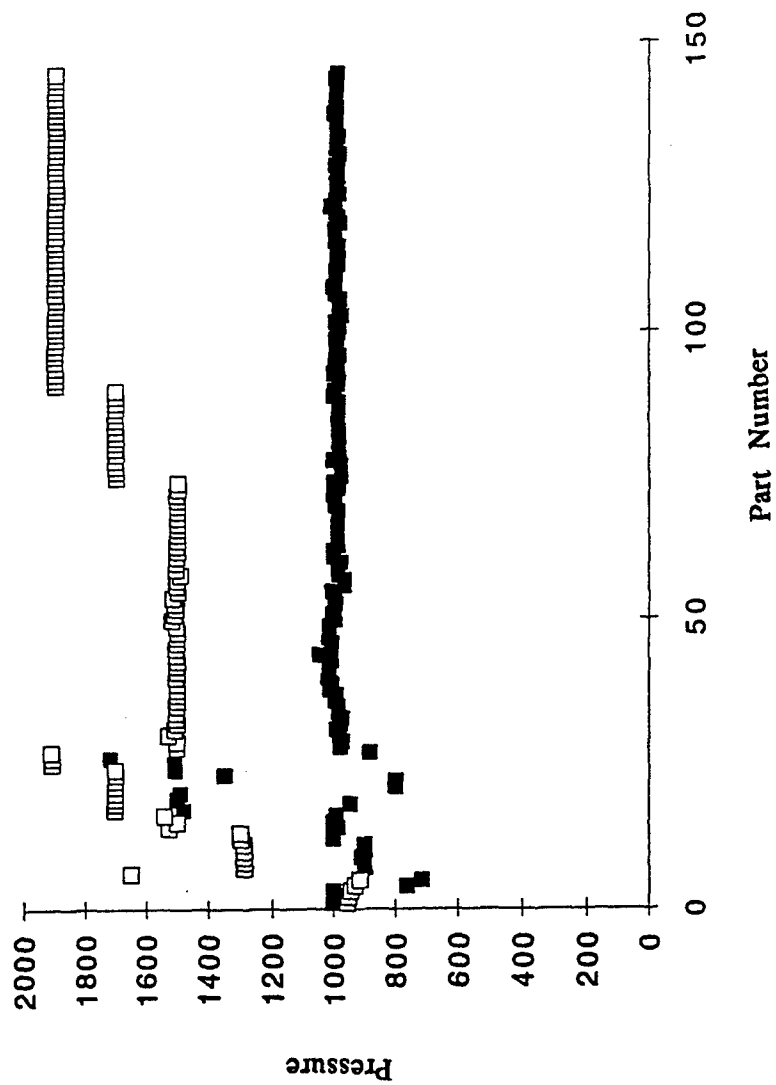


Figure 4 Injection and Packing Pressure vs Part Number

CFT SERIES 4 H-C PROGRAM

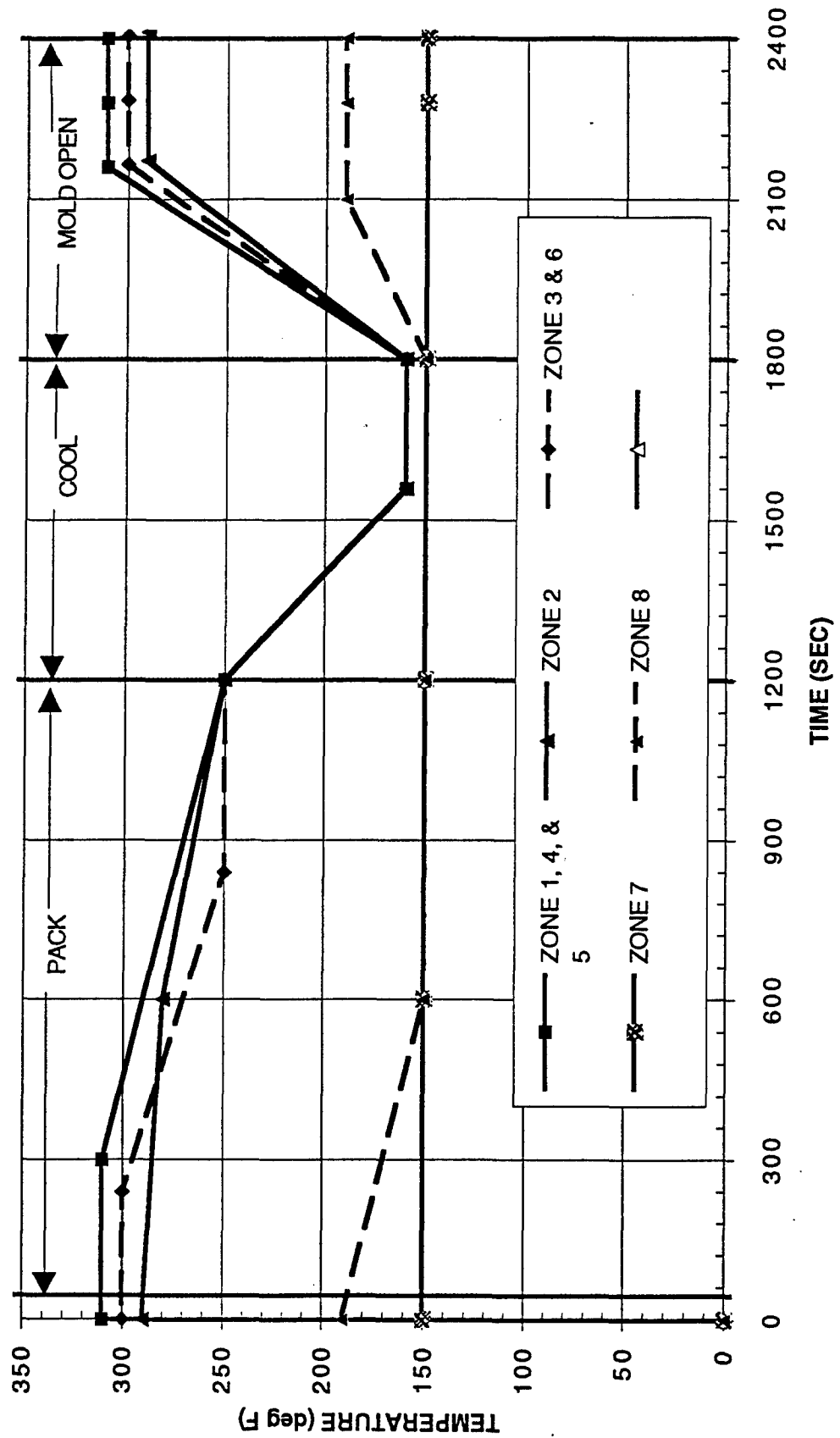


Figure 5. Mold Zone Temperatures for CFT Molded in the 4th Series

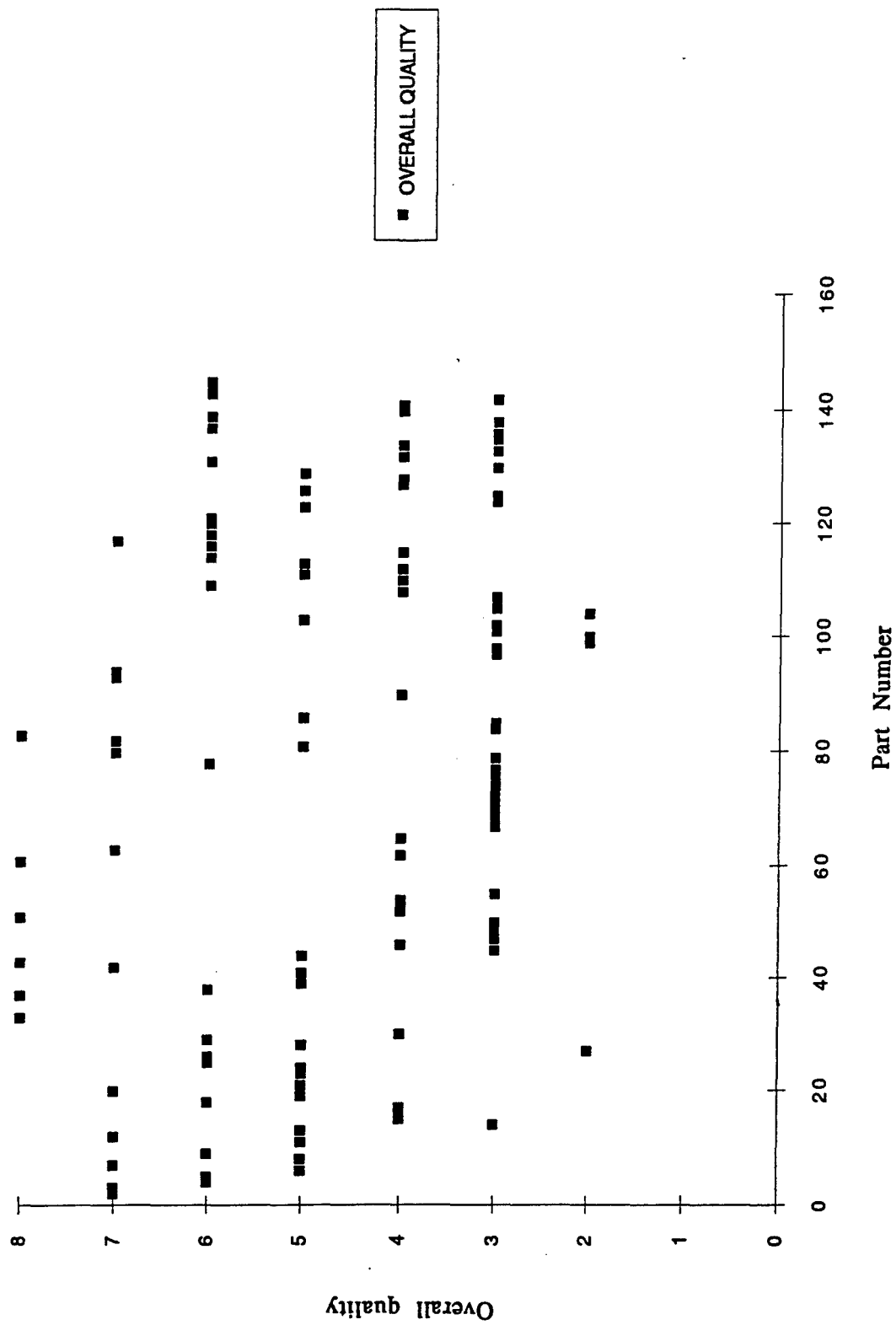
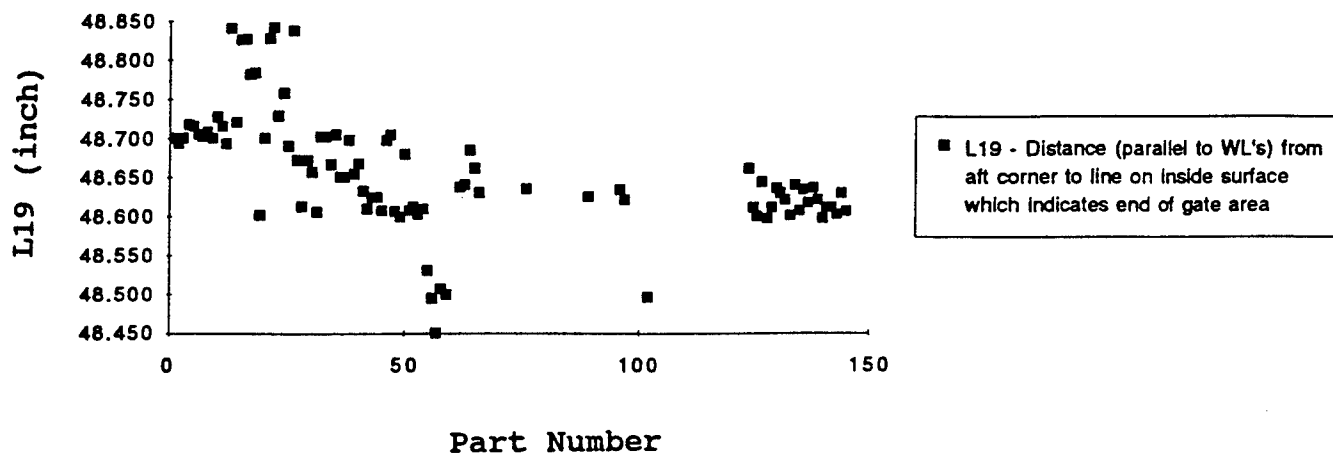
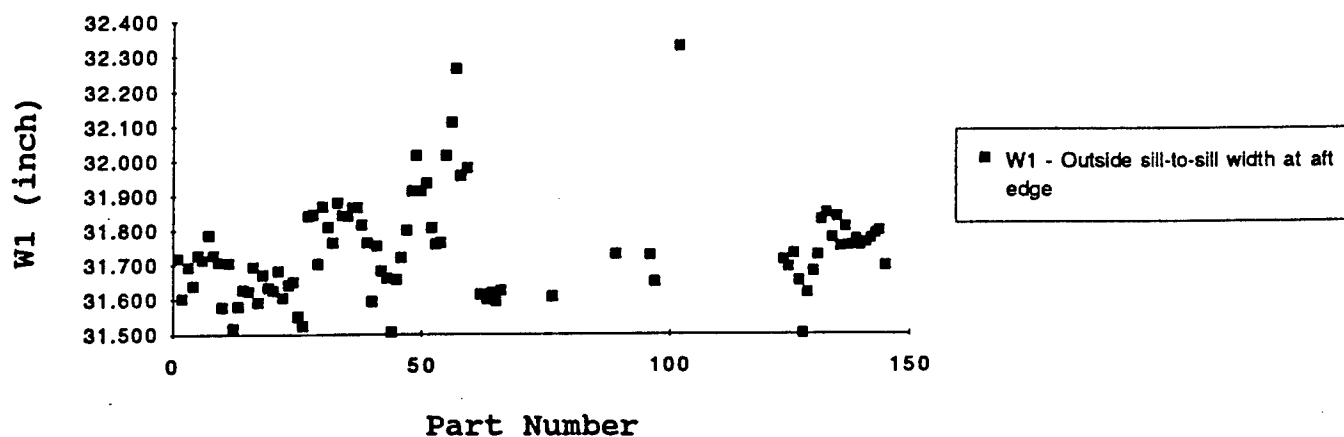


Figure 6. Overall quality vs Part Number



Overall length vs Part Number



Outside sill-to-sill width vs Part Number

Figure 7. Overall length (L19) and Outside Sill-to-sill Width (W1) vs Part Number

CFT DROP DART COUPON MEASUREMENT SHEET

Flow Direction

Coupon A, Center Line, Fwd

Thickness measurements
taken with micrometer,
and recorded to nearest
0.001".

.7542	.7580	.7571
.7557		.7574
.7581	.7607	.7589

Coupon B, Port

.7490	.7516	.7538
.7508		.7552
.7518	.7550	.7563

Coupon C, Stbd

.7565	.7551	.7544
.7577		.7552
.7589	.7588	.7563

.7634	.7632	.7658
.7666		.7680
.7686	.7686	.7696

Coupon D, Center Line, Aft

Figure 8. Micrometer Thickness Data Masurement for CFT No. 139

F-16 Canopy P/N 183100-01 S/N 492

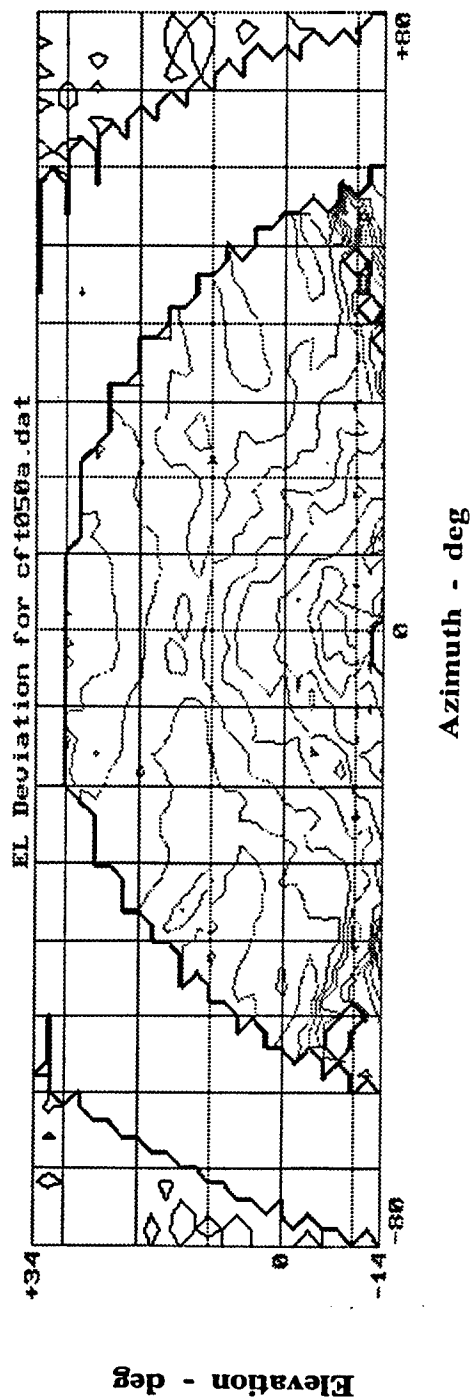
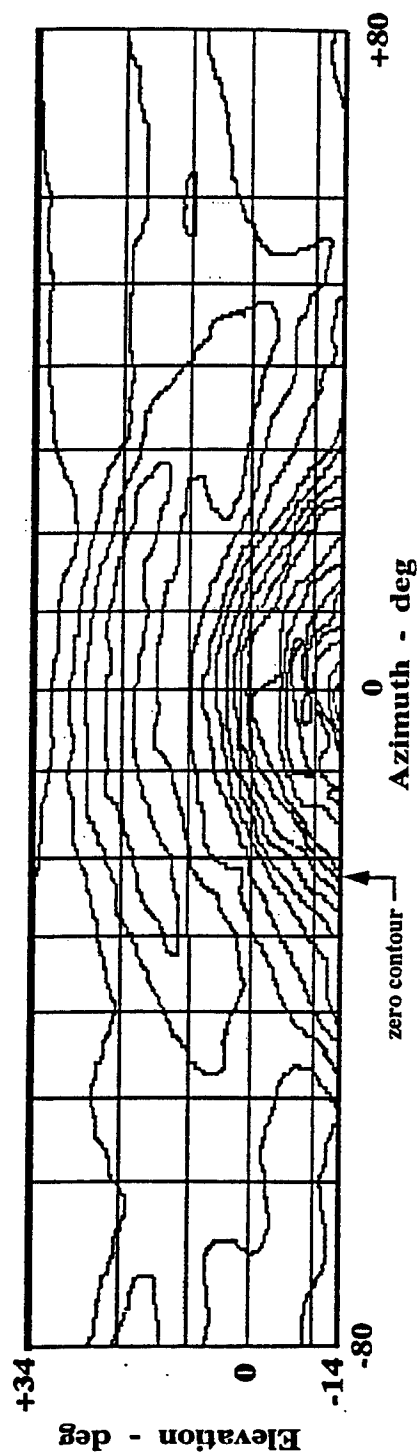


Figure 9. Angular Deviations for F-16 Canopy (top) and CFT (bottom).

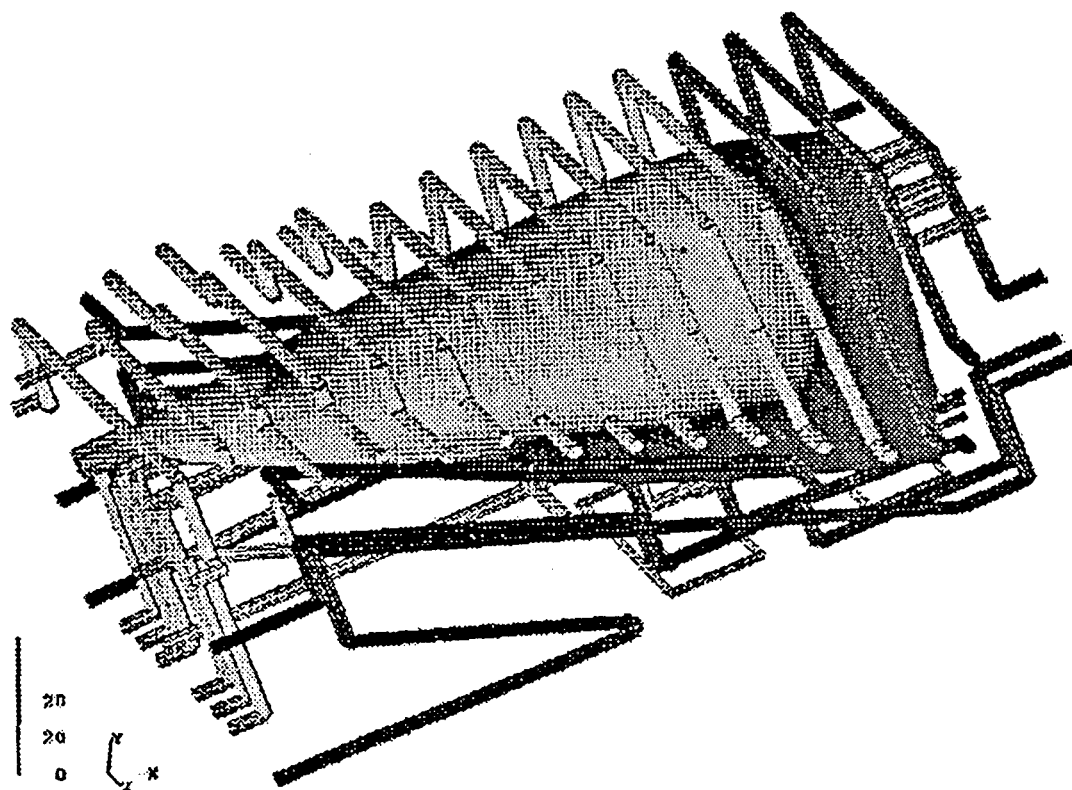


Figure 10. Simulation Model and Cooling Channel for CFT Molding

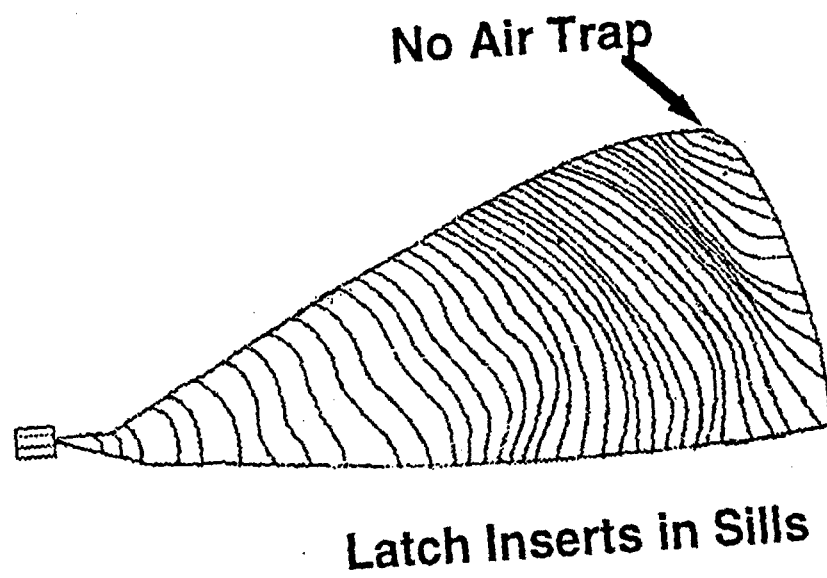
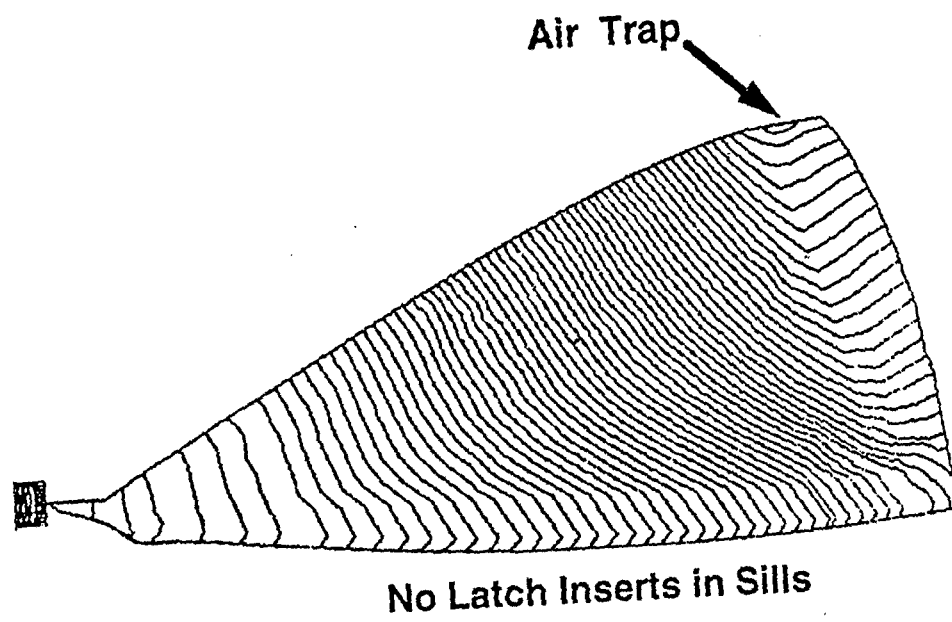
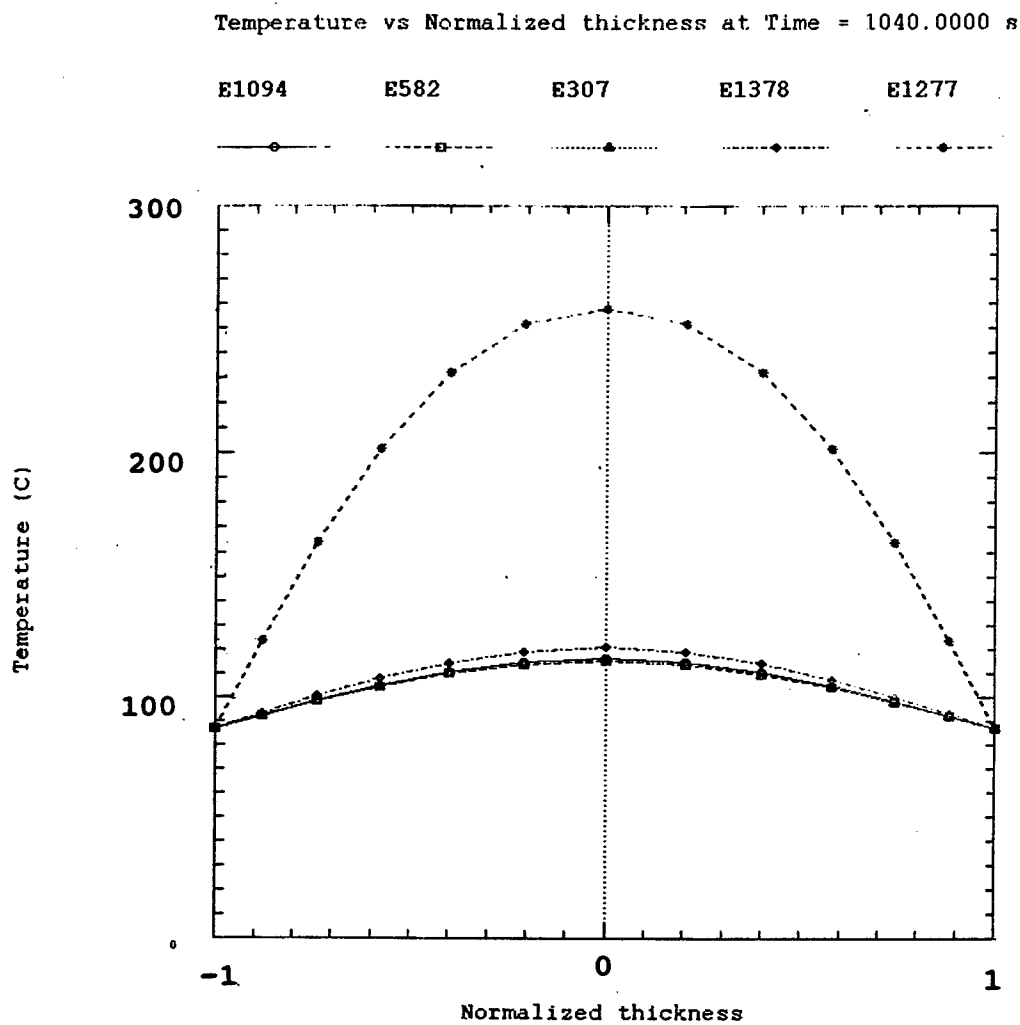


Figure 11. Flow Front Advancement without and with Inserts



Element 1277 is in the aft arch, E1094 is in the gate area, while the other three are in the optical area.

Figure 12. Temperature Profile Across Part Thickness - an output from C-Pack

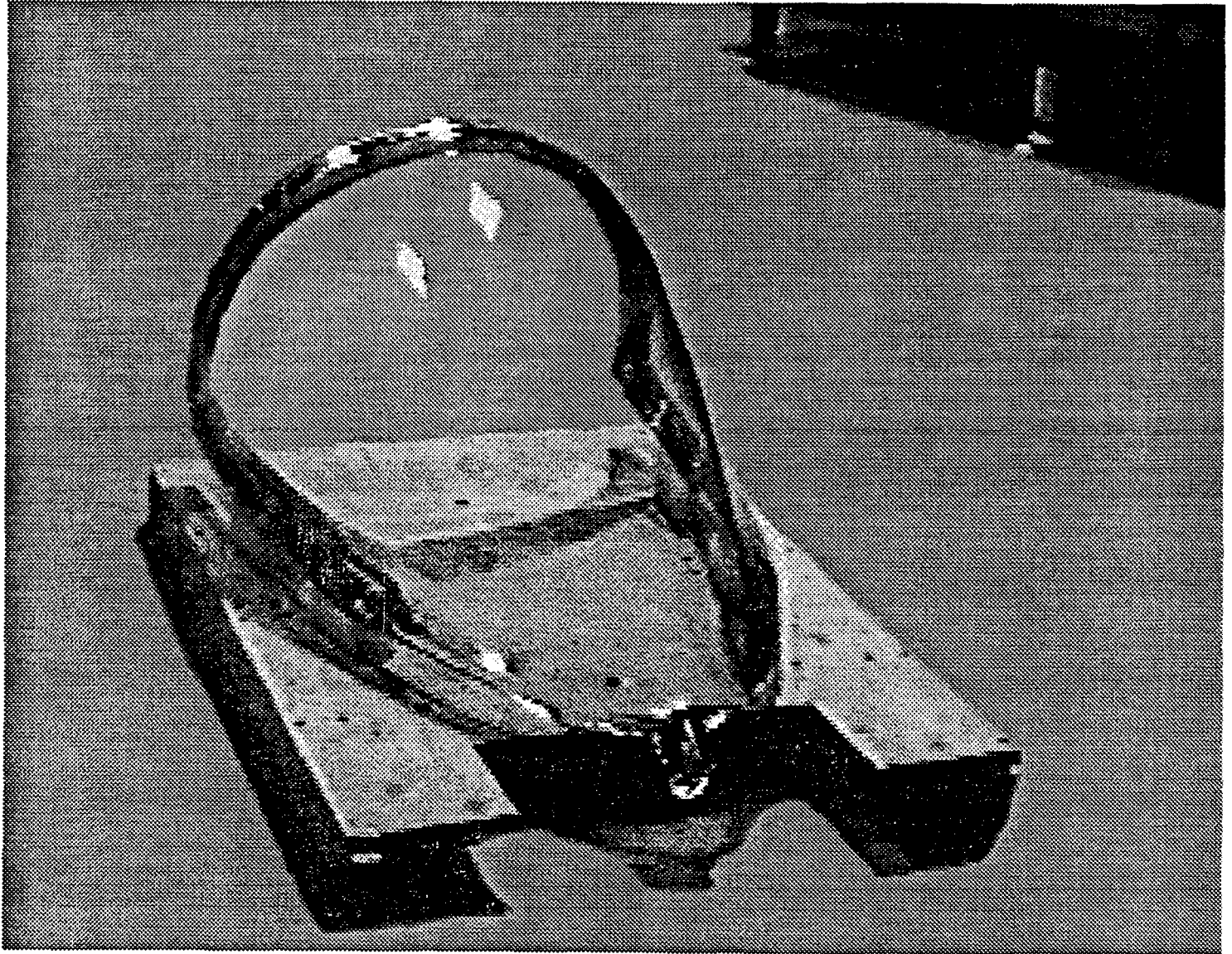


Figure 13. A typical molded CFT.

IMPLEMENTATION OF NOISE REDUCING MULTIPLE-SOURCE SCHLIEREN SYSTEMS

Steven H. Collicott
Assistant Professor
School of Aeronautics and Astronautics Purdue University
West Lafayette, IN 47907-1282

Final Report for:
Summer Research Extension Program (SREP)
Wright Laboratories

Sponsored by: Air Force Office of Scientific Research
Bolling AFB, Washington, D.C.
and
Purdue University

April 7, 1994

IMPLEMENTATION OF NOISE REDUCING MULTIPLE-SOURCE SCHLIEREN SYSTEMS

Steven H. Collicott
Assistant Professor
School of Aeronautics and Astronautics
Purdue University

Abstract

A problem exists with conventional schlieren systems in that they are sensitive to spatial density gradients in all planes along the optical axis between the source and cutoff. This effect is detrimental since spurious density gradients often create image noise which interferes with the signal being sought. Multiple-source schlieren systems seek to overcome this problem by reducing some of the volume that the system is sensitive to, or more specifically by being most sensitive to spatial density gradients within the test section. Previous research has shown that multiple-source schlieren systems reduce image noise. It is the purpose of this research to measure such effects. Noise reduction is quantified for noise occurring throughout systems with different source and cutoff grids. To accomplish this quantitative measure of noise reduction, images are digitized and two different regions of flow within these images are analyzed. Trends from these noise reduction effects are compared with theoretical predictions. These quantitative results allow the competent design of multiple-source schlieren systems with desired degrees of noise reduction.

IMPLEMENTATION OF NOISE REDUCING MULTIPLE-SOURCE SCHLIEREN SYSTEMS

Steven H. Collicott

INTRODUCTION

Schlieren systems are used for visualizing structures in flows that constitute sufficiently large amplitude spatial density gradients such as shock waves, expansion fans, and boundary layers. These systems have been successfully used for over 100 years to determine characteristics of supersonic flow structures. For the most part, these systems are used for flow visualization analysis. Deriving the most information from such images requires that clean, noise-free images be acquired. Unfortunately, low-noise images may be elusive when a conventional schlieren system is applied to certain facilities.

Conventional (single-slit) schlieren systems are sensitive to spatial density gradients outside the test section as well as inside it. In the past, these problems have been dealt with in the most obvious and simplistic ways. Minimizing thermal currents outside the test section as much as possible is essentially all that could be done. With the present interest in hypersonics, the noise problem in conventional schlieren systems may be especially important. In hypersonic tunnels, the problem is that the thermal currents outside the test section may contain larger spatial density gradients than the low density flow structures in the test section. Multiple-source schlieren systems seek to overcome these problems by being most sensitive to spatial density gradients within the test section.

It has been shown that multiple-source schlieren systems work to reduce the effects of noise[1, 2, 3, 4, 5, 6, 7], but these effects have yet to be quantified. Multiple-source schlieren systems are meant to decrease or eliminate the effects of unwanted noise outside the test section occurring from thermal currents in the room. These thermal currents can be caused by any number of sources including room drafts, convection currents from the cooling of nearby equipment, and people. Yet another key purpose is to increase the signal-to-noise ratio in cases of very low density (usually hypersonic) flow. These goals are achieved through the system having what is termed object plane or axial selectivity (or equivalently: reduced integration length). The analysis reported by these researchers over the years is not sufficient to accurately describe the noise reduction effects of these systems. Recent analysis by the authors[8] allows for key parameters which effectively describe the noise reduction properties of the system to be quantitatively determined. The measurement of such noise reduction effects described below allows for competent design of multiple-source schlieren systems with a pre-determined amount of noise reduction. This research attempts to quantify these noise reduction effects experimentally in order to extend the recent analysis into an actual aberrated system.

The experiments in this research quantify the noise reduction capabilities of the system for noise input at varying locations outside the test section of a supersonic wind tunnel. Objectives of this research include designing and implementing modifications to a classical single-source wind tunnel schlieren system with mirrors, creating repeatable image noise so as to provide a means of consistent measurement, and developing

methods of analyzing images for the purpose of quantifying the noise reduction capabilities of a particular system.

To quantify these noise reduction capabilities, data is taken with a noise mask positioned at several different locations outside the test section. These positions are in the central beam path between the two main mirrors along one leg of the schlieren. Images from these data positions are digitized and regions of interest within these images are analyzed with computational methods developed for this purpose. These methods quantify the noise reduction capabilities of the system by defining and determining quantities which can represent the amount of noise in a particular image.

Several effects predicted by analysis[8] are examined in these experiments. An attenuation of noise introduced at locations farther from the test section should be observed and quantified. The rate of reduction of this noise at locations farther from the test section should be proportional to the inter-beam angle between the slits of the source and cutoff grids. Also, the maximum attenuation of this noise should be proportional to the number of slits used for a single grid.

Qualitative studies of the multiple-source schlieren system are by far the most documented to date. Weinstein[5, 7] briefly reviews the work of earlier researchers. Both Boedeker[4] and Salyer[9], having more pages available, provide longer reviews. The work described below summarizes some of the pitfalls and problems with earlier systems as well as some of their successful results. This paper notes these qualitative effects where they occur, if only to reaffirm the implications of previous results and to allow some comparisons to be made between the similar systems studied.

The first known work directly addressing the noise reduction properties of a multiple-source modification of an existing wind-tunnel schlieren system is described by the authors in a previous paper[8]. Schlieren systems are known to be sensitive to spatial density gradients outside the test section as well as inside it, and it is shown that multiple-source schlieren systems effectively reduce the effects of this noise outside the central area of the test section. The paper indicates that minor modifications to conventional schlieren systems can be performed to give these benefits. Analysis of these modified systems shows that the noise reduction capabilities depend on the following (for an incoherent narrow band light source): the imaging system, the slit spacing, and the transverse length scale of the noise. All of these factors govern the depth of focus of the system. Also, the maximum attenuation of noise is shown to be proportional to the number of sources used.

Until the work presented in this paper, it is believed that no attempts have been made to quantify the noise reduction effects of the multiple-source schlieren system. Aside from the authors' previous paper, only Boedeker's work presents a thorough analysis of the system. The research described in this paper is focused on quantitative aspects of a modified traditional wind tunnel schlieren system with mirrors. Details and

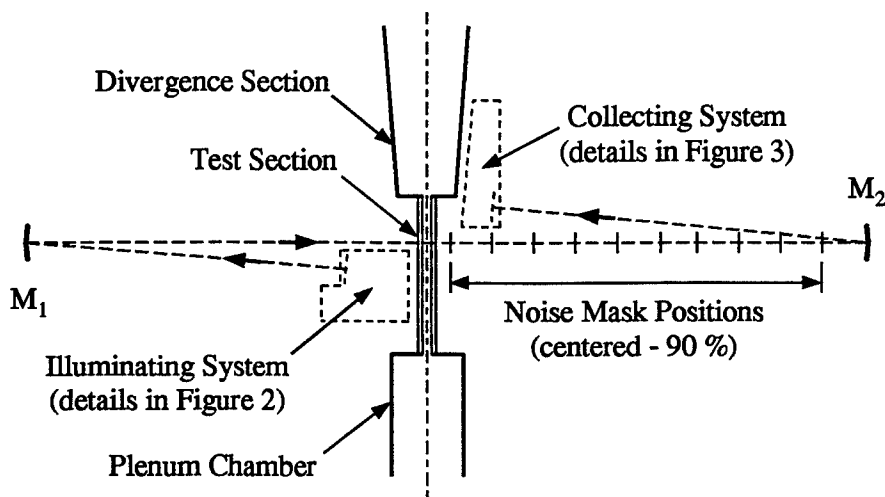


Figure 1: Multiple-source schlieren system with mirrors. See Figures 2 and 3 for details of illuminating and collecting optics.

further discussion of the present work can be found in a master's thesis due to be completed in February, 1994[9].

ANALYSIS

The difference between a conventional schlieren and a multiple-source schlieren is the illumination and the aperture. For illumination, the conventional schlieren uses a single source, while the multiple-source schlieren uses a series of sources arranged in a particular grid configuration. The layout of this grid configuration is usually a series of narrow slits which are oriented either vertically or horizontally, depending on the type of flow structures to be visualized. Other configurations are also possible, such as a series of points or a series of concentric circles, which are also chosen to best visualize the type of flow structures to be encountered. For the cutoff, the conventional schlieren has a single cutoff (generally a knife-edge), while the multiple-source schlieren has another grid configuration (generally a duplicate of the source grid). The combination of source grid and cutoff grid sends collimated beams through the test section at different angles, giving rise to the noise reducing effects characteristic of these systems. For a layout of the basic multiple-source schlieren system with mirrors, see Figure 1.

There exists an object plane in the system which gives the highest response in the image plane. This plane is in the central beam path between the two main mirrors where the centerlines of the individual beam paths cross. Although this plane is generally located in the center of the test section, it can be moved so that a 3-D flow structure could be probed if the integration length of the system is sufficiently small. This object plane of highest response can be moved by simply translating the entire system laterally (with respect to

the flow in the test section) either in one direction or the other, or by focusing with optics after the cut-off grid.

The location along the central beam path between the mirrors which has disturbances that are completely displaced from each other in the image plane is taken to be the outer limit of the integration length. Since this limit exists on both sides of the central image plane in the test section, the total integration length will be defined as twice this distance. This integration length is governed by two parameters: the inter-beam angle between adjacent slits on the source and cutoff grids, and the length scale of the noise. So, this integration length can be expressed as

$$L_I = \frac{2l_D}{\tan \alpha} \approx \frac{2l_D}{\alpha} \quad (1)$$

where l_D is a transverse length scale of the noise and α is the inter-beam angle between adjacent slits. Note that since integration length is dependent on length scale, disturbances having different length scales will be attenuated by differing amounts. This phenomenon is similar to how the depth of focus of an imaging system is also dependent on object transverse length scales.

From the analysis of Collicott and Salyer [8], the minimum integration length is found to be governed not by the fluid length scales, but by the diffractive response of the optical system itself. Specifically, the minimum integration length is defined as

$$(L_I)_{\min} = \frac{4\lambda f}{\alpha^2 h} \approx \frac{4\lambda f^3}{a^2 h}, \quad (2)$$

where λ is the central wavelength of the light, f is the focal length of the schlieren mirrors, h is the width of the source slits, and a is the slit spacing. It is assumed that the each cut-off slit blocks half of the image of the corresponding source slit.

As the location of a disturbance moves farther from the plane of highest response, images from this noise are spread out. Specifically, this noise reducing effect occurs due to the the images of noise disturbances not coinciding in the image plane when the noise source is outside the (central) plane of highest response. Only the images of disturbances that occur in this plane will coincide exactly in the image plane. There may exist a simple depth-of-field defocusing in the direction parallel to the long dimension of the source slit. This defocusing is in any imaging system with an extended source and sufficiently large aperture, and is not the topic of this work.

The noise in the image continues to decrease until the disturbances reach the outer limit of the appropriate integration length, where maximum noise reduction of the system occurs. The intensity of each of the individual images from disturbances outside the plane of highest response is a factor less than the intensity of the focused image of the noise structure, while their sum total intensity is equivalent to it. This implies that, for a greater number of images, individual intensities of each are lessened. To increase the number of images, the number of source slits used must increase. Finally, since the minimum amount of remaining

noise is proportional to the intensities of the completely offset images of the disturbances, the maximum attenuation of noise is proportional to the number of source slits used. Specifically, this maximum noise reduction factor can be written as[8]:

$$R_{\max} = \frac{1}{N} = \frac{(I_{\text{NOISE}})_{\min}}{(I_{\text{NOISE}})_{\max}}. \quad (3)$$

Here N represents the total number of source source slits used and I_{NOISE} is the image noise intensity. From Equation 3, it is evident that the response of the system to noise will never drop off entirely. So, even for the smallest integration length possible (which is governed by Equation 2), response to noise will never be eliminated, only reduced.

For a given length scale of noise, minimum integration length is achieved by maximizing inter-beam angle. To increase attenuation of noise, the number of sources used must increase. The maximum beam angle, described by $f/\#$, is governed by the quality of the optical system (i.e. the amount of optical defects or aberrations within the system). This puts a limit on the maximum beam angle available to the system. Since a maximum possible beam angle always exists, the following decisions must be made. If inter-beam angle is increased to obtain a smaller integration length, the number of sources used must decrease which then decreases the maximum attenuation of noise. The opposite case is also true. If the number of sources used is increased to obtain maximum attenuation of noise, inter-beam angle must decrease which then increases the integration length. Therefore, a design conflict exists in that a trade-off must be made between minimum integration length and maximum attenuation of noise.

As a summary of the characteristics of the multiple-source schlieren system useful for comparison with the conventional schlieren system, present are the following. The system is most sensitive to spatial density gradients inside the test section, while the conventional system is sensitive to spatial density gradients outside of the test section as well. There exists some degree of axial selectivity, (the integration length is selectable), while with the conventional system, axial selectivity does not exist, and as such, the integration length is non-selectable and generally quite large.

A detailed optical analysis of the entire system has not been presented here. The work of this paper focuses on measuring the noise reduction properties of these systems. So, only the parameters which are necessary to do this have been presented. Parameters such as sensitivity and contrast are useful for other purposes, but the methods used to quantify the noise reduction capabilities of these systems do not require them. As such, they are not included here. Also, simple geometrical analysis has been presented by numerous other researchers, so a repetition of the same analysis is not appropriate here either. For more of the analysis presented in this section, see Reference [8].

EXPERIMENT

The multiple-source schlieren system used is of the standard Z-formation type commonly used with mirrored systems. The two main mirrors used for collimation are spherical front-surface mirrors with 6 inch

diameter and 60 inch focal length. The distance between the mirrors is 12 feet 3 1/2 inches. The illumination and collection optics are positioned 60 inches from their respective mirrors, and approximately 5 degrees off-axis. This geometry makes the system symmetric and also gives a 1:1 magnification from the source grid to cutoff grid. This 1:1 magnification is beneficial for the system in that the source and cutoff grids are exact duplicates of one another, which makes their construction easier since no magnification factors are involved.

The illuminating system (Figure 2) is made up of a light source, a series of plane mirrors and lenses, and the source grid. The light source is a 100 Watt mercury arc lamp. Expanding optics are used to increase the collimated beam diameter from 1 inch to 2 inches for maximum grid coverage. Plane mirrors are used to redirect the beam for the purpose of compacting the overall system, which is necessary due to the physical constraints imposed by the wind tunnel. A plane mirror is used to turn the beam 90 degrees onto a plano-concave lens with a -150 mm focal length and 40 mm diameter. This lens spreads the beam, and a plane mirror reflects it into a lens of 300 mm focal length and 95 mm diameter. This collimates the beam, which is then incident on the source grid. Attached to and in front of the source grid is a ground glass plate which disperses the light from each slit. This allows each slit to have the same illumination characteristics. The entire illuminating system including the source grid is on a base with two angular degrees of freedom, pitch and yaw, defined while facing the first collimating mirror. This allows precise alignment of the beam direction.

The collecting system is made up of the cutoff grid, a plane mirror, a converging lens, and the camera. The cutoff grid is mounted on a rack and pinion traverse system for fine focusing of the source grid image onto the cutoff grid. Since the lines on the grid are horizontal, a vertical adjustment is also necessary. For this adjustment, a translating stage with a micrometer drive is mounted perpendicularly on the traverse, allowing fine cutoff adjustments of precisely known amounts. Rotational alignment of the grids is done by hand. After the cutoff grid, a plane mirror redirects the light into a lens which is an achromatic doublet with a 200 mm focal length and 40 mm diameter. This last lens focuses the light onto the CCD array, as depicted in Figure 3.

The grids used are of two types, from here on referred to as the large slit grids and the small slit grids. The large slit grids are created by photocopying computer generated lines of chosen dimensions onto transparencies. This method works once a black marker is used to further darken the lines. Once a grid configuration is chosen for a given system, it is advisable to create a higher-quality transparency. The small slit grids are 50 line per inch Ronchi rulings. It is noted that the etched side of the grid is placed away from the ground glass plate so that chosen lines can be masked off directly on the edges defining the slits. With both the small slit grids and large slit grids, lines are masked off with black electrical tape to form the proper grid configurations.

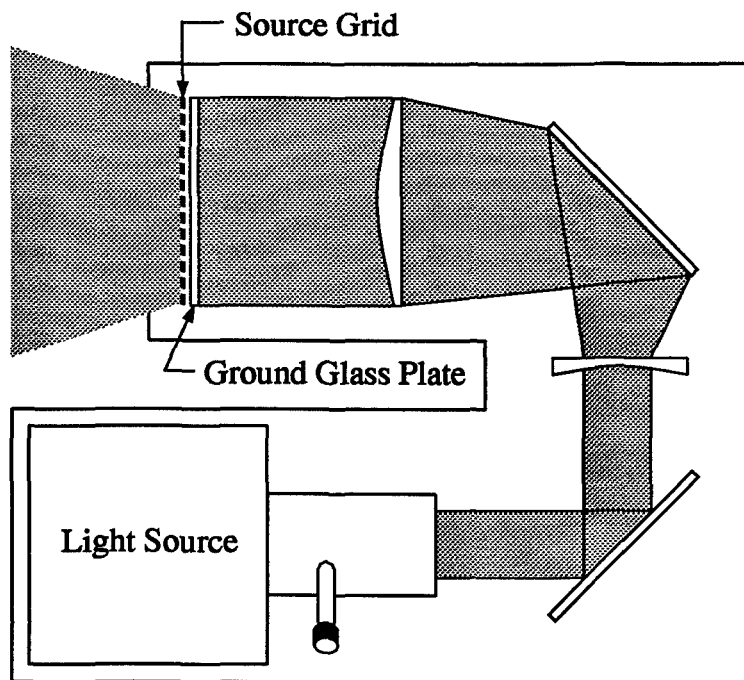


Figure 2: Illuminating optics. See Figure 1 for placement within the system.

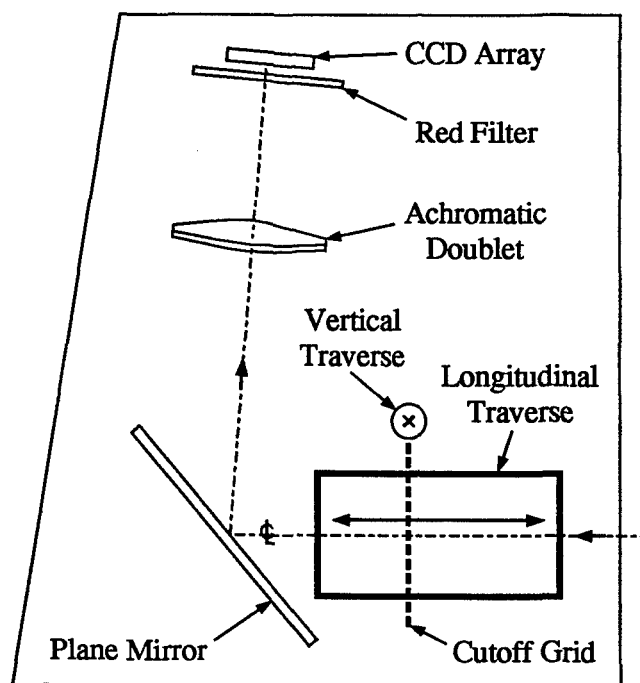


Figure 3: Collection optics and image plane. See Figure 1 for placement within the system.

The object in the test section is a wedge in a Mach 2.5 flow. Images of the test region are acquired with a CCD array camera and recorded on video tape in Super VHS format. The camera has an array size of 8.8mm by 6.6mm with a resolution of 768 pixels horizontally and 493 pixels vertically. Since the source of the schlieren system is continuous and the framing rate of the camera is the standard video rate, the images are not time resolved. To insure that all images of a particular data run have approximately the same overall intensity, the auto gain control on the CCD camera is used. A PC frame grabber is used to digitize (approximately a 7-bit gray scale) selected images from the SVHS tape.

Two regions of interest in each digitized image are selected. One is a 128 by 128 pixel area of undisturbed flow ahead of the test body and shocks. This region is of interest since the only effects here are the effects of noise. The other region of interest is the image of an oblique shock wave. To obtain the shock region, the entire image is first skewed to make the oblique shock wave vertical in the image. The 128 by 128 pixel region is then cut out with the shock centered in the image. These two regions are chosen because they bound the density gradients present in the flow.

To measure the noise reduction capabilities of the system, a consistent source of noise is needed. Noise is introduced into the system with a speckle pattern noise mask, created by exposing a holographic plate to a speckle pattern of known length scale. The holographic plate is developed and bleached to make the pattern mostly transparent. This changes the pattern into a phase disturbance rather than an amplitude disturbance, although a small amount of absorption remains. The phase disturbance of the bleached speckle pattern simulates the effects that thermal currents of the same length scale have on the phase of the incident wavefront. The speckle size used in the present work is 3mm. Note again that the length scale of the noise affects the integration length of the system, or equivalently, the axial selectivity.

For a parametric study of the response of the multiple-source schlieren system to noise at differing locations outside the test section, data is taken for different grid configurations. Nine different configurations are studied with two sets of source and cutoff grids, a large slit grid and a small slit grid. For the large slit grid, the following configurations are used: single slit (L1), 3 slit narrow spacing (L3N), 3 slit wide spacing

Table 1: Source grid configuration data.

Grid Label	# of slits	Slit Width (mm)	Spacing (mm)	Length (mm)
L1	1	1.5	N.A.	12.
L3N	3	1.5	6.0	12.
L3W	3	1.5	12.	12.
L5	5	1.5	6.0	12.

(L3W), and 5 slit (L5). The effects of slit length are not studied since they are known and can be explained without additional data being taken. For the small slit grid, the following configurations are used: single slit (S1), 3 slit narrow spacing (S3N), 3 slit wide spacing (S3W), 5 slit (S5), and 49 slit (which is the maximum number possible with the Ronchi ruling). Table 1 presents dimensional data for the grids.

Note that the single slit cases are taken to represent the conventional schlieren system results and are used for comparison purposes. The maximum slit configurations for both the large slit grid and the small slit grid are limited by the 2 inch collimated light beam from the illuminating system. Also, all grids are oriented with the slits running horizontally. This particular orientation makes the system most sensitive to spatial density gradients in the vertical direction.

The noise mask is positioned at 10 different locations outside the test section. These positions are in the central beam path along one leg of the schlieren system between the test section and the second focusing mirror. The specific noise mask positions are: directly centered between the mirrors, 10, 20, 30, 40, 50, 60, 70, 80, and 90 percent of the distance from the centered position to the second focusing mirror. Note that the centered position is not in the center of our test section, but is instead $2\frac{1}{8}$ inches from the outside wall of the test section. Regarding other parameters, the plenum chamber pressure is approximately 40 psig for each case and the flow in the test section is Mach 2.5.

RESULTS

For qualitative results, a simple visual assessment is performed on the data images for the systems with different grid configurations. Figures 4, 5, 6, and 7 are examples of the raw image data. Figure 4 is a photograph acquired with a single-slit schlieren system and noise input 10% of the distance between the test section and the second mirror. The effects of the noise mask are considerable; shocks are barely visible, and expansion fans are overwhelmed. Compare this with Figure 5, which is the five-slit system. Each slit is the same dimension as the single slit in Figure 4, and the separation is four slit widths. Figures 6 and 7 are from the narrow (L3N) and wide (L3W) spaced triple slits, respectively.

Note the greatly reduced magnitude of the speckle pattern, and the great increase in the visibility of shock waves and expansion fans in the multiple-slit images. The remaining pattern from the noise is due to defocusing in the horizontal direction caused by the long dimension of the slits. Images of this type are processed for all grid configurations and noise inputs. All multiple slit configuration images (see reference [9] for the complete set of images) possess shock structures, expansion fans, and the model in the test section which are clearly more visible than in the images from the standard systems. Also, the overall visibility increases as the noise is input closer to the mirror.

The quantitative analysis performed on the images from the systems with different grid configurations is done for two different regions within each image of data. In regions of uniform flow, histograms of the pixel

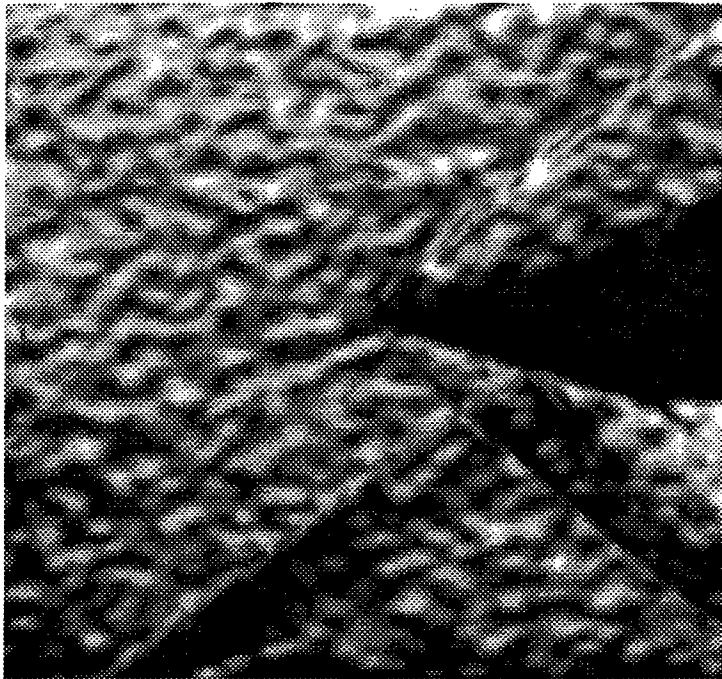


Figure 4: Photograph from a traditional single-slit schlieren system (L1 grid). Noise is input 10% of the distance from the test section to the second mirror.

grey scale values in a uniform region of the flow are used. For the response of the system to shock waves, RMS values for the deviation of the peaks of the shock waves are computed.

The response of the system to the most basic of signals is its response to the uniform region of flow in the test section. This still allows for all of the sources of noise to be present in the system, and most importantly still includes the boundary layers on the test section walls as well as all of the other sources of noise referred to earlier. Understanding how the system responds to this most basic flow signal allows for simple first estimate quantitative noise reduction measurements to be made.

For the following uniform region analysis, the area of interest of the data images is the region of undisturbed uniform flow ahead of the test body and shocks. All of the images used for analysis were 128 by 128 pixel portions cut out of the original data images.

Histograms of the pixel grey scale values from images in the uniform flow region are used as a basis for quantifying the noise reduction of the system. By determining the radius of gyration of the histograms, which is analogous to the radius of gyration of a solid body, a reliable means of determining the noise reduction of the system is accomplished.

For a solid body, the radius of gyration can be computed from a knowledge of the center of mass location and the integral moments of inertia summed about it. In the case of the histograms of the pixel grey scale

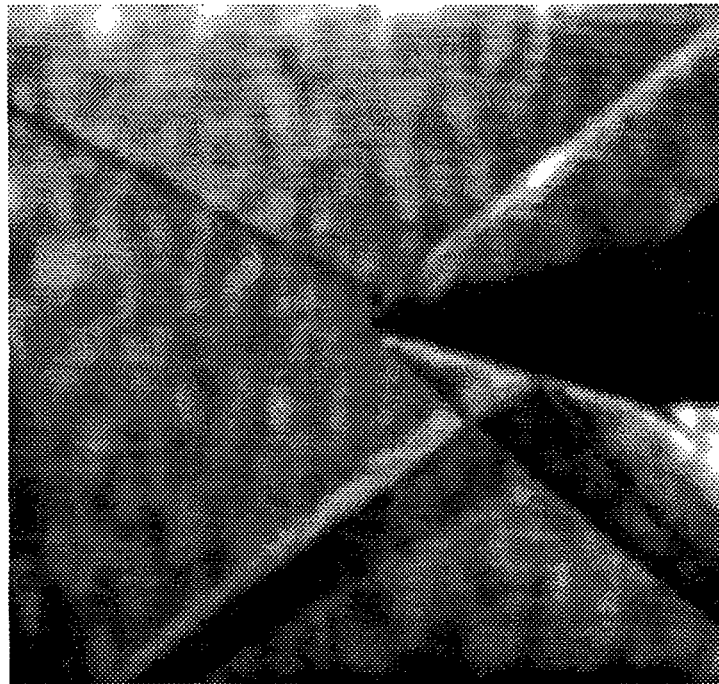


Figure 5: Photograph from a five-slit modification (L5 grid) of an existing single-slit schlieren system. Same noise input and flow field as in Figures 4, 6, and 7.

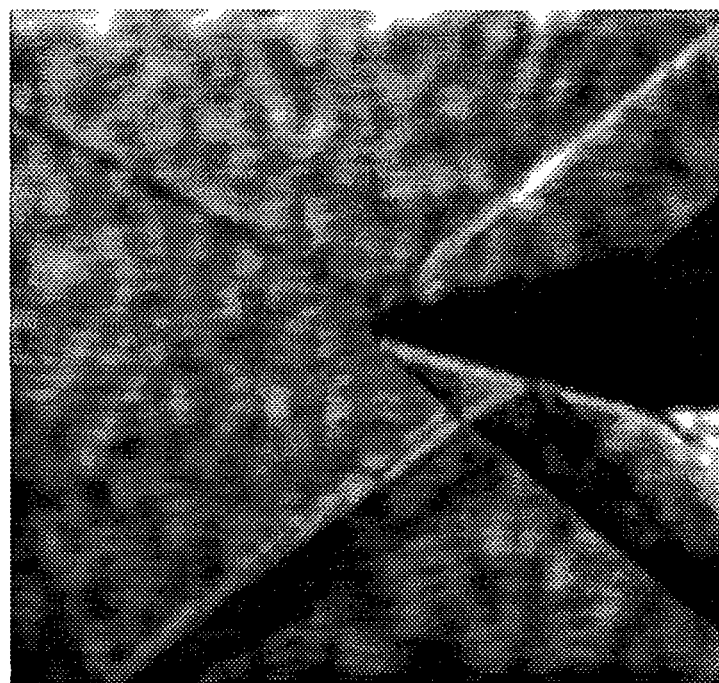


Figure 6: Photograph from a three-slit schlieren system of narrow spacing (L3N grid). Same noise input and flow field as in Figures 4, 5, and 7.

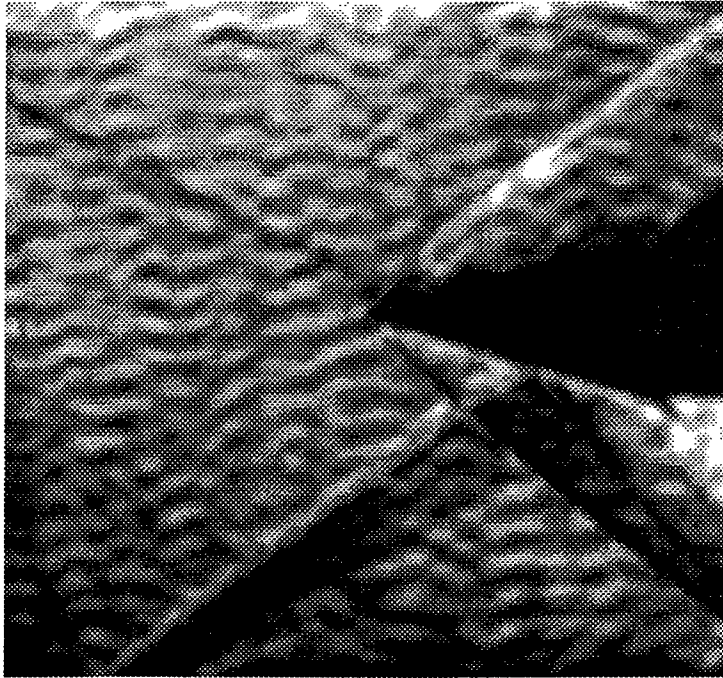


Figure 7: Photograph from the widely spaced three-slit modification (L3W grid). Same noise input and flow field as in Figures 4, 5, and 6. Inferior to the narrow (L3N) grid.

values, an analogous radius of gyration is computed. Each pixel with its corresponding grey scale value is analogous to a small unit of mass, and the average intensity or average grey scale value of the image is analogous to the center of mass. The difference between the grey scale value of each pixel and the average intensity grey scale value is analogous to the radius from the center of mass to the small unit of mass. The moments of inertia about the so-called center of mass are computed accordingly for each pixel and summed so that the radius of gyration of the histograms is given by

$$r = \left[\frac{1}{n_{tot}} \sum_{I=0}^{255} n_p(I)(I - \bar{I})^2 \right]^{1/2}, \quad (4)$$

where $n_p(I)$ is the number of pixels at intensity (or grey scale level) I , n_{tot} is the total number of pixels ($n_{tot} = 128^2$ in the data presented below), and \bar{I} is the average intensity or average grey scale level.

For an image with high noise content, i.e. one that contains small adjoining regions of either very dark and very bright pixels, the overall range of pixel grey scale values is large and covers most of the 8 bit grey scale range. The resulting histogram is broad and flat, indicating a wide range of pixel intensities and a noisy image. For an image with low noise content, the image appears to be more uniform and the range of pixel grey scale values is much smaller so that the image appears to be closer to one uniform intensity. The

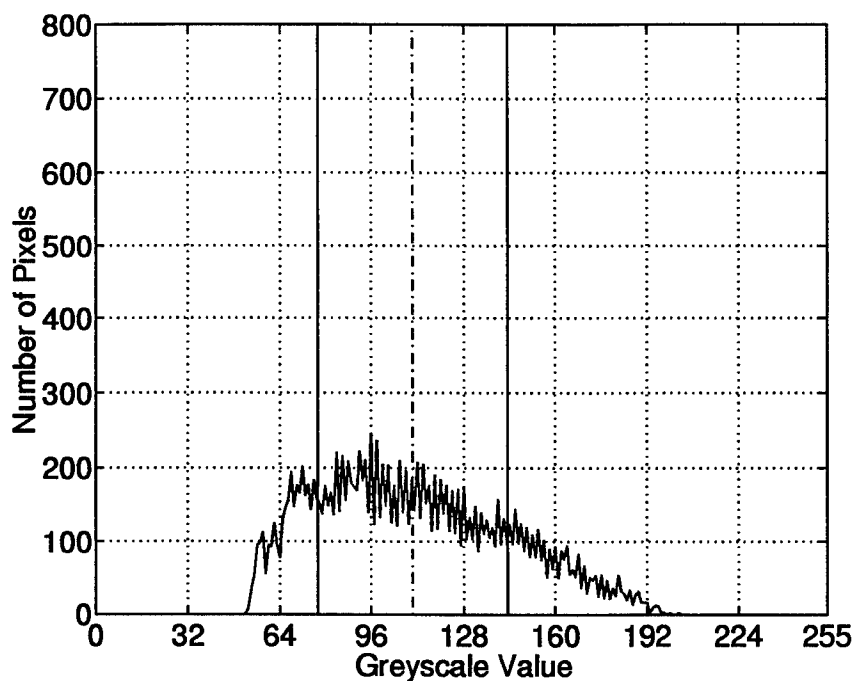


Figure 8: Grey scale histogram of uniform flow region. Single slit (L1 grid) with noise input at 10% of the distance from test section to mirror.

resulting histogram for the low noise image is more of a narrow spike at the center of the narrow band of pixel intensities.

The radii of gyration computed for the images of lower noise levels are significantly less than the radii for the relatively high noise images. This is to be expected since the histograms of the images of relatively high noise levels are much broader and their individual pixel intensities vary greatly from the mean. Figures 8 and 9 are examples of these attributes. Figure 8 is the histogram compiled from Figure 4, and Figure 9 is compiled from the image in Figure 5. The vertical broken line is marks the mean value of the pixel intensities, and the vertical solid lines are located one radius on either side of the mean. Visual interpretation of the relative widths of the histograms is consistent with the magnitude of this measure.

In some cases, the individual pixel intensities vary enough as to saturate one end of the spectrum of grey scale values. This reduces the radius of gyration only slightly because the majority of pixels are not saturated. Since this generally only occurs in cases of high noise levels, the radii of gyration for the images of high noise content are slightly closer to the ones for images of relatively low noise content, and the estimate of noise reduction is a conservative one in these cases.

Plotting radius of gyration versus noise mask position for the different systems allows a reliable quantitative measure of noise reduction to be made for each individual system and for a comparison of systems with

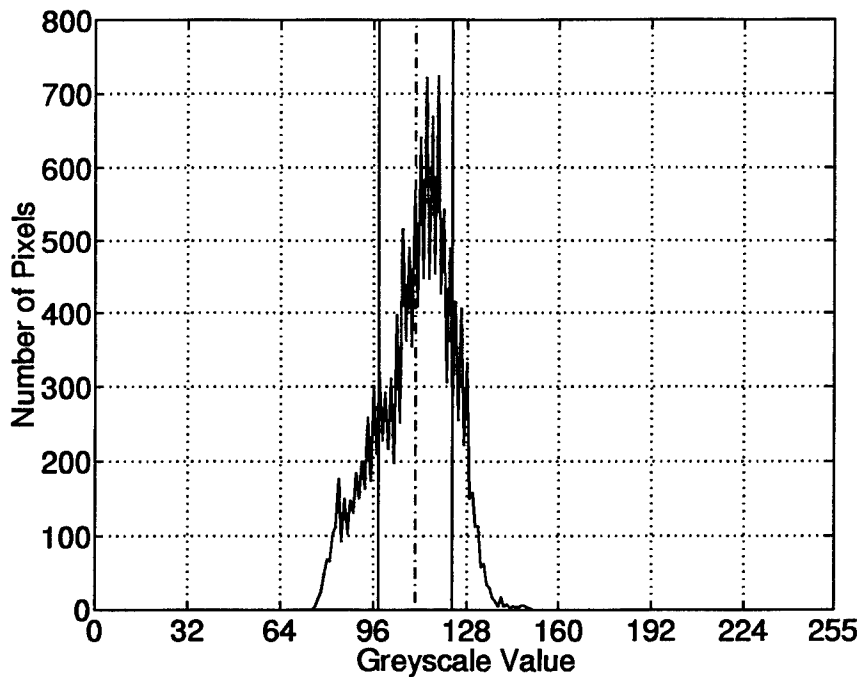


Figure 9: Grey scale histogram of uniform flow region. Five slits (L5 grid) with noise input at 10% of the distance from test section to mirror.

different source and cut-off grids. Figure 10 indicates how the radius of gyration decreases as the noise moves farther away from the test section. The ratios of these values for systems of different grid configurations give quantitative results for the noise reduction capabilities of a particular system. It is worth noting that the triple slit case with 6 mm spacing (L3N) performs better than the triple slit grid with 12 mm spacing (L3W). This indicates that the slits located 12 mm from the axis are less effective at reducing noise. The similarity between the performance of the five-slit grid (L5) and the three-slit narrow grid (L3N) is another indication of the poor performance of the slits 12 mm from the axis. The mirror diameter is approximately 150 mm. It is believed that the poor performance of the outer slits is somehow linked to the aberrations of the system. For example, astigmatism blurs an image slightly, which would infer better noise reduction, but at the same time, the depth-of-field is also increased. Apparently this depth-of-field increase is contributing to the reduced effectiveness of the out slits.

The single-slit (L1) line in Figure 10 demonstrates the noise reduction capability present because of the long dimension of the source slit. This affects the image statistics in only one transverse dimension, and the multiple slits are required to reduce noise with structure in the other direction. It is doubtful that thermal currents would be parallel and perfectly aligned with the long dimension of the slit. Thus a two-dimensional noise-reduction capability, such as a series of long slits, is required. Note that extension of the concept of

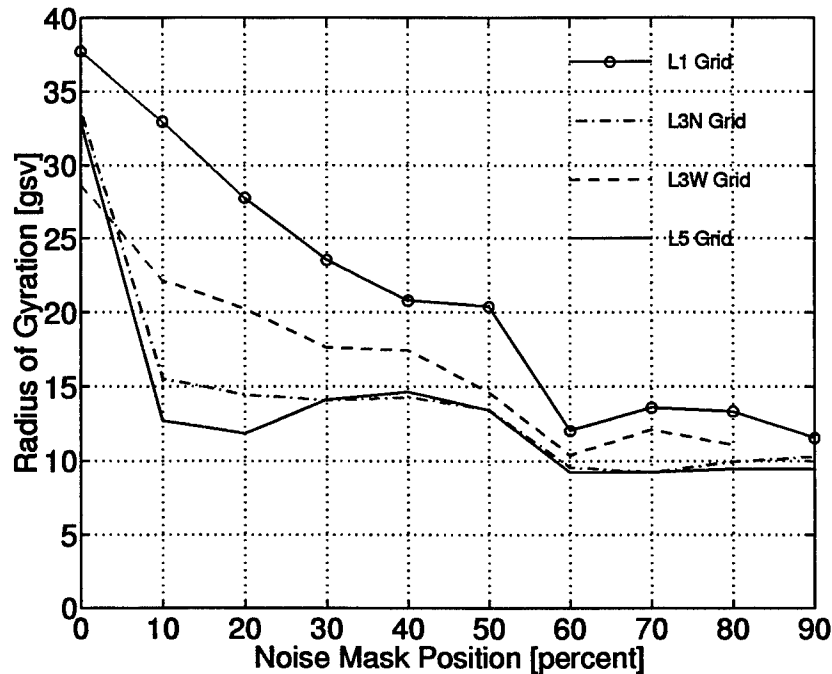


Figure 10: Radius of Gyration Comparisons, L1, L3N, L3W, and L5 Grids. Results of Figures 4, 5, 6, and 7 are the intersection of each curve with the vertical grid line at the 10% location.

a long slit to two dimensions, i.e., a large square source, fails because it will have minimal sensitivity as a schlieren system[10].

The response of the multiple-source schlieren system to a standard test section signal such as a shock wave is also important when characterizing the effectiveness of the system. In order to effectively design a system to reduce noise due to various effects, the response of the system to this standard signal needs to be determined. Essentially, what needs to be known is how much the noise interferes with the sought after signal and how much the signal improves when the noise moves farther away from the test section.

All cases studied here use an oblique shock wave emanating from the lower portion of the test section as a signal. For ease in computations, the image was sheared at the proper angle so as to make the shock vertical. The chosen portion of the image was then cut out to make a 128 by 128 pixel image of the shock with the shock lying vertically in the center of the image.

The deviation of where the peak intensities in the near shock location occur is used as a quantitative measure of the noise reduction of the system. Essentially, the more the so-called peak of the shock wave deviates from the known shock location (a vertical line in the center of the image), the noisier the signal is, thus indicating less noise reduction by the system.

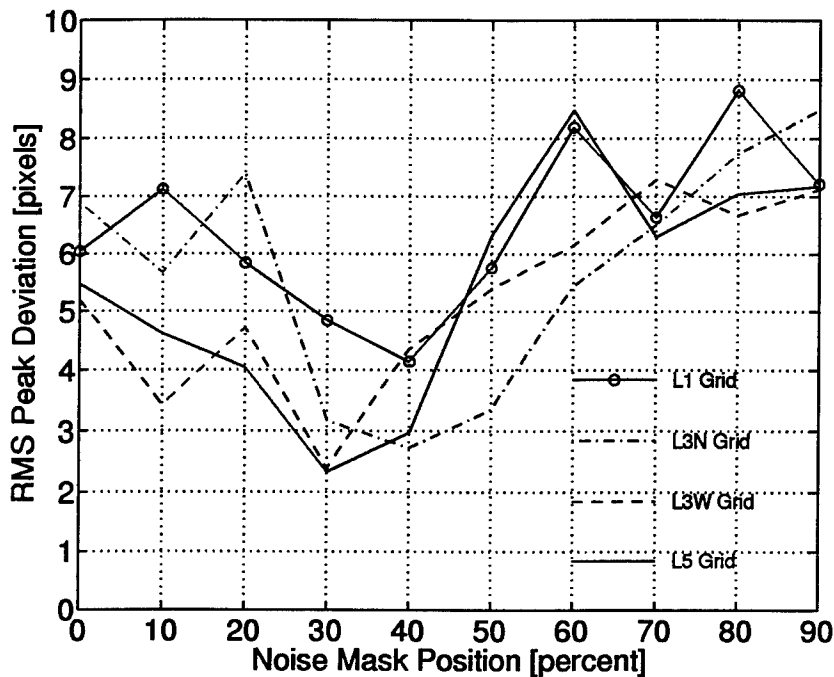


Figure 11: RMS Peak Deviation Comparisons, L1, L3N, L3W, and L5 Grids.

For a given shock width region, which is specified as a vertical band down the center of the image, the horizontal location of the highest intensity pixel(s) within the shock width band is found for each row. The deviation of the location of these peak pixels from the vertical center line of the image (which is the known actual shock location) is computed as an RMS value along the entire length of the shock.

The RMS peak deviation calculation is slightly dependent on the size of the shock width band region chosen. If the selected region is too small, i.e. the local peaks for each row lie outside the boundaries of the shock width band region, the computed RMS peak deviation appears smaller than it should be. In all cases studied, the shock width band region is chosen to be the center twenty five percent of the images. This particular value is used since it allows the chosen shock width band to encompass most of the visibly blurred shock wave, thus allowing a full range to be used for shock peak deviation calculations.

Plotting the RMS peak deviation versus noise mask position makes possible a quantitative measurement of the noise reduction for the particular system in question. Of course, this method is only used for noise reduction measurements with a shock wave for a signal. Figure 11 illustrates how the calculated RMS values decrease as the noise moves farther away from the test section. Accordingly, smaller RMS peak deviation values are indicative of images with less noise content. Ratios of RMS peak deviations for differing noise mask positions of different systems gives quantitative results for the noise reduction capabilities of a particular system when compared to a single slit conventional schlieren system configuration using the same size grid.

CONCLUSIONS

It is shown that simple multiple-source modifications to an existing schlieren system provides a practical means of reducing image noise. The noise is typically caused by thermal currents outside the test section. Currents closest to the test section fail to be attenuated significantly. Thus a system with image noise generated by turbulent boundary layers on the test section windows is a more difficult case to cure than is a drafty room. The results are especially encouraging for improving image quality in some low-density hypersonic facilities.

This research demonstrates that the quantification of noise reduction in a particular system can be performed with simple image analysis. Two methods quantify the noise reduction capabilities of each system for two important regions of each image. Knowledge of noise reduction as measured for uniform flow regions and for shock visibility allows the competent design of multiple-source schlieren systems with a desired amount of noise reduction. Consistent with earlier analysis[8], this design boils down to a trade-off between the maximum attenuation of noise and the size of the region near the test section in which the system is most sensitive to density gradients. The size of this region, often called the "integration length", is governed by the inter-beam angle, while the maximum attenuation of noise is governed by the number of slits. These objectives are conflicting due to a limited maximum overall beam angle governed by the F-number of the system. Therefore, either a relatively small number of sources with large inter-beam angles can be used to have a short integration length, or a relatively large number of sources can be used with accordingly small inter-beam angles to give a maximum attenuation of noise but with a longer integration length.

Quantification of noise reduction in regions of uniform flow is found to be simpler than in the regions of shock waves. A single numerical value, computed from the grey scale histogram, appears to correlate well with visual observation of the images. Visual observations of shock wave visibility appear to track the trends of the uniform region. This has the economic benefit of permitting set-up and evaluation of multiple-source schlieren modifications at large facilities without the need to operate the tunnel.

The experimental results for a system with $F/10$ spherical mirrors used 5 degrees off-axis demonstrates that the practical maximum grid size is approximately 15% of the mirror diameter. That is, the outermost source slits at this grid size contribute minimally to the noise reduction. It is reasonable to expect that existing schlieren systems with parabolic, and especially off-axis parabolic, mirrors will have a larger maximum for the practical grid size. Such systems are inherently less aberrated than the spherical mirror systems. Regardless, the results show that simple modifications to existing mirrored schlieren systems can improve the quality of images in the presence of thermal currents.

OFF-AXIS PARABOLIC SCHLIEREN SYSTEM

The experiments at Purdue were performed with a schlieren system built from spherical mirrors. The schlieren system of the TGF facility at WPAFB is built from off-axis parabolic mirrors. The only concern

about the difference is to accurately apply data gathered from the spherical mirror system to the parabolic system. Of primary interest is the off-axis position at which a source and cut-off slit pair fail to perform well. In the F/10 spherical system, the slit at about 15 parabolas are superior to the spherical mirrors, but just how much better needs to be understood prior to designing the outer-most slit for the TGF schlieren.

Determination of the spherical versus off-axis parabolic mirror performance is made by use of an exact ray-tracing optical design code, Oslo Series 3 from Sinclair Optics. The license for the code was acquired, and renewed, with funds from several sources within Purdue. Comparison between the two schlieren systems is made based on the size and location of exact ray-trace spot diagrams, and modulation transfer functions (MTF). Aberration theory is not applicable because neither system possesses rotational symmetry.

In the simplest interpretation, results of these computations show that the off-axis parabolic mirrors should permit the maximum off-axis slit position to be approximately triple that of an equivalent f-number spherical mirror. This is computed for F/10 mirrors with 6 degrees total bending of the axis by the mirror. Results also show that there may well exist an optimal off-axis position of the off-axis parabolic mirrors which differs from the paraxial design position. This is an area for further work. Figure 12 presents modulation transfer functions computed for the out-most pair of slits of the L3N system (top) and corresponding slits in the off-axis parabolic system, but located three times as far from the axis. Note that the MTF curves are very similar, especially in their widths. The computed spot size diameters also compare favorably. For the on-axis slit, the parabolic system is orders of magnitude superior. The off-axis parabolic system even operates diffraction limited within a small region near the axis.

These computed comparisons of the two types of schlieren systems lead to the conclusion that the outer-most slit in the TGF system can be three times further from the axis as it was in the spherical mirror system, when measured as a percentage of mirror diameter. Further analysis of the distortions of the systems could be performed, but the parabolic system should be superior again in this area, so there is a little factor of safety in the design. Distortion will not vary with f-number, so the differing f-numbers won't diminish this factor.

The limit on grid spacing in the TGF facility turns out not to be the performance of the grid-to-grid imaging system, but rather the lens speed (f-number) required after the second grid. That is, following the cut-off grid, a lens images the transmitted light onto the final image plane. Thus the imaging lens diameter sets a limit on the maximum slit spacing. The system designed uses commercially-available stock lenses. Larger, better, and other systems may certainly be designed by specifying custom lenses or additional off-axis parabolic mirrors.

HARDWARE DESIGN FOR THE TGF

Because the grid system in the Purdue experiments throws away a substantial portion of the light, a more efficient system is designed for the TGF tunnel. The wider slit spacings assist in this matter by

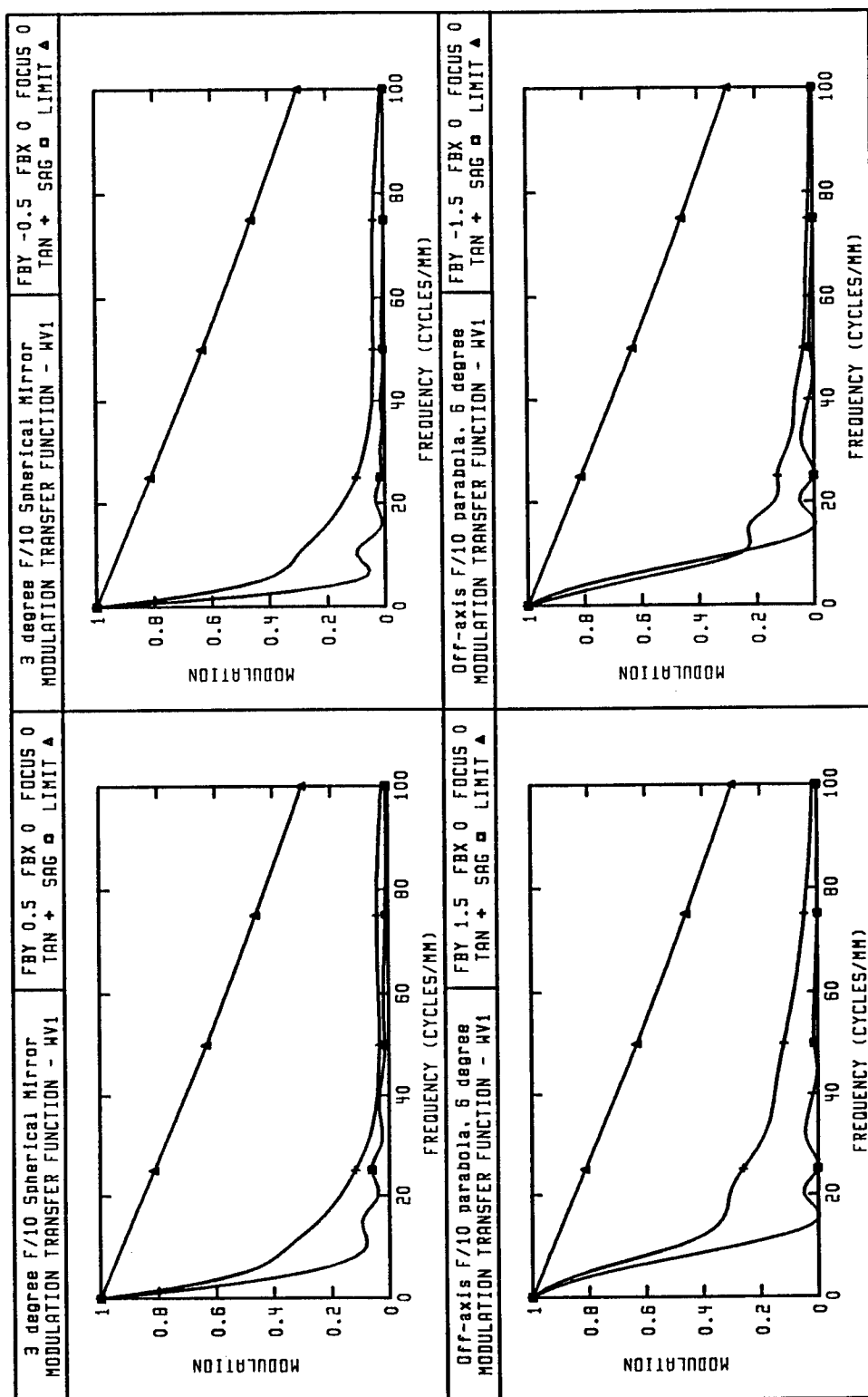


Figure 12: Modulation transfer functions for the grid-to-grid imaging of spherical and off-axis parabolic schlieren systems. Top row is for the spherical mirrors, bottom row is for the off-axis parabolic mirrors.

opening up room for placement of optics. A five-slit system is designed, occupying approximately 15% of the wind-tunnel window diameter. Slit thickness is similar to the slit in the existing schlieren system. Thus the multiple-slit system should provide comparable sensitivity as the present system, with the same lamp, but with noise reduction. As pointed out above, the number of slits and the slit spacing compete. The design specified herein differs substantially from the published designs of Weinstein[11]. This is not cause for concern, because there are differing goals. Additionally, the analysis performed by the P.I. for the 1992 AFOSR Summer Faculty Program, and the experiments performed under this contract, provide a foundation of knowledge about the details of the system performance. A few, widely spaced pairs of slits will reduce noise in a wide range of noise length scales, and also create a desired shortening of the "integration length". Noise reduction will be as much as 80%.

Figure 13 is a schematic of the overall source optics. Slit thickness is set by the F/7.5 cylindrical lenses, slit length is a maximum of 60 mm (they can easily be masked off to be smaller), and slit spacing is 16 mm. Larger slits can be formed by inserting a ground glass, or opal glass, plate in contact with a source-slit mask. This combination would then be placed a couple of millimeters closer to the cylinder lenses than in the case without a ground glass plate. The larger slits may sacrifice some sensitivity, but only to the point of reducing sensitivity to that of the existing system (while still maintaining the noise-reduction system). It may be that the beam from the Oriel lamp can not be focused tighter than 1 mm, in which case the 1 mm slits can be used without a ground- or opal-glass plate.

The telescope is made up of a negative plano-concave lens and a positive achromatic doublet. Focal lengths are -600 mm and 1250 mm, respectively. The negative lens is Melles-Griot part 01 LPK 065/078, and the positive doublet lens is Spindler & Hoyer part 32 2318, which includes the anti-reflection coating. The negative lens is used to mitigate the spherical aberration, which, along with axial color, is the dominant source of aberration affecting this type of system. Actually, the quality of collimation does not appear to be an issue in this design, so the present system should suffice. The flattest side of each lens face each other, with a separation of 13.83 inches. This optimal spacing is determined from exact ray-trace design. Of course, installation will likely fall short of this precision, but 13.83 inches is the goal. Give or take 1/16 inch in this dimension will not be cause intolerable flaws.

Figure 14 is a dimensioned drawing of the frame for the five cylinder lenses. The five cylindrical lenses are used in place of the grid in the Purdue experiments. The lens array makes far more efficient use of the lamp power than grids do. The trade-off is that alignment is more tedious, but it should not be prohibitive. When machining this frame, bear in mind that the most critical dimensions are the spacing and parallelism of the bottom edges of the five cut-outs. The slender portions between lenses carry minimal, if any, loads, and mainly serve as lens apertures. As such, the small dimensions are not of consequence to strength of the mount or stability of the lens positions.

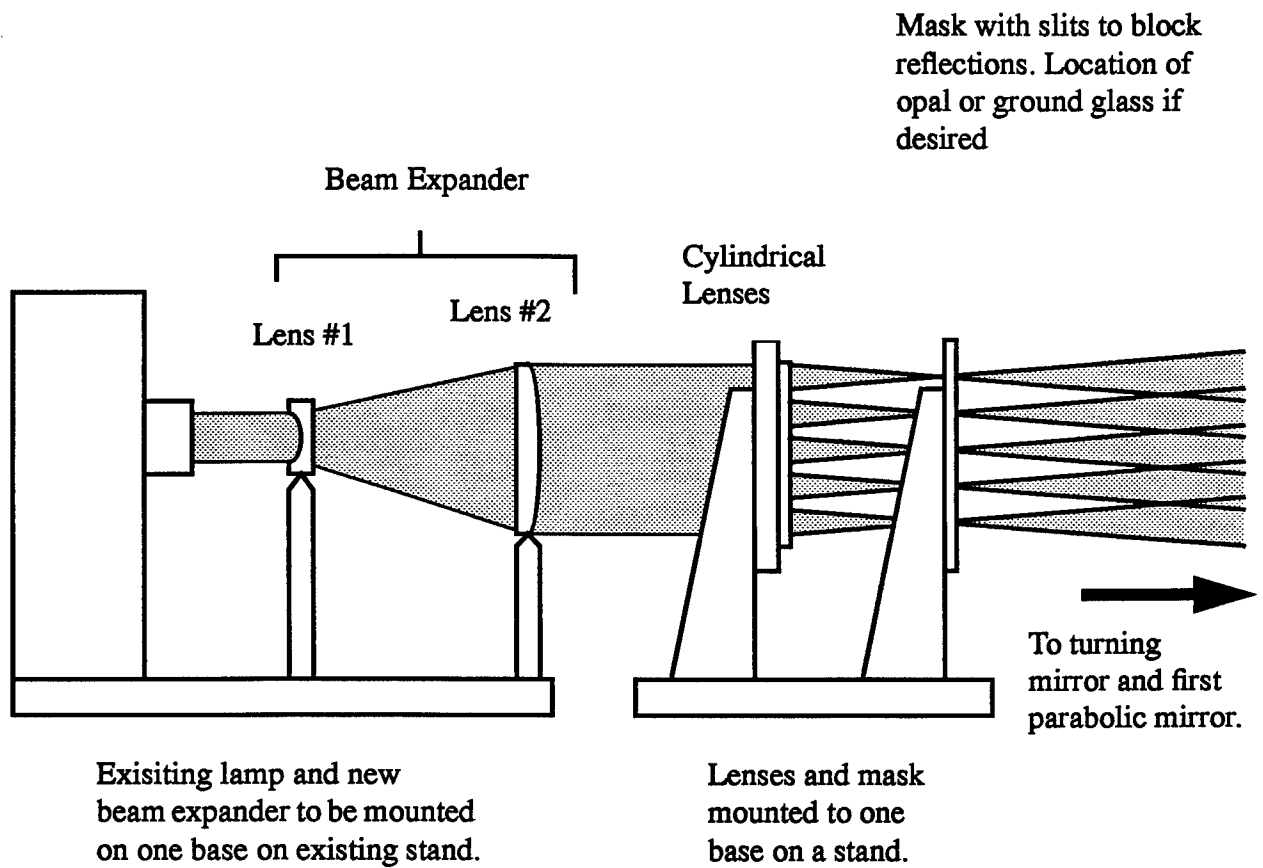


Figure 13: Schematic of the new illumination optics. Mounting to existing floor-mounted posts should include fine vertical adjustment and leveling capability.

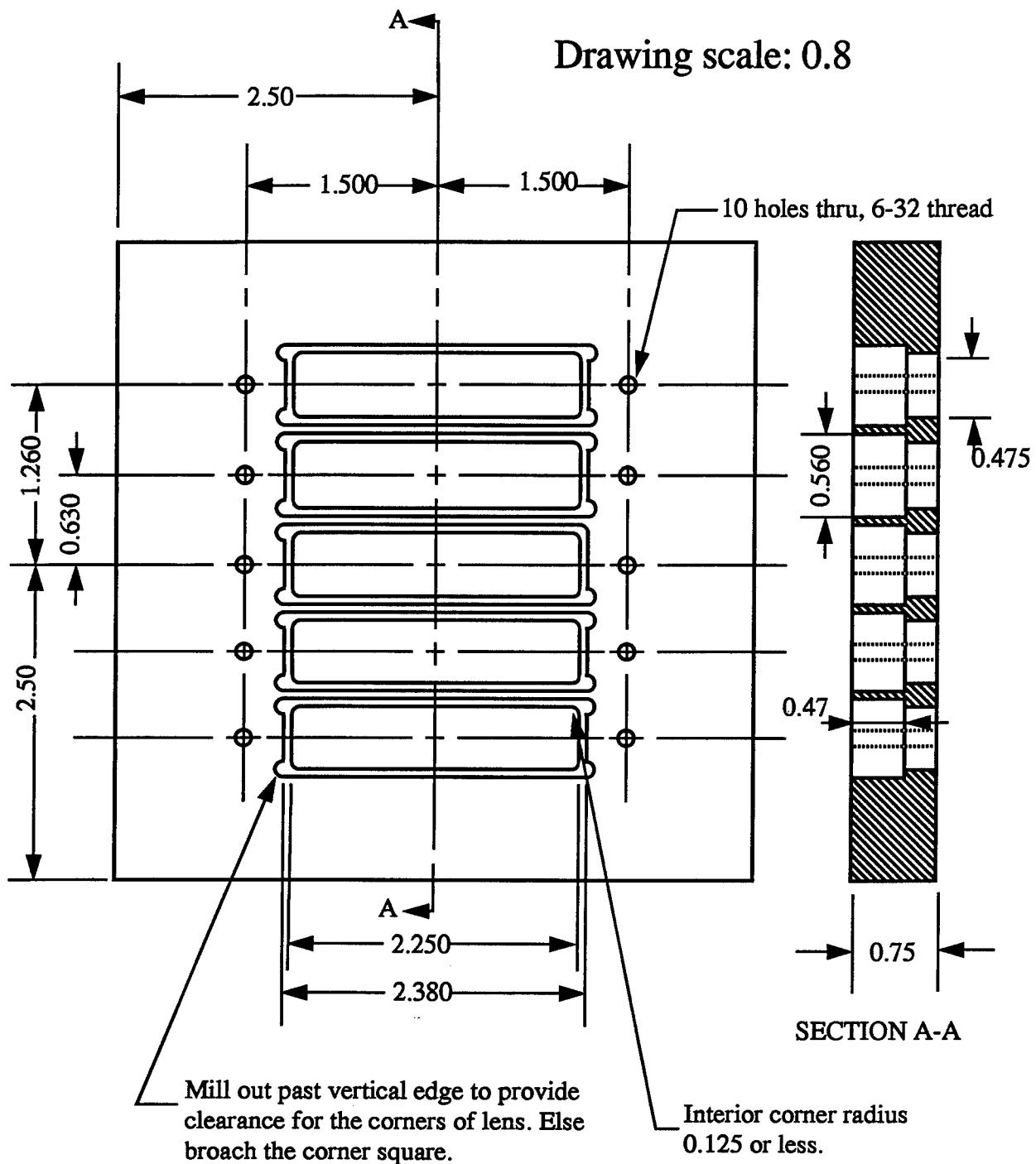


Figure 14: Lens frame for mounting the five cylindrical lenses. Aluminum, steel, or brass would be acceptable. Overall dimensions and thickness are not critical. Spacing and parallelism of the bottom edges of the slits are most critical. All dimensions plus or minus 0.001.

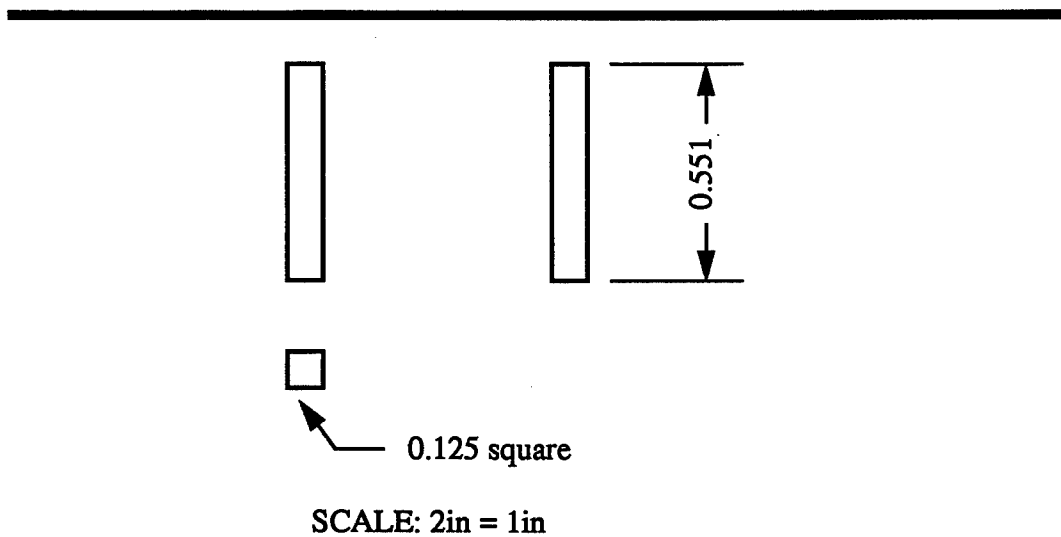
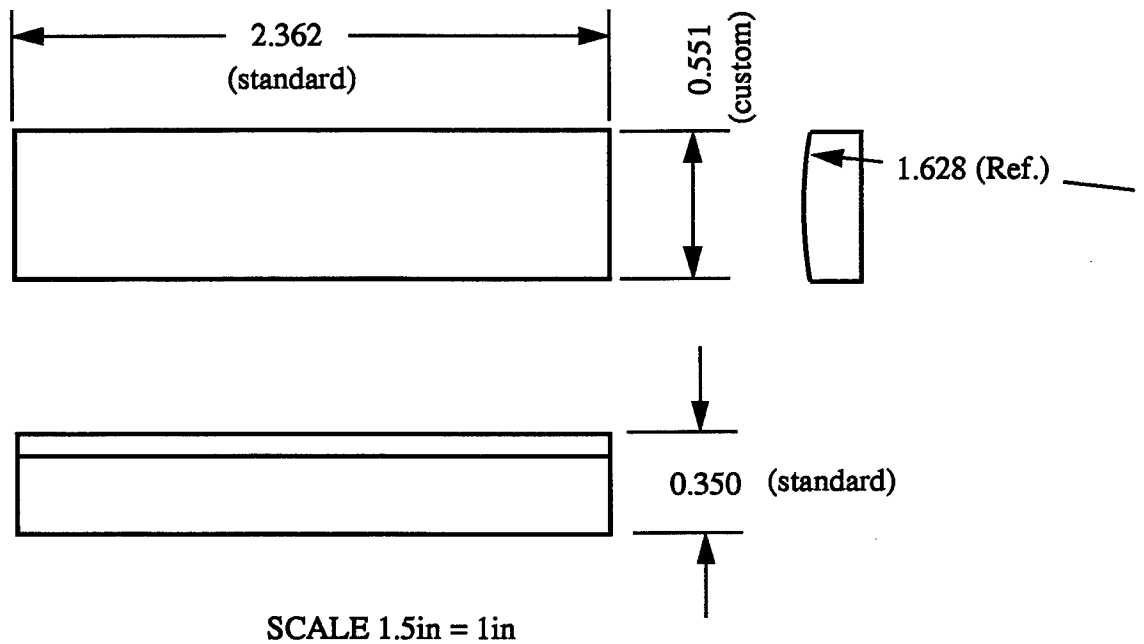


Figure 15: Cylindrical lens and pad dimensions. Lens perimeters are ground down from the stock lens size from Melles-Griot. The pads are to be nylon or similar resilient material.

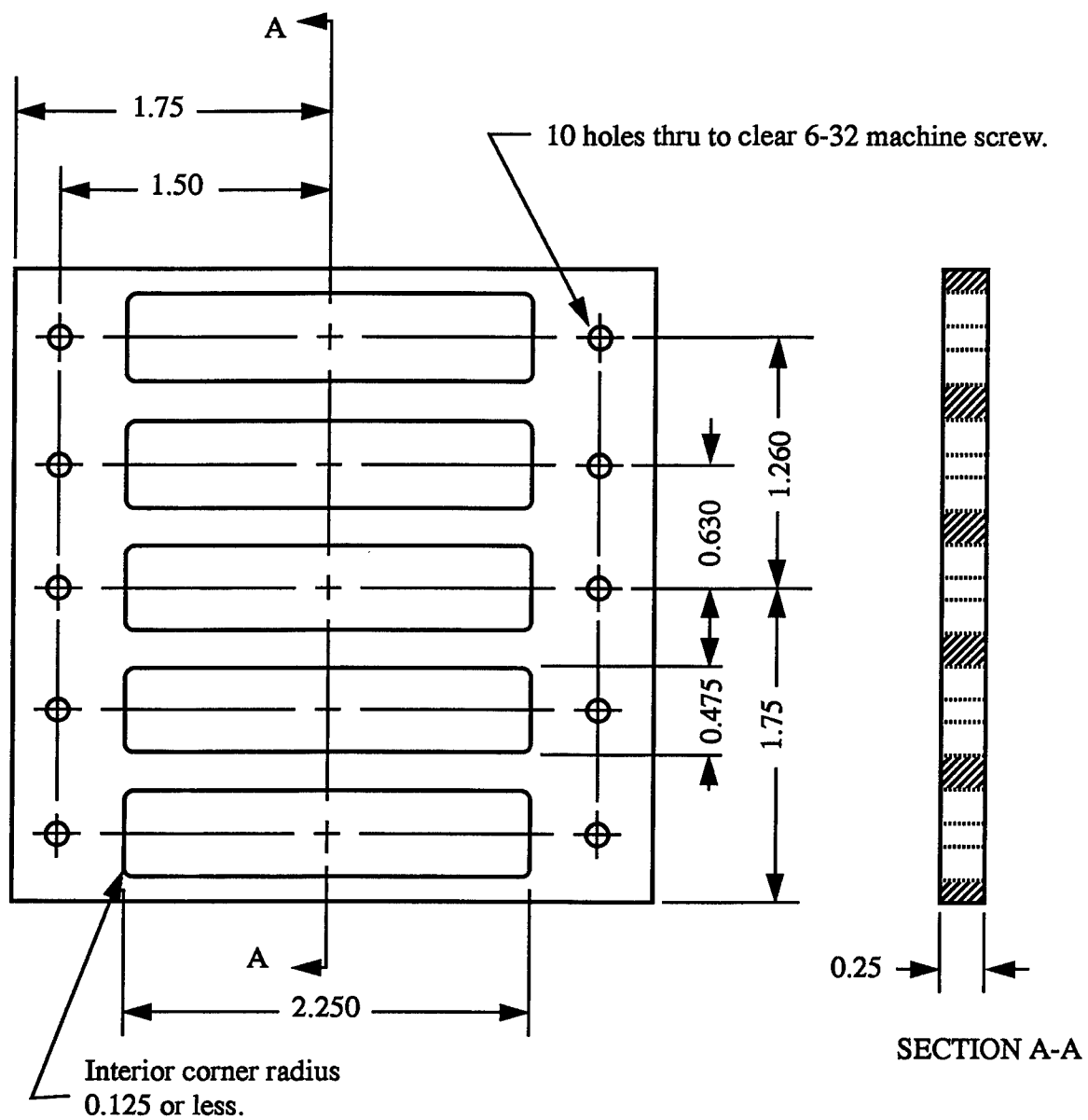


Figure 16: Clamping plate for the lens frame.

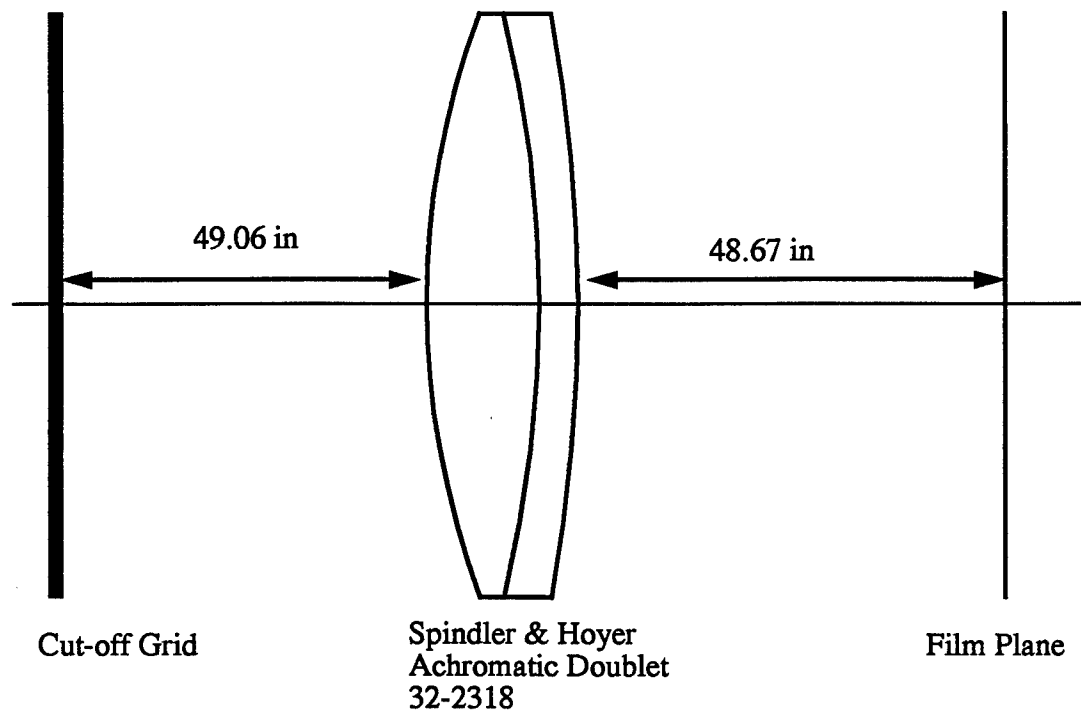


Figure 17: One possible choice for the imaging optics to follow the cut-off grid. Great flexibility exists in this part of the system.

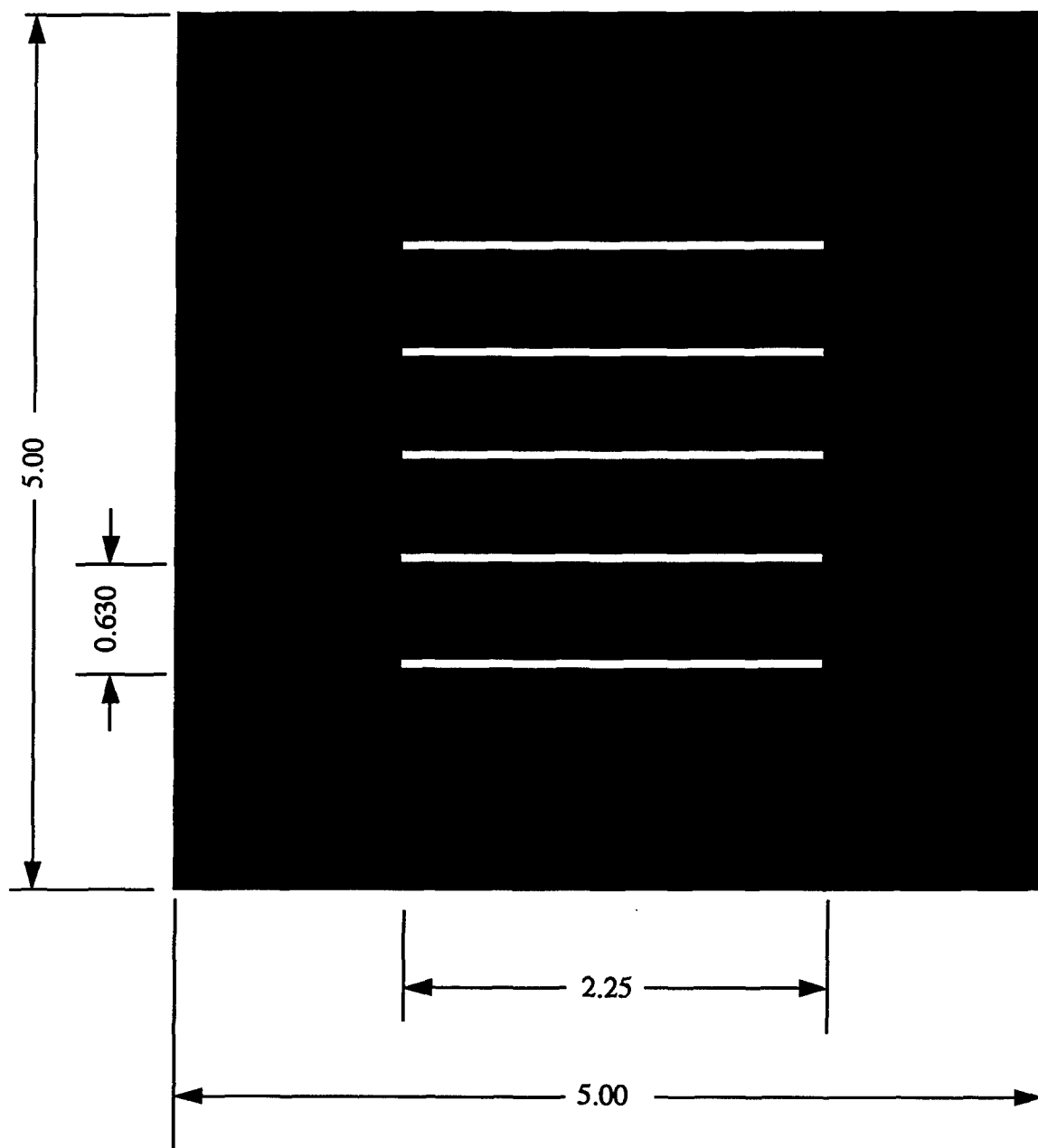


Figure 18: Lay-out of the required cut-off grid. Mount on a fine vertical traverse. Roll adjustment about the optical axis will be useful.

Cylindrical lenses are Melles-Griot part 01 LCP 155/078, cut or ground down to a height of 14mm (0.5512in), as shown in Figure 15. It is recommended that the cutting be done by the manufacturer prior to application of the anti-reflection coating. Shown in the bottom portion of Figure 15 is the nylon, or similar, pads used at each end of the curved face of the lens. The pads rest between the lens and the cover plate (Figure 14), or may even be bonded to the cover plate to simplify installation.

Figure 17 shows the imaging optics. Considerable flexibility exists in the optics that follow the cut-off grid. The present design is pretty much the simplest design, similar to a couple that are in use in our labs. The magnification is sized to fit the image directly on the existing 2-1/4 inch format camera. A viewing screen could also be used. The cut-off grid (Figure 18) must be manufactured with care. A photographic recording of the image of the source slits is an option, but unlike other published systems, it is not a necessity. Painted glass or five independently adjustable metal slits are two other options.

ACKNOWLEDGEMENTS

This research is supported through the 1992 AFOSR Summer Faculty Program, and the 1993 AFOSR Summer Research Extension Program, subcontract 93-144. Technical supervision is provided by Dr. George Seibert of Wright Labs. Experiments were performed by Mr. Terry Ray Salyer, and comprise much of his masters thesis at Purdue. Mr. Salyer developed much of the successful data processing methods used to quantify the image noise levels.

References

- [1] R. A. Burton. A modified schlieren apparatus for large areas of field. *Journal of the Optical Society of America*, 1949:907-908, Nov. 1949.
- [2] A. Kantrowitz and R. L. Trimpi. A sharp-focusing schlieren system. *Journal of Aeronautical Science*, 17(5):311-314, May 1950.
- [3] R. W. Fish and K. Parnham. Focusing schlieren systems. Technical Report IAP 999, ARC, Nov. 1950.
- [4] Laurence R. Boedeker. Analysis and construction of a sharp focusing schlieren system. Master's thesis, MIT, 1959.
- [5] Leonard M. Weinstein. Large-field high-brightness focusing schlieren system. *AIAA Journal*, 30(7):1250-1255, July 1993.
- [6] S. Price Cook and Ndaona Chokani. Quantitative results from the focusing schlieren technique. In *AIAA 31st Aerospace Sciences Meeting*, 1991. AIAA Paper number AIAA 93-0630.

- [7] Ehud Gartenburg, Leonard M. Weinstein, and Edwin E. Lee, Jr. Aerodynamic investigation with focusing schlieren in a cryogenic wind tunnel. In *AIAA 11th Applied Aerodynamics Conference*, 1993. AIAA Paper number AIAA 93-3485.
- [8] Steven H. Collicott and Terry Ray Salyer. Noise reduction properties of a multiple-source schlieren system. In *24th AIAA Fluid Dynamics Conference*, July 1993. AIAA paper number AIAA-93-2917.
- [9] Terry Ray Salyer. Quantitative noise reduction measurements of a multiple-source schlieren system. Master's thesis, Purdue University, School of Aeronautics and Astronautics, 1994. Expected in February.
- [10] H. W. Liepmann and A. Roshko. *Elements of Gas Dynamics*. Wiley & Sons, New York, 1957.
- [11] Leonard M. Weinstein. An improved large-field focusing schlieren system. In *AIAA 29th Aerospace Sciences Meeting*, 1991. AIAA Paper number AIAA 91-0567.

NOMENCLATURE

a	source slit spacing.
D	diameter of mirror or lens.
f	focal length of mirror or lens.
$F/\#$	F-number of an optic.
h	width of source slits.
\bar{I}	Mean intensity.
I_{NOISE}	intensity of image noise.
I	Pixel intensity or grey scale level.
L_I	integration length.
l_D	length scale of noise disturbance.
N	total number of source slits used.
$n_p(I)$	Number of pixels at intensity I .
n_{tot}	Total number of pixels.
R_{max}	maximum noise reduction factor.
r	Radius of gyration of histogram.
α	angle between adjacent beams.
λ	central wavelength of light.

TARGET CLASSIFICATION USING FUZZY IMAGE ALGEBRA NEURAL NETS

Dr. Jennifer Davidson
Assistant Professor

Rashmi Srivastava
Research Assistant

Department of Electrical and Computer Engineering
Iowa State University
Ames, IA 50011

Final Report for:
Research Initiation Program
Armament Laboratory
WL/MNGS Eglin AFB, Florida

Sponsored by:
Air Force Office of Scientific Research
Bolling Air Force Base, Washington, D.C.

and

Iowa State University

February 1994

TARGET CLASSIFICATION USING FUZZY IMAGE ALGEBRA NEURAL NETS

Dr. J. L. Davidson
Department of Electrical and Computer Engineering
Iowa State University

Abstract

Automatic Target Recognition using Fuzzy Image Algebra Neural Networks (FIANN) is studied. The network uses an activation function based on the generalized mean that offers a range of mapping functions from linear to the nonlinear fuzzy morphological. The FIANN is used in a heterogenous network structure for classifying tanks by the range data part of LADAR data. The network combines a feature extractor followed by a pattern recognizer for tank classification. Supervised training combines stochastic learning and gradient descent techniques, a new approach for this network. The input for the network is the range data converted to elevation or height form. The output of the network is one class from a total of three classes representing two tanks and one nontank object. This net achieved an 80% correct classification rate with a 25% rate of false alarm.

Contents

I	Introduction	8-4
II	Data	8-6
III	Fuzzy Image Algebra Neural Network (FIANN)	8-11
IV	Network Architecture and Training	8-19%[% Printer
V	Implementation & Results	8-23
VI	Conclusions & Future Research	8-29
VII	Acknowledgments	8-30
	Bibliography	8-31

TARGET CLASSIFICATION USING FUZZY IMAGE ALGEBRA NEURAL NETS

J. L. Davidson and R. Srivastava

I. Introduction

An artificial neural network (ANN) is a complex dynamical system that is inherently parallel in nature. ANNs are complex nonlinear dynamical systems that can perform a variety of tasks such as pattern recognition, optimization, and function determination. By nature of its methodology, an ANN solution can be more robust in nature than those from conventional methods. ANNs can be used for the solution of problems where the data may be noisy, incomplete, as well as where classical methods perform poorly, such as in automatic target recognition (ATR) problems.

This report presents a neural network application to target classification using a new type of neural network called the Fuzzy Image Algebra Neural Network (FIANN) [Gader, 1992]. Most pattern classification schemes make use of linear convolutional values or morphological structuring elements as pattern features that can be learned by a neural net. The FIANN, however, has an activation function based on the generalized mean. This function theoretically offers a variety of mapping functions, ranging from linear to the nonlinear fuzzy morphological.

The United States Air Force (USAF) is interested in new methodologies that are both versatile and accurate in solving ATR problems. This report details the efforts of Dr. Jennifer Davidson, Principal Investigator (PI), and her graduate student Rashmi Srivastava, in using the FIANN to solve a tank classification problem on LADAR data. LADAR range images provide a topographic mapping of the visible portion of the target

through direct measurement of the range to points on the target. The LADAR data used for this investigation has the added advantage of low expense and high resolution. The objective is to classify the tanks in the image data by type. The range data is first converted to elevation data, which is input to the net for classification. A two tiered approach is used, consisting of a feature extractor followed by a pattern classifier. First, a subimage of the target is extracted and converted into elevation form. That subimage is divided into overlapping rectangular zones, with the expectation that a partially occluded object can still carry forward enough information from fewer zones to the neural network for object identification. Linear convolution is carried out on each zone to provide feature information about the object, and the convolution values are passed to the top layer of the network. The top layer performs pattern classification on the features.

Previous approaches to ATR on range images have used model based approaches where the target is matched with 2-dimensional and 3-dimensional target templates [James Bevington and Lee, 1992], or image features are matched against model features based on an object description called attributed relational graph (ARG) [Li, 1992]. Morphological approaches make use of structuring elements, which are ideally suited for analysis of range images due to their inherently geometric nature [Krishnapuram and Gupta, 1992]. Also, they can handle features of known physical size [Verly and Delanoy, 1993].

The architecture of the FIANN is heterogenous. Generalized image algebra operations are used to obtain fuzzy morphological or linear operations. The parameters for the generalized operations are learned in a fashion similar to standard backpropogation. The lower layer of the net is trained using gradient descent. The upper, decision-making layers

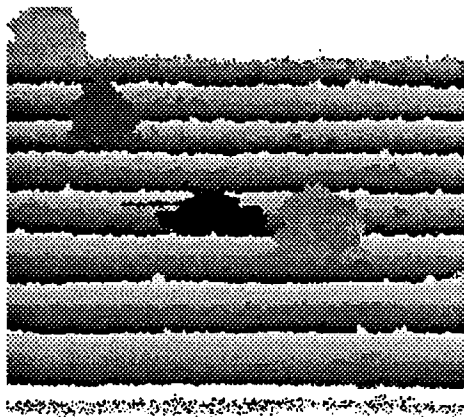
are trained using a combination of stochastic learning and gradient descent. Our results show that with proper training and selection of parameters, the network can perform classification. For instance, for one tank and one nontank class, correct classification was obtained 90% of the time (with, however, 60% false alarm).

The report is organized as follows: Section II consists of a description of the data used in the research and the preprocessing necessary to prepare it for input to the neural net. Section III introduces the fuzzy image algebra neural net and discusses the learning rules we used. Section IV details the architecture and training scheme for the neural network used in this specific target identification problem. Section V contains the results, and Section VI presents conclusions and suggestions for future research.

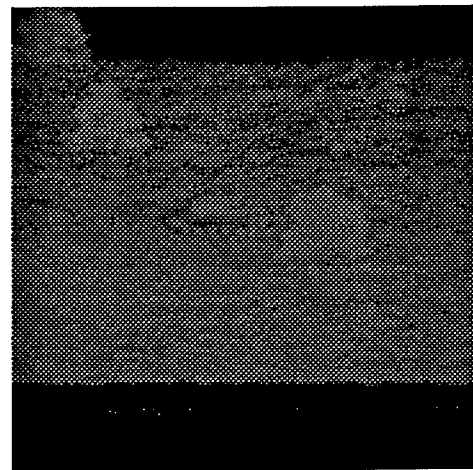
II. Data

The type of data used for this research is LADAR data collected by LTV. This data is visually very good and has very high resolution, of the order of 0.1 milliradians in both vertical and horizontal directions. LADAR data consists of two types of information at every pixel location. The first is the distance, in some unit, from the sensor to the sensed object in the real world. This is termed *range* data. The range data values varied from 1 to about 2000 units. The second value is the *intensity* of the returned signal, hence called intensity data. This data had a range of values from about 1 to 255. Certain approaches to ATR use both range and intensity data [Hackett and Shah, 1989], but for our classification problem, we made use of the range data. Even though the intensity data has greater visual contrast and hence appears to carry more information, it is the range data which carries more information. See Figure 1 for a sample of range and intensity

data. From the range data an elevation image can be constructed using simple geometric and trigonometric rules. Thus, there is 3-dimensional geometrical shape information in the range data that is not available in the intensity data. Further, the range data has excellent vertical and horizontal resolution, typically on the order of 6" or a foot. The range resolution along the line of vision is just as good.



Range Image



Intensity Image

Figure 1. 256 x 256 Range image and intensity image
of the same scene with an M60 tank in the foreground.

Converting Range Data to Elevation Data

The range images from the LADAR data typically consist of size 256 x 1024 pixels, and most contain one or more vehicles. The vehicles are tanks, trucks and jeeps. The natural terrain consists of trees, bushes, sandhills, and the like. The range image is first histogram equalized and then a small subimage consisting of one vehicle is extracted. See Figure 2 for a sample range subimage. The extraction process was manual, i.e.,

the vehicle coordinates were determined by looking at the image, and the rectangular window to be extracted was determined. An image processing software called Khoros could also be used for this purpose. Khoros is a public-domain software that allows, among other things, windowing of images, and also gives exact coordinates at any point in the image. Further research could be carried out to perform automatic extraction of the vehicle subimage. In any case, the subimage is then converted to elevation data using the Cartesian Method as follows [Kweon and Kanade, 1992].



Figure 2. M60 Tank range subimage.

The position of a point in the Cartesian coordinate system can be derived from the measured range value and the direction of the sensor beam at that point, both of which are available from the data we used. Figure 3 shows the range measurement (ρ) and the direction of the sensor beam which is specified by its vertical (ϕ) and horizontal (θ) scanning angles. The two angles are derived from the row and column position in the range image (r, c) by the equations

$$\theta = \theta_0 + c * \Delta\theta$$

$$\phi = \phi_0 + r * \Delta\phi$$

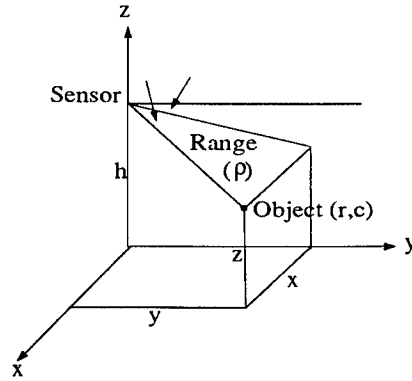


Figure 3. Geometry of the range sensor

The variables ϕ , θ , and (r, c) in Figure 3 have the following definitions:

ρ : Range measurement.

ϕ : Vertical Scanning Angle (Initial value ϕ_0 , Increment $\Delta\phi$).

θ : Horizontal Scanning Angle (Initial value θ_0 , Increment $\Delta\theta$).

(r, c) : Range image coordinates.

The x , y , z coordinates are then obtained using the following equations based on simple trigonometry and geometry.

$$x = \rho * \sin\theta$$

$$y = \rho * \cos\phi * \cos\theta$$

$$z = \rho * \sin\phi * \cos\theta$$

The resulting transformed image is called the elevation image. The missing data points in this image are filled in using a variation of bilinear interpolation.

Interpolation and Scaling

One of the main drawbacks of the Cartesian method is that it introduces nonuniform samples in Cartesian space. Even though the range finder scans with equal angle intervals,

the Cartesian map is progressively more sparse at points further from the sensor. It therefore becomes necessary to employ an interpolation scheme to fill in the missing data. The following steps are carried out during this datafill operation.

1. The x, y, z values are mapped into an image whose dimensions extend from 0 to the maximum value of x calculated for the columns, and 0 to maximum value of y calculated for the rows. An even grid is created and all missing z values are left empty.
2. A variation of the bilinear interpolation scheme is used to fill in the data.
 - a. Let $a \in R^X$ be the incomplete elevation image and $b \in R^X$ be the filled image. X is of size Rows x Cols, where Rows = maximum x dimension and Cols = maximum y dimension.
 - b. We check for a string of zeros in a row in between two nonzero z values. Let the two nonzero values be at locations (i,j) and (i+l,j). Then the values in between are given by:

$$\text{for } r = i, i + l$$

$$b(r, j) = (a(i, j) + a(i + l, j)) / (i - r)$$

- c. If a boundary location has a zero value, we look for the nearest non zero values along the row and along the column and average these. A point with this value is assumed outside the boundary point and interpolation carried out as in (b).
3. These interpolated elevation images vary in size from 100 x 200 to 50 x 50. It is necessary, therefore, to scale them to a standard size to input to the neural net. The size used for our analysis was 30 x 50.

4. The elevation image is scaled to a size 30 x 50 by convolving it with a shrinking, averaging template.

a. If X is an $M \times N$ rectangular array and $a \in R^X$. Let Y be a $P \times Q$ rectangular array and $b \in R^Y$ where $P < M$, $Q < N$. We write

$$M = U * P + R \quad U, V, R, S \text{ are integers}$$

$$N = V * Q + S \quad 0 \leq R \leq M, 0 \leq S \leq N$$

b. If $(R, S) = (0, 0)$ then define $t \in (R^X)^Y$ as follows:

if $(1, 1) \leq (i, j) \leq (R, S)$ then

$$t_{(i,j)}(h, k) = \begin{cases} \frac{1}{(u+1)(v+1)} & \text{if } ((i-1)(u+1)+1, (j-1)(v+1)+1) \\ & \leq (h, k) \leq (i(u+1), j(v+1)) \\ 0 & \text{otherwise} \end{cases}$$

if $(R+1, S+1) \leq (i, j) \leq (P, Q)$ then

$$t_{(i,j)}(h, k) = \begin{cases} \frac{1}{uv} & \text{if } ((i-1)u+1, (j-1)v+1) \leq (h, k) \leq (iu, jv) \\ \text{otherwise} \end{cases}$$

c. Then the scaled image is $b = a \oplus t$

5. The data is now in a form where it can be input to the neural net for classification.

III. Fuzzy Image Algebra Neural Network (FIANN)

Artificial neural nets are most often used as pattern classifiers. Essentially they perform a mapping from an input object space to an output classification space. Typically these mappings are determined by an optimization procedure where the error between input and known output is minimized. This 'training' phase must be carried out using

data, which, for the sake of good results, is statistically representative of the data to be classified. Further, neural nets can be fairly good at determining complex relationships between input data and the classification representations. Although neural networks do not have a very rigorous or broad mathematical foundation, they have been used to solve a wide variety of problems and have produced very acceptable results in many applications. They have been used for pattern recognition, speech and image processing, data forecasting, and a multitude of such tasks. Lippmann [Lippmann, 1987] gives a wide variety of networks for pattern classification.

Classical neural networks consist of a collection of nodes interconnected with weights, and an algorithm for passing data in and out of the system. Classical neural networks combine the information at a particular node as follows:

$$C_j = f \left(\sum_{i=0}^N w_{ji} a_i \right),$$

where C_j is the node value at an upper level node j , a_i is the node value at a lower level node i , and node i is connected to node j by weight w_{ji} . The function f is called an activation function and is usually nonlinear, such as the sigmoid function.

The activation function of the FIANN is not of the standard sigmoidal form. It is motivated by the generalized mean which is useful for defining generalized template operations. This is because the generalized mean can represent both linear and morphological operations.

The generalized mean for a set of numbers $\{x_i\}$ is given by:

$$g(x_1, x_2, \dots, x_n) = \left[\sum_{i=1}^n w_i x_i^P \right]^{1/P}$$

Here, x_i represents the input fuzzy class memberships and w_i can be viewed as relative importance factors for different criterion. Also, we must have $x_1 + x_2 + \dots + x_n = 1$ [Krishnapuram and Lee, 1992].

One of the properties of the generalized mean that makes it attractive is that the mean value always increases with an increase in P , that is, if $-\infty < P < +\infty$, then we can obtain all values from the minimum to the maximum of the data set. Thus, the whole range of fuzzy operations from intersection to union and anything in between can be approximated. An interesting feature is that $P = -1$ gives the harmonic mean, $P = 0$ gives the geometric mean, and $P = 1$ gives the arithmetic mean.

We first define the operands involved in the fuzzy image algebra neural net. Let $\mathbf{X} = \mathbf{Z} \times \mathbf{Z}$ be the coordinate set, where \mathbf{Z} is the set of integers. An image on \mathbf{X} with values in the closed interval $[0,1]$ is a function $\mathbf{a}: \mathbf{X} \rightarrow [0,1]$. A template on \mathbf{X} is a function $\mathbf{t}: \mathbf{X} \rightarrow [0,1]^{\mathbf{X}}$. The maximum support, S_0 of the template \mathbf{t} and minimum support S_1 are defined by

$$S_i(\mathbf{t}_{(\mathbf{j},\mathbf{i})}) = \left\{ (\mathbf{i},\mathbf{j}) \in \mathbf{X} : \mathbf{t}_{(\mathbf{j},\mathbf{i})} \neq \mathbf{i} \right\} \quad \mathbf{i} \in \{0,1\} \quad (1)$$

For the remainder of the report, we will use the subscript \mathbf{ji} to designate (\mathbf{j},\mathbf{i}) for templates to ease the notation.

The generalized mean has two important properties which make it a very flexible operator and very useful in pattern recognition problems. These are as follows:

1. Fuzzy erosion property: The first of these properties is as follows. If

$$w_{ji} = \frac{1}{N_j} \quad \text{for all } i, j$$

$$\text{and } P \rightarrow -\infty$$

$$\text{then } c \rightarrow a \boxminus_f t,$$

where $c = a \boxminus_f t$ represents the fuzzy erosion of image a with template t and is defined by:

$$c_j = \bigwedge_{i \in S_1(t_{ji})} r(1 - t_{ji} + a_i)$$

In effect the weighted fuzzy erosion represented by b should approximate the fuzzy erosion of image a with template t when the above conditions are met.

2. Convolution property: The second property is, if,

$$P = 1$$

$$t_{ji} = 1 \quad \text{for all } i, j$$

$$\text{then } c = a \oplus w,$$

where $c = a \oplus w$ is given by:

$$c_j = \sum_{i \in S_0(t_{ji})} a_i * w_{ji}.$$

If w is translation invariant then $a \oplus w$ represents linear convolution.

These two properties make the activation function of the FIANN very interesting. However, the key point in using this activation function is that this activation function is differentiable. This allows us to derive a gradient descent learning algorithm using the chain rule.

Governing Equation for the FIANN

The governing equation for the fuzzy image algebra neural net is $b = a \boxdot g$

$$b_j = \left[\sum_{i \in S_0(t_{ji}) \cap S_1(t_{ji})} w_{ji} * r[1 - t_{ji} + a_i]^P \right]^{1/P} \quad (2)$$

Here, b represents the weighted fuzzy erosion of image a with a parametrized template group g given by : $g = (t, w; P)$ where t and w are image algebra templates and P a parameter. Here a is an image with values in $[0,1]$. The ramp function $r(x)$ is defined by:

$$r(x) = \begin{cases} 0 & x < 0 \\ x & 0 < x < 1. \\ 1 & 1 < x \end{cases}$$

See Figure 4 for a graph of r . The supports S_0 and S_1 are defined in Eq. (1).

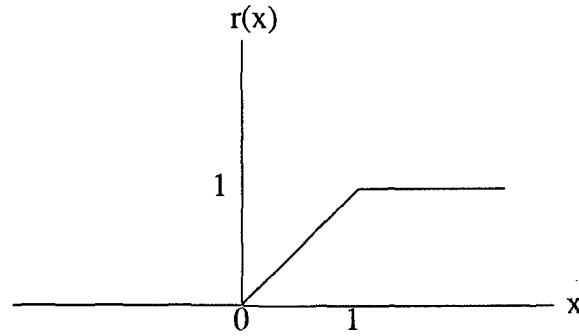


Figure 4. The ramp function r .

The weighted fuzzy erosion between a and g is carried out over an image area which represents the intersection of the maximum and minimum supports of t .

The input to the network is an image. We train on N pairs of data, each pair consisting of an image a_k and a desired output d_k ; $k = 1, \dots, N$. We wish to find a template group g

that minimizes the sum of the squares of the difference between the actual and desired output:

$$E = \sum_{k=1}^N \sum_{(i,j) \in X} E_k^2(i,j)$$

where

$$E_k(i,j) = [(a_k \boxminus g - d_k)(i,j)]$$

$$d_k = a_k \boxminus_f \tilde{t}$$
(3)

where \tilde{t} is the ideal template for fuzzy erosion.

Learning Schemes

Two learning schemes were implemented on the FIANN.

1. Gradient Descent
2. Stochastic Learning

Gradient Descent

1. In this method the cost function is minimized by following the gradient of E.
2. Algorithm:
 1. The templates t , w are randomly initialized to values in $[0,1]$. Parameter P is randomly initialized to some large negative number.
 2. Training pairs of input image a_k and desired output image d_k are presented to the net.
 3. Error E is calculated and generalized template g modified using the gradient descent learning rules.
 4. Steps 2–3 are repeated until error falls below acceptable level.

3. Training Rules:

- For Template **w**: The weights w_{ji} are updated following the gradient of E as follows:

$$w_{ji}^{new} = w_{ji}^{old} - \eta_1 \frac{\partial E}{\partial w_{ji}},$$

where

$$\frac{\partial E}{\partial t_{ji}} = \sum_{k=1}^N (f_j^k - d_j^k) \frac{\partial f^k}{\partial t_{ji}},$$

and

$$\frac{\partial f^k}{\partial w_{ji}} = \frac{2w_{ji}}{p\|w\|^2} (f^k)^{1-P} \left(r[1 - t_{ji} + a_i]^P - (f^k)^P \right).$$

Further the value of $\frac{\partial f^k}{\partial w_{ji}}$ is nonzero only when $r(1 - t_{ji} + a_i) \in [0, 1]$ and this holds true for all the partials. The computation of $\frac{\partial f^k}{\partial t_{ji}}$ and $\frac{\partial f^k}{\partial P}$ is the same as for w_{ji} .

- For Template **t**: Learning equations for template **t** are as follows:

$$t_{ji}^{new} = t_{ji}^{old} - \eta_2 \frac{\partial E}{\partial t_{ji}}$$

$$\frac{\partial f^k}{\partial t_{ji}} = \frac{-2w_{ji}}{\|w\|^2} (f^k)^{(1-P)/P} \left(r[1 - t_{ji} + a_i]^{P-1} \right).$$

The value of the parameter η is determined by the training set size [Eaton and Olivier, 1992].

- For Parameter **P**: The equations for updating **P** are as follows:

$$P^{new} = P^{old} - \eta_3 \frac{\partial E}{\partial P}$$

where

$$\frac{\partial f^k}{\partial P} = \frac{(f^k)^{1-P}}{P^2} \sum \frac{w_{ji}^2}{\|w\|^2} (m_{ji}^k)^P \ln(m_{ji}^s)^P - (f^k)^P \ln((f^k)^P)$$

and where

$$m_{ji}^k = r[1 - t_{ji} + a_i].$$

Stochastic Learning

1. Random optimization methods use Gaussian probability density functions to generate random search vectors. In this method we randomly perturb one of the weight vectors and if the resultant cost function is lower we select this vector and start gradient descent at this point. This technique allows us to move about in the error space and jump out of local minima [Bartlett, 1994].
2. Algorithm:
 1. The templates \mathbf{t} , \mathbf{w} are randomly initialized to values in $[0,1]$. Parameter P is randomly initialized to some large negative number.
 2. Calculate initial cost E^{old} .
 3. Make small random changes to one of the templates \mathbf{t} , \mathbf{w} or to parameter P . Calculate cost E^{new} .
 4. If $E^{\text{new}} < E^{\text{old}}$ then goto step 5. Else repeat step 2.
 5. Keep the new weight set and discard the old.
 6. Now carry out gradient descent for a fixed number of times.
 7. If error is less than some predetermined acceptable cost, end training, else goto step 3.
 8. Repeat steps 3–7 until convergence.

IV. Network Architecture and Training

The network consists of an input layer, two hidden layers and an output layer. The training data, an elevation image of size 30 x 50 with values in the closed interval [0,1], is input to the net. The image is divided into sections of size 6 x 8 with an overlap of two rows and two columns. Each of these subimages is connected to one node of the first hidden layer. This calls for a total of 56 nodes in the first hidden layer. Thus the information contained in 1500 input image points is mapped onto 56 points. Essentially, the first hidden layer acts as a feature detector. It attempts to learn the features of different sections of the image. The information from this layer is further condensed into 14 nodes in the next layer. Here, too, there is only partial interconnection between the layers. Four successive nodes in the first hidden layer are connected to one node in the second hidden layer. The second hidden layer allows the net to learn image features more efficiently. Finally, the 14 nodes from this layer are completely connected to three output layer nodes. This layer gives the results of the classification. Only one node at a time will be high representing a particular tank or vehicle, e.g., node 1 high implies that the input image was an M60 type tank. The network architecture and training schemes are shown in Figure 5. We now give a step by step description of net operation and training.

1. An elevation image of size 30 x 50 with values in [0,1] is input to the first layer of the net. The image is divided into subimages of size 6x8 which overlap with adjacent images by 2 rows and 2 columns.
 - a. Each of these subimages is connected to one hidden node in the first hidden layer.

This layer has a total of 56 nodes. A simple linear convolution is performed

between the subimage and the node to combine the information along all the data points in the subimage. Multiple template groups are used for the image, one for each subimage. Let these be represented by $g1 = (t1, w1, P1)$.

- b. Four successive first hidden layer nodes are connected to one second hidden layer node. The multiple templates used here are represented by $g2 = (t2, w2, P2)$.
- c. Finally, the second hidden layer nodes are completely connected to the three output layer nodes. This template is represented by $g3 = (t3, w3, P3)$.

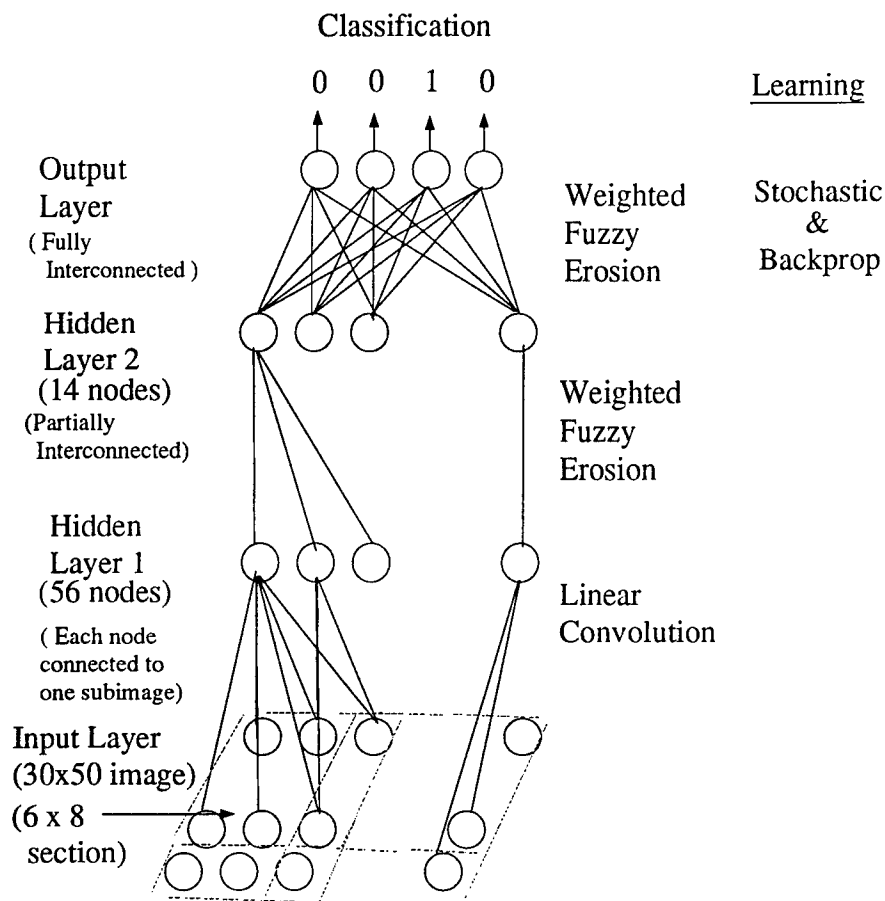


Figure 5.

2. The \mathbf{t} and \mathbf{w} templates associated with the generalized templates are initialized randomly to values in $[0,1]$. The parameter P is initialized to some negative number. In **g1**, $P1 = 1$, since we are trying to simulate the linear convolution property of the generalized mean. All the templates are translation invariant.
3. The output at all the nodes in the hidden and output layers is calculated successively, using weighted fuzzy erosion, as follows:

$$b_j = \left[\sum_{i \in S_0(t) \cap S_1(t)} w_{ji} * r [1 - t_{ji} + a_i]^P \right]^{1/P}$$

4. Training the network: A modification of the standard backpropagation training rule is used.

a. Output Layer:

- As each successive input is presented to the net, the output at the final layer and the error associated with the input are calculated. The weight vectors for **g3** are perturbed and the output and error recalculated until we obtain a weight vector which gives us a lower error for that image. This is done for each of the training images. The total error is now calculated using Equation (3).
- Gradient descent is carried out for about 10 iterations using the equations given in the previous section.
- The weights for the output layer are then updated a final time using the following equations based on the backpropagation delta rule.

$$w_{ji}(t+1) = w_{ji}(t) + \Delta w_{ji}(t) \quad \text{where,} \quad (4)$$

$$\Delta w_{ji}(t) = \eta \delta_j a_i + \alpha [\Delta w_{ji}(t-1)], \quad \text{and,}$$

$$\delta_j = (d_j - o_j) \frac{\partial f_j}{\partial a_j},$$

for an output node j connected to a lower node i through weights w_{ji} . The weights for template t are updated similarly

b. Hidden Layers:

- Here too a combination of stochastic learning and gradient descent is used for training the net. This time, the weight vectors for g_2 are perturbed and values calculated at the hidden and output nodes till a lower error surface is obtained.
- Starting at this error surface gradient descent is carried out for 10 iterations and finally the weights are updated one last time using the delta rule. In the backpropagation neural net these delta values are passed back through the weights or synapses, so that the error value for a hidden layer node (i) is taken as a weighted sum of the errors of the nodes in the layers above to which it is connected. Thus the value of δ_j for a hidden node is as follows:

$$\delta_i = \frac{\partial f_i}{\partial a_i} \sum_{j=1}^n w_{ji} \delta_j,$$

for a hidden node i connected to an upper node j through a synapse w_{ji} and n is the number of synapses for node i . The weights for t and w are updated using Equation (4) and this delta value.

- c. These steps are repeated until the net converges or the error at the output nodes is very small, of the order of 10^{-3} as compared to an initial error of about 20.

- d. The network is now trained and ready for classification.

V. Implementation & Results

The net implementation was carried out in two stages. In the first stage a one layer FIANN was designed whose training data consisted of N pairs: an input image and a corresponding desired output image. The FIANN's erosion and convolution properties were tested and optimal training rules obtained. In the second stage, a multilayer FIANN was implemented to carry out target classification. A more detailed description of the two stages now follows:

I. Testing the FIANN's Erosion and Convolution Properties:

a. Erosion Property

- *Implementation:* A 1 layer net was implemented in which the number of nodes equalled the number of pixels in the input image. The input was an image of certain size (16 x 16, 64 x 64) and the desired output was its corresponding fuzzy eroded image obtained as follows:

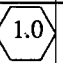
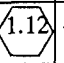
$$c_j = \bigwedge_{i \in S_1(t_{ji})} r(1 - t_{ji} + a_i)$$

The generalized template \mathbf{g} was initialized such that $w_{ji} = 1/N_j$ for all i, j , where $N_j = |S_0(t) \cap S_1(t)|$, template \mathbf{t} and parameter P are randomly initialized.

- *Training:* The net was trained to 'learn' a template \mathbf{g} such that weighted fuzzy erosion of input \mathbf{a} with this template would produce the same output

image as would the fuzzy erosion of \mathbf{a} with $\tilde{\mathbf{t}}$, where $\tilde{\mathbf{t}}$ is some template commonly used for fuzzy erosion. Several different training rules had to be applied before an optimal training rule was obtained. The one layer net was trained using three different learning schemes. These were:

- Stochastic Learning
 - Simulated Annealing
 - Gradient Descent
-
- *Results:* Figure 6 shows the template values obtained for the fuzzy erosion case with the different learning schemes. As can be seen none of the templates match the original template. However, it should be noted that the operations of fuzzy erosion and weighted fuzzy erosion are algebraically different operations, hence two different templates could produce the same output with these two operations. The lowest error, calculated using equation (3), was obtained using the stochastic learning algorithm. Simulated Annealing and gradient descent, both did not give good results for this property.

Original Template			Template from gradient descent training		
.333	.083	.333	-0.58	-0.06	0.41
.416		.416	0.75		-3.7
.333	.083	.333	0.0	-1.01	0.35

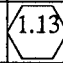
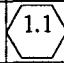
Template from Simulated Annealing			Template from Stochastic Learning		
0.9	-.484	1.227	.401	.102	.388
.484		.444	.544		.391
.603	.516	.066	.333	.09	.54

Figure 6. Results for erosion property.

b. *Convolution Property*

- *Implementation:* This was tested similarly on a one layer net where number of nodes equalled the number of pixels. Generalized template \mathbf{g} was initialized such that $P = 1$ and $t_{ji} = 1$ for all i, j .
- *Training:* The net was trained to 'learn' a template \mathbf{g} such that weighted fuzzy erosion of input \mathbf{a} with \mathbf{g} would be equivalent to convolution of \mathbf{a} with template \mathbf{w} given by:

$$c_j = \sum_{i \in S_0(t_{ji})} a_i * w_{ji}.$$

- *Results:* This property was tested using the gradient descent scheme. This learning method gave fairly good results. As can be seen in Figure 7, the template values do not correspond to one another but the template shown below produced an image closest to the desired image.


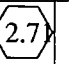
Original Template			Template from gradient descent training		
.333	.083	.333	4.06	3.08	5.6
.416		.416	4.51		5.89
.333	.083	.333	3.85	3.54	6.89

Figure 7. Results for convolution property.

II. Target Classification using a Multilayer FIANN

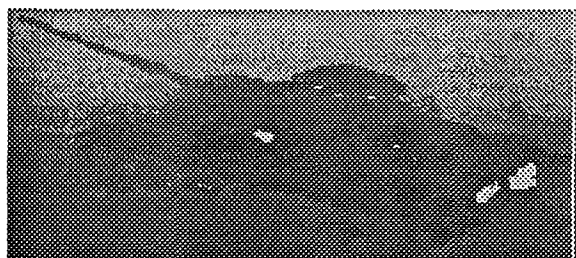
- *Implementation:* The network architecture and learning rules are explained in the previous section. The net was trained to give three possible classification results:
 - Tank of type M60.
 - Tank of type M53.
 - Nontank.
- *Results:* The results obtained are given in the tables in Figures 8 and 9. "False alarm" signifies a nontank object identified as a tank. The recall data was a combination of training data and new inputs. Sample range images for the three classes can be seen in Figure 10.

Training Data		Recall Data		%Classified correctly		False Alarm
M60	Non-tanks	M60	Non-tanks	M60	Non-tanks	
6	4	10	5	90%	40%	60%

Figure 8. Results for one tank and one nontank class.

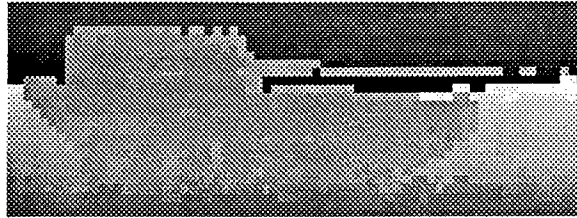
	Training Data		Recall Data	% Classified as the correct tank	% Classified as the wrong tank	False Alarm
Run 1	M60	6	6	50%	50%	-
	M53	6	6	100%	0%	-
	Non-tanks	4	4	50%	-	50%
Run 2	M60	10	10	80%	20%	-
	M53	5	5	80%	20%	-
	Non-tanks	4	4	75%	-	25%

Figure 9. Results for two tank and one nontank class.



M60 Range Image

Figure 10. Range images of the three input classes. (Continued . . .)



M53 Range Image



Nontank Image (Tree)

Figure 10. Range images of the three input classes.

Considering the complexity of the network, the FIANN gave a reasonably good performance on the range data. Initially only two classes were used, one tank and one nontank. Six different images of the M60 tank, and 4 images of the general terrain, taken from several range images at different angles and range offsets, were used as net input. In this case the net classified the tank correctly 90% of the time. However, the net did not perform well on nontank data and gave only 40% correct classification with a false alarm rate of 60%. When two different tanks were used as training data the results were not as good. The net seemed to be biased towards the class of M53 artillery type tanks

and classified them correctly each time. With the class of M60 type tanks, the rate of correct classification was only 50%. The nontank targets were also classified correctly only 50% of the time, with a false alarm rate of 50%. More simulations of the data are being performed and will be available for future reference.

It should be noted here that all of the data used for training purposes was real data. This data was extracted from several different range images, each having a different range offset and sensor angle. The horizontal and vertical resolutions also varied in these images. The elevation data obtained was very sparse and had to be filled in using linear interpolation. Thus, the data used was very noisy, and this could be a reason for the inconsistent results.

VI. Conclusions & Future Research

The FIANN has potential as a pattern classifier, although more research needs to be performed to determine its appropriateness for this type of pattern classification. The network's differentiable activation function, based on the generalized mean, requires careful selection of initialization points and parameters. The training schedule for the FIANN, as formulated in our research, is a complex combination of several different training schemes. Hence, parameter selection is a critical factor in network training. The results for one tank and one nontank data, using random initialization procedures, were promising. With a greater number of classes the results deteriorated somewhat, and a more detailed investigation of the system needs to be performed.

A great deal of future research is possible with the FIANN. Selection of initial starting points for the weight vectors, finding optimum values for the various parameters used

in training and weight update, as well as different training schemes for the net are all areas of interest. Further, the network architecture proposed in the report, which is a variation of the standard backpropagation net, is just one type of architecture possible. For example, this net could be modified to have different numbers of hidden layers and nodes. A totally different architecture, one that is not based on the backpropagation algorithm, could also provide more experimentation. The network's performance on data other than elevation data would be an indicator of its pattern recognition capabilities. A more efficient conversion from range to elevation data, such as the locus method proposed in [Kweon and Kanade, 1992] could be explored to improve performance of the system.

VII. Acknowledgments

The authors acknowledge the generous support of AFOSR and the Armament Laboratory at Eglin AFB, including focal points Ms. Karren Norris and Dr. Patrick Coffield, on this project.

Bibliography

- [Bartlett, 1994] Eric B. Bartlett. A stochastic training algorithm for artificial neural networks. *Neurocomputing*, 6(1):1–13, 1994.
- [Eaton and Olivier, 1992] Harry A. C. Eaton and Tracy L. Olivier. Learning coefficient dependence on training size. *Neural Networks*, 5:283–288, 1992.
- [Gader, 1992] Paul D. Gader. Template generation for pattern classification. *Proc. of the 1992 SPIE Image Algebra and Morph. Image Proc. III*, 1769:72–81, 1992.
- [Hackett and Shah, 1989] K. Hackett and Mubarak Shah. Segmentation using intensity and range data. *Optical Engineering*, 28:667–674, June 1989.
- [James Bevington and Lee, 1992] Randy Johnston James Bevington and Joel Lee. A modular target recognition algorithm for ladar. *Second Automatic Target Recognizer Systems and Technology Conference*, pages 91–104, 1992.
- [Krishnapuram and Gupta, 1992] R. Krishnapuram and S. Gupta. Morphological methods for detection and classification of edges in range images. *Journal of Mathematical Imaging and Vision*, 2:351–374, 1992.
- [Krishnapuram and Lee, 1992] R. Krishnapuram and J. Lee. Fuzzy-set-based hierarchical networks for information fusion in computer vision. *Neural Networks*, 5:335–350, 1992.

- [Kweon and Kanade, 1992] In So Kweon and Takeo Kanade. High resolution terrain map from multiple sensor data. *IEEE Trans. on Pattern Analysis and Machine Intelligence*, 14:278–292, Feb. 1992.
- [Li, 1992] S. Z. Li. Towards 3d vision from range images: An optimization framework and parallel networks. *Computer Vision, Graphics and Image Processing*, 55(3):231–260, May 1992.
- [Lippmann, 1987] R.P. Lippmann. An introduction to computing with neural nets. *ASSP Magazine*, 4:4–22, Nov. 1987.
- [Verly and Delanoy, 1993] Jacques G. Verly and Richard L. Delanoy. Adaptive math morphology for range imagery. *IEEE Transactions on Image Processing*, 2(2):272–275, Apr. 1993.

TURBULENT HEAT TRANSFER IN COUNTER-ROTATING DISK SYSTEM

**Jamie S. Ervin
Assistant Professor
Department of Mechanical and Aerospace Engineering**

**University of Dayton
300 College Park
Dayton, OH 45469-0210**

**Final Report for:
Research Initiation Program
Wright Laboratory**

**Sponsored by:
Air Force Office of Scientific Research
Bolling Air Force Base, Washington, DC**

and

University of Dayton

December 1993

TURBULENT HEAT TRANSFER IN COUNTER-ROTATING DISK SYSTEM

Jamie S. Ervin
Assistant Professor
Department of Mechanical and Aerospace Engineering
University of Dayton

Abstract

A state-of-the-art gas turbine design that implements counter-rotating blades has recently been submitted to the Air Force, resulting in the need for an experimental analysis of the associated convective heat transfer. To meet this need, a fundamental study of the turbulent heat transfer and fluid flow between two counter-rotating disks has been initiated. Flow visualization by means of a laser light sheet has been used to extract qualitative details of the unsteady velocity field. Preliminary heat transfer measurements for the case of an imposed constant heat flux on one disk indicate that for a given mass flow rate, there may be an optimum rotation rate that maximizes the heat transfer. Furthermore, the Rossby number, Ro , may be used to correlate local Nusselt numbers.

TURBULENT HEAT TRANSFER IN COUNTER-ROTATING DISK SYSTEM

Jamie S. Ervin

INTRODUCTION

Counter-rotating turbine stages may be used in future high-bypass-ratio engines which eliminate the requirement for stator blades, thus reducing engine weight. A state-of-the-art gas turbine design that implements counter-rotating blades has been recently submitted to the Air Force and is shown in Figure 1. This innovative design has resulted in the need for an experimental analysis of the associated convective heat transfer. The turbulent flow in a gas turbine engine is extremely complex, and measurements in operating engines are difficult and expensive. As a consequence, rotating disk systems with radial outward flow are sometimes used to model the convective heat transfer. The simple geometry of a rotating disk system removes many of the complications associated with real engines, and yet, still offers basic insight into the nature of heat transfer processes in real engines. To meet this need, a fundamental study of the turbulent heat transfer and fluid flow between two counter-rotating disks with source flow has been initiated.

BACKGROUND

The velocity field in a counter-rotating disk system with turbulent source flow is extremely complex. The fluid velocity vector has a component in the tangential direction from shear stresses induced by moving surfaces. The mean radial velocity decreases with increasing radial distance from the source as the fluid moves through an increasing cross-sectional area. For non-isothermal systems, buoyancy forces resulting from centrifugal and Coriolis accelerations present additional flow complexities. Furthermore, as the radius tends to zero, flow separation and recirculation may occur.

Few experimental studies of the turbulent flow in counter-rotating disk systems exist in the literature and there appears to be no investigations of the heat transfer in counter-rotating disk systems. Batchelor (1951) and Stewartson (1953) considered solutions to the Navier-Stokes equations for laminar isothermal flow between counter-rotating disks that were infinite in extent. Dijkstra and van Heijst (1983) considered a theoretical and

experimental study of laminar flow between two counter-rotating disks, one of which was shrouded. Wavy instabilities were observed for some rotational speeds. Graber et al. (1987) experimentally determined torque coefficients for co-rotating disks, counter-rotating disks, and a rotor-stator combination of disks. The measurements were largely bulk averages with no quantified characteristics of the turbulence given. Later, Daniels et al. (1991) measured moment coefficients in a test rig that included a stationary peripheral shroud. Gan et al. (1993) performed laser doppler anemometer measurements and presented time averaged velocities in the radial and tangential directions for isothermal source flow between two counter-rotating disks. In these previous isothermal studies, the effects of varying inlet geometry or inlet velocity profile have not been examined, and the effect of disk spacing on the turbulent flow field is unknown and has not been quantified. It is believed that inlet geometry, inlet velocity profile, and disk spacing will greatly affect the downstream flow field. No detailed measurements of the turbulence intensities or Reynolds stress profiles are available in the literature. Furthermore, no turbulent heat transfer measurements have been made.

OBJECTIVES

From the above review of prior work, it is apparent that there has been a void in the fundamental understanding of the turbulent flow and heat transfer in counter-rotating systems. This study attempted to partially fill this void with the following objectives:

- To correlate dimensionless parameters which correctly express the observed physics and provide a meaningful representation of the experimental results. It is of interest to determine the effect of Re , Re_θ , Tu , g/D , and d/D on local Nu .
- To study quantitative details of the turbulent velocity field by laser doppler anemometry by means of fiber optics.
- To consider qualitative details of the complex velocity field by flow visualization with a laser light sheet.
- To explore various means of inducing very high turbulence intensity levels which would augment the heat transfer in counter rotating systems.
- To examine the effects of a peripheral shroud on the flow field and convective heat transfer.

APPARATUS

An overall view of the experimental arrangement is shown in Figure 2. One of the 61 cm diameter parallel disks is fabricated from optically transparent polycarbonate, and the other consists of an insulated heater assembly in an aluminum shell. Different polycarbonate disks with either 2.54 cm or 5 cm inlet diameters were constructed to determine the influence of d/D on the resulting flow and heat transfer, and a transparent polycarbonate shroud was attached to some of these for studies of ambient gas ingress. To reduce possible flexing of the polycarbonate disk, the disks are in an orientation parallel with the gravity vector. The disks are each mounted to a pulley driven shaft, which are in turn, connected to two speed-controlled 20 hp ac motors by belts. The angular speed of each disk can then be independently controlled up to 1750 rpm, and the spacing between the disks is set by adjusting the shaft bearings. Air flows from the 15 hp blower which produced mass flow rates in the range from 0.008 to 0.017 kg/s through a calibrated orifice meter and enters the center of the rotating, unheated polycarbonate disk by means of a non-rotating pipe. The air then impinges on the heated disk, flowing radially outward. More specific details of the experimental components are given in the following paragraphs, beginning with the heater disk assembly.

The heater disk assembly, shown in Figure 3, is composed of a retaining aluminum cylindrical shell which contains polyurethane insulating material below a laminated heater. This laminated heater consists of three layers: a heater element etched from an electrically resistive material on a printed circuit board, an electrically insulating, but thermally conducting epoxy, and an inconel outer surface (0.05 mm thick). The heating element is etched to provide a uniform coverage of 90% of the available surface area, insuring a uniform wall heat flux with the imposed constant voltage. A single piece of inconel is used for the outer surface of the heater because it does not readily form surface oxides which results in a nearly constant emissivity over the temperature range of -134 °C to 560 °C. As a result, reasonable estimates of radiative losses can be made. Eleven Type J 30 gage thermocouples are also attached to the underside of the inconel surface as shown in Figure 4 for local temperature measurement and for verification of future liquid crystal temperature measurements. The thermocouple wire passed through the rotating shaft of the heater disk assembly and was connected to a mercury slip ring which accommodated five thermocouples, and the thermocouples associated with the second through fifth position of Figure 5 were chosen

for the experiments described here. The thermocouple extension wires were connected to a stable electronic reference junction and to a Hewlett Packard multiplexer for PC based data acquisition. The heated disk is powered by means of a German-silver power slip ring assembly which can transmit up to 80 amps at 1000 rpm. The power source was capable of providing a maximum of 15 kW of power to the resistance heater. Voltage measurement across a calibrated shunt electrically in series with the heated surface permits determination of the current, and voltage measured across the heated surface allows the calculation of the power supplied.

Image acquisition of the light reflected from particles in the light sheet produced by an Nd YAG laser with the optics shown in Figures 6 and 7 is performed by means of a high speed color video camera system, which provides an effective framing rate of 200 frames per second. The camera is focused directly through (or from above as in Figure 7) the rotating polycarbonate disk to capture either reflected light from flow visualization or from the liquid crystal surface temperature measurements for the optical determination of local Nu as described in Farino et al. (1993). It was intended that Thermochromic Liquid Crystal (TLC) be painted on the heated disk surface, and the color response of the TLC coatings would provide a full-field two-dimensional temperature distribution. However, the required image analysis hardware and software for color-hue interpolation did not arrive at the time of the writing of this report, but are expected in January 1994.

When velocity measurements are desired, the probing rays from the laser system can enter from the spacing between the disks or through the polycarbonate disk. However, the required anemometry hardware did not arrive at the time this report was written, but is expected in early 1994.

PROCEDURE AND DATA REDUCTION

For determination of the local heat transfer coefficients, the desired mass flow rate and heat flux were adjusted. The surface temperature of the heated disk was monitored until changes were less than 0.1 °C over a one hour time. At this point for the stationary disks, the shunt, heater assembly, pressure transducer, and thermocouple voltages were recorded for calculation of the heat flux, thermocouple temperatures, and mass flow rate. Subsequently, different steady-state conditions were reached in approximately 45 minutes following initiation of counter-rotation, and again voltages across the shunt and heater assembly were recorded together with

thermocouple voltages and pressured transducer voltages.

With

$$q'' = h (T_s - T_\infty) \quad (1)$$

the local heat transfer coefficient, h , could be calculated. In equation (1), q'' is the net heat flux to the flowing air, T_s is the outer surface temperature of the heater, and T_∞ is the ambient temperature. q'' can be calculated from:

$$q'' = q''_{\text{total}} - (q''_{\text{rad}} + q''_{\text{loss}}) \quad (2)$$

where q''_{total} is the calculated total power supplied to the heater assembly. With this surface, q''_{rad} was less than 20 W/m², and q''_{loss} was estimated to be less than 45 W/m². The appropriateness of T_∞ in equation (1) may be questionable, and a local bulk temperature might be more physically meaningful. However, because of the physical constraints of the experiment, a local bulk temperature is difficult to measure. A mean bulk temperature calculated from measurements at the inlet and exit from the disks may be more appropriate. It must be pointed out that in the results which follow, equation (1) was used, but this will be corrected in future tests. With h known, Nu_r can then be calculated from:

$$Nu_r = \frac{hr}{k_f} \quad (3)$$

where Nu_r is the local Nusselt number, r is the radial location, and k_f is the thermal conductivity of the air. Since the thermal conductivity of the air could not be evaluated from an average bulk temperature, the ambient temperature was used.

For the flow visualization portion of the tests, ignited smoke incendiaries were placed in the explosion proof vessel of Figure 8 that was then slightly pressurized above ambient pressure by compressed air. The blower was set at the desired flow rate and the motors connected to the disks were then switched on. The seeded air

flowed into the inlet of the disks through a tube that passed through the stationary pipe that was connected to the rotating polycarbonate disk, and the high-speed video camera was activated.

Uncertainties in the thermocouple measurements are on the order of 0.5 °C, and uncertainty in the measured mass flow rate is less than one percent for the flow range considered. Uncertainties in the measured heat flux and rotation rate were less than one percent for the tests described here.

RESULTS

Flow Visualization

Figure 9 presents initial results of the flow visualization of the turbulent flow between shrouded stationary disks with a mass flow rate of 0.008 kg/s and a gap between the disks of 3.8 cm. The diameter of the inlet to the disk cavity is 2.54 cm. In this series of frames which are sequential in time, the light sheet is parallel to the disks. A wedge-shaped portion of the flow is visible, as is the rim of the polycarbonate disk. Near the center of the disks dark circular rings develop and subsequently move down stream. At the inlet where the rings form, the flow separates and vortices are periodically shed. As can be seen from the sequence, these vortices impart swirl to the flow, and the turbulent flow between the two motionless disks is inherently unsteady. For the same conditions but without the shroud which reduced the height of the gap at the exit plane from 3.8 cm to 0.6 cm, the ingress of air from the surrounding was observed. Flow visualization for counter-rotating disks was not finished in time for the writing of this report, as the supply of smoke devices was temporarily exhausted and are being procured.

Heat Transfer Measurements

Figure 10 presents local Nu_r as defined in equation (3) for the shrouded counter-rotating disks. For these series of tests, q'' was 413 W/m², the mass flow rate was 0.01487 kg/s, g was 3.8 cm, and d was 2.54 cm. As expected, the largest heat transfer rates from the heated disk occur near the stagnation region for small r/R . The lowest heat transfer rates were for the stationary disks, and the greatest heat transfer rates in the region from $0.08 < r/R < 0.5$ were for a rotation rate of 200 RPM. It was initially expected that the test with the greatest rotation rate or rotational Reynolds number, Re_θ , would provide the greatest heat transfer effectiveness with all other parameters

held constant. Hence, it was presumed that the 600 RPM test of Figure 10 would have the greatest heat transfer for all radial locations. However, this was not the case, as the experiment with a rotation rate of 200 RPM had the greatest heat transfer rate. This means that for a given imposed heat flux and flow rate, there is an optimum rotation rate for the greatest heat transfer.

If the Rossby number, Ro , which is the ratio of inertial forces to Coriolis forces, is considered as in Figure 11, it appears that increasing Ro results in increasing Nu_r for $0 < r/R < 0.5$. In other words for r/R less than 0.5, where stagnation effects may still dominate, inertial forces control the heat transport. This trend reverses for larger radii. At r/R equal to 0.83, the smallest Ro corresponds to the largest Nu_r . This might be intuited since inertial forces are expected to become less important as both viscous and Coriolis forces become more dominate for large radii.

Experiments were performed comparing (although the data is not presented here), with all other parameters held constant, the effect of co-rotating both disks or rotating only the unheated disk on the measured heat transfer. In all experiments, the counter-rotating results had greater measured heat transfer rates at the same radii on the heated disk. Further statistical details of the flow field will be forthcoming.

CONCLUSIONS

The heat transfer was greatest for the counter-rotating case when compared to the rotor-stator, co-rotating, or stationary disk configuration. In addition for the counter-rotating tests, the heat transfer near the stagnation region was greater than at other radial locations. The Rossby number appeared to correlate local Nusselt numbers for a given flow rate and heat flux.

ACKNOWLEDGMENTS

The Principal Investigator would like to acknowledge the AFOSR for making this research possible. In addition, Mr. Scott Mann and Mr. Anthony Paris are acknowledged for their diligent work. Appreciation is also extended to Dr. Richard Rivir of the Aero-Propulsion Division of Wright Laboratory for his very helpful comments and suggestions.

REFERENCES

- Batchelor, G.K., "On A Class of Solutions of The Navier-Stokes Equations Representing Steady Rotationally-Symmetric Flow," *Quart. J. Mech. Appl. Math.*, 4, pp. 29-41, 1951.
- Daniels, W., Johnson, B., and Graber, D., "Aerodynamic and Torque Characteristics of Enclosed Co/Counter Rotating Disks," *J. Turbomachinery*, 113, pp. 67-74, 1991.
- Dijkstra, D. and van Heijst, G., "The Flow Between Two Finite Rotating Disks Enclosed By A Cylinder," *J. Fluid Mech.*, 128, pp. 123-154, 1983.
- Farino, D., Hacker, J., Moffat, R., and Eaton, J., "Illuminant Invariant Calibration of Thermochromic Liquid Crystals," Presented at the 29th National Heat Transfer Conference, Atlanta, Ga, 1993.
- Gan, X., Kilic, M., and Owen, J., "Flow Between Contra-Rotating Discs," Presented at The International Gas Turbine and Aeroengine Congress and Exposition, Cincinnati, Ohio, May 1993.
- Graber, D., Daniels, W., Johnson, B., "Disk Pumping Test," United Technologies Corp., Pratt and Whitney Report for Aero Propulsion Laboratory, Air Force Wright Aeronautical Laboratories, Wright-Patterson AFB, Report AFWAL-TR-87-2050, September 1987.
- Owen, J. and Rogers, R., Flow and Heat Transfer in Rotating-Disc Systems. Volume 1-Rotor-Stator Systems, Research Studies Press LTD., Somerset, England, 1989.
- Stewartson, K., "On The Flow Between Two Rotating Coaxial Discs," *Proc. Camb. Phil. Soc.*, 49, pp. 333-341, 1953.

NOMENCLATURE

g = gap spacing, m

h = local convective heat transfer coefficient, $W/m^2\ ^\circ C$

k_f = thermal conductivity of air, $W/m\ ^\circ C$

m = mass flow rate, kg/s

Nu_r = local Nusselt number, hr/k_f

r = radial location, m

R = disk radius, m

Re_θ = rotational Reynolds number, $\omega R^2/\nu$

Ro = Rossby number, $m/2\pi\rho R^2 g\omega$

ω = rotational speed, rad/s

ν = kinematic viscosity, m^2/s

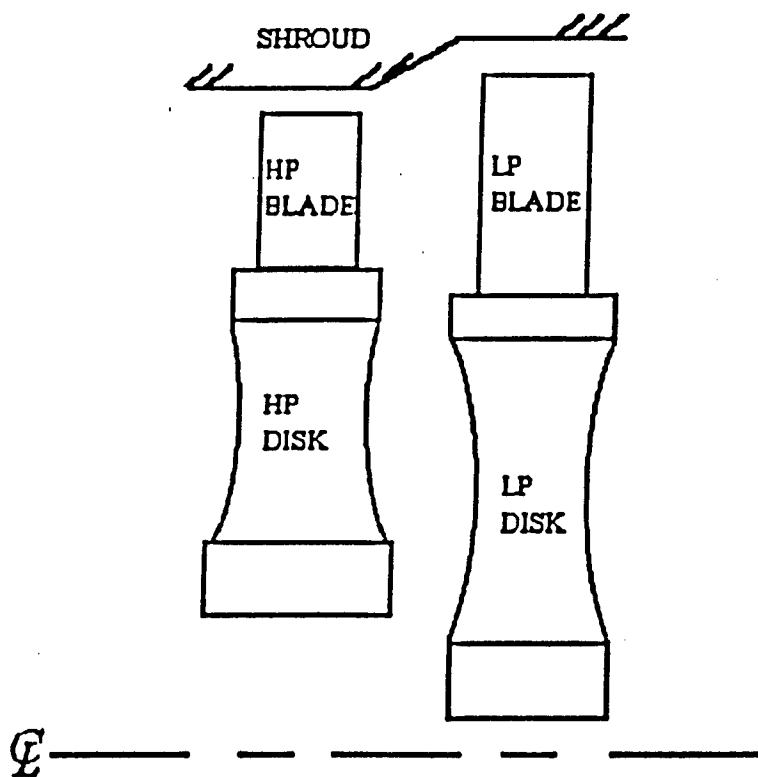


Figure 1 Counter-rotating, vaneless design

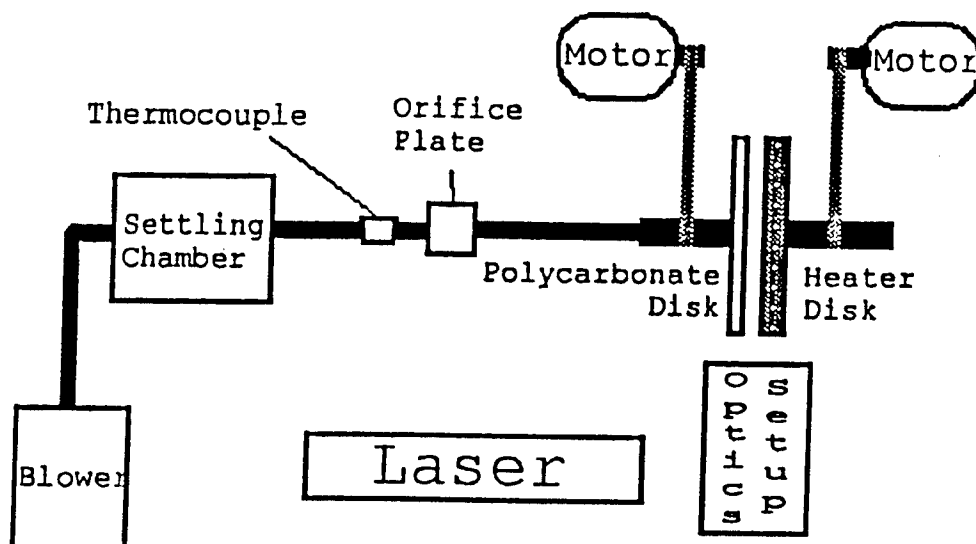


Figure 2 Experimental arrangement

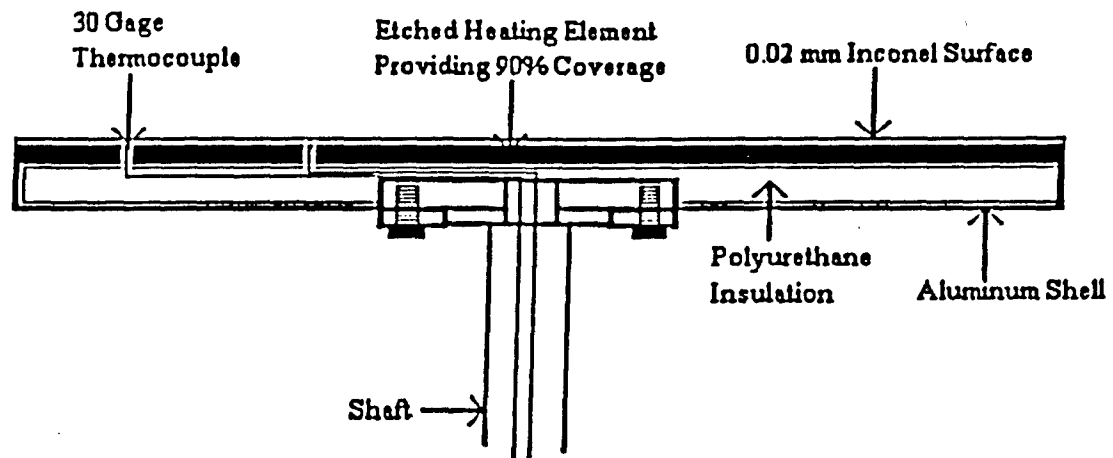


Figure 3 Sectional view of disk which produced uniform heating

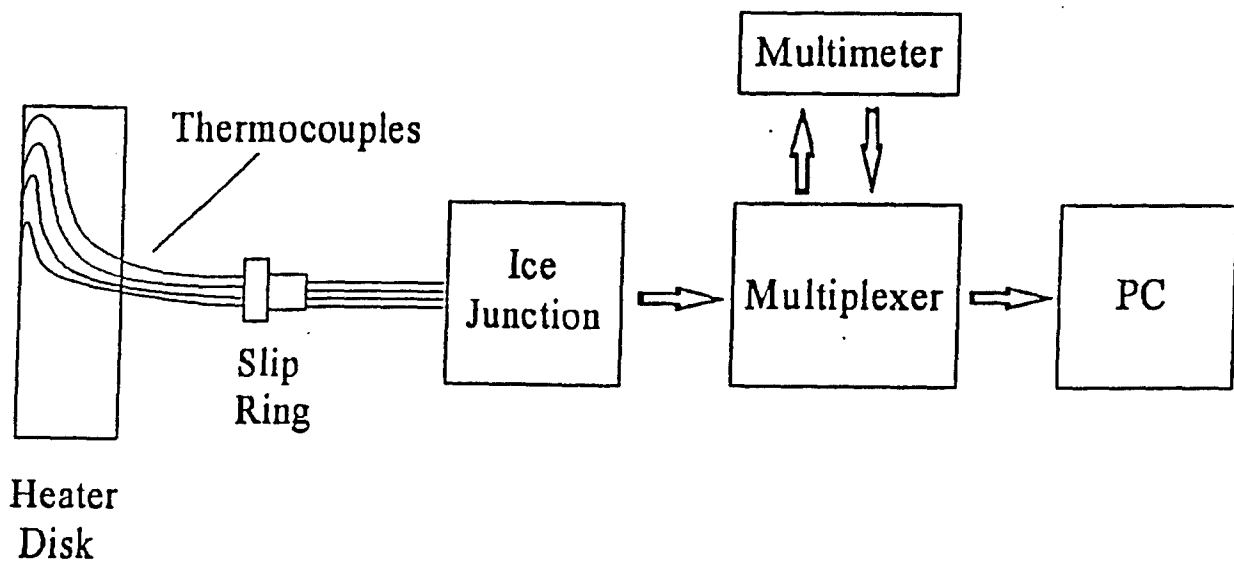


Figure 4 Thermocouple location within heated disk assembly and data acquisition equipment

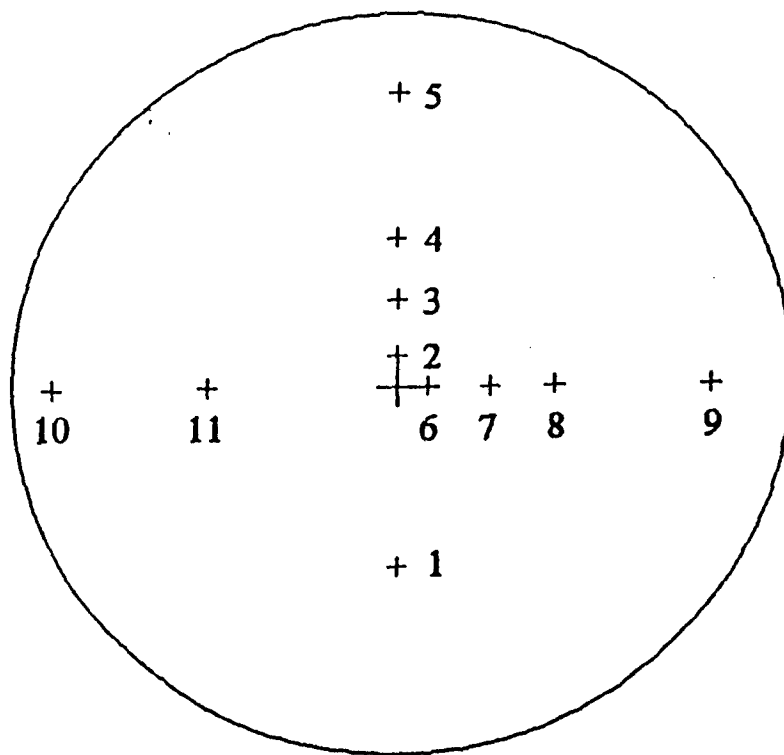


Figure 5 Location of thermocouples on heated disk (only four locations were used in these tests)

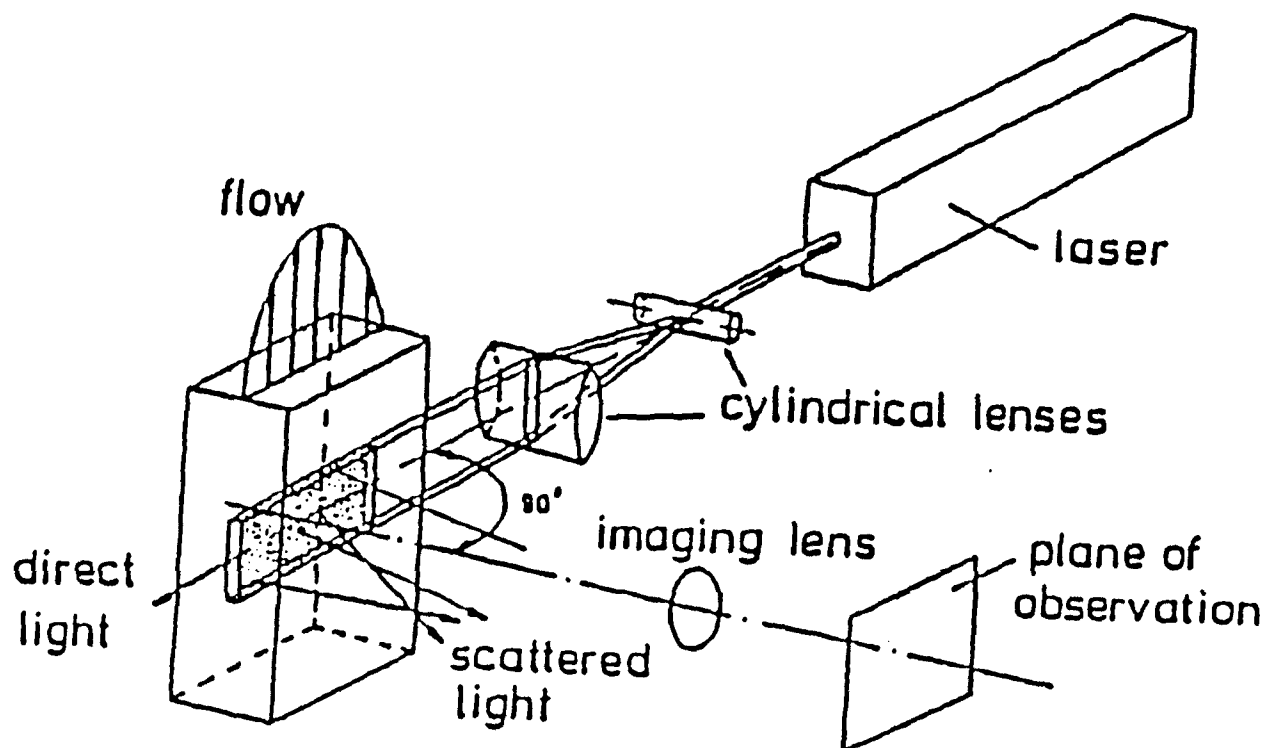


Figure 6 Optics for producing a laser light sheet

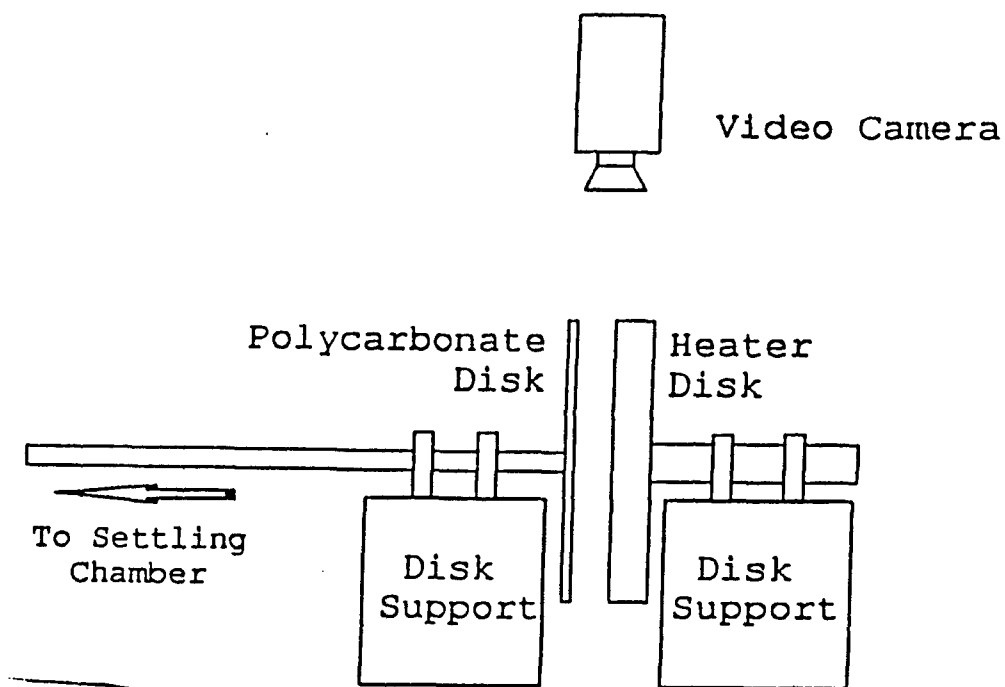


Figure 7 Polycarbonate disk and heater disk with camera view normal to rotational axis

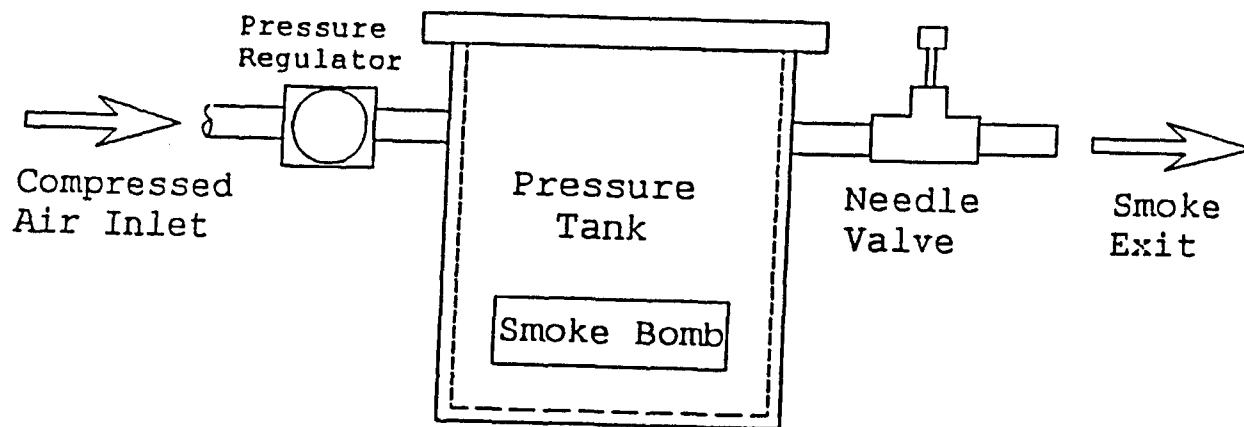


Figure 8 Equipment for seeding the flow

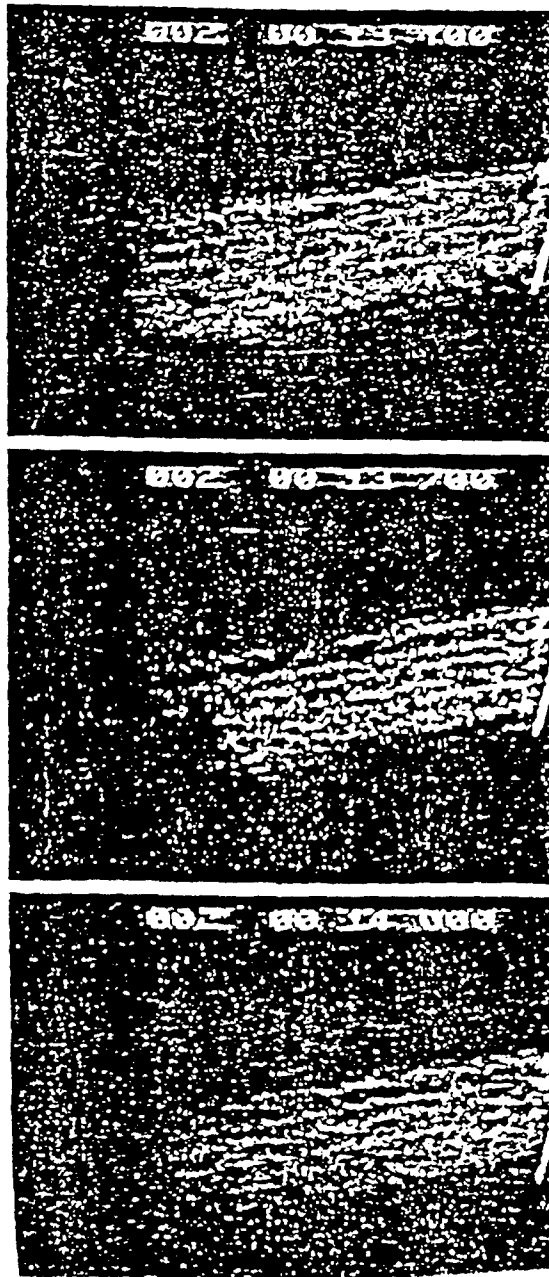


Figure 9 Flow visualization results for turbulent flow between stationary disks

Figure 10 Local Nu For Counter-Rotating Shrouded Disks

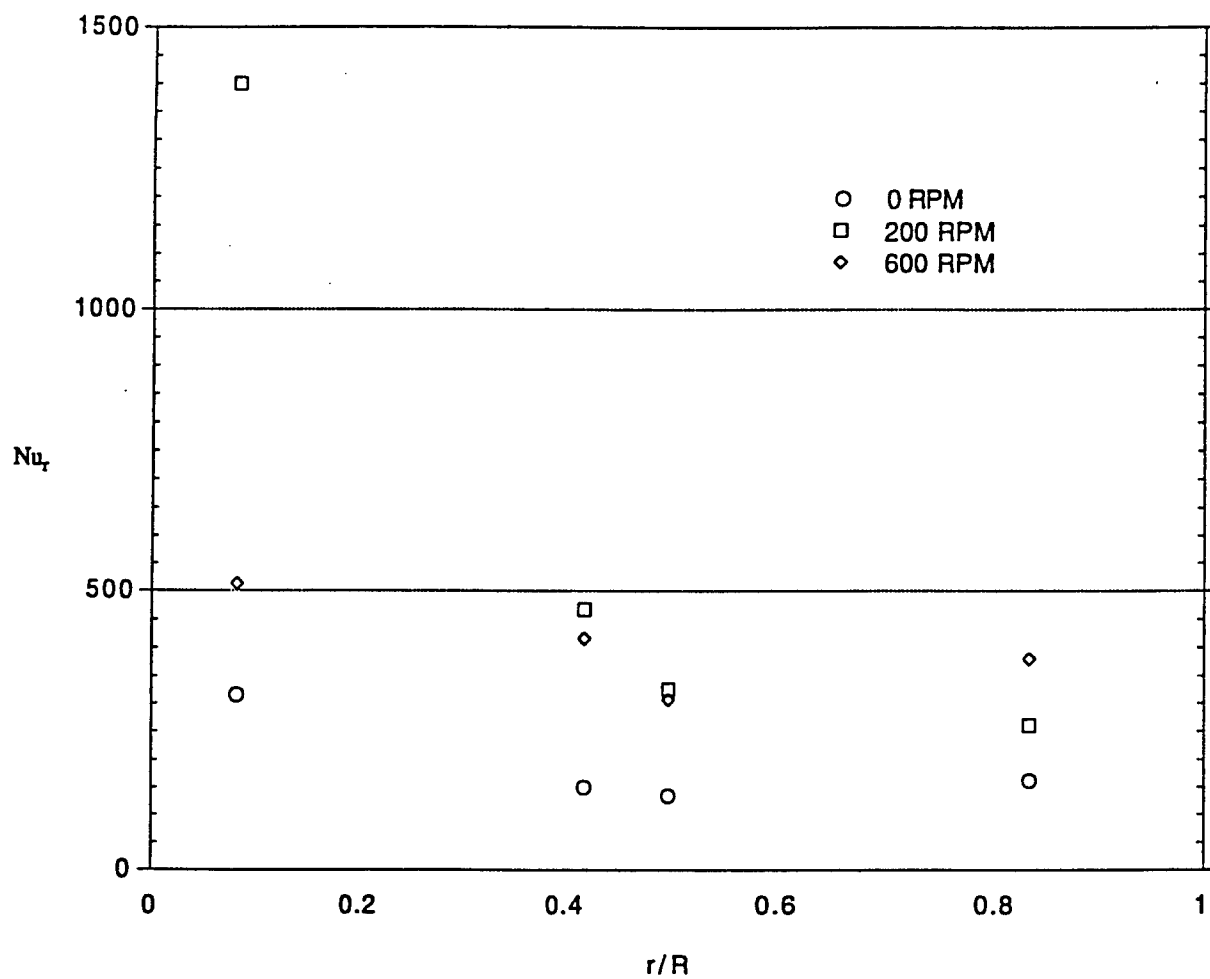
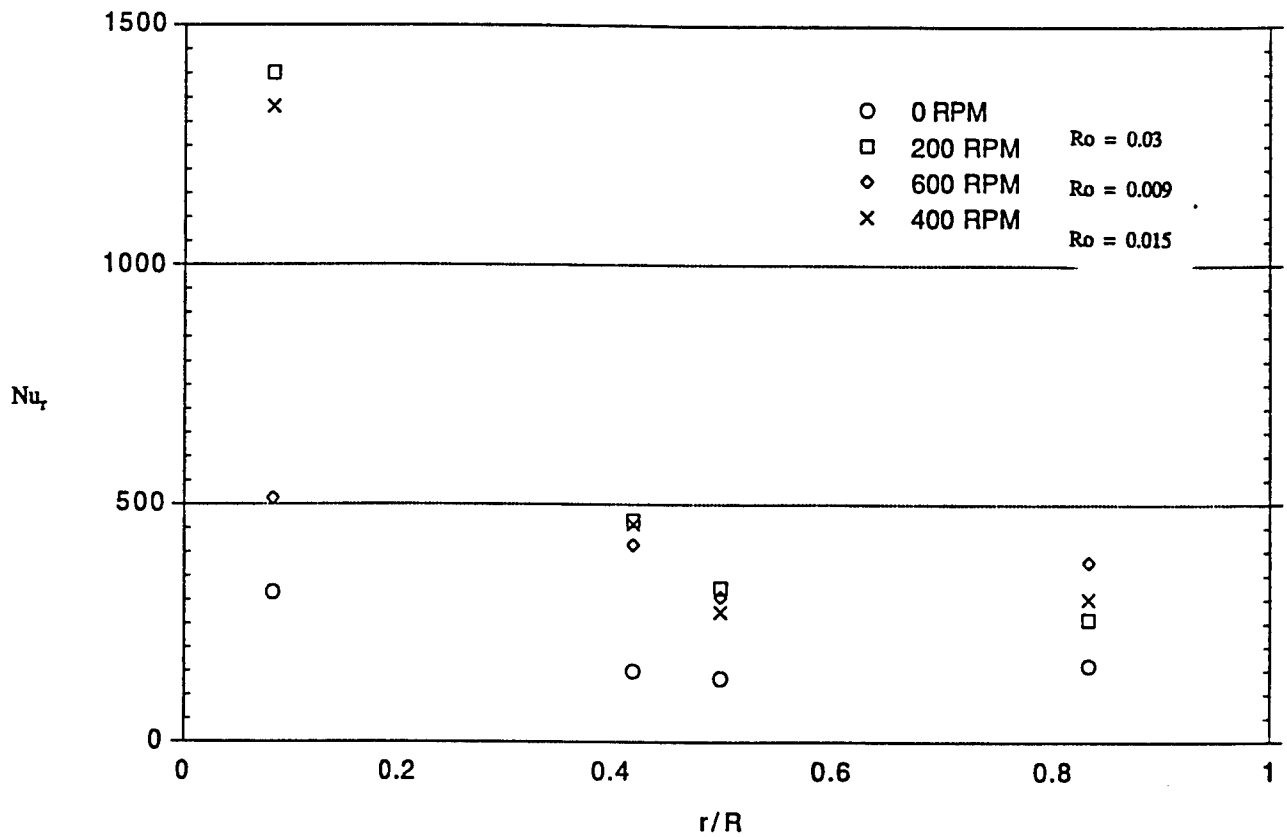


Figure 11 Local Nu For Counter-Rotating Shrouded Disks



MODELING OF BIOMATERIALS FOR NON-LINEAR OPTICAL APPLICATIONS

E. K. Karikari
Research Assistant
Department of Materials Science & Engineering

and

B. L. Farmer
Professor
Department of Materials Science & Engineering

University of Virginia
Charlottesville, VA 22903

Final Report for:
Research Initiation Program
Wright Laboratory, Materials Directorate

Sponsored by:
Air Force Office of Scientific Research
Bolling AFB, Washington DC

and

University of Virginia

January 1994

MODELING OF BIOMATERIALS FOR NON-LINEAR OPTICAL APPLICATIONS

E. K. Karikari

Research Assistant

Department of Materials Science & Engineering

University of Virginia

and

B. L. Farmer

Professor

Department of Materials Science & Engineering

Abstract

The effect of spiropyran chromophore isomerization on poly-L-alanine having the peptide backbone in the α -helical or β -sheet conformations have been investigated using molecular mechanics (MM) and molecular dynamics (MD) calculations. Two variations of the spiropyran chromophore, the indoline and benzothiazoline derivatives were studied in detail. The effect of the chromophores on two copolymers, the hexapeptide poly(gly-ser-gly-ala-gly-ala) and the septipeptide poly(asp-arg-leu-ala-ser-tyro-leu) were also investigated. These polypeptides are compositionally representative of the naturally occurring amino acid sequences in silk and wool, having respectively, the β -sheet and α -helical conformations.

Molecular mechanics results indicate that an increase in energy of 30 - 50 kcal occurs when the spiropyran chromophore is attached to the β - and α -poly-L-alanine respectively. Results from molecular dynamics simulations show that the α -helix or the β -sheet conformation of poly-L-alanine is destabilized by the open and closed forms of the chromophore, with the open form exerting a larger influence. The larger influence exerted by the merocyanine results, in part, from the distortion of the α -helical framework due to the formation of a hydrogen bond between the oxygen (in the NO_2 group) in the merocyanine chromophore and the carboxylic group of the first alanine residue in the peptide chain. These results are in agreement with those calculated for a spiropyran-modified poly-L-glutamate system. Similar results were observed for the chromophore-copolymer systems.

MODELING OF BIOMATERIALS FOR NON-LINEAR OPTICAL APPLICATIONS

E. K. Karikari and B. L. Farmer

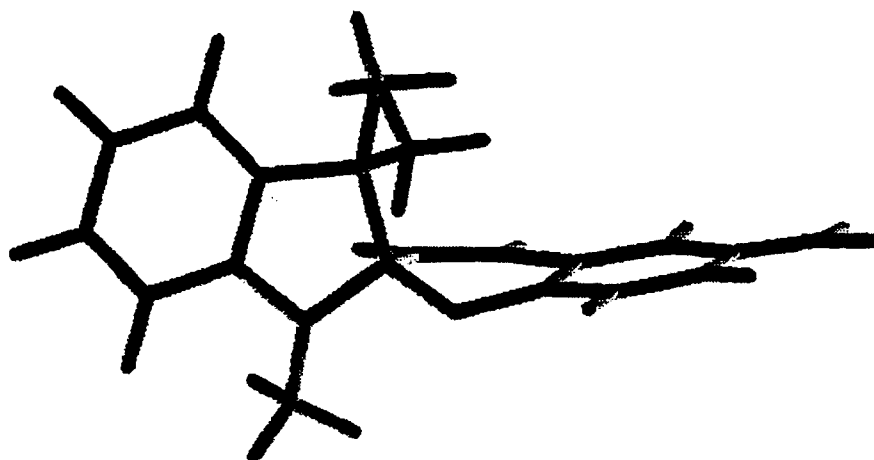
INTRODUCTION

Photochromic biopolymers are polypeptides with substituent non-linear optical (NLO) chromophores. These materials are being extensively investigated by the Air Force as potential non-linear optical materials for laser hardening applications. Studies of the structures of biologically-synthesizable materials that may exhibit NLO response should contribute insight and understanding for the invention of such complex biomaterials having defined structures and controlled optical properties. Helix-to-random coil transitions in polypeptides are induced by factors such as changes in polarity of a solvent, temperature, and pH. Such transitions also occur when azo dyes and spiropyran chromophores are coupled to a polypeptide backbone (1 - 7). The polypeptide-chromophore systems are photoresponsive and consequently undergo changes in their peptide backbone conformation. This observation has spurred research interest in such photochromic-polypeptide systems as models for coupling photochemistry with backbone conformational changes. They are attractive systems because they can exist in definite ordered structures such as α -helix or β -sheet conformations.

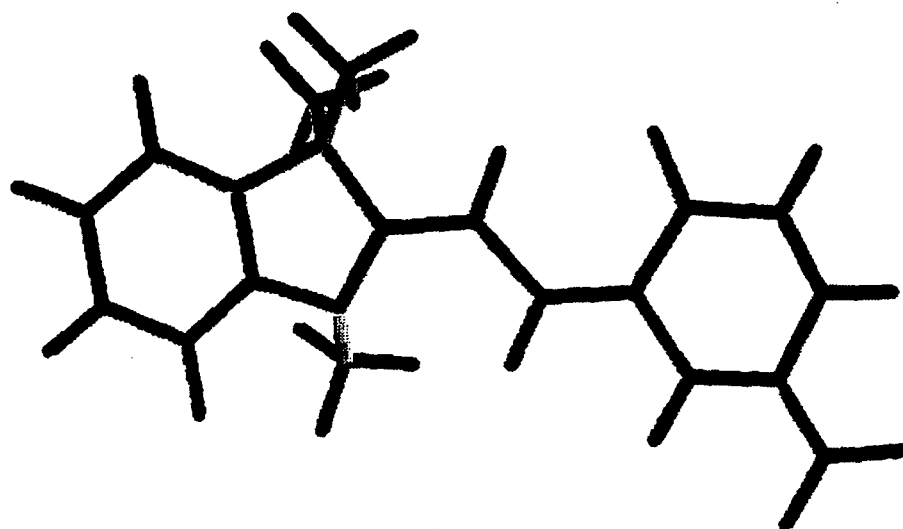
The chromophores investigated here are the spiropyrans (Fig. 1). In its closed form, the indoline, (left) and benzopyran, (right) fragments of the spiropyran molecule are linked by a spiro carbon atom having tetrahedral sp^3 hybridization. The two fragments are thus orthogonal to each other. Upon irradiation with light in the UV region of the electromagnetic spectrum, spiropyrans undergo ring scission converting from the colorless, closed form to a colored, open merocyanine form (Fig. 2).

Current applications of the spiropyrans include high resolution photography, optical devices, variable transmission devices, photovoltaic and holographic systems (8).

Ring opening occurs by heterolytic dissociation of the bond between the spiro carbon and the pyran oxygen atoms, followed by molecular rearrangement. The central carbon atom becomes sp^2 hybridized and the indoline and benzopyran moieties become coplanar. This facilitates delocalization



(a) closed form



(b) open merocyanine form

Figure 1. Open and closed forms of indoline spiropyran

of the π electrons between the indoline and benzopyran fragments giving rise to an intense absorption band in the visible portion of the spectrum. Thermal energy or absorption of visible light causes the closed, spiropyran structure to re-form slowly.

Two variations of the spiropyran chromophore, the indoline and benzothiazoline derivatives (Fig.1 and Fig. 3 respectively) have been investigated. Steric factors would be considerably different in the benzothiazoline derivative since it lacks the 3'-methyl substituents (9).

When the spiropyran is appended to a polypeptide, accumulation of charged merocyanine groups along the peptide chain can alter the chain conformation. This in turn influences the photochromic behavior of the spiropyran. Conformational calculations (7) on spiropyran-modified poly-L-glutamate shows that the polypeptide chain conformation is perturbed by the open and closed forms of the chromophore, with the open form exerting a larger influence on the peptide chain.

Various stable conformations exist in polypeptide backbones. These include the left-handed and right-handed α -helices, the extended β -sheet, the PGI and PGII helices found in polyglycine, and PPI and PPII helices found in poly-proline. The present molecular modeling calculations focused on

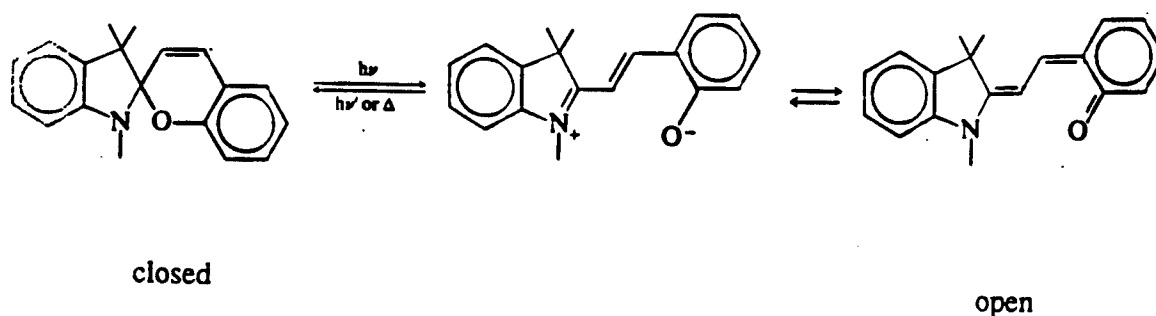


Fig. 2. Reversible photochromism in spiropyran

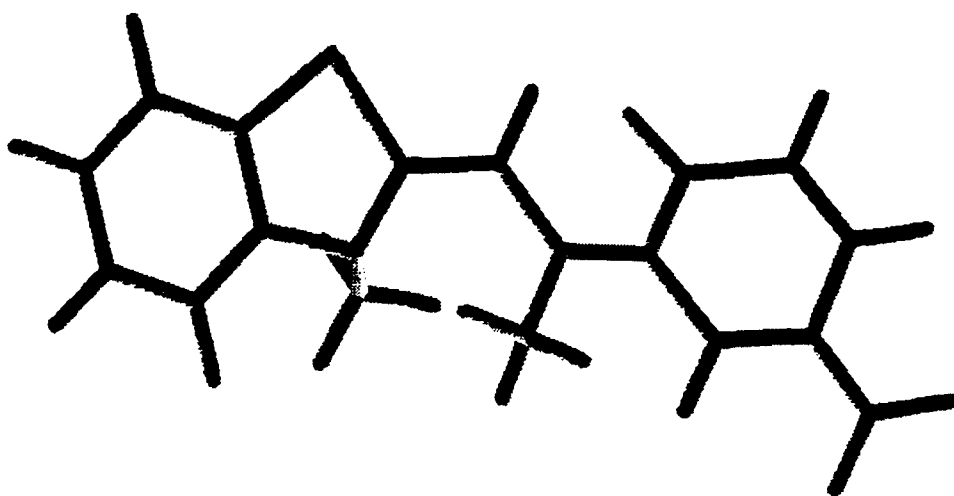


Fig. 3. Benzothiazoline-spiro-benzopyran

polypeptide-spiropyran systems in which the polypeptide chain was initially in the α -helical or extended β -sheet conformation. Both homopolymer and copolymer chains have been considered. Poly-L-alanine, a homopolymer, in both the α -helix and β -sheet conformations was studied in detail. Poly-L-alanine was chosen because it is the simplest polypeptide found experimentally to adopt both the α -helical and β -sheet conformations. Though the most stable conformation of an isolated poly-L-alanine molecule is the α -helix, X-ray diffraction studies (10, 11) show that the molecule can also exist in an antiparallel β -sheet conformation in fibers mechanically stretched in steam or treated with suitable solvents.

The copolymers investigated were the hexapeptide poly(gly-ser-gly-ala-gly-ala) and the septipeptide poly(asp-arg-leu-ala-ser-tyro-leu). These peptides are compositionally representative of

the naturally occurring amino acid sequences in silk and wool, having respectively, the β -sheet and α -helical conformations.

Previous work (7) modeled the spiropyran-peptide system by attaching the spiropyran as a pendant side-group on the polymer. We have investigated the effects of alternate locations for the chromophore on the conformations of various polypeptides. For example, both open and closed forms were used as a blocking group at the amino terminus of the peptide. We also investigated systems in which two polypeptide chain segments were attached to the chromophore. This could leave the helical or β -sheet segments collinear, and thus able to order easily, perhaps into a liquid crystalline phase. Furthermore, the presence of the chromophore could preclude crystallization and stabilize the liquid crystalline phase. Upon irradiation with light, formation of the merocyanine would cause the α -helix segments to become non-collinear, thus disrupting the packing of the liquid crystalline phase. Not only would the material become colored, its opacity would also change as a result of disrupting of the molecular packing. On the other hand, the packing of the polypeptide segments may substantially alter the ability of the spiropyran to open and close, affecting its sensitivity to UV radiation and the kinetics of its color change.

PROCEDURE

Computational molecular modeling calculations were carried out using SYBYL Molecular Modeling Software Package (version 6.01) (12).

SYBYL/BIOPOLYMER module was used to model the peptide chain conformations to be attached to the indoline and thiazole derivatives of the spiropyran chromophore. The biopolymer modeling uses the concept of a monomer and builds and modifies structures on a residue by residue basis. The polypeptides were modeled as α -helices and β -sheets consisting of 7 amino acid residues.

It has been reported (13) that the minimum peptide main chain length for α -helix formation corresponds to 7 amino acid residues. The C-terminus was blocked by an N-methyl amide (-HNCH_3) group, while the chromophore was used as a blocking group at the N- terminus of the peptide. The peptide-chromophore structures modeled were minimized using MAXIMIN2 which is a full-relaxation energy minimization scheme provided in the SYBYL environment. The default minimization procedure (Powell method) was used. This is an iterative method in which the atomic coordinates are modified from one iteration to the next in order to lower the energy of the structure. The method is similar to the conjugate gradient method, but uses more advanced rules to determine the descent direction. Figures 4a and 4b show two α -poly-L-alanine chains attached to the closed and open forms of the spiropyran chromophore (designated as $\text{pA}[\alpha]\text{-S-pA}[\alpha]$ and $\text{pA}[\alpha]\text{-M-pA}[\alpha]$ respectively). Shown in Figures 5a and b are β -chains from the same biopolymer attached to the spiropyran chromophore (designated as $\text{pA}[\beta]\text{-S-pA}[\beta]$ and $\text{pA}[\beta]\text{-M-pA}[\beta]$).

Molecular mechanics (MM) was used to generate and evaluate conformations and packing characteristics. Molecular dynamics (MD) was used to evaluate the effect of a chromophore on the conformational properties of the polypeptide and to address the issue of molecular flexibility in the system. The conformational calculations took into account electrostatic interactions. These were calculated by a partial charge method (the Del Re method) which employs the concept of localized bond orbitals. The Tripos force field treats hydrogen bonds as non-directional and electrostatic in nature. Although hydrogen bonds are not explicitly handled by this force field, during calculations, hydrogen bond energies are accounted for by scaling the van der Waals interactions between the hydrogen bond acceptors (N, O) and hydrogens bonded to H bond donors (N, O).

MM and MD calculations are based on a classical description of the bonding in a molecular system. Bond lengths, bond angles, torsion angles and non-bonded interactions are described in terms of force constants derived from a large body of vibrational and crystallographic data. (16). Each cycle of energy minimization can be thought of as a step in conformational space, while each cycle of

molecular dynamics advances time in the order of femtosecond time steps. The MM approach is primarily concerned with geometrical optimization of molecular conformations by finding the structural geometry that results in the lowest total potential energy. The Tripos Force Field, which was used for the MM and MD calculations, describes the potential energy as a function of bond stretches, bond angle bends, non-bonded interactions and torsion angle twists for each atom pair or set. The total potential energy of the molecule is the summation of the contributions by individual potential functions.

$$PE = \Sigma E_{\text{stretch}} + \Sigma E_{\text{bend}} + \Sigma E_{\text{torsion}} + \Sigma E_{\text{vdw}} + \Sigma E_{\text{elec}} \quad (1)$$

where E_{stretch} = bond stretching energy term, E_{bend} = angle bending energy term, E_{torsion} = torsional energy term, E_{vdw} = van der Waals energy term (Leonard Jones non-bonded potential), and E_{elec} is the energy due to electrostatic interactions.

MD is an extension of the molecular mechanics method of conformational analysis, employing the same semiempirical potential energy functions and associated force field to evaluate atomic interactions. MD calculations incorporate kinetic (i.e. thermal) energy to provide a dynamic view of the system as a function of time and/or temperature. The atomic positions and velocities are iteratively computed over femtosecond (fs) time steps to provide a description of the natural molecular motions available to the system at the prescribed temperature. In simple terms, the MD calculations proceed as follows. First the force acting on each atom is computed from the derivative of the potential energy) for all the interactions (bond stretches, bond angles, torsions and van der Waals) in the system.

$$\partial E / \partial r_i = F = m_i (d^2 r_i / dt^2) \quad \text{-----} (2)$$

Subsequent numerical integration of the classical Newtonian equations of motion ($F = ma$, $v = at$) using the Verlet (or Leapfrog) method (17) yields the individual atomic velocities and new atomic positions. In the Verlet method, the velocity is calculated at odd half integral multiples of Δt , while

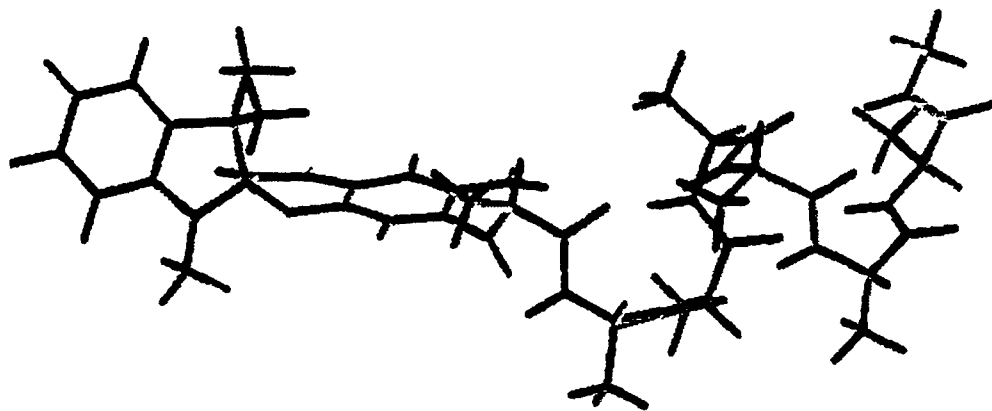


Fig. 4a. Model of pA[α]-S-pA[α]

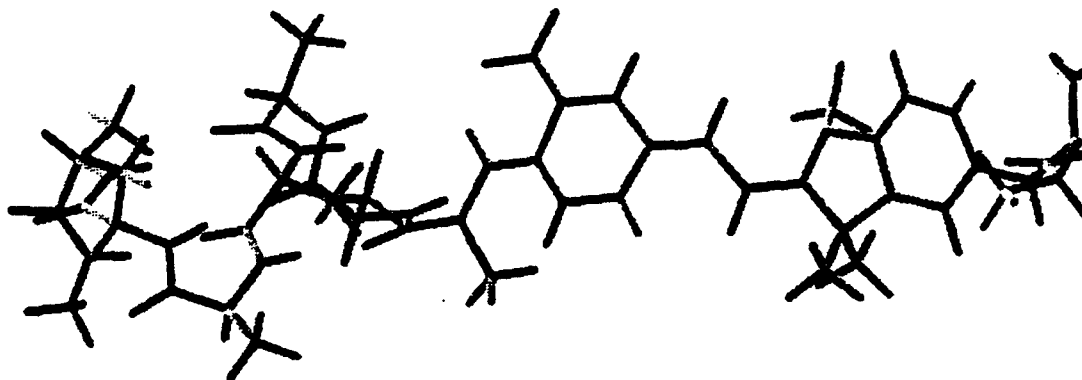


Fig. 4b. Model of pA[α]-M-pA[α]

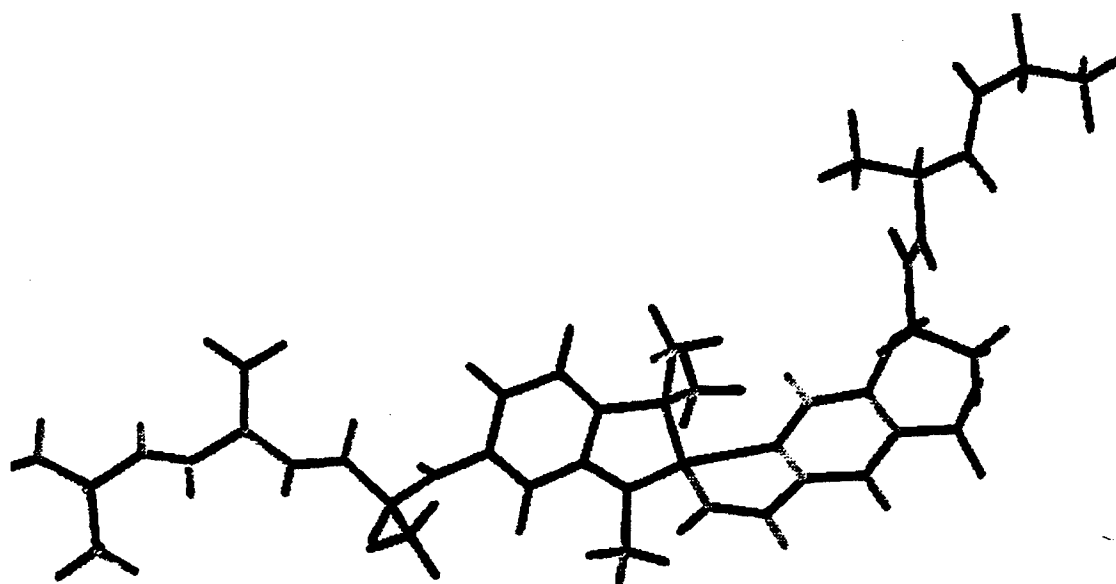


Fig. 5a. Model of pA[β]-S-pA[β]

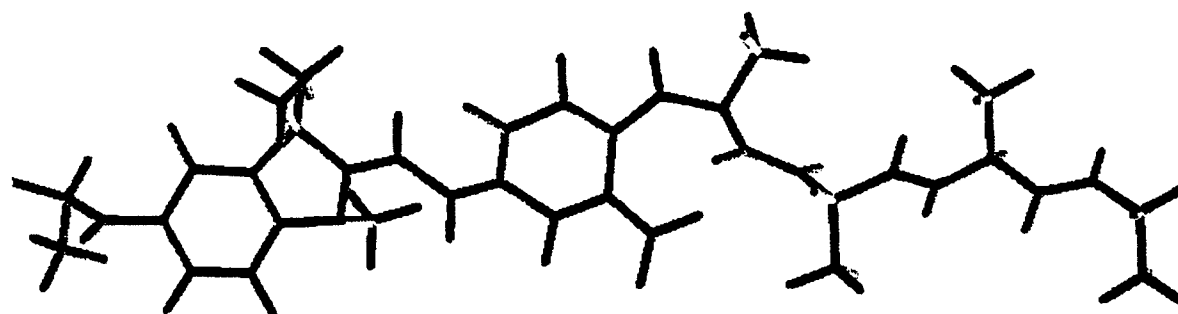


Fig. 5b. Model of pA[β]-M-pA[β]

the position is calculated at integral multiples of Δt . The velocities of the atoms are then scaled at each time step to the specified temperature of the simulation using the equation:

$$3Nk_B T = \sum m_i v_i^2 \quad \text{----(3)}$$

where T is the absolute temperature, k_B is the Boltzman's constant, m_i and v_i are the mass and velocity of the i th atom, and N is the total number of atoms. After one time step (1 fs) these scaled velocities bring the atoms to new positions and modify the forces they experience. The forces are once again evaluated and the procedure is repeated until the simulation accumulates a specified number of time steps. A detailed description of MD is given by McCammon (18).

MD was used to simulate the natural molecular motions of the chromophore-bound polypeptides at 300 K. Initially the system was heated from 0 K to the target temperature of 300 K in 50 K increments. The total simulation time employed was 62,000 fs including 10,000 fs each of heating and equilibration stages of the computation. The time step used for each simulation was 1 fs. Nonbonded interaction lists were updated every 25 fs and molecular trajectories were saved every 50 fs. The nonbonded cutoff distance was 8.0 Å and all atoms were included explicitly in the simulation. The simulation was carried out without of solvent. This would represent the molecule as it might exist and behave in vacuo.

RESULTS AND DISCUSSION

The Tripos force field in SYBYL version 6.01 was used in the molecular mechanics and molecular dynamics calculations. The force field has been shown (12) to produce molecular geometries close to the crystal structures of a variety of organic molecules and biopolymers.

Calculations using the Tripos force field were found (12) to compare well with the Amber force field, developed primarily for biopolymer calculations.

Energetics of the spiropyran-biopolymer models

Table 1 shows the potential energies for the indoline spiropyran-polypeptide systems with the peptide backbone in the helical or beta sheet conformation. Also included in the calculations are the energies of an unsubstituted poly-L-alanine in both α -helical or β -sheet conformations, and having a total length comparable to that of each of the biopolymer-chromophore systems. Table 2 shows a similar calculation for the biopolymers coupled to benzothiazoline-spiro-benzopyran. The results show a significant increase in energy (about 50 kcal/mol) upon derivatizing α -poly-L-alanine with the merocyanine form of the chromophores. The results also show that the minimum energy conformation of the polypeptide-chromophore system is the α -helix irrespective of the type of chromophore. The large difference in energy between the unsubstituted α -helical and β -poly-L-alanine is due to the fact that the calculations were done on an isolated chain of β -poly-L-alanine in which the stabilization effect of intermolecular hydrogen bonding is absent. It should be pointed out that a gain in stabilization energy (comparable to that of the helix) of the β -conformation is achieved through intermolecular hydrogen bonding between stacked parallel or antiparallel sheets.

Effect of polypeptide backbone on structure of chromophore

The optimized-geometry (shown in Figure 2) of the merocyanine- α -poly-L-alanine model shows that the biopolymer chains cause a negative twist of dihedral angle 1 of the chromophore. For

Table 1. PE (in kcal/mol) of indoline spiropyran-poly-L-alanine models.

Polypeptide-chromophore system	E kcal/mol
pA[α]-S	64.9
pA[α]-M	80.1
pA[β]-S	92.0
pA[β]-M	103.1
pA[α]	32.3
pA[β]	74.0

Table 2. PE (in kcal/mol) of benzothiazoline spiropyran-poly-L-alanine models.

Polypeptide-chromophore system	E kcal/mol
pA[α]-S	82.4
pA[α]-M	85.7
pA[β]-S	88.0
pA[β]-M	112.3
pA[α]	32.3
pA[β]	74.0

example, after energy minimization, a negative twist of this dihedral angle occurs when two α -helical poly-L-alanine chains are attached to the chromophore. This results in a change of the dihedral angle from 177.5 to -173.6°. A similar negative twist of this dihedral angle was observed (7) for the merocyanine analog of a spiropyran-substituted poly-L-glutamate system. However, when β -poly-L-alanine chains are attached to the merocyanine, no negative twisting of the dihedral angles is observed. The reason might be due to the absence of intramolecular H-bonds in the beta

conformation. Intramolecular H-bonds are responsible for the stability of the helix. Results for the benzothiazoline-spiro-benzopyran show a similar negative twist of dihedral angle 1 upon attaching α -poly-L-alanine chains.

Molecular Dynamics Results

The amount of motion that occurred during the molecular dynamics simulation was observed by plotting the end-to-end distance (between the amide N of residue 1 and the carbonyl carbon of residue 7) as a function of time. Tables 3 and 4 show the statistical analysis of the end-to-end distance of the α -helical and β -chains of poly-L-alanine derivatized with the open and closed forms of indoline spyropyran.

Table 3. Statistical analysis of end-to-end distance of α -poly-L-alanine

	pA[α]-M	pA[α]-S	pA[α]
average (Å)	12.71	8.07	11.92
Std deviation (Å)	2.05	1.93	0.94

Table 3. Statistical analysis of end-to-end distance of β -poly-L-alanine

	pA[β]-M	pA[β]-S	pA[β]
average (Å)	10.62	5.50	11.40
Std deviation (Å)	3.00	2.72	1.05

Results show that there is a measurable increase in standard deviation in the end-to-end distance of both α - and β -poly-L-alanine chains as a result of the presence of both forms of the chromophore. For example, the statistical analysis indicates a two-fold increase in the standard deviation in the end-to-end distance of α -poly-L-alanine in the presence of the open form of the chromophore. For both conformations of poly-L-alanine, the deviations are higher when the chromophore is in the open form. The presence of the closed form of the chromophore forces the peptide chain in both the α -helical or β -sheet conformation into more compact structures as indicated by the average distance. Shown in Figures 7 and 8 are plots of end-to-end distance for the closed and open indoline spiropyrans attached to α -poly-L-alanine and β -polyalanine respectively.

From the above results, it is seen that the merocyanine form of the chromophore destabilizes the biopolymer backbone more than the closed form does. This result is consistent with that obtained (7) for a spiropyran-modified poly-L-glutamate. The larger influence exerted by the open form results, in part, from the destabilization of the α -helical framework due to the formation of a hydrogen bond between the NO_2 group on the merocyanine chromophore and the first alanine residue in the peptide chain. Another reason may be due to the fact that the chromophore's presence disrupts the hydrogen bonding network in the helix which reduces the stability of the helix, hence the observed higher standard deviation in the end-to-end distance. The extent of helical backbone distortion depends on the attachment site on the chromophore. The fluctuations in the peptide backbone attached on the indoline part of the chromophore are higher than that attached on the benzopyran side. Standard deviations of 2.72 Å and 2.25 Å were calculated for the chains attached to the indoline and pyran rings respectively of the open form of the chromophore.

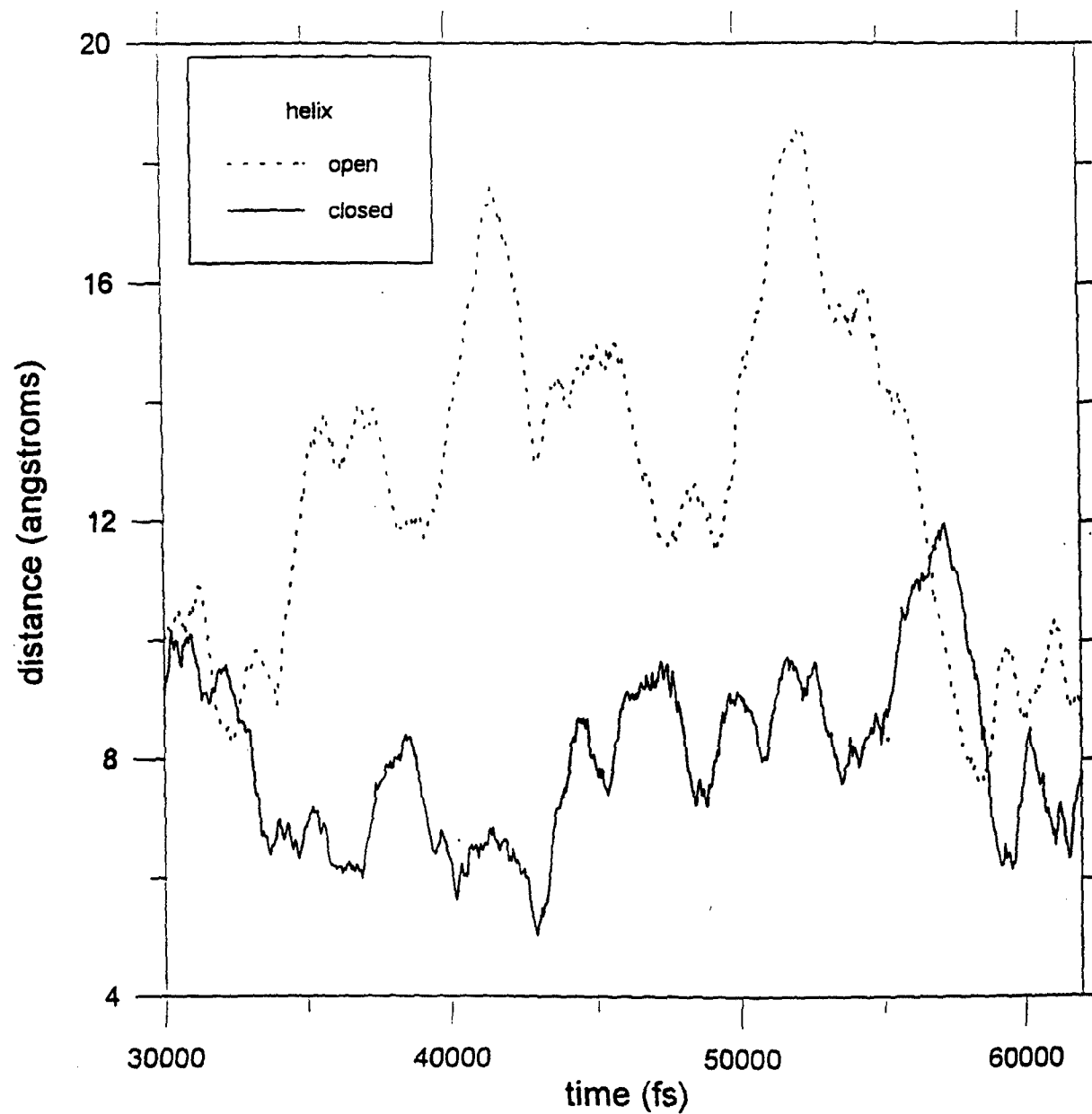


Fig. 7. End-to-end distance as a function of time

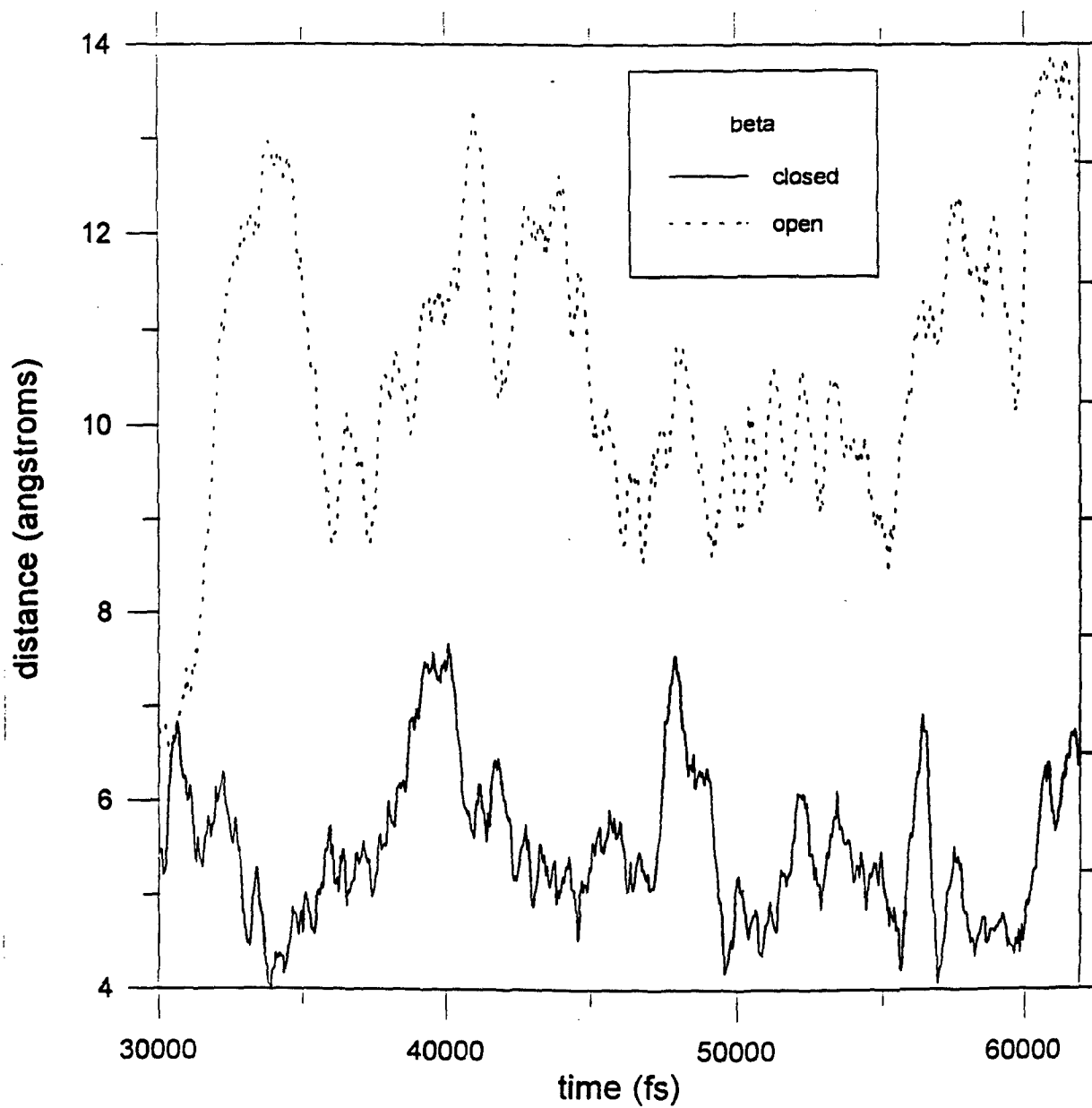


Fig. 8. End-to-end distance as a function of time

The β -sheet conformation is more distorted than the helix. This may be due to the fact that the α -helix is stabilized by intramolecular hydrogen bonding which is absent in the β -conformation. The β -sheet is stabilized by intermolecular hydrogen bonding between parallel or anti-parallel sheets. During the dynamics, the β -sheet conformation gained occasional stability by the formation of hydrogen bonds between the i th and $(i+2)$ th, or i th and $(i+3)$ th amino acid residues as the beta structure randomized. However, the number of hydrogen bonds formed were less than found in the helical systems.

Shown in Tables 4 and 5 are the statistics of the end-to-end distance when the chromophores are attached to copolymer chains. It can be seen that the merocyanine form distorts the peptide chains more than the closed form does, as found for the homopolymer chains.

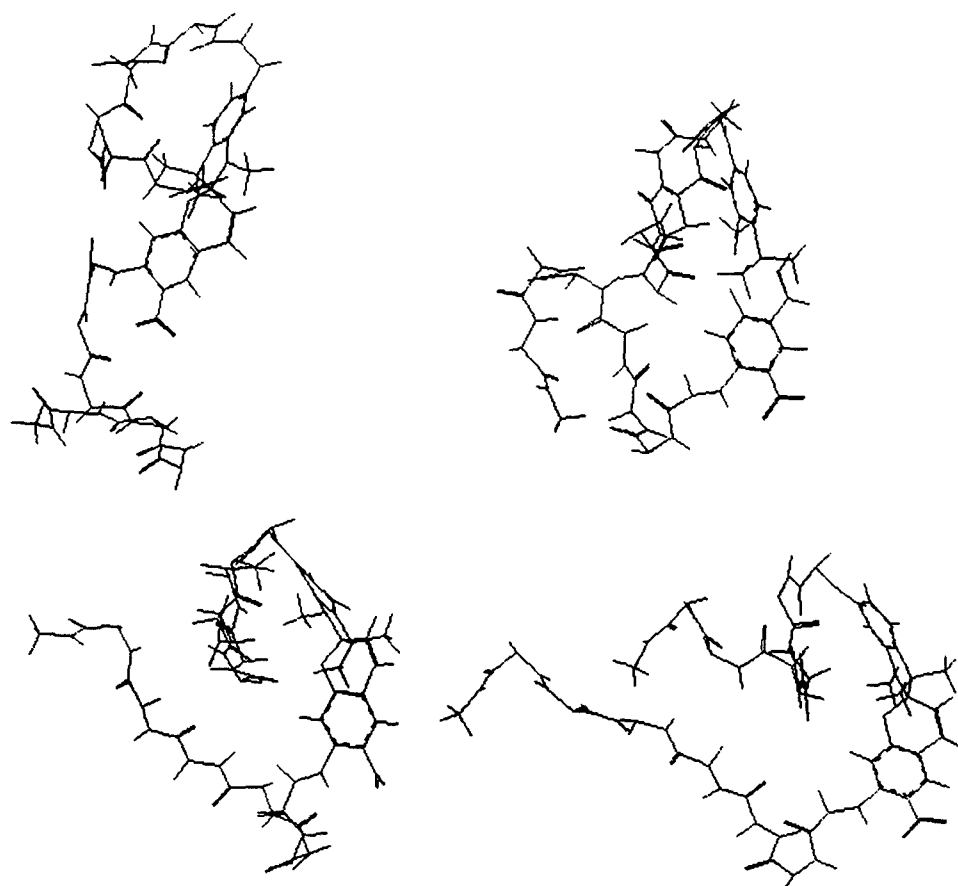
Table 4. Statistical analysis of end-to-end distance of α -poly(asp-arg-leu-ala-ser-tyr-leu)

	GSGAGA[α]-M	GSGAGA[α] S
average (Å)	11.98	5.60
Std deviation (Å)	1.58	1.06

Table 5. Statistical analysis of end-to-end distance of β -poly(gly-ser-gly-ala-gly-ala)

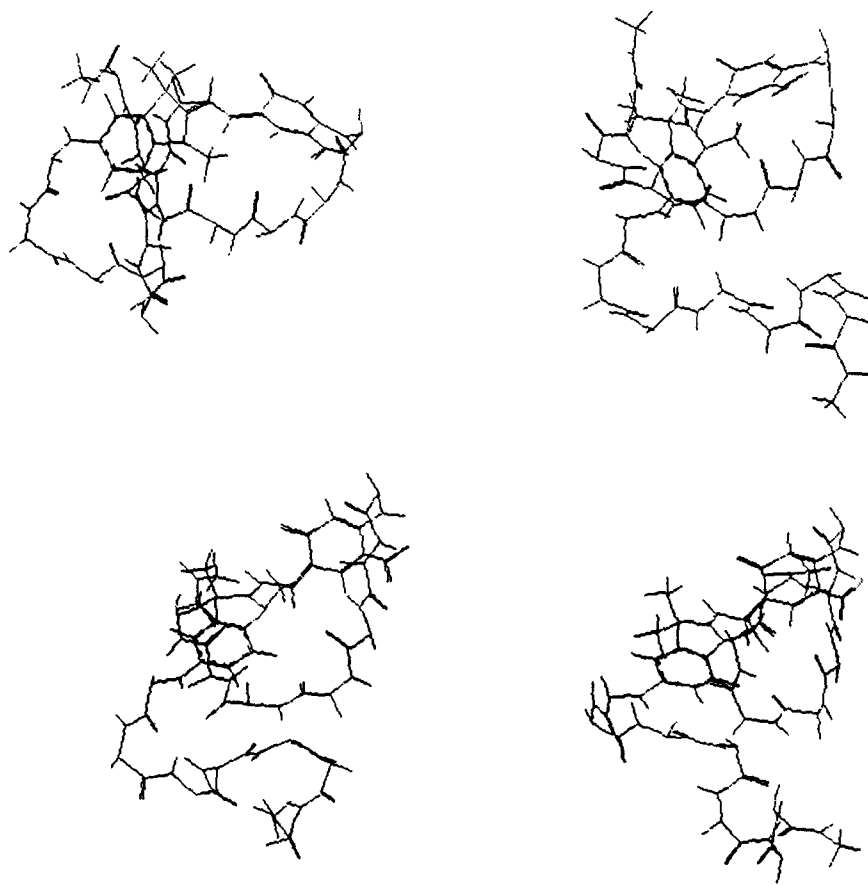
	GSGAGA[β]-M	GSGAGA[β] S
average (Å)	6.91	13.87
Std deviation (Å)	1.95	1.65

Figures 9 and 10 show the molecular conformations of the polypeptide-chromophore systems at 30 to 60 ps simulation at 300 K. The sidechains are omitted for the sake of clarity. Figure 11 shows the molecular conformations of α -helical poly-L-alanine without the chromophore at 300 K. Some portions of the helices remained intact in the unsubstituted poly-L-alanine during the simulation while none was observed in the chromophore-substituted α -poly-L-alanine. This shows that the



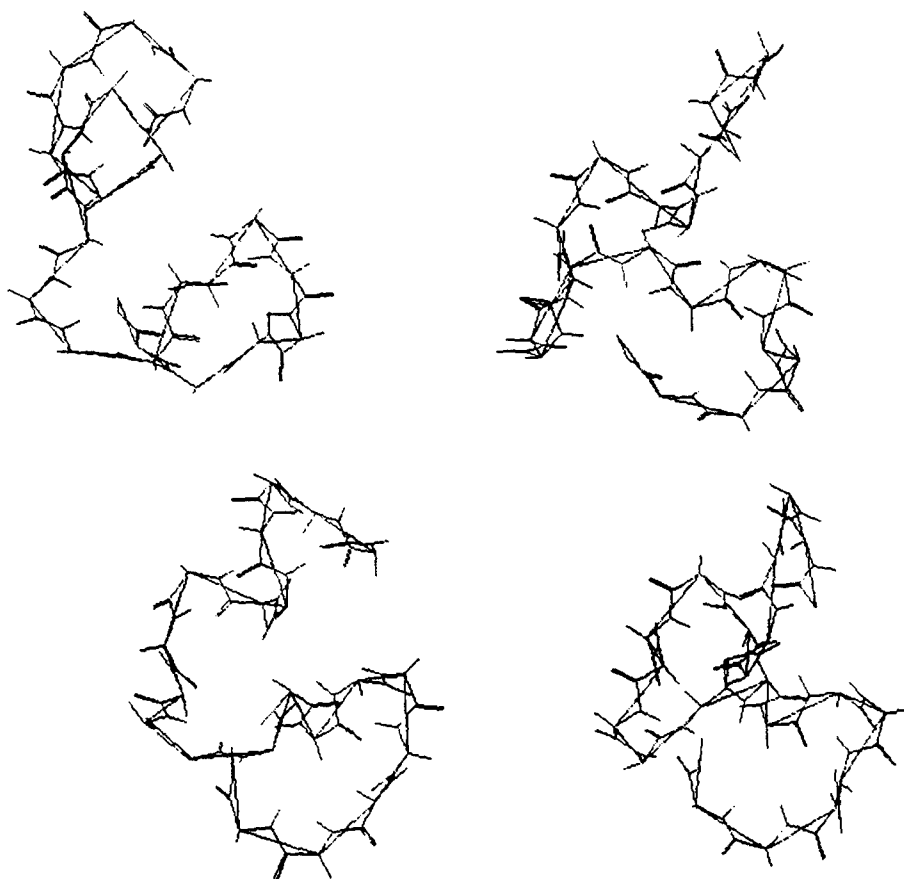
closed spiropyran substituted α -poly-L-alanine

Figure 9. Peptide chain motions at 30 to 60 ps of MD simulation.



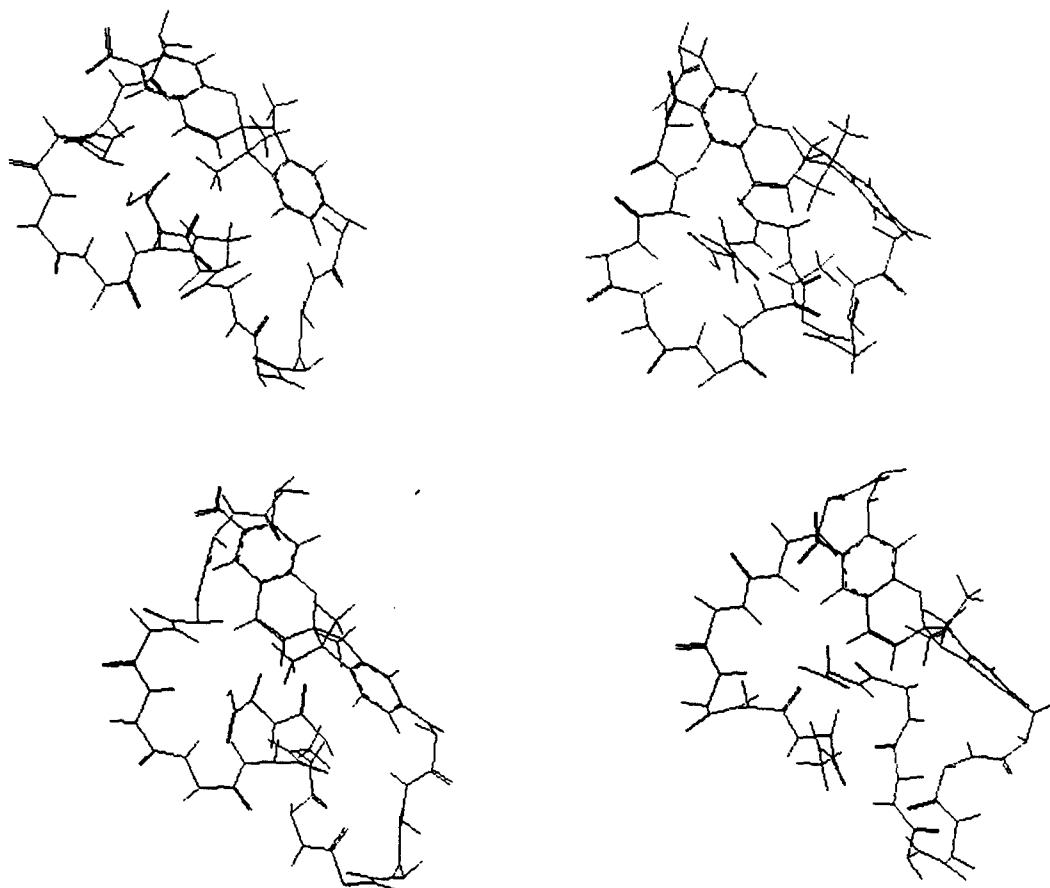
merocyanine substituted α -poly-L-alanine

Figure 10. Peptide chain motions at 30 to 60 ps of MD simulation.



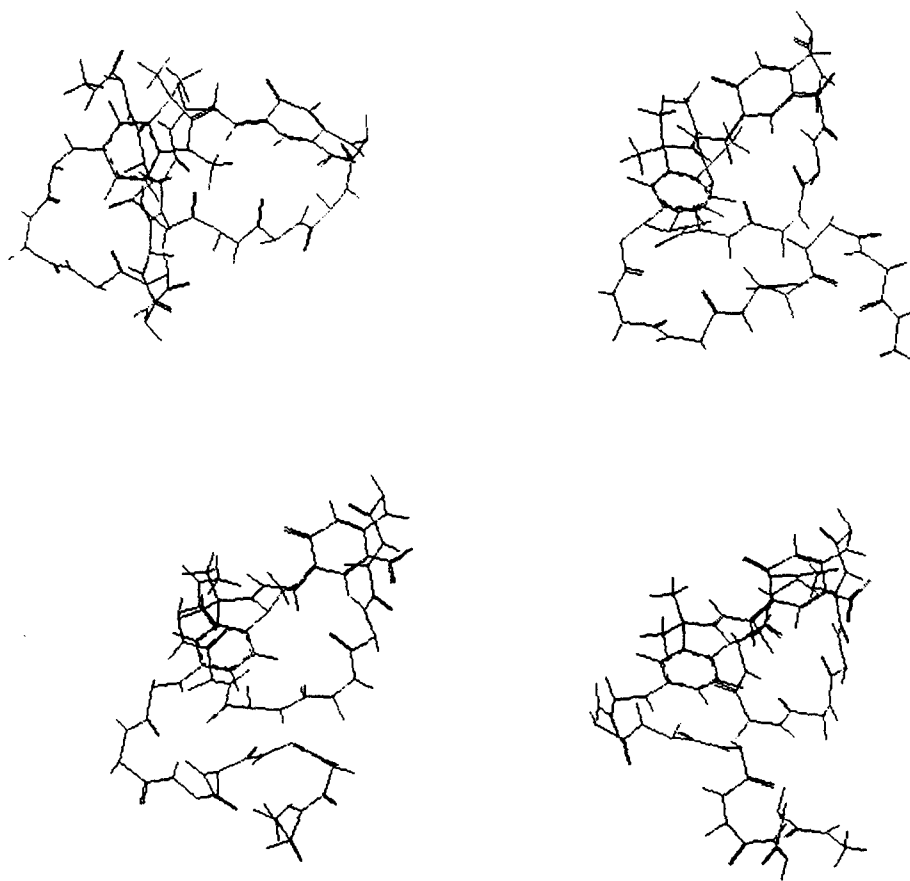
unsubstituted α -poly-L-alanine

Figure 11. Peptide chain motions at 30 to 60 ps of MD simulation.



closed spiropyran substituted β -poly-L-alanine

Figure 12. Peptide chain motions at 30 to 60 ps of MD simulation



merocyanine substituted β -poly-L-alanine

Figure 13. Peptide chain motions at 30 to 60 ps of MD simulation.

presence of the chromophore disrupts the hydrogen bonds causing a randomization of the helix.

An alternative way of viewing the degree of motion in the peptide chain occurring during the simulation is by studying the angular variation in the ϕ and ψ dihedral angles, defining the structure of the peptide. The ϕ and ψ dihedral angles measure the torsions about the rotationally permissive bonds in the backbone of the amino acid residues, and hence, are the most important internal coordinates in determining the peptide chain conformation. For a peptide chain in the α -helical conformation, the values of the ϕ and ψ dihedral angles are -58° and -47° respectively while for the β -sheet the values are -139° and 135° . The scatter plots in Figures 14 and 15 indicate that larger fluctuations in the poly-L-alanine chains occurs upon derivatizing with the spiropyran chromophore as compared to the unsubstituted poly-L-alanine. The Ψ values for the unsubstituted α -poly-L-alanine remain close to the ideal value, while large excursions of this dihedral angle occur for the chromophore-bound poly-L-alanine systems. The fluctuations are slightly higher in the merocyanine-substituted poly-L-alanine systems. Similar results are found for the chromophore-copolymer systems.

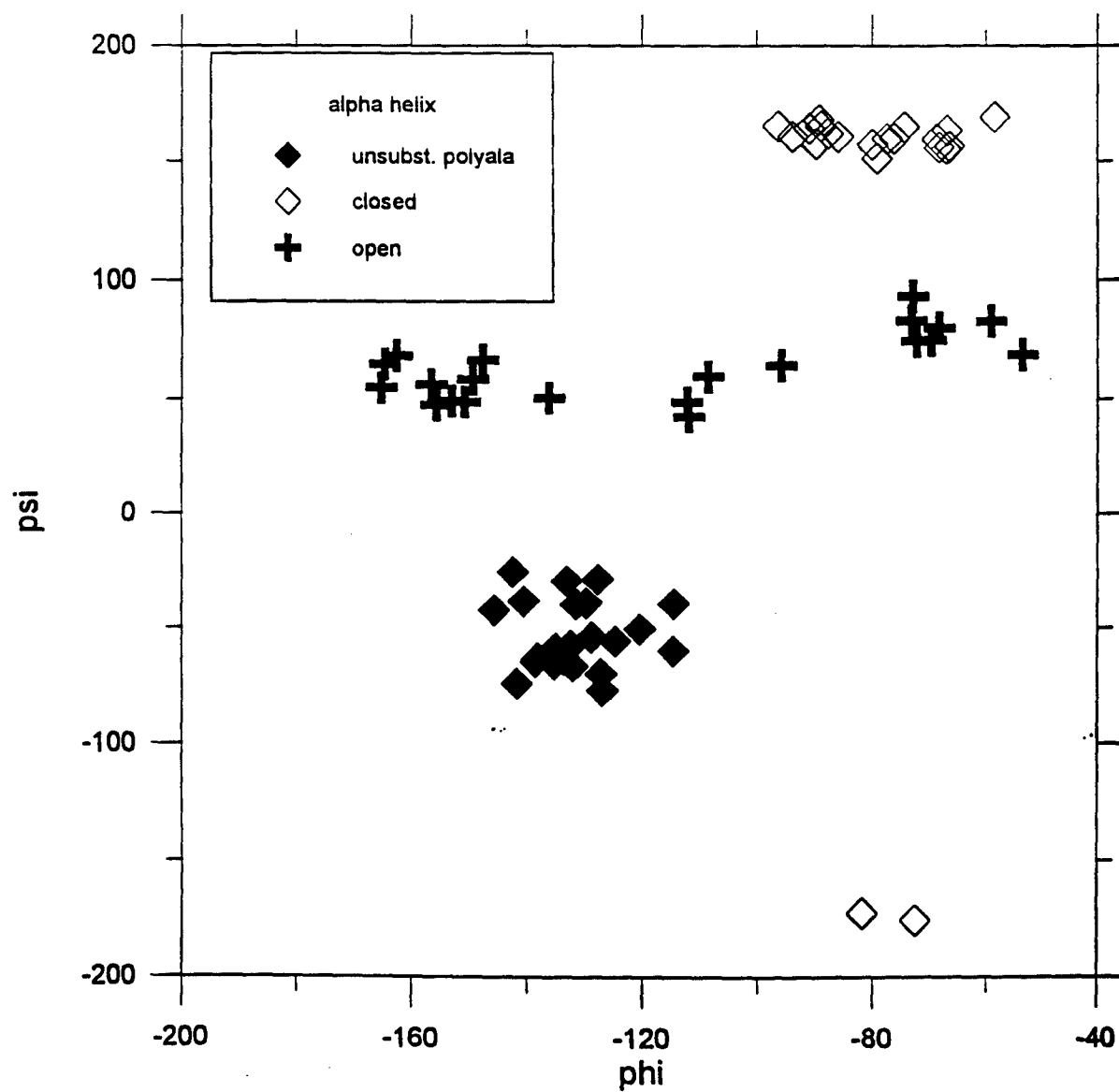


Figure 14. ψ vs. ϕ

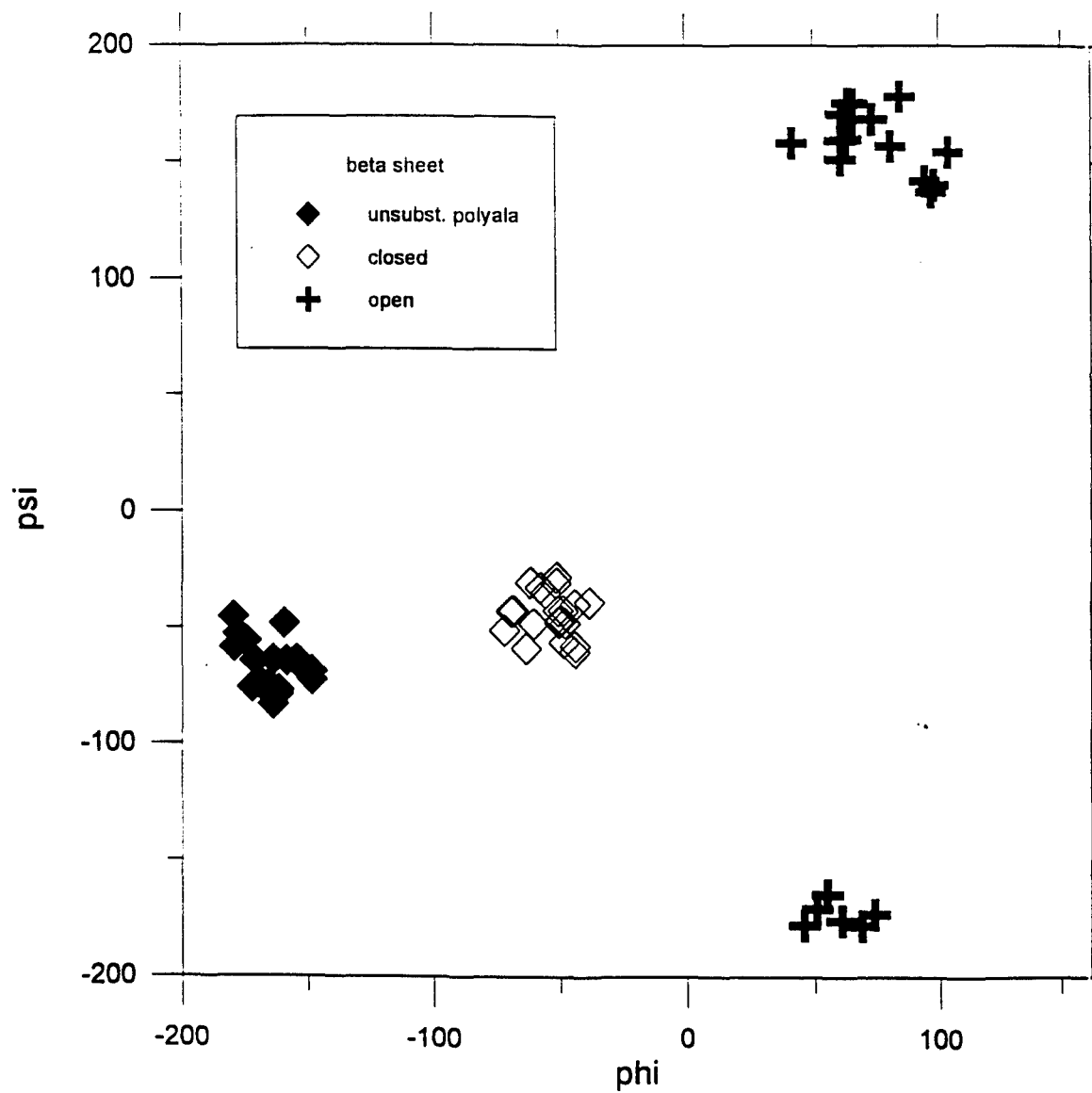


Figure 15. ϕ vs ψ

CONCLUSIONS

Computational chemistry methods were used to explore the properties of poly-L-alanine-chromophore and copolymer-chromophore systems. Molecular mechanics was used to generate and evaluate conformations for the the chromophore-biopolymer system. Results on poly-L-alanine and the copolymers indicate that an increase in energy of about 30-50 kcal occurs when the spiropyran chromophore is attached to β - or α -poly-L-alanine respectively. Molecular dynamics simulations were used to evaluate the effects of the spiropyran chromophore on the conformational properties of the polypeptide and to address the issue of molecular flexibility in the chromophore-biopolymer system. Results from the simulations show that the α -helix or the β -sheet conformation of poly-L-alanine is destabilized by the open and closed forms of the chromophore, with the open form exerting a larger influence. The larger influence exerted by the merocyanine results, in part, from the distortion of the α -helical framework due to the formation of a hydrogen bond between the oxygen (in the NO_2 group) in the merocyanine chromophore and the carboxylic group of the first alanine residue in the peptide chain. These results are in agreement with those calculated for a spiropyran-modified poly-L-glutamate system.

Similar results were observed for the chromophore-copolymer systems.

References

- (1) Vandeweyer, P.H., Smets, G., J. Polym. Sci., 1970, 8, pp. 2364-2374.
- (2) Cooper, T.M., Obermeier, K.A., Crane, R.L., Photochem.& Photobiol., 1992, 55, pp. 1-7.
- (3) Suzuki, Y., Ozawa, K., Hosoki, A., Ichimura, K., Poly. Bull., 1987, 17, pp. 285-291.
- (4) Yamamoto, H., Miyagi, Y., Nishida, A., Tagagishi, T., Shima, S., J. Photochem., 39, 343-350.
- (5) Ueno, A., Takahashi, K., Anzai, J., Osa, T., J. Am. Chem. Soc., 1981, 103, 5410-6415.
- (6) Ciardelli, F., Fabbri, D., Pieroni, O., Fissi, A., J. Am. Chem. Soc., 1989, 111, pp. 3470-3472.
- (7) Pachter R., Cooper, T.M., Natarajan, Obermeier, K.A., L.V., Crane, R.L., Adams, W.W., Biopolymers, 1992, 32, pp. 1129-1140.
- (8) Guglielmetti, R., "4n + 2 systems: spiropyrans", Review of Photochromism, by Bertelson, p. 314.
- (9) Robillard, J., Caulfield, H.J., Industrial applications of Holography, Oxford University Press, 1990, p. 151.
- (10) Bamford, C.H., Brown, L., Elliott, A., Hanby, W.E., Trotter, I.F., Proc. Roy. Soc., 1953, B141, p. 49.
- (11) Bamford, C.H., Elliott, A., Hanby, W.E., Synthetic Polypeptides, Academic Press, NY, 1956.
- (12) SYBYL version 6.01, Tripos Associates, Inc., St. Louis, MO.
- (13) Benedetti, E., Di Blasho, B., Pavone, V., Pedone, C., Toniolo, C., Crisma, M., Biopolymers, 1992, 32, pp. 453-456
- (14) Clark, M., Cramer, R.D. III, Opdenbosch Van, N., J. Comp. Chem., 10, 1989, p. 982.
- (15) Buckert, Ulrich, D.C., Norman, A.L., Molecular Mechanisms ACS Monograph, 1982, 177.
- (16) Sorensen, R. A., Liau, W.B., Boyd, R.H., Macromolecules, 1980, 13, pp. 1178-1183.
- (17) Verlet, L., Phys. Rev., 1967, 159, p. 98.
- (18) McCammomn, J.A., Harvey, S.C., Dynamics of proteins and Nucleic acids, Cambridge University Press, NY, 1987.

AN EXACT METHOD FOR RANGE CALCULATION
IN A DIVERGENT BINOCULAR IMAGING SYSTEM

Simon Y. Foo
Assistant Professor
Department of Electrical Engineering
FAMU/FSU College of Engineering

Florida State University
Tallahassee, FL 32306

Final Report for:
Summer Research Extension Program
Wright Laboratory

Sponsored by:
Air Force Office of Scientific Research
Bolling Air Force Base, Washington, D. C.

December 1993

AN EXACT METHOD FOR RANGE CALCULATION IN A DIVERGENT BINOCULAR IMAGING SYSTEM

Simon Y. Foo
Assistant Professor
Department of Electrical Engineering
Florida State University

Abstract

This report presents an exact method for range calculation in a divergent binocular imaging system. Unlike conventional stereo imaging systems, the sensors of this divergent binocular imaging system are placed on a convex cylindrical surface. An important consideration when choosing algorithms or methods for range calculation is speed. The advantage of our stereo vision technique is that it only requires few simple calculations, and therefore this method is most suitable for realtime applications where speed is critical.

AN EXACT METHOD FOR RANGE CALCULATION IN A DIVERGENT BINOCULAR IMAGING SYSTEM

Simon Y. Foo

Introduction

There are numerous situations, particularly in military systems, where a fast moving observer (e.g., a projectile) with passive imaging sensors wishes to determine the location of a stationary or moving target. For example, in passive airborne automatic acquisition systems, it may be necessary to determine range to a candidate target for use in the target classification algorithms. In general, depth or range information can be obtained from (i) a single monocular image by a variety of "depth cues" such as size and occlusion; (ii) binocular images by simple triangulation; (iii) sequential motion images from a single camera by analyzing the optical flow; (iv) field strength of energy transmission measurements.

Mapping a three-dimensional scene onto a two-dimensional image plane is a *many-to-one* transformation, i.e., an image point does not uniquely determine the location of a corresponding world point, as pointed out by Fu, Gonzalez, and Lee [1], and Gonzalez and Woods [2]. The missing depth information can be obtained by using stereo imaging techniques. The concept in stereo or binocular imaging is quite simple: If two images of an object taken at different viewpoints can be placed in correspondence, the intersection of the lines of sight from two matching image points determines a point in three-dimensional space. The most difficult task in this technique is that of identifying corresponding points from the two images, a task commonly called pixel registration. One way of achieving this is to use correlation or template matching. The idea is to take a patch of one image and *correlate* it against the other image, finding the location of best match in the second image. Unfortunately, correlation is an expensive operation requiring $O(n^2m^2)$ multiplications and additions for an m -by- m patch and n -by- n image. The method of "light striping", first proposed by Will and Pennington [3] and later studied extensively by Popplestone et. al. [4], can be used to aid the matching of corresponding points in two images. A single plane of light is projected onto a scene causing a stripe of light to appear. The illuminated surface is then segmented into surfaces which simplifies the point matching process.

This research report summarizes earlier work by Foo [5] where an exact method to extracting range information for fuze applications is presented. Unlike conventional stereo imaging systems, the sensors of this divergent binocular imaging system are placed

on the perimeter of a convex cylindrical surface. An important consideration when choosing algorithms or methods for range calculation is speed. The advantage of this stereo vision method is that it only requires few simple calculations, and therefore it is most suitable for realtime applications where speed is critical.

A Divergent Binocular Imaging System for Range Calculation

As discussed earlier, it is possible to obtain range information by using a divergent binocular imaging technique. If two images from different viewpoints can be placed in correspondence, then the intersection of the lines of sight from two matching image points determines a point in three-dimensional space. This technique is conceptually simple:

- (1) Consider two images separated by a baseline.
- (2) Register points between the two images.
- (3) Derive the equations of the two lines from the image planes to the target.
- (4) Intersect the lines.

The result is the object's position in three-dimensional world coordinates.

This above concepts form the basis of this passive ranging technique, as shown in Figure 1. The line from the target through lens i to image plane i can be described by

$$\bar{x}_i = \bar{x}_{Li} + \alpha_i(\bar{x}_{Li} - \bar{x}_{Ri}) \quad (1)$$

where

- | | |
|---------------------------------|--|
| \bar{x}_i | : any point on the line, |
| \bar{x}_{Li} | : one known point on the line |
| $(\bar{x}_{Li} - \bar{x}_{Ri})$ | : a known segment giving the direction of the line |
| α_i | : a scalar (to be determined) |

In three-dimensional space, the position of target, i.e., \bar{x} , is given by the point of closest approach between the two lines \bar{x}_1 and \bar{x}_2 . The distance between any two points on the lines, squared, is given by

$$d^2 = (x_1 - x_2)^2 + (y_1 - y_2)^2 + (z_1 - z_2)^2 \quad (2)$$

where

$$x_1 = x_{L1} + \alpha_1(x_{L1} - x_{R1})$$

$$x_2 = x_{L2} + \alpha_2(x_{L2} - x_{R2})$$

and

$$\begin{aligned}
(x_1 - x_2)^2 = & (x_{L1} - x_{L2})^2 + \alpha_1^2 (x_{L1} - x_{I1})^2 + \alpha_2^2 (x_{L2} - x_{I2})^2 \\
& + 2\alpha_1 (x_{L1} - x_{L2})(x_{L1} - x_{I1}) \\
& - 2\alpha_2 (x_{L1} - x_{L2})(x_{L2} - x_{I2}) \\
& - 2\alpha_1 \alpha_2 (x_{L1} - x_{I1})(x_{L2} - x_{I2})
\end{aligned}$$

The same applies for the y's and the z's. The positions of the centers of lens 1 and 2 relative to the global origin are

$$\bar{x}_{L1} = \begin{pmatrix} R \sin \Theta \\ R \cos \Theta \\ 0 \end{pmatrix}, \quad \bar{x}_{L2} = \begin{pmatrix} -R \sin \Theta \\ R \cos \Theta \\ 0 \end{pmatrix}$$

where R is the radius of curved surface, and Θ is the angle of lens from y-axis. Similarly, the positions of image points on image planes 1 and 2 relative to the global origin are

$$\bar{x}_{I1} = \begin{pmatrix} (R-f) \sin \Theta + u \cos \Theta \\ (R-f) \cos \Theta - u \sin \Theta \\ z \end{pmatrix}, \quad \bar{x}_{I2} = \begin{pmatrix} -(R-f) \sin \Theta + u \cos \Theta \\ (R-f) \cos \Theta + u \sin \Theta \\ z \end{pmatrix}$$

where image position on image plane is (u, z) and f is the focal length. After summing all the terms of equation (2), the result is

$$d^2 = C_0 + C_1 \alpha_1^2 + C_2 \alpha_2^2 + C_3 \alpha_1 + C_4 \alpha_2 + C_5 \alpha_1 \alpha_2 \quad (3)$$

where C 's are constants. To find the intersection between the two lines, we minimize equation (3) with respect to α_i , i.e.,

$$\frac{\partial(d^2)}{\partial \alpha_1} = 2C_1 \alpha_1 + C_3 + C_5 \alpha_2 = 0$$

$$\frac{\partial(d^2)}{\partial \alpha_2} = 2C_2 \alpha_2 + C_4 + C_5 \alpha_1 = 0$$

or

$$\begin{pmatrix} 2C_1 & C_5 \\ C_5 & 2C_2 \end{pmatrix} \begin{pmatrix} \alpha_1 \\ \alpha_2 \end{pmatrix} = \begin{pmatrix} -C_3 \\ -C_4 \end{pmatrix} \quad (4)$$

From equation (4), we solve for α_1 and α_2 , and calculate either \bar{x}_1 or \bar{x}_2 using equation (1). This gives the target's position relative to the global origin, and hence the relative distance to the target is determined.

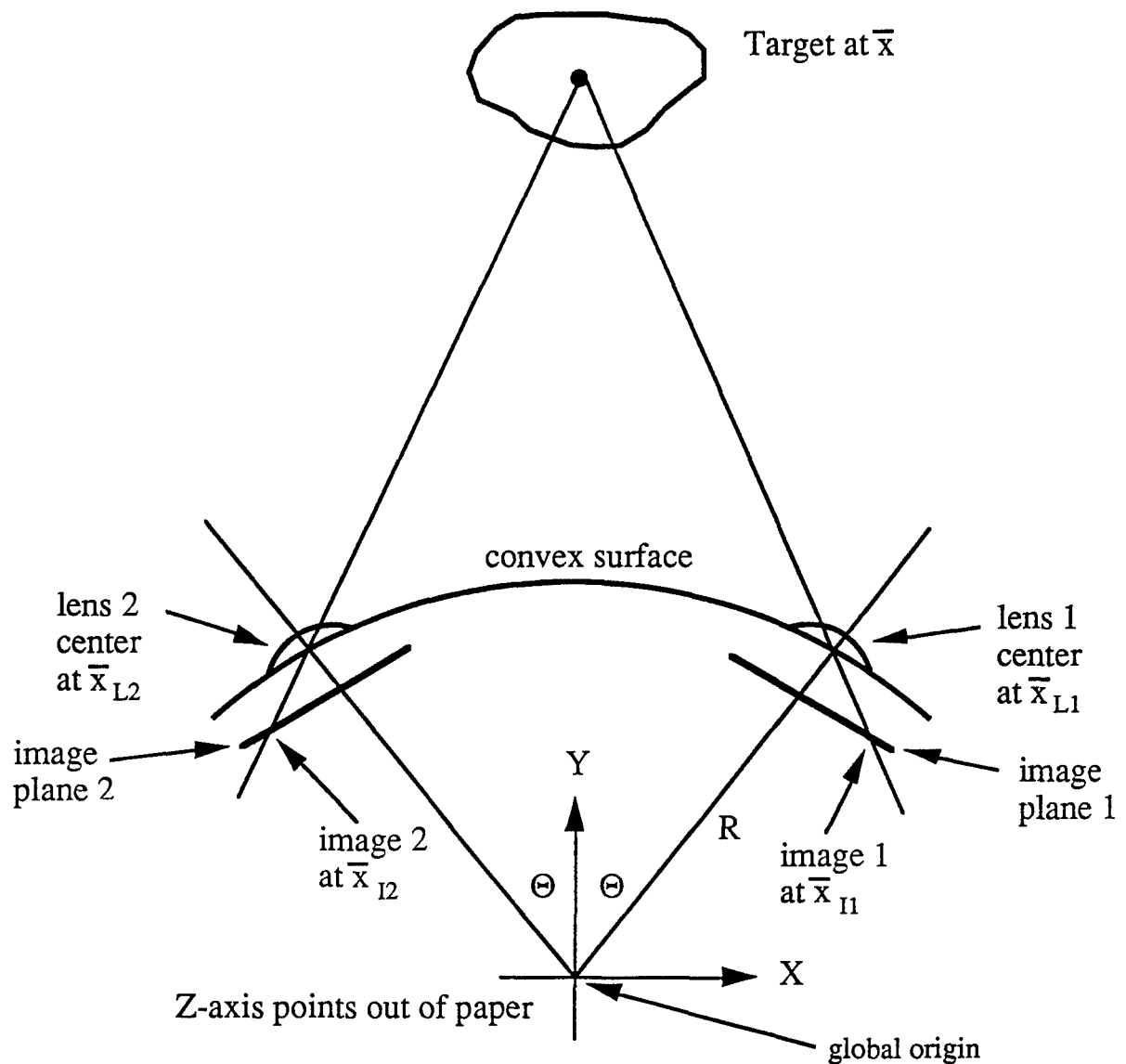


Figure 1. Passive ranging in a divergent binocular imaging system.

Test Platform: A Single Camera Stereo Vision System

A simple test platform is developed to prove the correctness of the mathematical model of divergent binocular imaging developed by Foo [5] for calculating the position and range of a target. The test platform consisted of a single video camera, a camera positioning table, and a computer image digitizing and analysis system. To simplify the correspondence problem, a pin-point light source is used to simulate a target. Software is written to locate the center of the light source in the two images and to calculate the distance to the target. The results of the experiments support the correctness of the mathematical model.

As shown in Figure 1, the system parameters of a divergent binocular imaging system are defined as follows:

- R : system radius, i.e., the distance along the optical axis from the global origin to the lens center,
- F : focal length, i.e., the distance from the optical center of the lens to the imaging plane, and
- Θ : the angle between the optical axis and the Y axis.

The constants R , F , and Θ are determined by the system configuration and choice of lens. The two vectors, (u_1, Z_1) and (u_2, Z_2) , are the unknowns. These vectors lie on the plane of their respective imaging surfaces and represent the location of the target image.

A single camera is mounted on a movable arm that pivots about a fixed point on the positioning table. This allowed the simulation of stereo vision with a single camera. Camera mounting holes are placed at two-inch increments along the camera arm to allow for variation of radius. An arrangement of predetermined registration pins and a locking mechanism allows the camera mounting arm to be easily positioned at a desired angle Θ . This single camera stereo vision system is depicted in Figure 2.

Using a single camera offers several advantages. The one-camera system eliminates error that would be introduced by differences between different lenses. The need for two digitizers or a video multiplexer is also eliminated. In addition, to allow the use of lenses with different focal-lengths, R and Θ has to be adjustable. Meeting this goal with a one-camera system is mechanically less complex.

The ULTRAK model K-204 video camera was chosen for its compact size (2x2.375x4.375 inches) and solid state image sensor. A solid state image sensor has well defined dimensions simplifying the determination of the image plane points (u_1, Z_1) and (u_2, Z_2) . Other features of camera include low power consumption, composite video output, and standard lens mount. A camera data sheet is included in Appendix A.

A digitizer and frame buffer (TARGA+) acquires 512x485x8-bit image data from the camera's video output. The Imagescale Plus software package, developed by Electronic Imagery, Inc., and custom software developed to implement the stereo imaging model, is used for image processing.

Acquisition of Stereo Image Data

For a given target position, the values for R , F , and Θ are chosen so that a target image is formed on the image sensor at both camera positions, i.e., Θ and $-\Theta$. The minimum distance for which the target image can be seen from both camera positions is given in terms of the parameters R and Θ by

$$Y_{\min} = R \cos \Theta + \frac{R \sin \Theta}{\tan(FOV - \Theta)}$$

where FOV is the field-of-view of lens. After choosing appropriate values for the parameters the following procedure is performed:

- (1) The pin point light source simulating the target is positioned and the intensity of the background set low enough to insure that none of the pixel values representing the background are saturated. However, the pixel values representing the target are to be saturated.
- (2) The camera mounting arm is secured at one position. Using Imagescale the digital image data is captured and saved to a file called IMAGE1.TGA.
- (3) Now, the camera mounting arm is secured at the second position. Using Imagescale the digital image data was captured and saved to a file called IMAGE2.TGA.
- (4) The RANGER Program (a custom software which implements the stereo vision passive ranging technique) is executed.

The RANGER Program

The primary computer program developed for this project is called RANGER. It performs several basic tasks. First it searches the digital image data from IMAGE1.TGA and determines the coordinates of the saturated pixel cluster. The cluster centroid is calculated and is taken to represent the target image position (u_1, Z_1). This procedure is repeated for IMAGE2.TGA to locate the target image position (u_2, Z_2). These coordinates are then transformed from the image plane coordinate systems to the global coordinate system. The set of linear equations describing the system are then solved for α_1 and α_2 using Equation (4). Finally, the target's global coordinates and range are calculated.

In this system, the focal length is a critical value. As pointed out by Ray [6], the focal length marked on a lens is rounded to the nearest integer value. The program FOCALTST, a modified version of RANGER, is developed to accurately determine the focal length F of a lens from experimental data. FOCALTST has as its input the Up - Zp coordinates from Image 1 and Image 2 for a target at a known distance from the global origin. FOCALTST produces a look up table which contains incremental values of F and the corresponding calculated distance. The focal length of the lens is determined from this table by matching the calculated distance with the known distance.

Experiments

A series of experiments was conducted to confirm the mathematical model governing passive ranging with divergent binocular imaging. Two of these experiments, Lens Distortion and the Pin-Hole, will be discussed in this section. These experiments investigate the effects of lens distortion on range. It is well known that lenses introduce some radial distortion (Krotkov [7]) which affects range calculations. The lens used, a Rainbow Model H612, 6 mm, C-mount lens with iris and focus, was found to have these radial distortions. The Lens Distortion experiment showed that large distortion effects were present, and the Pin-Hole experiment showed that it was a lens effect only.

Lens Distortion Experiment

It is a common industry practice to publish the focal length of a general-purpose lens rounded to the nearest integer value. For our project, however, a more precise value is required. The first objective of this experiment is to determine the actual focal length.

A program called FOCALTST was used to determine the actual focal length of the lens. FOCALTST has as its input the Up - Zp coordinates from Image 1 and Image 2 for a target at a known distance from the global origin. FOCALTST produces a look-up table, as shown in Table 1. The table contains incremental values of focal length and the corresponding calculated distance. The focal length of the lens was determined from this table by matching the calculated distance with the known distance. The Up - Zp coordinates of a target placed on the Y axis (the system center-line) were used. The focal length was determined to be 0.2522 inches (or 6.41mm).

The other issue we are concerned with is geometric distortion caused by imperfections in lenses. Simple lenses made of ordinary elements form geometrically distorted images on flat surfaces. This distortion, known as barrelling and pincushion, cause straight lines in the object to appear curved in the image. The degree of distortion in an image is a function of the radial distance from an object point to the optical axis.

Since the mathematical model is developed for an ideal lens, this distortion is expected to introduce error in the system. A second objective of this experiment is to detect and characterize the error caused by the geometric distortion present in the lens.

Distortion affects both the apparent focal length F and the range. To minimize distortion effects, F is calculated by FOCALTST for a known target position on the system center-line. With the actual value of F , ranges can now be calculated using the RANGER program for unknown target positions over a limited region. An object was ranged at 20 points on the X-Y plane as shown in Figure 3. The points were at a constant distance from the global origin and evenly spaced across the system's field of view.

Table 2 summarizes the output of the RANGER program using the data from Table 1 and a focal length of 6.41mm. The table contains the calculated coordinates (X,Y,Z) and the range R. Figure 3 shows graphs of the data in Table 2. For $|\alpha| > 12^\circ$, we observed that the error increases rapidly. At $\pm 20^\circ$ the error in range is in excess of 300%.

Figure 4(a) shows the graph of the range data. From this graph it is observed that the range error is a function of the target's distance from the system's center-line. Figures 4(b), (c), and (d) compares the expected X, Y, and Z coordinates, respectively, with those reported by the ranging system. As observed from the plots, the error in the calculated X, Y, and Z coordinates are functions of the target's distance from the center-line.

Geometric distortion in a lens is more severe when light rays pass through a lens near the edge of a lens element. When the target was placed on the system center line, the effects of distortion were minimal and equal in both images. However, when the target was placed at the $\pm 20^\circ$ position, light rays travel nearly through the center of one lens while entering at the extreme edge of the other. This suggests increasing error as the target moves away from the center line. This is consistent with the symmetry of the data represented in Figure 4. The focal length determined in this experiment includes the effects of this distortion.

To verify that the error between the experimental and the actual range data is a lens effect only, the Pin-Hole experiment was conducted.

Pin-Hole Experiment

Although a pin-hole lacks the light gathering ability and magnification factor of a lens, a pin-hole will form an image without radial distortion. To confirm that the range errors seen in Figure 4 was a lens effect only, the lens was replaced with a pin-hole. Range data was collected using the same experimental set-up and procedure as the Lens Distortion experiment. Using the FOCALTST program, the apparent focal length F of the pin-hole lens was first determined to be 0.2705 inches. With the actual value of F , ranges

were calculated using the RANGER program for unknown target positions over a limited region. An object was ranged at 20 points on the X-Y plane as shown in Figure 3.

Figures 5(a) and 5(b) show the resulting range data and X-coordinate data, respectively. We observed that the margin of error in the range and X-coordinate calculations were almost negligible. This figure confirms the correctness of the mathematical model with a pin-hole where radial distortion caused by lenses can be eliminated.

Conclusion

An exact method to range calculation in a divergent binocular imaging system has been presented. The major advantage of this passive ranging method is speed without too much sacrifice in accuracy. Furthermore, the accuracy of this passive ranging approach can be improved with better correlation techniques for pixel registration. Foo's [5] model is based on a distortionless lens. The Pin-Hole experiment confirms the correctness of this model. The Lens Distortion experiment shows that lenses introduce radial distortion which affects ranging. Practical systems will require the light gathering capabilities and magnification of lenses. Thus the choice of a lens will be a significant issue. Alternatively, a lens model could be included to compensate for radial distortions.

References

- [1] K. S. Fu, R. C. Gonzalez, and C. S. G. Lee, Robotics: Control, Sensing, Vision, and Intelligence, McGraw-Hill, New York, 1987.
- [2] R. C. Gonzalez and R. E. Woods, Digital Image Processing, Addison-Wesley, 1992.
- [3] P. M. Will and K. S. Pennington, "Grid coding: a preprocessing technique for robot and machine vision," *Artificial Intelligence* 2, 3/4, Winter 1971, pp. 319-329.
- [4] R. J. Popplestone, C. M. Brown, A. P. Ambler, and G. F. Crawford, "Forming models of plane-and-cylinder faceted bodies from light stripes," *Proc. of 4th IJCAI*, September 1975, pp. 664-668.
- [5] S. Y. Foo, "Passive ranging and roll-angle approximation for fuze application," Technical Report, Eglin AFB, FL, August 1992.
- [6] S. F. Ray, The Photographic Lens, Focal Press, London, 1979, pp. 68 and 108.
- [7] E. P. Krotkov, Active Computer Vision by Cooperative Focus and Stereo, Springer-Verlag, New York, 1989, p. 60.

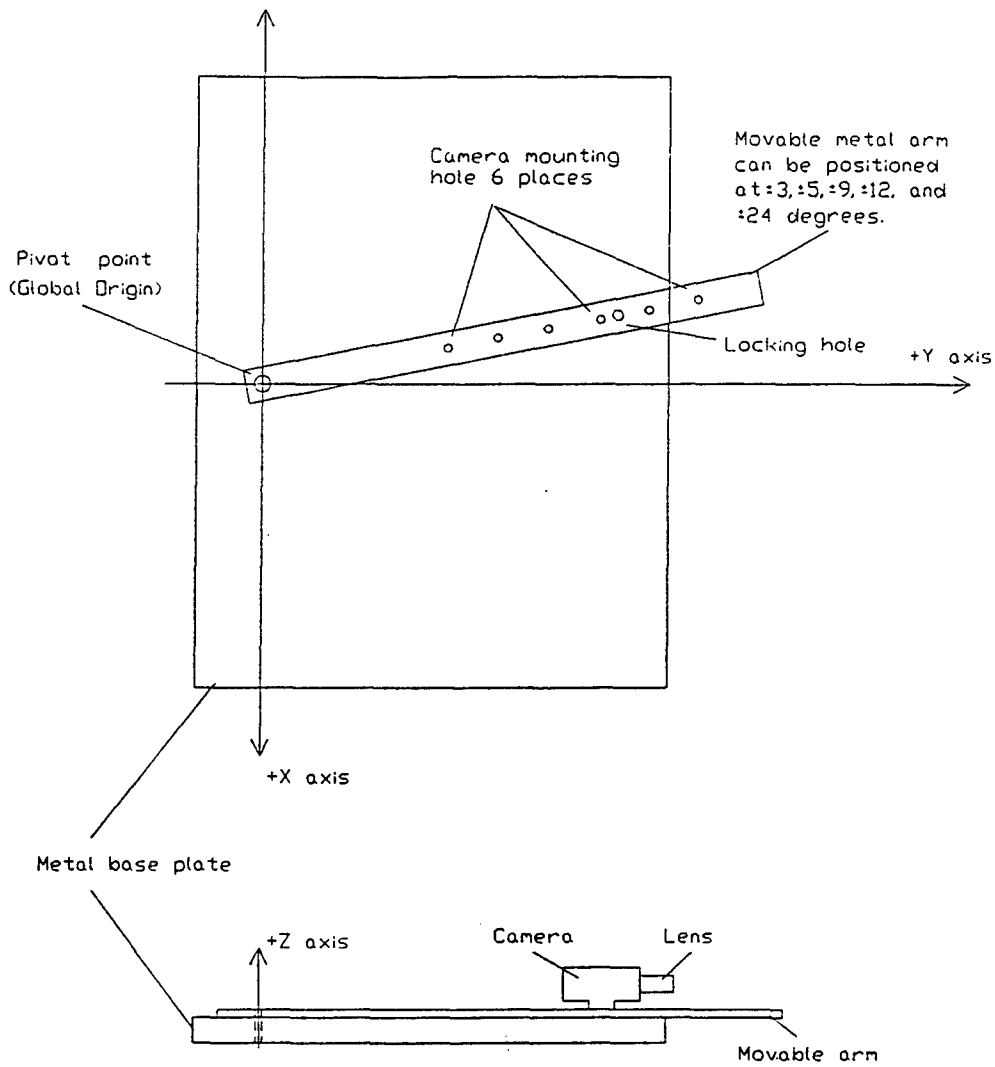


Figure 2. A single-camera test platform used for stereo imaging.

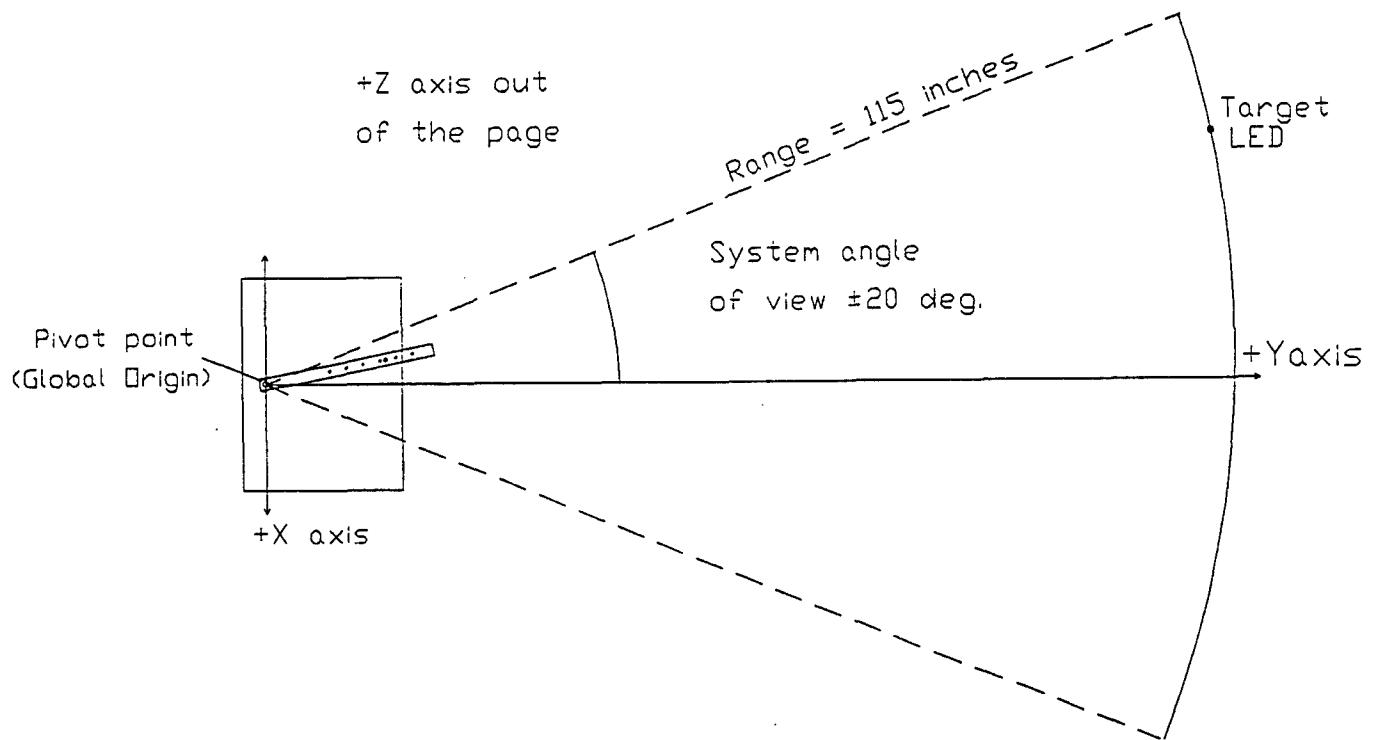
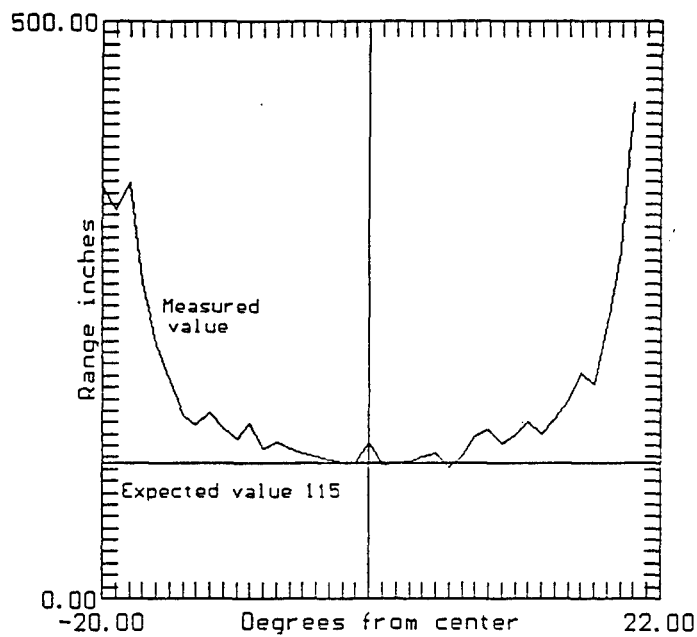
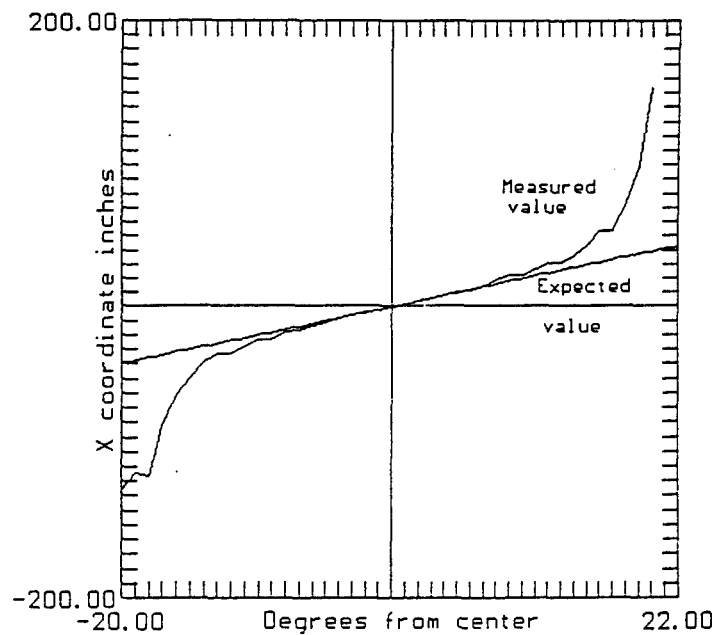


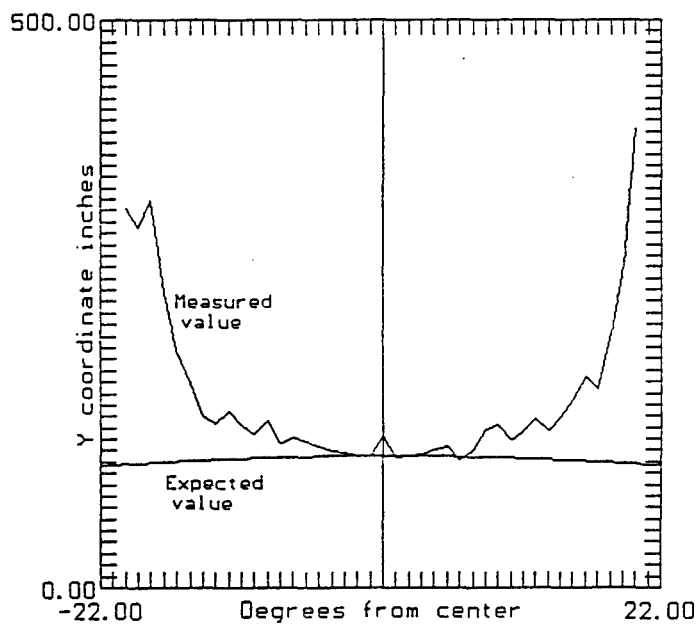
Figure 3. The setup used to collect data for a target on the X-Y plane at a constant distance from the global origin.



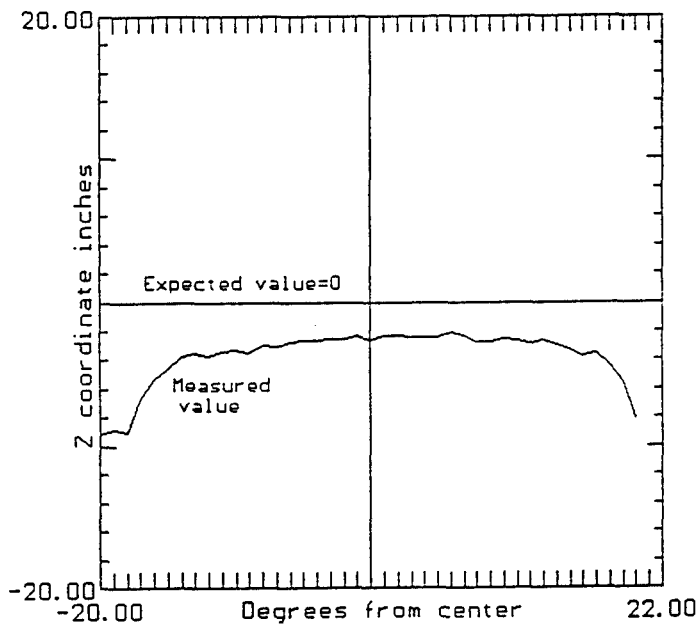
(a)



(b)



(c)



(d)

Figure 4. Graphs of the Lens Distortion experimental data: (a) the reported range, and (b) the corresponding X-coordinates, (c) the Y-coordinates, and (d) the Z-coordinates.

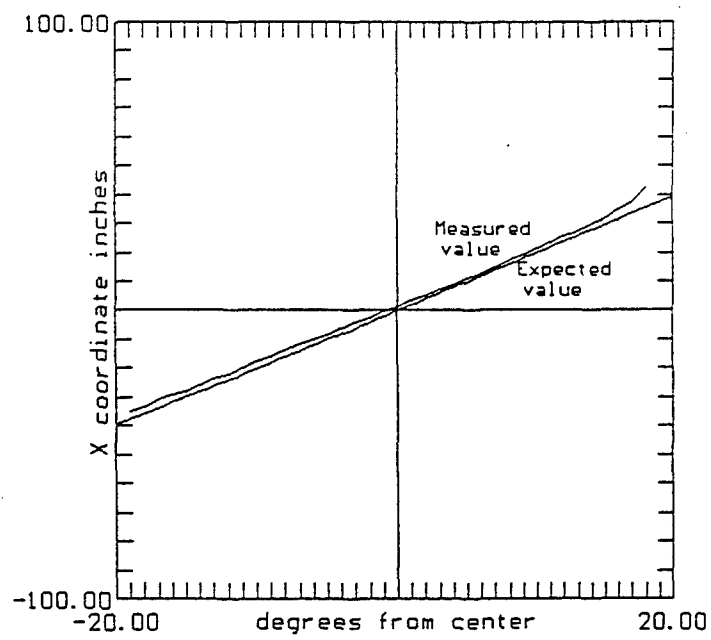
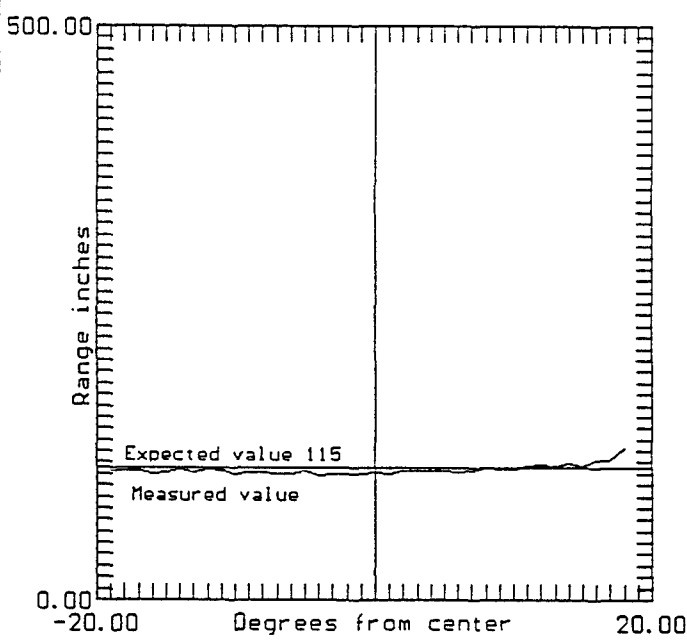


Figure 5. Graphs of Pin-Hole experimental data: (a) the reported range, and (b) the corresponding X-coordinates.

α	up_1	Zp_1	up_2	Zp_2
-20°	22	222	85	224
-19°	32	222	95	223
-18°	43	223	105	224
-17°	53	223	115	224
-16°	64	223	126	224
-15°	74	223	136	224
-14°	84	223	146	225
-13°	94	224	156	224
-12°	105	224	166	225
-11°	115	224	176	225
-10°	125	224	186	224
-9°	135.5	224	195.5	225
-8°	145	224	205.5	225.5
-7°	155	224	215	225
-6°	165	225	225	226
-5°	175	225	235	226
-4°	185	225	245	226
-3°	195	225	255	226
-2°	205	225	265	226
-1°	214	226	274	227
0°	225	226.5	284	227
1°	234	226	294	227
2°	244	226	304	227
3°	254	226	314	227
4°	264	227	324	227
5°	274	227	334	227
6°	283	227	344	227.5
7°	293.5	227	354	228
8°	303	227	363	227
9°	314	227	374	228
10°	323	227	384	228
11°	333	227	394	228
12°	343	227	404	228
13°	353	227	415	228
14°	363	227	425	228
15°	373	227	435	228
16°	383	227	445	228
17°	393	227	456	228
18°	403	228	466	228
19°	413	228	476	228
20°	424	228	487	228

Table 1. Image coordinates in pixels.

α	X	Y	Z	D
-20°	-126.72	331.92	-9.12	355.40
-19°	-113.92	314.67	-8.86	334.78
-18°	-116.35	338.89	-9.07	358.42
-17°	-82.49	257.60	-6.81	270.57
-16°	-61.31	207.35	-5.41	216.30
-15°	-48.91	178.40	-4.60	185.04
-14°	-37.99	150.66	-3.72	155.42
-13°	-33.39	143.30	-3.52	147.18
-12°	-33.43	154.83	-3.72	158.45
-11°	-27.99	142.58	-3.40	145.35
-10°	-23.69	133.66	-3.26	135.79
-9°	-23.60	146.52	-3.51	148.45
-8°	-17.89	126.57	-2.94	127.86
-7°	-16.48	132.04	-3.12	133.10
-6°	-13.52	126.82	-2.81	127.57
-5°	-10.88	122.76	-2.71	123.27
-4°	-8.48	119.63	-2.63	119.96
-3°	-6.24	117.29	-2.58	117.48
-2°	-4.13	115.64	-2.53	115.75
-1°	-2.30	114.70	-2.35	114.75
0°	-0.23	132.17	-2.71	132.20
1°	1.69	114.36	-2.35	114.40
2°	3.71	115.06	-2.36	115.15
3°	5.78	116.38	-2.39	116.54
4°	8.10	120.19	-2.40	120.49
5°	10.49	123.15	-2.47	123.62
6°	11.11	110.67	-2.15	111.25
7°	14.39	120.44	-2.32	121.32
8°	18.95	137.55	-2.79	138.88
9°	22.40	141.86	-2.79	143.64
10°	22.28	128.83	-2.51	130.77
11°	26.27	136.89	-2.68	139.41
12°	31.06	147.03	-2.90	150.30
13°	31.13	136.40	-2.67	139.93
14°	36.83	148.40	-2.93	152.93
15°	44.02	163.90	-3.27	169.74
16°	53.35	184.27	-3.71	191.87
17°	53.25	173.36	-3.47	181.39
18°	73.81	222.76	-4.38	234.71
19°	99.53	280.78	-5.59	297.95
20°	153.06	401.98	-8.13	430.21

Table 2. Target coordinates and range data.

INVESTIGATIONS INTO THE ROLE OF SULFUR AND PHENOLIC COMPOUNDS IN THE DEPOSIT
FORMATION OF JET FUELS

Ann P. Gillman, M.S.
Research Associate
and
William D. Schulz, Ph.D.
Department of Chemistry

Eastern Kentucky University
337 Moore
Richmond, KY 40475

Final Report for:
Research Initiation Program
Research and Development Laboratories
Culver City, CA 90230

Sponsored by:
Air Force Office of Scientific Research
Wright-Patterson Air Force Base
Dayton, Ohio

and
Eastern Kentucky University

August 1993

INVESTIGATIONS INTO THE ROLE OF SULFUR AND PHENOLIC COMPOUNDS IN THE DEPOSIT FORMATION OF JET FUELS

Ann P. Gillman
William D. Schulz
Department of Chemistry
Eastern Kentucky University

ABSTRACT

Analysis of deposits formed by two U.S. Air Force jet fuels in a simple, static, well controlled thermal flask test suggested two distinctly different mechanisms for deposit formation. Non-hydrotreated Jet-A fuels rapidly produce crystalline, high melting deposits upon thermal stress. These deposits are insoluble in highly polar solvents such as acetone. Hydrotreated fuels, on the other hand, produced primarily amorphous, low melting acetone soluble gums with little or no insoluble solid material. Caustic extracts from the non-hydrotreated fuels were nearly totally phenolic in composition, ranging from phenol through C_6 substituted phenol and C_2 naphthalenols. Caustic extracts from the hydrotreated fuels contained less than one-half the amount of phenols than the non-hydrotreated extracts. These phenols were of lower molecular weight, through C_4 . These extracts also contained non-phenolic compounds such as carboxylic acids and substituted furanones. Phenols act as fuel antioxidants (1), which may explain the different oxidative characteristics of these two different fuel groups.

Sulfur containing compounds were detected in non-hydrotreated fuels through Gas Chromatography-Atomic Emission Detection. These fuels are relatively high in sulfur but under 0.3 %. Sulfur compounds were not detectable by Mass Spectrometry in extracted concentrates of unstressed fuels, extracts of stressed fuels or deposits.

A surrogate fuel containing a 12 component, representative fuel matrix, was doped with phenolic and organo-sulfur compounds. The yield of total insolubles from these tests were very consistent with results from tests on non-hydrotreated jet fuels. GC-MS provided compositional analysis of fuel soluble gums, acetone soluble gums and solids. GC-AED spectroscopy showed that sulfur atoms concentrated into the deposits upon thermal stress, in both the non-hydrotreated fuel and the doped surrogate.

INTRODUCTION

Fuel deposits are the limiting factor in the temperature to which a fuel can be heated. Deposits formed in aircraft systems by thermal decomposition of fuel can clog filters, fuel feed arms, nozzles, augmentor feeds and exchange tubes. Heat generated by advanced aircraft components such as avionics, environmental controls, hydraulics and engines must be exchanged to fuel. Since fuels act as a sink for this environmental heat, increased thermal stability has become more important as to accommodate the sophistication and performance of modern aircraft.

To study the effects of thermal oxidation of jet fuels, we developed a flask test system for stressing fuels rapidly and with repeatability. To avoid the chemical complexity of real petroleum derived fuels, a 12 component JP-8 surrogate fuel was prepared. It contains a reasonable compound formulation that is representative of the chemical classes found in real fuels. This fuel was used to develop test methods to apply to real reference jet fuels (POSF 2747 and POSF 2827) that are known to behave differently in other tests. Separation of solid oxidation products was done through filtration. Chemical composition was determined by thermal desorption and pyrolysis/GC-MS. Fuel oxidation products were concentrated and isolated by solid phase extraction and characterized via GC-MS. Elemental analysis was performed on unstressed fuel samples, stressed samples containing fuel soluble gums, acetone soluble gums and solids. Extent of oxidation was determined using Fourier Transform IR peak integration of alcohol and carbonyl absorbance regions.

Oxidation products are universally defined as the following: 1; Soluble gums are those that remain soluble in the fuel upon thermal stress. 2; Insoluble gums are deposits that settle from the fuel but are soluble in polar solvents such as acetone. 3; Insoluble solids are hard, crystalline deposits that are insoluble in non-polar and polar solvents.

Numerous studies have been conducted on the low temperature liquid phase autooxidation of pure hydrocarbons of the types found in distillate fuels (2) Such reactions are free radical chain reactions where the initial products are hydroperoxides (3):

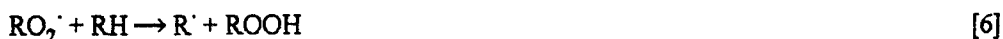
Formation of alkyl peroxide



Initiation



Propagation



Termination



Studies using the static thermal flask test have indicated a division in mechanisms of fuel deposition. Several features of the two different observed pathways are distinct. The first "oxidative" deposition is typical of model compounds such as dodecane, our 12 component surrogate and baseline standard jet fuels such as JP-7, JP-TS and POSF 2747. In the flask test, these fuels oxidize very rapidly, forming a second liquid phase and deposits that are gummy and essentially all acetone soluble. The deposits are highly amorphous, low melting and surface adherent. They are composed mainly of compounds also found by extraction of thermally stressed fuel; that is, fuel soluble gums consisting of alcohols, carboxylic acids, aldehydes, ketones and substituted furanones. The concentrations of these products, and of the gums, increase gradually with time during thermal stress. The alternate pathway is a "non-oxidizing" pathway that is characteristic of fuels such as POSF 2827, POSF 2857 and the surrogate fuel when doped with phenolic and organo-sulfur compounds.

Fuel specification reports of ASTM tests conducted on these fuels show increased acid numbers and mercaptan sulfur amounts in the non-hydrotreated fuels (4). High acid numbers could result from increased concentrations of phenolic compounds and/or the formation of sulfonic acids. These fuels form crystalline solids with little or no gums. They oxidize slowly with an apparent induction period under flask test conditions suggesting a "non-oxidizing" mechanism.

Further investigation into these mechanisms involved doping the surrogate fuel with an alkyl-substituted phenol, coupled with an organo-sulfur compound from one of the following classes: thiol, thiophenol, thiophene and sulfide. Each fuel was thermally stressed for 24 hours at 175 °C with flowing oxygen at 100 mL/min.

This research effort represents a combined study of the deposition characteristics of fuels and the role of phenols and sulfur compounds in the proposed "non-oxidizing" deposit mechanism by doping the thermally stable surrogate fuel with phenolic and various organo-sulfur compounds. Upon evaluation of oxidation products and deposits formed from these doping experiments, an attempt was made to elucidate a general mechanism and to lay the ground work for possible interruption of the mechanism by either fuel treatment or fuel additives (3).

EXPERIMENTAL

Materials: JP-8 surrogate fuel, blended from Aldrich™ experimental reagent grade chemicals (Figure 1), reference jet fuels POSF 2747, 2827 and 2857. POSF 2747 is a known thermally stable, hydrotreated fuel, 2827 and 2857 are non-hydrotreated fuels. Figure 1. shows the doping chemicals used in this study. Solvents used were methanol, petroleum ether, hexane and acetone. All chemicals were purchased from Aldrich Chemical Co. Inc., Milwaukee, WI.

Table 1. Dopants Used in Thermal Stress Experiments.

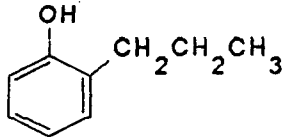
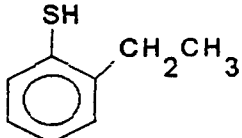
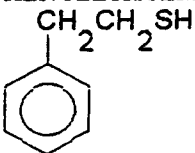
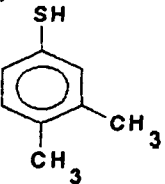
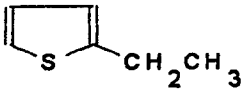
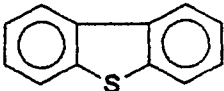
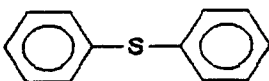
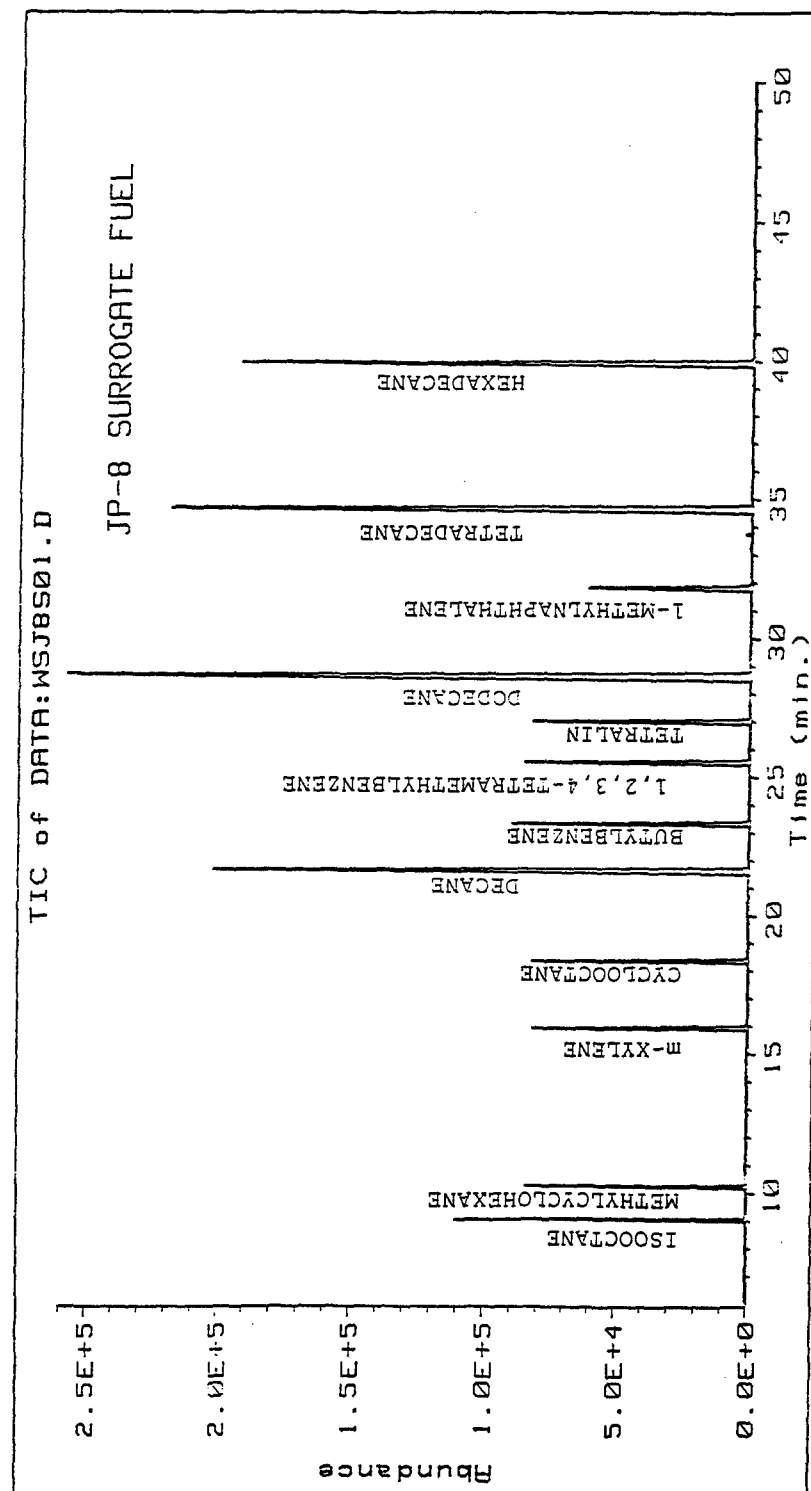
COMPOUND	MOLECULAR WEIGHT (g/m)	B.P. (°C)
2-PROPYLPHENOL 	136.19	224-226
2-ETHYLTHIOPHENOL 	138.23	203-205
PHENYLETHYLMERCAPTAN 	138.23	217-218
3,4-DIMETHYLTHIOPHENOL 	138.23	218
2-ETHYLTHIOPHENE 	112.19	132-134
DIBENZOTHIOPHENE 	186.26	332-333
PHENYLSULFIDE 	186.28	296

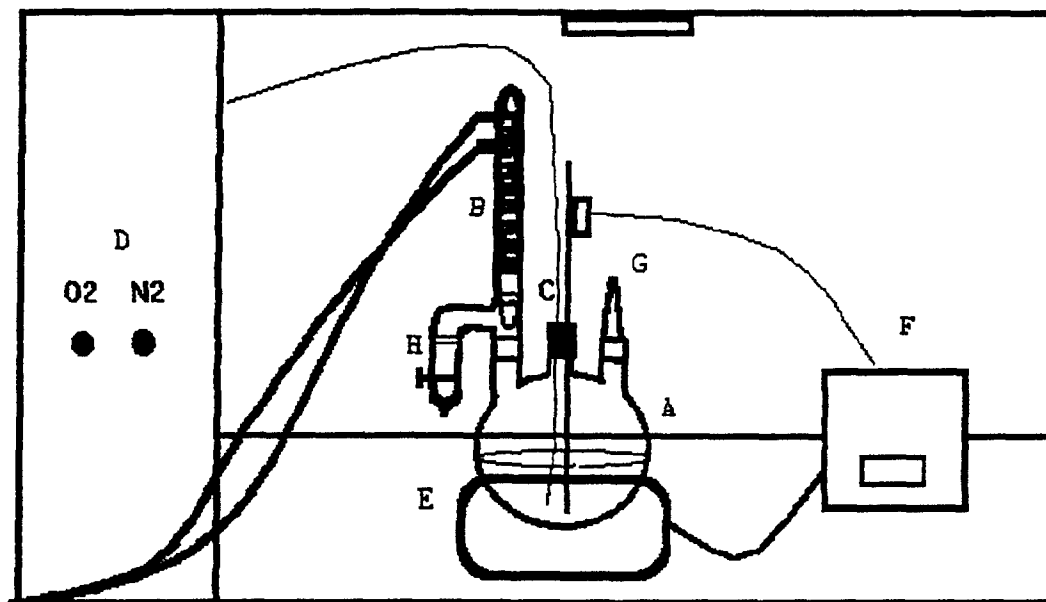
Figure 1. Total Ion Chromatogram of JP-8 Surrogate Fuel



Equipment: A static flask test was designed to simplify and accelerate deposit formation in the fuels.

Figure 2 is a schematic diagram of the flask test.

Figure 2. Thermal Flask Test Apparatus.



A; Approximately 30 mL of fuel is housed in a 50 mL 24/40 round bottom boiling flask. B; Refrigerated coolant is supplied via Friedrich™ condensers attached to the boiling flask by Claissen™ adaptors. C; The center opening of the flask and adaptor is used to position the thermometer and nitrogen/oxygen gas feed lines. Gas feed lines are of 0.53 mm Megabore™ deactivated, polyimide coated fused quartz capillaries inserted through Virton-B™ thermometer seals and positioned to within 0.6 mm of the bottom of the flask. D; Either inert nitrogen or oxidizing oxygen gas can be delivered to the flask via valved system. E; Flasks are heated by fabric mantles, controlled by 120 volt Therm-o-watch™ sensors, clipped directly to the thermometer to maintain 175 °C. G; Access to fuel during the stress period. H; A Dean-Staerk™ trap was used to collect an aqueous phase that was produced by POSF 2747.

Insoluble solids were collected by vacuum filtration on Osmonics™ 0.45 μ silver membrane filters. Filters were washed with acetone, placed in Pyrex™ 60 x 15 mm glass culture dishes and dried in vacuo (20 - 30 Torr, 80 °C) 36 - 48 hours and reweighed. Acetone soluble gums were collected as filtrate, solvent evaporated to dryness with inert nitrogen, dried in vacuo and reweighed.

Fuel soluble oxidation products were concentrated and separated using 1.0 g Bakerbond™ silica gel solid phase extraction cartridges. Concentrated oxidation products were collected in pre weighed culture tubes upon elution with methanol. Solvent was evaporated under nitrogen. Extract weight was determined by weight difference then samples were rediluted with 1.0 mL methanol.

The oxidation and chromatographic procedures were followed by GC-MS and GC-AED to determine trouble spots and track the success of the method. Polar extracts were analyzed on a Hewlett Packard™ 5890 Series II gas chromatograph with HP 5890 mass selective detection, perfluorotributylamine (PFTBA) autotune conditions (@ 2,200 EMV) scanned from 35 to 550 m/z with an eight minute solvent delay. Samples were injected (~2 mL) via HP 7673 auto-injector splitless. The column was 50 M, 0.25 mm i.d., 0.5 µm DB-5. Temperature program was -40 °C for six minutes, 10 °C/min to 50 °C, then 3 °C/min to 280 °C with a 17.33 minute hold.

Acetone soluble and insoluble deposits were analyzed by thermal desorption and pyrolysis/GC-MS using a CDS™ model 1000 "Pyroprobe". Samples were contained in a 2 x 20 mm quartz tube. Thermal desorption was at 200 and 280 °C with the interface at these temperatures. For pyrolysis at 450, 750 and 1100 °C, the interface was at the maximum of 325 °C (350 °C set). Temperature ramp was 5 °C/ms and the probe was fired for 99.99 seconds. Elemental composition (C, H, N, & O %) of liquid and solid fuel samples was measured on a LECO™ CHN-93 elemental analyzer.

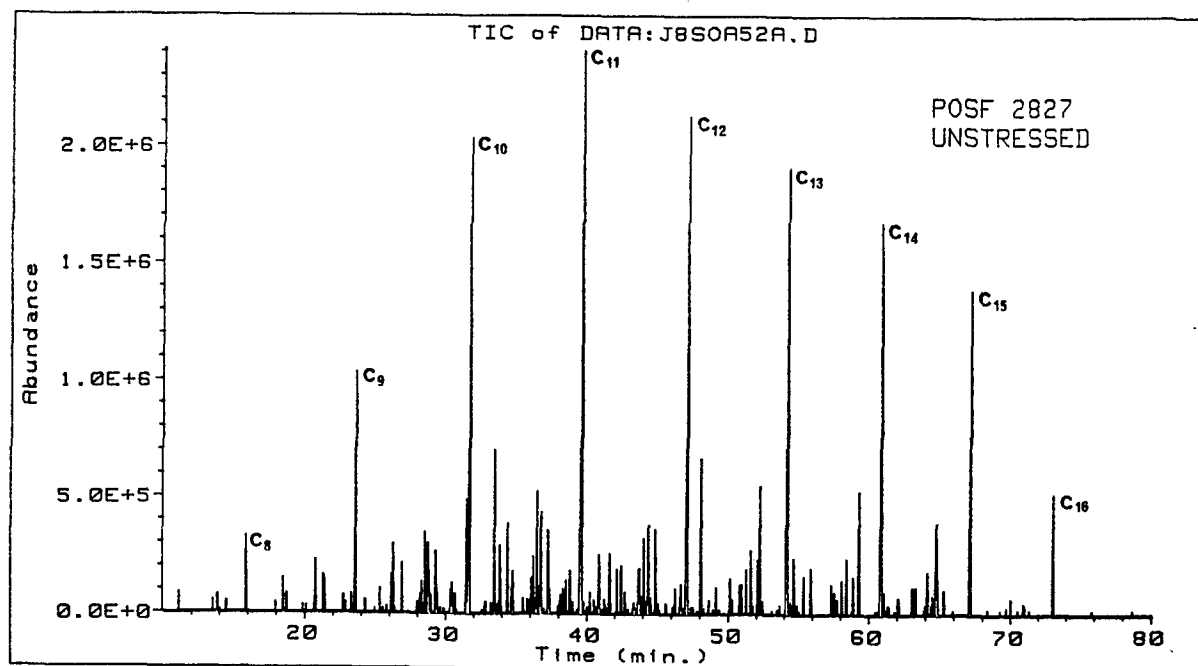
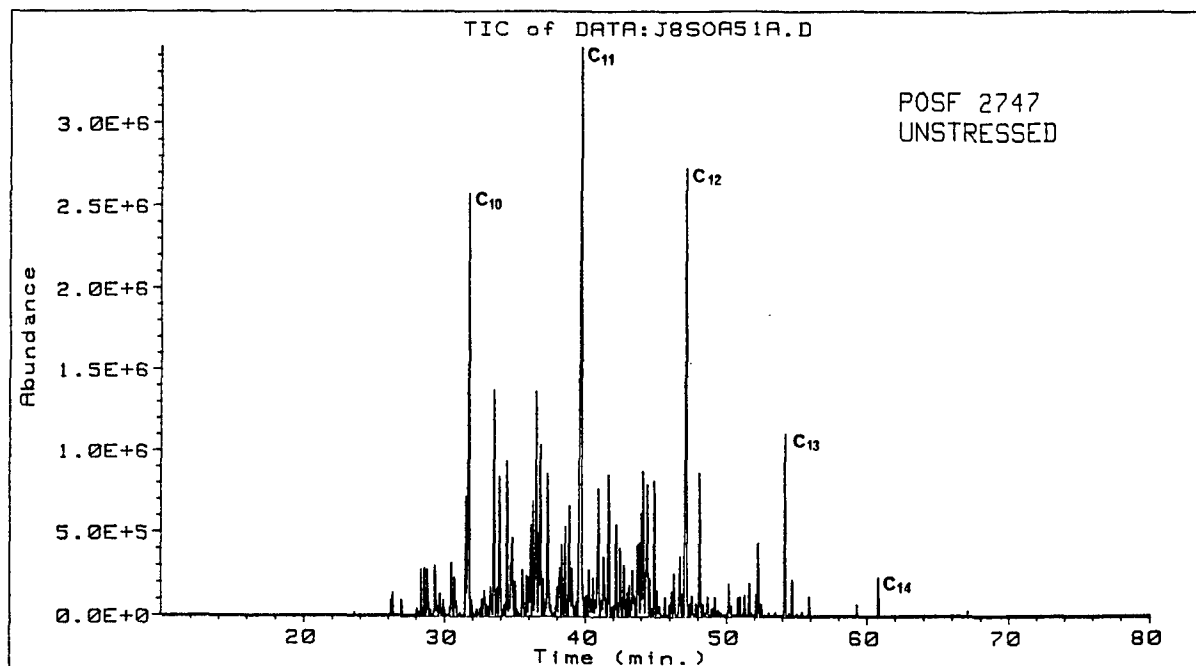
Extent of oxidation was monitored using a Mattson™ "Galaxy" 4020 Fourier Transform infrared spectrometer with Advanced First™ software on an MS-DOS™ based data station and operation. Liquid fuel samples were housed in a Spectra-Tech™ baseline horizontal attenuated total reflectance cell. -OH and C=O concentrations were determined by peak integration of absorbancy regions 3600-3080 cm⁻¹ and 1815-1640 cm⁻¹. These areas were compared with standards of 3 molar 1-dodecanol and 3.33 molar 2-octanone in unstressed surrogate fuel.

DISCUSSION

Analysis of Oxidative Behavior Using Two Classes of Jet Fuels: GC-MS chromatograms show contrasting chemical compositions of hydrotreated and non-hydrotreated jet fuels. Figures 3 and 4 illustrate that POSF 2747 (hydrotreated) contains normal hydrocarbons ranging from C_{10} to C_{14} with a large number of C_4 substituted benzenes. POSF 2827 (non-hydrotreated) contains a much broader boiling range of C_8 to C_{16} hydrocarbons mixed with substituted alkanes and about the same concentration of aromatic compounds as 2747. Figures 5 and 6 are total ion chromatograms of caustic extractable substances from these fuels. Both extracts are primarily phenolic. The only obvious difference is that 2827 has substituted phenols of greater molecular weight than 2747. 2827 has a much larger concentration of phenols. Figure 5 (2747) is five times the injection volume of Figure 6 (2827).

Upon thermal stress these fuels behave very differently as earlier indicated. Final gravimetric analysis of deposits formed by POSF 2747 indicates that this fuel produces a significant amount of acetone soluble gums with very little solids. Although 2747 forms a greater measurable quantity of deposits, they are essentially all acetone soluble. Approximately two-thirds of the deposits produced by POSF 2827 are acetone insoluble as shown in Figure 7.

Figures 3 & 4. Total Ion Chromatograms of Unstressed POSF Fuels 2747 and 2827.



Figures 5 & 6. Total Ion Chromatograms of Caustic Extracts of Unstressed POSF Fuels 2747 and 2827.

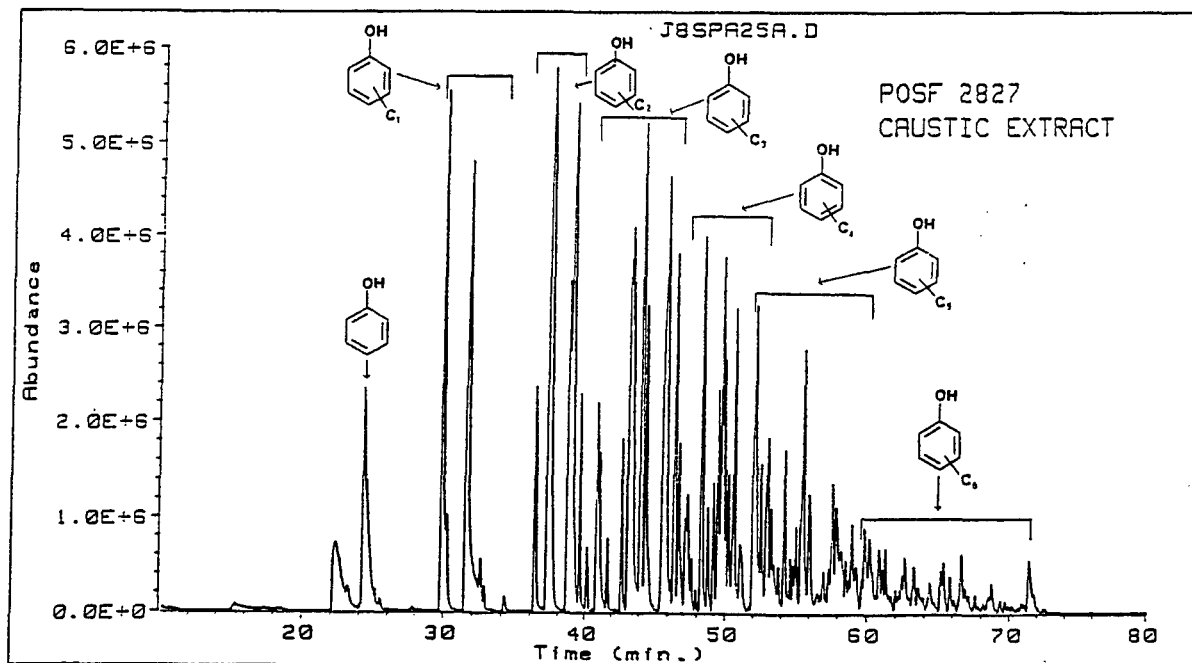
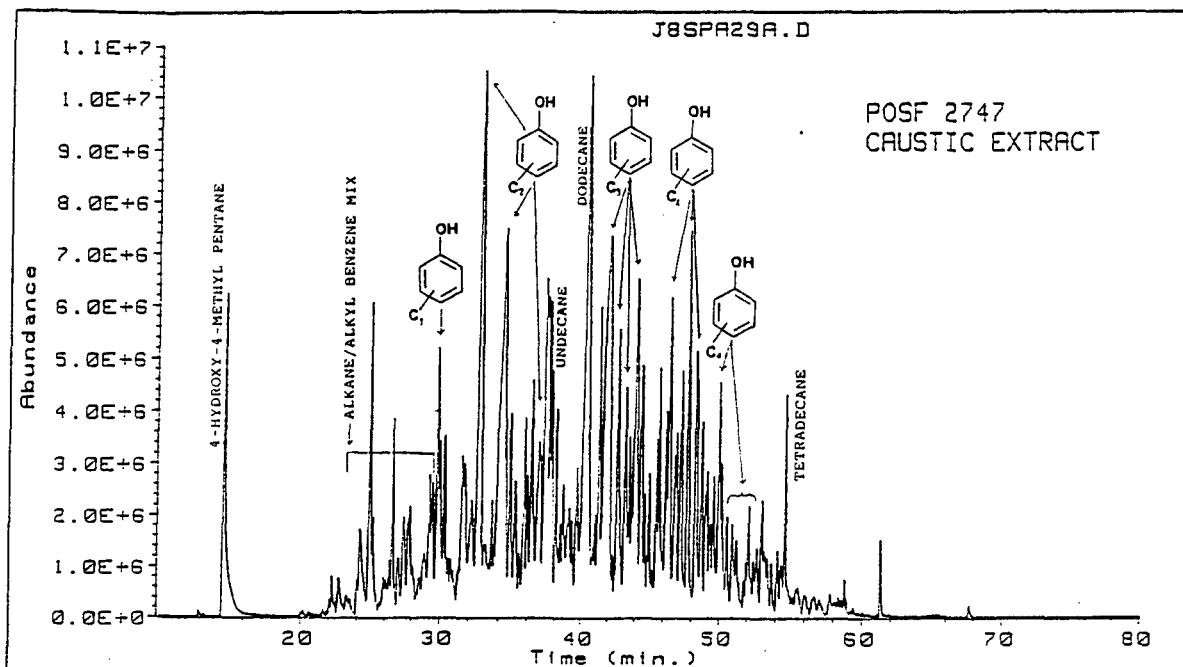
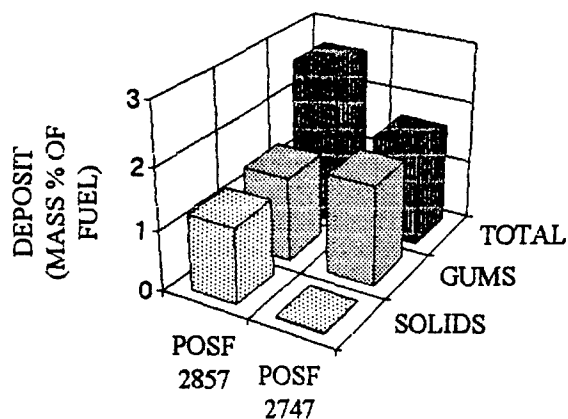


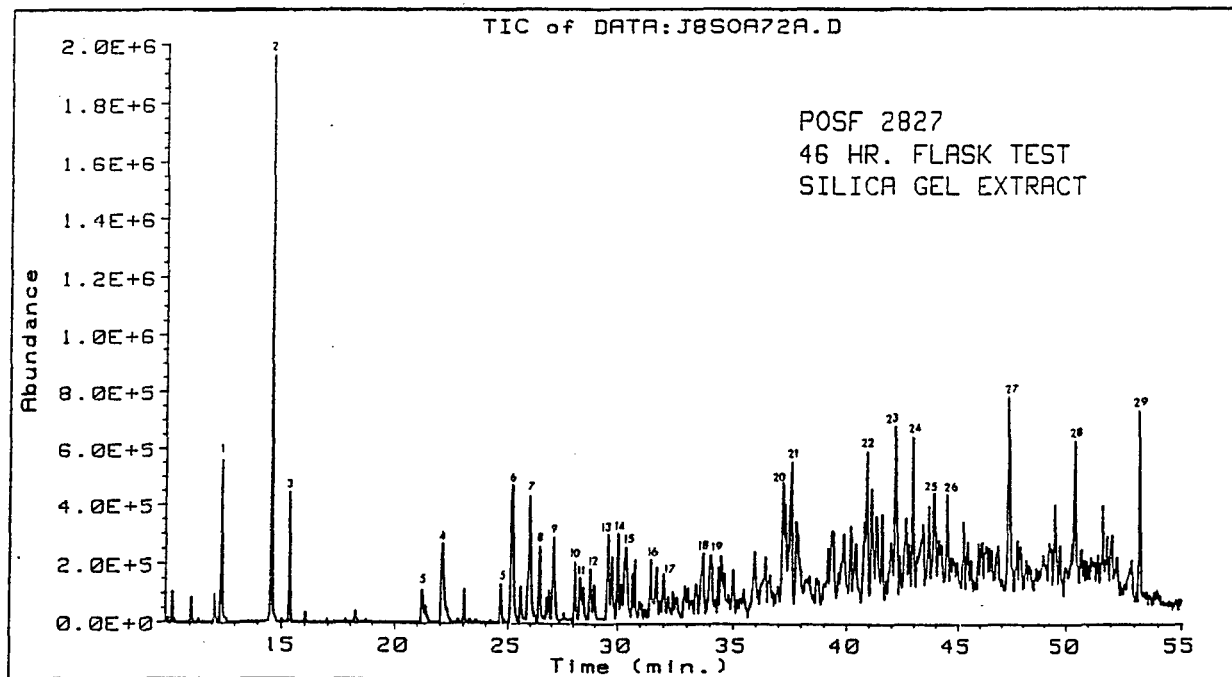
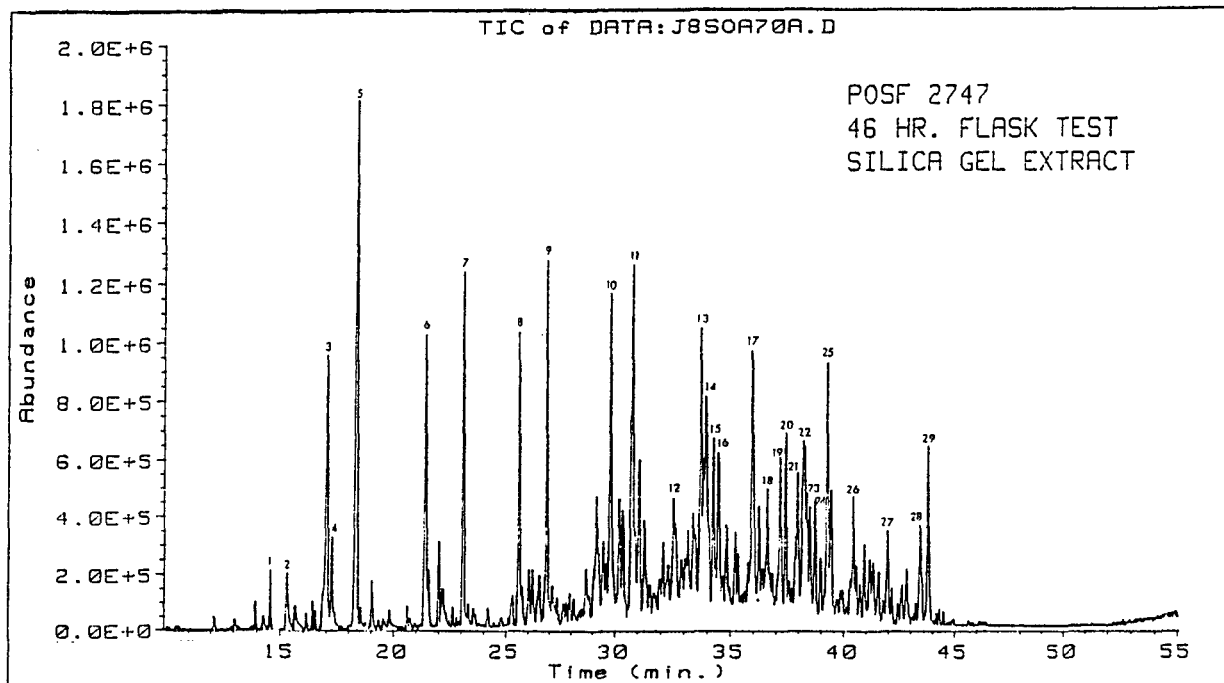
Figure 7. Deposits Formed by POSF 2747 and 2827. 46 Hour Flask Test @ 175 C With Oxygen Flow ~100 mL/min.



The chemical matrices of fuel soluble gums, acetone soluble gums and insoluble solids contrast greatly between POSF 2747 and 2827. Figures 8 and 9 are total ion chromatograms of silica gel extracts of fuel soluble oxidation products from 2747 and 2827. The 2747 extract is rich in oxygenates, primarily aldehydes, alcohols, ketones, furanones and carboxylic acids (Table 2). Table 2 lists the contrasting phenolic nature of oxidation products formed by 2827. Another interesting feature is that 2747 forms an immiscible polar layer upon thermal stress, containing mainly low-boiling carboxylic acids, alcohols and aldehydes (Figure 10, Table 3).

Figures 8 & 9. Total Ion Chromatograms of Silica Gel Extracts of POSF Fuels 2747 and 2827.

Both Fuels Were Stressed for 46 Hours.



This observation coupled with quantitative FT-IR analysis of alcohol and carbonyl production, provides evidence that two separate pathways of deposition are occurring. Table 4 illustrates the relative rates of oxidation product production of these two fuels and the surrogate fuel over an eight hour stress period.

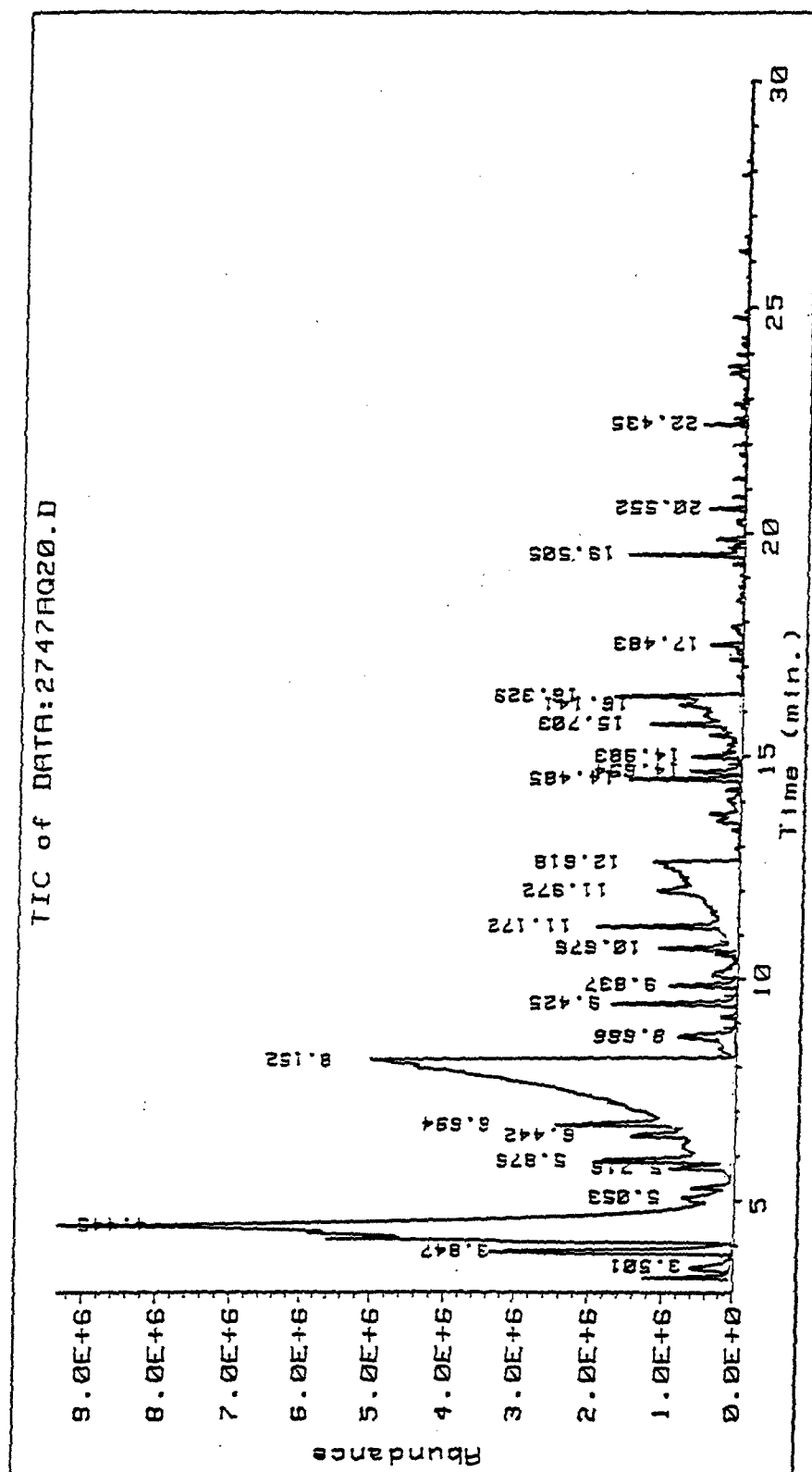
Table 4. FTIR Analysis of Alcohol and Carbonyl Production.

STRESS TIME (hrs.)	PREDICTED CONCENTRATION (m/L)					
	JP-8S		2747		2827	
	OH	C=O	OH	C=O	OH	C=O
0.3	0.028	0.039	0	0	0	0
0.6	0.028	0.039	0	0	0	0
1.3	0.035	0.049	0	0.017	0	0
2	0.047	0.066	0.039	0.056	0	0
4	0.123	0.174	0.069	0.099	0	0
6	0.223	0.316	0.291	0.416	0	0
8	0.349	0.494	0.759	1.088	0	0
INSOLUBLES (mg/mL)		2		3.8		4.8

Tables 2 & 3. Peak Identification for Figures 8 & 9.

Identification of Chromatographic Peaks for J8SOA70A.D. Extracted Oxidation Products from POSF-2747.			Identification of Chromatographic Peaks for J8SOA72A.D. Extracted Oxidation Products from POSF-2827.		
Peak #	Rt (min.)	Compound	Peak #	Rt (min)	Compound
1.	14.59	3,3-dimethyl-2-hexanone	1.	12.43	1-propoxypentane
2.	15.32	dihydro-2(3H)-furanone	2.	14.59	3,3-dimethyl-2-hexanone
3.	17.06	dihydro-5-methyl-2(3H)-furanone	3.	15.34	2,2-dimethylpentanol
4.	17.24	tetrahydro-2H-pyran-2-one	4.	22.08	4-methylphenol
5.	18.37	4,4-dimethyl-dihydro-2(3H)-furanone	5.	24.66	ethylphenol
6.	21.43	substituted furanone	6.	25.18	dimethylphenol
7.	23.10	5-ethylidihydro-5-methyl-2(3H)-furanone	7.	25.98	dimethylphenol
8.	25.59	5-propyl-dihydro-2(3H)-furanone	8.	26.43	dimethylphenol
9.	26.86	3-ethyl-2,5-furandione	9.	27.09	dimethylphenol
10.	29.83	5-butylidihydro-2(3H)-furanone	10.	28.07	2-propylphenol
11.	30.80	2-undecanol	11.	28.13	propylphenol
12.	32.55	1,3-isobenzofurandione	12.	28.78	propylphenol
13.	33.76	5-pentylidihydro-2(3H)-furanone	13.	29.58	ethylmethylphenol
14.	33.97	sec-butylethylbenzene	14.	30.03	trimethylphenol
15.	34.28	1-ethyl-3-(1-methylethyl)-benzene	15.	30.26	C ₃ phenol
16.	34.49	substituted 2,5-furandione	16.	31.46	C ₄ phenol
17.	35.96	4-methylisobenzofurandione	17.	31.70	C ₄ phenol
18.	36.62	substituted furanone	18.	33.70	substituted tetrahydrofuranone
19.	37.19	3-methylisobenzofurandione	19.	34.45	decanol
20.	37.45	5-hexylidihydro-2(3H)-furanone	20.	37.19	methylisobenzofurandione
21.	37.97	methyl-1(3H)-isobenzofurandione	21.	37.57	undecanol
22.	38.20	methyl-1(3H)-isobenzofurandione	22.	40.90	substituted benzoic acid
23.	38.29	methylisobenzofurandione	23.	42.17	dimethylbenzopyran-2-one
24.	38.75	2,4,6-trimethylphenyl-1-ethanone	24.	42.95	alkene
25.	39.29	4-methylphthalic acid	25.	43.69	p-cyclohexenylphenol
26.	40.42	5,6-dimethyl-3(2H)-benzofuranone	26.	44.52	methylnaphthoquinone
27.	41.95	dimethylbenzofuranone	27.	47.31	substituted phenol
28.	43.41	ethylmethylbenzofuranone	28.	50.38	methoxyphenanthrene
29.	43.79	ethylmethylbenzofuranone	29.	53.20	substituted furandione

Figure 10. Total Ion Chromatogram of Polar Phase Produced From POSF 2747. 24 HR. Flask Test @ 175 °C.



Rate of fuel oxidation was evaluated by quantitatively measuring IR absorbancy regions of 3500 cm^{-1} (-OH) and 1700 cm^{-1} (C=O) against those of internal standards containing 0.08 to 0.50 molar dodecanol and octanone. This test indicated that deposit formation is independent of oxygen supply and that solid formation is inverse to ease of oxidation. GC-AED analysis (Figures 11 and 12) also indicate that 2747 consumes oxygen rapidly, forming a large number of detectable oxygen containing compounds.

Figure 11. GC-AED Chromatogram of Unstressed POSF 2827 & 2747

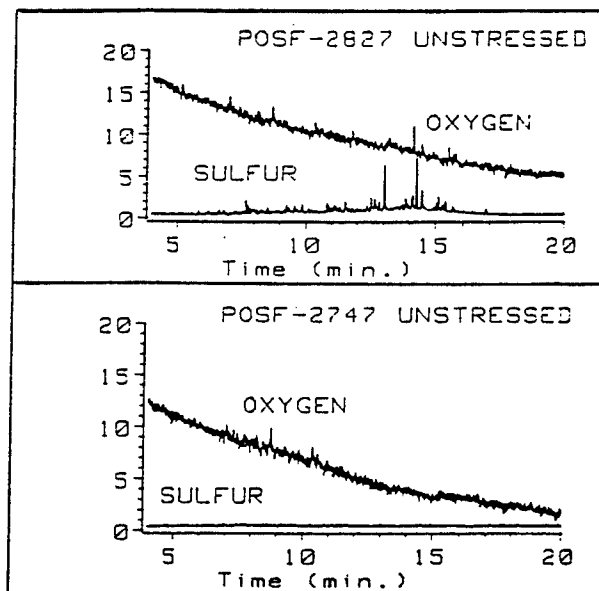
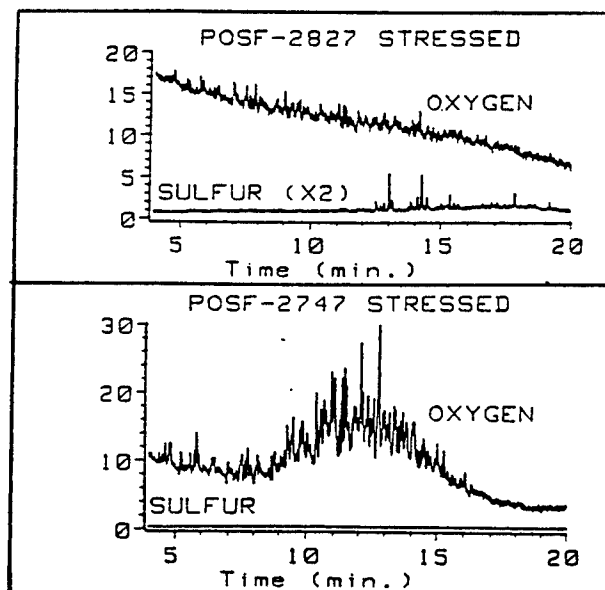


Figure 12. GC-AED Chromatogram of Stressed POSF 2827 and 2747.



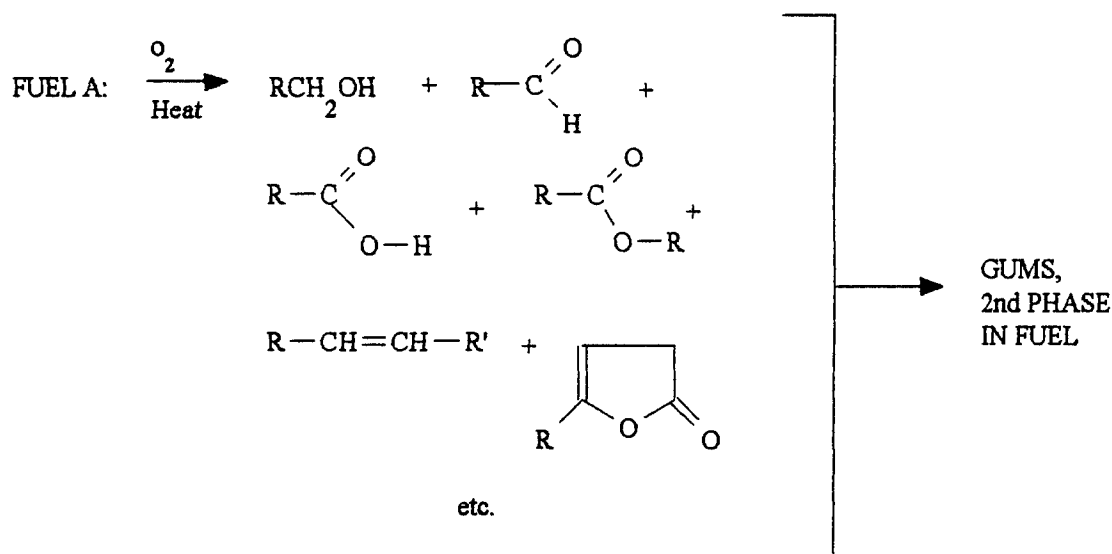
Figures 11 and 12 also indicate the present of significant amounts of sulfur containing compounds in 2827 while finding no detectable sulfur in 2747. Sulfur compounds appear to be intimately involved in the chemical reactions which take place under thermal stressing. Figure 12 illustrated that sulfur atoms in stressed 2827 decreased by more than a factor of two (4). These data support the theory of "oxidizing and "non-oxidizing" pathways and their relationship to deposit formation. GC-AED analysis of sulfur compounds provided the initial information that lead to further investigation into the role of sulfur in deposit formations through doping studies with the surrogate fuel.

Table 5 contains elemental analysis data of the working fuel, POSF 2827 and the surrogate doped with 3,4-dimethylthiophenol and 2-propylphenol . These data clearly suggest that sulfur compounds are involved in deposit formation by the increased sulfur concentration found in the deposits.

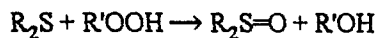
Table 5. C, H, N, S, O LECO™ Elemental Analysis (%) of Several Fuel Samples. Stressed Samples Were for 46 Hours at 175 °C With Oxygen Flow at ~100 mL/min.					
Fuel	C	H	N	S	O
POSF 2827	83.7	13.0	0.11	0.25	2.94
POSF 2827 (stressed)	82.4	12.7	0.17	0.18	4.55
POSF 2827 (gums)	70.9	6.2	0.20	0.50	22.20
POSF 2827 (solids)	68.9	5.5	0.10	0.40	20.30
JP-8S + 0.02 % 2-propylphenol + 0.1 % 3,4-dimethylthiophenol (stressed)	82.5	12.8	0.11	0.13	4.46
JP-8S + 0.02 % 2-propylphenol + 0.1 % 3,4-dimethylthiophenol (gums)	70.6	5.3	0.20	1.70	22.20
JP-8S + 0.02 % 2-propylphenol + 0.1 % 3,4-dimethylthiophenol (solids)	71.6	4.3	0.30	1.60	21.70

LECO data, when compared to deposit yield, indicate that sulfur compounds tend to cause fuels to be more thermally unstable as well as to investigate production of significant amounts of insoluble materials upon thermal stress.

This theory was investigated further by using a series of organo-sulfur compounds coupled with 2-propyl phenol, doped into the surrogate fuel and then stressed 24 hours with oxygen supply at ~100 mL/min. Deposits were collected and identified by thermal desorption/pyrolysis GC-MS. The surrogate fuel and the surrogate doped with only phenol showed heavy oxidation. Total ion chromatograms of the silica gel extracts of stressed fuel are abundant in alcohols, carboxylic acids and carbonyl compounds. Judging from oxidized products formed, the results suggest that reaction occurs via the following "oxidizing" mechanism:

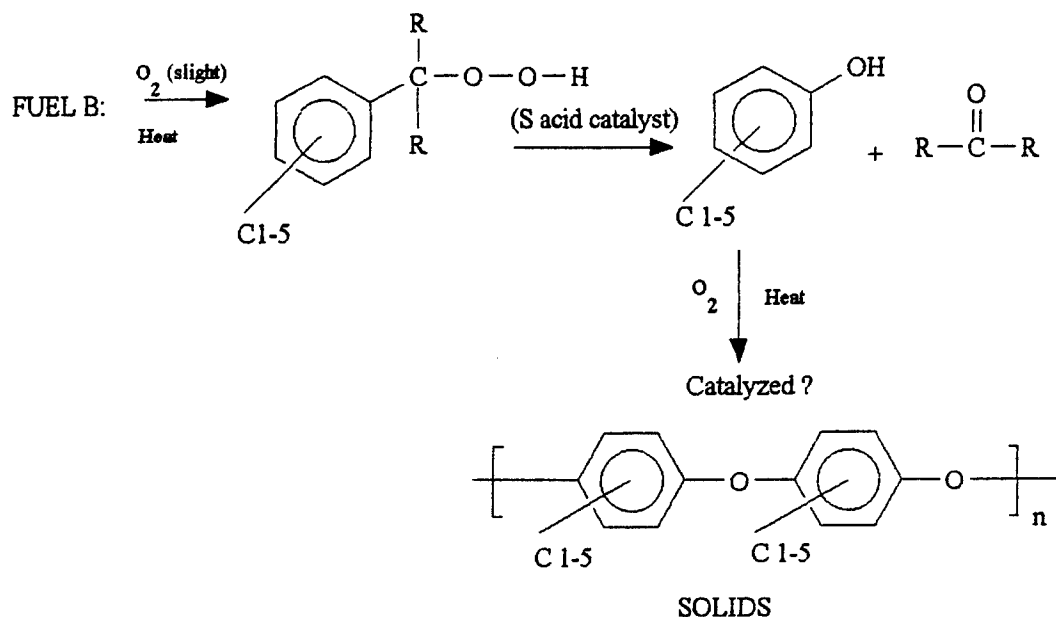


Divalent sulfur compounds are commonly used in the polymer industry as secondary antioxidants (5). These compounds reduce hydroperoxides to alcohols.

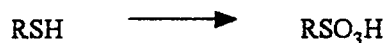


Solids from all doped samples with the exception of phenylsulfide and those without sulfur at all, revealed sulfur compounds to be concentrated, in their unreacted form, in the deposits. Early elution (~3 min.) of sulfur dioxide, seen in pyrograms of the surrogate doped with mercaptan and thiophenic compounds, is also indicative of thermal decomposition of sulfur containing compounds. Sulfur compounds were not recovered or detected in the silica gel extracts of these fuel samples.

These samples produced substantial amounts of acetone insoluble solids and a minimal gums. Chromatograms of their silica gel extracts showed only slight oxidation. These results suggested a different "non-oxidizing" mechanism which can be represented as:

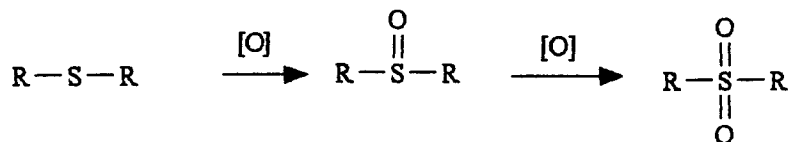


Thiol sulfur (-SH) oxidize to sulfonic acids by the following reaction (6):

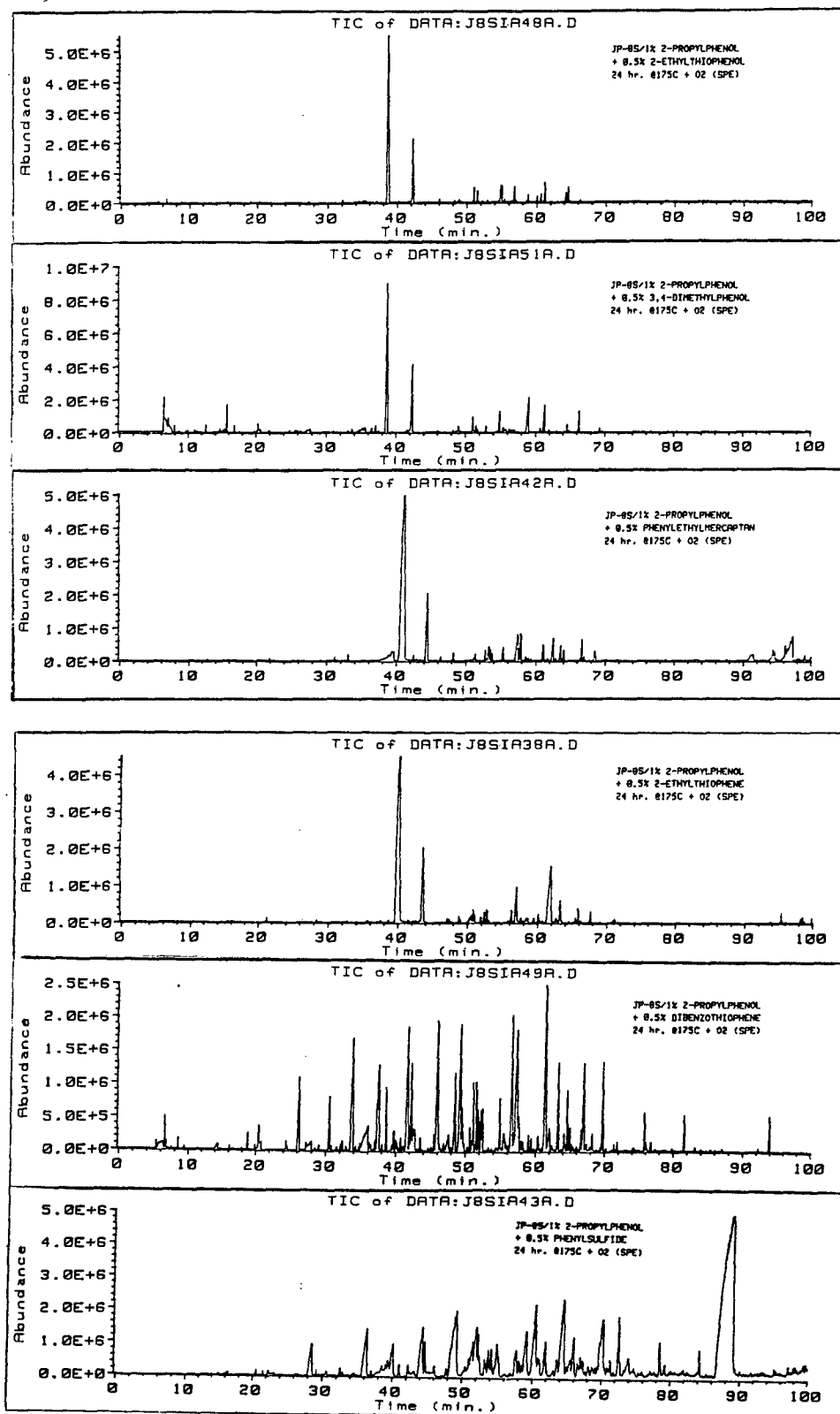


This reaction can occur in the presence of an acid catalyst or by autoxidation via atmospheric oxygen (5). These sulfonic acids can act as catalysts in the proposed "non-oxidizing" mechanism. Sulfonic acids formed from thiols are presumed to catalyze the breakdown of hydroperoxides.

Thiophenic sulfur (C-S-C) does not follow the same oxidation scheme. These compounds tend to oxidize stepwise to form sulfoxides and sulfones (7).



Figures 13 a-f. Total Ion Chromatograms of SiOH Extracts of JP-8 Surrogate with 1.0 % 2-propylphenol & 0.5% Sulfur Compounds. 24 hr. Thermal Stress @ 175 °C with Flowing Oxygen @ 100 mL/min.

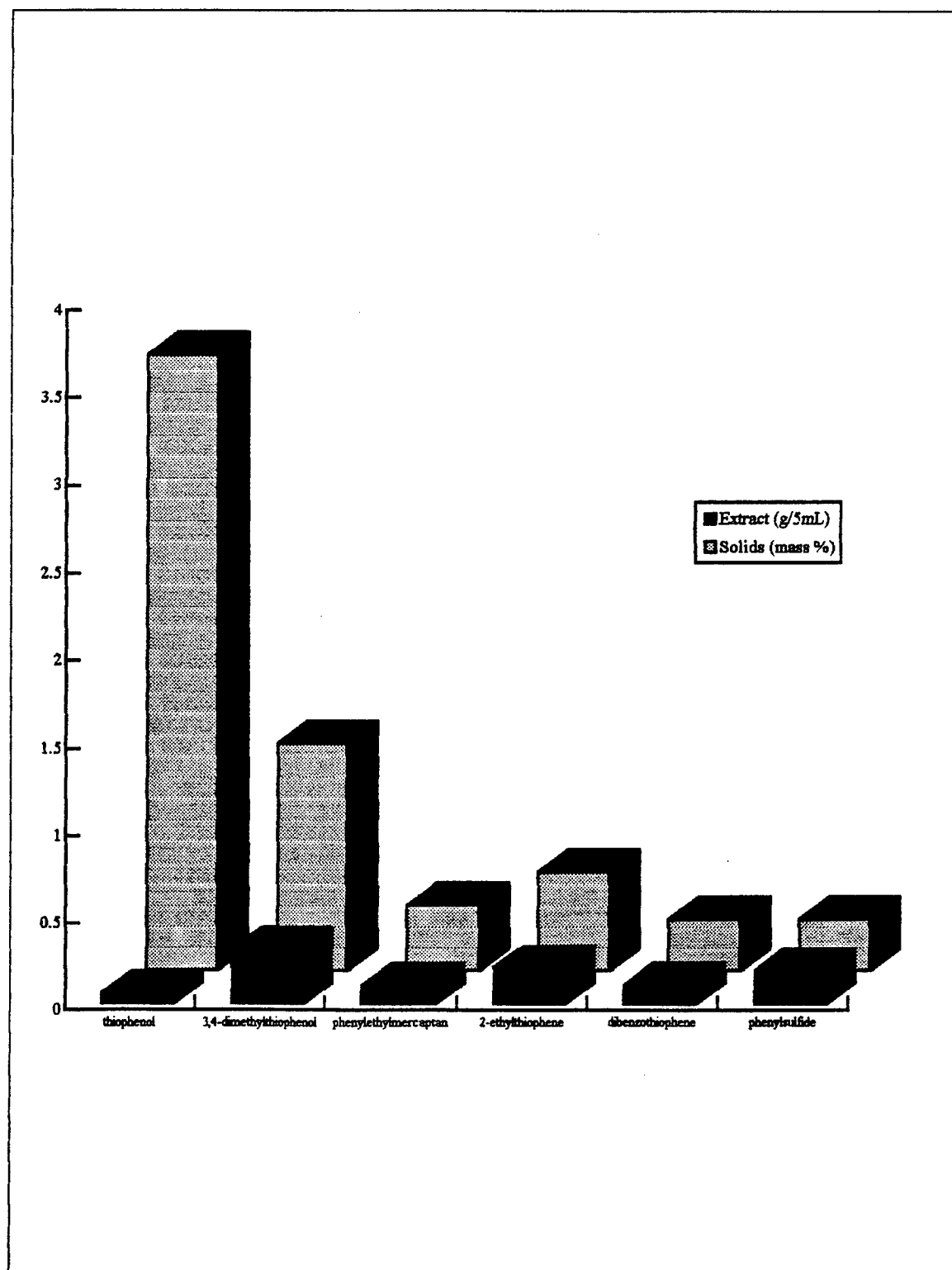


The obvious difference in these fuel extracts is that samples doped with thiols produce few oxidized species while samples doped with thiophenes produce numerous oxidation products. None of the unoxidized sulfur compounds were found in the extract chromatograms. Extracts from samples containing thiols (Figures 13a-c) gave mainly phenols, ketones and various other oxygenated aromatics. These samples represent the "non-oxidizing" mechanism. 2-propylphenol is the largest chromatographic peak at ~40 minutes.

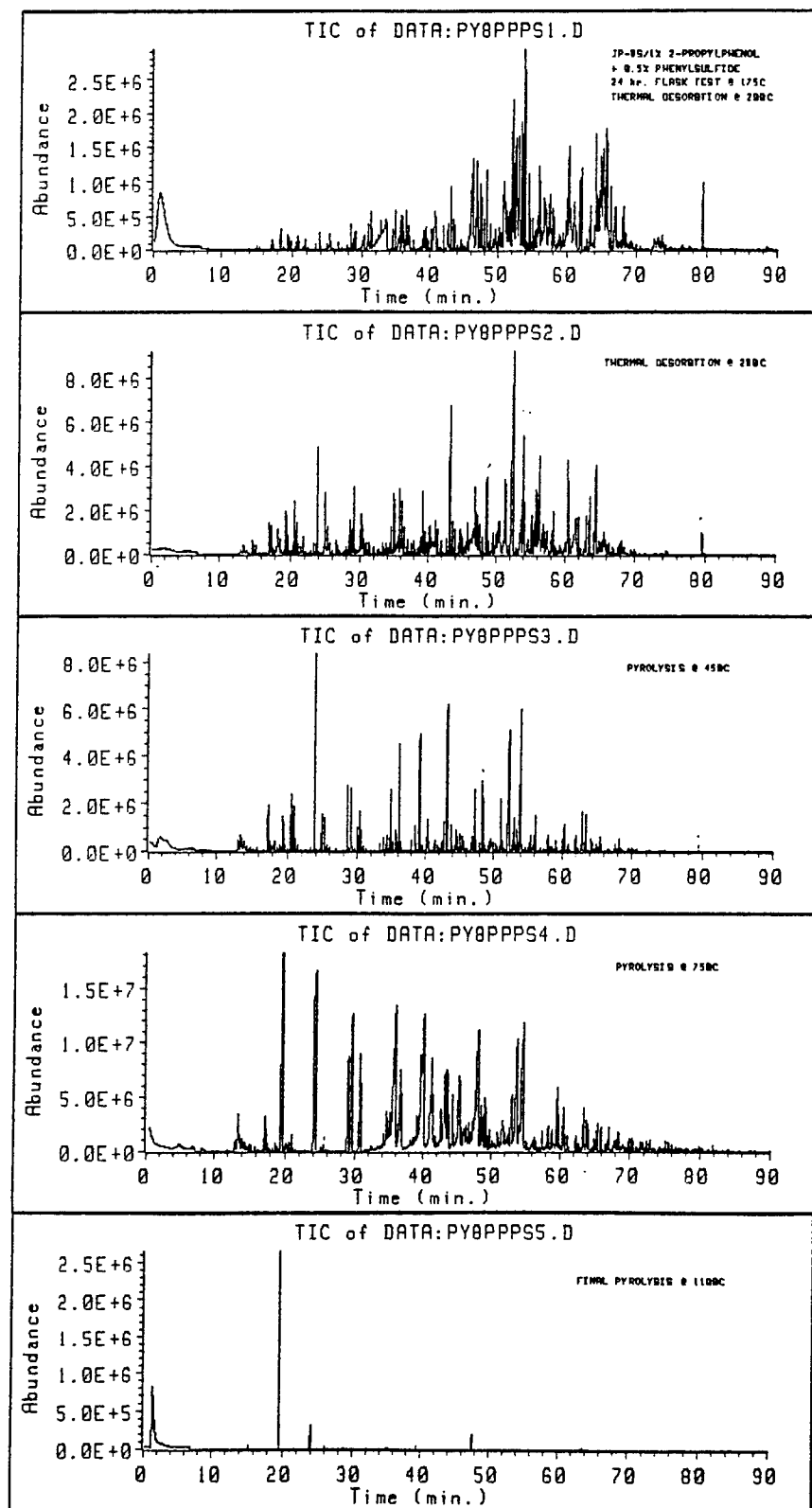
"Oxidized" chromatograms from fuels containing thiophenes and the thioether, show high concentrations alcohols and carbonyl compounds. 2-propylphenol nearly disappeared, indicating that it either became further oxidized or rearranged to form various other oxygenated products. The respective sulfones were found in each chromatogram. The dioxide of 2-ethylthiophene (144 m/z) was found in Figure 13 d at ~62 min., co-eluted with other compounds. The corresponding sulfones of dibenzothiophene and phenylsulfide (218 m/z each) were found in Figure 13 e and 13 f at ~94 and 88 minutes, respectively.

The amount of solids formed in these experiments is found to be inverse to both the mass of soluble oxidation products and the number of oxidized species formed. This observation is illustrated by comparison of solid mass to total ion chromatograms of silica gel extracts (Figures a-f). Figures a-f are placed in ascending order of oxidation. Note the abundance scale for each chromatogram. Figure 14 illustrates the inverse relationship of solid formation to the mass of soluble oxidation products (as obtained by solvent evaporation and weighing of solid phase extracts).

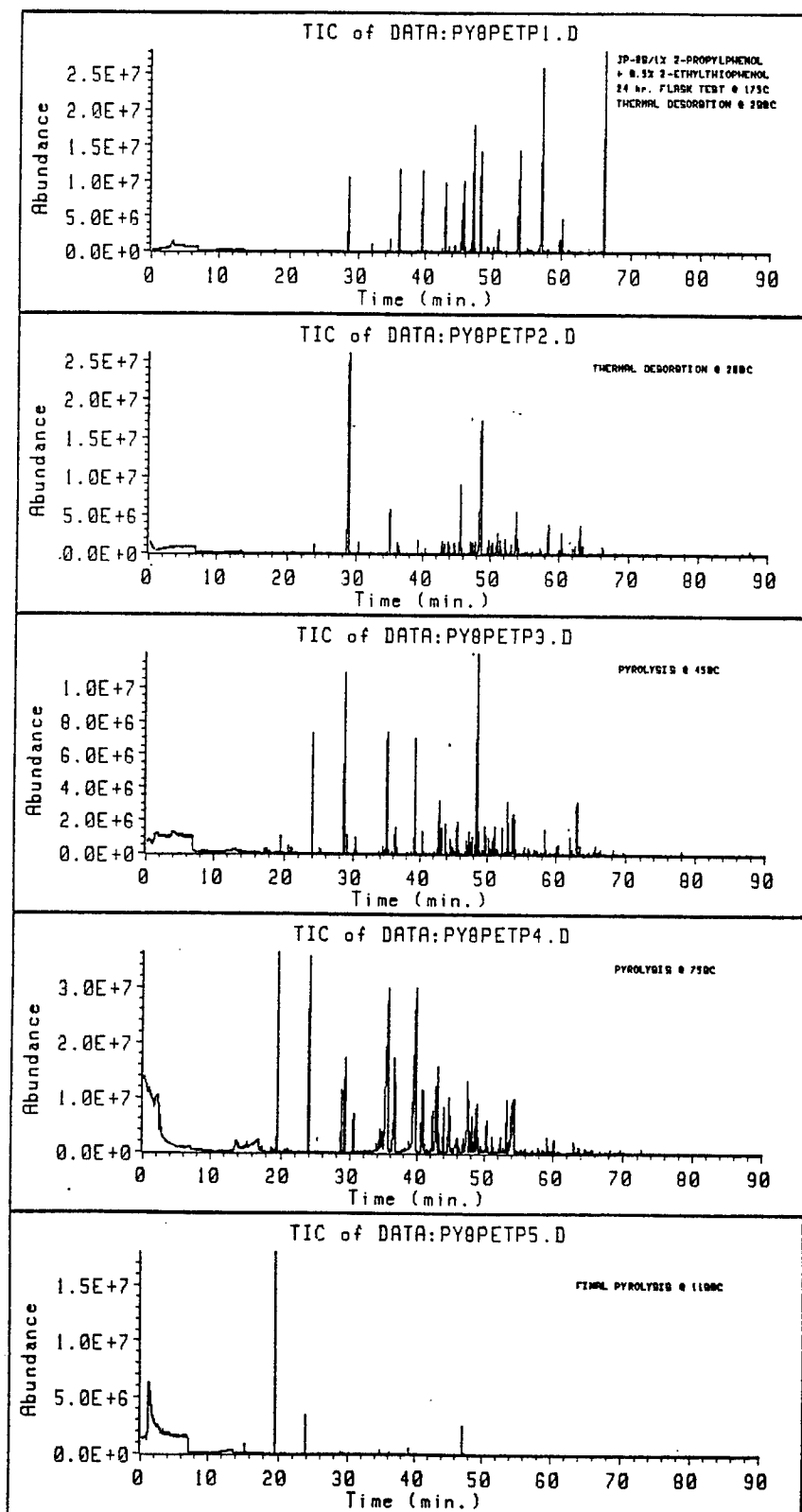
Figure 14. Comparison of Solids and Soluble Oxidation Products (Extracts) From JP-8 Surrogate Doped With 2-propylphenol & Organo-Sulfur Compounds & Thermally Stressed for 24 hrs. @ 175 °C



Figures 15 a-e. Sequential Thermal Desorption/Pyrolysis Total Ion Chromatograms of JP-8S Doped With 1.0 % 2-propylphenol and 0.5 % Phenylsulfide. 24 hr. Flask Test @ 175 °C With O₂ @ 100 mL/min.



Figures 16 a-e. Sequential Thermal Desorption/Pyrolysis Total Ion Chromatograms of JP-8S Doped With 1.0 % 2-propylphenol and 0.5 % 2-ethylthiophenol. 24 hr. Flask Test @ 175 °C With O₂ @ 100 mL/min.



Figures 15 a-e and 16 a-e are contrasting chromatograms of two extremes, of oxidation vs. non-oxidation. Figures 15 a-e are total ion chromatograms of solids formed by the surrogate fuel when doped with 1.0 % 2-propylphenol and 0.5 % phenylsulfide. Figures 16 a-e are chromatograms from the solids of the surrogate doped with the same percentages of 2-propylphenol and 2-ethylthiophenol. Figures a-e are sequential thermal desorption/pyrolysis compositional separations of the solids. The series of chromatograms have common features, as follows: A: Thermal desorption at 200 °C separated yield mostly adsorbed fuel components. B & C: 280 °C and 450 °C, produce the majority of information useful for differentiating the nature of the solids. 280 °C is on the edge of thermal desorption/pyrolysis with 450 °C being gentle pyrolysis. D: 750 °C and similar, but less useful than pyrolysis at 450 °C, because of more extensive pyrolytic rearrangement. E: 1100 °C is extreme pyrolysis of highly condensed carbonaceous matter giving essentially only benzene and naphthalene, in all cases.

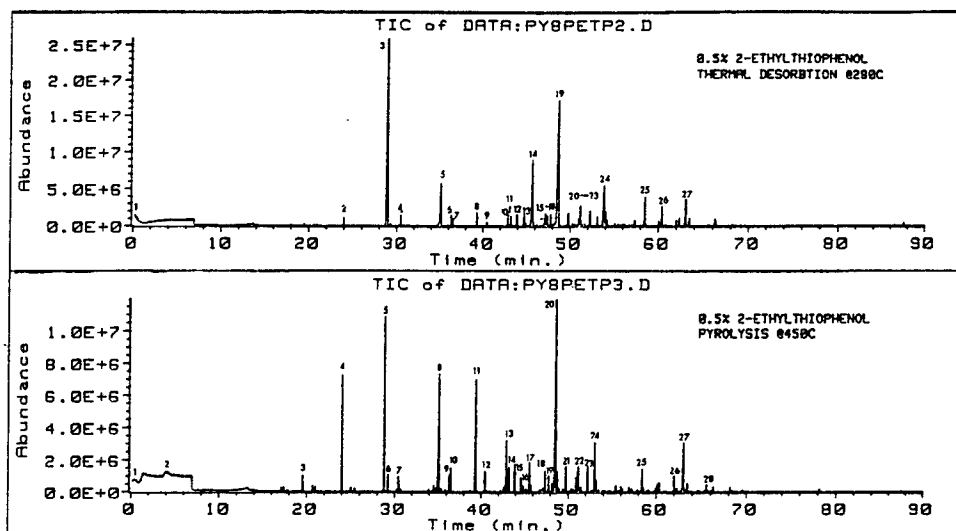
The major difference between these sets of chromatograms is the extreme complexity of the chromatograms from phenylsulfide doped surrogate and the simplicity of those from doping with the thiophenol. The surrogate with phenylsulfide shows extensive oxidation illustrated by the numerous peaks in the chromatograms. On the other hand, the chromatogram containing 2-ethylthiophenol contains few peaks, most representing phenols and few other oxidation products. This sample produced nearly 2X more measurable solids than the sample with phenylsulfide.

Mechanistic clues to the contrasting oxidation patterns are noted in the two series of chromatograms. No unoxidized sulfur compounds were found in either series. However, oxidized species were found in both. The un-oxidized chromatograms containing 2-ethylthiophenol contain phenylethylsulfonic acid (175 m/z) at ~63 minutes. The early elution of SO₂ is also indicative of degradation of thermally unstable sulfonic acids that were probably formed during the oxidative stress. Doped phenol content remained high (~48.5 min.). This probably indicated that the phenol remains un-oxidized (un-reacted) like many other fuel components. The presence of substituted phenols and cresols indicate phenol production almost certainly catalyzed by the action of sulfonic acids on the hydroperoxides formed at the α-hydrogen of the aromatic fuel components of aromatic fuel species.

In contrast, solids from the surrogate doped with phenylsulfide contained mainly substituted alkanes, alkenes, benzenes and carbonyls. No SO₂ was detected but a substantial peak representing phenylsulfone (218 m/z) was found at ~79.5 minutes. Doped phenol (~48.5 min.) was significantly lower in this series than in the thiol series. This may indicate that substituted phenols are further oxidized to other aromatic compounds in the absence of catalytic sulfonic acids.

Thermal desorption (280 °C) and pyrolysis (450 °C) of the surrogate doped with six different sulfur compounds detail the contrasting chemical matrix of the solids. Figures 14 a & b through 19 a & b are total ion chromatograms of thermally desorbed and pyrolyzed solids formed from thermal stress of the surrogate doped with 1.0% 2-propylphenol and 0.5 % 2-ethylthiophenol, 3,4-dimethylthiophenol, phenylethylmercaptan, 2-ethylthiophene, dibenzothiophene and phenylsulfide respectively. Their compositional matrices are listed in Tables 6a & b through 11a & b.

Figures 14 a & b. Thermal Desorption @ 280 °C and Pyrolysis @ 450 °C of Solids Formed From JP-8S Doped With 1.0 % 2-propylphenol & 0.5 % 2-ethylthiophenol.



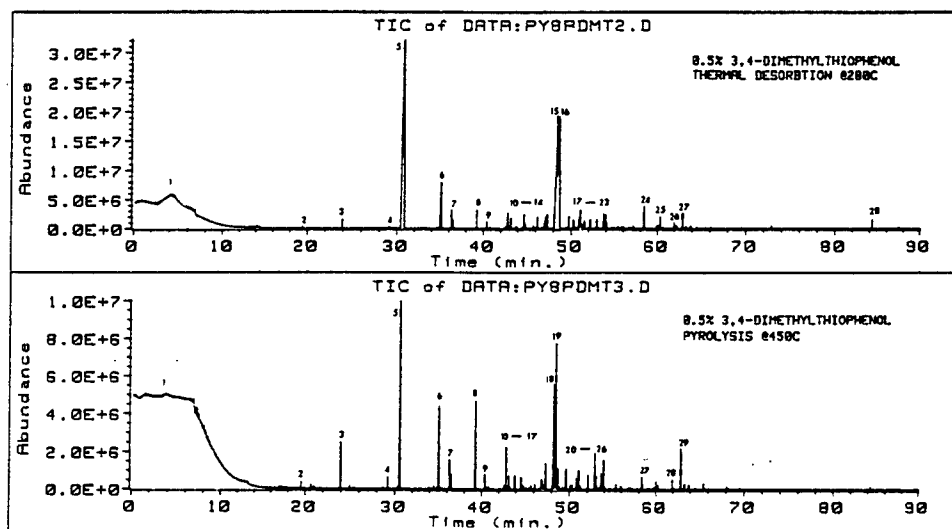
Tables 6 a & b. Compound Identification for Figures 14 a & b.

Peak #	Rt (min.)	Compound @ 280 °C	Rt (min.)	Compound @ 450 °C
1.	0.25	Sulfur dioxide	0.50	Carbon dioxide
2.	24.08	Toluene	3.98	Sulfur dioxide
3.	28.97	Ethylbenzene	19.56	Benzene
4.	30.48	Styrene	24.01	Toluene
5.	35.12	Phenol	28.82	Ethylbenzene
6.	36.34	Trimethylbenzene	29.24	Xylene
7.	36.51	Benzofuran	30.47	Styrene
8.	39.31	Cresol	35.13	Phenol
9.	42.79	Methylphenylethanone	36.33	Trimethylbenzene
10.	42.91	Methylbenzofuran	36.52	Benzofuran
11.	43.95	1,2,4,5-tetramethylbenzene	39.37	Cresol
12.	44.78	2-ethylphenol	40.42	Cresol
13.	45.73	Dimethylphenol	42.91	Methylbenzofuran
14.	47.09	2-ethylthiophenol*	43.26	1,2,4,5-tetramethylbenzene
15.	47.19	Benzenediol	43.92	2-ethylphenol
16.	47.42	Hydroxybenzenepropane	44.63	Dimethylphenol
17.	47.83	Naphthalene	45.62	2-ethylthiophenol*
18.	48.71	?-thiophene	47.37	Naphthalene
19.	49.80	2-propylphenol*	47.82	?-thiophene
20.	51.14	C ₄ benzene	48.58	2-propylphenol
21.	52.29	2,4,5-trimethylphenol	49.76	C ₄ benzene
22.	53.10	Dihydroindeneone	51.18	C ₄ phenol
23.	53.86	C ₄ phenol	52.21	2,3-dihydro-1H-indeneone
24.	58.51	Methylnaphthalene	53.02	C ₄ phenol
25.	58.51	Pentenylphenol	58.42	Pentenylphenol
26.	62.00	Phenylethylsulfonic acid**	62.01	Phenylethylsulfonic Acid**
27.	63.07	Naphthalenol	63.02	Naphthalenol
			65.54	Methylnaphthalene

*Dopant

**Oxidized dopant

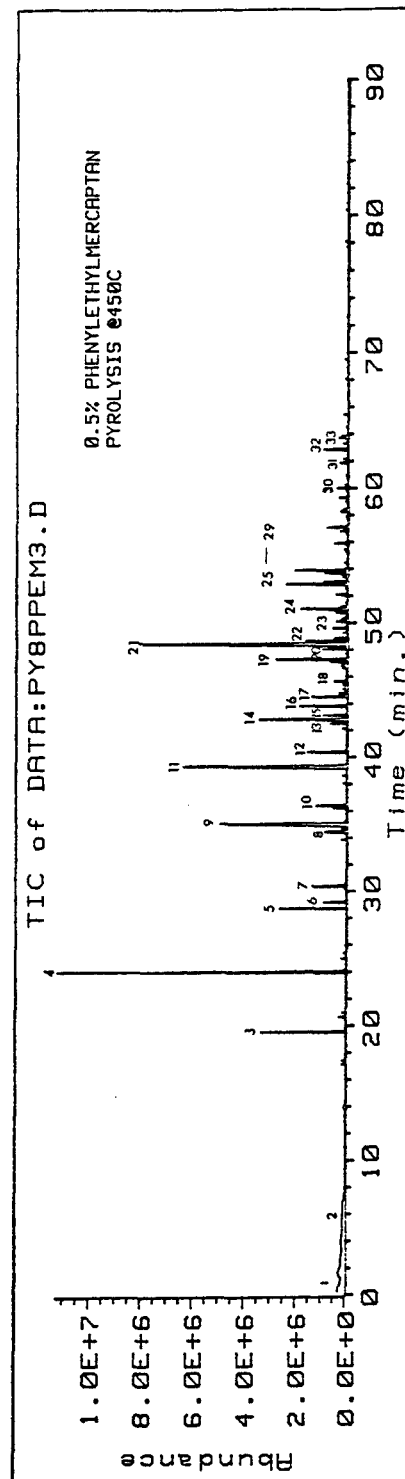
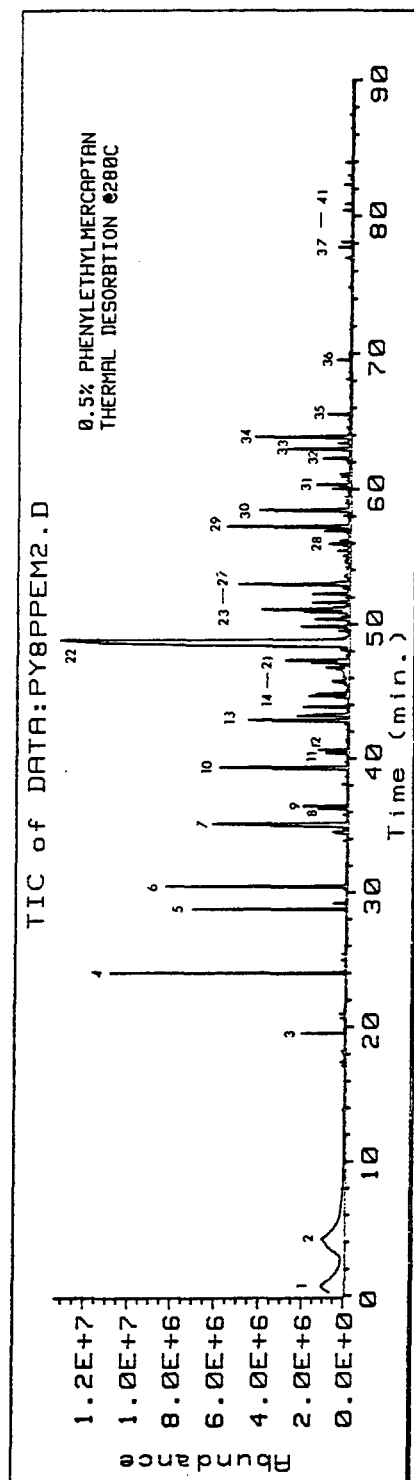
Figures 15 a & b. Thermal Desorption @ 280 °C and Pyrolysis @ 450 °C of Solids Formed From JP-8S Doped With 1.0 % 2-propylphenol & 0.5 % 3,4-dimethylthiophenol.



Tables 7 a & b. Compound Identification for Figures 15 a & b.

Peak #	Rt (min.)	Compound @ 280 °C	Rt (min.)	Compound @ 450 °C
1.	0-15	Air/sulfur dioxide mix	0-15	Air/sulfur dioxide mix
2.	19.54	Benzene	19.53	Benzene
3.	23.96	Toluene	23.95	Toluene
4.	29.23	Ethylbenzene	29.20	Ethylbenzene
5.	30.86	Xylene	30.54	Xylene
6.	35.12	Phenol	35.04	Phenol
7.	36.34	Trimethylbenzene	36.26	Trimethylbenzene
8.	39.28	Cresol	39.30	Cresol
9.	40.46	Cresol	40.40	Cresol
10.	43.22	2-methylbenzofuran	42.85	Phenylpropenal
11.	43.75	C ₃ benzene	43.21	C ₄ benzene
12.	44.73	Dimethylphenol	43.86	Ethylphenol
13.	46.24	Dimethylphenol	44.55	C ₇ phenol
14.	47.37	Naphthalene	44.83	Phenylpropenal
15.	48.46	2,3-dimethylthiophenol*	45.70	Benzaldehyde
16.	48.72	2-propylphenol*	46.15	Ethylphenol
17.	49.79	C ₄ benzene	47.33	Naphthalene
18.	50.40	C ₄ naphthalene	48.23	3,4-dimethylthiophenol*
19.	50.95	Substituted benzofuran	48.49	2-propylphenol
20.	51.09	2,4,5-trimethylphenol	48.72	Dimethylbenzofuran
21.	52.98	C ₄ phenol	49.67	Cyclooctatrienedione
22.	53.99	Methylnaphthalene	50.80	Dimethyloctayne
23.	57.18	Substituted aromatic	50.99	Trimethylphenol
24.	58.45	dihydroxypropylbenzene	52.14	2,3-dihydro-1H-indeneone
25.	61.99	2,3-dimethylphenolsulfonic acid**	52.92	C ₄ phenol
26.	63.00	Naphthalenol	53.11	Methylnaphthalene
27.	72.88	Substituted aromatic	53.93	Dihydromethanonaphthalene
28.	84.31	Substituted aromatic	61.94	3,4-dimethylphenylsulfonic acid**
29..			62.93	Naphthalenol

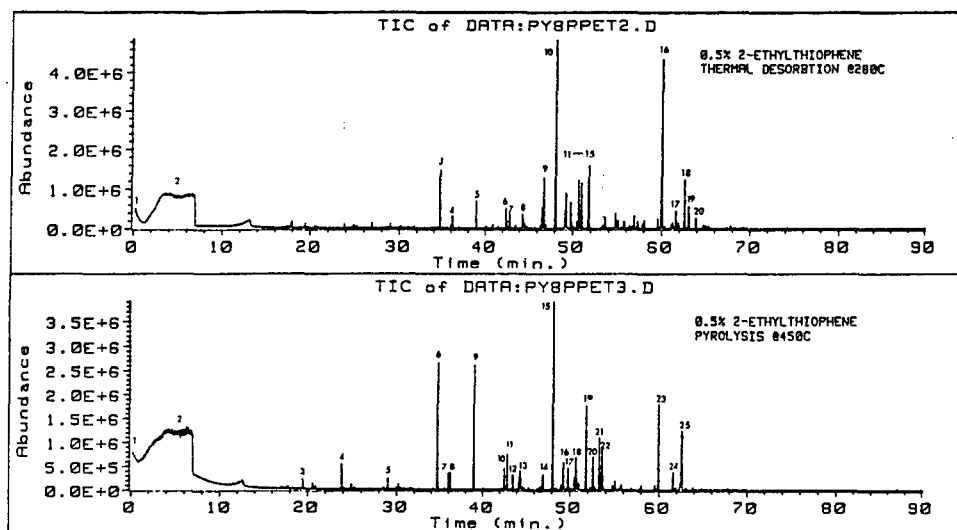
Figures 16 a & b. Thermal Desorbition @ 280 °C and Pyrolysis @ 450 °C of Solids Formed From JP-8S Doped With 1.0 % 2-propylphenol & 0.5 % PhenylethylMercaptan.



Tables 8 a & b. Compound Identification for Figures 16 a & b.

Peak #	Rt (min.)	Compound @ 280 °C	Rt (min.)	Compound @ 450 °C
1.	0.70	Carbon dioxide	0.40	Carbon dioxide
2.	4.32	Sulfur dioxide	4.55	Sulfur dioxide
3.	19.55	Benzene	19.54	Benzene
4.	24.01	Toluene	24.01	Toluene
5.	28.75	Ethylbenzene	28.70	Ethylbenzene
6.	30.42	Styrene	29.16	Xylene
7.	35.15	Phenol	30.37	Styrene
8.	36.24	Trimethylbenzene	34.45	Benzaldehyde
9.	36.45	Benzofuran	35.07	Phenol
10.	39.33	Cresol	36.40	Benzofuran
11.	40.42	Cresol	39.33	Cresol
12.	42.82	Methylbenzofuran	40.39	Cresol
13.	43.17	1,2,4,5-tetramethylbenzene	42.49	Dimethylphenol
14.	43.28	Benzeneethanol	42.84	Methylbenzofuran
15.	43.82	2-ethylphenol	43.14	Ethyl dimethylbenzene
16.	44.66	dimethylphenol	43.80	Ethylphenol
17.	44.82	Dihydromethylbenzofuran	44.51	Dimethylphenol
18.	45.74	Hydroxyphenylethanone	45.66	2-hydroxyphenylethanone
19.	46.79	Phenylethylmercaptan*	47.31	Azulene
20.	47.14	Benzenediol	48.03	Isopropylbenzaldehyde
21.	47.33	Naphthalene	48.48	2-propylphenol*
22.	48.80	2-propylphenol*	48.66	Dimethylbenzofuran
23.	49.84	Substituted aromatic acid	51.05	C ₄ phenol
24.	50.89	Dihydromethylbenzofuran	52.63	2,3-dihydro-1H-indeneone
25.	51.10	2,4,5-trimethylphenol	52.86	C ₄ phenol
26.	52.29	2,3-dihydro-1H-indeneone	53.05	Methylnaphthalene
27.	52.96	C ₄ phenol	55.89	Propyltetralin
28.	55.42	Methylbenzocarboxyaldehyde	57.08	?-thiophene
29.	57.24	?-thiophene	59.28	Methoxypropenylphenol
30.	58.46	Dihydroxypropylbenzene	59.99	Dimethylnaphthalene
31.	60.34	Substituted benzene	61.85	Phenylethylsulfonic acid**
32.	61.95	Phenylethylsulfonic acid**	62.86	Methylnaphthalenol
33.	62.98	Naphthalenol	63.80	Dihydromethoxynaphthalene
34.	63.86	?-thiophene		
35.	65.53	Anthracene		
36.	69.54	Methyldibenzofuran		
37.	77.15	Substituted methoxybenzene		
38.	80.40	Substituted phenylether		
39.	80.88	?-thiophene		
40.	82.29	Substituted aromatic		
41.	83.92	Substituted anthracene		

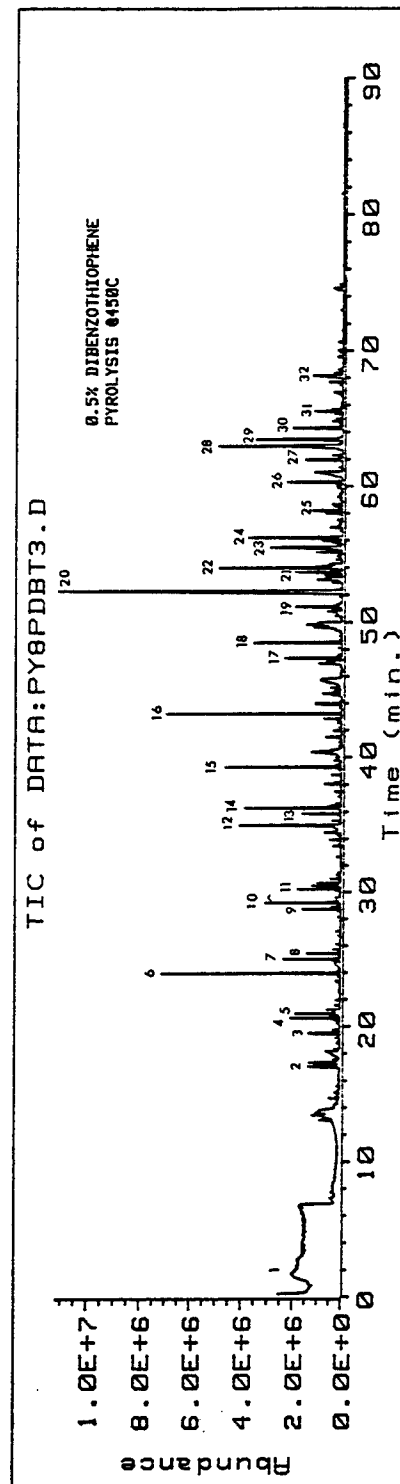
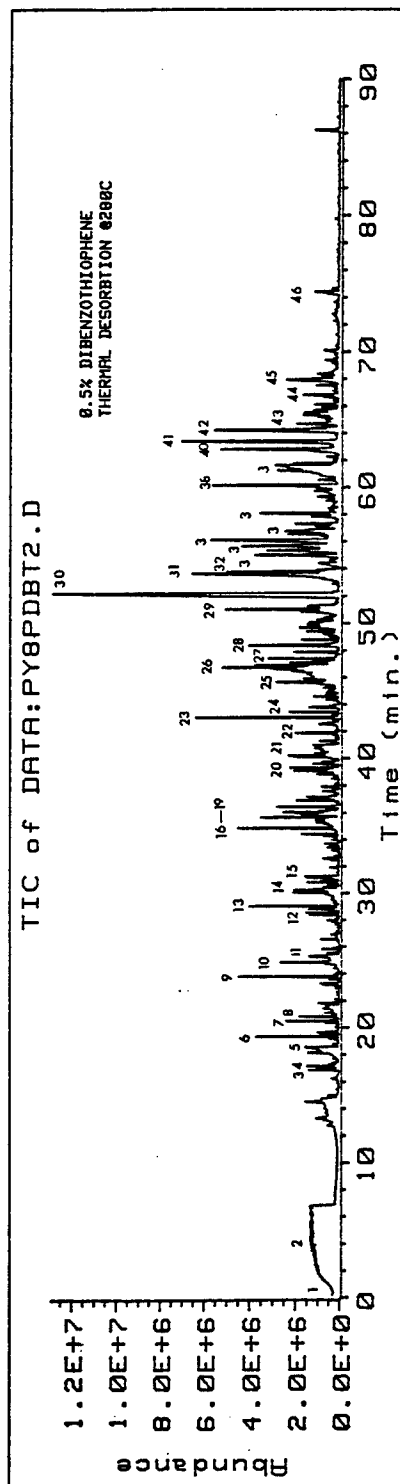
Figures 17 a & b. Thermal Desorption @ 280 °C and Pyrolysis @ 450 °C of Solids Formed From JP-8S Doped With 1.0 % 2-propylphenol & 0.5 % 2-ethylthiophene.



Tables 9 a & b. Compound Identification for Figures 17 a & b.

Peak #	Rt (min.)	Compound @ 280 °C	Rt (min.)	Compound @ 450 °C
1.	0.25	Carbon dioxide	0.30	Carbon dioxide
2.	3-5.50	Air/Sulfur dioxide mix	3.15	Air/sulfur dioxide mix
3.	34.70	Phenol	19.47	Benzene
4.	36.16	Benzofuran	23.82	Toluene
5.	38.93	Cresol	28.99	Ethylbenzene
6.	42.41	Hexyneol	34.71	Phenol
7.	44.61	C ₄ benzene	35.98	C ₃ benzene
8.	44.34	2-ethylphenol	36.17	Benzofuran
9.	46.79	Substituted benzene	38.96	Cresol
10.	48.11	2-propylphenol*	42.52	Methylindole
11.	50.67	2,4,5-trimethylphenol	42.87	1,2,4,5-tetremethylbenzene
12.	51.61	2,3-dihydro-1H-indeneone	43.53	Ethylphenol
13.	55.00	Indenedione	42.35	C ₂ phenol
14.	56.89	Tricycloundecane	46.60	C ₂ phenol/aromatic mix
15.	59.55	Benzofuran	48.12	2-propylphenol*
16.	60.02	Substituted phenol?	49.27	C ₄ benzene
17.	61.60	Substituted benzene/aromatic mix	50.69	C ₃ phenol
18.	63.04	Naphthalenol	51.82	2,3-dihydro-1H-indeneone
19.	63.81	Propenyloxybenzene	52-57	C ₄ phenol
20.			53.58	Methylnaphthalene
21.			55.04	Phenylcarboxaldehyde
22.			59.96	Mixed phenol
23.			61.58	Substituted aromatic
24.			62.57	Naphthalenol
25.			63.04	Naphthalenol

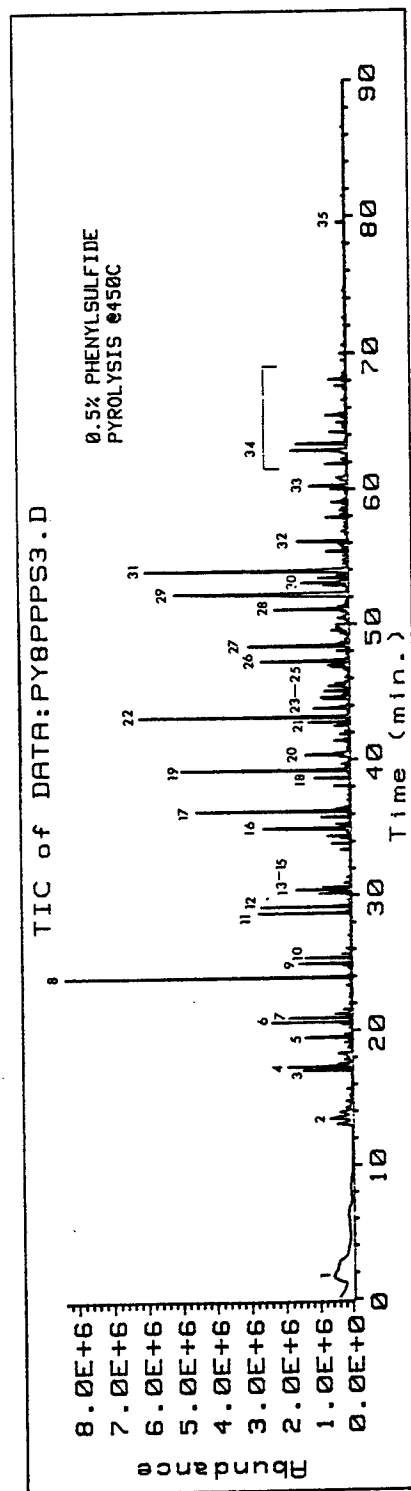
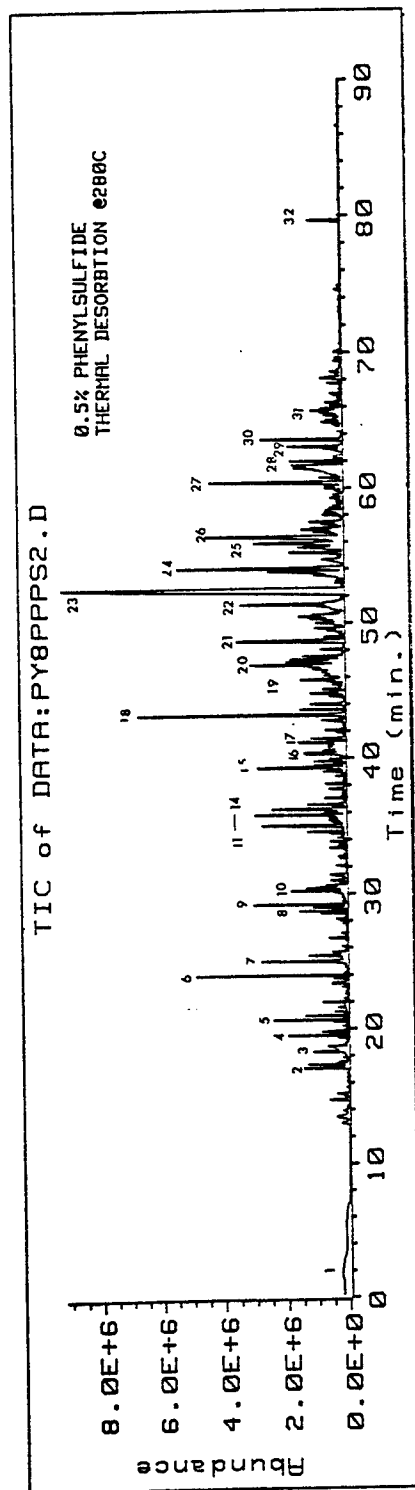
Figures 18 a & b. Thermal Desorption @ 280 °C and Pyrolysis @ 450 °C of Solids Formed From JP-8S Doped With 1.0 % 2-propylphenol and 0.5 % Dibenzothiophene.



Tables 10 a & b. Compound Identification for Figures 18 a & b.

Peak #	Rt (min.)	Compound @ 280 °C	Rt (min.)	Compound @ 450 °C
1.	0.75	Carbon dioxide	1.70	Carbon dioxide
2.	0.75-7.00	Air	17.07	Hexene
3.	16.88	Hexene	19.47	Benzene
4.	17.07	Butanol	20.85	Heptene
5.	18.16	Hexadiene	20.98	Heptane
6.	19.36	Benzene	23.97	Toluene
7.	20.50	Heptene	25.01	Octene
8.	20.83	Heptane	25.43	Octane
9.	23.81	Toluene	28.73	m,p-xylene
10.	24.84	Octene	29.23	o-xylene
11.	25.28	Octane	30.43	Styrene
12.	28.39	Ethylbenzene	35.02	Phenol
13.	29.03	Xylene	35.87	Alkene
14.	30.24	Styrene	36.30	1,2,4-trimethylbenzene
15.	30.84	Cyclooctadiene	39.27	o-cresol mixed
16.	34.89	Phenol	43.25	1,2,4,5-tetramethylbenzene
17.	35.67	Nonene	47.36	Naphthalene
18.	36.08	Trimethylbenzene	48.52	2-propylphenol*
19.	36.46	Decene	51.14	2,3,6-trimethylphenol
20.	39.33	Cyclooctanedieneone	52.32	2,3-dihydroindene-1-one
21.	40.13	Mixed alcohol	53.69	1,3-isobenzofurandione
22.	41.89	Mixed diene	54.00	Methylnaphthalene
23.	43.03	C ₄ benzene	55.52	Isobenzofuranone
24.	43.44	C ₄ alkenylbenzene	56.25	Diphenyldiethanone
25.	45.67	Butylcyclopropene	58.23	Ethylbenzylfuran
26.	46.77	Dodecenes	61.99	Methylnaphthalenediol
27.	48.42	Mixed alkene	63.03	Naphthalenol
28.	49.23	2-propylphenol*	63.48	Naphthalenol
29.	51.04	C ₃ phenol	64.33	C ₅ phenol
30.	52.21	2,3-dihydro-1H-indeneone	65.56	Methylnaphthalenol
31.	53.66	Isobenzofurandione	68.20	Methylnaphthalenol
32.	53.86	Methylnaphthalene	74.62	Dimethylnaphthalenol
33.	55.02	Indene-1H-dione		
34.	55.67	Phenylethylene bis ethanone		
35.	56.15	Isobenzofuranone		
36.	56.54	Tetradecene		
37.	58.13	Benzofuran		
38.	60.19	C ₃ benzene		
39.	62.15	Dihydronaphthalenone		
40.	62.84	Naphthalenol		
41.	63.44	Naphthalenol		
42.	64.27	Mixed isobenzofurandione		
43.	64.50-67.00	Alkane/aromatic mix		
44.	68.00	C ₆ benzene		
45.	74.43	Naphthalene/alkene mix		
46.	86.27	Dibenzosulfone***		

Figures 19 a & b. Thermal Desorption @ 280 °C and Pyrolysis @ 450 °C of Solids Formed From JP-8S Doped With 1.0 % 2-propylphenol and 0.5 % Phenylsulfide.



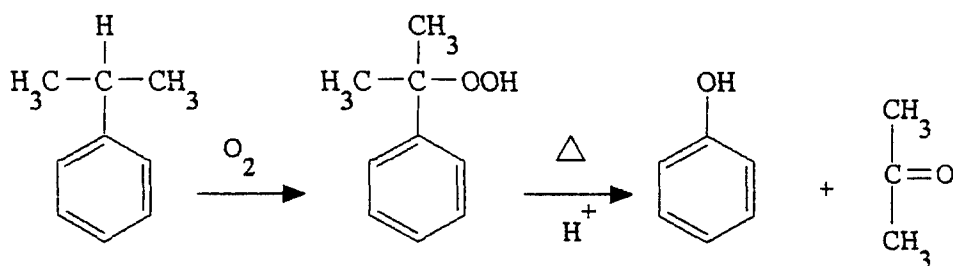
Tables 11 a & b. Compound Identification for Figures 19 a & b.

Peak #	Rt (min.)	Compound @ 280 °C	Rt (min.)	Compound @ 450 °C
1.	1.58	Carbon dioxide	1.72	Carbon dioxide
2.	17.35	Hexane	13.50	Substituted alkane
3.	18.29	Hexadiene	17.10	Hexene
4.	19.50	Benzene	17.36	Hexane
5.	20.65	Heptene	19.35	Benzene
6.	23.48	Toluene	20.66	Heptene
7.	25.01	Octene	21.00	Heptane
8.	28.72	Ethylbenzene	24.00	Toluene
9.	29.05	Xylene	25.01	Octene
10.	30.40	Styrene	25.42	Octane
11.	34.60	Heptanol	28.74	Ethylbenzene
12.	35.06	Phenol	29.30	Xylene
13.	35.84	Decene	30.19	Substituted heptene
14.	36.25	Trimethylbenzene	30.49	Xylene
15.	39.29	Propenylbenzene	30.67	Nonane/xylene mix
16.	40.32	Octanol	35.02	Phenol
17.	41.18	Dihydrobenzofuran	36.29	Trimethylbenzene
18.	43.27	C ₄ benzene	38.69	2,3-dihydro-1H-indene
19.	44-46.50	Substituted alkanes	39.29	Cresol
20.	46.93	Dodecene	40.41	Cresol
21.	48.68	2-propylphenol	42.82	Methylbenzofuran
22.	51.36	Trimethylphenol	43.26	1,2,4,5-tetramethylbenzene
23.	52.58	2,3-dihydro-1H-indeneone	43.85	2-ethylphenol
24.	54.07	Methylnaphthalene	44.68	C ₇ phenol
25.	55.92	1,1'(1,3-phenylene)bis-ethanone	45.14	Methyl-1H-indene
26.	56.45	Isobenzofuranone	47.34	Naphthalene
27.	60.21	C ₅ phenol	48.47	2-propylphenol*
28.	61.50	Trimethylbenzoic acid	48.47	Trimethylphenol
29.	63.06	Naphthalenol	51.15	2,3-dihydro-1H-indeneone
30.	65.71	Tetrahydromethanonaphthalene	52.35	Methylnaphthalene
31.	79.62	Phenylsulfoxide**	53.10	Methylnaphthalene
32.			54.03	C ₄ benzene
33.			56.21	Substituted phenol
34.			62.93-68.13	Naphthalenols
35.			79.58	Phenylsulfoxide**

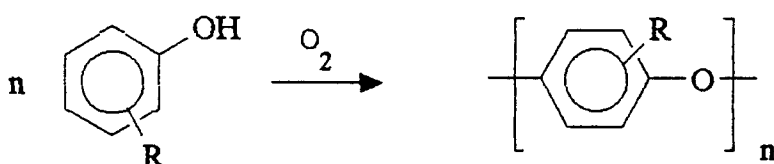
CONCLUSION

Stressed fuel samples that contained mercaptan sulfur formed significant amounts of insoluble solid deposit. GC/MS revealed the conversion of thiols to sulfonic sulfonic acids during thermal oxidative conditions. The production of these sulfonic acids seemed to inhibit oxidation and played a catalytic role in deposit formation.

A well known industrial process for the syntheses of phenol is by oxidation of isopropyl benzene (cumene) to cumene hydroperoxide. The hydroperoxide is converted by aqueous acid into phenol and acetone (8).



This type of mechanism is probably representative of the "non-oxidizing" mechanism in which sulfonic acids act catalytically on the α hydrogen of aromatic fuel components leading to the formation of phenols. These phenols can oxidatively couple to form phenolic oligomers (9) with high thermal stability.



Phenols are the predominate functionality found in jet fuel solids recovered from aircraft engines (1). This implies that phenolic coupling is a major contributor to the formation of deposits. The implication of phenolic oxidative coupling as a major mechanism in deposit formation is supported by the work of Hazlett (10) and other fuel researchers. Oxidative coupling is wide-spread in nature, and can occur in the presence of air, with or without catalysis (10,11). The apparent disappearance of 2-propylphenol in the extracts and solids of samples doped with thiophene and thioether compounds could be the result of oxidation of the phenol or thermal rearrangement into other aromatic species. In contrast, the substantial abundance of 2-propylphenol in samples doped with thiols could result from the antioxidant effect of sulfonic acids

formed during the stress. In this case the phenol would remain as an unreacted species and the acids would catalyze the production of phenols from hydroperoxides. These phenols then couple and become a primary component for production of the solid matrix for the build up of acetone insoluble solids. Cumulative data on the production of gums, solids, soluble gums and degree of oxidation from tests conducted during this study are displayed in Table 12.

Table 12. Cumulative Analytical Data From Dopant Studies on JP-8 Surrogate Fuel.

Surrogate + Dopant	Gums	Solids Mass % of Fuel	Total	SiOH Extract* mg/~3mL Fuel	Molarity (m/L)**		
					[-OH]	[C=O]	[Sum]
1% 2-propylphenol+0.5% 2-ethylthiophenol O ₂ 24 hr	0.57	0.91	1.48	29.00	0.60	0.02	0.62
1% 2-propylphenol+0.5% phenylethylmercaptan O ₂ 24 hr.	0.30	0.35	0.65	107.50	0.21	0.30	0.51
1% 2-propylphenol+0.5% 3,4-dimethylthiophenol O ₂ 24 hr.	0.38	1.30	1.68	32.00	N/A	N/A	N/A
1% 2-propylphenol+0.5% dibenzothiophene O ₂ 24 hr.	4.70	0.30	5.00	110.20	N/A	N/A	N/A
1% 2-propylphenol+0.5% phenylsulfide O ₂ 24 hr.	2.43	0.29	2.72	191.50	0.00	1.76	1.76
1% 2-propylphenol+0.5% 2-ethylthiophene O ₂ 24 hr.	4.13	0.58	4.71	210.20	0.00	0.00	0.00
JP-8 Surrogate O ₂ 24 hr.	3.32	0.06	3.38	122.70	0.00	3.48	3.48
POSF 2747	13.72	0.48	14.20	N/A	N/A	N/A	N/A
POSF 2827	1.23	0.60	1.83	N/A	N/A	N/A	N/A
10.3mg (0.04 mg) SiOH Extract from 2827 O ₂ 24 hr.	2.45	0.91	3.36	232.50	0.00	3.48	3.48
1% 2-propylphenol+0.5% 2-ethylthiophenol No O ₂ 24 hr.	0.05	0.04	0.09	40.50	0.00	0.00	0.00
1% 2-propylphenol+0.5% 2-ethylthiophene No O ₂ 24 hr.	0.00	0.04	0.04	22.40	0.00	0.00	0.00
1% 2-propylphenol+0.5% 2-ethylthiophenol+0.3% phenol-d6 O ₂ 24 hr.	0.71	1.70	2.40	77.50	1.36	0.33	1.69
1% 2-propylphenol+0.5% 2-ethylthiophenol+0.3% phenol-d6 O ₂ 10 hr.	0.38	0.39	0.77	33.00	N/A	N/A	N/A
1% 2-propylphenol+0.3% phenol-d6 O ₂ 24 hr.	1.71	0.16	1.87	155.80	1.10	1.90	3.00
1% 2-propylphenol+0.3% phenol-d6 O ₂ 10 hr.	0.93	0.02	0.95	99.00	N/A	N/A	N/A

*SiOH extract: Represents volues for "soluble gums".

**Data from FTIR of filtered fuel samples based on alcohol and ketone standards.

LITERATURE CITED

1. Gillman, A.P., Thesis, "Determination of Chemical Mechanisms for the Oxidation and Deposit Formation of Aviation Turbine Fuels", Eastern Kentucky University, Richmond, KY, 1993.
2. Bramford, D.H. and Tipper, C.F., Eds., Comprehensive Chemical Kinetics, Vol. 16, Elsevier Scientific Publishing Company, NY, 1980.
3. Lowery, T.H. and Richardson, K.S., Mechanism and Theory in Organic Chemistry, Harper & Row Publishers, 3rd ed., p. 780, 1987.
4. Heneghan, S.P., et. al., "Static Tests for the Evaluation of Fuel Additives", 30th Aerospace Science Meeting & Exhibit, Reno, NV, January, 1992.
5. Schulz, W.D., "Thermal Desorption-GC-MS Determination of Solid Products of Jet Fuel Oxidation", Abstracts, 34th Rocky Mountain Conference on Analytical Chemistry, Paper #15, August, 1992.
6. Stevens, M.P., *Journal of Chemical Education*, 70, #7, pp. 535-538, July, 1993.
7. Fuson, R.C., Reactions of Organic Compounds, John Wiley & Sons, Inc., NY, 1962.
8. Boyd, R.N. and Morrison, R.T., *Organic Chemistry*, 3rd Ed., Allyn & Bacon, Inc., 1979.
9. Seymor, R.B. and Carraher, C.E., Polymer Chemistry, 2nd Ed., Marcel Dekker, Inc., 1988.
10. Hazlett, R.N. and Power, A.J., "The Role of Phenols in Distillate Fuel Stability", 2nd International Conference on Long Term Storage Stabilities of Liquid Fuels, San Antonio, TX, October, 1986.
11. Musso, H., *Oxidative Coupling of Phenols*, Taylor, W.I. and Battersby, A.R., Eds., Marcel Dekker, NY, 1967.

AEROELASTICITY OF AN AIRFOIL TEST RIG
AT LOW INCIDENCE

Gary M. Graham
Associate Professor
Department of Mechanical Engineering
Ohio University
257 Stocker
Athens, Oh 45701

and

Lizhong Huang
Research Assistant
Ohio University

Final Report for:
Summer Research Extension Program

Sponsored by:
Air Force Office of Scientific Research
Bolling Air Force Base, Washington, D.C.

March 1994

AEROELASTICITY OF AN AIRFOIL TEST RIG
AT LOW INCIDENCE

Gary M. Graham
Associate Professor
Department of Mechanical Engineering
Ohio University
257 Stocker
Athens, Oh 45701

and

Lizhong Huang
Research Assistant
Ohio University

Abstract

The normal force loading on a NACA 0015 airfoil undergoing a rapid step-like maneuver has been measured using strain gauges in the Ohio University tow tank. The motivation for the experiments was to experimentally study airfoil indicial response aerodynamics. Because the test rig experiences large acceleration rates as well as significant aerodynamic loads during the step, an important issue is the degree to which aeroelastic reactions deform the structure and influence the strain gauge output. This report describes an aeroelastic analysis of the O.U. test rig. The analysis is based on the mode superposition method for structural dynamics and linear airfoil theory. The analysis is compared with the experimental strain gauge data and shows that aeroelastic reactions following the step are significant. The equations of aeroelasticity are solved in closed form.

AEROELASTICITY OF AN AIRFOIL TEST RIG AT LOW INCIDENCE

Gary M. Graham and Lizhong Huang

Introduction

The present report describes a continuation of research initiated and reported under grant AFOSR-89-0502. The focus of the research has been an experimental and analytical investigation of airfoil indicial response aerodynamics as related to the convolution integral formulation for unsteady airfoil loading.

The convolution integral formulation for the lift on a flat plate airfoil in arbitrary motion has been derived in Reference[1]. The formulation requires an indicial lift function which by definition is the transient lift response to a step change in angle of attack. The indicial lift response for a flat plate airfoil experiencing a step change in angle of attack due to plunge was first derived by Wagner. In Reference [1], Wagner's function is derived under the assumption of small perturbations using a Fourier integral of Theodorsen's function for harmonic motions. At the onset of the step Wagner's function jumps instantaneously to one-half the steady state lift. Also derived in Reference[1] is Kussner's function for the lift on a flat plate airfoil entering a sharp-edged gust. The initial lift in this case is zero and approaches steady state as the gust overtakes the airfoil. In the case of a 2D airfoil of finite thickness, Reference [2] shows that for an airfoil having a trailing edge with a finite angle of convergence the indicial lift at the step onset is zero. This suggests that the subsequent transient lift for finite airfoils at small incidence may be similar in form to Kussner's function. Reference [2] cites other numerical studies for finite airfoils which appear to agree with the zero initial lift result. Reference [3] uses the Laplace transform method to derive the lift transfer function for a number of airfoil motions. The Laplace domain formulation includes the indicial lift function and results are presented using Kussner's function to describe the indicial lift.

Reference [4] describes a tow tank study designed to measure the normal force response of a NACA 0015 airfoil experiencing sudden step-like changes in angle of attack by rotation about the quarter. The motivation for these experiments was to study airfoil indicial response aerodynamics as defined in the theory of nonlinear mathematical modeling for aerodynamic systems [5]. These experiments involved strain gauge load cell measurements of the transient normal force loading on an airfoil undergoing a sudden change in angle of attack of approximately $\Delta\alpha = +1^\circ$. The angle of attack prior to the step onset (α_0) was steady and was varied from run-to-run over the range $2^\circ < \alpha_0 < 60^\circ$.

In the experiments of Reference [4] the test rig may experience large inertial and aerodynamic loading due to the rapid starting and stopping required to impart the step. Therefore, an important issue is the degree to which aeroelastic reactions deform the structure thereby influencing the output of the strain gauge bridge. Knowledge of these reactions is useful in comparing these strain gauge data with the theoretical indicial responses of Wagner and Kussner. This report describes an aeroelastic analysis of the Ohio University tow tank test rig. The model is based on the mode superposition method for structural systems and classical linear airfoil theory. The Laplace transform method is used to solve the equations of aeroelasticity in closed form.

Ohio University Tow Tank

A schematic of the O.U. tow tank is shown in Figure 1a. The facility consists of a large tank with a six inch chord NACA 0015 airfoil suspended vertically in the water with a submerged length of 42.0 inches. A carriage moves in translation at 2 ft/s ($Re = 9.5E4$) along roller bearings fixed to I-beams which span the tank. The airfoil is driven in rotation by a drive shaft fixed to the airfoil quarter chord at one end, and coupled to a 3.5 hp stepper motor/gear box apparatus at the other end. Figure 1b shows details of the drive shaft and airfoil. Shown here are dimensions in inches, and a numbering scheme (1 through 23) defined for the purpose of discretizing the mass of the structure as will be discussed in detail. The drive shaft has a number of variations in cross section over the length of the shaft which must be considered in modeling the aeroelastic response of the structure. Near the middle of the drive shaft is a machined rectangular section which has a strain gauge load cell adhered to the shaft. The load cell section is discretized into mass elements 5 through 9 with the strain gauges located at the centroid of element 7. The strain gauge circuit is electrically compensated to be sensitive to chord normal forces only. The upper most mass element 1 is made of steel while all other parts are aluminum. The modulus of elasticity (E) for steel was taken to be 30×10^6 psi, and for the aluminum was measured to be 7.3×10^6 psi. The modulus of rigidity (G) was taken to be 10×10^6 psi for the steel and for aluminum 4×10^6 psi. The area moment of inertia of the airfoil about the chord line is 0.12 in^4 and the center of mass of the airfoil is located 1.335 inches aft of the pitch axis at the quarter chord. The polar moment of inertia of the airfoil about the pitch axis is 6.71 in^4 . The densities of steel and aluminum were taken to be 0.3 and $0.1 \text{ lb}_m/\text{in}^3$. The mass of the airfoil per unit length is $0.1598 \text{ lb}_m/\text{in}$.

Theoretical Linear Normal Force Response for Small Angles of Attack

In an incompressible flow at small incidence, the theoretical linear normal force coefficient response of an airfoil given an instantaneous step change in angle of attack by *rotation* about the quarter chord is related to the indicial lift function, $\Gamma(t)$, and is given by:

$$C_N(t) = C_{N0} + \pi \Delta \alpha \left[\delta(t-0) + \frac{1}{2} \delta'(t-0) \right] + 2 \pi \Delta \alpha \left(\Gamma(t) - \Gamma'(t) \right) \quad (1a)$$

where C_{N0} is the initial normal force, $\Delta \alpha$ is the step amplitude, δ' is the time derivative of the Dirac delta function δ , and Γ' is the time derivative of Γ . The first two terms in brackets in Equation 1 are generalized functions [6] which describe the noncirculatory component of the loading, while the last group of terms gives the circulatory component. For a flat plate airfoil the indicial function can be represented by a two pole curve fit to Wagner's function:

$$\Gamma(t) = [1 - 0.165e^{-0.0455t} - 0.335e^{-3t}] \quad (1b)$$

As has been pointed out, for an airfoil with a finite trailing edge angle it may be more appropriate to use Kussner's function in which case:

$$\Gamma(t) = [1 - 0.5e^{-.13t} - 0.5e^{-t}] \quad (1c)$$

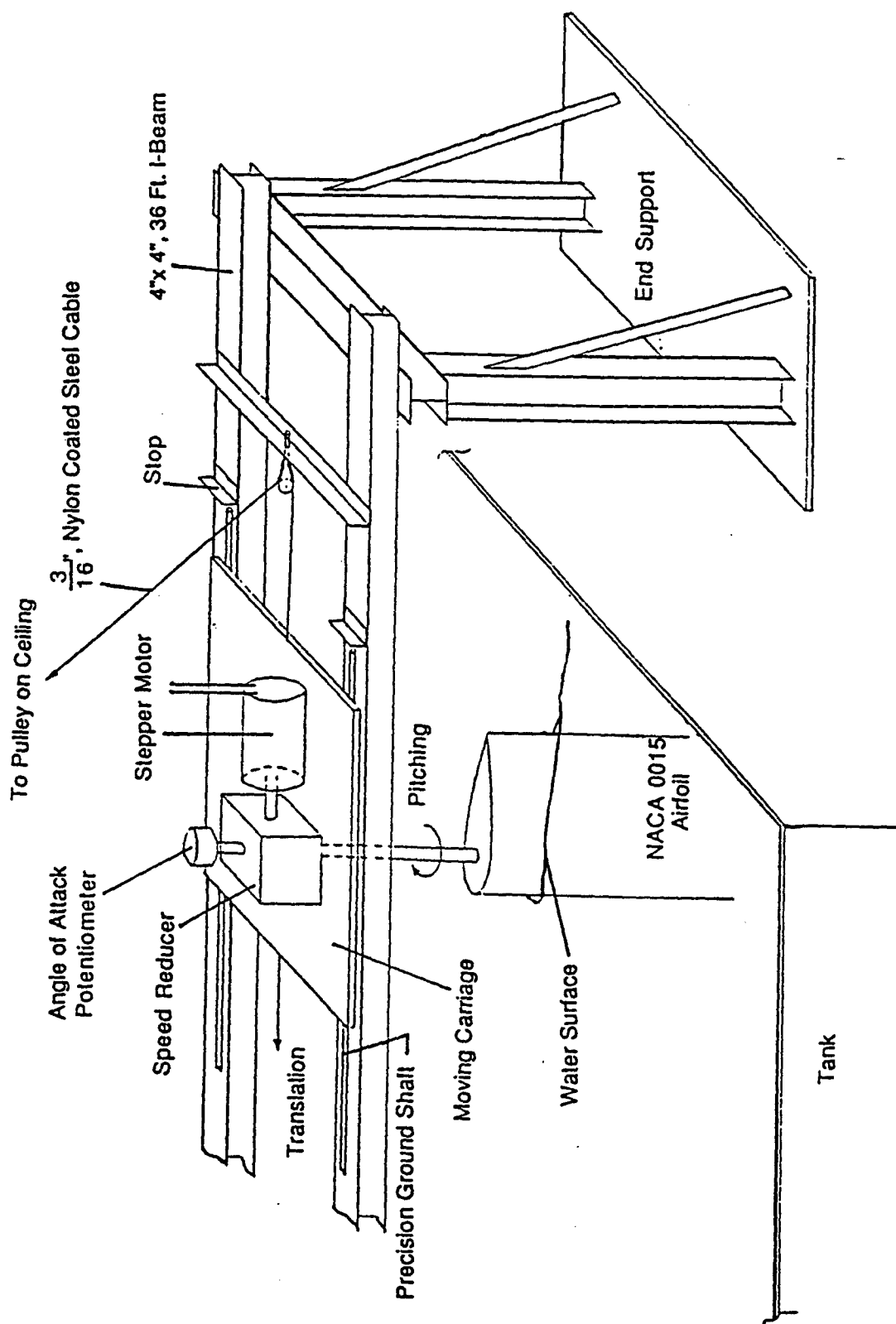


Figure 1a. Ohio University Tow Tank Facility

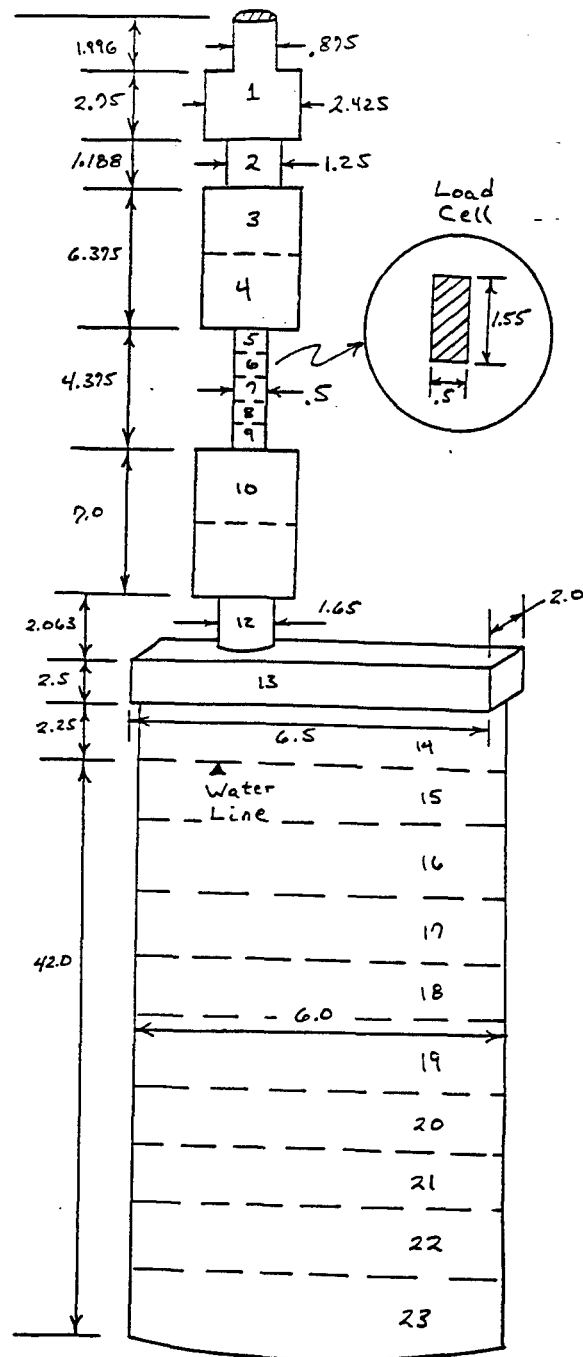


Figure 1b. Test rig

Transient normal force responses of a NACA 0015 airfoil undergoing sudden step-like changes in angle of attack by rotation have been measured in the Ohio U. tow tank. Figure 2 shows angle of attack data for a typical run (small spikes are electrical noise). The onset angle is 2.09° and the step amplitude is approximately $+1.25^\circ$. The motion resembles, to a reasonable approximation, a small amplitude ramp motion. Equation 1 is compared below with the experimental strain gauge data corresponding to the motion of Figure 2. To facilitate the comparison, the coefficient 2π (for a flat plate airfoil) on the circulatory part in Equation 1 has been replaced by the static normal force curve slope (for the present NACA 0015) which has been measured in an independent test [4]. This substitution is necessary for the response of Equation 1 to approach the same steady state as the experimental response.

Aeroelastic Analysis

The present analysis is based on a combination of the mode superposition method for a forced structural dynamic response [7], and linear airfoil theory formulated in terms of the convolution integral for the loading on an airfoil in arbitrary motion [1]. The structure to be modeled has been shown in Figure 1b. Because the pitch axis (drive shaft axis) does not coincide with the center of mass of the lower part of the structure (mass elements 13-23), it is necessary to consider the coupling between the normal and torsional aeroelastic degrees of freedom.

System Representation

As illustrated in Figure 1b, the structure has been discretized into 23 mass elements which are considered to be concentrated at the centroid of each element. Under the influence of aeroelastic loading, the masses will deflect normal to the airfoil chord referred to here as the normal degree of freedom (NDOF), as well as in torsion about the pitch axis hereafter referred to as the TDOF. The lowest nine masses (15-23) represent the submerged portion of the airfoil, and masses 5 through 9 correspond to the rectangular cross section load cell. Masses are concentrated on the load cell to obtain good resolution of the deformation and strain. In the TDOF, the mass elements are replaced by polar mass moment of inertia elements. For the TDOF analysis, the structure is discretized in the same way as the NDOF for elements 1 through 12, however, elements 13 through 23 are lumped into a single inertia element giving a total of 13 inertia elements. The reduction in elements in the TDOF is based on the fact that the torsional stiffness of both the mounting block (element 13) and airfoil are much larger than the drive shaft, and consequently the mounting block and entire airfoil experience nearly the same TDOF deflection. The resulting discretized structure may be described mathematically in terms of a diagonal mass matrix $[M]$, a symmetric NDOF flexibility matrix $[AN]$, a diagonal polar mass moment of inertia matrix $[J]$, and a symmetric TDOF flexibility matrix $[AT]$. The flexibility coefficient $AN(i,j)$ is by definition the deflection of mass i due to a unit force applied at mass j , while $AT(i,j)$ gives the angular rotation of polar inertia i due to a unit torque applied to inertia j . The matrix $[AN]$ has been computed by assuming the structure to deform as a cantilever beam and integrating the second order differential equation for the elastic beam curvature [8]. A condition of continuous slope is applied at discontinuities in area moment of inertia of the drive shaft. The matrix $[AT]$ has been computed using mechanics for shafts in torsion [9]. The analytically derived flexibility matrices have been validated to some extent by loading the structure and measuring the deflection at selected points. For example, the analytical value of $AN(15,15)$ is $3.4143e-3$ in/lb_f while the experimental

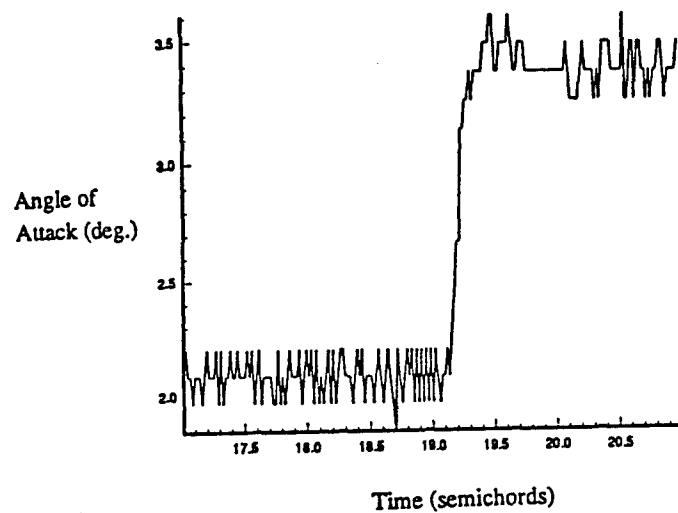


Figure 2. Angle of Attack Data for Indicial Response Test

value is 3.516×10^{-3} in/lb_f. The NDOF stiffness matrix [KN] and TDOF stiffness matrix [KT] are computed by inverting [AN] and [AT], respectively, and has been done using an IMSL subroutine.

Eigenvalue Problem

The system matrices above have been used to solve the eigenvalue problem for the natural frequencies and mode shape vectors of the system. The eigenvalues (natural frequencies) and eigenvectors (modal vectors) have been computed using the IMSL subroutine EVCGR. In the mode superposition analysis, the two lowest NDOF modes (NDOF1 and NDOF2) have been used, while for the TDOF only the lowest fundamental mode has been retained. The corresponding modal vectors are plotted in Figure 3 and given numerically in Table 1. The modal vectors are designated below as ϕ_{N1} , ϕ_{N2} , and ϕ_T for the NDOF1, NDOF2, and TDOF, respectively.

Table 1. Modal Vectors for NDOF1, NDOF2, and TDOF

i	ϕ_{N1}	ϕ_{N2}	ϕ_T
1	0.003	-0.002	0.0392
2	0.0011	-0.0073	0.0647
3	0.0025	-0.0156	0.0983
4	0.0156	-0.0922	0.1178
5	0.0229	-0.1332	0.2080
6	0.0270	-0.1542	0.3687
7	0.0318	-0.1778	0.5294
8	0.0375	-0.2038	0.6900
9	0.0439	-0.2319	0.8507
10	0.0620	-0.3067	0.9417
11	0.0928	-0.4287	0.9629
12	0.1189	-0.5252	0.9867
13	0.1416	-0.6019	1.0000
14	0.1661	-0.6790	1.0
15	0.2090	-0.7609	1.0
16	0.2803	-0.7984	1.0
17	0.3642	-0.7455	1.0
18	0.4581	-0.6027	1.0
19	0.5595	-0.3783	1.0
20	0.6661	-0.0871	1.0
21	0.7760	0.2522	1.0
22	0.8877	0.6202	1.0
23	1.0000	1.0000	1.0

*The position of element i is located at the centroid of the element (see Figure 1b).

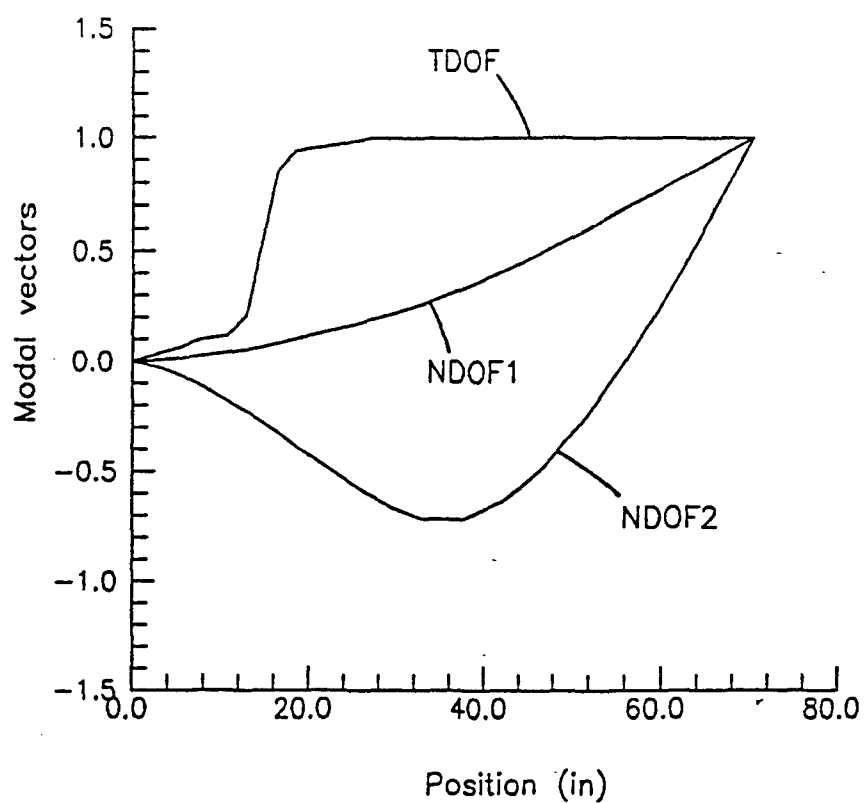


Figure 3. Modal Vectors.

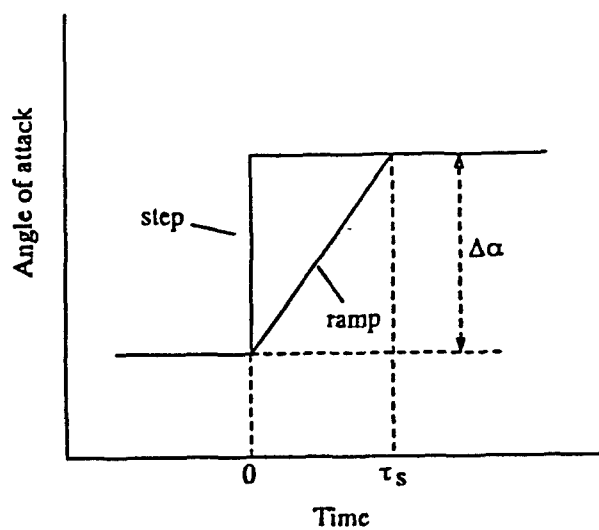


Figure 4. Step and Ramp Input Motions

The nondimensional natural frequencies ($\omega b/U$) for the NDOF modes were computed to be $\omega_{N1} = 6.374$ and $\omega_{N2} = 26.985$, and for the TDOF $\omega_T = 65.782$. Notice that the initial part of the angle of attack data (the ramp) of Figure 2 has a slope nearly the same as a sine function with a nondimensional frequency near 50. This frequency is, in a sense, the excitation frequency. Because the NDOF2 and TDOF natural frequencies are near the excitation frequency, it is appropriate to consider these modal responses. Apparent mass and inertia effects tend to reduce the *aeroelastic* frequencies even further.

Structural Dynamics Model

The aeroelastic structural response of the O.U. test rig has been modeled using the mode superposition method and classical linear airfoil theory. For modeling the rigid body rotation of the rig, a rotation degree of freedom (RDOF) is introduced. The RDOF is used to simulate the change in angle of attack of the structure due to the rotation imparted by the stepper motor. The NDOF and TDOF as defined above simulate only deformations relative to the instantaneous position of the top of the drive shaft where both the NDOF and TDOF deflections are always zero.

In the NDOF and TDOF, the deflections of the structure are given by the normalized mode shape vectors multiplied by time dependent modal amplitudes. The total deflection of the structure is defined by:

$$\begin{aligned} \mathbf{v}_N(t) &= \phi_{N1}q_1(t) + \phi_{N2}q_2(t) \\ \mathbf{v}_T &= \phi_T g(t) \\ \alpha(t) &= p(t) \end{aligned} \tag{2}$$

where \mathbf{v}_N and \mathbf{v}_T are the deflection vectors in the NDOF and TDOF, respectively, and $\alpha(t)$ describes the RDOF motion. The quantities $q_1(t)$, $q_2(t)$, and $g(t)$ are the modal amplitudes and the generalized coordinates of the system. The scalar RDOF motion variable $p(t)$ is the magnitude of the nominal angle of attack as the structure is pitched and is an input to the model. This is the angle measured by the rotational potentiometer illustrated in Figure 1a.

Substituting Equations 2 into the equations of motion for the system and using the orthogonality of the modal vectors w.r.t. the system mass and stiffness matrices to uncouple the modal equations [7] yields the following three generalized equations of motion:

$$\begin{aligned} M_1 \ddot{q}_1 + K_1 q_1 &= \phi_{N1}^T F \\ M_2 \ddot{q}_2 + K_2 q_2 &= \phi_{N2}^T F \\ J \ddot{g} + C_T \dot{g} + K_T g &= \phi_T^T T \end{aligned} \tag{3}$$

where the generalized system properties are scalar quantities given by:

$$M_1 = \phi_{N1}^T [M] \phi_{N1}, \quad M_2 = \phi_{N2}^T [M] \phi_{N2}, \quad J = \phi_T^T [J] \phi_T$$

$$K_1 = \phi_{N1}^T [KN] \phi_{N1}, K_2 = \phi_{N2}^T [KN] \phi_{N2}, K_T = \phi_T^T [KT] \phi_T \quad (4)$$

$$C_T = 2\zeta_T J \omega_T$$

The damping term in the last of Equations 3 is included to account for a small amount of rotational "play" in the airfoil drive shaft which tends to cause oscillations in TDOF to damp out. In Equation 4, ζ_T is the damping ratio which was estimated to be 0.05 and ω_T is the natural frequency in the TDOF. The solution of Equations 3 for the generalized coordinates $q_1(t)$, $q_2(t)$, and $g(t)$ subject to a prescribed RDOF input parameter $p(t)$, is described below.

Aeroelastic Normal Forces

The normal force acting on the structure is decomposed into a rigid body force vector, F_R , associated with the RDOF, an aeroelastic force vector, F_A , due to time dependent aeroelastic deflections along the span of the airfoil, and an inertial force vector, F_I , so that in Equations 3, $F = F_R + F_A + F_I$.

The rigid body force vector is the ideal aerodynamic loading response to a step change in angle of attack due to rotation about the quarter chord. These aerodynamic forces are exerted only on the submerged part of the airfoil represented by masses 15 through 23 of Figure 1b. For a given motion input $p(t)$, the vector F_R at any time, t , at or after the step is given by :

$$F_{Ri} = 0, \quad i = 1, 2, \dots, 14$$

$$F_{Ri}(t) = \pi L_i \left\{ \dot{p}(t) + \frac{1}{2} \ddot{p}(t) \right\} + C_{N\alpha} L_i \int_0^t \left(\dot{p}(\tau) + \ddot{p}(\tau) \right) \Gamma(t-\tau) d\tau \quad (5)$$

$$, i = 15, 16, \dots, 23$$

where $C_{N\alpha}$ is the static normal force curve slope, L_i is the span of the i^{th} airfoil element, and $\Gamma(t-\tau)$ is the indicial lift response given by either Equation 1b or Equation 1c. Notice that F_R is not a function of the generalized coordinates $q_1(t)$, $q_2(t)$, and $g(t)$ since in the ideal response the loading is given by (rigid body) 2-D airfoil theory alone. Notice also that if $p(t)$ is a unit step function of amplitude $\Delta\alpha$ and L_i is unity, Equation 5 becomes identical to Equation 1a.

The aeroelastic force vector is also based on the convolution integral formulation for an airfoil in arbitrary motion, and again acts only on the submerged part of the airfoil. For the pitch axis at the quarter chord the loading is:

$$F_{Ai} = 0, \quad i = 1, 2, \dots, 14$$

$$F_{Ai}(t) = \pi L_i \left\{ -(\phi_{N1i} \ddot{q}_1(t) + \phi_{N2i} \ddot{q}_2(t)) + \phi_{Ti} \left(\dot{g}(t) + \frac{1}{2} \ddot{g}(t) \right) \right\} +$$

$$C_{N\alpha} L_i \int_0^t \left[-(\phi_{N1i} \ddot{q}_1(\tau) + \phi_{N2i} \ddot{q}_2(\tau)) + \phi_{Ti} (\dot{g}(\tau) + \ddot{g}(\tau)) \right] \Gamma(t-\tau) d\tau \quad (6)$$

$$, i = 15, 16, \dots, 23$$

where ϕ_{N1i} and ϕ_{N2i} are the values of the NDOF1 and NDOF2 mode shapes at element i , respectively, and ϕ_{Ti}

is the value of the TDOF mode shape. The negative sign on the NDOF terms is due to the sign convention adopted.

The inertial loading arises from the fact that the centroids of masses 13 through 23 do not coincide with the pitch axis. Thus, angular acceleration about the pitch axis produces an inertial normal force which acts at the centroid. The inertial force vector is:

$$\begin{aligned} F_{Ii} &= 0 & , i &= 1, 2, \dots, 12 \\ F_{Ii}(t) &= m_i r_i \{ \phi_{Ti} \ddot{g}(t) + \ddot{p}(t) \} & , i &= 13, 14, \dots, 23 \end{aligned} \quad (7)$$

where m_i is the mass of element i and r_i is the distance from the pitch axis to the centroid.

Aeroelastic Moments

The moments acting on the inertial elements of Figure 1b are also decomposed into a rigid body moment vector, T_R , an aeroelastic moment vector, T_A , and an inertial moment vector, T_I , giving a total moment of: $T = T_R + T_A + T_I$. The rigid body moment and the aeroelastic moment act only on the submerged part of the airfoil. The expressions for these components are simplified by the fact that the circulatory normal force acts at the quarter chord (for a flat plate airfoil) giving a zero moment arm in the present study. For a NACA 0015 airfoil the circulatory normal force (at $Re \sim 10^5$) acts within 2% fraction of chord from the quarter chord and on this basis has been neglected. The rigid body moment for rotation about the quarter chord is:

$$\begin{aligned} T_{Ri} &= 0 & , i &= 1, 2, \dots, 14 \\ T_{Ri}(t) &= -\pi L_i \{ \dot{p}(t) + \frac{3}{8} \ddot{p}(t) \} & , i &= 15, 16, \dots, 23 \end{aligned} \quad (8)$$

The aeroelastic moment vector acting on an airfoil in arbitrary motion with the pitch axis at the quarter chord is given by:

$$\begin{aligned} T_{Ai} &= 0 & , i &= 1, 2, \dots, 14 \\ T_{Ai}(t) &= \pi L_i \{ \frac{1}{2} (\phi_{N1i} \ddot{q}_1(t) + \phi_{N2i} \ddot{q}_2(t)) - \phi_{Ti} (\dot{g}(t) + \frac{3}{8} \ddot{g}(t)) \} & , i &= 15, 16, \dots, 23 \end{aligned} \quad (9)$$

The inertial moment vector is:

$$\begin{aligned} T_{Ii} &= 0 & , i &= 1, 2, \dots, 12 \\ T_{Ii}(t) &= m_i r_i (\phi_{N1i} \ddot{q}_1(t) + \phi_{N2i} \ddot{q}_2(t)) - J_i \ddot{p}(t) & , i &= 13, 14, \dots, 23 \end{aligned} \quad (10)$$

where J_i is the mass moment of inertia of element i .

Input Rigid Body Motion

Two input motions have been considered and are illustrated in Figure 4. The first motion is a step function input of magnitude $\Delta\alpha$ and the second input is small amplitude ramp modeled after the experimental angle of

attack of Figure 2. These motions are expressed mathematically by:

$$p(t) = \Delta\alpha \mu(t-0) \quad (\text{step}) \quad (11a)$$

$$p(t) = \frac{\Delta\alpha}{\tau_s} t (\mu(t-0) - \mu(t-\tau_s)) + \Delta\alpha \mu(t-\tau_s) \quad (\text{ramp}) \quad (11b)$$

where μ is the unit step function, and τ_s ($=0.13$ semichords) is the ramp duration which is determined from the experimental angle of attack data. One of Equations 11a or 11b is substituted into Equations 5, 7, 8, and 10 and the generalized forces and moments are formulated by performing the vector multiplications indicated on the RHS of Equations 3. The result is three simultaneous second order differential equations in terms of the generalized coordinates $q_1(t)$, $q_2(t)$, and $g(t)$.

Solution of the Generalized Equations of Motion

The Laplace transform method is used to transform the three generalized differential Equations 3 into three algebraic equations which are linear in terms of the transformed generalized coordinates. These equations are solved simultaneously for the transformed generalized coordinates as functions of the Laplace variable, s . The inverse Laplace transform is performed to transform these solutions to the time domain to obtain $q_1(t)$, $q_2(t)$, and $g(t)$. The Laplace transform of each of Equations 3 can be done by hand using standard tables. To perform the extensive algebra required in the solution, the computer program MACSYMA has been used. MACSYMA is capable of symbolic mathematics required in the solution of the simultaneous equations in terms of the Laplace variable s . The resulting equations of motion in the Laplace transform domain are quite long and are omitted here for brevity. Once the Laplace transforms have been done the solution proceeds by first rearranging, using MACSYMA, the system of three equations into the following form:

$$\{X(s)\} = \{R(s)\} P(s) \quad (12)$$

Here, $\{X(s)\}$ is a 3x1 vector given by:

$$\{X(s)\} = \begin{Bmatrix} Q_1(s) \\ Q_2(s) \\ G(s) \end{Bmatrix} \quad (13)$$

where $Q_1(s)$ is the Laplace transform of $q_1(t)$, $Q_2(s)$ of $q_2(t)$, and $G(s)$ of $g(t)$. In Equation 12, $P(s)$ is the Laplace transform of the motion input parameter $p(t)$ (Equation 11) and the 3x1 vector $\{R(s)\}$ is an aeroelastic transfer function which is a function of the Laplace variable s only.

Substitution of a particular input motion, $P(s)$, into Equation 12 gives the solution for the generalized coordinates in the Laplace domain. For the step input of Equation 11a, the result for each generalized coordinate is in the form of a quotient of two polynomials in s , wherein the numerator is a tenth order polynomial and the denominator is an eleventh order polynomial. The inverse Laplace transform is accomplished by decomposing the quotients using partial fractions into functions which can be inverted by hand. In the partial fraction decomposition MACSYMA has been used to find the roots of the polynomial in the denominator. The denominator has five real roots which can be traced directly to the constants appearing in the indicial response function, Γ . The denominator further has three pairs of complex conjugate roots which

represent the oscillatory (harmonic) response of the structure at the three frequencies associated with the NDOF1, NDOF2, and TDOF. The numerical values of the frequencies of the harmonic response can be traced to the mass (including apparent mass) and stiffness terms in the governing aeroelastic equations. The set of simultaneous equations for the undetermined constants in the expansion terms has been solved using the IMSL subroutine LSARG.

The solutions for the generalized coordinates $q_1(t)$, $q_2(t)$, and $g(t)$ can be represented generally by the function $f(t)$ which has the following form:

$$f(t) = A - Be^{-bt} - Ce^{-ct} - De^{-dt} - Fe^{-ft} + e^{-ht}(G\sin\omega_1 t + H\cos\omega_1 t) + e^{-jt}(J\sin\omega_2 t + K\cos\omega_2 t) + e^{-mt}(M\sin\omega_3 t + N\cos\omega_3 t) \quad (14a)$$

where the constants are given in the following table. The constants in Tables 2 and 3 were computed using the Wagner function for the indicial lift function, Γ .

Table 2. Constants for Generalized Coordinates for Step Input

	$q_1(t)$	$q_2(t)$	$g(t)$
A	1.241e-2	1.196e-4	0
B	-1.333e-3	-4.401e-6	-9.421e-9
C	-6.816e-4	-1.412e-5	7.451e-9
D	-3.123e-3	1.513e-5	-1.558e-7
F	-7.615e-5	-4.179e-5	2.095e-9
G	8.408e-3	-3.066e-5	-5.537e-5
H	2.042e-2	-9.538e-5	-4.836e-5
J	7.322e-4	7.162e-3	-3.272e-4
K	1.403e-4	1.661e-3	-5.603e-5
M	-1.585e-2	-7.001e-3	-2.075e-2
N	-2.374e-4	2.455e-4	7.555e-4

The remaining constants apply to each of $q_1(t)$, $q_2(t)$, and $g(t)$

$$b = -0.04522$$

$$c = -0.04565$$

$$d = -0.2877$$

$$f = -0.29989$$

$$h = -0.55591$$

$$j = -0.49752$$

$$m = -2.71184$$

$$\omega_1(\text{NDOF1}) = 2.23361$$

$$\omega_2(\text{NDOF2}) = 12.186$$

$$\omega_3(\text{TDOF}) = 52.2147$$

For the sudden ramp input of Equation 11b, the solution in the Laplace domain for each generalized coordinate is in the form of an eleventh order polynomial in s divided by a twelfth order polynomial. The solutions for $q_1(t)$, $q_2(t)$, and $g(t)$ in the time domain can be represented by a function of the form: $f(t) - \mu(t-\tau_s) f(t-\tau_s)$ (e.g. $q_1(t) = f(t) - \mu(t-\tau_s) f(t-\tau_s)$), where τ_s is the ramp duration (0.13 semichords), and $\mu(t-\tau_s)$ is the unit step function. The "shifting" in time of the function $f(t-\tau_s)$ is due to the exponential terms in the Laplace transform of those terms containing $\mu(t-\tau_s)$ in Equation 11b. In the ramp case, $f(t)$ has the form:

$$f(t) = A + Et + Be^{-bt} + Ce^{-ct} + De^{-dt} + Fe^{-ft} + e^{-ht}(G\sin\omega_1 t + H\cos\omega_1 t) + e^{-jt}(J\sin\omega_2 t + K\cos\omega_2 t) + e^{-mt}(M\sin\omega_3 t + N\cos\omega_3 t) \quad (14b)$$

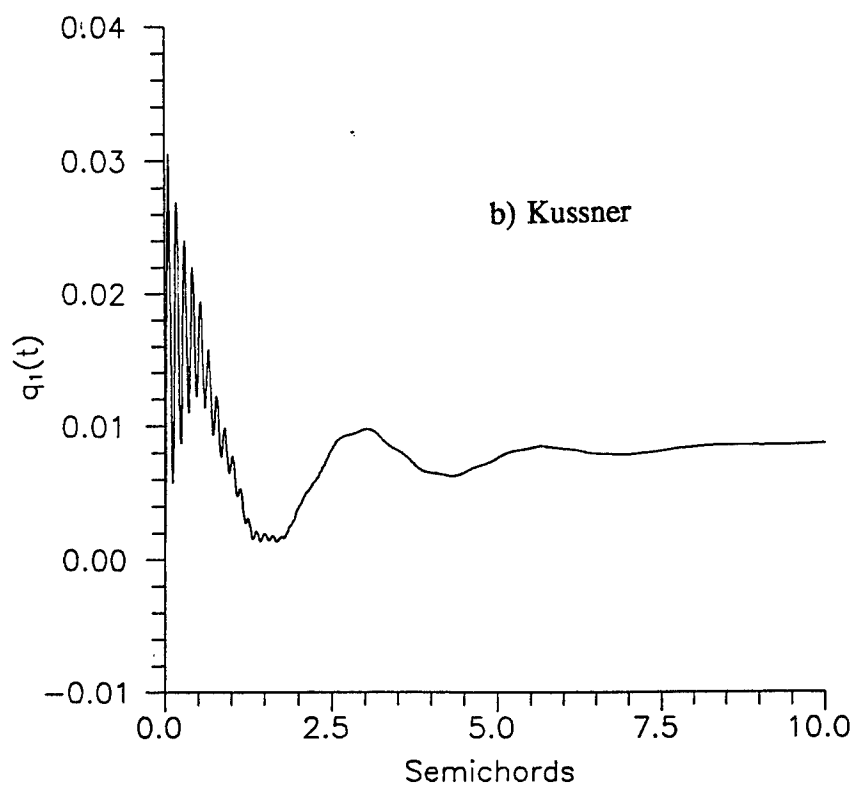
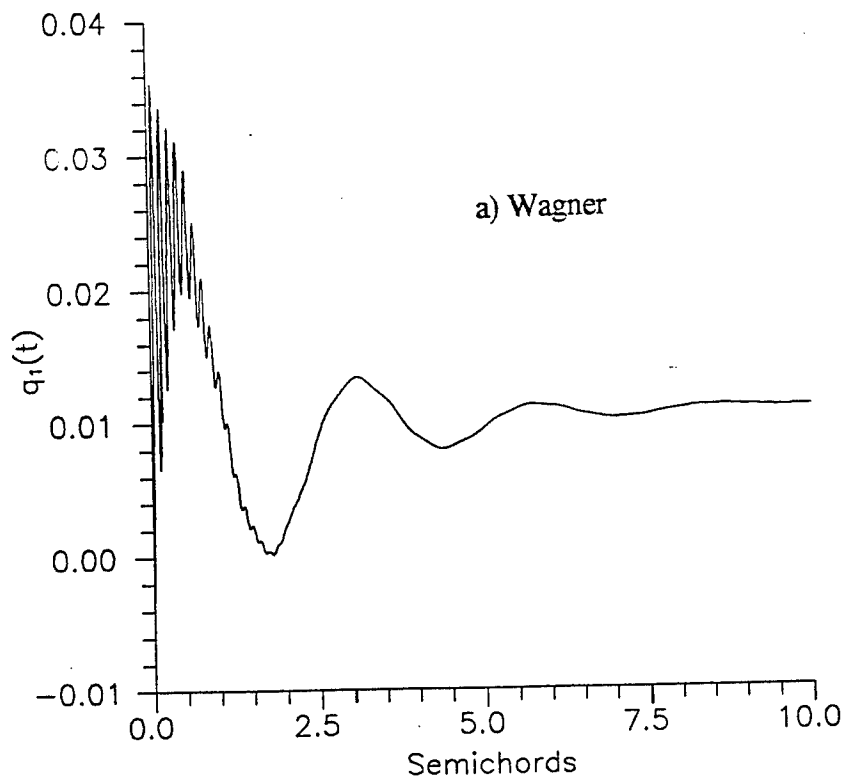
Notice the ramp motion gives rise to a term proportional to time t . This might be expected since the ramp motion produces an upwash at the 3/4 chord proportional to t . For times beyond τ_s , this term goes to $E\tau_s$ ($=\text{const}$) and combines with A to give the steady state lift. The constants in $f(t)$ and are given in the following table.

Table 3. Constants for Generalized Coordinates for Sudden Ramp Input

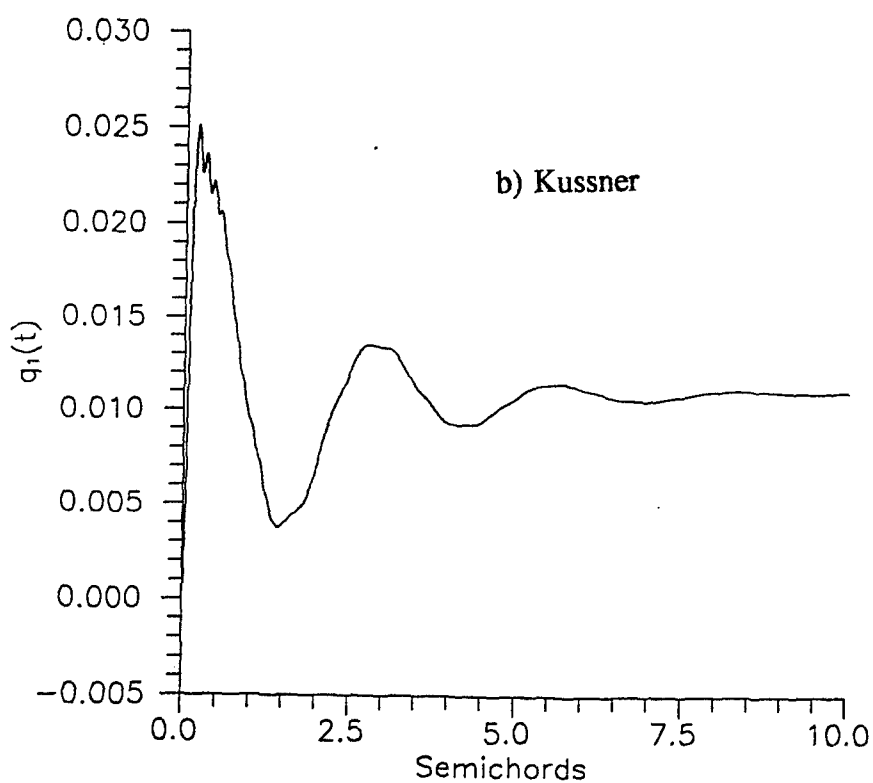
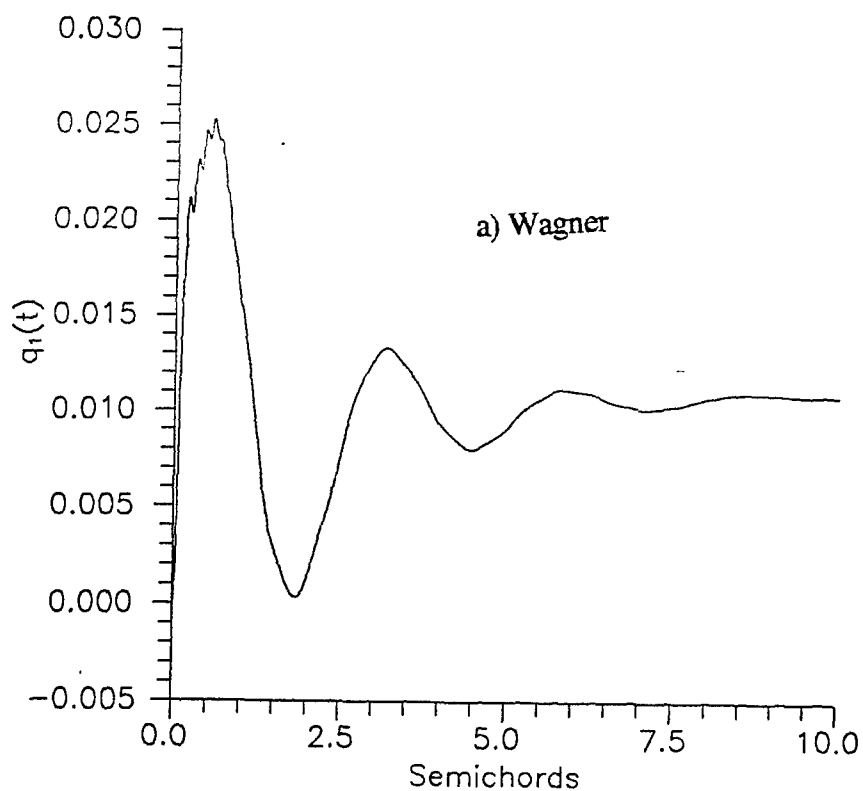
	$q_1(t)$	$q_2(t)$	$g(t)$
A	-0.319	-2.534e-3	-2.868e-4
B	0.328	-1.394e-3	3.474e-6
C	1.982e-2	4.338e-3	-2.641e-7
D	4.587e-2	-2.434e-5	1.952e-6
E	9.529e-2	9.186e-4	0
F	-4.210e-6	3.426e-6	-1.834e-8
G	-3.150e-2	1.363e-4	1.152e-4
H	3.633e-2	-1.557e-4	-1.448e-4
J	-3.567e-5	-6.068e-4	3.344e-5
K	4.638e-4	4.542e-3	-2.055e-4
M	1.788e-4	8.112e-5	1.330e-4
N	-2.317e-3	-1.024e-3	-3.045e-3

*The values of the remaining constants are the same as given in Table 2.

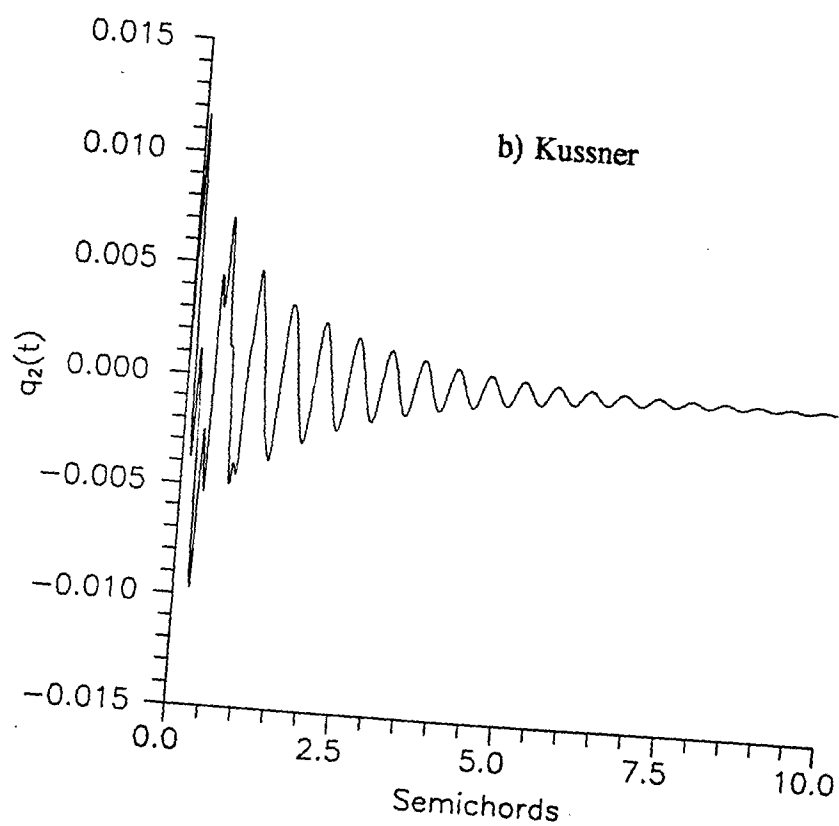
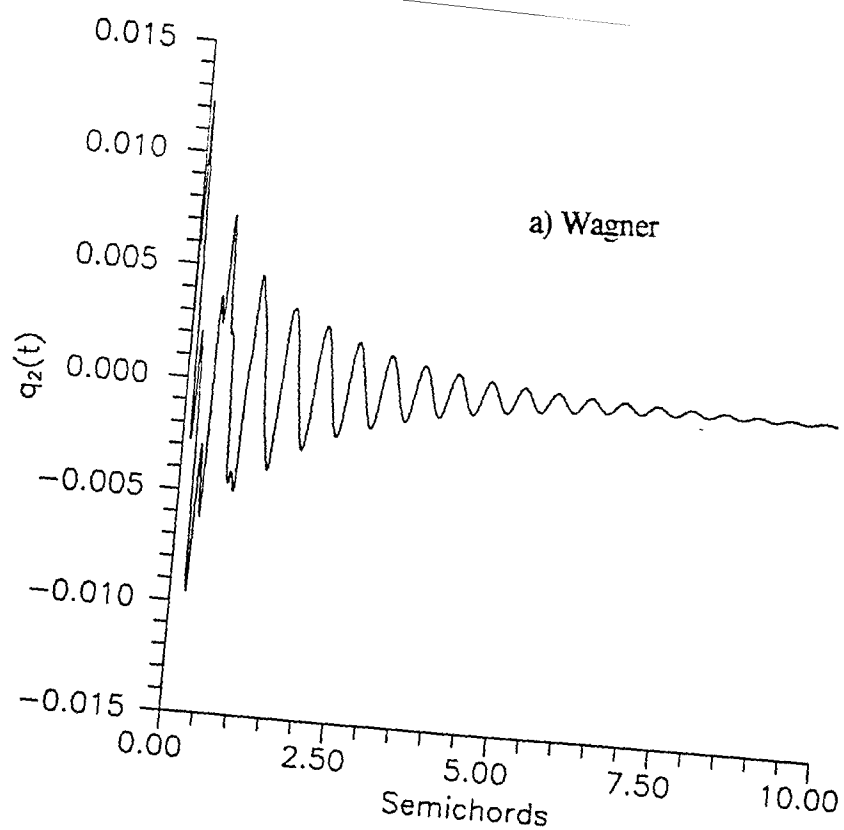
The above solutions are in closed form and have the mathematical properties that might be anticipated. That is, the exponential terms giving the response to a circulatory build-up in lift after the motion input, and an oscillatory component which occurs at three distinct frequencies that arise due to the modal coupling in the forcing terms on the RHS of Equations 3. Notice the reduction in the frequencies in the results above from the natural frequencies (given previously) in the respective modes due to apparent mass effects. The solutions given above are plotted in Figures 5a-l where the modal coupling can be observed in the frequency content of each modal solution. The solutions are given for both the step and ramp motions and have been calculated using



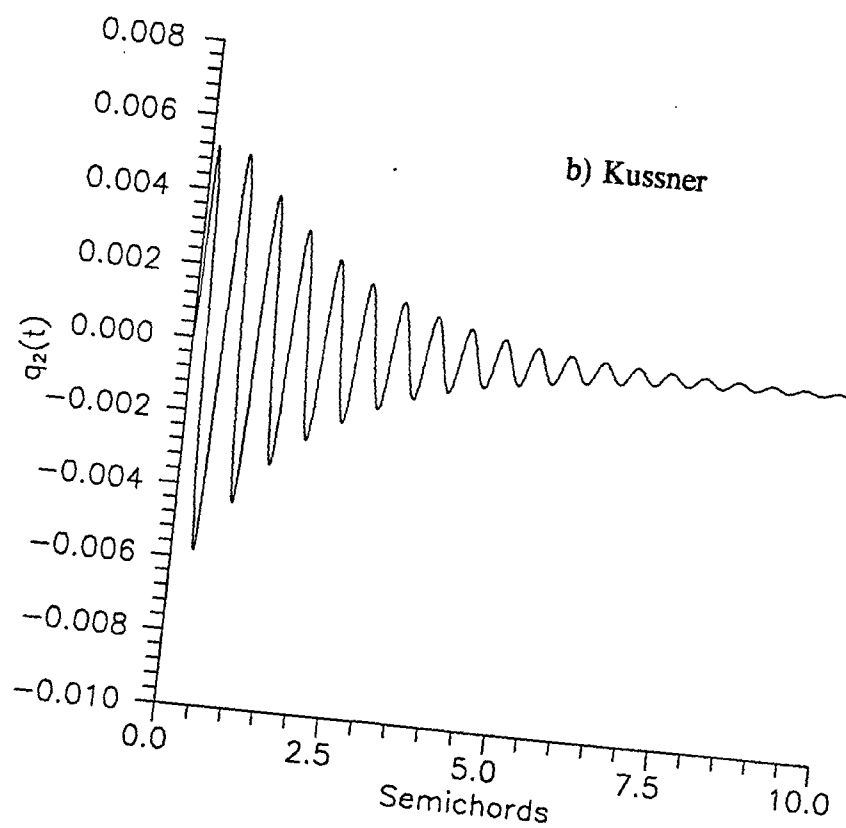
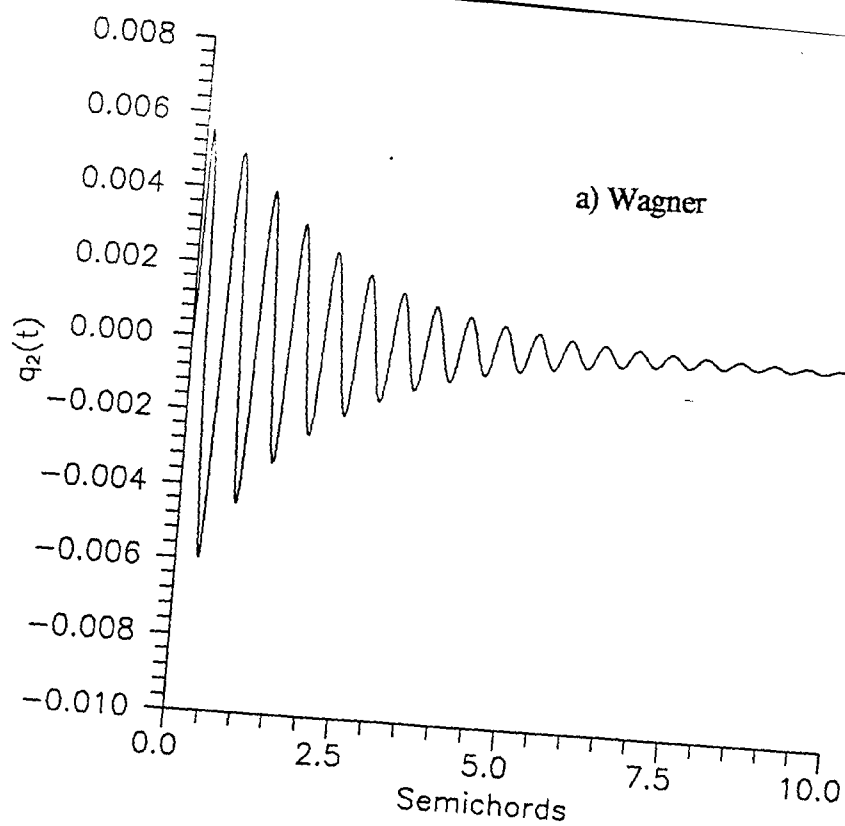
Figures 5a and 5b. Step Solution for the NDOF1 Generalized Coordinate $q_1(t)$ using:
a) Wagner function, b) Kussner function



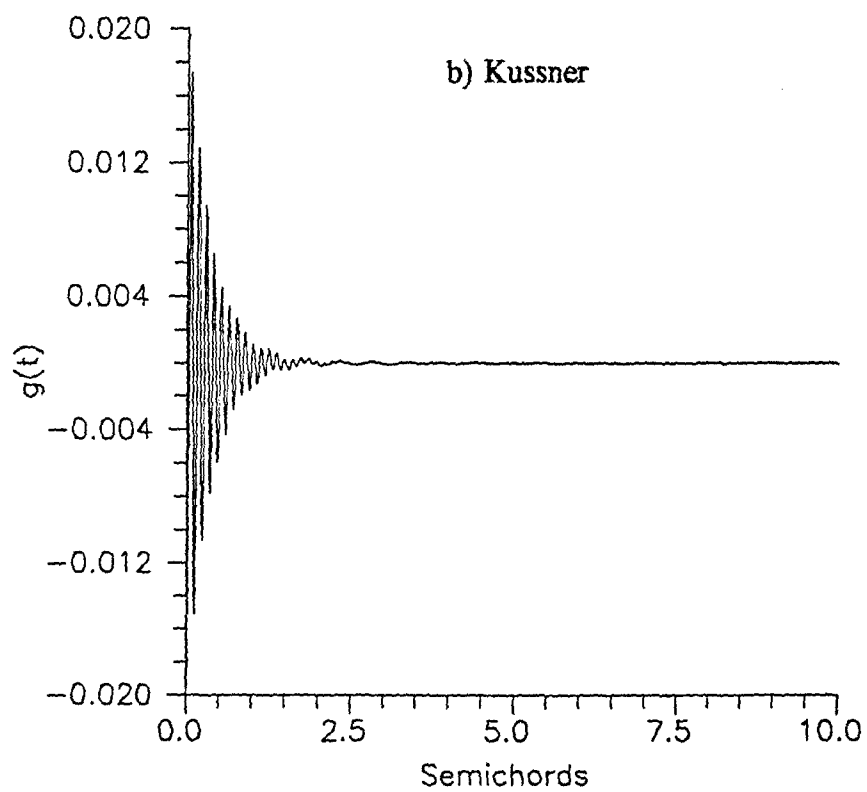
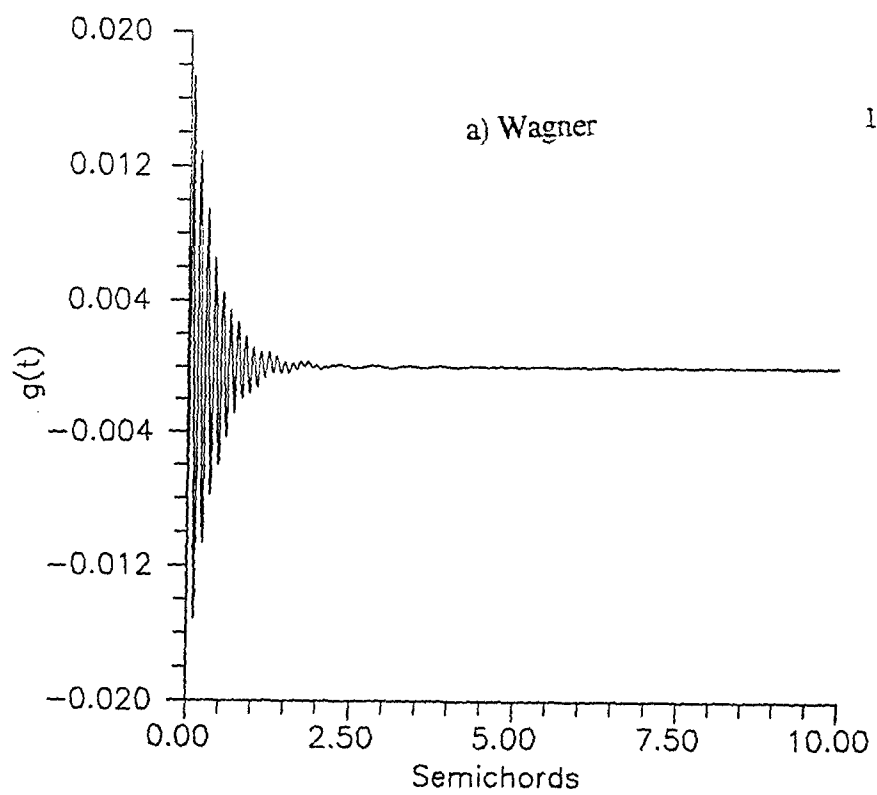
Figures 5c and 5d. Ramp Solution for the NDOF1 Generalized Coordinate $q_1(t)$ using:
a) Wagner function, b) Kussner function



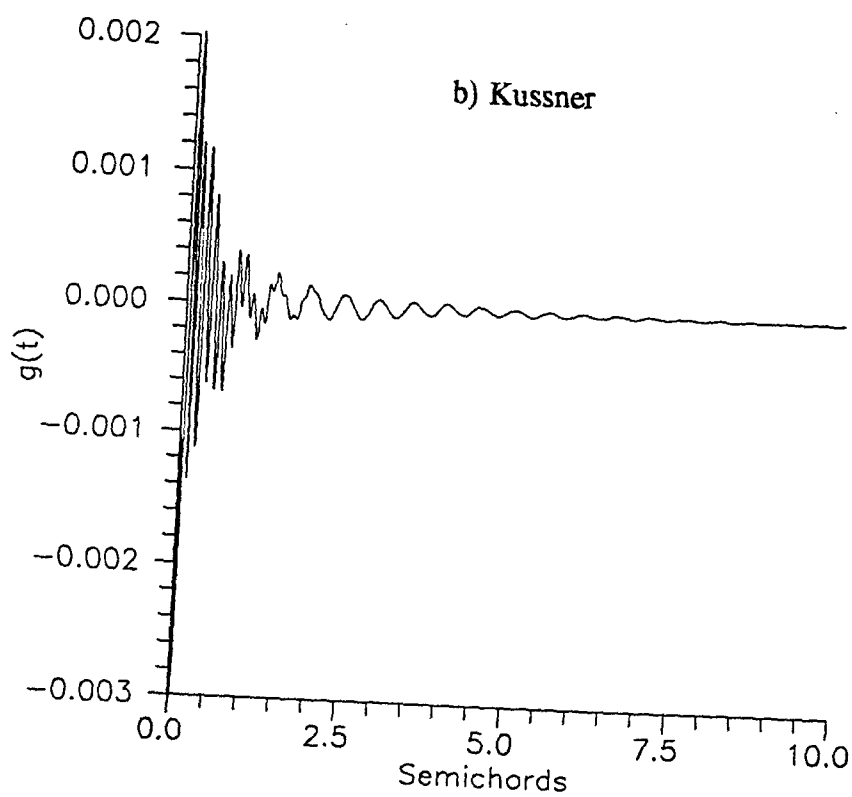
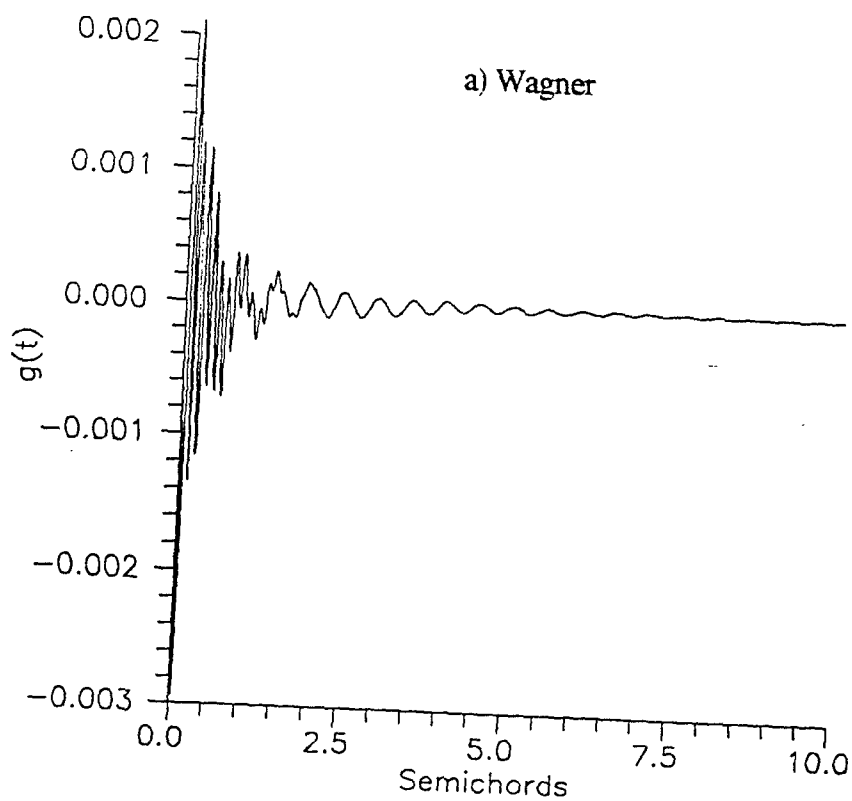
Figures 5e and 5f. Step Solution for the NDOF2 Generalized Coordinate $q_2(t)$ using:
a) Wagner function, b) Kussner function



Figures 5g and 5h. Ramp Solution for the NDOF2 Generalized Coordinate $q_2(t)$ using:
a) Wagner function, b) Kussner function



Figures 5i and 5j. Step Solution for the TDOF Generalized Coordinate $g(t)$ using:
a) Wagner function, b) Kussner function



Figures 5k and 5l. Ramp Solution for the TDOF Generalized Coordinate $g(t)$ using:
a) Wagner function, b) Kussner function

both the Wagner function and the Kussner function as the indicial lift. The conditions are indicated in the caption of each figure. As might be expected the step input tends to excite the higher frequency TDOF more than the ramp input.

It is of course possible to input other motions than those of Equations 11a and 11b. For example, the trigonometric function: $p(t) = (\Delta\alpha/2\pi)(\omega_s t - \sin\omega_s t)(\mu(t-0) - \mu(t-\tau_s)) + \Delta\alpha\mu(t-\tau_s)$ may be used to represent the step, where $\omega_s = 2\pi/\tau_s$. This function has continuous first and second derivatives. The solution for the generalized coordinate is of the form $f(t) - \mu(t-\tau_s) f(t-\tau_s)$, where:

$$f(t) = A + Et + (U\sin\omega_s t + V\cos\omega_s t) + Be^{-bt} + Ce^{-at} + De^{-dt} + Fe^{-ft} + e^{-ht}(G\sin\omega_1 t + H\cos\omega_1 t) + e^{-jt}(J\sin\omega_2 t + K\cos\omega_2 t) + e^{-mt}(M\sin\omega_3 t + N\cos\omega_3 t) \quad (14c)$$

Notice that the period of ω_s is τ_s and consequently, the harmonic terms containing ω_s cancel identically for times greater than τ_s (according to $f(t) - \mu(t-\tau_s) f(t-\tau_s)$). The results for this input are similar to the ramp input and are not presented here.

Calculation of the Sensible Normal Force at the Load Cell

The purpose of the present analysis is to determine the effects of aeroelasticity on the output of the strain gauge load cell used in the experiments described above. In these experiments the strain gauge output is interpreted ideally as that due to a moment exerted by a normal force applied at the midspan of the submerged part of the airfoil (point loads were applied here to calibrate the strain gauge bridge). In reality, however, this is not the case since the strain gauge output is determined solely by the instantaneous beam curvature at the cell. This curvature is due, not to aerodynamic loading alone, but rather the total aeroelastic structural response.

From beam theory the moment at the center of the load cell (centroid of element 7) is related to the beam curvature by:

$$M_{LC}(t) = EI \left\{ q_1(t) \frac{d^2\phi_{N1}}{dx^2} \right\}_7 + q_2(t) \frac{d^2\phi_{N2}}{dx^2} \Big|_7 \quad (14)$$

where x is measured along the span. The second derivative has been computed numerically from the NDOF mode shapes for elements 5 through 9 using a five point numerical derivative given by Richardson's extrapolation method [10]. A time dependent "sensible" normal force acting at the midspan of the submerged portion of the airfoil which produces the same moment as that given by Equation 14 may then be defined for comparison with experimental normal force data. For this purpose, the moment arm between the mass 7 and the midspan is $L_{LC} = 37.0$ in. These results are presented in the form of a sensible normal force coefficient defined as:

$$C_N(t) = C_{N0} + \frac{M_{LC}(t)/L_{LC}}{\rho U^2 b L} \quad (15)$$

where C_{N0} is normal force at the origin of the motion, ρ is the density of water, and L is the submerged airfoil length (42.0 in), U and b are the freestream velocity and the semichord length, respectively.

Results

Sensible force calculations using the present model are compared below with the experimental normal force data of Reference [4]. A comparison is also made with recent accelerometer data taken on the Ohio U. tow tank rig undergoing the motion illustrated in Figure 2. In these tests an accelerometer (PCB Flexcel Series 336A) was placed on mass 13 (see Figure 1b) with the accelerometer centered on the pitch axis. The accelerometer data have been integrated once and put in the form of velocity. The present model can predict velocity at any point on the structure by taking the time derivative of Equations 2. The accelerometer data and normal force data below were acquired in separate runs.

Sensible Force and Accelerometer Comparisons

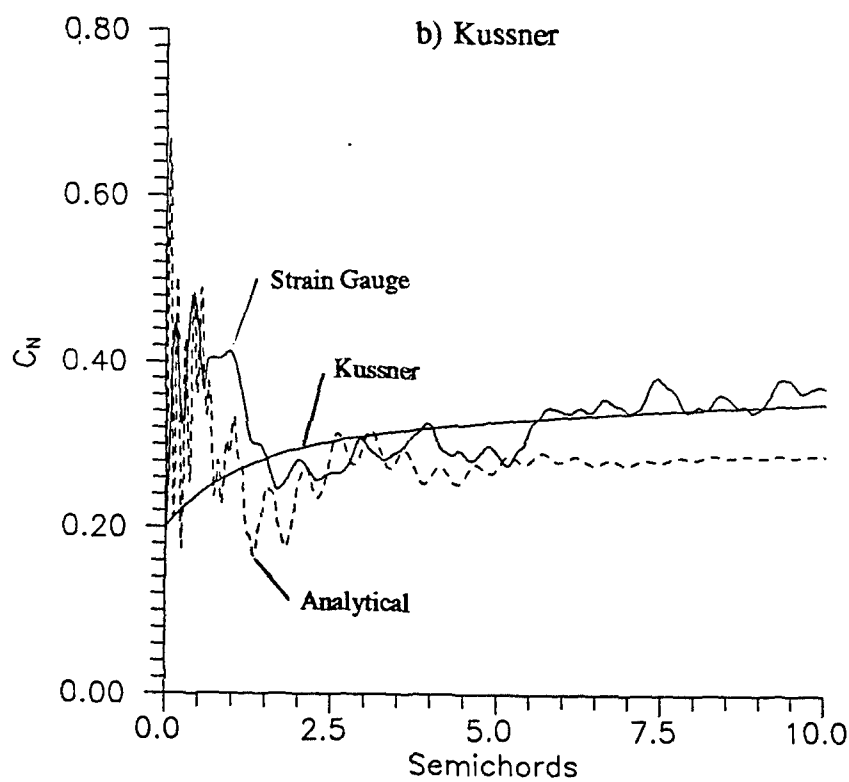
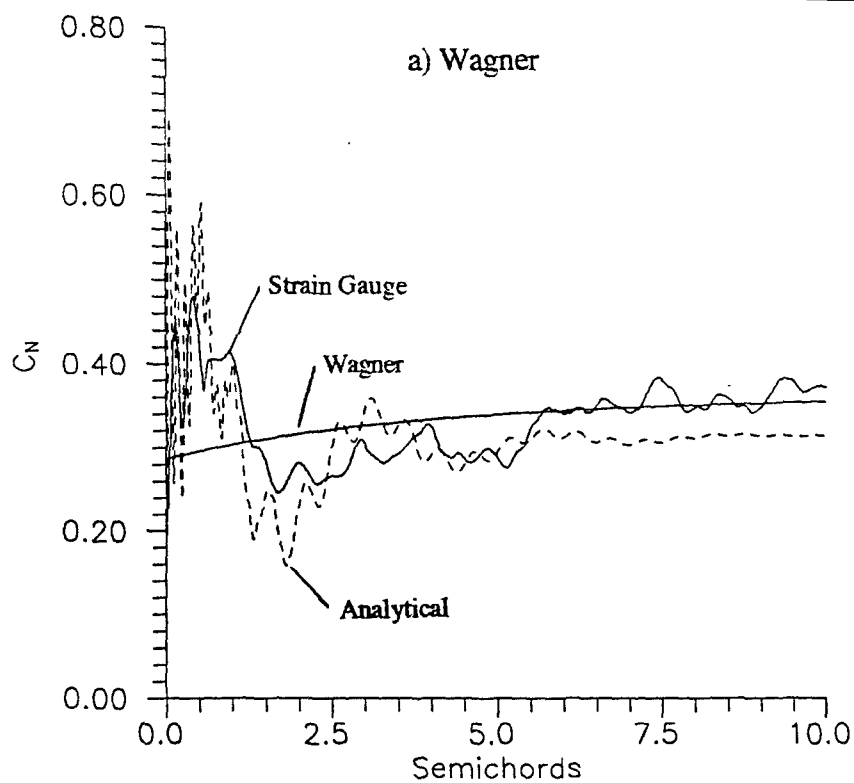
The two motion inputs given by Equations 11a and 11b have been considered. The sensible force corresponding to the step input is compared with experimental strain gauge data in Figures 6a and 6b. Figure 6a has been computed using Wagner's function and Figure 6b has been computed using Kussner's function. Also shown is the theoretical response based on the Wagner function and Kussner function, respectively. There are three frequencies present in the aeroelastic model. The lowest frequency has a period of approximately 2.5 semichords and is associated with the NDOF1 fundamental mode. The second frequency has a period of about 0.5 semichords and is due to the NDOF2 mode, and the third highest frequency with a period near 0.1 semichord is due to the coupling between the TDOF and the NDOF1 and NDOF2. It is clear that aeroelastic reactions have caused significant deviation from the theoretical response particularly before about 2 semichords.

The sensible force based on the aeroelastic response with the sudden ramp input of Equation 11b is illustrated in Figures 6c and 6d. The response directly after the motion inception is in better agreement with the strain gauge data than the step input results. A comparison of the aeroelastic response of Figures 6a,b and 6c,d indicates that the step input of excites the NDOF and TDOF coupling more than the sudden ramp motion. The experimental data exhibit discernible oscillations, which in the analytical force, are associated with the NDOF2 mode. Notice from Figures 5g,h that the NDOF2 oscillations require a significant period of time to damp out. It should be noted that the uncertainty in the experimental data is near 10%.

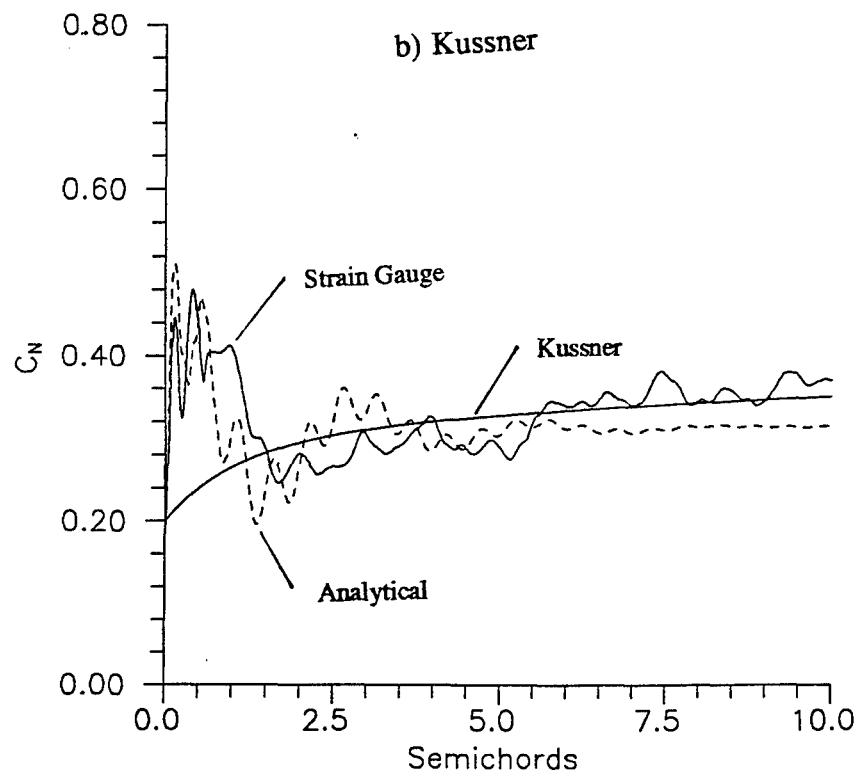
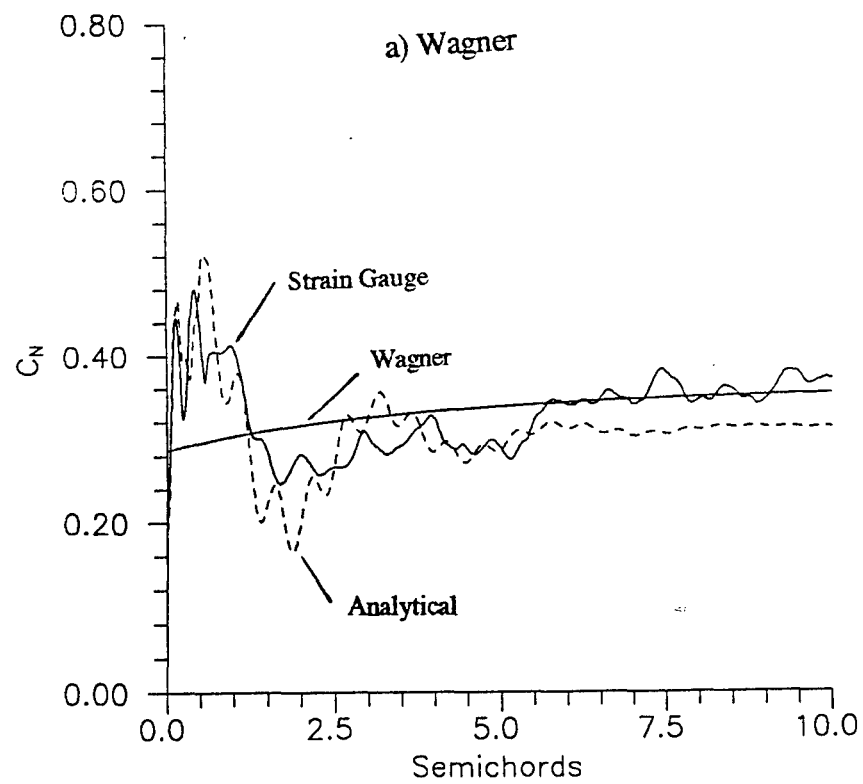
A comparison between the aeroelastic analysis using motion 1 step input and accelerometer data is shown in Figure 7a (based on Wagner function). The accelerometer data have been integrated numerically and put in the form of velocity data. Again, the use of the step function input excites the TDOF mode more than the experimental data indicates. The use of the sudden ramp motion gives the results of Figure 7b (based on Wagner function) where the agreement between the experimental data and the analysis is very good. Use of Kussner's function gives results similar to those in Figures 7a and 7b.

Conclusion

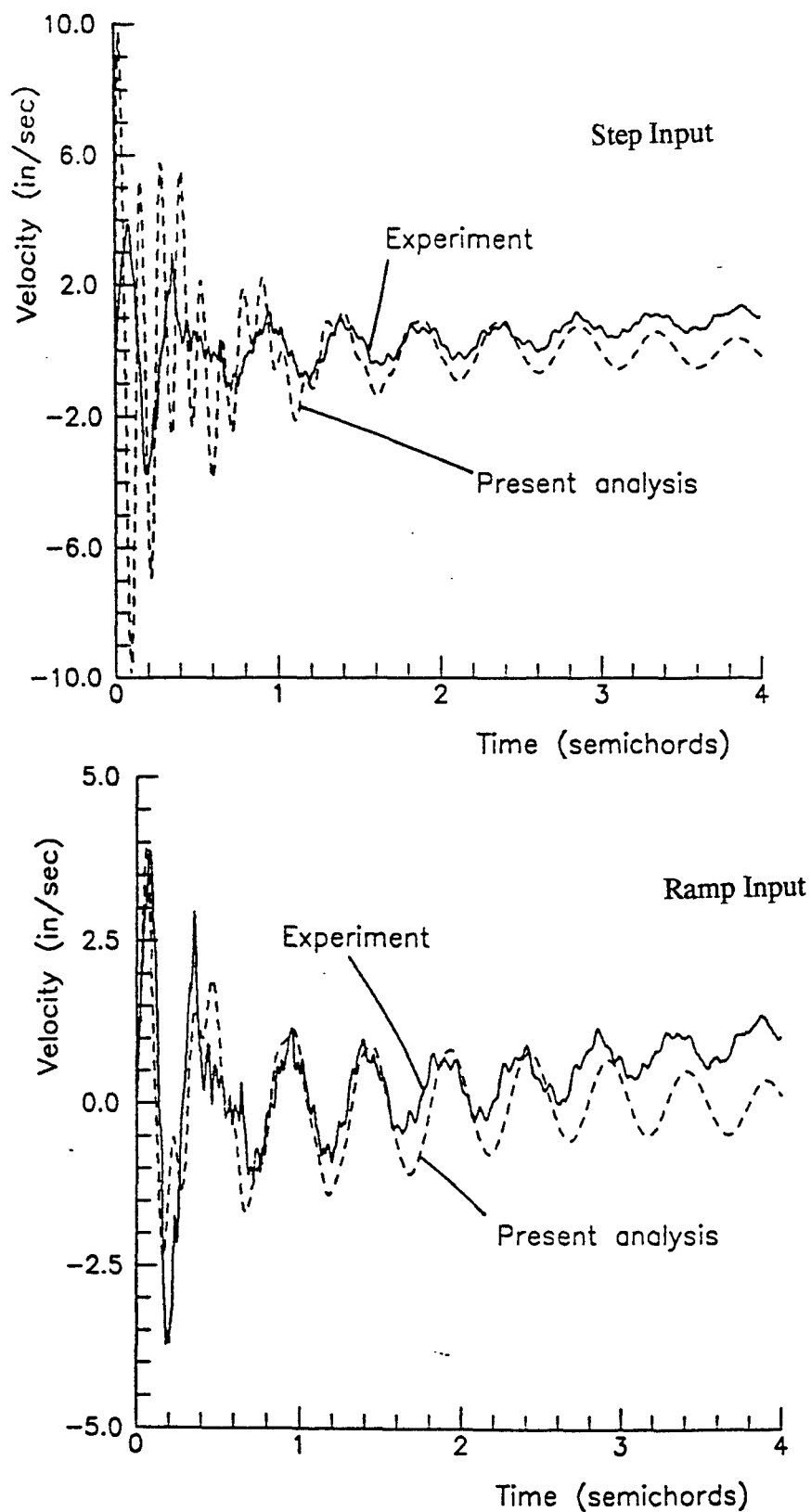
The present analysis has been conducted to determine the effect of aeroelastic reactions on airfoil indicial response tests conducted in the Ohio U. tow tank. The analysis has been validated to a reasonable level of accuracy by comparing with strain gauge and accelerometer data. The results indicate that aeroelasticity causes significant deviation from the 2-D theoretical response shortly after the motion inception. The focus of future



Figures 6a and 6b. Sensible Force Results for Step Input using: a) Wagner function, b) Kussner function



Figures 6c and 6d. Sensible Force Results for Ramp Input using: a) Wagner function,
b) Kussner function



Figures 7a and 7b. Comparison of Velocity Predictions (using Wagner function) and Integrated Accelerometer Data for Step and Ramp Input Motions

research will be to use the present aeroelastic model as a basis for correcting the indicial response strain gauge data of Reference [4] for aeroelastic effects. In some sense, this amounts to working the present analysis in reverse. That is, in the present analysis we are given an indicial lift function, and for a given motion we compute the aeroelastic response. In the reverse problem we are given an aeroelastic response for a given motion, and we seek to compute the indicial lift function which produces the response.

Acknowledgement

This work was further supported under AFOSR Grant F49620-93-0030, under the management of Major Danial Fant, USAF. The authors are grateful to Mr. Jerry E. Jenkins of Wright Laboratories for his valuable suggestions during the course of this project.

References

- ¹Bisplinghoff, R.L., Ashley, H., and Halfman, R.L., *Aeroelasticity*, Addison-Wesley, Boston, Mass., 1957.
- ²Chow, C.Y. and Huang, M.K., "The Initial Lift on an Impulsively Started Airfoil of Finite Thickness," *J. Fluid Mechanics*, vol. 118, pp. 393-409, 1982.
- ³Beddoes, T.S., "Practical Computation of Unsteady Lift," *Vertica*, vol. 8, pp. 55-71, 1984.
- ⁴Graham, G. M., Islam, M. and Jenkins, J. E., "Nonlinear Normal Force Indicial Responses for a 2-D Airfoil," AIAA Paper No. AIAA-91-2866-CP, New Orleans, La., Aug. 12-14, 1991 .
- ⁵Tobak, M. and Schiff, L.B., "Aerodynamic Mathematical Modeling-Basic Concepts," AGARD Lecture Series No.114, Paper 1, March 1981.
- ⁶Kaplan, W.K., *Advanced Calculus*, Addison-Wesley Publishing Co., 2nd ed., pp. 515-521.
- ⁷Clough, R.W. and Penzien, J., *Dynamics of Structures*, McGraw Hill Publisher, 1975.
- ⁸Fung, Y.C., *An Introduction to the Theory of Aeroelasticity*, Dover Publications, New York, 1969.
- ⁹Higdon, A. et al., *Mechanics of Materials*, Wiley and Sons, Inc. Publisher, New York, 1960.
- ¹⁰Burden, R.L., Farres, J.D., and Reynolds, A.C., *Numerical Analysis*, Prindle, Weber & Schmidt Boston, Ma., 1980, p.185.

VIRTUAL REALITY INFORMATION PRESENTATION TECHNOLOGY
FOR AVIONICS

Elmer A. Grubbs
Assistant Professor
Department of Engineering

New Mexico Highlands University
Las Vegas, New Mexico 87701

Final Report for:
Summer Research Extension Program

Sponsored by:
Air Force Office of Scientific Research
Bolling AFB, Washington D.C.
and
New Mexico Highlands University
Las Vegas, New Mexico

December 1993

VIRTUAL REALITY INFORMATION PRESENTATION TECHNOLOGY
FOR AVIONICS

Elmer A. Grubbs
Assistant Professor
Department of Engineering
New Mexico Highlands University

ABSTRACT

This report is on a continuation of work begun during the summer 1992 as a researcher under the Air Force Office of Scientific Research (AFOSR) at Wright Laboratory's Avionics Directorate, (WL/AAAF). This project builds upon the results of the participation in WL/AAAF's avionics Virtual Reality (VR) research. Specifically, we have enhanced the VR three dimensional (3-D) presentation technology invented during the summer, and extended the research into other related areas. The technology that provides three dimensional television viewing has been extended to computer monitors. Additionally, work has been done to enhance the picture quality, extend the work from black and white to color, and to begin the capability of supporting multiple monitors. The prototype system has been redesigned to simplify it and make it more reliable and easy to move around. Several additional 3-D techniques have been investigated. This work will provide an added dimension and reduce costs to the visualization of avionics related information such as flight simulation, out-the-window displays, plotting of numerical data, and avionics software documentation.

VIRTUAL REALITY INFORMATION PRESENTATION TECHNOLOGY FOR AVIONICS

Elmer A. Grubbs

INTRODUCTION

Virtual reality is fast becoming a very important technology. It seems that it has the potential to enter into nearly every portion of the nation's research and development communities. It will be especially important in the Air Force Laboratories. The Avionics Directorate will be deeply involved in using this technology to help solve avionics related problems. One of the important hardware concerns is how to display the three dimensional data to the user. Up to this point there have been two general approaches to this problem. The first is to use a head mounted display (HMD). This is two television monitors mounted in a helmet or set of goggles, that give the user a left and right picture to produce the three dimensional display. The second approach involves using a single television set or computer with some kind of glasses to separate the picture into left and right displays. Much introductory, but exciting work was done during the summer of 1992 on this second approach. The thrust of the work has been continued by the projects discussed in this report. In the work that follows, in most cases the references are to television, but the computer display is also a television, so in this report the two terms are synonymous.

The concept of three dimensional display of television pictures has been around for almost as long as television has. The methods of the past have not successfully presented watchable, high quality images. Recently, with the development of liquid crystal diode (LCD) glasses, the technology has

reached the point where high quality images are now producible. Two problems remain: either the picture suffers from an annoying flicker at thirty hertz, or the television equipment has to be expensively modified to provide the 3-D effect. During the summer, this researcher filed two patent disclosures on 3-D television that allow the use of standard broadcast television equipment to produce flicker free 3-D pictures. The work has now been extended and expanded to provide additional capabilities.

The original work provided black and white pictures only. The work has now been extended to color. The prototype introduced artifacts into the picture. These artifacts can now be eliminated based on the results of this research. The work has been extended to computer systems, thus providing three dimensional, flicker free pictures, with no modifications or electrical attachments to the computer itself. Additionally, work has begun on another method for providing three dimensional display of pictures on television, computer or the printed page, and on a three dimensional volumetric display unit, which provides three dimensional picture without the use of HMD's, glasses or eye focusing techniques.

DISCUSSION OF PROBLEM

Shortly after the commercialization of television, researchers began working on adding a third dimension to the two already present on the TV display. To present a three dimensional display requires that two cameras

be used, one representing the left eye, and one representing the right eye. Both pictures need to be broadcast and then received by the television, and the images then need to be separated and sent to the correct eye. Early attempts produced a generally unacceptable picture. These designs used techniques that either required expensive modifications to the television receiver or used a color difference to broadcast the two pictures simultaneously. At the receiver end, the viewer wore glasses that were red on one lens and blue on the other, thus filtering out the incorrect image for each eye. The 3-D effect was minimal.

Recently, LCD technology has provided the ability to build a pair of glasses, where each lens can be turned on and off separately, up to a frequency of about ninety hertz. Now the 3-D problem becomes solvable. We simply broadcast the left eye information first, and while it is being broadcast, open the left lens of the LCD glasses. As soon as a screenful of left eye information is sent, we flip a switch and send information from the right eye for one field. Unfortunately, up to this point, there have still been major problems. Using the standard television field rates, information for each eye can only be presented at thirty hertz. Since the brain notices anything below about fifty hertz, this presents an annoying flicker when viewing a 3-D picture presented in this way. In order to solve this problem, the television set needs to be modified to use a higher field rate to eliminate the flicker. This of course costs a great deal of money, and again reduces its usefulness as a commercial product. Please refer to figure one for a block diagram of this general approach.

During summer 1992, we have filed two patent disclosures that solve both problems. Left and right eye information are multiplexed in a fashion that increases the frequency and greatly reduces the flicker. Additionally, circuitry does not need to be attached to the television set in order to derive the signal to drive the glasses, and in fact, no modifications to the television scan rate are required. Off the shelf video equipment is used with no modifications. One variant uses an attachment to the RF input of the television or an optical connection to the screen, but that is all. Using these techniques, 3-D television becomes available to anyone with a standard television set or computer.

Several artifacts are introduced into the television picture due to the multiplexing of the two signals. One of the efforts of this proposal has been to investigate the removal of these artifacts. Secondly, research has been done under this grant to apply the techniques to computer systems, in this case an Intel 486 based personal computer system. These computers use the same basic technique for scanning the pictures to be displayed, and each line on the screen is available to the user. A circuit has been built and software written such that the user simply runs a program, and views the screen using an inexpensive circuit attached to a pair of LCD glasses to see the 3-D effect. The research supported under this grant has also extended the technique to use in a color system.

Additionally, a technique has been investigated which presents the left and right eye pictures simultaneously side by side. By focusing at a point in front of the pictures, the viewer seems to see the two images converge

into a single 3-D picture. By presenting the images using two television receivers in a dark room, and by prefocusing the viewer's eyes at the proper location before turning on the pictures, the 3-D image seems to appear before the viewer. This technique requires that the viewer wear polarized glasses for best results.

All of these techniques require the user to wear glasses to observe the effect. Another method uses a rotating screen upon which images are projected. As the screen turns, new images are projected based on calculations of what part of an object would appear at any location in space. The image appears to be three dimensional and requires no viewing aids. As part of this research a simple model of this device, called a volumetric display device was constructed. It will be tested at a later time.

Finally, part of the equipment was purchased for a study of multiple display devices. This was intended to be the beginning of a study of the feasibility of implementing a media room, that is one where the viewer is surrounded by television or computer images. A very inexpensive room could be built using the techniques developed as part of this research. At the present time, construction of such a room costs in excess of one million dollars. This part of the study was not completed due to time constraints.

METHODOLOGY

Using the methods outlined in two patent disclosures, a system was constructed consisting of two color cameras, a multiplexor box, a power supply, a color burst generator, a color television receiver, an up converter, and a pair of LCD glasses. See figure two for a block diagram of the system. See figure three for pictures of the assembled and constructed circuitry. Figure four shows a close up of the multiplexor box, designed and built for this project. It is a third generation prototype which has been constructed in a small box which allows the equipment to be moved easily and quickly, and interfaces easily to multiple multiplexor boxes which will be used to test the multiple monitor systems.

After assembling the equipment, we first worked on a high frequency amplifier to handle the increased demands for implementing a color picture. Next we investigated the removal of various artifacts in the picture including horizontal black lines across the face of the picture, and vertical intensity differences. Special circuitry was constructed which allowed us to independently move as a function of time the turn on and turn off signals for both the right and left lenses of the LCD glasses. A circuit was built and added to the multiplexor which synchronized the multiplexor action to the television field rate.

A computer system was built up using an Intel 486 microprocessor. Please see figure five for a block diagram and figure six for a picture. An interface box was built which captures the frame rate of the computer display, and synchronizes the LCD glasses to the frame rate. Using windows and C++, we programmed several demonstrations into the computer. The first

was a colored cube which was stationary on the screen. The other one was a rotating colored cube. The programs consisted of the code necessary to create and move the colored cube, as well as presenting it in two views, one a right eye view and one a left eye view, and synchronizing the display to the computer's frame rate while at the same time incorporating the multiplexing technique. We spent time during this period minimizing the effect of the artifacts.

A few of the items necessary for investigating the use of multiple monitors were purchased, and will be used in subsequent projects. See figure seven for a block diagram.

An experiment was constructed using two cameras and two television receivers and a pair of polarized glasses. Please see figure eight for the diagram. The idea here is to present the left eye picture to the left eye and the right eye picture to the right eye using the polarizer. Since the pictures are always there, there is no flicker. The pictures can be presented by one or two televisions or computer screens. For a demonstration of the technique, please see the pictures in figure nine. Cross your eyes by focusing on a finger or pencil held about twelve inches in front of the figure. Move your finger back and forth while focusing on it, but glancing at the figure until the two pictures merge into one 3-D picture.

Finally, a primitive prototype was constructed to test the idea of a volumetric display unit. Figure ten contains a drawing of such a device, and figure eleven contains a picture of the first prototype. The device consists of four rotating vanes, each containing 25 LEDs in a square matrix. The

turning on and off of the LEDs is controlled by a computer. As the vanes turn the computer calculates which LEDs are inside of the figure to be displayed, and lights them up. LEDs outside of the figure to be displayed are not lit up. The vanes turn quickly enough so that everything but the LEDs appear to be invisible.

RESULTS

The television system was built and tested. It presented 3-D pictures in color of an aircraft coming toward the camera and appearing to land. The results were such that many people viewing the aircraft moved their head by reflex action as the aircraft moved toward them. The vertical line artifacts were not able to be completely removed by the timing adjustment circuitry. The lines are caused by the finite turn on and turn off time of the LCD glasses (on the order of 1 to 2 msec). Figure twelve shows a graph of the light allowed through the right and left lenses as they are driven by a square wave with extremely fast rise and fall times. LCD glasses are available now with turn on and turn off times of 20 to 50 usec, which would eliminate the lines, but they are still expensive (\$3000). As the price drops to under \$100, these glasses will become more available.

An optical system has been designed and built to perform measurements of the television screen as viewed through the LCD glasses, so that the

intensity of the visible radiation that reaches the eyes can be measured as a function of vertical distance from the top of the television receiver. These measurements have not yet been taken, but will be in the next month. We will focus the cameras on a uniform background and measure the intensity of the light coming off of the television receiver. By placing either large filters in front of the television screen or smaller ones in front of the cameras, we will be able to eliminate the intensity differences. Although smaller filters in front of the cameras sounds like the better idea, it is complicated by the fact that the filters need to be placed outside of the near field of the cameras, not right on the lenses. See figure thirteen for a diagram of the equipment that will be used to take these measurements. There is still a small amount of flicker present in the pictures, especially on large light areas, but this is eliminated easily by reducing the intensity of the television screen, or by placing filters in front of the lenses of the LCD glasses. The flicker from the room light is completely eliminated.

The results of the computer system were even more striking. There is no flicker on the screen, no intensity differences, and the lines were eliminated in this case by using a black background, and making sure that the objects displayed did not cross the horizontal black lines. Of course the faster glasses will eliminate the black lines under all conditions. The quicker scan rate and higher persistence of the monitor are responsible for the elimination of the other artifacts as mentioned above. The cube that was displayed appeared to be located between the screen and about three inches

outside of the screen. The rotating cube at one point in the rotation came out of the screen toward the viewer. Of course, other than the LCD glasses, there were no expensive modifications or additions to the computer system to achieve the 3-D pictures.

There are several problems with the computer system. So far, we have used only simulations of objects. We still need to purchase a frame grabber, and interface it to the computer to look at real objects. The method only works with 486/35 Mhz machines, the other 486 machines are too slow to present the graphics fast enough for the method to be functional. Finally, the higher frame rate of the computer (72 Hz) causes the turn on and turn off of the LCD glasses to beat against the 120 Hz of the florescent lights, producing a flicker. This can be solved by using incandescent lighting, natural lighting, or by using a different frame rate on the monitor.

There are no results of the multiple monitor system to report at this time. Two additional cameras were purchased, and another television receiver and a VCR are available for testing, but no tests have been run at this time.

Tests were run using the two picture system as described in the previous section. Outside observers had trouble resolving the two pictures into one 3-D picture.

The volumetric display unit is only partially constructed at this time. About one half of the mechanical work is done, but little electronic circuitry is built and nothing has been interfaced to the computer. Also no programming has been done at this point. This work will be completed at a

future time. It is hoped that this prototype will allow us to investigate methods which will make construction of a practical prototype possible at a future date by allowing us to investigate ideas for improving the method.

Please see figure fourteen for a summary of the budget for this project and figure fifteen for the project schedule.

CONCLUSIONS

The work accomplished by this contract has taken a major step ahead in implementing the ideas developed in summer 1992. The television system is much improved and after the optical intensity measurements are taken, and new LCD glasses purchased, it is expected that quality 3-D television pictures will be available. The computer pictures already are very good quality. The method of displaying two pictures side by side shows great potential especially for such things as battlefield 3-D views to a limited audience. The volumetric display device, if perfected would be extremely useful to the Air Force Laboratories. All of these potential products are extremely low cost devices. They all are at the edge of the state of the art. Since the Avionics Directorate will likely be deeply involved in virtual reality research and development, the funds expended on this project have been well spent and hold the potential of saving the Air Force a significant amount of money.

REFERENCES

1. Communications of the ACM, June 1992.
2. "A Flicker Free 3-D Picture on Standard Television Equipment," July 1992, Patent disclosure, Elmer A. Grubbs.
3. Popular Science, June 1988, pp. 58 - 63, 110.
4. Proceedings of the Conference of Optics and Photonics applied to Three-dimensional Imagery, 1979, Volume 212, pp. 40 -47.
5. "Television Interface Circuitry for 3-D Viewing," June 1992, Patent disclosure, Elmer A. Grubbs.

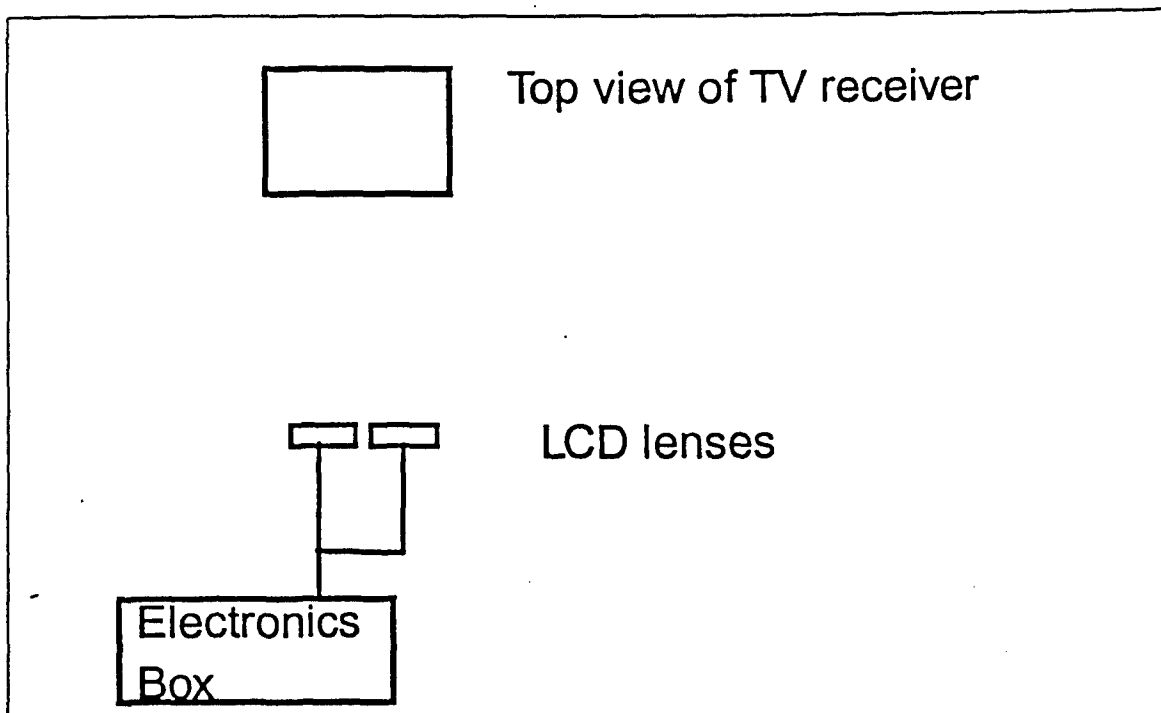
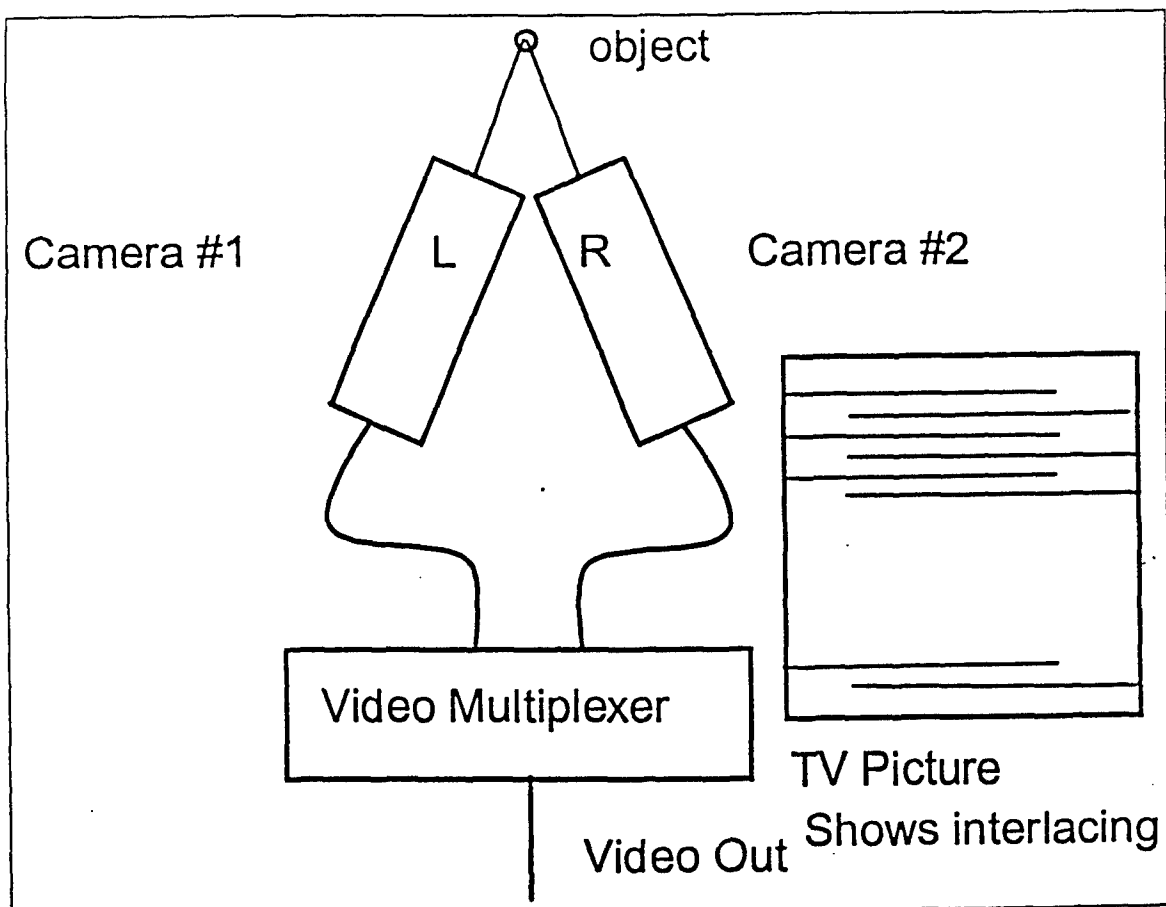


Figure one

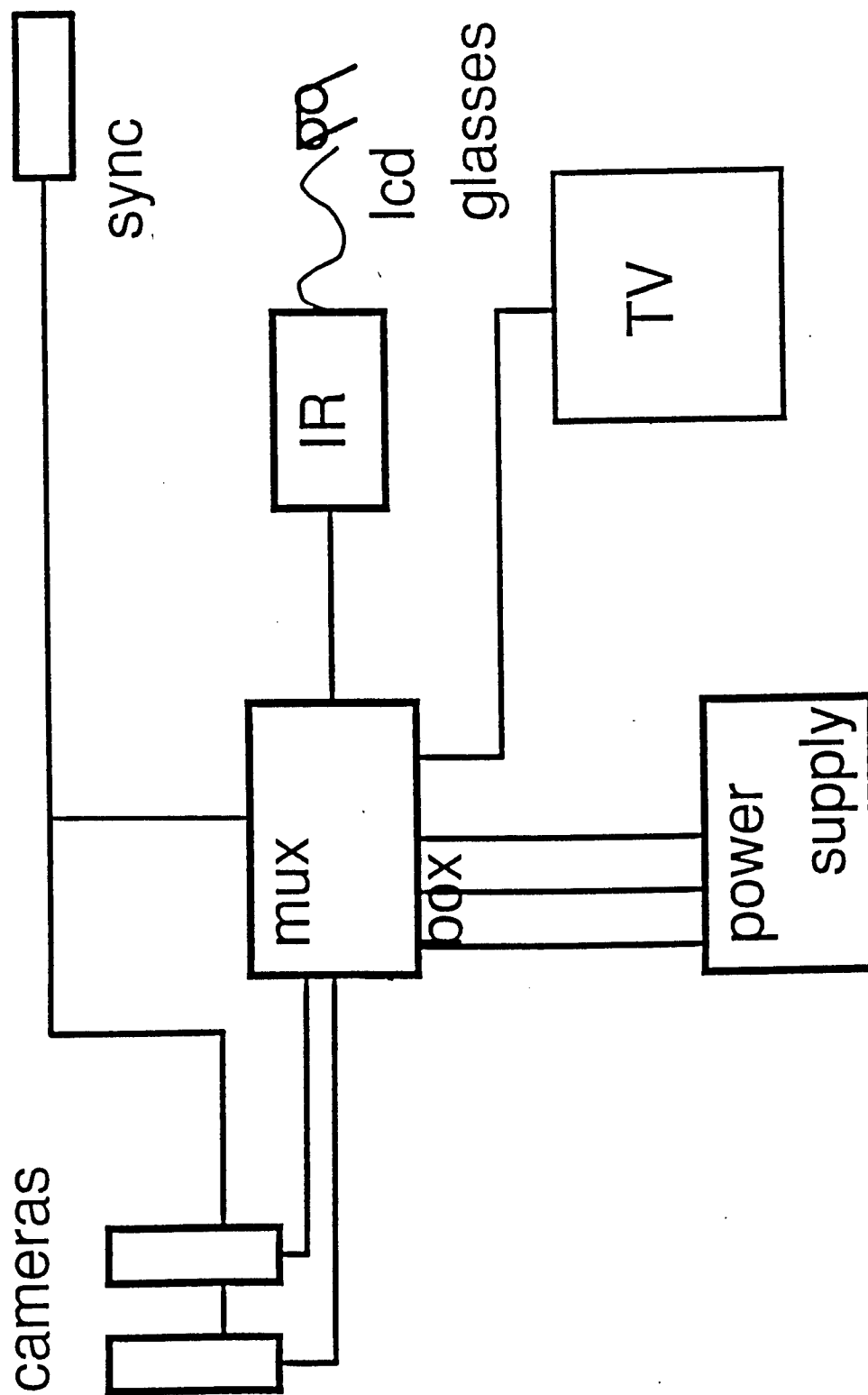


figure two, video system block diagram

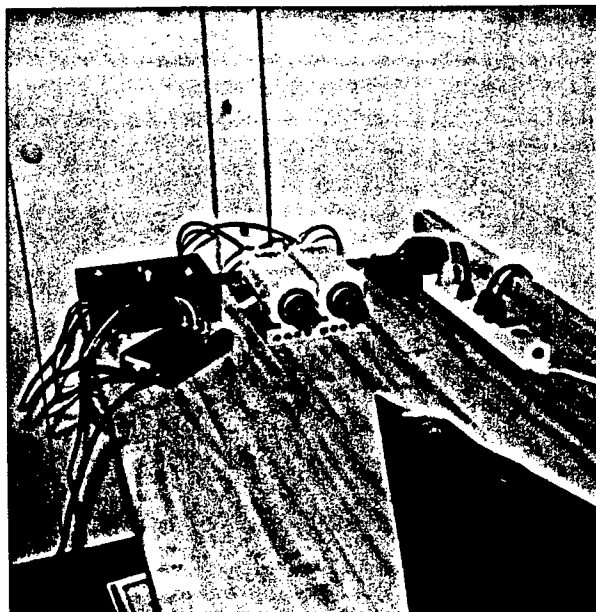


Figure 3

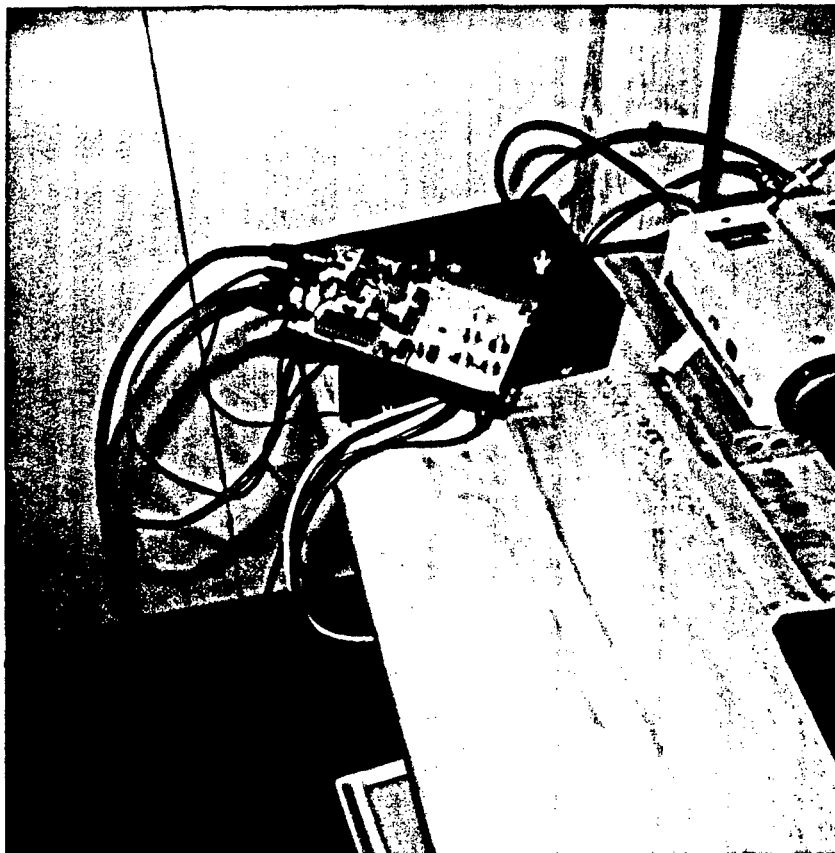
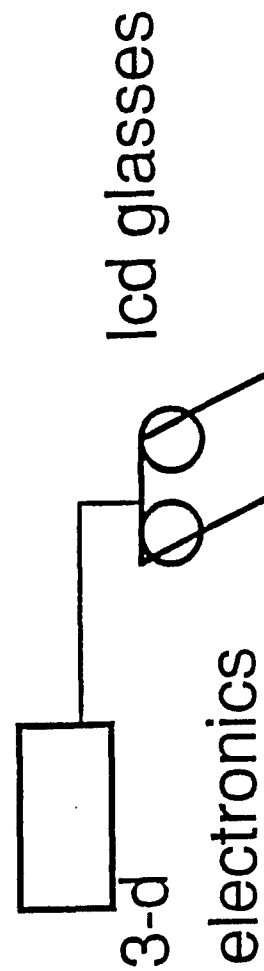
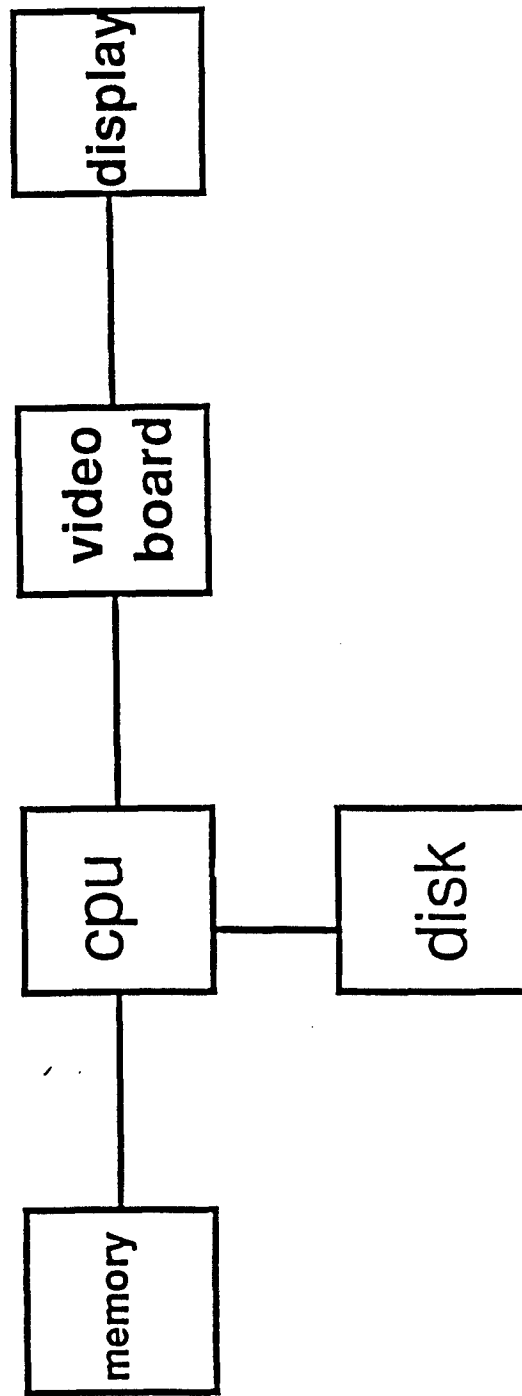


Figure 4



computer system block diagram

Figure 5



Figure 6

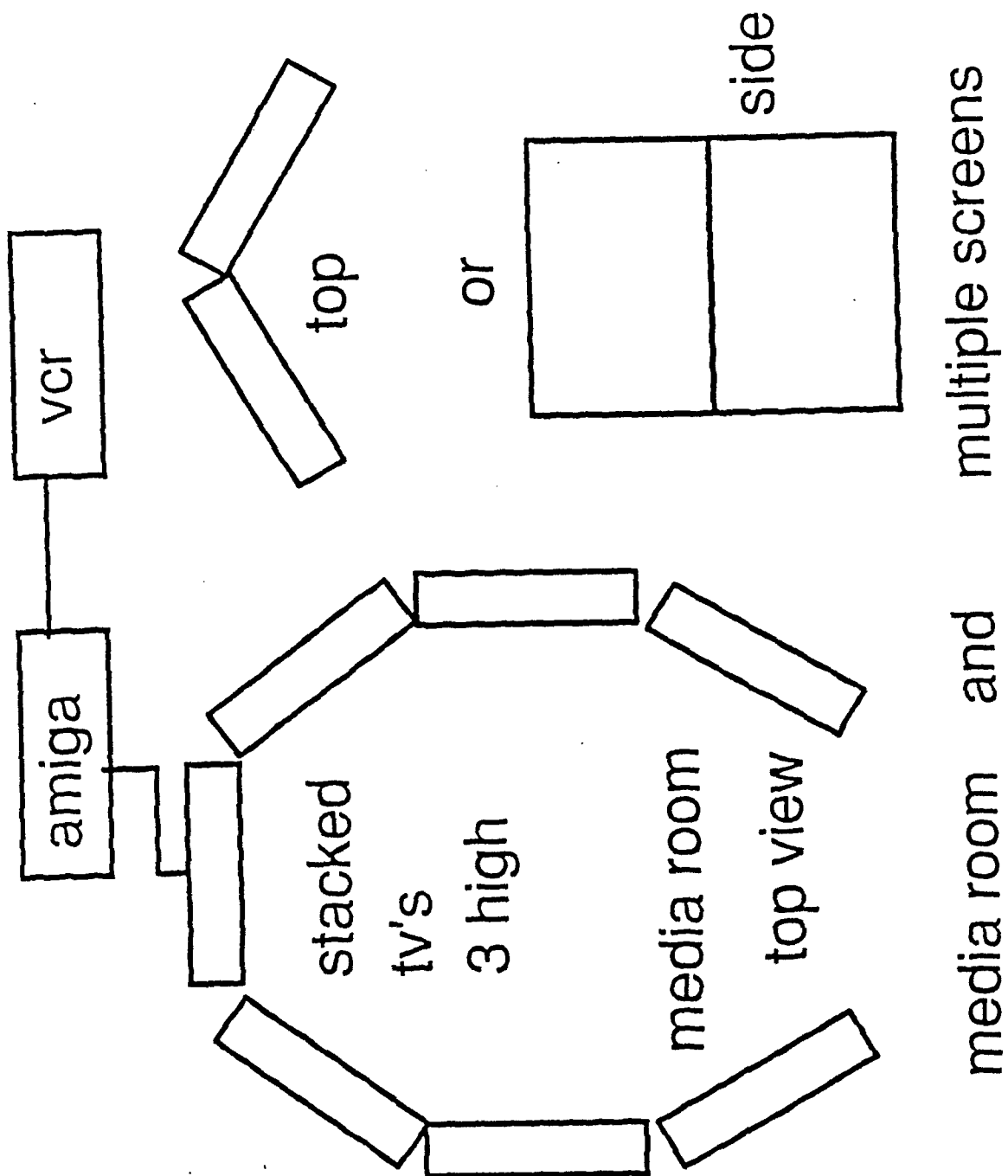


Figure 7

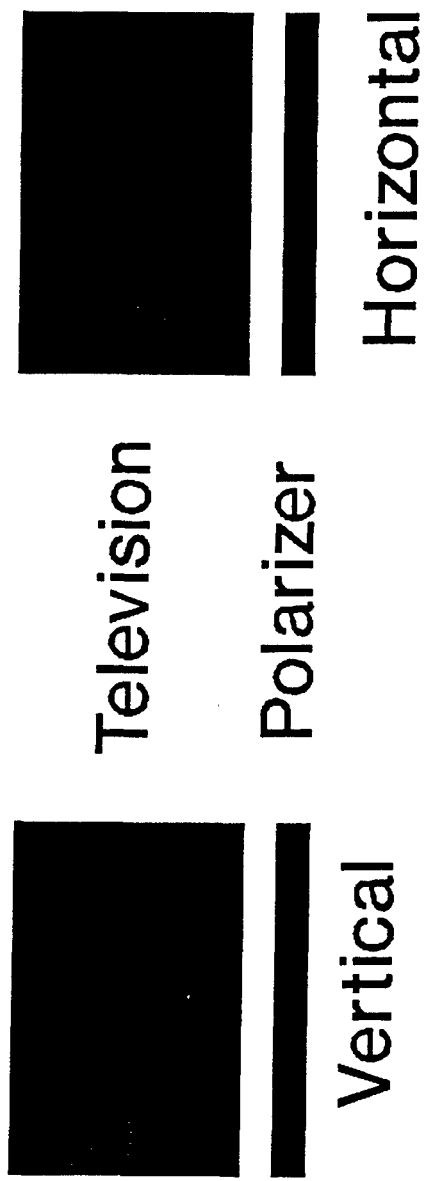
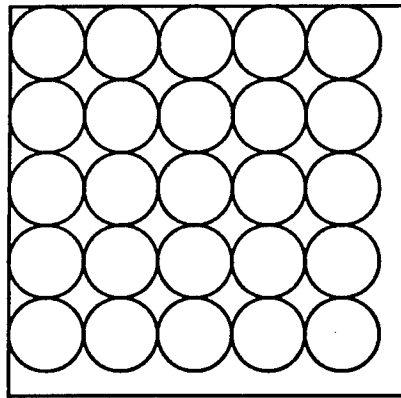


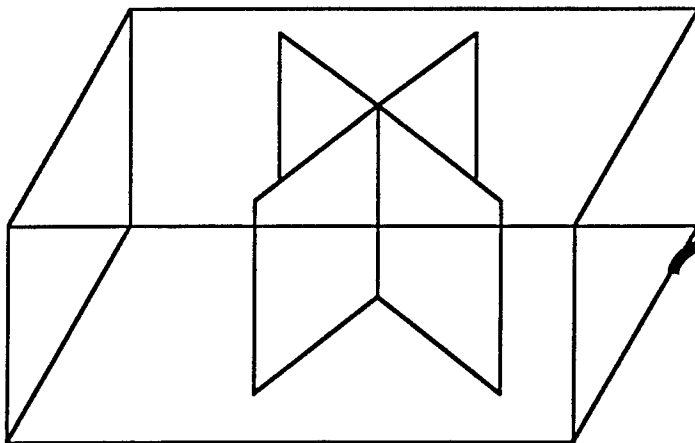
Figure 8



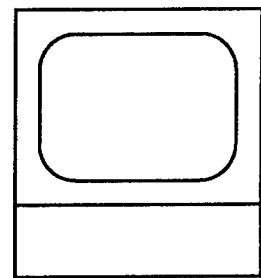
Figure 9



LED Board



Volumetric display



Computer

Figure 10

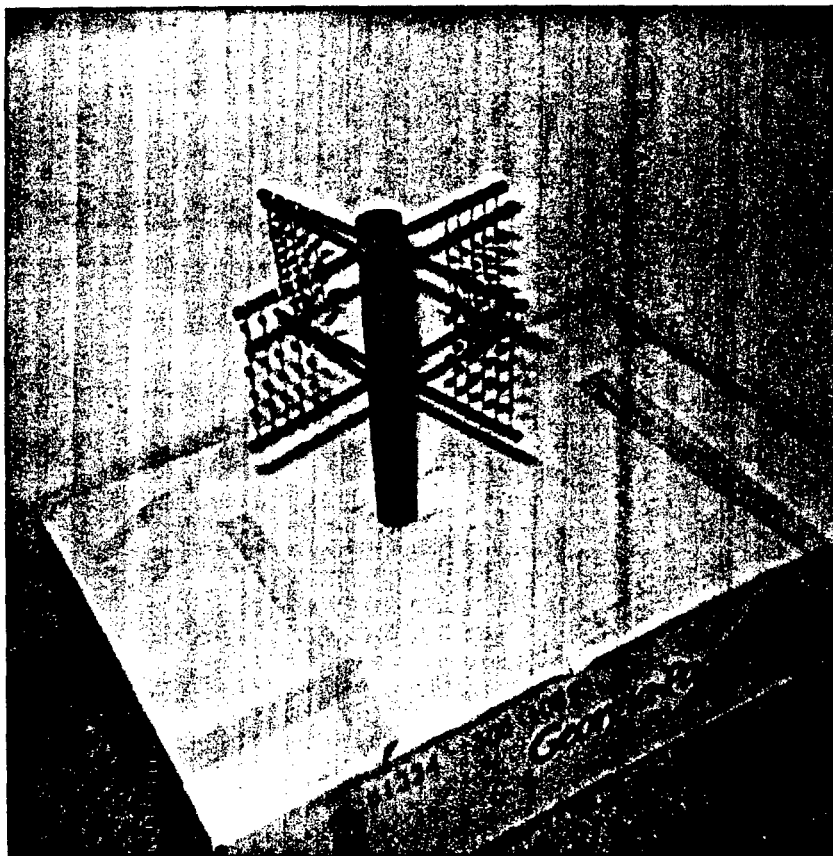


Figure 11

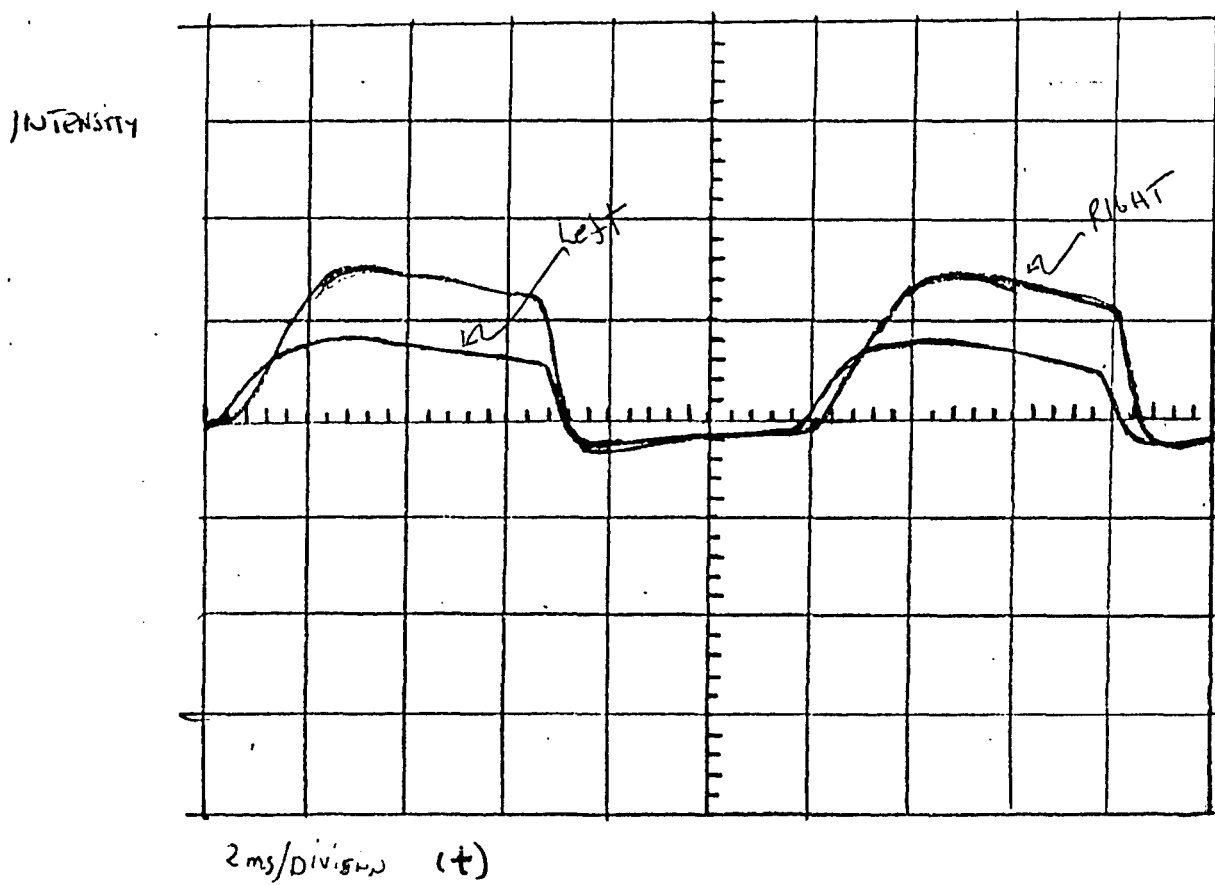


Figure 12

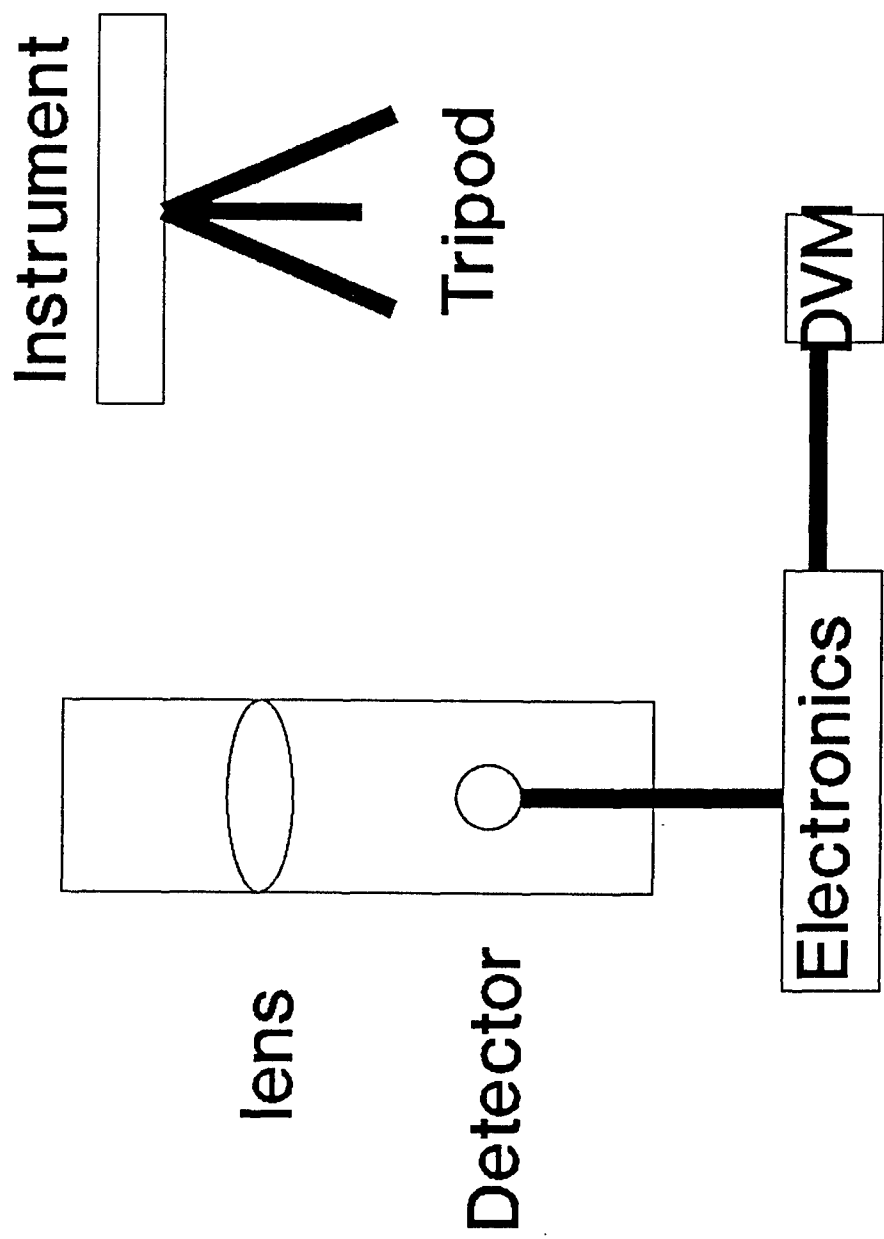


Figure 13

BUDGET

	allocated	expended
1. Salary	\$8,480	\$8,480
2. Fringe	\$2,205	\$2,205
3. Equipment	\$4,800	\$4,607
4. Consulting subcontract	\$1,500	\$1,400
5. Travel	\$ 600	\$ 554
6. Indirect	\$2,415	\$2,415
7. Total	\$20,000	\$19,661

Figure 14

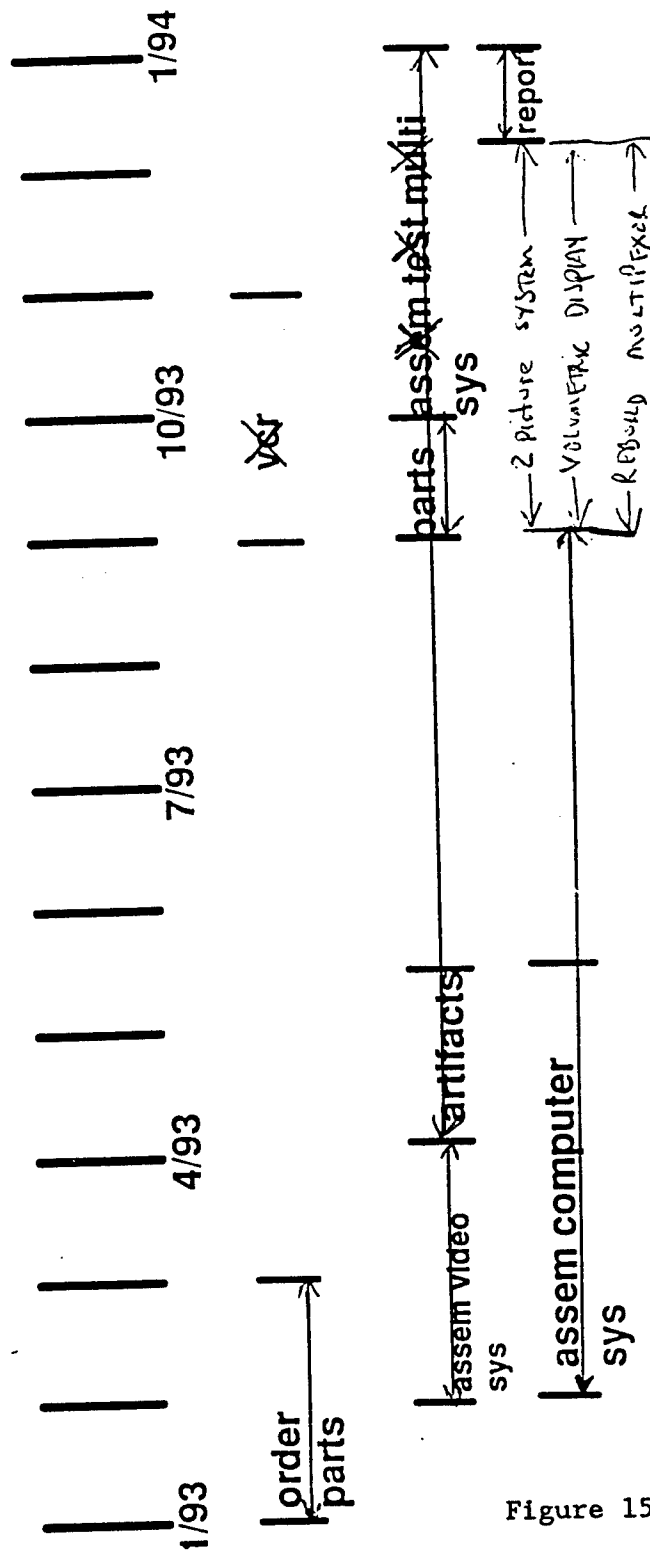


Figure 15

scheduled of tasks

THERMAL STABILITY
OF AN
SCS-6/Ti-22Al-23Nb COMPOSITE

Ian W. Hall
Associate Professor and Chairman
Materials Science Program

University of Delaware
Newark, DE 19716-3106

Final Report for:
Research Initiation Program
WL/MLLM
Wright-Patterson Air Force Base

Sponsored by:
Air Force Office of Scientific Research
Bolling Air Force Base, Washington, D.C.

and

University of Delaware

February 1994

THERMAL STABILITY
OF AN
SCS-6/Ti-22Al-23Nb COMPOSITE

I. W. Hall
Associate Professor and Chairman
Materials Science Program
University of Delaware
Newark, DE 19716-3106

ABSTRACT

Titanium aluminide matrix composites have been subjected to isothermal exposure treatments in an inert atmosphere at temperatures up to 800°C and for times up to 1000 hours. The specimens have been examined by transmission and scanning electron microscopy in order to investigate the effect of these treatments on the fiber/matrix interfacial reaction. The products of these reactions have been identified and are primarily carbides and silicides based upon TiC and Ti₅Si₃. The reaction layer increases a little in thickness with increasing exposure times and temperatures but the thermal stability characteristics of this composite appear to be superior to those of comparable systems.

THERMAL STABILITY OF AN SCS-6/Ti-22Al-23Nb COMPOSITE

1. INTRODUCTION

Among various titanium aluminide based intermetallic matrix composites, the SCS-6/Ti-22Al-23Nb system is believed to be one of the most promising candidates for high temperature applications. The matrix material, Ti-22Al-23Nb (all compositions hereafter are in at.%), consists of three phases, the relative proportions of which depend upon heat treatment: these are α_2 (Ti_3Al), an orthorhombic phase (Ti_2AlNb) and a β phase. The strength of this Ti-22Al-23Nb sheet and foil was shown to be consistently higher than that of the Ti-22Al-11Nb material from which this alloy was developed [1].

It was found that a dual phase mixture of α and β_0 in the near-surface region of the Ti-22Al-23Nb foil could be created, and is believed to occur because of Al depletion during vacuum annealing operations. This modified layer on the foil is believed to be beneficial during the manufacturing of the SCS-6/Ti-22Al-23Nb composite. More importantly, it may persist after the consolidation of the composite and therefore restrict the reactions at the fiber and matrix interface and prevent the occurrence of the β -depleted zone [1,2] which has been found in most other SCS-6/titanium aluminide systems and which was detrimental to obtaining optimum mechanical properties of the composites.

Previous studies [3,4] indicated that the fiber/matrix reaction zone products of the SCS-6/Ti-22Al-23Nb composite were essentially analogous to those found for the SCS-6/Ti-22Al-11Nb composite. The product species were TiC and Ti_5Si_3 , and related phases such as $(\text{Ti,Nb})\text{C}$, $(\text{Ti,Nb})_5(\text{Si,Al})_3$ and $\text{Al}(\text{Ti,Nb})_3\text{C}$ distributed in separate layers. The only difference was the total thickness of the reaction zone, which was $0.6\mu\text{m}$ in the as-fabricated SCS-6/Ti-22Al-23Nb composite while it was $1.6\mu\text{m}$ in the SCS-6/Ti-22Al-11Nb composite. Also no β -depleted zone was present in the SCS-6/Ti-22Al-23Nb composite [5].

In spite of the work done so far, thermal stability of the SCS-6/Ti-22Al-23Nb composite remains as one of the least investigated among a number of areas which will ultimately determine its use in structural applications. It was shown that the microstructure of monolithic alloy sheets of Ti-23.2Al-24.4Nb changed appreciably over a period of 1000 hours with isothermal exposure at temperatures as low as 500°C [6]. Later investigation on the panels of the same material, consolidated by diffusion bonding of 5-ply modified foils, suggested that the final stable microstructure present in the Ti-23.2Al-24.4Nb alloy would consist of the orthorhombic and disordered beta phases after exposure at high temperatures, but

below the beta transus, for a very long time [7]. As for the effects which might occur with long-term isothermal exposure of the SCS-6/Ti-22Al-23Nb composite, little was known at the outset of this work. The purpose of the present investigation was, therefore, to characterize the fiber/matrix interfaces of long term, isothermally exposed samples and to interpret the kinetics in the reaction layer. The effects of long-term exposure to high temperatures upon the microstructure of the matrix were also examined.

2. EXPERIMENTAL

The 4-ply composite panels examined in this work were fabricated by diffusion bonding of modified Ti-22Al-23Nb foils and unidirectional SCS-6 fibers. The base-line material for the study was the composite in the as-fabricated condition with no further heat treatment.

Samples about 5mm by 6mm were cut from the composite panels 0.8mm thick and subjected to the heat treatments designed to simulate long term exposure to temperatures in the anticipated use range. The schedule of heat treatments was as follows:

- i) 500°C for 500 hours;
- ii) 500°C for 1000 hours;
- iii) 600°C for 500 hours;
- iv) 700°C for 500 hours;
- v) 800°C for 500 hours;
- vi) 800°C for 1000 hours;

Because of the interest in obtaining information about the reaction zone between fiber and matrix, specimens were further prepared in such a way that the fiber was perpendicular to the plane of the thin foil. As the thickness of the panels was only about 0.8mm, nickel electroplating was applied to build up a thickness of about 5mm. Slices about 0.4mm thick were cut from the electroplated sample to obtain the transverse cross section view of the composite. Some slices were then core drilled to get 3mm diameter TEM disc specimens and the others were mounted and further prepared for SEM observations. The disc was mechanically ground and polished from one side to a thickness of approximately 200µm with successively finer grit diamond compounds. For both of the TEM foils and the SEM specimens the final-polishing was performed on a vibratory polisher with a low-nap cloth. Extreme care was taken to obtain a flat surface which was crucial to the final quality of the specimen. The foil was then carefully dimpled from the other side until perforation just occurred and then ion milled at 4kV and 0.5mA gun current and at a tilt of 12 degrees for about 8 hours.

The specimens were examined principally in a Philips 400T transmission electron microscope equipped with scanning transmission electron microscopy (STEM) capability and a energy dispersive spectrometry (EDS) system: an operating voltage of 120kV was employed for all the TEM work. An ISI WB-6 scanning electron microscope was also used. A windowless EDS detector was available on the SEM but not on the TEM.

3. RESULTS

Although all specimens have been examined, the differences between them are not very great as we move to higher temperatures and longer times. Consequently, and in order to avoid needless repetition, only the extreme cases will be reported below unless it is deemed appropriate to make specific observations on the intermediate conditions.

3.a SEM Observations

3.a.i As-fabricated

A low magnification view of the as-fabricated composite is shown in Fig. 1. In regions where the fiber spacing was small there were some macroscopic defects in the matrix resulting from incomplete composite consolidation.

As will be seen more clearly later, the matrix microstructure consisted of three phases, which appeared as dark gray, light gray and white. The dark gray phase was identified as α_2 , the light gray phase was the orthorhombic phase and the white phase was β . Grains close to and between the fibers were, relatively, larger than those far away from them. Also, around the fiber there appeared to be a greater volume fraction of the dark gray α_2 phase.

The original surface of the foil before consolidation consisted of essentially two phases, as mentioned in the Introduction above. This dual phase region was about $5\mu\text{m}$ in thickness and Figure 2 shows that it persists mainly next to those fiber surfaces which were normal to the axis of consolidation. The region was considerably thinner in areas between the fibers of each layer because it had undergone a larger percent strain during consolidation. However, away from this dual phase region, there was an α_2 rich region which extended for about $15\mu\text{m}$. The grain size in this region was relatively large.

Figure 3 shows the interface area between the surfaces of two matrix foils. Along this interface the dual phases, β +O, were still detectable. A region of large grains with a large fraction of α_2 phase was adjacent to this dual phase region. In the matrix near the fiber and transverse to the pressing direction, the fraction of β

phase was found to be somewhat less than that shown in Fig. 2 where the fiber was almost enclosed by the original surface of the matrix foil.

Quite unexpectedly, a relatively large fraction of α_2 was seen lying adjacent to the modified dual phase region. Although the reasons for this are not clear it may be related to the strain gradients which arise during the manufacturing processing cycle. A more likely possibility, however, is that it is a result of carbon diffusion from the surface layer of the fiber and the fiber itself. Windowless EDS analysis indeed indicates the presence of carbon in the matrix near the fiber but the levels are too low for useful further comment at this time. Enrichment in carbon, an alpha stabilizer, would result in an increased volume fraction of α_2 : the extreme surfaces layer though, which was already depleted in the alpha stabilizing aluminum, would retain a predominantly O+ β microstructure. Further work is being undertaken using EELS to characterize more fully the structure of this near-fiber region.

Figure 4 shows a typical area of the matrix near the fiber: the consolidation direction is vertical. Along with the equiaxed O phase, some plate-like O is visible within the β . There is a large volume fraction of α_2 in this field of view. The thickness of the reaction layer is seen to be about 0.5 μ m but little detail is visible within it because i) it is very fine and ii) there is such a wide range of contrast that the SEM cannot be adjusted to reveal microstructural details in the fiber, the matrix and the reaction layer simultaneously.

3.a.ii 500°C for 1000 hours

The matrix structure of the composite after this heat treatment was basically the same as that of the as-fabricated composite, when observed by SEM. Figure 5 shows a typical low magnification view, in which the original modified surface region of the foils remained at the bond-line of the foils. This modified structure was also seen to be distributed discontinuously around the fiber as before.

In Fig. 6, the plate-like O phase in the β close to the fibers is seen to be disappearing. It appears that a process of $O \rightarrow \beta (+ \alpha_2?)$ began to take place when the composite was thermally exposed. Limited grain growth was observed in the matrix but generally no fundamental morphological change occurred in the matrix.

Figure 7 shows the matrix structure adjacent to the fiber edge: the pressing direction is again vertical. Relatively, less β phase was found in the matrix there, again, no doubt, because the surface of the foil is severely stretched in this region. This reduced β fraction had no obvious effect on the reaction zone thickness. A hint of detail can now be seen in the reaction layer, indicating that it is composed of two separate layers.

3.a.iii 800°C for 1000 hours

After being exposed at 800°C for 1000 hours, the structure of the matrix material, Fig. 8, still appeared to be quite stable. No substantial changes in the matrix morphology were found.

The matrix inhomogeneity arising from the deformation processing was still present, as shown in Fig. 9. A process of $O \rightleftharpoons \beta + \alpha_2$ seems to be occurring since those regions of the matrix which contain a large volume fraction of O also contain a very small fraction of β and no α_2 . Again it is clear that there were regions where the modified surface of the original foil was not able to cover the fiber completely and Figs. 9 & 10 show that less β phase was detected in these regions.

In Fig. 11, some microporosity is observed in the reaction zone. This might concentrate at the inner or outer edge of the reaction zone and grow into micro-cracks. The total thickness of the reaction zone in this composite, which had been exposed to a high temperature for a long time, was about 1 μm which is significantly smaller than those of other composite systems even in their as-fabricated conditions [4].

Observations at intermediate temperatures provided no new information concerning the phase transformations or reaction layer growth in this composite and, consequently, will not be reported here.

3.b TEM Observations

TEM analysis was carried out with an emphasis on the examination of the reaction zones. The nature of the reaction products was determined by electron diffraction and energy dispersive X-ray spectroscopy (EDS). It was found that the phases and their sequence of layers were similar in the reaction zones of the composites with different heat treatments, the principal difference lying in their respective thicknesses. The extreme difficulty of making TEM specimens of this material generally precludes obtaining samples which illustrate the sequence of reaction layers and matrix structure in one location. Nevertheless, traversing around the periphery of a fiber (or the hole left by a fiber) allows the whole sequence to be tracked at different locations as seen in Fig. 12.

3.b.i As fabricated

Figure 13(a) shows the typical interface structure of the as-fabricated composite. The fiber is at the left and adjacent to it is a layer of very fine equiaxed grains and microporosity. The fine-scale of the reaction products in this

layer makes it all but impossible to obtain diffraction patterns from individual grains in this layer. However, based on its morphology, analysis of spotty electron diffraction ring patterns and the EDS analyses, it was deduced that TiC is the principal constituent of this layer. A typical EDS spectrum from this region, Fig. 13(b) shows that some Nb and Si is also present so it is composed of (Ti,Nb,Si)C, possibly with some (Ti,Nb)₅Si₃ (Carbon cannot be identified in the current TEM). The identification is in agreement with the work of other researchers [4, 5].

The intermediate layer was made up of columnar-like grains of TiC though EDS analysis indicated very slight amounts of Nb and Si as well. The grains were of sufficient size to be identified with reasonable certainty by selected area diffraction and with great confidence by the convergent beam technique. Figure 14(a), shows typical [001] diffraction patterns obtained from one of these grains; the 4-fold symmetry confirms the cubic symmetry based on the f.c.c. TiC structure. Figure 14(b) shows the EDS spectrum from one such grain.

Next to the matrix was a layer of grains which were somewhat elongated circumferentially. They were analyzed by EDS and CBD and found to correspond to (Ti,Nb)₅Si₃, Fig. 15.

Adjacent to the fibers, the matrix contained a very high dislocation density because of the high residual stresses present. The β , O and α_2 phases were all identified in various locations, Fig. 16 shows a β grain containing O platelets.

3.b.ii 500°C for 500hrs.

The interface structure of the specimen treated at 500°C for 500 hours is shown in Fig.17. It is clear that there is little morphological difference between the reaction products in this heat treated specimen and the as-fabricated specimen apart from a slight coarsening of the grains in the first fine-grain layer. The compositions of the different layers were also found to be essentially unchanged from the as fabricated specimen.

3.b.iii 800°C for 1000hrs

However, in the specimen exposed at 800°C for 1000 hours, several changes, including noticeable growth of the outer layer, had occurred. The second layer had coarsened somewhat and its composition had also changed slightly. The major changes, though, were the appearance of a new phase at the second/third reaction layer interface and a considerable thickening of the third layer itself, Fig 18. In some cases, grain coalescence had occurred leading to very long grains within the third layer as shown in Fig. 19(a). The new phase appearing after this treatment is indicated in Fig. 19(a), at the interface between the second and third

layers. An EDS spectrum from this grain is shown as Fig. 19(b) indicating a significantly different composition from that of the typical $(\text{Ti,Nb})_5\text{Si}_3$ of the third layer. This phase has not yet been unambiguously identified.

The interface structure is drawn schematically in Fig. 20 on the basis of the experimental observations. Table 1 gives the thicknesses of the reaction layers. It was noticed that the relative growth rate of different layers were quite different.

The thickness of the inner layer did not change very much as a function of heat treatment schedule although more microporosity and voids were found in this layer for samples exposed at 800°C for 1000 hours. The columnar intermediate layer might have been expected to have a high growth based upon consideration of the diffusivities of species and the large amount of grain boundary area. While this layer did have a higher growth compared with the outer layer at first, the latter turned out to have the more dominant growth at a later stage of the isothermal exposure to a temperature of 800°C.

Table 1 Thicknesses of the reaction layers*

Thickness (μm)	Inner layer	Intermediate layer	Outer layer	Total
As-fab.	0.22	0.23	0.2	0.65
500°C/500h	0.2	0.25	0.18	0.63
800°C/500h	0.2	0.3	0.19	0.69
800°C/1000h	0.16	0.25	0.53	0.94

* Because of time and representative sampling constraints, reliable thickness data for the rest of specimens remain to be obtained.

Based on the configuration of the reaction products in Fig. 20 and other experimental observations, an attempt was made to analyze the diffusion and reaction processes at the interface and get a better understanding of the kinetics of formation of the reaction layers.

4. DISCUSSION

4.a General

It must be emphasized at the outset that, while this investigation has already provided much information concerning the thermal stability of the composite, in view of the limited time available this is regarded as a preliminary report. Further work is still under way and will be reported in due course.

The first and clear conclusion of the results to date and presented above is that the SCS-6/Ti-22Al-23Nb composite does not undergo serious interfacial fiber/matrix reaction even at relatively long times at 800°C. The thickness of the

reaction layer increased by only $\sim 0.3\mu\text{m}$ after the most severe isothermal exposure treatment investigated and there was scant evidence of serious deleterious effects such as crack or pore nucleation. Second, the interfacial reaction products are, to a first approximation anyway, very similar to those found in other related systems such as SCS-6/Ti-6Al-4V and SCS-6/Ti-24Al-11Nb. Hence, further development of this system can be undertaken with considerable confidence that experience gained in comparable composites can be translated directly to this system. There are, however, still uncertainties concerning i) the effect of the fibers themselves upon the matrix structure and ii) the identity of some of the reaction products.

It has been demonstrated that the matrix has a surface skin, the microstructure and composition of which differ from the bulk. It is believed that this microstructure contributes to the reduced reactivity of the fiber/matrix couple and is related to the increased presence of the β phase, or increased concentration of β -stabilizing elements, at the interface. The fiber itself and its protective coating are potent sources of carbon which normally stabilize the (α or) α_2 phase so this is normally present at the interface. The present observations suggest the possibility that either the fibers may be tailored for improved compatibility with the matrix by coating with a specific β -stabilizing element, or that the matrix itself could be thus treated. The former approach is conventional, expensive and reasonably advanced in practical terms whereas the author is not aware of significant efforts being undertaken in the latter, and potentially vastly cheaper, approach.

Current extension of this work is being focused upon:

- a) identification of the new reaction products
- b) establishing the effect of interstitials upon the matrix microstructure and,
- c) calculation and analysis of thermodynamic data for the potential interfacial phases in the Ti-Al-Nb-Si-C system with a view to tailoring it to produce thermodynamically stable phases.

The background for the latter investigation forms the remainder of this report.

4.b Reactive Diffusion at the Interface

The reactions at most composite interfaces can be described in terms of reactive diffusion which involves:

- i) chemical reactions at the interface between phases, and,
- ii) interdiffusion of elements through various phases present.

Wagner was perhaps the first to make a series of calculations for diffusion in systems consisting of more than one phase [8, 9] and developed a parabolic relationship between the displacement of the phase boundary and the time. In his

calculations, a major simplification among many was that equilibrium compositions were maintained at the phase boundaries and the diffusion process was the controlling step for the growth of phases. Later, using a different approach based on Fick's first law, Kidson obtained similar results for the growth of diffusion layers in binary systems[10]. He also defined the conditions under which the phases that would have been present according to the phase diagram might not grow to observable widths in the diffusion zone. What seemed to be debatable for the theories developed by Wagner, Kidson and many other investigators such as Heumann and Shatynski *et al.* [11,12] was that they took no account of the rate of chemical reactions.

Considerations of the chemical reaction step and the diffusion route in the multiphase diffusion were made in some more recent work [13,14]. But most of the theories of reactive diffusion have been based upon single or multi-phase binary diffusion couples. As for the reactive diffusion theory concerning real systems containing more than two elements, little relevant literature exists.

From the present experimental observations, several questions became manifest, principal among which were:

- i) Are all the thermodynamically possible phases present in the reaction zone?
- ii) What governs the spatial sequence of the phase layers?
- iii) What is the time dependence of the phase growth?
- iv) Are the phase growth rates diffusion controlled or reaction controlled?

Answers to these questions are crucial to the further technological development of this type of composite.

4.c Thermodynamic considerations

It has been argued that a two phase region would never be present in a diffusion couple. The validity of this assertion for a binary system can be made clear by following arguments.

Suppose that there exists a two phase region ($\alpha+\beta$) in a bar consisting of two components, as shown in Fig. 21, where α and β could be solid solutions and/or miscible compounds. The chemical potential of component A, $\mu_A(X_A, T, P)$, at constant temperature and pressure along the bar is also schematically plotted in the figure. Because of the constant chemical potential of component A, and therefore that of component B which can be determined using the Gibbs-Duhem equation, within the region II, no atoms can diffuse out of it. The net effect of the diffusion in region I and III is, therefore, that β phase would transform into α phase at the interface of I and II and α phase would transform into β phase at the interface of II and III resulting in the shrinking of region II.

An identical conclusion to the problem above can be obtained by a discussion of the phase rule which states that, at constant temperature and pressure:

$$F = C - P - M$$

where F = degree(s) of freedom;
 C = number of component(s);
 P = number of phase(s);
 M = number of independent chemical reaction(s).

For the present case, $C=P=2$ and $M=0$ in the region II. So $F=0$, which means that the composition and the fraction of the phases in the region are constant and no chemical potential gradient can exist within it. Therefore, no force will be available for atomic movement since $f_i = \frac{\partial \mu_i}{\partial x}$.

However, in the case of systems containing more than two components, the picture of the interface structure of a diffusion couple may become much more complicated. It is usually believed that distinct phase layers can still be expected there. While this is true in many cases, there are quite as many observations, such as those described in the references [15] and [16], which reveal very complex interfaces. In fact, multiphase diffusion layers are thermodynamically possible in a diffusion couple with more than two components.

As an illustration, let us consider a ternary system. Suppose a two phase region is formed in a diffusion couple, as shown in Fig. 22. At constant temperature and pressure, the phase rule indicates that in this dual phase region there is one degree of freedom if no independent chemical reaction occurs ($C=3$, $P=2$, $M=0$, $F=1$). The composition of the phases and, therefore, the average composition of this dual phase region may change according to the tie lines in the isothermal Gibbs triangle in Fig. 22 while a local phase equilibrium can be maintained at the same time. Since the chemical potential of each species, $\mu_i(X_A, X_B, T, P)$, depends on the composition of the system, it can be expected that there will be a chemical potential gradient along the bar in the region because of a gradient of the composition. So diffusion through the region will occur. The region may grow if there is a net flux of atoms into the region, or remain unchanged in dimension if a steady state of flux through the region can be maintained or even shrink if there is a net flux of atoms towards the outside of the region.

In metal and intermetallic matrix composites, the interface products are usually chemical compounds with only limited miscibilities. It is also quite

common for some of these compounds such as TiC type to have an ordered crystal structure. These situations impose some extra restrictions on the degree of freedom ($M \neq 0$) or the diffusivity of species. This may account for the commonly observed single phase layer structure at the interface of composites.

From our observations of the interface of the SCS-6/Ti-22Al-23Nb composite, it was inferred that the inner dual phase layer was formed at an early stage of the processing cycle through chemical reactions. Once it had been formed its growth was negligible or, since more microporosity was observed in this inner layer for specimens exposed at 800°C for 1000 hours, the layer might even have been shrinking.

4.d Diffusivity in a columnar layer

A section of the columnar-like (second) layer normal to the grain boundary and the layer boundary is shown schematically in Fig. 23. Obviously, the overall diffusivity of species in this layer may be greater than the lattice diffusivity alone because of an extra parallel flux through the grain boundaries. Suppose D_l and D_b are the lattice diffusion coefficient and the grain boundary diffusion coefficients respectively. For a sufficiently long time the concentration gradient within the grain bulk and along the grain boundary can be shown to be almost the same if assumptions are made similar to those of Fisher [17]. Therefore, there are two corresponding fluxes:

$$J_l = -D_l \frac{\partial c}{\partial y} \quad J_b = -D_b \frac{\partial c}{\partial y}$$

and the overall flux is the sum of these:

$$J = \frac{d}{d+\delta} J_l + \frac{\delta}{d+\delta} J_b = -\left(\frac{d}{d+\delta} D_l + \frac{\delta}{d+\delta} D_b\right) \frac{\partial c}{\partial y}$$

where d is the average grain size in the circumferential direction and δ is the thickness of grain boundary. So the overall diffusivity is given by:

$$D = \frac{d}{d+\delta} D_l + \frac{\delta}{d+\delta} D_b \approx D_l + \frac{\delta}{d} D_b$$

Clearly, diffusion may be enhanced by a columnar grain structure, especially when the average size is small. Present observations did not show the expected rapid growth of this columnar-like intermediate layer in the SCS-6/Ti-22Al-23Nb composite. The explanation for this may lie in the respective magnitudes of the diffusion coefficients or in the kinetics of the layer growth. Further consideration must, therefore, be given to the kinetics of cooperative layer growth.

4.e Growth kinetics of intermediate and outer layers

Among the five diffusing species in the composite system, carbon has the highest diffusivity. There was evidence [18] that C was the only diffusing species in $\text{TiC}_{(1-x)}$. Current EDS analyses revealed that Si and Al also showed much compositional variation and, hence, diffusion over the range of the interface area. Furthermore, to form the reaction products as identified in the reaction layer, some redistribution of Ti and Nb is indispensable. So the overall picture of the reactive diffusion was really very complicated. But from a phenomenological point of view, some descriptions and semi-quantitative analysis might still be possible. The reaction at the interface of the SCS-6/Ti-22Al-23Nb composite might be qualitatively pictured in this way:

The inner layer was formed at once by chemical reactions occurring at the start of the processing cycle. No appreciable growth of this layer could be observed thereafter. It simply acted as a highly diffusive path and a source of nuclei for the intermediate layer and even for the outer layer. The intermediate $(\text{Ti,Nb})\text{C}_{(1-x)}$ layer would grow without any incubation period until a critical thickness was reached, and then its growth would slow down. One possible reason for this was that the diffusion path for Ti and Nb from the matrix was somehow blocked by the outer layer. More noticeable growth was observed for the outer layer. It is possible that while there was no difficulty in obtaining the elements Ti, Nb and Al from the matrix for this forefront layer, the element Si could also reach this layer fairly easily through the highly diffusive inner layer and intermediate layer.

The theory of Kidson [10] provides an explanation for the relative width of phase layers in the diffusion zone. In Fig. 24, if the distance measurement is referred to the Matano interface and the concentrations at the interface are assumed constant and equal to the equilibrium values, the rate of advance of the interface is given by

$$\begin{aligned} |C_{\alpha\beta} - C_{\beta\alpha}| \frac{d\xi_{\alpha\beta}}{dt} &= J_{\alpha\beta} - J_{\beta\alpha} \\ &= -D \left(\frac{\partial C}{\partial x} \right)_{\alpha\beta} + D \left(\frac{\partial C}{\partial x} \right)_{\beta\alpha} \end{aligned} \quad (1)$$

where the flux of material is assumed from left to right. Since the system fulfills the conditions for the Boltzmann theorem, the concentration $C(x, t)$ may be expressed as a function of a single parameter $\lambda = \frac{x}{t^{1/2}}$ and

$$\frac{\partial C}{\partial x} = \frac{1}{t^{1/2}} \frac{dC}{d\lambda} \quad (2)$$

If, as has been assumed, the concentrations remain constant at the interface, then the value of the parameter λ , in terms of which C is expressed, must be constant. Since $dc/d\lambda$ is again a function of λ alone, it is also constant at the interface. Thus (1) may be written as

$$\frac{d\xi_{\alpha\beta}}{dt} = \left[\frac{(DK)_{\beta\alpha} - (DK)_{\alpha\beta}}{C_{\alpha\beta} - C_{\beta\alpha}} \right] \frac{1}{t^{1/2}} \quad (3)$$

where $K_{ij} = \left(\frac{dC}{d\lambda} \right)_{ij} = t^{1/2} \left(\frac{\partial C}{\partial x} \right)_{ij}$ is constant at the interface. Integrating (3):

$$\xi_{\alpha\beta} = 2 \left[\frac{(DK)_{\beta\alpha} - (DK)_{\alpha\beta}}{C_{\alpha\beta} - C_{\beta\alpha}} \right] t^{1/2} = A_{\alpha\beta} t^{1/2} \quad (4)$$

Equation (4) exhibits the parabolic time dependence of the interface movement. For a three phase system as shown in Fig. 25, applying equation (4) to both of the interfaces as before:

$$\xi_{\alpha\beta} = 2 \left[\frac{(DK)_{\beta\alpha} - (DK)_{\alpha\beta}}{C_{\alpha\beta} - C_{\beta\alpha}} \right] t^{1/2} \quad (5)$$

$$\xi_{\beta\gamma} = 2 \left[\frac{(DK)_{\gamma\beta} - (DK)_{\beta\gamma}}{C_{\beta\gamma} - C_{\gamma\beta}} \right] t^{1/2} \quad (6)$$

The width of the β phase layer as a function of time is simply

$$\begin{aligned} W_{\beta} &= \xi_{\beta\gamma} - \xi_{\alpha\beta} \\ &= 2 \left\{ \left[\frac{(DK)_{\gamma\beta} - (DK)_{\beta\gamma}}{C_{\beta\gamma} - C_{\gamma\beta}} \right] - \left[\frac{(DK)_{\beta\alpha} - (DK)_{\alpha\beta}}{C_{\alpha\beta} - C_{\beta\alpha}} \right] \right\} t^{1/2} \\ &= B_{\beta} t^{1/2} \end{aligned} \quad (7)$$

Again a parabolic relationship is derived. This equation also predicts that when $B_{\beta} \leq 0$, the β phase will not appear or may disappear if it had already formed for some reason.

As mentioned before, one of the weakness of this theory is that it fails to consider the effect of chemical reactions at the interface. There are few theories

which take into account of the effect of chemical reactions on the layer growth [13, 14]. While they are usually oversimplified, these theories do explain some specific phenomena in experiments.

Suppose there is only one species, e.g. A, diffusing through the couple in which a compound AB is formed, Fig. 26. Let C'' be the equilibrium concentration and C' the actual concentration at the AB/B interface. The concentration at the other interface remains constant and is equal to C . By Fick's law:

$$J_1 = D \frac{C - C'}{\xi} \quad (8)$$

assuming D is independent of composition and the concentration distribution is linear. The species A builds up at the interface of the compound AB and B. If AB is formed through a first order reaction, its rate

$$J_2 = K(C' - C'') \quad (9)$$

where K is the reaction constant. Philibert introduced two slowness parameters K^{-1} and ξ/D and the rate of the interface can then be expressed as:

$$\frac{d\xi}{dt} = \left(\frac{1}{K} + \frac{\xi}{D} \right)^{-1} \quad (10)$$

where K and D are directly proportional to K and D . For a particular case with only two intermediate phases as shown in Fig. 27, the growth rates of the layers are

$$\frac{d\xi_1}{dt} = \left(\frac{1}{K_1} + \frac{\xi_1}{D_1} \right)^{-1} - \left(\frac{1}{K_2} + \frac{\xi_2}{D_2} \right)^{-1} \quad (11)$$

$$\begin{aligned} \frac{d\xi_2}{dt} = & \left(\frac{1}{K_2} + \frac{\xi_2}{D_2} \right)^{-1} + \left(\frac{1}{K_3} + \frac{\xi_2}{D_2} \right)^{-1} \\ & - \left(\frac{1}{K_1} + \frac{\xi_1}{D_1} \right)^{-1} \end{aligned} \quad (12)$$

From (12), it is clear that for $\frac{d\xi_2}{dt}$ to be positive, ξ_1 must obey an inequality of the form: $\xi_1 > \xi_1^* + f(\xi_2)$. Yet as the phase AB grows, $\frac{d\xi_2}{dt}$ decreases. Such coupling effect may be an explanation for the growth phenomena observed at the SCS-6/Ti-22Al-23Nb composite interface. While this approach provides a qualitative basis

for understanding the sequence and thicknesses of the various reaction products it cannot yet provide a quantitative model with predictive capabilities. Further work is progressing in this area to develop that capability.

5. REFERENCES

1. J. A. Graves *et al.*, in Intermetallic Matrix Composites, edited by D. B. Miracle *et al.* (Mater. Res. Soc. Proc. 273, Pittsburgh, PA 1990) pp. 31-42.
2. R. G. Rowe, in Microstructure/Property Relationships in Titanium Aluminides and Alloys, (Y. -W. Kim & R. R. Boyer. eds.) TMS, Warrendale, PA, (1991) p.387.
3. P. R. Smith *et al.*, in Intermetallic Matrix Composites, edited by D.B. Miracle *et al.* (Mater. Res. Soc. Proc. 273, Pittsburgh, PA 1990) pp. 43-52.
4. C. G. Rhodes in Intermetallic Matrix Composites, edited by D.B. Miracle *et al.* (Mater. Res. Soc. Proc. 273, Pittsburgh, PA 1990) pp. 17-29.
5. S. F. Baumann *et al.* , *Metall. Trans. A*, 1990, Vol. 21A, pp. 1559-1569.
6. I. W. Hall, Microstructural Evolution of Ti-23.2Al-24.4Nb, Final Report for Summer Research Program, Wright Laboratory, WPAFB, 1992.
7. I. W. Hall, Long-Term Thermal Stability of a Ti-23.2Al-24Nb Intermetallic Alloy, Final Report for Summer Research Program, Wright Laboratory, WPAFB, 1993.
8. W. Jost, Diffusion in Solids, Liquids, Gases (Academic Press, 1952) 69.
9. C. Wagner, *Acta Metall.* 17 (1969) 99.
10. G. V. Kidson, *J. Nucl. Mater.* 3, 1 (1961) 21-29.
11. T. Heumann, *Z. Phys. Chem.* 209 (1952) 168.
12. S. R. Shatynski *et al.*, *Acta Metall.* 24 (1976) 1071.
13. J. Philibert, *Appl. Surf. Sci.* 53 (1991) 74-81.
14. V. I. Dybkov, *J. Mater. Sci.* 21 (1986) 3078-3084.
15. S. F. Baumann, *et al. Metallurgical Transactions*, 21A (1990) 1559-1569.
16. C. Jones, *et al. J. Mater. Res.*, Vol. 4, No.2, (1989) 327-335.
17. J. C. Fisher, *J. Appl. Phys.*, 22 (1951) 74.
18. F. J. J. van Loo *et al. Metallurgical Transactions*, 20A (1989) 403-411

6. FIGURE CAPTIONS

- Fig. 1 A typical low magnification view of the as-fabricated composite.
- Fig. 2 The original dual phase region near the fiber.
- Fig. 3 The interface between two matrix foils.
- Fig. 4 Matrix /fiber interface. Consolidation direction vertical.
- Fig. 5 A low magnification view of the composite treated at 500°C for 1000 hours.
- Fig. 6 Fiber/matrix interface after 1000hrs at 500°C showing disappearance of the plate-like O phase within β grain. Consolidation direction vertical.
- Fig. 7 The matrix structure at fiber edge; consolidation direction vertical.
- Fig. 8 Typical structure after exposure at 800°C for 1000 hours.
- Fig. 9 Deformation inhomogeneity in the matrix after exposure at 800°C for 1000 hours. Consolidation direction top left to bottom right.
- Fig. 10 A region of matrix with less β phase near the fiber.
- Fig. 11 Microporosity in the reaction zone after exposure at 800°C for 1000 hours.
- Fig. 12 Periphery of matrix showing reaction layers.
- Fig. 13(a) A typical interface structure of the as-fabricated composite.
- Fig. 13(b) EDS spectrum from the first reaction layer.
- Fig. 14(a) Diffraction patterns from one of the second layer grains, indexable as $[001]_{\text{TIC}}$. (CBED patterns, very slightly off-zone axis)
- Fig. 14(b) EDS spectrum from one of the second layer grains in as-fabricated specimen..
- Fig. 15 EDS spectrum from third reaction layer grain in as-fabricated specimen.
- Fig. 16 A β grain containing O platelets.
- Fig. 17 A typical interface structure of the composite exposed at 500°C for 500 hours. Fiber at left.
- Fig. 18 Third layer of the interface in composite exposed at 800°C for 1000 hours. Fiber at top.
- Fig. 19(a) A very long grain in the outer layer.
- Fig. 19(b) EDS spectrum of the small grain indicated in Fig. 19(a)
- Fig. 20 Schematic diagram of the interface structure.
- Fig. 21 A pseudo-dual phase region in a binary system.
- Fig. 22 A ternary system and its Gibbs triangle.
- Fig. 23 A sketch of the intermediate layer in reaction zone.
- Fig. 24 The displacement of phase layer in a diffusion zone with one growing phase.
- Fig. 25 A diffusion zone with three phases.
- Fig. 26 Diffusion through the couple in which a compound is formed.
- Fig. 27 A diffusion couple with two layers of intermediate phases.

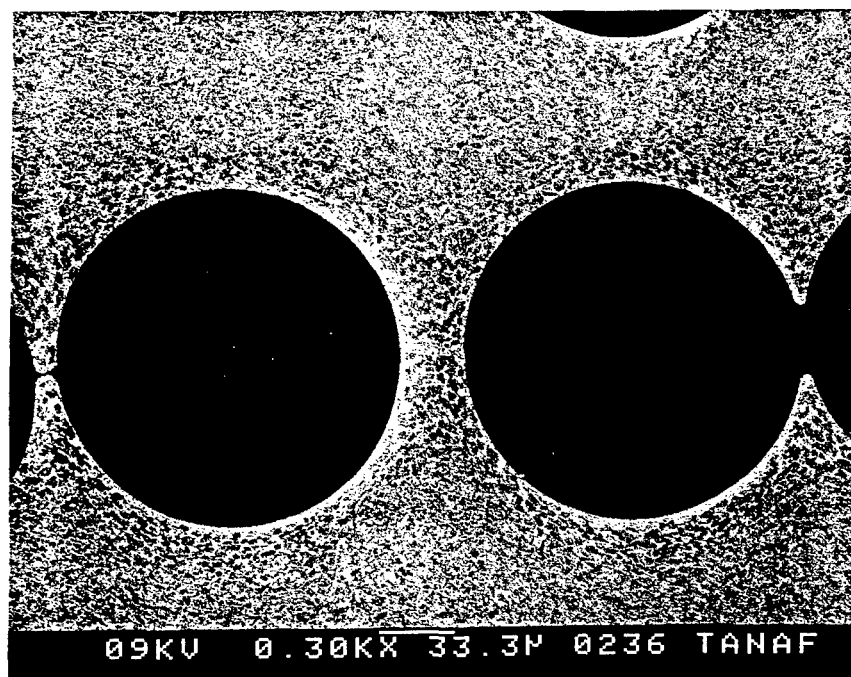


Fig. 1 A typical low magnification view of the as-fabricated composite.

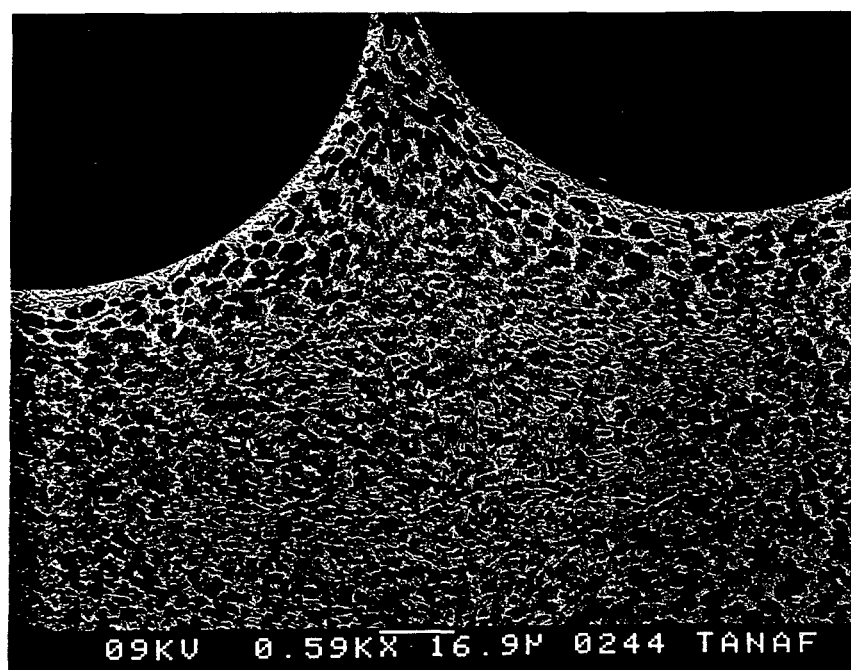


Fig. 2 The original dual phase region near the fiber.

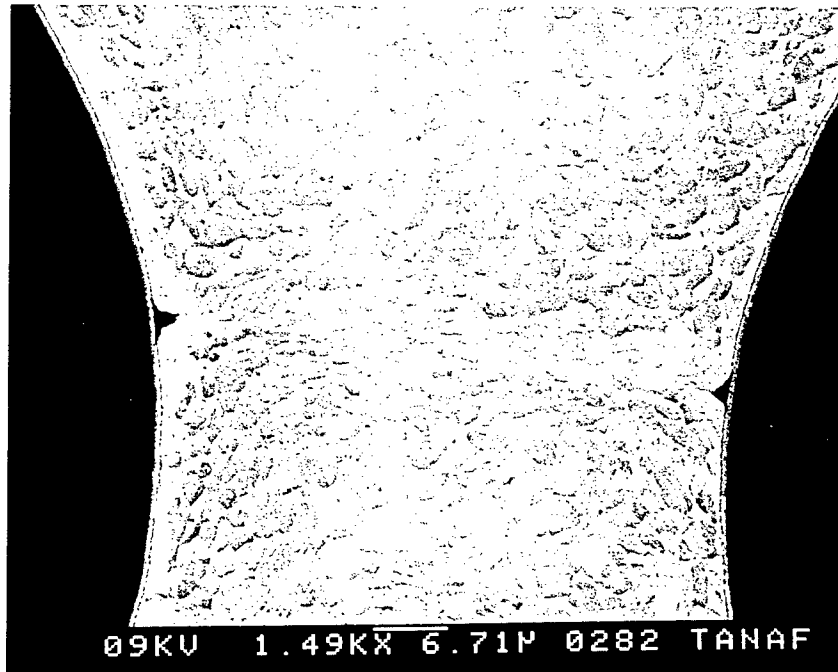


Fig. 3 The interface between two matrix foils.



Fig. 4 Matrix /fiber interface. Consolidation direction vertical.

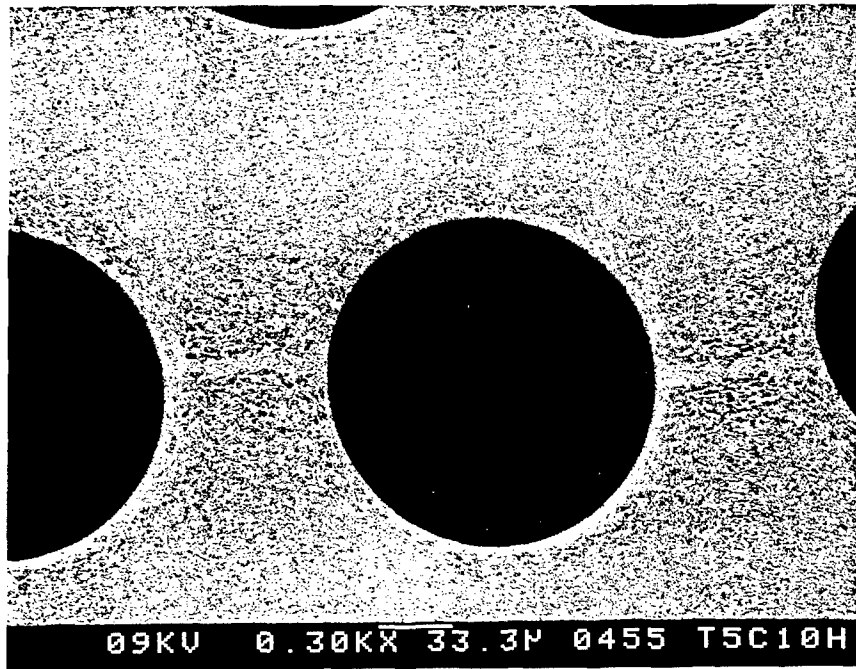


Fig. 5 A low magnification view of the composite treated at 500°C for 1000 hours.

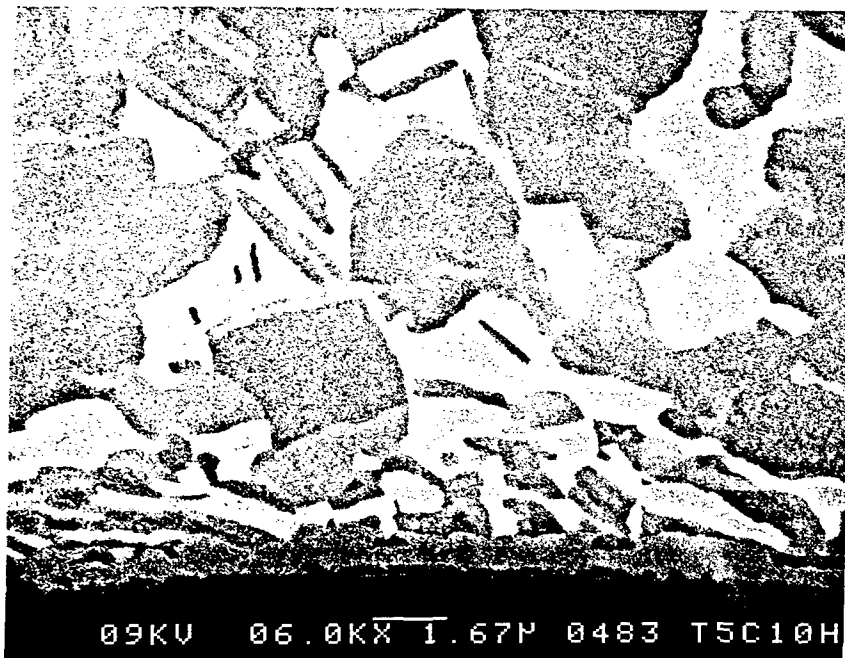


Fig. 6 Fiber/matrix interface after 1000hrs at 500°C showing disappearance of the plate-like O phase within β grain. Consolidation direction vertical.

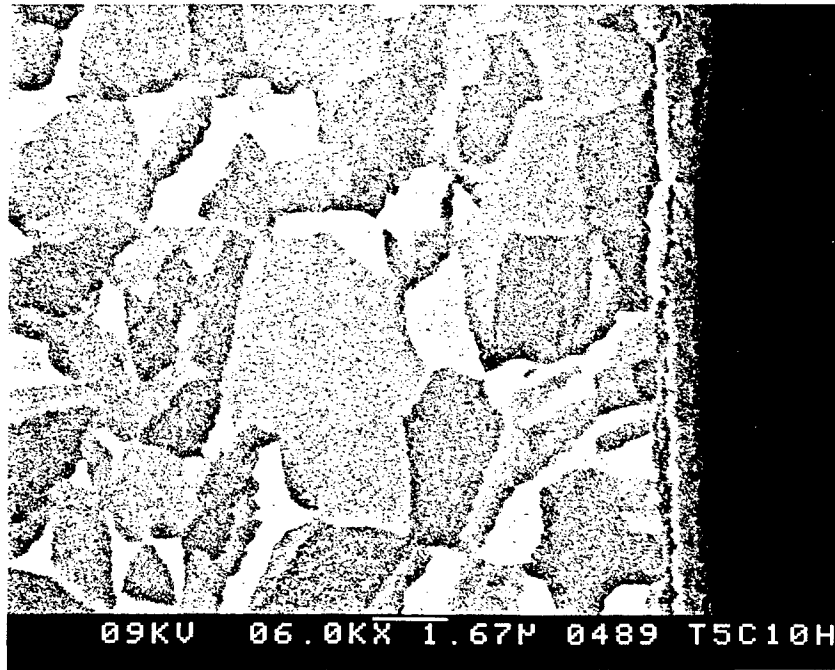


Fig. 7 The matrix structure at fiber edge; consolidation direction vertical.

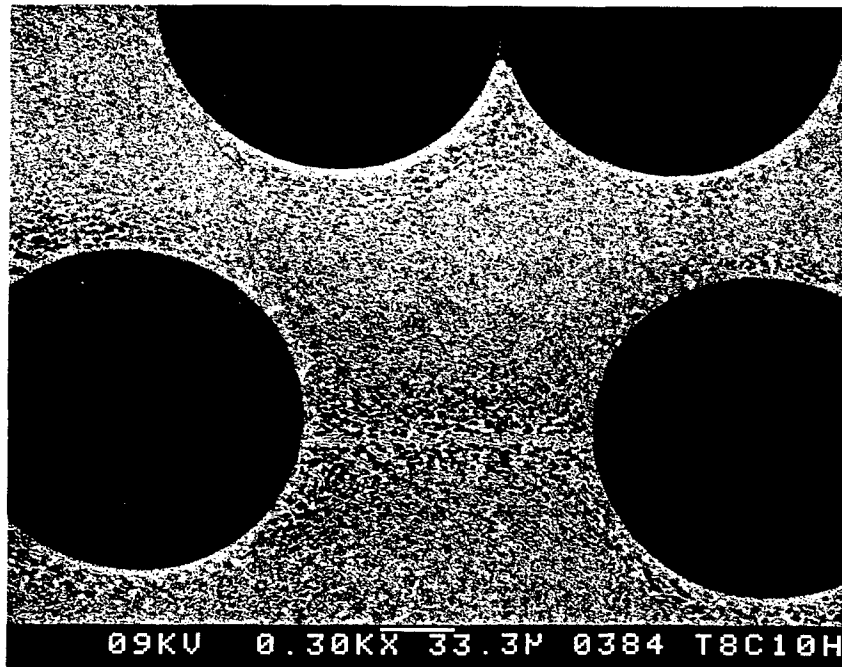


Fig. 8 Typical structure after exposure at 800°C for 1000 hours.

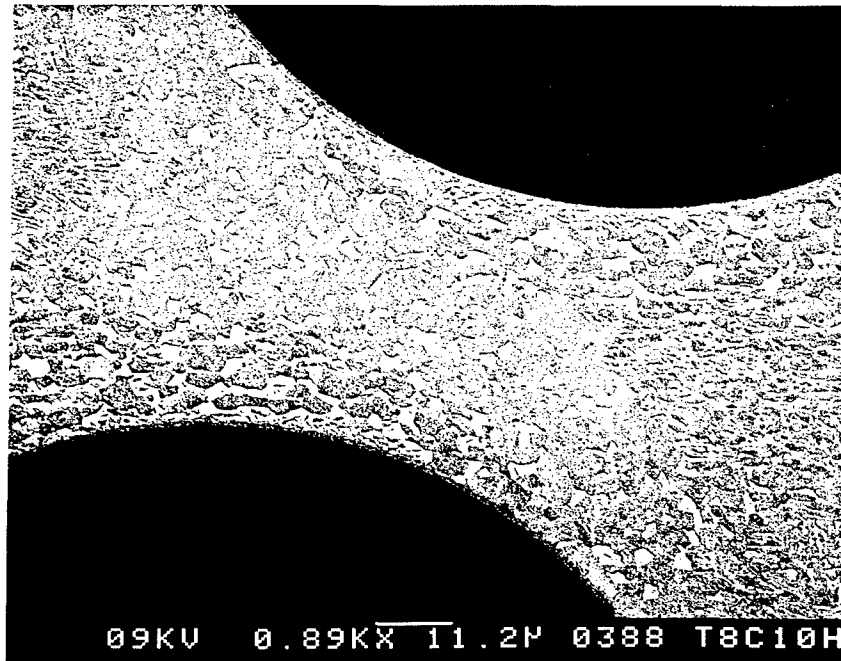


Fig. 9 Deformation inhomogeneity in the matrix after exposure at 800°C for 1000 hours. Consolidation direction top left to bottom right.

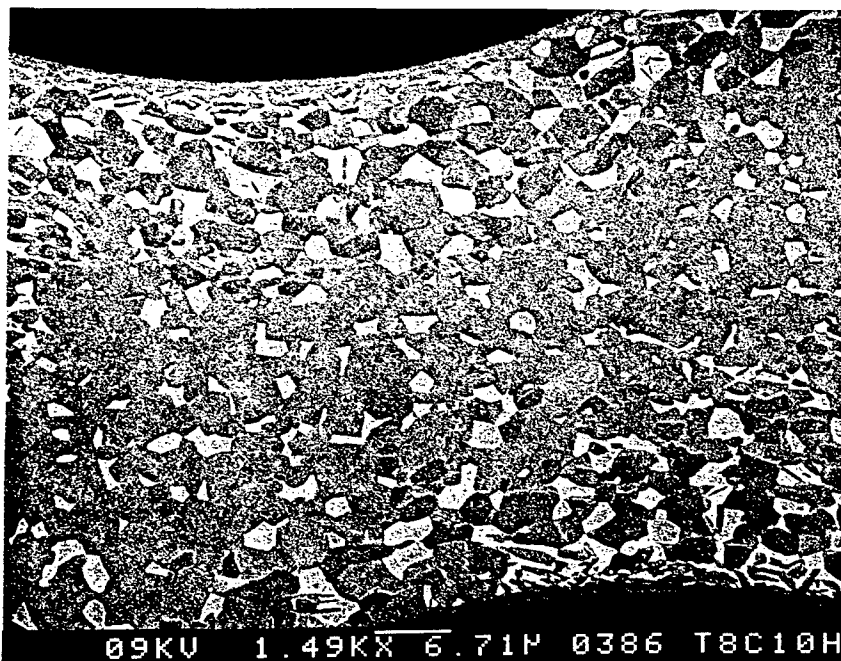


Fig. 10 A region of matrix with less β phase near the fiber.

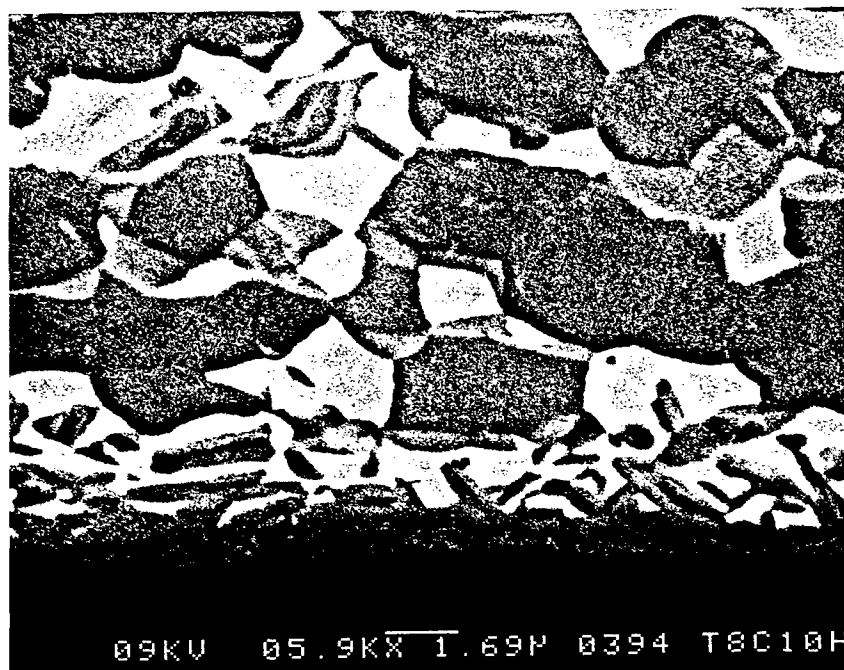


Fig. 11 Microporosity in the reaction zone after exposure at 800°C for 1000 hours.

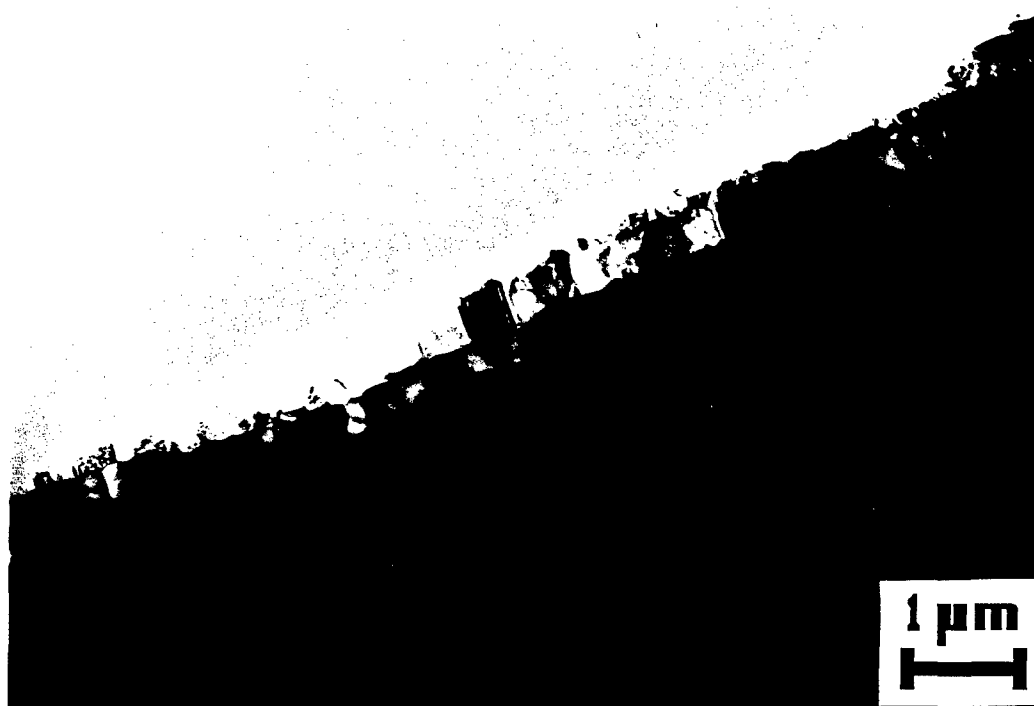


Fig. 12 Periphery of matrix showing reaction layers.



Fig. 13(a) A typical interface structure of the as-fabricated composite.

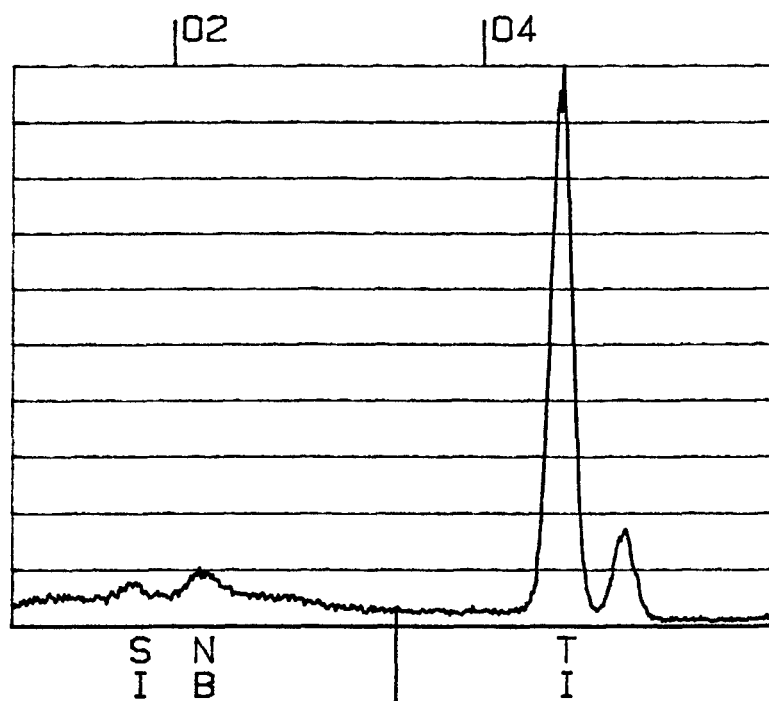


Fig. 13(b) EDS spectrum from the first reaction layer.

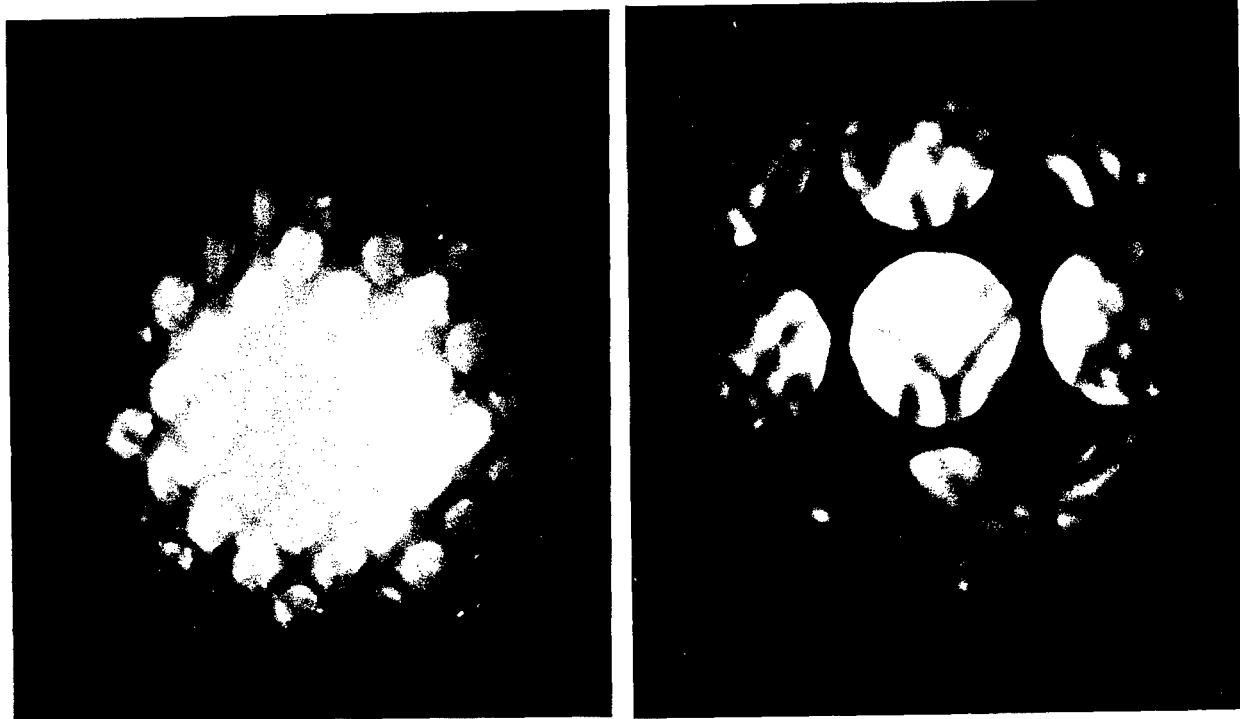


Fig. 14(a) Diffraction patterns from one of the second layer grains, indexable as $[001]_{\text{TIC}}$. (CBED patterns, very slightly off-zone axis)

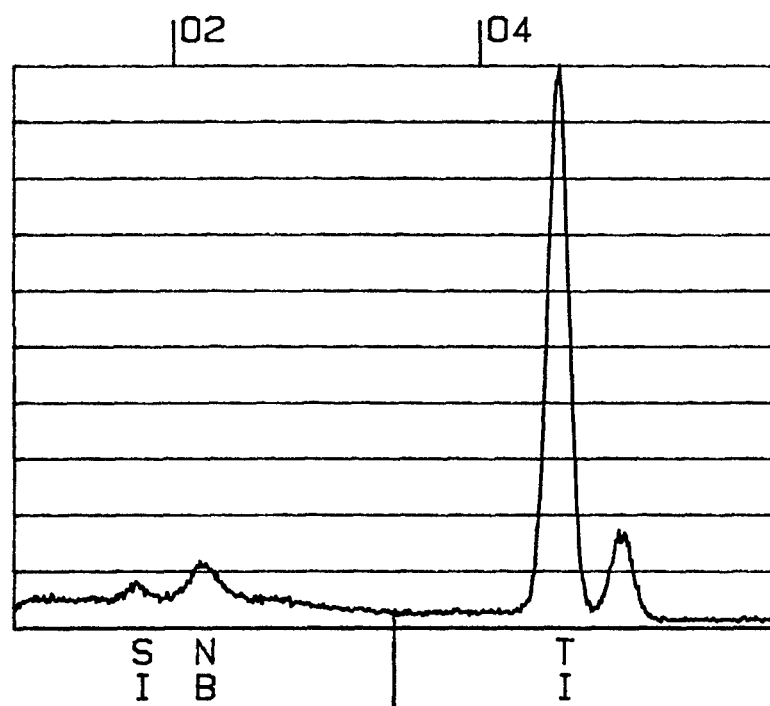


Fig. 14(b) EDS spectrum from one of the second layer grains in as-fabricated specimen..

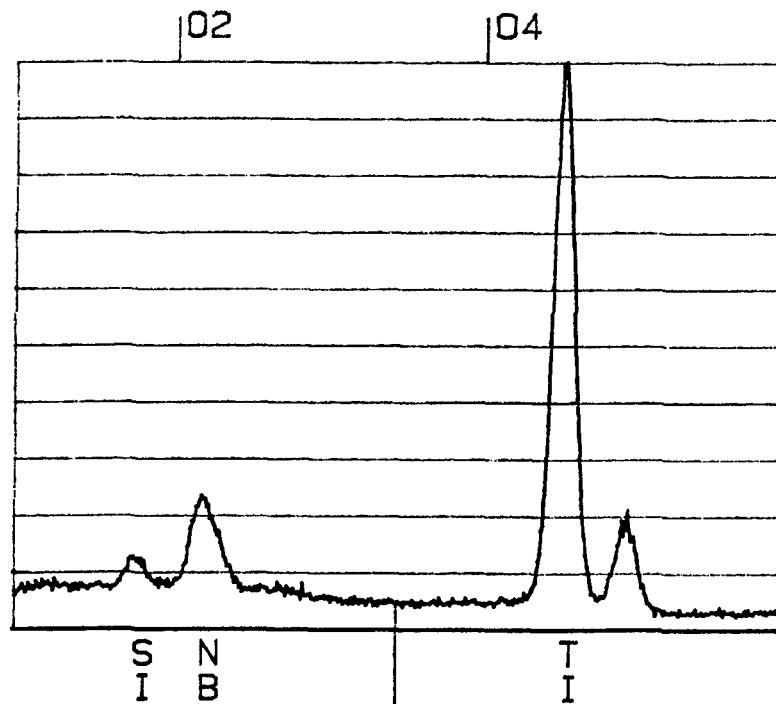


Fig. 15 EDS spectrum from third reaction layer grain in as-fabricated specimen.

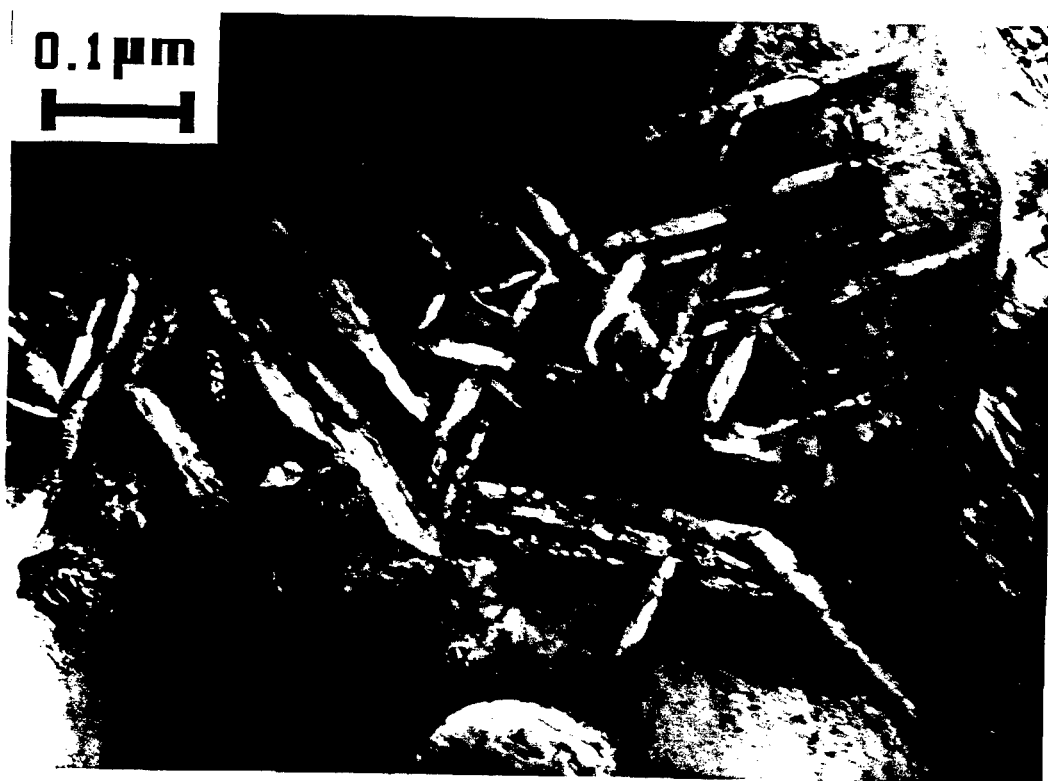


Fig. 16 A β grain containing O platelets.



Fig. 17 A typical interface structure of the composite exposed at 500°C for 500 hours. Fiber at left.



Fig. 18 Third layer of the interface in composite exposed at 800°C for 1000 hours. Fiber at top.

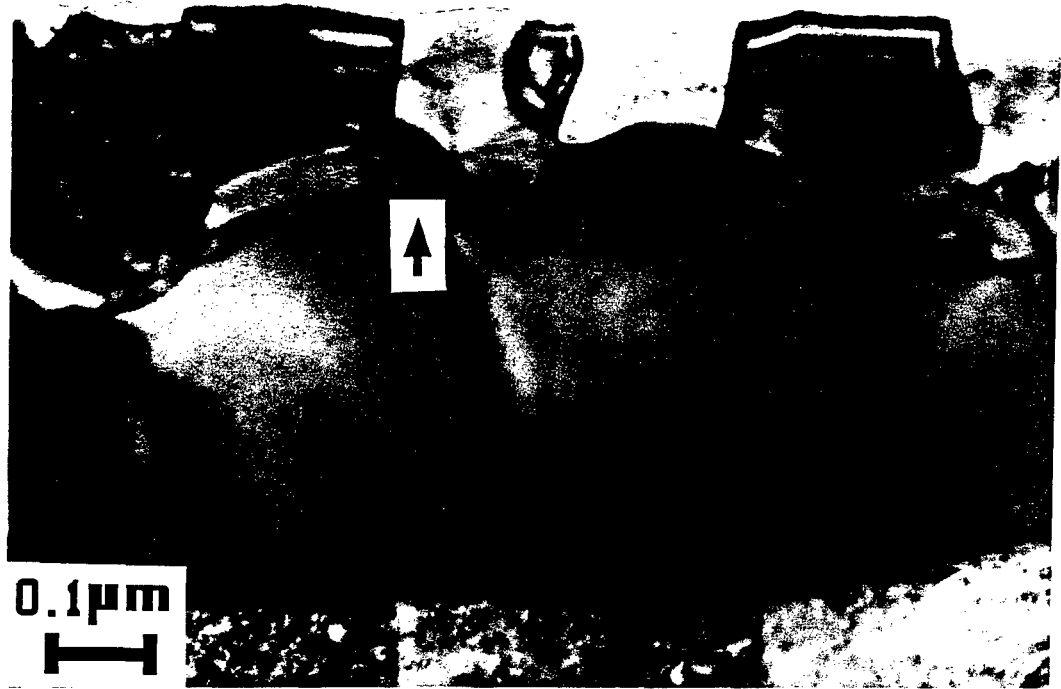


Fig. 19(a) A very long grain in the outer layer.

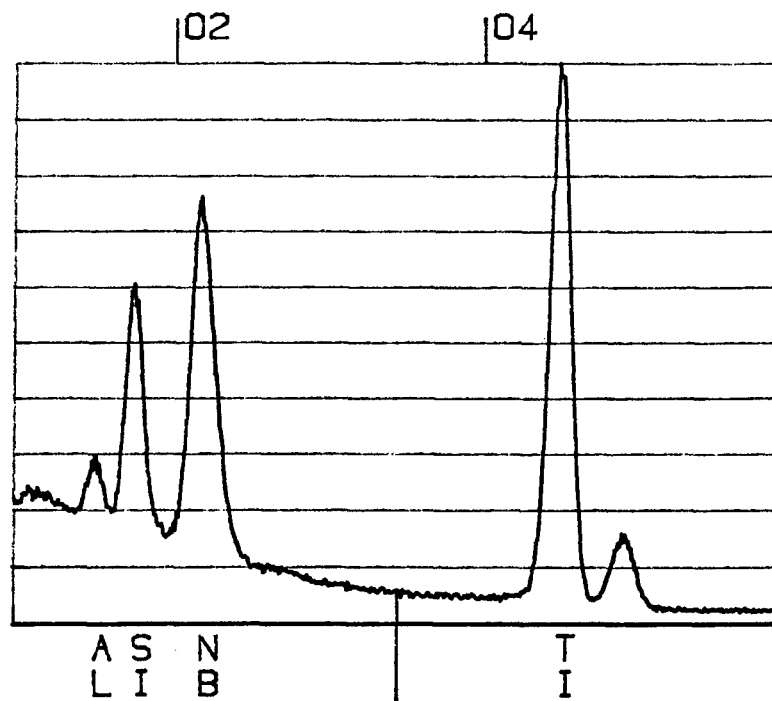


Fig. 19(b) EDS spectrum of the small grain indicated in Fig. 19(a)

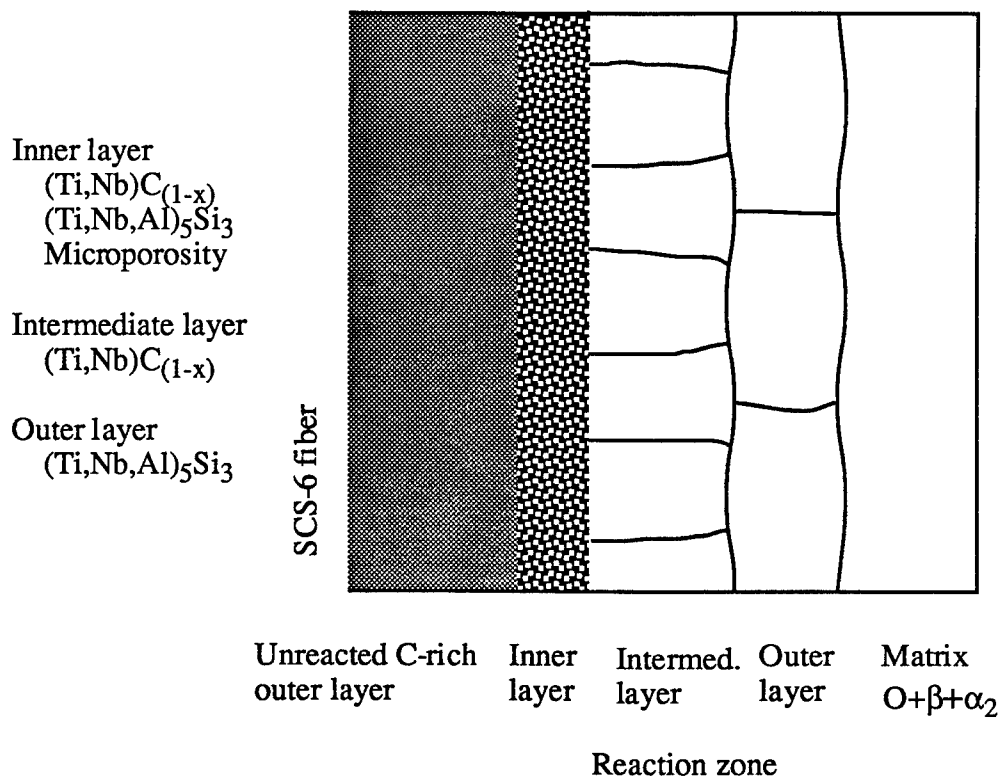


Fig. 20 Schematic diagram of the interface structure.

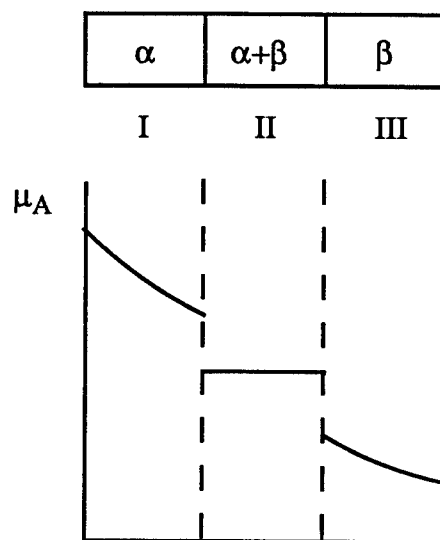


Fig. 21 A pseudo-dual phase region in a binary system.

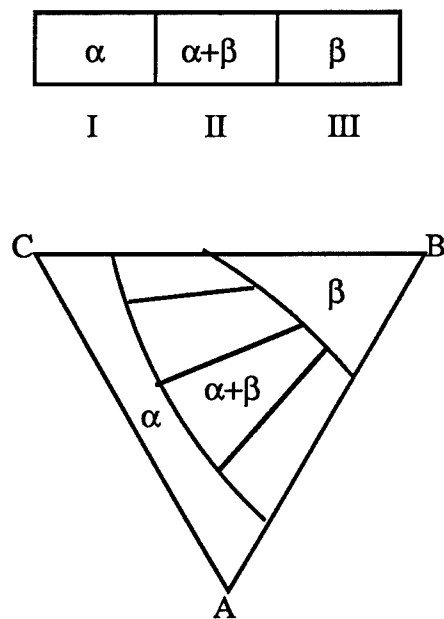


Fig. 22 A ternary system and its Gibbs triangle.

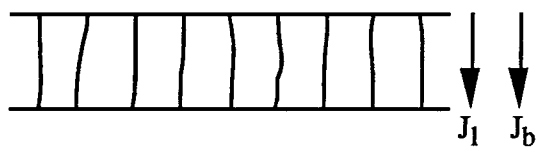


Fig. 23 A sketch of the intermediate layer in reaction zone.

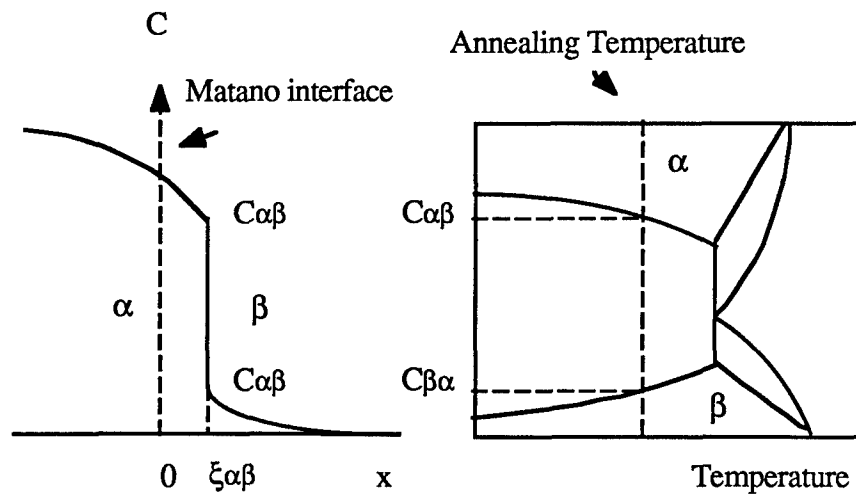


Fig. 24 The displacement of phase layer in a diffusion zone with one growing phase.

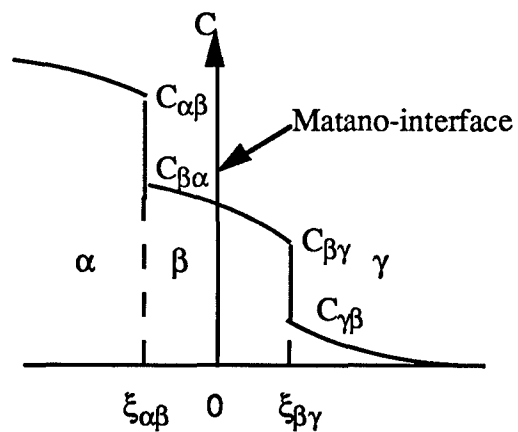


Fig. 25 A diffusion zone with three phases.

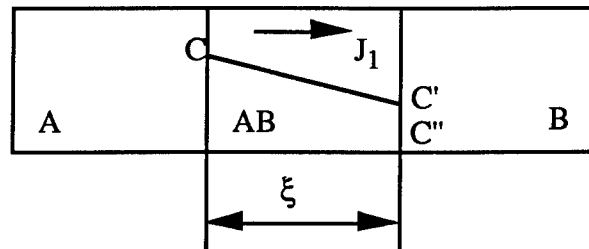


Fig. 26 Diffusion through the couple in which a compound is formed.

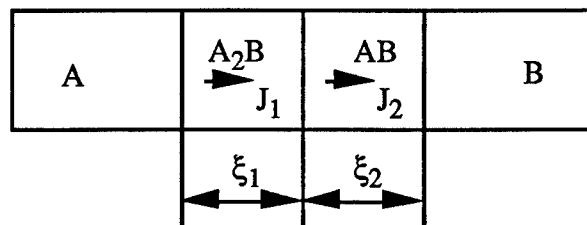


Fig. 27 A diffusion couple with two layers of intermediate phases.

**INVESTIGATION OF THE COMBUSTION CHARACTERISTICS OF CONFINED
COANNULAR JETS WITH A SUDDEN EXPANSION (TASK 150 COMBUSTOR)**

**Paul O. Hedman, Professor
David K. Pyper, Stephan Schmidt, and David L. Warren, Master Candidates
Departments of Chemical Engineering and Mechanical Engineering
Brigham Young University
Provo, Utah 64602**

**Final Report for:
Summer Research Extension Program
Aero Propulsion and Power Laboratory
Wright-Patterson AFB, OH 45433**

**Sponsored by
Air Force Office of Scientific Research
Boiling Air Force Base, Washington D.C.,
and
Brigham Young University
Advanced Combustion Engineering Research Center**

December 1993

INVESTIGATION OF THE COMBUSTION CHARACTERISTICS OF CONFINED COANNULAR JETS WITH A SUDDEN EXPANSION (TASK 150 COMBUSTOR)

Paul O. Hedman, Professor
David K. Pyper, Stephan Schmidt, and David L. Warren, Master Candidates
Departments of Chemical and Mechanical Engineering
Brigham Young University

Abstract

This third research initiation program uses data from two previous AFOSR Research Initiation Grants at BYU and three AFOSR Summer Faculty Research Programs at WPAFB. The previous studies provided lean blow out data; flame structures from still, video, and PLIF images of the OH radical; and limited LDA gas velocity data from practical fuel injectors in a geometrically simple burner. Measurement of air flow partitioning through the dome and injector passages with an analysis of images and gas velocity data have helped explain basic mixing and combustion patterns.

The focus of this third research initiation grant was to: 1) collect CARS gas temperature data; 2) evaluate the effect of side air injection on flame structure, 3) complete the evaluation of geometrical effects on lean blow out; 4) make limited gas composition measurements in fuel rich corner recirculation zones; 5) install and check out the operation of a LDA system for gas velocity measurements; 6) investigate the feasibility of burning ethanol in the Task 150 burners; and 7) analyze and interpret results obtained in this study and in the previous research initiation and summer faculty research programs.

Single shot CARS gas temperature data were collected for the T100, T150-LS, and T150-HS burners at 500 slpm air flow and at fuel equivalence ratios of 0.75, 1.00, 1.25, and 1.50. The use of a ethanol fuel in the combustors was demonstrated. The effect of side air injection on flame structure was determined for both propane and ethanol fuels. The investigation into the effects of burner geometry on LBO was completed. In addition, the effects of oxygen partial pressure on lean blow out was investigated. Limited gas composition measurements were obtained in the fuel rich corner recirculation zones. The LDA system was installed, but problems with the argon-ion laser prevented the completion of check out tests.

Analysis of instantaneous PLIF images of OH radical, LDA measurements of mean and rms velocity, and CARS measurements of mean and rms gas temperatures in the same burner operating at the same conditions has provided a unique set of measurements to help understand the mean and turbulent characteristics of the very complicated processes associated with a practical injector operating in a combustor that closely represents a real gas turbine combustor. A complete presentation of all of the results of this study is not possible within the page constraints of this report. Additional findings can be found in three technical papers that have been submitted for presentation, and in two M.S. theses that have been prepared.

INVESTIGATION OF THE COMBUSTION CHARACTERISTICS OF CONFINED COANNULAR JETS WITH A SUDDEN EXPANSION (TASK 150 COMBUSTOR)

Paul O. Hedman, David K. Pyper, Stephan Schmidt, and David L. Warren

INTRODUCTION

This study has continued the investigation of the operational characteristics of a combustor that was designed to "specifically reproduce recirculation patterns and LBO processes that occur in a real gas turbine combustor" (Sturgess, et al., 1990). During the summer of 1990, a study was begun at Wright-Patterson Air Force Base (WPAFB) to investigate the combustion characteristics of the Task 100 combustor which operates with confined coannular fuel and air jets with a sudden expansion (Hedman, 1990). Subsequently, a AFOSR research initiation grant was funded to incorporate a practical, swirling injector into the Task 100 Combustor, install combustor hardware provided by WPAFB at Brigham Young University (BYU), and conduct limited checkout and lean blow out combustion experiments (Pyper and Hedman, 1991). This Task 150 combustor uses practical swirling injectors provided by Pratt & Whitney Aircraft Co. and the combustion chamber of the simple Task 100 burner. This unique configuration allows complex diagnostic measurements to be measured in a geometry that embodies most of the features of an actual jet engine combustor in a nearly axisymmetric configuration. Figure 1 illustrates the combustion facility used at BYU to operated the Task 100 and Task 150 burners. Figures 2 and 3 show schematic drawings of the Task 100 and Task 150 combustors. The specific details of the fuel and air deliver into the Task 100 and the fuel injector and dome areas of the Task 150 combustor are illustrated. Identical Pratt-Whitney Task 100/150 combustors are installed in the Combustion Laboratory at BYU (Pyper and Hedman, 1991).and at (WPAFB).

The principal investigator and a graduate student participated in second and third summer research programs at Wright-Patterson AFB during the summers of 1991 and 1992 (Hedman and Warren, 1991; Hedman and Warren, 1992). The primary effort during the 1991 summer faculty research program was to assemble Task 150 hardware, and investigate its basic operational behavior. It was found that the flame exhibited very different operating characteristics as the fuel equivalence ratio was changed. Film images and video tape of the various operating modes as a function of fuel equivalence ratio were obtained. Measurements of the fuel equivalence ratio at lean blow out as a function of air flow rate were also obtained with and without the addition of a nitrogen diluent to the air stream. During the 1992 summer faculty research program at Wright Patterson Air Force Base, planar laser induced fluorescence (PLIF) images the OH radical were obtained for both the Task 100 and Task 150 burners configurations as well as extensive gas velocity measurements using a laser Doppler anemometer (LDA).

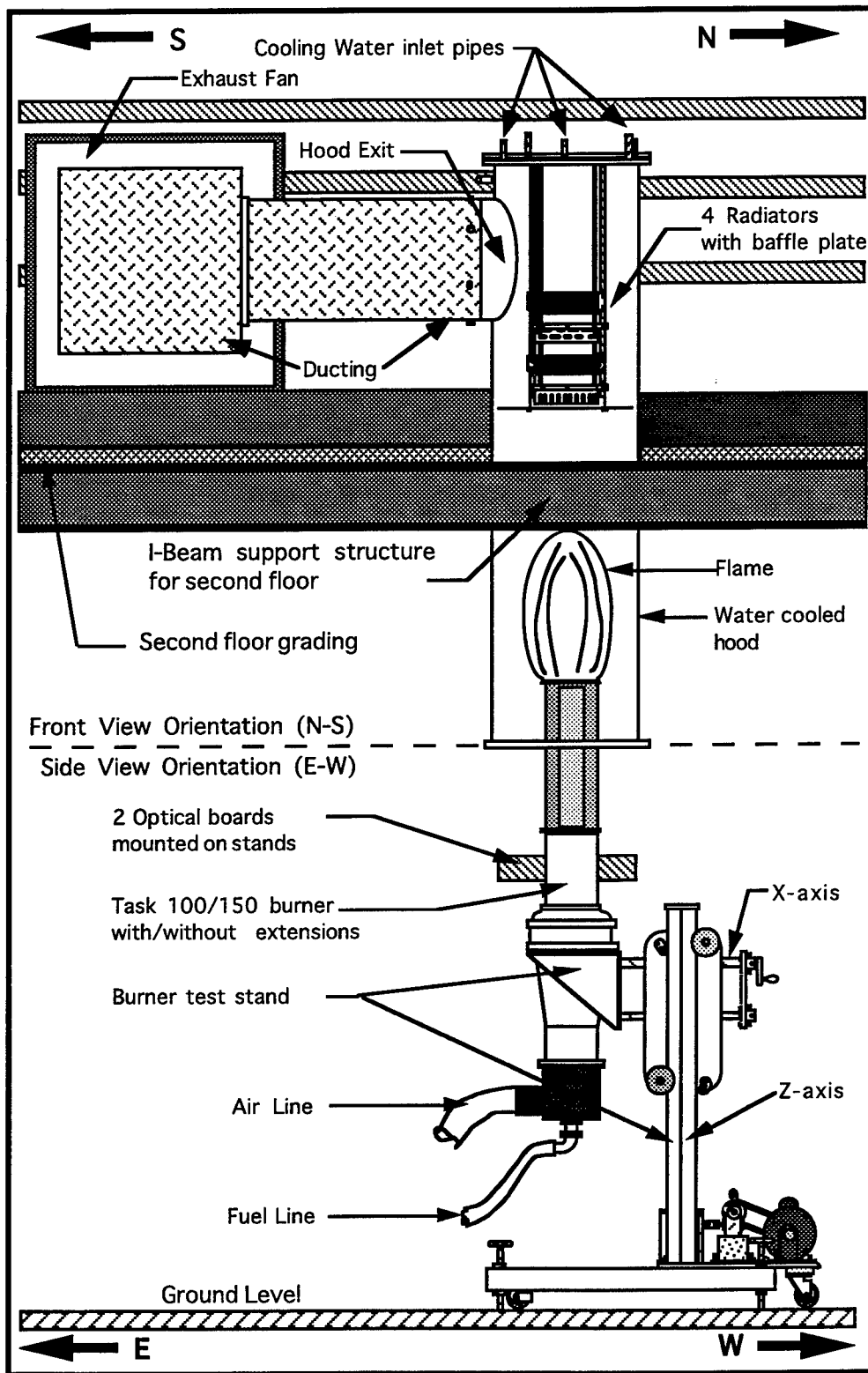


Figure 1 - Schematic of the Air Force Burner Test Facility

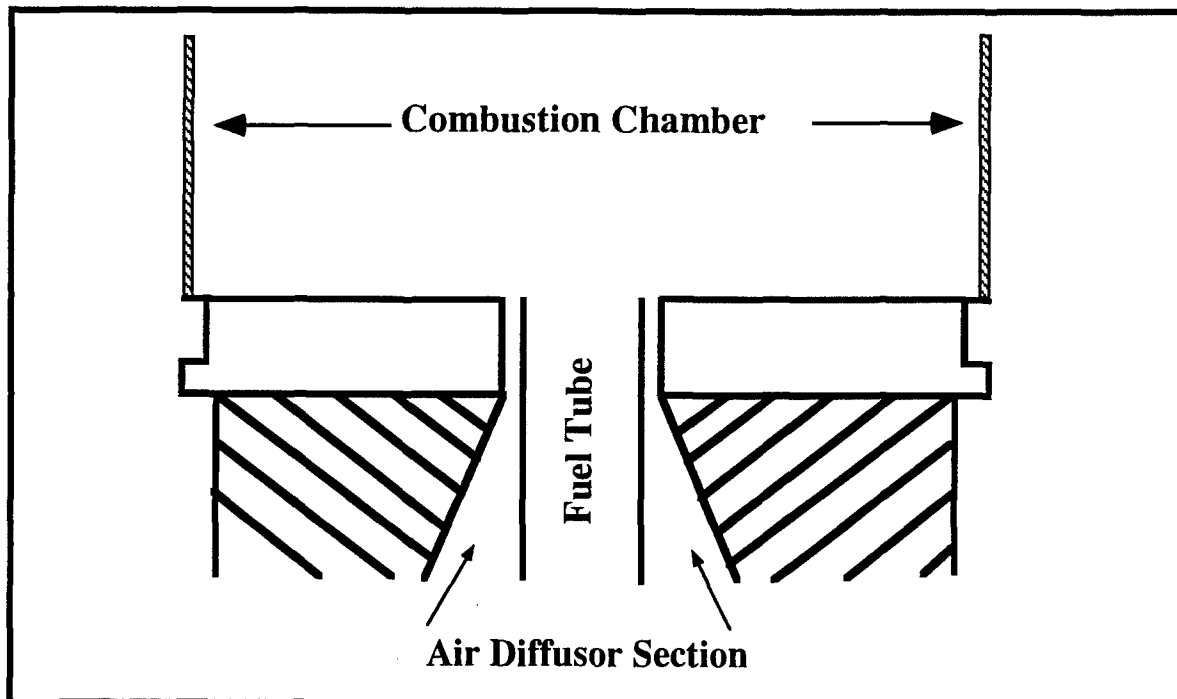


Figure 2 - Schematic Drawing of the Task 100 Burner

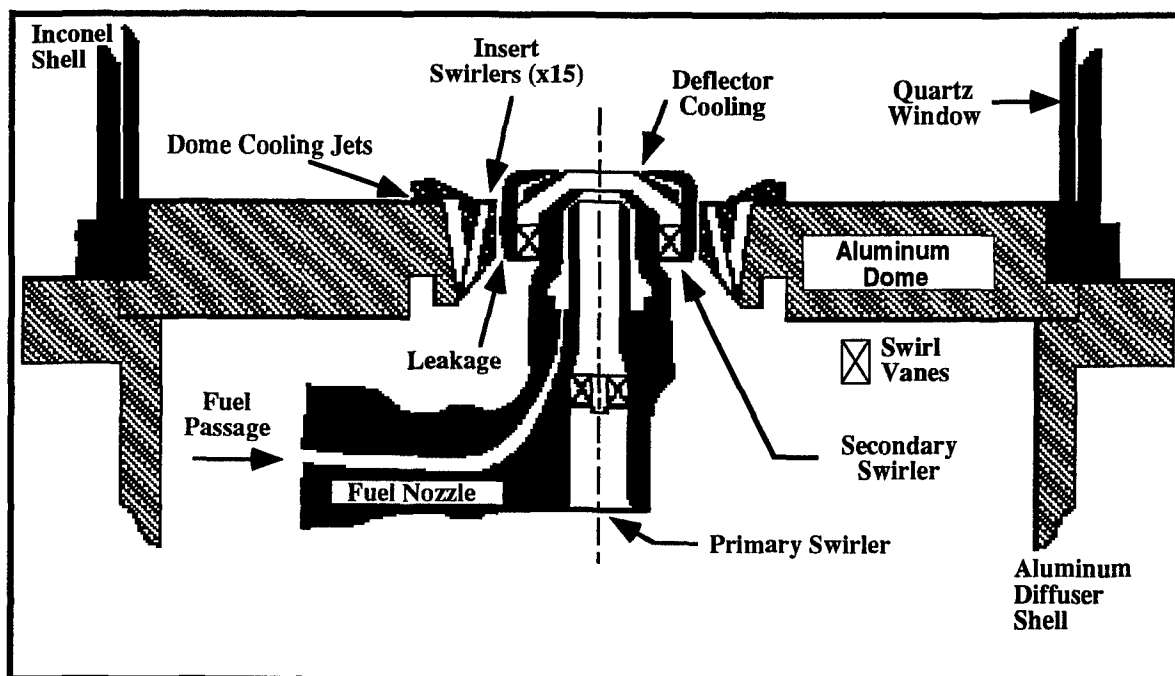


Figure 3 - Schematic Drawing of the Task 150 Burner

During the second research initiation grant (Pyper, et al., 1992) measurements to evaluate the effect of flow partitioning, and measurements to determine the effect of geometry and operating condition, including the effect of nitrogen dilution, on lean blow were completed. In addition, flame visualization was made using film photographs of Mie scattered images from sheets of laser light to evaluate flame structure.

The partitioning of the flows through the dome jets, the insert jets, the primary air swirler and the secondary air swirler has also been determined previously. The effect of fuel flow on the pressure drop across the injectors and its effect on the flow partitioning was also investigated by introducing CO₂ (same molecular weight as propane) into the fuel passage at varying flow rates (Hedman and Warren, 1991). How the air flows partition between the various flow passages in an injector seems to have a major impact on how that injector operates.

Measurements in the Task 100 or the Task 150 burners from the three summer research programs or the two research initiation programs have included: fuel equivalence ratio at lean blow out, wall temperature and pressure, imaging of the flame using a film and video cameras, imaging of a seeded flame using Mie scattering from a sheet of laser light, imaging of the flame structure using planar laser induced fluorescence (PLIF) from OH radical, and gas velocity measurements using a laser Doppler anemometer (Hedman, 1990; Hedman and Warren, 1991; Hedman and Warren, 1992; Pyper and Hedman, 1991, and Pyper, et al., 1992). Additional data that has not been fully analyzed is available from a related study completed by members of the research staff from SRL, Inc. (Post and Vilimpoc, 1992). A number of important insights into the operation of the burner and lean blow out mechanism have been drawn from the results of the five programs. Nevertheless, there remained a need for some additional data, particularly gas temperature data, and a great need existed to completely analyze and interpret the experimental results already obtained.

OBJECTIVES

The objective of this third research initiation program was to develop an understanding of the physical and chemical phenomena which contribute to the transitions from attached to lifted flames and to lean blow out. A second objective of the program was to collect instantaneous, in situ gas velocity data, gas temperature data, and images of the flame structure for comparison to computer simulations of the combustion process (Roquemore, et al., 1991). The overall research program has depended on the participation in three summer faculty research programs at Wright-Patterson Air Force Base, and the related research initiation grants. Each summer program and each research initiation grant have contributed to the overall understanding of the problem, but have been limited to a specific set of measurements. Sufficiently different sets of experimental data have now been collected to permit an integrated analysis and interpretation of the results to be made. A third objective of this specific research

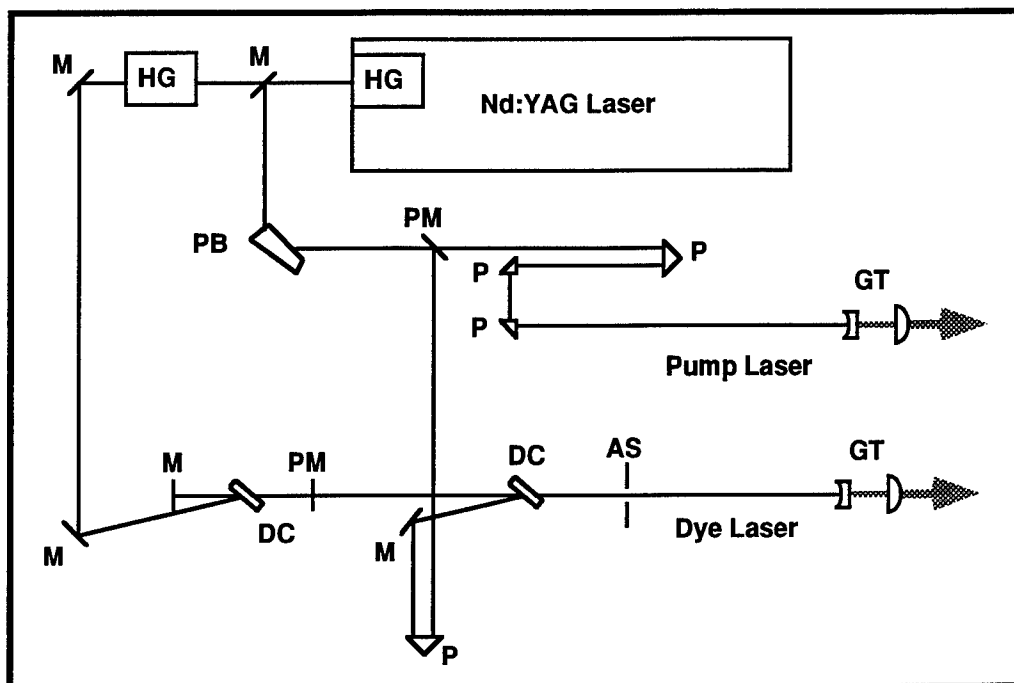
initiation grant was to complete the analysis and interpretation of the data collected in earlier parts of the overall study, and prepare an appropriate final report, M.S. Theses, and peer reviewed technical papers that summarize the findings. It is hoped that several reviewed journal articles will be published from the data and analysis conducted.

This study extended the work completed in the previous summer faculty research programs, and the companion research initiation programs. The work in this third research initiation program was done using the Task 100 combustor and the Task 150 combustor with the high swirl (HS) and low swirl (LS) fuel injectors provided to the project by WPAFB and Pratt-Whitney Aircraft Co. There were seven specific tasks that were to be completed during the course of the program. These include: Task 1 - Local Gas Temperature Measurements using coherent anti-Stokes Raman spectroscopy (CARS); Task 2 - Evaluation of Flow Partitioning (Side Air Injection); Task 3 - Lean Blow Out Measurements; Task 4 - Gas Composition Measurements; Task 5 - Local Gas Velocity Data; Task 6 - Feasibility of Burning Liquid Fuels (notably liquid ethanol) in the Task 150 Combustor; and Task 7 - Analysis and Interpretation of Experimental Results.

In general, all of the tasks as described in the work statement were completed. Some hardware difficulties with the argon-ion laser delayed the installation of the LDA system. Consequently, only the installation of the LDA system was completed. The planned checkout tests were not completed. All of the CARS temperature measurements that were planned were completed, as were the effect of side air injection on the flame structure. Not only was the use of liquid ethanol as a fuel demonstrated, but the effect of side air injection on liquid ethanol fueled flames was also determined. Because of the page constraints of this report, only example results are included in the following sections. Additional results are being presented in various technical papers that have been submitted to the International Gas Turbine Conference (Sturgess, et al., 1994), and to the 25th International Combustion Institute Meeting (Hedman, et al., 1994). Theses are also being prepared that summarize the work in great detail (Pyper, 1994; and Warren, 1994).

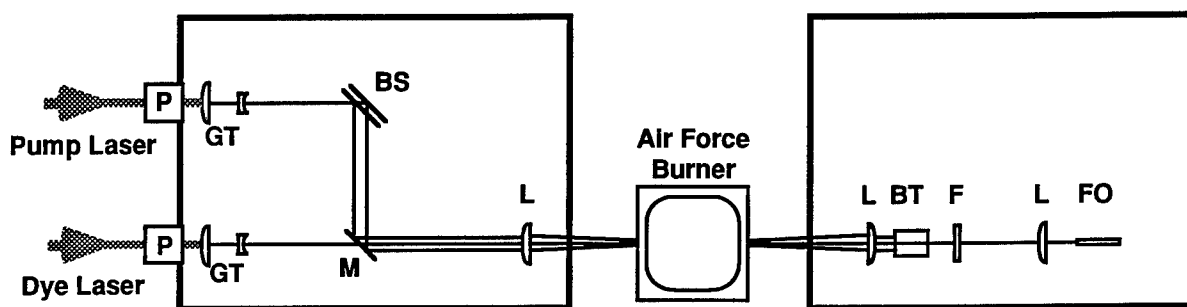
CARS MEASUREMENTS OF GAS TEMPERATURE

The BYU CARS instrument has been described in detail by Boyack and Hedman (1990); Hancock, et al., (1991), and Hancock, et al., (1992). A diagram of the main optical table modified for use in this study, is shown in Figure 4. The frequency doubled Nd:Yag laser was used to provide the pump beams for the CARS folded BOXCARS phase matching and to pump the broad band dye laser beam. Secondary optic tables were located near the reactor. A periscope consisting of a pair of two-inch right angle prisms transported each laser beam from the height of the laser table to the height of the tables near the burner. Once on the secondary optic table, the two beams were configured into the folded BOXCARS phase



AS: Auto Shutter	M: Mirror
DC: Dye Cell	P: Prism
GT: Galilean Telescope	PB: Pellin-Broca
HG: Harmonic Generator	PM: Partial Mirror

A) CARS Laser Table



BS: Beam Splitter	GT: Galilean Telescope
BT: Beam Trap	L: Lens
F: Filter	M: Mirror
FO: Fiber Optic to Spectrometer	P: Prism System

B) Optical Tables Adjacent to Combustor

Figure 4 - Schematic of CARS Instrumentation

matching geometry. The diagnostic volume was an ellipsoid in shape, and was about 1.6 mm in length and 150 mm in diameter. The CARS signal was focused into the end of a 50 mm fiber optic cable and conveyed to 1024 photo diode array in the spectrometer, digitized in a Optical Multichannel Analyzer, and collected and stored with a Macintosh Quadra 800 computer. Each single shot CARS spectra was analyzed by comparing the experimental CARS spectra for nitrogen to libraries of nitrogen spectra generated at discrete temperatures using spectral programs provided by Sandia National Laboratories (Palmer, 1989).

The CARS temperature data measurements were made at locations and test conditions to closely correspond with the velocity data sets collected at WPAFB. There was a limitation in the ability to take CARS temperature data near the combustor wall. The diagnostic volume formed with the powerful CARS lasers could not be positioned away from the combustor centerline without damaging the quartz windows. Thus, optical access was restricted to about ± 30 mm each side of the centerline on a $Y=0$ mm axis. . Nevertheless, instantaneous gas temperature measurements were obtained over the complex combustion zone near the fuel injector.

Five-hundred separate data points were collected at each diagnostic location. Four complete data sets were obtained for the Task 100, the Task 150-LS, and the Task 150-HS burners at fuel equivalence ratios of 0.75, 1.00, 1.25, and 1.50 and at an air flow rate of 500 slpm. Thus, direct comparisons of the flow field determined from the gas velocity (LDA) and the temperature field determined from the CARS measurements are possible at the fuel lean ($\phi = 0.72$ versus 0.75) and at the very fuel rich ($\phi = 1.49$ versus 1.50) cases. In addition, the temperature measurements at $\phi = 1.00$ and $\phi = 1.25$ allow the changes in temperature distributions to be seen as the fuel equivalence ratio changes from fuel lean to fuel rich.

The instantaneous local gas temperature measurements have been used to generate two-dimensional iso-contour plots that map both the mean and RMS (standard deviation) gas temperature measurement across the various flame zones in the combustor. These contour plots are shown in Figures 5 and 6 for the Task 100 burner, Figures 7 and 8 for the Task 150-LS burner, and in Figures 9 and 10 for the Task 150-HS burner. Each contour plot was generated from the centerline to the + 33 mm location using commercial computer software (Spyglass Transform, 1993). The plot was then duplicated, flipped horizontally, and both the original and mirrored plots combined with a scaled schematic drawing of the appropriate combustor. The composite symmetrical presentation clearly shows the various temperature zones with respect to the injector. The odd numbered figures (Figure 5, 7, and 9) presents the distribution of the mean gas temperature across the combustion zone. The even numbered figures (Figure 6, 8, and 10) present the distribution of the RMS gas temperature across the combustion zone.

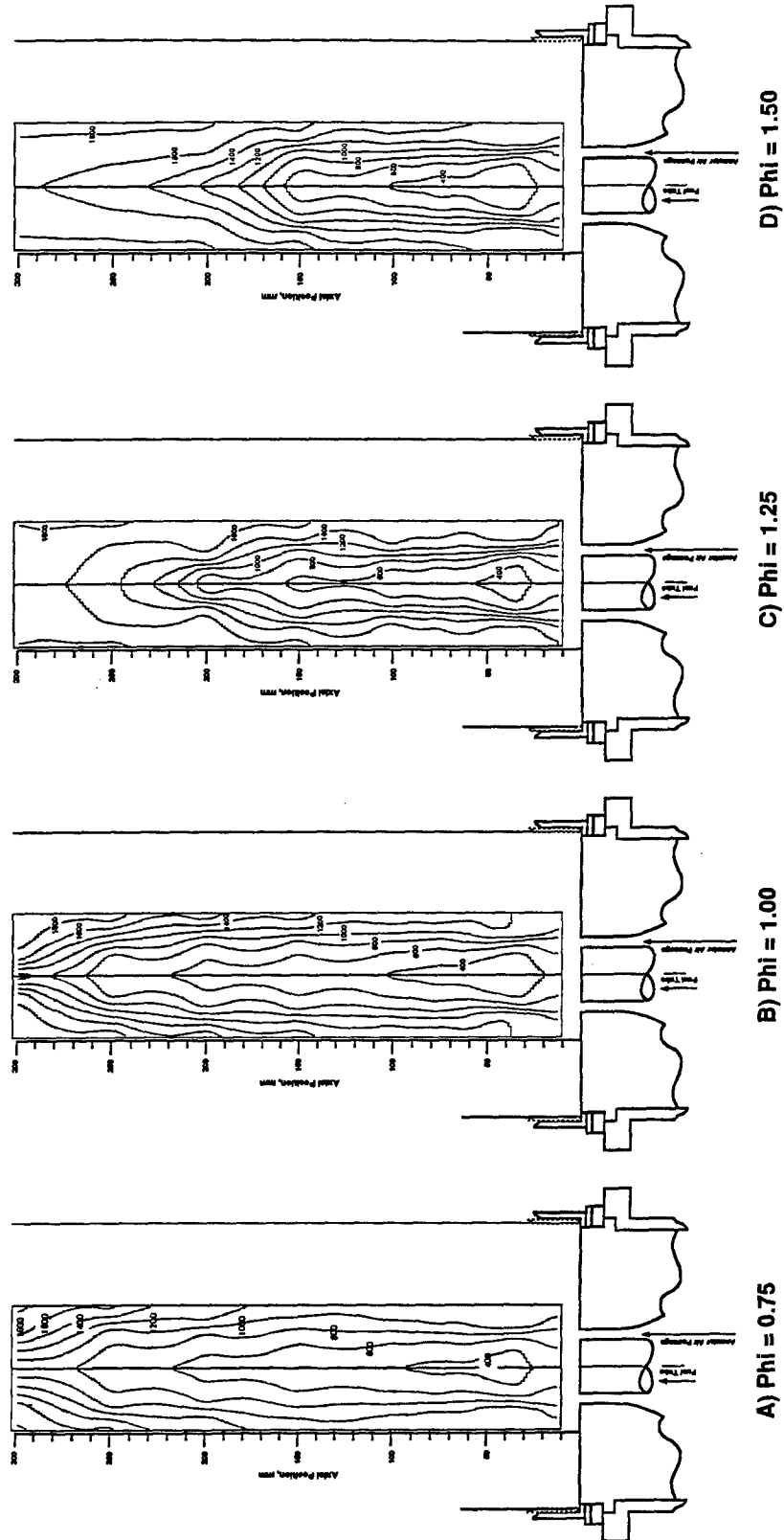


Figure 5 - Mean Isothermal Gas Temperature Contours
(Task 100 Burner, 500 slpm Air flow)

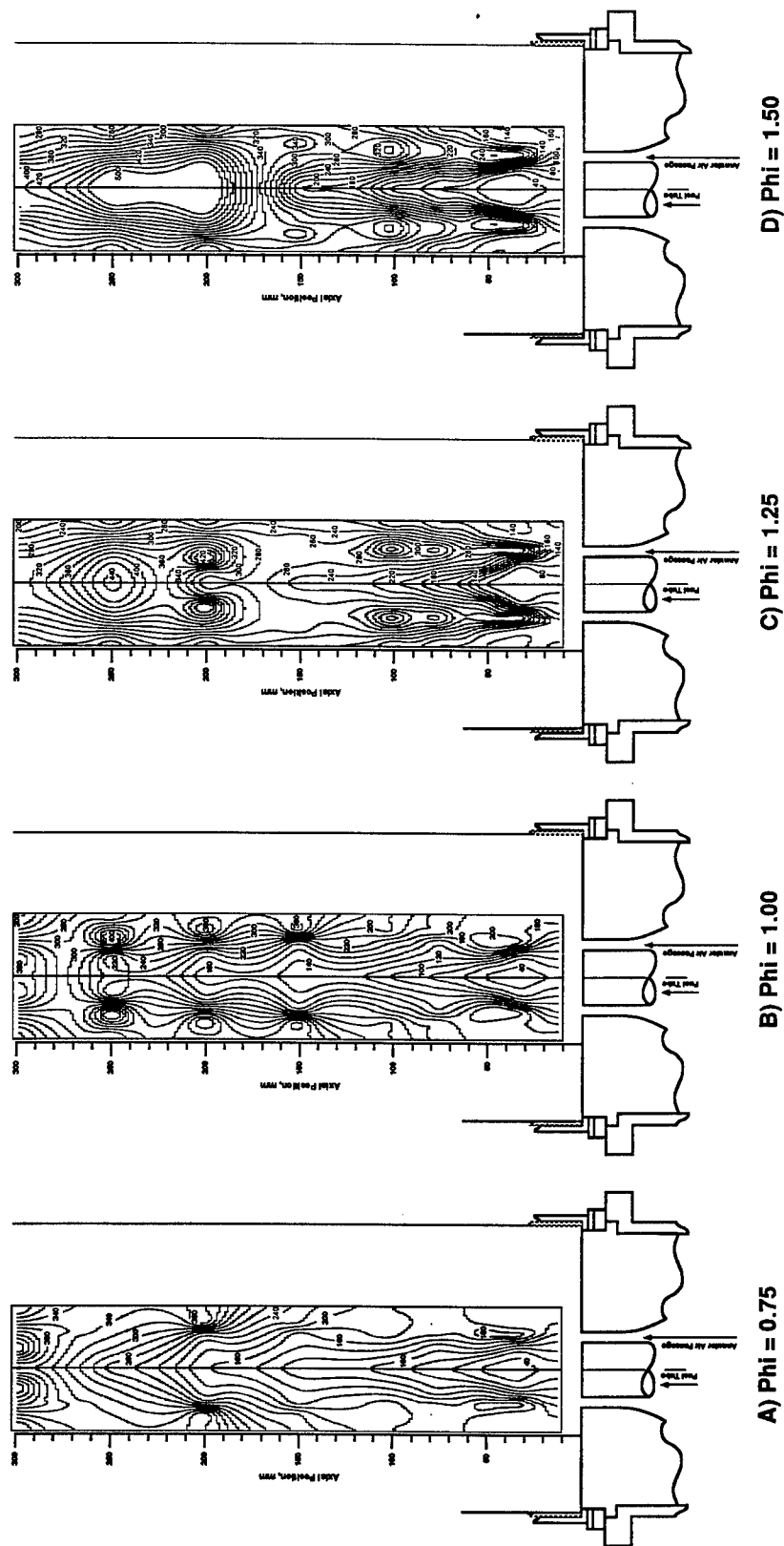
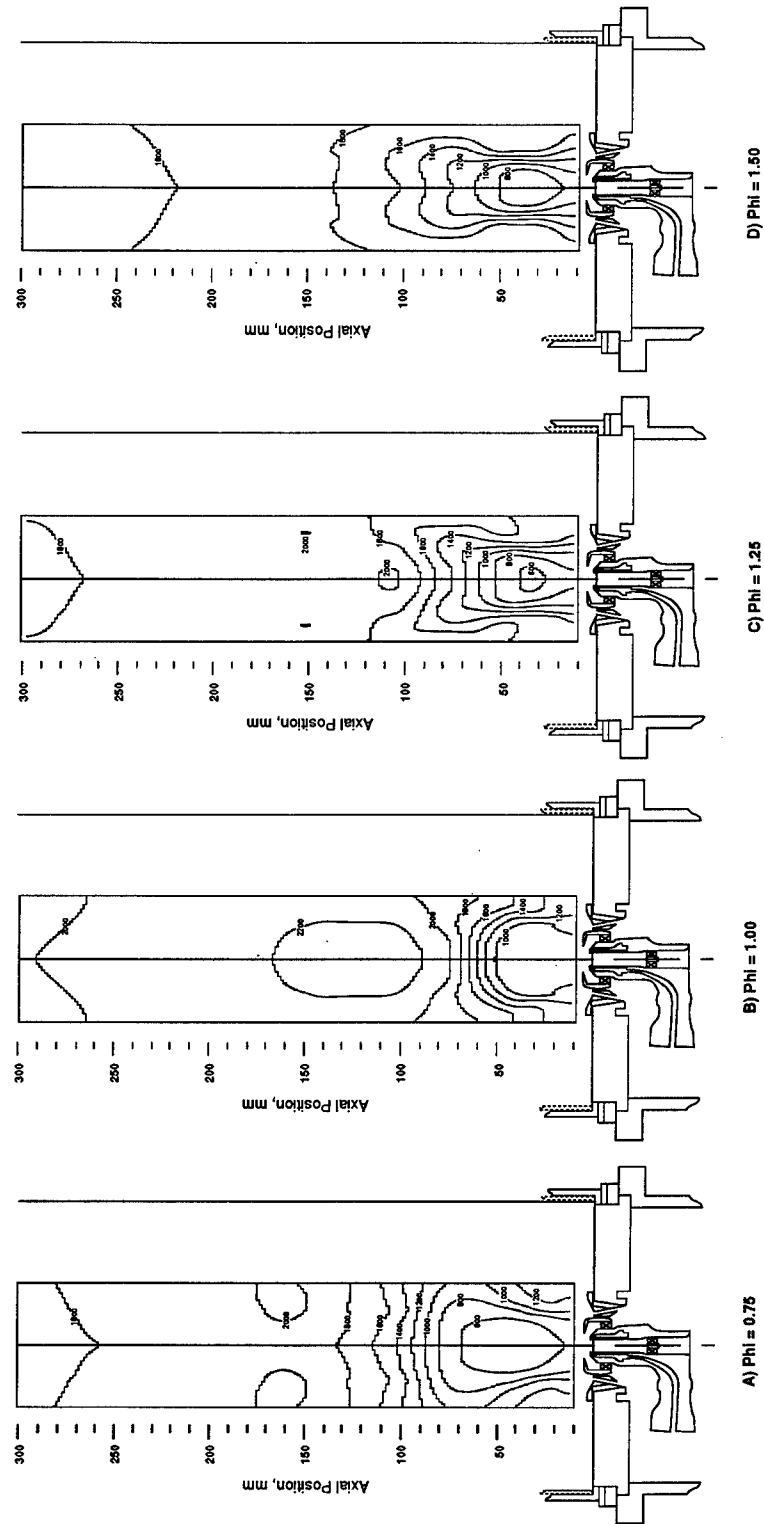
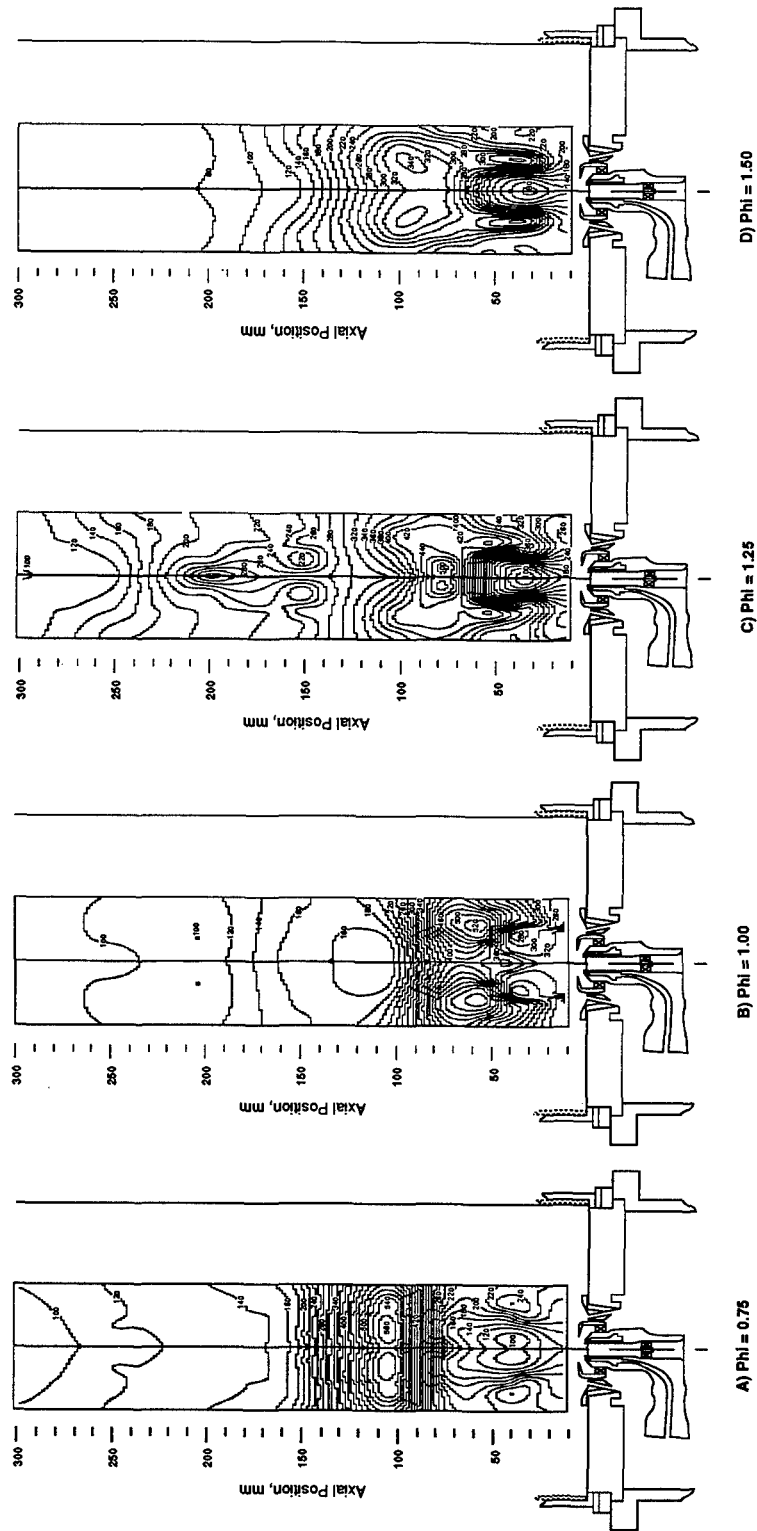


Figure 6 - RMS Isothermal Gas Temperature Contours
(Task 100 Burner, 500 slpm Air flow)



**Figure 7 - Mean Isothermal Gas Temperature Contours
(Task 150-LS Burner, 500 slpm Air flow)**



**Figure 8 - RMS Isothermal Gas Temperature Contours
(Task 150-LS Burner, 500 slpm Air flow)**

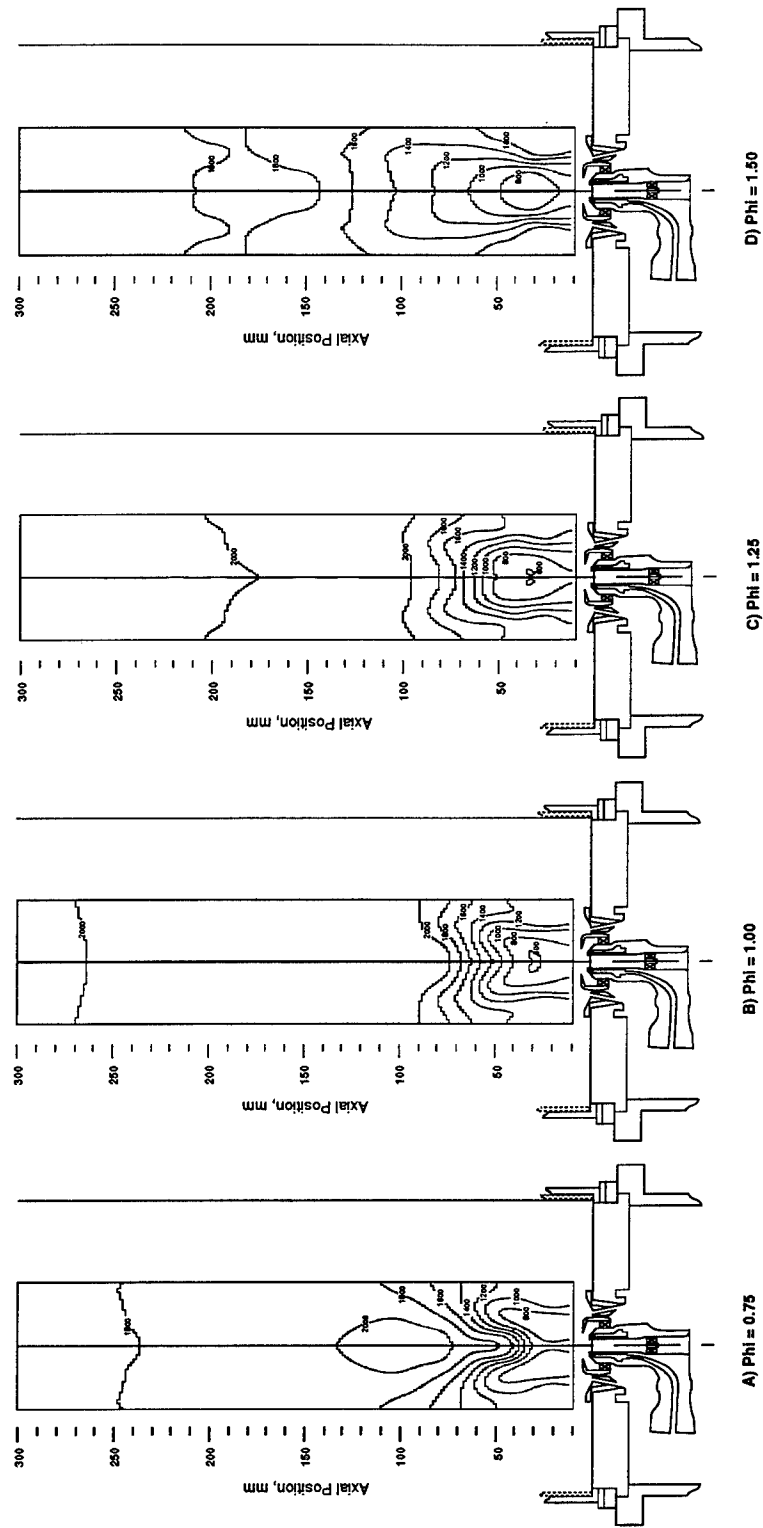
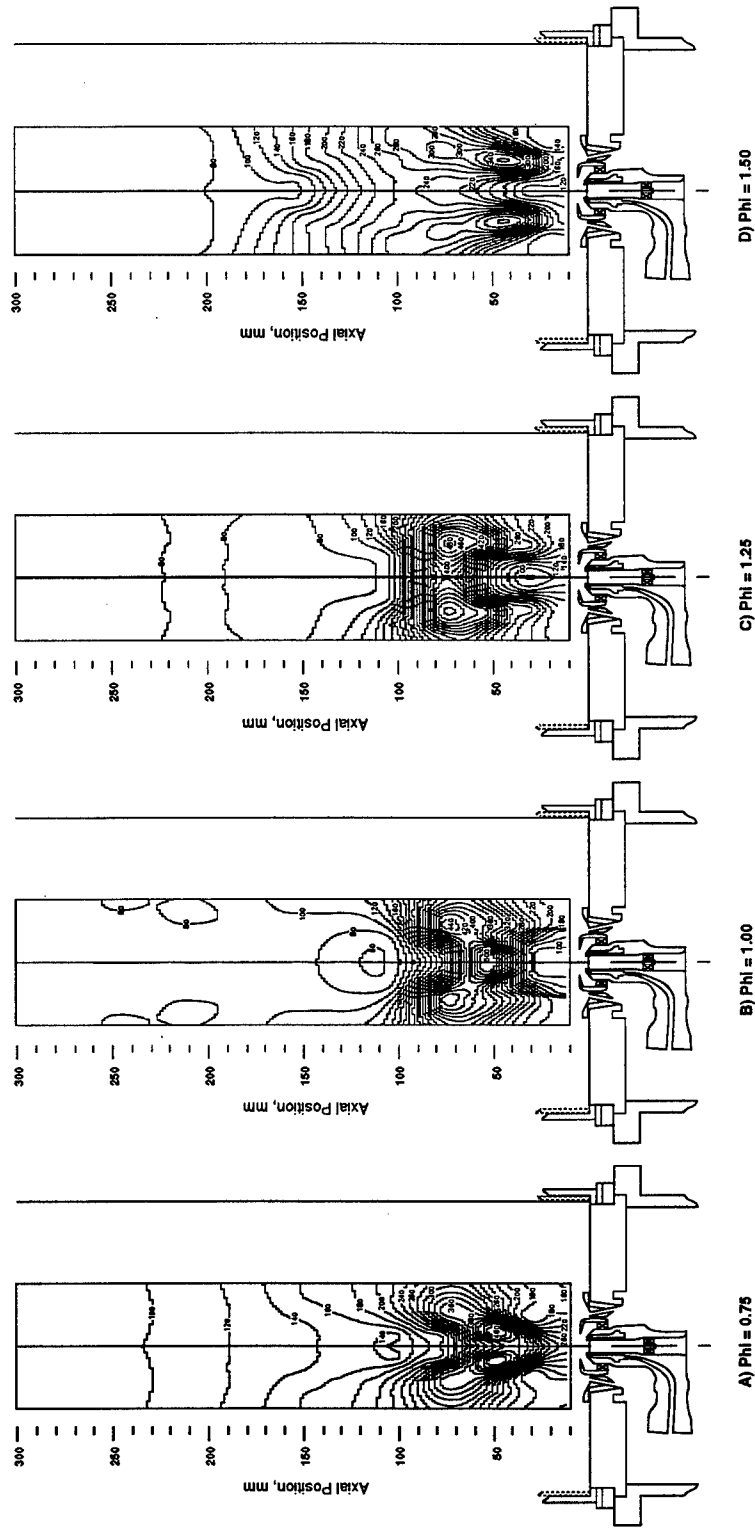


Figure 9 - Mean Isothermal Gas Temperature Contours
(Task 150-HS Burner, 500 slpm Air flow)



**Figure 10 -RMS Isothermal Gas Temperature Contours
(Task 150-HS Burner, 500 slpm Air flow)**

The temperature iso-contours for the Task 100 burner, as shown in Figure 5, vary considerably as the fuel equivalence ratio is varied from a fuel lean condition ($\phi = 0.75$) to a fuel rich case ($\phi = 1.50$). In the fuel lean case, the highest temperatures are associated with a flame zone that seems attached to an upper recirculation zone. As the fuel equivalence ratio is increased, the highest temperature zone moves to the outside edge of the diffusion flame, and higher temperatures are observed near the dome of the combustor at $\phi = 1.50$. In each fuel equivalence ratio case, there is a relatively cold zone (ca 400 K) on the centerline of the burner, just above the fuel tube. The shape of this zone changes somewhat as fuel equivalence ratio changes, which suggests that there is some effect of the heat release on the fluid dynamics.

An analysis of the probability density function of the gas temperature data has shown a rather narrow PDF in regions of nearly uniform gas temperature, either hot or cold. These regions also seem to correspond to regions of nearly uniform velocity. However, in regions of large velocity gradient, a large gradient in gas temperature also seems to exist. In these high gradient regions, a large value of RMS gas temperature occurs. This has suggested that the iso-contour maps of RMS gas temperature will show regions in the flame where large gradients, and high turbulence exist. This seems to be supported in Figure 6, where significant structures are evident in the RMS temperature contour plots. The shape, intensity, and location of these structures varies widely as fuel equivalence ration is changed from $\phi = 0.75$ to $\phi = 1.50$. The RMS contour plots seem to show the major recirculation zones in the flame where the flame is stabilized. These recirculation zones have also been seen in the LDA gas velocity data, the PLIF images of OH, and in visual images of the flame. The observations thus far on the implications of these RMS gas temperature structures has been limited by the scope of this study. Nevertheless, this data does provide considerable insight into the combustion phenomena of the Task 100 burner.

The two-dimensional iso-contour plots of mean and RMS gas temperature for the Task 150-LS burner are shown in Figures 7, and 8. Figure 7 (mean temperature) shows low temperature zones near the outlet of the injector which extends to the insert jets. This zone appears to be bounded by the insert jets, which form a cup around the swirling air where the combustion is taking place. The gas immediately outside this cup is recirculated hot products from the combustion zone mixed with cold air from the dome jets. A funnel-like flame structure is evident in the both the mean and RMS plots. This funnel like structure has also been seen in visual images of the flame. The location of the peak temperatures changes dramatically as the fuel equivalence ratio is increased from the fuel lean condition to the fuel rich condition. In the fuel lean experiments, the peak temperature is located near the centerline, and is associated with the down stream recirculation zone. As the fuel equivalence ratio is increased, the peak temperature zone moves outward, and becomes associated with the additional air being injected through the insert jets. In the

$\phi = 1.50$ case, there is a suggestion the peak temperature lies outside the main flame zone associated with the injector, and is most likely the highest in the corner recirculation zone.

Figure 7 also shows a significant change in the peak temperatures associated with the changes in operating condition. The peak temperature occurs in the stoichiometric case, and is close to the predicated adiabatic flame temperature of 2273 K. Peak temperatures are lower in both the fuel lean and fuel rich cases. This figure also shows that the temperature field has become relative uniform by about the 150 mm axial location for each flame condition. Given the wide variety of flame shapes exhibited by the burner over the range of fuel equivalence ratios tested, this uniformity probability can be attributed to a relatively stable downstream recirculation zone. The LDA velocity data also showed uniformity downstream of about 150 mm.

Figure 8 presents the RMS iso-contours of gas temperature at each of the experimental fuel equivalence ratios tested. As with the Task 100 results, the highest RMS values seem to be associated with regions of high gradient and high turbulence. Interesting structures can be seen which change significantly as fuel equivalence ration is changed. The area of highest RMS temperature appears to be toroidal in nature approximately 20 mm in diameter and 50 mm downstream of the injector. This area of high RMS temperature is also in an area of high RMS velocity and is a region of very turbulent, unsteady, combustion.

Figures 9 and 10 present the mean and RMS gas temperature iso-contours plots for the Task 150-HS burner, respectively. These figures are very similar to the figures shown for the LS burner. Peak temperatures are about the same, and the flame seems to move from being attached to a recirculation zone near the injector for the fuel lean case to being attached to the insert jets for the fuel rich case. Figure 9 (mean temperature) shows a low temperature zone near the outlet of the injector which extends to the insert jets, which is similar to that observed with the LS burner. This zone also appears to be bounded by the insert jets. As with the LS burner, the gas immediately outside the insert jets is recirculated hot products from the combustion zone mixed with cold air from the dome jets. A tornado-like flame structure is evident in the both the mean and RMS plots. This tornado like structure is even more pronounced in this HS case. The location of the peak temperatures also changes dramatically as the fuel equivalence ratio is increased from the fuel lean condition to the fuel rich condition. As with the LS case, the peak temperature is located near the centerline in the fuel lean experiments, but is near the insert jets in the fuel rich case

Figure 10 presents iso-contours of RMS gas temperature for the HS case. As with the Task 100 and Task 150-LS results, the highest RMS values seem to be associated with regions of high gradient and high turbulence. As with the LS case, interesting structures can be seen which change significantly as fuel

equivalence ration is changed. The area of highest RMS temperature also appears to be toroidal in nature approximately 20 mm in diameter and 50 mm downstream of the injector. This area of high RMS temperature is also in an area of high RMS velocity and is a region of very turbulent, unsteady, combustion. Interesting funnel shaped and toroidal shaped structures are present, the location and intensity of which changes dramatically as fuel equivalence ration is changed.

EVALUATION OF FLOW PARTITIONING (SIDE AIR INJECTION)

One of this years tasks was to perform a study of how the flame structure and stability in the burner was affected by injecting air into the sides of the burner. In order to facilitate the air injection, the burner required a few modifications. New burner side walls were designed and manufactured. Figure 11 shows a schematic drawing of the burner with the added air injection ports. The two opposing side walls contained the air injection ports, two on each side as shown in the figure. The set of four injection ports were located at various axial positions so the effect of air injection into different flame zones could be investigated. The axial locations began at 25 mm and was incremented at a 25 mm interval to a position of 175 mm above the dome of the burner. Each of the four individual injectors provided 1/4 of the total injected air volume. The active injectors were connected to a pressurized air tank via copper tubing, while the unused injectors were plugged to prevent leakage.

Test were performed using the Task 150-HS burner configuration with a primary air flow rate of 500 slpm at $\phi = 1.25$ and $\phi = 1.5$ using both gaseous propane and liquid ethanol as fuel, and side air injection rates of either 100 or 200 slpm. Each of the four tests was performed at each injector location for both the propane and ethanol fuels. The tests were recorded on video tape for later analysis. Figure 12 and Figure 13 contain digitized contour images of selected injection tests captured from the video tapes using the computer video editing capabilities available in the laboratory. Complete copies of the video tapes will be sent to Drs. G. J. Sturgess at Pratt & Whitney and W. M. Roquemore at Wright-Patterson Air Force Base.

Figure 12 shows example effects on the flame structure of injecting 200 slpm of air at four discrete locations in the propane flame at a $\phi = 1.5$. The flame without air injection is approximately 150 mm long, slightly lifted and has a fairly even intensity throughout its structure. Injection at a position of 25 mm causes the bottom of the flame to be attached to the injection jets and reduces the flame length to about 50 mm, producing a very bright, intense disk-like flame. The flame is very stable at this point. Injecting the air at a position of 75 mm also produces a very stable flame. In this case the flame is also very bright and intense, having a slight funnel shape with the top being at the level of the injection jets and the bottom being lifted about 25 mm. Injecting the air at a position of 125 mm produces a stable flame with a flat top at the level of the injection jets and a bottom lifted approximately 25 mm. When injecting at a position of

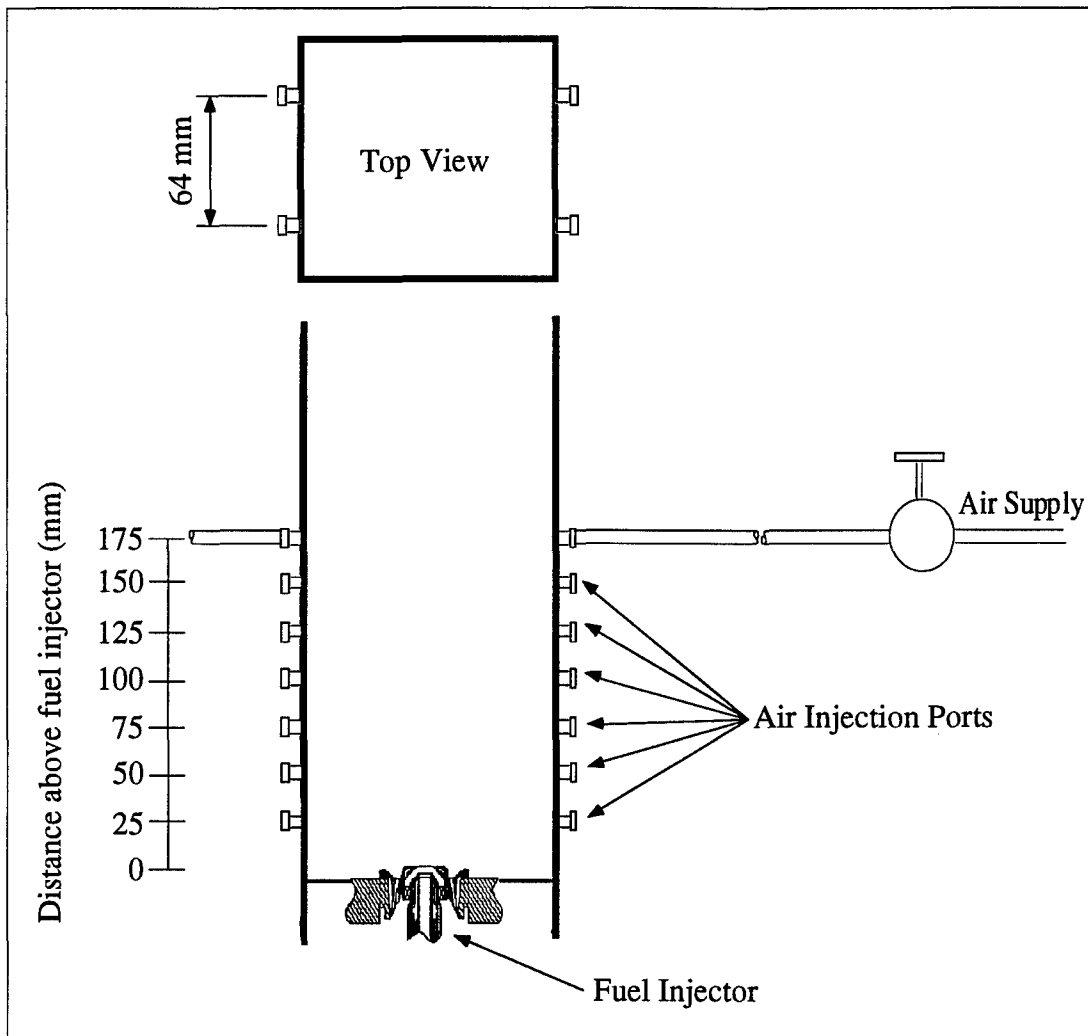


Figure 11 - Schematic of Air Injection on Task 150-HS Burner.

75 mm the flame also has a flat top at the level of the injection jets and a lifted bottom, but it also has a secondary set of flames attached directly to the incoming air jets.

The air injection tests using ethanol as fuel were performed using the same conditions and burner configuration as with the propane fuel. The ethanol was stored in a sealed pressure tank and forced out by means of a bladder in the tank which was attached to a high pressure air system. This configuration allowed for very precise ethanol flow rate regulation. Earlier attempts to feed the ethanol by just pressurizing the fuel tank with nitrogen were less that successful. Nitrogen, which had dissolved into the liquid alcohol fuel, would form gas bubbles in the fuel feed line which would interrupt the fuel flow and extinguish the flame. The use of a pressurized bladder within the fuel tank solved this problem.

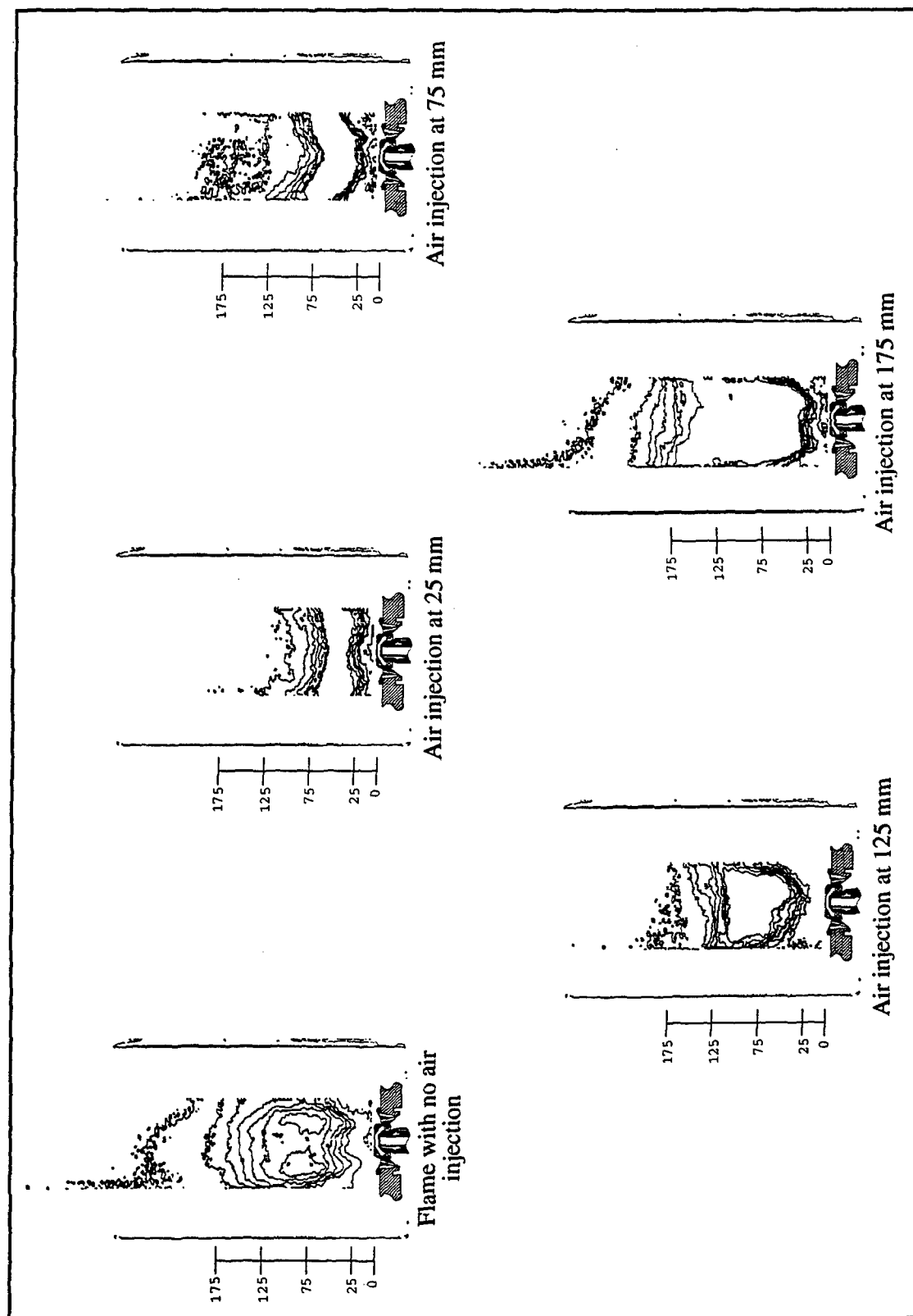


Figure 12. Effect of Side Air Injection on Flame Shape in the Task 150-HS Burner
($\Phi = 1.50$, Gaseous Propane Fuel, 500 slpm Air Flow with Side Air Injection of 200 slpm)

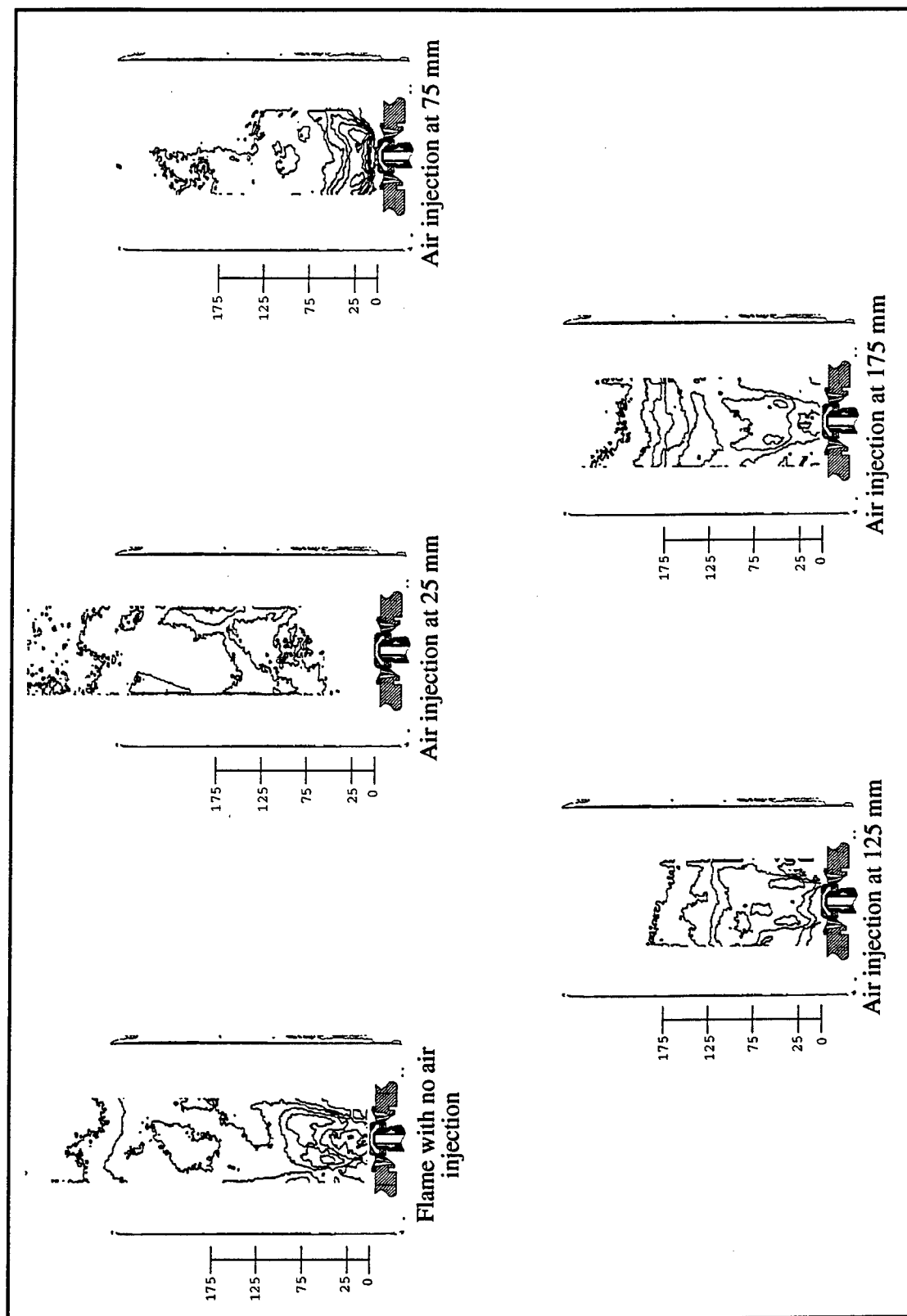
Figure 13 shows digitized contour images for the ethanol flame. The ethanol flame looks very different from the propane flame. At a $\phi = 1.5$ and with no air injection the ethanol flame is about 125 mm long and completely attached with a large orange soot cloud filling the rest of the burner. Injecting 200 slpm of air at 25 mm produced a very unstable lifted flame which appeared to burn off the walls of the burner. When the air was injected at a position of 75 mm the flame was crunched down below the injection jets and there was only a slight orange soot cloud. Injection at 125 mm produced a stable, attached flame with the top of the flame being at the level of the injection jets. In this case the orange soot cloud completely disappeared. Air injection at 175 mm produced a flame similar to the propane flame at the same test conditions, the top of the flame was level with the injection jets and there were secondary flames attached to the incoming air jets, the major difference being that the ethanol flame was attached to the injector. As with injection at 125 mm the orange soot cloud is not present.

Analysis of the air injection test results has shown that air injection has a significant effect on the flame structure and stability. In addition, these test have also demonstrated the feasibility of using liquid fuels in the Task 150-HS burner configuration.

INSTALLATION AND CHECKOUT OF THE BYU LDA SYSTEM

During this study, a 5 Watt argon-ion laser, purchased with other funds, was to be incorporated into the LDA system, and the system was to be set up on the Air Force Burner and operationally checked out. Unfortunately, there were technical problems with the argon-ion laser that required it being shipped back to the manufacturer twice for repair. This delayed the installation of the instrument until near the end of the program. Consequently, only the installation of the system was completed during this study. It is anticipated that checkout tests and additional LDA velocity data will be collected with support from the BYU ACERC program. This data is important to other BYU programs as well as the Air Force. Any additional data collected will be made available to the researchers at WPAFB and Pratt & Whitney Aircraft Company.

The LDA system setup at the BYU Combustion Laboratory consists of a Four Beam-Two Color system. This system makes the simultaneous measurement of two orthogonal velocity components possible. Depending in which direction the burner is traversed, either axial and tangential or axial and radial velocity components can be measured. The system also has one Bragg Cell, which is used to apply a frequency shift to the set of beams which measure the axial velocity component. The frequency shifting allows for the measurement of both positive and negative axial velocity components. The current optical alignment of the LDA system allows for data acquisition in the back scatter mode. A schematic of the optical setup is shown in Figure 14. The data acquired will be analyzed using a Macintosh computer and software written by Larry Goss at SRL Inc.



**Figure 13 - Effect of Side Air Injection on Flame Shape in the Task 150-HS Burner
($\Phi = 1.50$, Liquid Ethanol Fuel, 500 slpm, Air Flow with Side Air Injection of 200 slpm)**

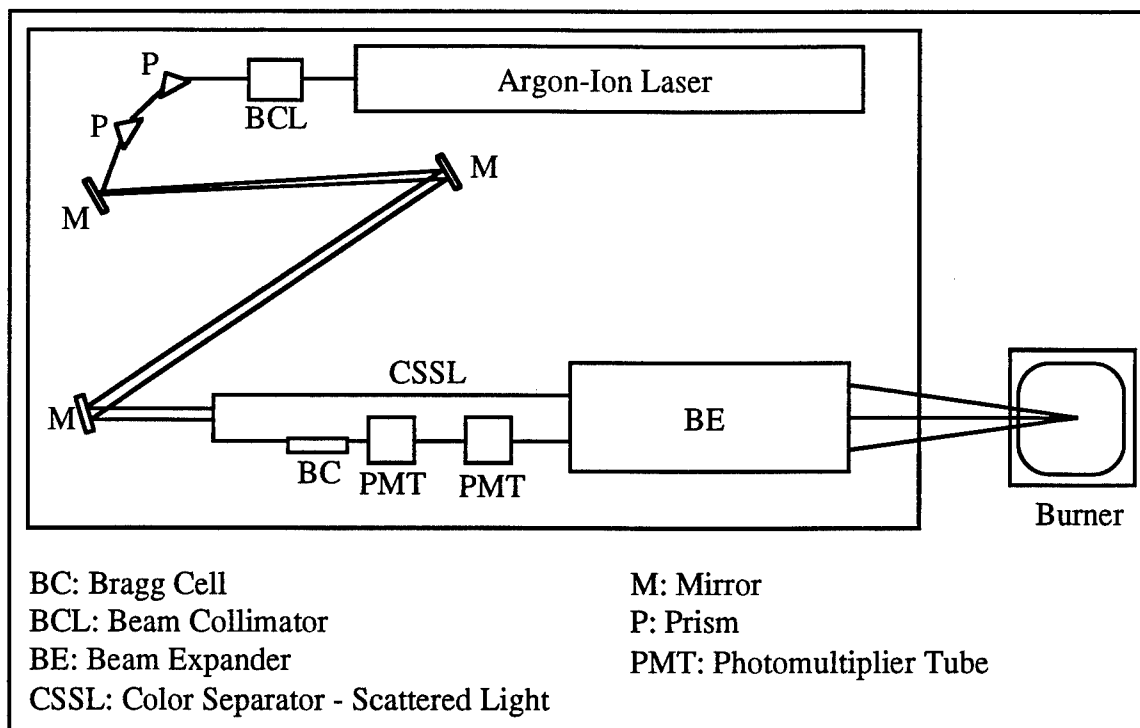


Figure 14 - Schematic of LDA System in Backscatter Mode.

LEAN BLOW OUT MEASUREMENTS

The effect of geometry (chamber extension, and exit orifice restriction) on the fuel equivalence ratio at lean blow out were examined and reported in a previous study (Pyper, et al., 1992). Additional LBO measurements were conducted in this study and further analysis of the results was completed. Only a brief presentation of the LBO experiments conducted during this study are presented below. A detailed presentation of results is contained in the M.S. Thesis of Pyper (1994).

Effects of O₂ Partial Pressure on Lean Blow Out Measurements. The effects of partial pressure of oxygen on LBO were examined by adding nitrogen to the combustion air to lower the oxygen partial pressure or by adding oxygen to the combustion air to increase the partial pressure of oxygen. Lean blow out measurements were completed in the Task 100, Task 150-LS and Task 150-HS burners. The test matrix used is summarized in Tables 1 and Table 2. Table 1 shows the different gas composition used and Table 2 gives the burner geometry and corresponding air flow rates. Only one nominal air flow rate was chosen per burner.

Table 1
Gas Composition and Partial Pressure of Oxygen for N₂/O₂ LBO Tests
(Two Data Points were Collected per Row)

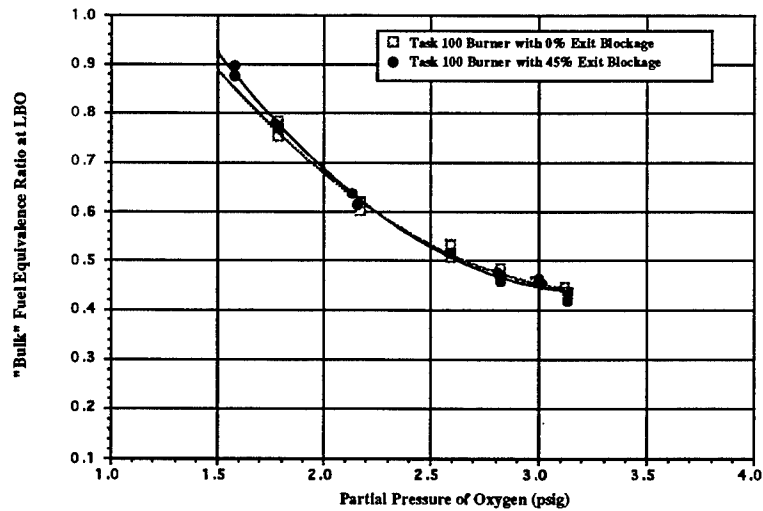
O ₂ Content	Mole Percent O ₂	Mole Percent N ₂	Partial Pressure O ₂ (psia)
Deficient	12	88	1.764
Deficient	15	85	2.205
Deficient	18	82	2.646
Normal Air	21	79	3.087
Excess	24	76	3.528
Excess	27	73	3.969
Excess	30	70	4.410

Table 2
Burner Setup and Air Flow Rates for N₂/O₂ LBO Tests

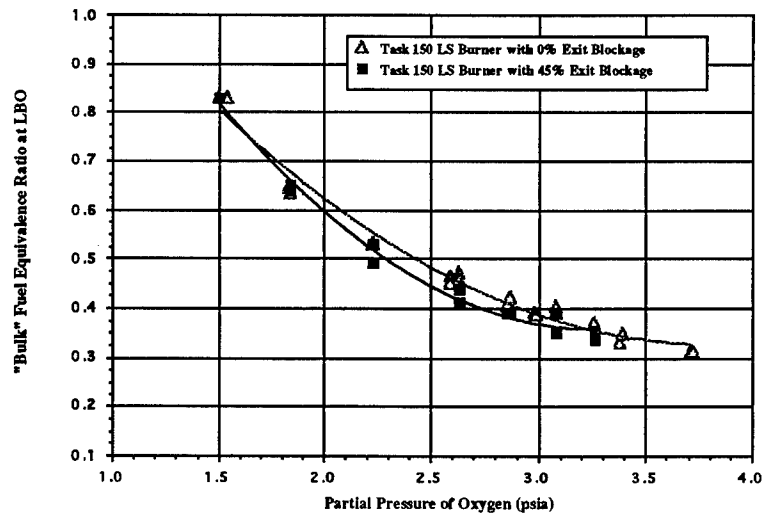
Burner Type	Air Flow Rate	Burner Configurations
Task 100 Burner	1000 slpm	10 inch Ext. with 0% or 45% Exit Blockage
Task 150 LS Burner	500 slpm	10 inch Ext. with 0% or 45% Exit Blockage
Task 150 HS Burner	500 slpm	10 inch Ext. with 0% or 45% Exit Blockage

The effects of excess oxygen on LBO varies greatly from the effects of excess nitrogen (lack of oxygen) on LBO as noted in Figure 15. As the partial pressure of oxygen (P_{O_2}) is increased, the ϕ_{LBO} is not decreased as much as the same increase in the partial pressure of nitrogen (or decrease of P_{O_2}). The lean flammability limit of hydrocarbons rarely differs between air and oxygen because the excess oxygen in the lean condition has the same thermophysical properties as nitrogen. This is better understood by considering the results of rich and lean flammability limits in pure oxygen (Lewis and von Elbe, 1987). The values of ϕ_{LBO} in pure oxygen is only a fraction less than that of air. Therefore, an increase in partial pressure of oxygen provides some increase in the flame's ability to maintain a lower value of ϕ_{LBO} . The limit to which a combustion system can operate with increasing P_{O_2} is the lean flammability limit of pure oxygen with that fuel. Further investigation of basic combustion characteristics of LBO with changing P_{O_2} may lead to increased understanding of lean limit flame extinction.

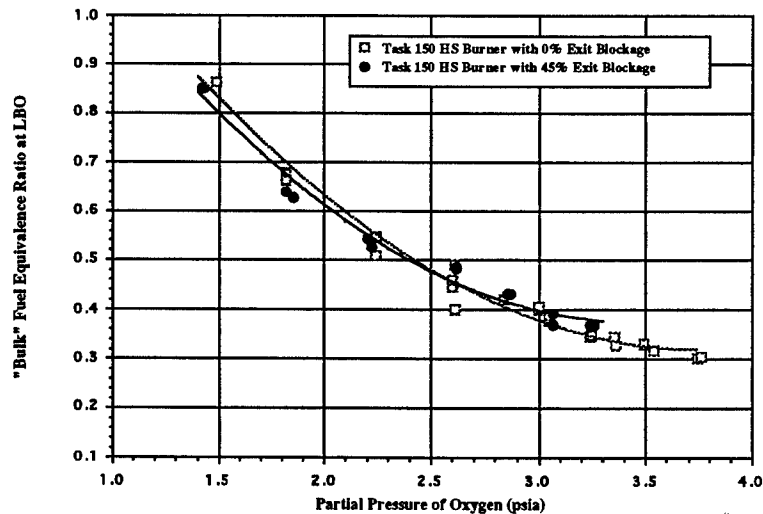
CFD Predictions of Geometrical Effects on Task 100 Burner Near LBO. It was observed from previous studies (Hedman et al., 1992, Pyper 1994) that different burner geometries (i.e. 10 inch combustion extension and exit restriction plates) caused significant effects in LBO for the Task 100 burner. It was believed that the back pressure produced from the exit restriction plates was influencing the weak recirculation zones found in the Task 100 burner enough to effect flame stability near LBO. Since only limited gas velocity data are available for the Task 100 burner, it was desired to apply computer



A) Task 100 Burner, 10 inch Extension, 1000 slpm Air Flow



B) Task 150-LS Burner, 10 inch Extension, 500 slpm Air Flow



C) Task 150-HS Burner, 10 inch Extension, 500 slpm Air Flow

Figure 15 - Effect of Oxygen Partial Pressure on Fuel Equivalence Ratio at LBO

modeling to better understand the influence of the extension and exit restriction plates on the fluid dynamic mechanisms governing LBO.

Fluid dynamic predictions using Fluent, a CFD code (Fluent User's Guide, 1990), were made to evaluate the effects of the 10 inch extension and all exit restriction plates on the recirculation patterns in the Task 100 burner at an air flow rate of 1000 slpm. Fluent model predictions were made for no 10 inch extension and with the 10 in extension for four different flow conditions and two different exit restrictions(Pyper, 1994). The combustion input parameters (air and fuel flow, etc.) were based on actual LBO conditions for that particular burner geometry. A two step global kinetic mechanism was employed with Arrhenius rate coefficients for propane taken from Westbrook and Dryer (1981). The burner was modeled with a two-dimensional asymmetric grid. A summary of all the input variables for the case with no exit plate and no 10 inch extension and for the case with the 62% plate and 10 inch extension are given in Pyper (1994).

It was suggested and then verified that the Task 100 burner had weak recirculation zones due to the non-swirl aspect of the burner. This was observed in the LBO data which was affected by changing orifice plates when no 10 inch extension was present and the removal of such effects once the 10 inch extension was in place (Hedman et al., 1992, and Pyper, 1994). It was suggested that the extension altered the mixing patterns enough within the combustor that the stability envelopes remain quite constant with increasing air flow rate and increased exit restrictions once the 10 inch extension was attached. A example of one of the simple qualitative analyses of the possible effects of exit blockage plate and combustion chamber extension on the Task 100 burner stability envelope near LBO is shown in Figure 16. The first observation from the CFD investigation is the apparent difference between the predicted lower recirculation zones between cases (a) and (b). The disturbance in the flow fields caused by the back pressure of the 62% restriction plate in case (b) appears to be slightly affecting the lower recirculation zones beneath it. The flame at LBO for either case stabilized at about two thirds up in the combustion chamber. This is about where the predicted slight differences in stream lines between case (a) and case (b) are noted. This slight disturbance in flow fields confirms the suspicion of the top recirculation zones, produced by the exit restriction plate, interacting or coupling with the lower zones and causing a wider stability envelope for increasing exit restriction plate as noted in Figure 16 The second observation was that even though the restriction plate in case (d) caused top recirculation zones as in case (b), the 10 inch combustion chamber extension seems to have provided sufficient space (volume and length) to uncouple any effects that the top recirculation zones may have had on the bottom zones. The CFD predictions, though far from conclusive, seem to confirm the suspected flow behavior.

Effects of Burner Geometry on LBO in Task 150 Technology Combustors. The effects of all burner geometries on LBO for the Task 150 LS and HS burners were investigated according to the test

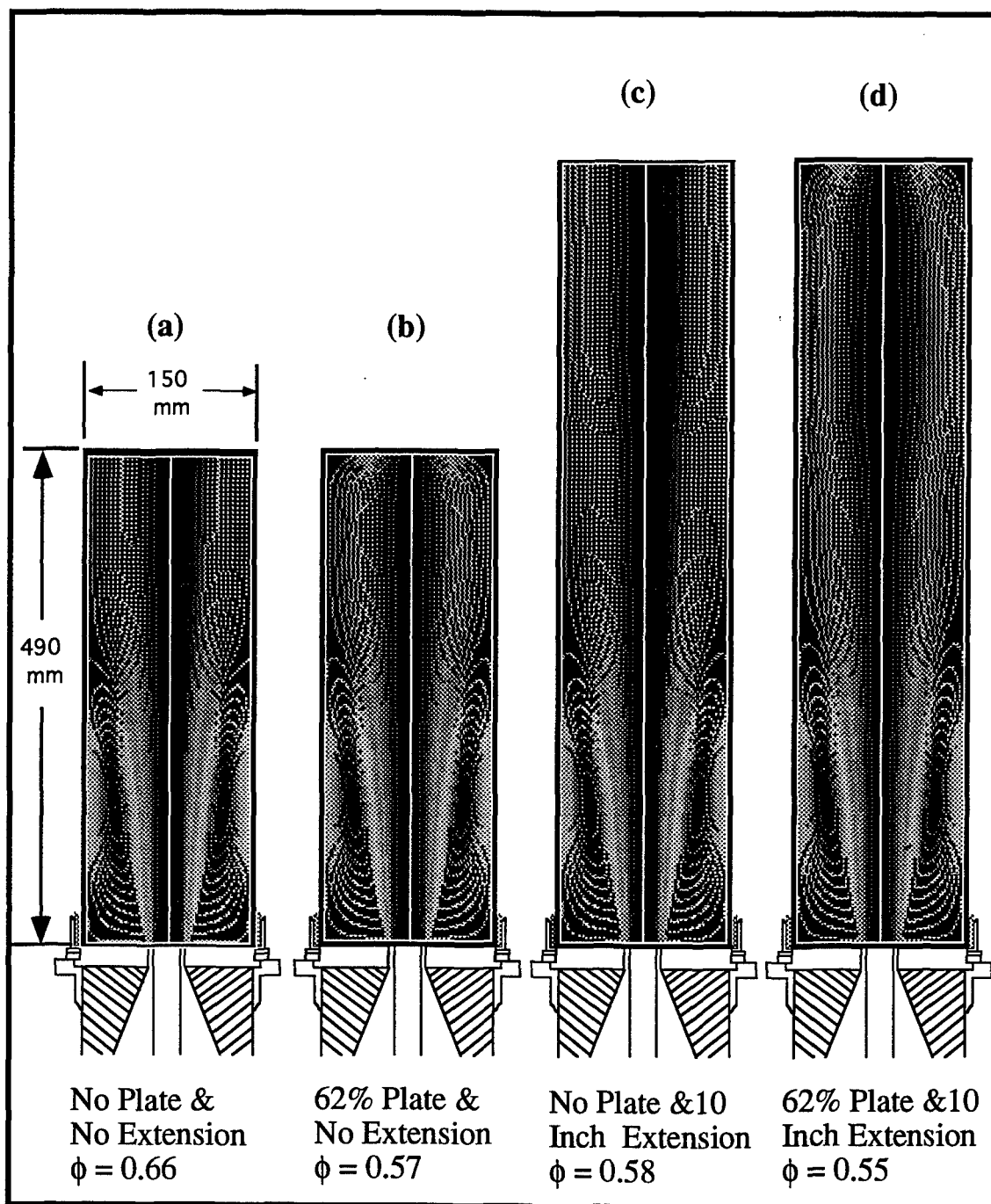


Figure 16 - Four Simulated Stream Function Contours for the Task 100 Burner at 1000 slpm of Air with Varying Geometries, Values of Phi Shown for LBO Conditions

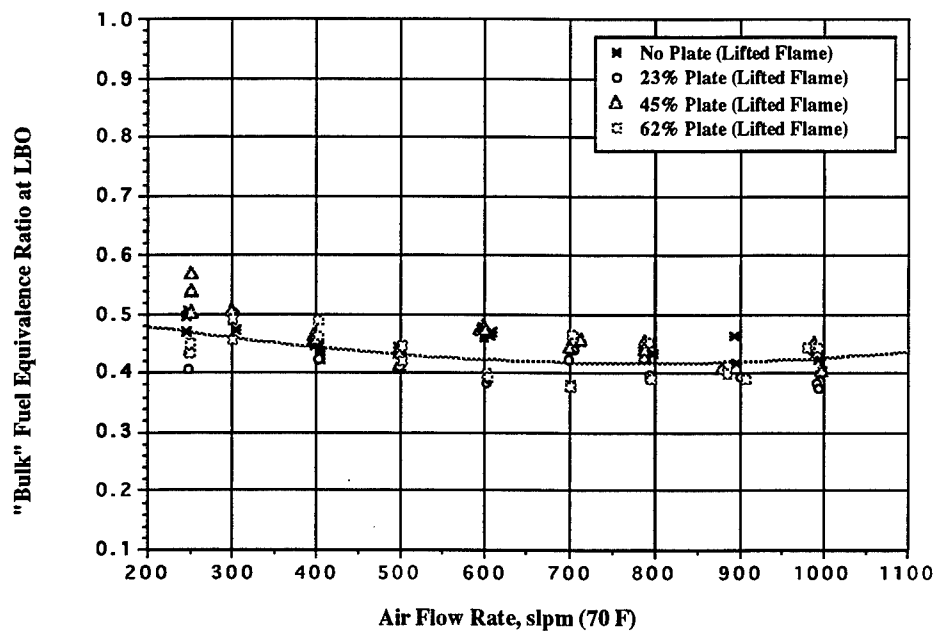
matrix shown in Table 3. A sample of the results of varying burner geometry on LBO for the Task 150 LS technology combustors is shown in Figure 17a. In every case, the flame in the Task 150 LS always blew out from a lifted mode. This suggested that the flame was always stabilized in some down stream recirculation zone. There appeared to be no significant effect of exit plate restrictions or combustion chamber extension on LBO for the Task 150 LS burner. It appeared that the dominate mechanism governing LBO in the Task 150 LS burner was independent of geometric changes.

Table 3
LBO Test Matrix for Varying Geometry in Task 100 and Task 150 Burners

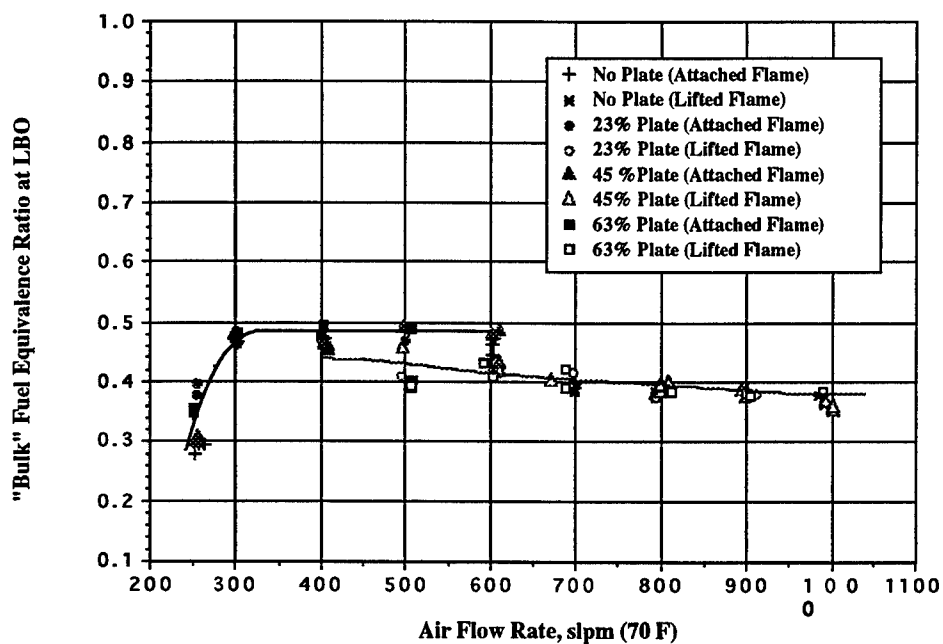
Burner Type	Air Flow Range (slpm)	Air Flow Increment (slpm)	Burner Extension	Burner Exit Restriction (plate size)
Task 150 LS and HS	250 - 500	50	0 & 10 inch	0%, 23%, 45%, 62%
Task 150 LS and HS	500 -1000	100	0 & 10 inch	0%, 23%, 45%, 62%

Figure 17b illustrates the effects of the three exit restrictions with 10 inch combustion chamber extension on LBO for the Task 150 HS burner. The flame would "blow out" in two different modes. At lower air flow rates (250 slpm to 600 slpm), the flame would blow out from an attached position on the nozzle. At higher air flow rates, the flame would lift and stabilize on a down stream recirculation zone prior to blow out just like the Task 100 and LS burners. In an intermediate air flow range (400 slpm to 600 slpm), both modes of blow out were observed (i.e. the flame would abruptly lift from the nozzle but, would then stabilize down stream). It is suggested that the recirculation patterns produced by the swirl aspect of the high swirl fuel injector greatly influence these two modes of flame stability. It appeared that the 10 inch extension and the different exit blockages again had little or no effect on the ϕ_{LBO} for the Task 150 HS burner. This trend was comparable to that observed with the Task 150 LS burner. Once the flame lifted in the HS burner, the LBO data trends resembled those of the LS burner.

Swirl Number Calculation and Swirl Effects on LBO. The swirls numbers for the low and high swirl fuel injectors used in the Task 150 burner were calculated as shown in Table 4. The swirl numbers were determined from the angles of the swirl vanes in each flow passage (Gupta, 1984). The combined swirl number was based on a mass flow weighted average of the two swirl passages. The primary swirl number for the HS injector is about 2.77 times larger than the swirl number for the LS primary swirl. This means that there is more radial velocity than axial velocity in the gas exiting the HS primary swirl than the LS primary swirl. The secondary swirl numbers for both injectors are almost the same. The reason for their difference is the slight dimensional differences in the secondary vane pack hub diameter of the two injectors. The total swirl number for the HS injector is about 1.34 times larger than the total swirl number



A) Task 150-LS Burner, 10 Inch Extension, Varying Exit Restrictions



B) Task 150-HS Burner, 10 Inch Extension, Varying Exit Restrictions

Figure 17 - Example LBO Data for the Task 150 Burner

for the LS injector. This characterization of swirl number for each injector can aid in understanding the effects of swirl passages on LBO.

Table 4
Calculated Swirl Numbers for the LS and HS Injectors at 500 slpm of Air

Task 150 Injector	Primary Swirl Number (S_p)	Secondary Swirl Number (S_s)	Total Swirl Number (S_T)
Low Swirl	0.69	1.21	1.05
High Swirl	1.91	1.24	1.41

The effect of swirl number has been found to be significant in understanding the observed lean blow out differences between the Task 150-LS and Task 150-HS burners. Presentation of the complete analysis is beyond the page limitations of this report. A more complete discussion of this effect is presented in the M.S. Thesis of Pyper (1994).

GAS COMPOSITION MEASUREMENTS IN THE TASK 100 AND 150-HS BURNERS

In order to meet one of this years objectives the experimental combustor facility was modified so that gas samples could be obtained from the flame zone. This was accomplished by using a side panel on the burner which contained small holes along a vertical line. A long hypodermic syringe was passed through one of the small holes and used to extract localized gas samples. These gas samples were analyzed with a gas chromatograph available in the laboratory.

Gas samples were drawn from both the Task 100 and Task 150-HS burner in order to determine the species present in the lower recirculation zone. One of the main objectives was to determine what fuel rich species were being transported into the corner recirculation zone when the burners were being operated fuel rich. Analysis of the gas samples showed a significant amount of methane and other undetermined fuel rich fragments at the rich conditions in the Task 100 burner, but no propane was detected. The samples from the Task 150-HS burner showed no significant amounts of any hydrocarbons. Table 5 summarizes the major species concentrations in dry mole percent for the Task 150-HS and Task 100 at $\phi = 1.5$ and $\phi = 0.75$.

FEASIBILITY OF BURNING LIQUID ETHANOL IN THE TASK 150 COMBUSTOR

One of this years objectives included the investigation of the feasibility of using liquid ethanol fuel with the Task 150-HS and Task 150-LS burner configurations. To feed the ethanol to the burner a new fuel system consisting of a pressure vessel, rubber bladder, pressurized air tanks, pressure regulator and a flow meter was constructed. The rubber bladder was placed inside the pressure vessel and connected to the pressurized air tanks via the pressure regulator. Once the bladder was

in place the pressure vessel was filled with ethanol and sealed. The bladder was then inflated and kept at a constant pressure of 30 psig. This provided a very consistent flow of ethanol as it was forced out of the tank by the expanding bladder. A flow meter was placed in the line after the pressure vessel to provide for exact flow measurement.

Table 5
Dry Mole Percent of Major Species.
 (All vertical and radial distances are given in millimeters)

Task 150-HS $\phi = 1.5$			
Species	Z=0 mm, R=30 mm	Z=38 mm, R=40 mm	Z=76 mm, R=55 mm
CO	-	1.1	4.6
CO ₂	11.6	8.3	10.9
N ₂	82.5	80.9	79.6
O ₂	5.9	9.7	4.9
CH ₄	-	-	-
Task 150-HS $\phi = 0.75$			
CO	-	-	-
CO ₂	6.5	4.2	7.1
N ₂	79.9	80.4	81.5
O ₂	13.8	15.4	11.4
CH ₄	-	-	-
Task 100 $\phi = 1.5$			
CO	9.0	6.3	8.2
CO ₂	7.7	9.4	8.5
N ₂	81.1	82.4	80.8
O ₂	1.2	1.3	1.6
CH ₄	1.0	0.6	0.8
Task 100 $\phi = 0.75$			
CO	-	-	-
CO ₂	7.1	6.5	7.9
N ₂	82.5	80.5	82.5
O ₂	10.4	13.0	9.6
CH ₄	-	-	-

Both burner configurations operated excellently. Air bubbles in the ethanol caused some initial unsteadiness, but this problem was removed by the installation of an air trap in the fuel supply line. Both burner configurations were run at stoichiometries varying from a rich flame at $\phi = 1.5$ to the lean blow out condition at $\phi = 0.22$.

It should be noted that there was very little soot formation on the windows of the combustion chamber while operating with the ethanol fuel. This suggests that it will be very feasible to make laser based optical diagnostic measurements with this liquid fuel.

Not only was the feasibility of operating the Task 150 burner on liquid fuel demonstrated, but a series of experiments were made where the effect of side air injection on flame structure, as discussed above, was determined.

ANALYSIS AND INTERPRETATION OF EXPERIMENTAL RESULTS

One of the objectives of this study has been to complete the analysis of data taken in the previous research initiation and summer faculty research programs. Because of the page constraints of this report, only examples of the more extensive analyses are included. Additional evaluation of results are being presented in various technical papers that have been submitted to the International Gas Turbine Conference (Sturgess, et al., 1994, and Hedman, et al., 1994a), and to the 25th International Combustion Institute Meeting (Hedman, et al., 1994b). M.S. theses are also being prepared that summarize the work in great detail (Pyper, 1994; and Warren, 1994).

Planner Laser Induced Fluorescence (PLIF) Imaging of OH Radical. PLIF (Planner Laser Induced Florescence) was used during a summer faculty research program at WPAFB to obtain instantaneous images of the flame zone (OH radical) in order to better understand the flow and reaction patterns in the burner. In these experiments, OH radicals were excited with a 10 ns pulse of ultra-violet (ca 283 nm) laser light. This approximately 75 mm high sheet of laser light was passed through centerline of the reactor. An intensified CCD camera, located normal to the laser sheet, captured the two-dimensional uv image from the fluorescence (ca 308 nm) of the OH radical. Images at different axial locations were obtained by moving the burner axially about 50 mm at a time. The PLIF images presented below are a collage of several images taken at different times, and at different axial locations. The images are placed in their respective positions with respect to the combustor, in order to show the representative flame structure. Instantaneous images as well as averaged images of 6 to 10 separate instantaneous images are shown.

It has been informative to correlate the OH radical images with the information known about the partitioning of the air flow rates through the various passageways of the nozzle. The local fuel equivalence ratios shown in Table 6 were calculated from the air flow through each of the different passageways and the total fuel flow. Implicit in these calculations are two assumptions. First, the fuel is assumed to mix uniformly within each combination of partitions before mixing with remaining air. Second, the fuel blockage effects (which would change the partitioning as a function of fuel flow) are assumed to be negligible. At this air flow (500 slpm), LBO occurs at a fuel equivalence ratio of about 0.5, which also corresponds to the lean flammability limit of propane air mixtures (Lewis and von Elbe, 1987)

Table 6
Local Fuel Equivalence Ratios Calculated from Total Fuel Flow and Combined Air Flows for each Combination of Injector, and Insert Jet Passageways.

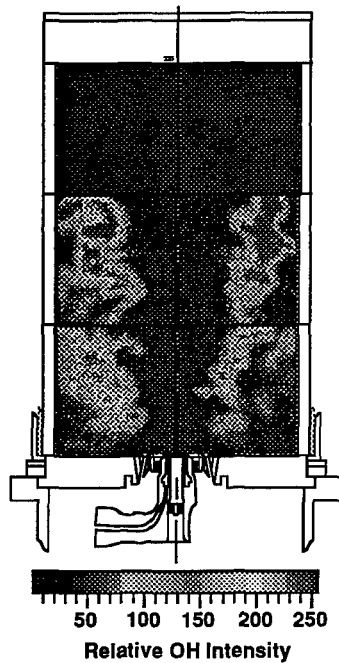
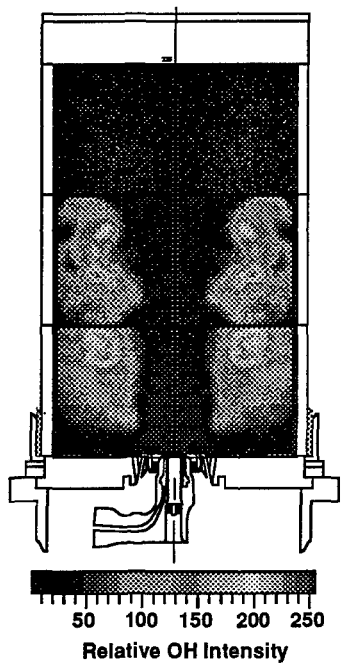
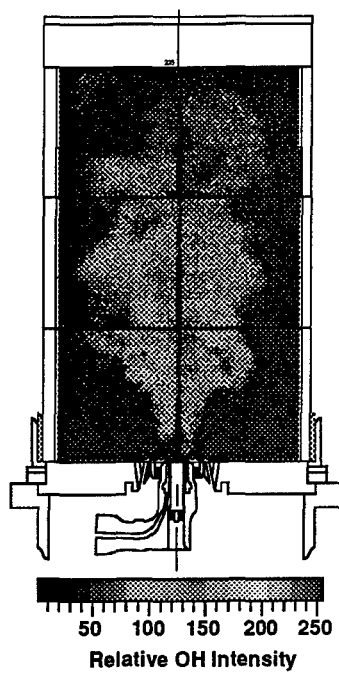
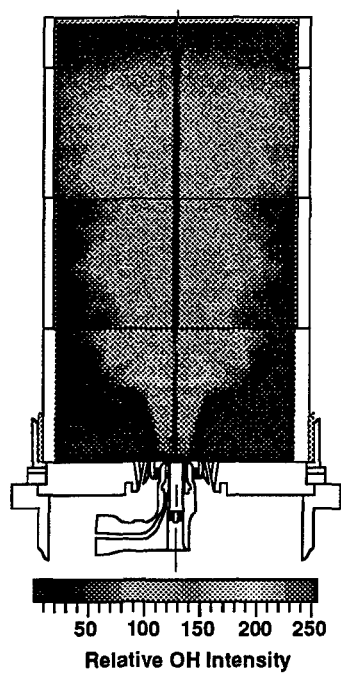
Overall Phi	Primary Swirler Phi	Primary+Secondary Swirlers Phi	Primary+Secondary Swirlers and Insert Jets Phi
0.62	4.17	1.11	0.80
1.08	7.26	1.94	1.39
1.49	10.02	2.67	1.92

With these assumptions in mind, and knowing the lean flammability limit for a propane-air flame is about $\phi = 0.5$ and the rich limit is about $\phi = 2.5$, some conclusions can cautiously be applied to these images. In every case, the air in the primary swirler alone does not provide sufficient oxidizer to permit combustion. Thus, the fuel must mix with at least the secondary swirled air before combustion is possible. With a fuel equivalence ratio of 0.62, the funnel like structure expected in a swirl stabilized flame is observed (Hedman, et al., 1994). As shown in Table 6, the local equivalence ratio for fuel combined with the air from the two swirled jets is 1.11, indicating little air from the insert jets is needed to complete the combustion.

As the overall fuel equivalence ratio is increased to 1.08, the swirled air/fuel mixture was still within flammability limits. What changed was the amount of fuel left for to mix with the insert jets. This additional fuel apparently burns on the shoulders of the funnel. As the overall fuel equivalence ratio is further increased to 1.49, the very fuel-rich swirled air ($\phi = 2.67$) can no longer support combustion. The characteristic funnel like structure of a swirl stabilized flame is no longer visible. The combustion is only taking place in the presence of air from the insert and dome jets.

Figure 18 presents PLIF images of the OH radical for two extreme fuel equivalence ratios, $\phi = 0.72$ and $\phi = 1.49$. The images for the $\phi = 0.72$ test condition are shown rather than the $\phi = 0.62$ condition shown previously (Hedman, et al., 1994), in order to provide more direct comparison to the LDA velocity and CARS temperature data sets discussed in previous sections of this report. The PLIF images of OH radical at $\phi = 0.62$ and $\phi = 0.72$ are essentially identical.

Two sets of images are presented. Images A and C are averaged images from 6 to 10 separate laser shots. Images B and D are representative instantaneous images. The averaged images represent the mean flame structure, while the instantaneous images give an indication of the complex instantaneous flame structure associated with the intense turbulent flow and reaction zones. The two sets of images provide support on the argument presented above, that the flame



**Figure 18 - Mean and Instantaneous PLIF Images of OH Radical
(Task 150-HS Burner, 500 slpm Air Flow Rate)**

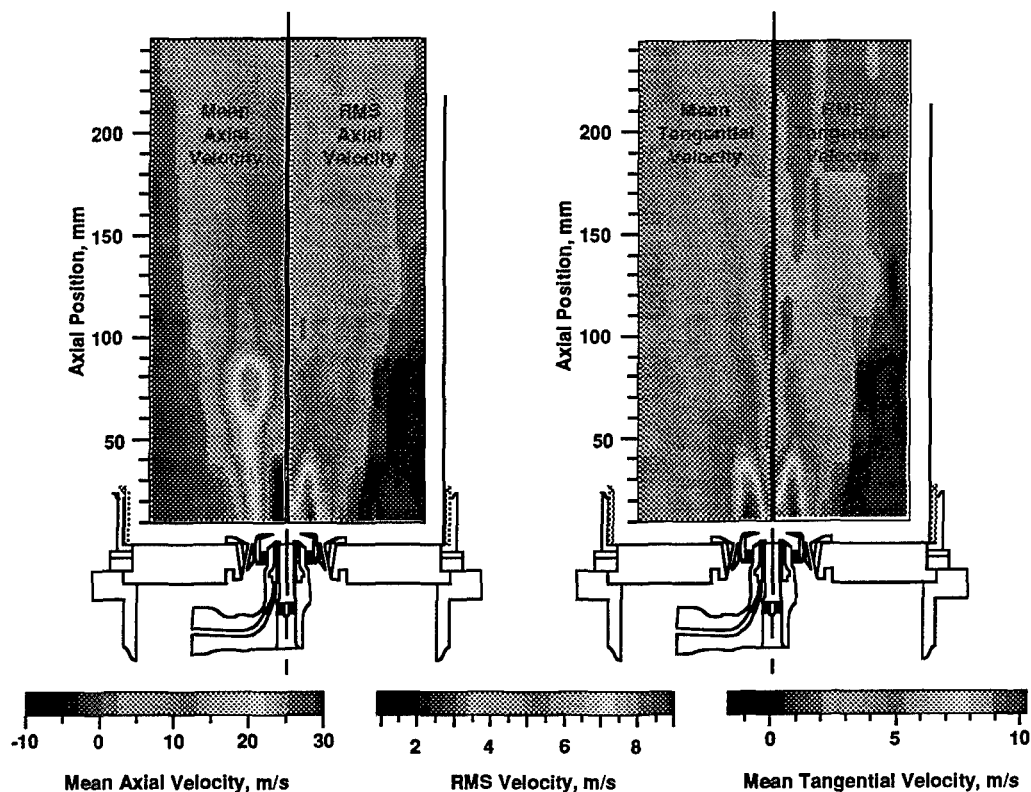
attaches to the burner when the local fuel equivalence ratio is within the flammability limits, but is extinguished when the local fuel equivalence ratio in this region of the burner exceeds the rich flammability limits for the propane-air system. The fuel rich images also support the contention that the overall fuel rich combustion is stabilized on the increased amount of air that comes from the insert jets.

Laser Doppler Anemometer (LDA) Measurements of Gas Velocity A two-component laser Doppler anemometer (LDA) was used at WPAFB during a summer faculty research program (Hedman and Warren, 1992), to measure gas velocity in the burner at fuel lean conditions ($\phi = 0.72$) where the flame attaches to the injector, and at fuel rich condition ($\phi = 1.49$) where the flame attaches to the dome and insert jets. This set of velocity data has allowed the effect of fuel equivalence ratio to be investigated for cases where major differences in the flame structure were evident. The velocity results are summarized in Figures 19 and 20 for the $\phi = 0.72$ and $\phi = 1.49$ cases respectively. Iso-contour plots of mean axial and tangential velocities and rms axial and tangential velocities are shown. The high axial and tangential velocities associated with the injection process are clearly evident. Areas of recirculation are evident on the centerline, just above the injector, and in the corner region between the combustor dome and wall.

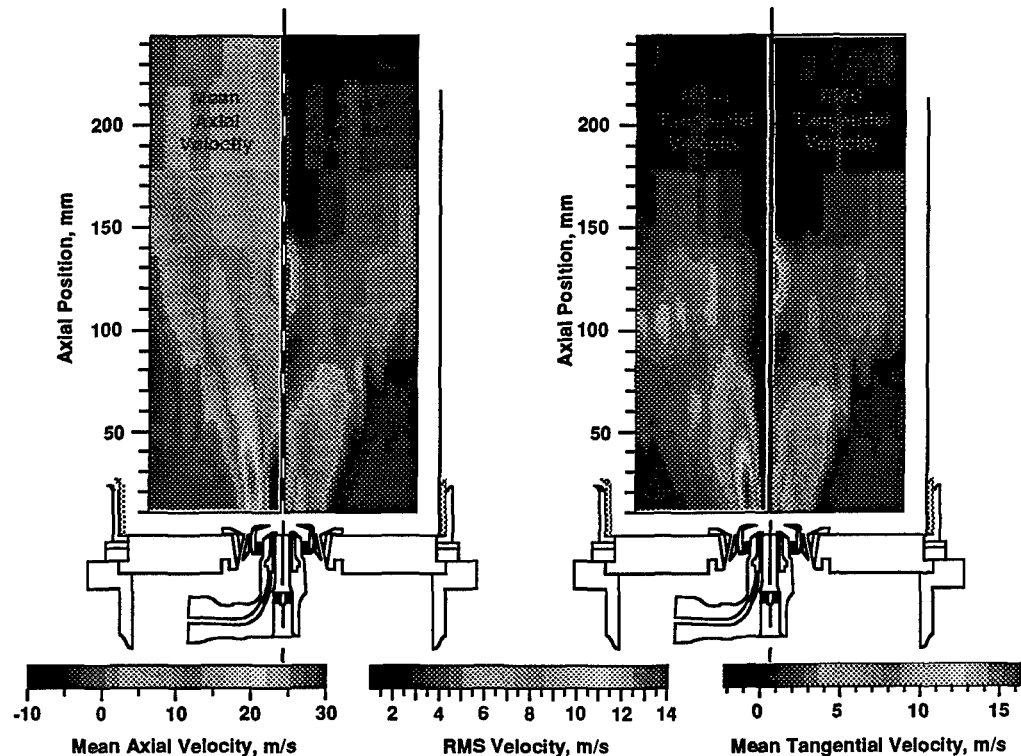
In a swirling flow, the major flow field forms a funnel shape with the low pressure central region drawing gases into a central recirculation zone. In these figures, the centerline axial velocities near the injector are negative. The negative velocity is quickly overcome, however, by a momentum transfer across the large velocity gradient and the expansion due to the combustion process.

Two recirculation zones exist between the central funnel shape and the wall of the combustor. The first zone, near the corner between the wall and the dome, is formed by the dome jets and rotates in a clock-wise direction in the mean axial velocity contour plots shown. This zone extends to about 30 mm above the dome but is not easily seen in the figures. The second recirculation zone rotates in a counter-clockwise direction in the mean axial velocity contour plot shown, and extends from about 30 mm to about 150 mm for the $\phi = 1.49$ case and to about 170 mm for the $\phi = 0.72$ case. The axial velocity profile becomes nearly flat by about 150 mm, a length equal to the diameter of the combustion chamber for both the $\phi = 0.72$ and $\phi = 1.49$ cases.

At the high ϕ condition, the highest axial velocity region has been relocated from 75 mm downstream (Figure 20) to a point attached to the dome (Figure 19). This variation corresponds to the flame location moving from near the injector ($\phi = 0.72$) to the insert jets ($\phi = 1.49$). The velocities in the recirculation zones outside the funnel shaped flow field are about the same magnitude in both cases. The tangential velocities are lower for the high ϕ case, but exhibit the



**Figure 19 - LDA Measurements of Axial and Tangential Velocity
(Task 150-HS Burner, 500 slpm Air Flow, $\Phi = 0.72$)**



**Figure 20 - LDA Measurements of Axial and Tangential Velocity
(Task 150-HS Burner, 500 slpm Air Flow, $\Phi = 1.49$)**

same general trends as the low ϕ case. The rms contour plots show similar structures and numerical values for both ϕ cases.

CONCLUSIONS

There have been many observations and conclusions drawn from this research initiation study and from the two previous research initiation and three summer faculty research programs. A detailed summary of all of the observations and conclusions is beyond the scope of this brief final report. A few of the more significant observations and conclusions is contained in the following paragraphs. Additional results are discussed in greater detail in various technical papers that have been submitted to the International Gas Turbine Conference (Sturgess, et al., 1994; and Hedman, et al., 1994a), and to the 25th International Combustion Institute Meeting (Hedman, et al., 1994b). Two M.S. Theses are also being prepared that summarize the work in great detail (Pyper, 1994; and Warren, 1994).

There have been considerable insights gained in this study into the operational characteristics of a practical injector operating in a combustor that closely simulates that of a real gas turbine engine. The PLIF images of the OH radical have dramatically illustrated the characteristics of swirling flames and the highly variable nature of the flame shape. The effect of the insert jets is conspicuous. Correlation of these OH radical images with the partitioning of the air flow rates through the various passageways of the nozzle has shown a consistent correlation between the local fuel equivalence ratio and the presence of flame structure. This supports an assumption of the fuel mixing with each passageway in turn from the inside-out.

The BYU CARS facility was successfully adapted to the burner facility, and CARS gas temperature measurements were obtained for the Task 150-HS burner at four different fuel equivalence ratios. LDA measurements were made at lean ($\phi = 0.72$) conditions where the flame attached to the injector, and at fuel rich conditions ($\phi = 1.49$) where the flame attached to the dome and insert jets. This has allowed the flow field effects to be determined for the two extremely different flame structures observed.

The main result of the Task 100 burner CFD investigation was that an apparent difference was noted in the lower recirculation zones due to an increase in exit restriction with no 10 inch combustion chamber extension. This confirmed the suspicion of the coupling of the top and bottom recirculation zones with increasing exit plate and no 10 inch extension. With the 10 inch combustion extension in place, an increase in percent exit restriction plates did little to cause the predicted upper recirculation zones to interfere with lower zones. The Fluent CFD results were qualitatively confirmed by the limited Task 100

burner LDA data. From the present analysis, the recirculation patterns and interactions in the Task 100 burner appeared dependent on burner geometry.

Essentially no effect in the stability loop was noted in the Task 150 LS and HS burners by adding the combustion chamber extension or the exit restriction plates. It was concluded that the different recirculation zones produced by these injectors had already stabilized the flame such that the addition of the extension or restriction plates did very little to affect the stability envelope. Therefore, the mechanisms governing LBO in the Task 150 LS and HS burners were independent of geometric changes in the burner length or exit restrictions.

The only real difference between the Task 150 LS and HS burners was the difference in the primary swirl. The primary swirl number for the HS injector was about 2.77 times larger than the swirl number for the LS primary swirl. The total swirl number for the HS injector is about 1.34 times larger than the total swirl number for the LS injector.

A swirl passage analysis in the Task 150 burner revealed the relationship of swirl passage to flame mode. The flame in the HS burner remained attached near LBO conditions at low air flow rates ($AF < ca\ 500\text{ slpm}$) because of the large swirl number in the primary swirl passage. Over all, the primary air swirl passage had little influence on the flame stability in the LS burner, thus allowing the flame to always remain lifted at LBO conditions. At higher air flow rates ($AF > 500\text{ slpm}$) the dominating swirl passage in the LS and HS burner was the secondary swirl passage with little influence from the primary swirl. This explained the similar LBO trends in both burners at increased air flow rates.

It was observed that the increase of partial pressure of oxygen caused a decrease in ϕ_{LBO} for all three combustors. Since mixing rates remained fairly constant at the nominal air flow rate tested, it was suspected that the increasing partial pressure of oxygen altered the combustion chemistry kinetics and the limiting intermediate step reactions (i.e. OH radical) which in turn allowed the flame to sustain lower values of ϕ_{LBO} .

ACKNOWLEDGMENTS

This study includes work done at WPAFB during three Air Force Office of Scientific Research (AFOSR) Summer Faculty Research Programs, and at BYU under this and two previous AFOSR Research Initiation Grants. Additional financial support has been received from the NSF sponsored Advanced Combustion Engineering Research Center (ACERC) located at Brigham Young University, Provo, Utah. Special thanks are also given to W. M. Roquemore, Dale Shouse and Melvin Russell at WPAFB, who provided support with instrumentation, the burner and facility modifications, and assisted materially in providing the burner for installation in the BYU Combustion Laboratory. Special thanks are in order for Larry Goss, Benjamin Sarka, and Daryl Trump at Systems

Research Laboratory, Inc. (SRL) in Dayton, Ohio. Their assistance in providing the instrumentation, facilities, and in making both the OH imaging measurements and the LDA measurements was essential to the success of this study. The special help of K. Y. Hsu, a Post Doctoral Researcher from the University of Iowa, in obtaining the PLIF images of the OH radical during one of the Summer Faculty Research Programs at WPAFB is also gratefully acknowledged. G.J. Sturgess from Pratt & Whitney Aircraft Company, in East Hartford, Connecticut has been a valuable resource in guiding many of the experiments conducted, and in providing insights into the interpretation of the results. Pratt and Whitney also provided the practical injectors that have been used in this study. Other students at Brigham Young University that have contributed to this study include Scott Blackham, and Jenai Christensen. Their help is also gratefully acknowledged.

REFERENCES

- Boyack, K.W., and Hedman, P.O., "Dual-Stokes CARS System for Simultaneous Measurement of Temperature and Multiple Species in Turbulent Flames," Twenty-third Symposium (International) on Combustion, The Combustion Institute, Pittsburgh, PA (1990)
- Fluent User's Guide, Version 4.0, Fluent Incorporated, Lebanon, NH, (1990).
- Goss, L.P., Personal Communication, Systems Research Laboratories, Inc., Dayton, Ohio (1992)
- Gupta, A.K., Lilley, D.G., and Syred, N, Swirl Flows, Abacus Press, Kent, UK (1984)
- Hancock, R.D., Hedman, P.O., and Kramer, S.K., "Coherent Anti-Stokes Raman Spectroscopy (CARS) Temperature and Species Concentration Measurements in Coal-Seeded Flames," Combustion and Flame, **71**, 593-604, (October, 1991)
- Hancock, R.D., Boyack, K.W., and Hedman, P.O., "Coherent Anti-Stokes Raman Spectroscopy (CARS) in Pulverized Coal Flames," Advances in Coal Spectroscopy, pg 373-407, ed by Henk L.C. Meuzelaar, Plenum Publishing Company (1992)
- Hedman, P. O., "Investigation of the Combustion Characteristics of a Confined Coannular Jet with a Sudden Expansion," Final Report, Contract No. F49620-88-C-0053, 1990 AFOSR Summer Faculty Research Program, Universal Energy Systems, Inc., Dayton, Ohio (July 20, 1990).
- Hedman, P.O. and Warren D.L., "Investigation of the Combustion Characteristics of Swirled Injectors in a Confined Coannular System with a Sudden Expansion," Final Report, AFOSR Summer Faculty Research Program, Research and Development Laboratories, Inc., Culver City, California (1991)
- Hedman, P. O., and Warren, D. L., Investigation of the Combustion Characteristics of Swirled Injectors in a Confined Coannular System with a Sudden Expansion," Final Report, AFOSR Research Initiation Program, Research and Development Laboratories, Inc., Culver City, California (1992).
- Hedman, P. O., Pyper, D. K., and Warren, D. L., "Investigation of the Combustion Characteristics of Confined Coannular Swirling Jets with a Sudden Expansion [Task 150]". Final Report for: Research Initiation Program Aero Propulsion and Power Laboratory Wright-Patterson AFB, OHIO 45433, (1992).
- Hedman, P.O., Sturgess, G.J., Warren D.L., Shouse, D., and Goss, L.P., "Observations of Flame Behavior from a Practical Fuel Injector Using Gaseous Fuel in a Technology Combustor," The 39th ASME International Gas Turbine & Aeroengine Congress & Exposition, The Hague, Netherlands (1994a)

- Hedman, P.O., and Warren, D.L., "Turbulent Velocity and Temperature Measurements from a Gaseous Fueled Technology Combustor with a Practical Fuel Injector," Submitted to 25th International Combustion Institute Bi-Annual Meeting, University of California, Irvine, California (1994b)
- Palmer, R.E., Sandia Report SAND89-8206 UC-13, Sandia National Laboratories, Livermore, California (1989)
- Pyper, D.K., and Hedman, P.O., "Investigation of the Combustion Characteristics of Confined Coannular Swirling Jets with a Sudden Expansion," Final Report, AFOSR Research Initiation Program, Universal Energy Systems, Inc., Dayton, Ohio (1991)..
- Pyper, D.K., Master of Science Thesis, Mechanical Engineering Department, Brigham Young University, Provo, "The Study of Non-Swirl and Swirl Non-Premixed Flame Stability Near Lean Blow Out and the Design of a Research Combustion Facility", M.S. Thesis, Department of Mechanical Engineering, Brigham Young University, Provo, Utah, (1994).
- Roquemore, W.M., Reddy, V.K., Hedman, P.O., Post, M.E., Chen, T.H., Goss, L.P., Trump, D., Vilimpoc, V., and Sturgess, G.J., "Experimental and Theoretical Studies in a Gas-Fueled Research Combustor," AIAA 91-0639, 29th Aerospace Sciences Meeting, Reno, Nevada (January 7-10, 1991)
- Sturgess, G. J., Sloan, D. G., Lesmerises, A. L. , Henneghan, S. P., and Ballal, D. R. "Design and Development of a Research Combustor for Lean Blow Out Studies", 35th International Gas Turbine and Aeroengine Congress and Exposition. Brussels, Belgium, (June 1990).
- Sturgess, G.J., Hedman, P.O., Sloan, D.G., and Shouse, D., "Aspects of Flame Stability in a Research Dump combustor," 39th International Gas Turbine and Aeroengine Congress and Exposition. The Hague, Netherlands (June 1994).
- Warren, D.L., Master of Science Thesis, Mechanical Engineering Department, Brigham Young University, Provo, Utah (in progress) (1994)
- Westbrook, Charles,K., and Dryer, Fredick, L., "Simplified Reactions Mechanisms of the Oxidation of Hydrocarbons Fuels in Flames", Combustion Science and Technology, Vol 27, pp 31-34, (1981).

**MORPHOLOGY OF HIGH-VELOCITY PERFORATION OF LAMINATED
PLATES USING DEPLY TECHNIQUE**

David Hui

Professor

Department of Mechanical Engineering

University of New Orleans

New Orleans, LA 70148

Final Report for:

Summer Research Extension Program

Wright Laboratory

Sponsored by:

Air Force Office of Scientific Research

Bolling Air Force Base, Washington, D.C.

December 1993

**MORPHOLOGY OF HIGH-VELOCITY PERFORATION OF LAMINATED
PLATES USING DEPLY TECHNIQUE**

David Hui
Professor
University of New Orleans
Department of Mechanical Engineering
New Orleans, LA 70148, USA

ABSTRACT

The work deals with the energy absorption of graphite/epoxy laminated plates due to spherical projectile impact. A scanning electron microscopic examination of a few fragments from the impact shows that the fracture surfaces of the matrix have some characteristic hacklemarks. An attempt is being made to determine if these hacklemarks are responsible for the considerable energy absorption of the impact.

Measurements of the distribution of the areas of perforation holes and delaminated region surrounding the holes were performed with automatic image analysis equipment after utilization of a stain-pyrolyze-deply procedure. The stain consisted of gold chloride solution. The shapes of the delaminated regions on each ply were outlined in white ink with a fine tip hobby paint brush for improved visibility in the permanent photographic record and image analysis.

INTRODUCTION

New composites manufactured from advanced fibers and specially selected resins are being increasingly considered for defeating high speed projectiles or ballistic threats. The ability of graphite/epoxy (Gr/Ep) composites for this purpose is being considered. The ability of such material clearly relates to its energy absorbing properties at very high strain rates (10^3 to 10^5s^{-1}), and the amount of material which is involved in the energy absorbing process (Brown and Egglesstone, 1989).

Initial work on energy absorption by 32-ply Gr/Ep composite plate subjected to a wide range of impact velocity was conducted in the ballistic test range of the Flight Dynamics Laboratory at the U.S. Air Force Wright-Patterson Air Force base, Ohio. Results of these tests have not yet been published but summarized by Altamirano (1991) and Mayer (1992) and is shown in Figure 1. The empirical relationship between the energy absorption function E , and the impact velocity V has been characterized by them as:

$$E = CV^n \quad (1)$$

Ballistic tests were also conducted at the U.S. Army Cold Regions Research and Engineering Laboratory, Hanover, New Hampshire on single and multiple ply laminates to study the impact damage and energy absorption characteristics. Common to both U.S. Air Force, Wright Laboratory test and the U.S. Army Cold Regions Laboratory (CRREL) test are some micrographs of fragments from the impact which contained very characteristic comblike hacklemarks.

The periodicity of hacklemarks due to impact and fracture is at present intriguing. As of now, there is no explanation reported in the literature for a satisfactory explanation of such periodicity. It is possible that such periodicity is a result of standing waves in the matrix, that is the resonance of the cavity between fibers. The wavelength of hacklemarks corresponds to the various modes of vibration and the periodicity to the shear yielding failure of the material. A basis for consideration of these hacklemarks as an energy absorption mechanism is discussed in the latter part of this paper.

ENERGY DISSIPATION IN PERFORATION IMPACT

The study of energy dissipation of laminated plates under perforation impact provides an estimate of the available energy which causes the various forms of damage to the composite plate.

Energy absorbed by the Gr/Ep plate can be computed from the following energy balance equation (Greszczuk 1982, Shivakumar et al. 1984):

$$E_A = E_c + E_b + E_m + E_d + E_f \quad (2)$$

where E_c = the energy expended in Hertzian contact indentation, E_b = the energy due to plate bending, E_m = the energy due to stretching of the middle plate surface, E_d = the energy due to permanent plate damage, and E_f = the energy due to friction, heating etc. Among all these energies, in the perforation type impact the permanent plate damage is the main source of energy absorption. Plate damage may include any or all of the following modes of failure: Matrix cracking,

delamination, fiber breakage, spalling, and shear plug out.

The high strain rate Hertzian contact deformation work has been conducted at CRREL using Hopkinson bar apparatus and is reported in detail in another paper in this conference (Dutta et al 1993) and earlier by Dutta et al (1992). As the projectile impacts the plate a given amount of energy is dissipated in causing the plate to flex before any irreversible damage process begins. Following the flexure the permanent damage and failure of the plate is initiated. As mentioned before, this phase is characterized by fiber breakage, fiber pullout, matrix crack, and delaminations. If the areas of delamination could be determined an estimate of the energy absorbed by the delamination process can be obtained. The next major source of energy absorption is in shear plug out. The plug out is a shear fracture conoid having smaller diameter on the impact side and larger diameter on the exit side. Florence (1969) estimated that the circular area over which the impact momentum is first distributed is the base diameter of the fracture conoid and is equal to the diameter of the projectile. The empirical observation of the cone angle is approximately 63° .

BALLISTIC TESTS

The ballistic experimental test facilities at CRREL is shown schematically in Figure 2(a) and by an assembly photograph in Figure 2(b). The entire facility is located in three adjoining rooms. The gun room is equipped with a 14.3 mm (9/16 in.) bore explosive powered gun which can be remotely operated from the control room. The barrel end and the projectile path is completely sealed with a steel pipe which passes through the wall of the gun room into the target room. The end of the seal pipe terminates into a specially designed plexiglass chamber, equipped to clamp the target test plates at the periphery for normal impact. The target test chamber is also completely sealed with the target located in the middle. The back plate of the chamber, made from plastic is replaceable after every shot. The projectile exiting through the back plate is captured by a sandbox located in the flight path opposite to an opening in the wall. For high velocity (>610 m/s, 2000 ft/s) tests the interior of the gun barrel, seal pipe and the test chamber must have a very high vacuum pressure which is achieved by connecting the pipe interior to a vacuum pump. For low velocity tests no vacuum is necessary.

The impact and exit velocities were measured using light activated chronograph screens used in pairs on both sides of the target. The output from the chronograph screen starts and stops a timer with 10^{-7} second accuracy.

To perform the tests the 12.7 mm (0.5 in) diameter steel sphere projectile is first located in the gun with a suitable sabot. The amount of gun powder necessary to propel the projectile at the desired velocity was first determined by trial runs. When the projectile crosses the light path of the first chronograph screen it starts the counting clock. When it passes the next one the signal from it stops the counting, thus displaying the time of travel on the time counter. By measuring the distance between the two light screens the projectile velocity is calculated.

The tests were performed on two types of Gr/Ep plates. The first system is identified as T300/984 unidirectional 8-ply laminate. The second system was a 30-ply AS-4/3502 laminate with a stacking sequence of

$$[(-45/0_2)_2/90/-45/0_2/-45]_s$$

No attempt was made to capture the fragments from the impact on the unidirectional composite. The focus of the unidirectional composite impact test was to identify the gross damage pattern developed on the composite at different velocities. The fragments from the quasi-isotropic composites were collected on the adhesive coated papers which lined the interior of the target chamber on both the impact and exit sides. Figure 3 shows one typical perforated plate of unidirectional Gr/Ep, and Figure 4 shows a carefully cut section through the 30-ply quasi-isotropic Gr/Ep. The results of only room temperature unidirectional plate impacts will now be discussed.

DAMAGE ANALYSIS

The damages in the unidirectional laminate were simple to interpret. Because of severe anisotropy of the stiffness and strength properties, only longitudinal cracks in fiber direction propagated. The primary failure in the impact zone was obviously indentation followed by fiber breakage, delamination, and finally shear plugging. Numerous longitudinal cracks split the specimens in a large number of longitudinal strips (Figure 3). Figure 5 shows the effects of velocity on the damage process of the unidirectional Gr/Ep. Notice that the shear plug out hole for the high velocity (4500 ft/s) impact has a much cleaner outline (Figure 5a) than the one at lower velocity (Figure 5b). It seems likely that at higher velocities more momentum is trapped in the shear plug than at low velocities. At lower velocities the fibers break upon impact of the projectile, and then flex with shear failures propagating longitudinally to the boundaries of the specimens.

Figure 6(a) shows a very low velocity (88.4 m/s, 291 ft/s) impact of the steel ball on the 30-ply Gr/Ep laminate. The energy of impact in this case was not sufficient to cause perforation. (Ballistic tests performed at the U.S. Airforce Wright Research Laboratory (Mayer 1992) show that the V_{50} velocities for this type of laminates would be about 137 m/s (450 ft/s). Nevertheless, the damage by delamination and fiber breakage did happen as evident from the slight bulging of the rear surface.

At velocities around V_{50} a typical damage looks like the one shown in Figure 6(b), which was obtained at 151 m/s (496 ft/s). The perforation was complete in this case.

The high velocity (975 m/s, 3200 ft/s) perforation type damage on these laminate was rather extensive. Figure 6(c) shows a cutout section through the perforation hole of the high velocity impact. The cutout was carefully made without disturbing the positions of broken lamina and fibers. Notice that the damages on both impact and exit sides are more extensive than at the center. Delamination damage is more in the rear side, whereas the impact end has more crushing and fiber breakage.

SEM ANALYSIS OF BALLISTIC FRAGMENTS

As mentioned before, the composite fragments from the 30-ply Gr/Ep target panels were collected on the adhesive coated paper, lining the target test chamber. The SEM of one of the particles shows very well developed hacklemark (Figure 7a). In the second particle (Figure 7b) the hacklemark is less developed but appears to be of higher frequencies. Similar hacklemarks were also noted by Mayer (1992) in the SEM analysis of fragments from ballistics tests on Gr/Ep at AFWL.

DISCUSSION

The results of non-perforated low velocity impact, perforated low velocity impact, and the perforated high velocity impact manifest the progressive failure mechanisms, one taking over the other, as the velocity increases. For example, in the nonperforated low velocity impact on the multiple ply laminate the Hertzian indentation was the major form of damage, whereas at higher velocities shear plug out with extensive compressive failure and delaminations were the main mechanisms.

The fractographic features and its relation to the failure are of interest to note. Very little information on the genesis of hacklemark formation is available in composites literature except that a large number of researchers have observed their presence related with brittle failure (Morris 1982, Richards-Frandsen and Naerheim 1983). It has been shown by Purslow (1986) that in static failure, the presence of the relatively stiff fibers increases the influence of shear stresses on the resin fracture and hacklemarks development under such conditions will be suppressed. However, Purslow observed that at relatively high strain rate of deformation and fracture matrix cleavage and hackle formation are common. SEM's of ballistic fragments of the Gr/Ep from two independent laboratories (WPAFB and CRREL) clearly show that above V_{50} there are indications of hacklemark development.

The hacklemarks present a periodic formation of sigmoidally shaped ridges and troughs running roughly parallel to the fiber direction and located in the matrix region between them. The spatial periodicity is manifested in a direction parallel to the fibers. This regular spatial periodicity is the first suggestive observation. The second observation is that the wavelength of these hacklemarks appears to increase as the distance between the neighboring fibers increase (Figure 7a). The wavelength of the hacklemark is of the order of inter-fiber distance. Sometimes, the ridges appear to be canted at an angle to the fiber axis.

It is appropriate now to examine the phenomenon of wavelength proportionality to fiber spacing at some depth. It is conceivable that the wavelength proportionality to fiber spacing would result if it were associated with or determined by a disturbance which propagates in the plane of two adjacent fibers from one fiber surface to the other at a fixed angle to their length direction and then was reflected back from the other fiber at an equal angle toward the first fiber, and the process then repeated. The distance between successive reflections from the same fiber then represents a wavelength. Its proportionality to interfiber separation follows from the geometric similarity of the construction of wave reflections. Such

constructions are current in models of the acoustic resonance frequencies of simple enclosures (Beranek and Leo, 1954).

The explanation offered here is that the hacklemarks result from intense resonant vibrations of the matrix polymer cavity contained between the points of closest proximity of two adjacent fibers. These oscillations are considered to be so intense that the brittle matrix polymer is pulverized in regions surrounding the antinodes of these standing wave vibrational modes. The shape of these hacklemarks are therefore reflections of both the failure stress criterion and the intensity of vibration present in the composite during the impact event.

We consider that the hacklemarks represent a significant augmentation of the surface area of a fragment and therefore also a correspondingly large store of surface free energy. We speculate that the spatial frequency must increase with the speed of impact since our observations had been that the total energy absorbed (as measured by the decrease in kinetic energy of the projectile) increased with the velocity of the impact and a higher spatial frequency would represent an increase in surface area assuming the amplitude of the undulations remained constant. It is also conjectured that if the spatial frequency of the hacklemarks did not increase with projectile speed, then perhaps the fractional coverage of the surface of a fragment by hacklemarks must reflect the increase in total impact energy absorbed. Of course, we are aware from the work of Dennis Grady (1982) at Sandia Laboratories, of the decrease in the mean size of fragments produced as the strain rate is increased which results in a greater density of the energy absorption per unit volume of the fractured and fragmented material. We have appropriated these results to the case of impact by postulating a proportionality between strain rate and projectile velocity. We now hypothesize that the hackle mark wave length is a function only of the inter-fiber space occupied by matrix, and the distance between transverse matrix and their characteristic length is associated with the rate of impact event. We should continue to expect that the percentage coverage of the interply surface region by hacklemarks should increase with the vehemence of the impact (that is, the strain rate or projectile arrival velocity) and that the amount of material missing from the region occupied by hacklemarks should likewise increase with the applied intensity of the impact.

The following are the main findings of the experimental investigation (see Samad 1993).

i) The effect of mismatch angle produces a decrease in the perforation threshold velocity as the mismatch angle of the layup increases amounting to about 17% when the angle increases from 11.25 to 90 degrees.

ii) The total area of the delamination regions created inside a plate decreases as the impact velocity is increased over the velocity range studied for all values of mismatch angle, with the delaminated area at the perforation threshold representing a least upper bound of the delamination.

iii) At the lower velocities the shapes of the delaminated regions resemble those produced during non penetrating impacts.

iv) Hole areas practically vanish at the lowest velocity suggesting that the projectile traverses a parted matrix crack

running parallel to the fiber direction near the perforation threshold.

v) The radius of the circle circumscribing the delaminated zones at low velocities increases with decreasing mismatch angle.

vi) The effect of the mismatch angle on type and magnitude of damage as well as energy exchange disappeared toward the upper limits of the impact velocity range.

vii) The fraction of the initial kinetic energy residing in the projectile upon completion of the impact approaches a constant asymptote with a value of .8 for the 32 ply thick plates studied independently of the value of the mismatch angle.

CONCLUDING REMARKS

Initial results from ballistic impact tests have shown increased energy absorption at higher impact velocities. An analysis of the energy partitioning between various mechanisms of energy absorption is important in understanding the ballistic impact resistance of the material. Laminated plates have a unique failure mechanism in the ability to delaminate, which is the most favorable mode of failure for preventing penetration. This study has attempted to relate this energy to the micrographic features of the fractures on the delaminated surfaces to the energy level (velocity level). Fracture surfaces from fragments of ballistic impact have shown a tendency to develop characteristic hacklemarks. Their developments have been related to the cavity resonance of the matrix between the fibers. Although qualitative indications point to the existence of these phenomena a quantitative analysis is still lacking.

ACKNOWLEDGEMENT

The first series of impact experiments was conducted at the Wright Laboratory under the guidance of Dr. Arnold Mayer and the second series of impact experiments was conducted under the guidance of Dr. Piyush K. Dutta of CRREL. Both Dr. Dutta and Dr. Mayer participated extensively through contribution of data, discussion, and advice in preparation of this paper. The work was funded by the U.S. Army Research Office through the ASSERT program and the AFOSR Research Initiation Program.

REFERENCES

- Altamirano, M.R., (1991). " Experimental Investigation of High and Low Impact Energy Absorption of A54/3502 Graphite/Epoxy Panels", M.S. Thesis, University of New Orleans.
- Beranek, L.K. and Leo, L., (1954). Acoustics, McGraw Hill.
- Brown, J.R., and Egglestone, G.T., (1989). Ballistic Properties of Composite Materials for Personnel Protection, MRL-TR-89-6, Published by Materials Research Laboratory, Victoria, Australia.
- Dutta, P.K. and Taylor, S., (1989). A Fractographic Analysis of Graphite/Epoxy Composites Subjected to Low Temperature Thermal Cycling, Proceedings of the International Symposium for Testing and Failure Analysis, 6-10 Nov, ASM International, Materials Park, Ohio, pp.429-435.
- Dutta, P.K., Hui, D. and Altamirano, M.R., (1991). Energy Absorption of Graphite/Epoxy Plates Using Hopkinson Bar Impact, USA Cold Regions Research and Engineering Laboratory, CRREL Report 91-20.
- Dutta, P.K., Farrell, K. and Hui, D., (1993). Influence of Low Temperature on Energy Absorption in Laminated Composites, Proceedings ICCM-9, Madrid.
- Florence, A.L., (1969). Interaction of Projectiles and Composite Armor Part II. Stanford Research Institute, Menlo Park, California, AMMRG-CR-69-15, August.
- Grady, D.E., (1982). Local Inertial Effects in Dynamic Fragmentation, J. of Applied Physics, Vol 53, No. 1, pp. 322-325.
- Greszczuk, L.B., (1982). Damage in Composite Materials Due to Low Velocity Impact Chapter 3 in Impact Dynamics (J.A.Zukas et al. Eds) John Wiley and Sons, New York, pp.55-94.
- Mayer, A., (1992). U.S. Air Force Wright Laboratory, Dayton, Ohio, Personal Communication.
- Morris, G.E., (1982). Nondestructive Evaluation and Flow Criticality for Composite Materials, ASTM STP 696, (R.B.Pipes, Ed.) pp.274.
- Purslow, D., (1986). Matrix Fractography of Fiber Reinforced Epoxy Composites, Composites, Vol. 17, No. 4, pp.289-303.
- Richards-Frandsen, R. and Naerheim, Y., (1983). Fracture Morphology of Graphite/Epoxy Composites", Vol 17, pp.105-113.
- Samad, M. A. (1993). "Delamination Damage and Energy Exchange from Penetrating Impact of Spiral Staircase Lay-up Composite Plates", MS thesis, University of New Orleans, Dept. of Mechanical Engineering.
- Shivakumar, K.N., Elber, W. and Illg, W., (1985). Prediction of Impact Force and Duration Due to Low-velocity Impact on Circular Composite Laminates, ASME Journal of Applied mechanics, Vol 55, pp.674-680.

List of Figures

Figure 1. Ballistic test results of 31-ply Gr/Ep plate 12.7-mm steel sphere impact. (Mayer, 1992).

Figure 2. (a) Schematic of CRREL ballistic test facility.
(b) Assembly of the CRREL ballistic test gun system.

Figure 3. A typical specimen of the unidirectional Gr/Ep specimen after test.

Figure 4. Section of a 30-ply Gr/Ep panel through the perforation.

Figure 5. Effect of velocity on the damage of unidirectional Gr/Ep plates:

- (a) High velocity: shear plug out.
- (b) Low velocity: no shear plug out.

Figure 6. (a) Very low velocity indentation impact.

(b) Low velocity impact damage.

(c) High velocity impact damage

Figure 7. (a,b) Impact fragment fracture surfaces:

Micrographs

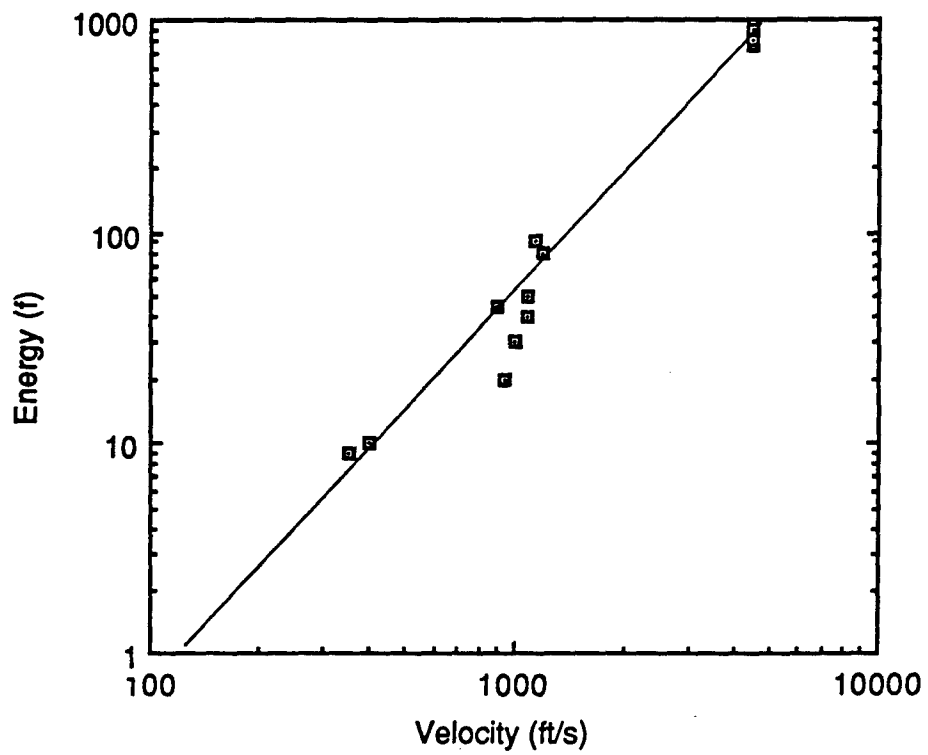


Figure 1. Ballistic test results of 31-ply Gr/Ep plate 12.7-mm steel sphere impact. (Mayer, 1992).

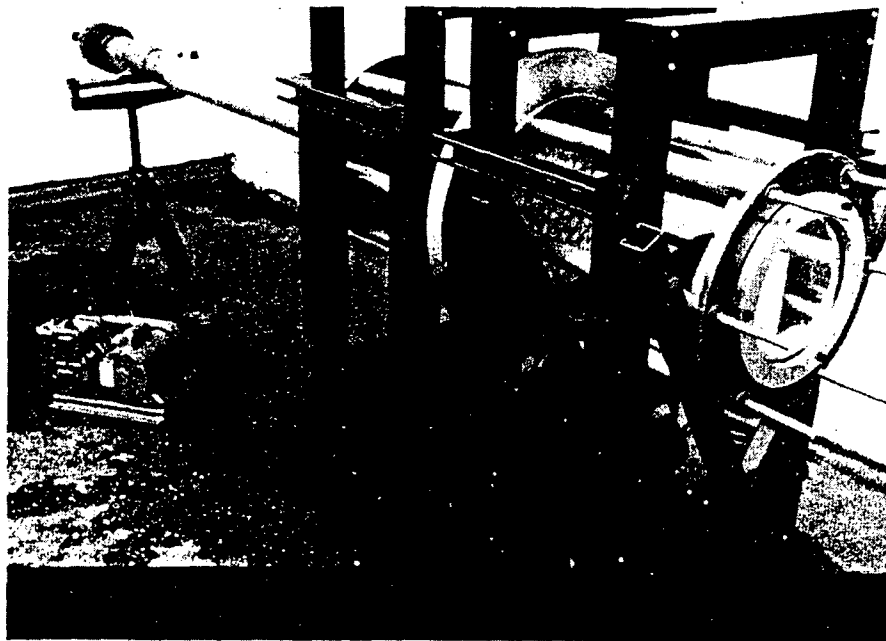
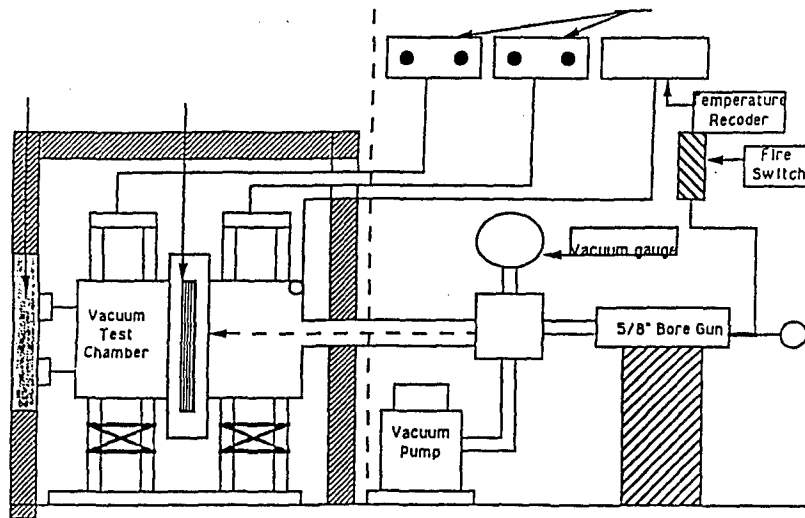


Figure 2. (a) Schematic of CRREL ballistic test facility.
 (b) Assembly of the CRREL ballistic test gun system.

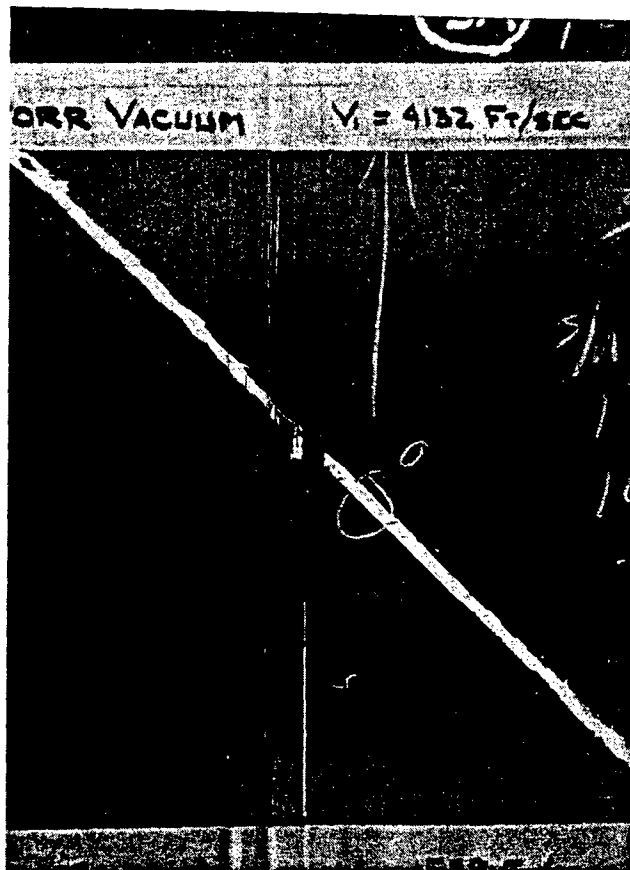


Figure 3. A typical specimen of the unidirectional Gr/Ep specimen after test.

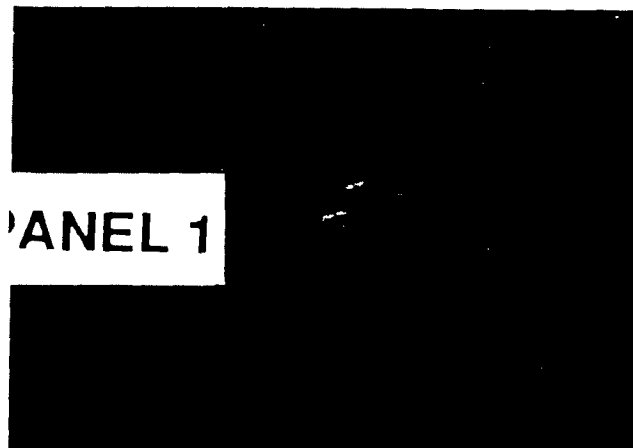


Figure 4. Section of a 30-ply Gr/Ep panel through the perforation.



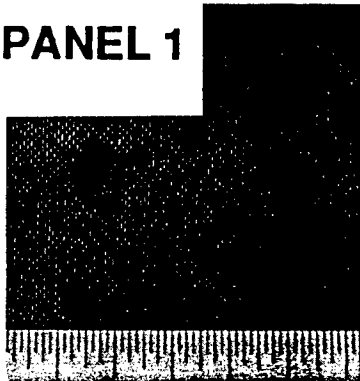
(a) High velocity: shear plug out.



(b) Low velocity: no shear plug out.

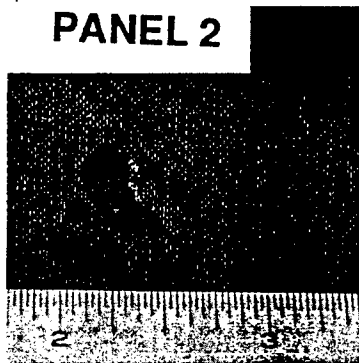
Figure 5. Effect of velocity on the damage of unidirectional Gr/Ep plates:

PANEL 1

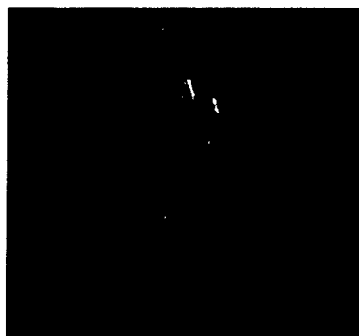


(a) Very low velocity indentation impact.

PANEL 2



(b) Low velocity impact damage.



(c) High velocity impact damage

Figure 6.



Figure 7a
Well-Developed Hacklemark
Fracture Surface



Figure 7b
Less-Developed Hacklemark
Fracture Surface